ASME
SETTING THE STANDARD

Journal of Fluids Engineering

Published Monthly by ASME

VOLUME 129 • NUMBER 8 • AUGUST 2007

Transactions of the ASME, Journal of Fluids Engineering (ISSN 0098-2202) is published monthly by The American Society of Mechanical Engineers, Three Park Avenue, New York, NY 10016. Periodicals postage paid at New York, NY and additional mailing offices.
POSTMASTER: Send address changes to Transactions of the ASME, Journal of Fluids Engineering, c/o THE AMERICAN SOCIETY OF MECHANICAL ENGINEERS, 22 Law Drive, Box 2300, Fairfield, NJ 07007-2300.
CHANGES OF ADDRESS must be received at Society headquarters seven weeks before they are to be effective. Please send old label and new address.

TECHNICAL PAPERS

(Contents continued on inside back cover)

This journal is printed on acid-free paper, which exceeds the ANSI Z39.48-1992 specification for permanence of paper and library materials. ♾™
♻ 85% recycled content, including 10% post-consumer fibers.

Journal of Fluids Engineering Volume 129, Number 8 AUGUST 2007

ANNOUNCEMENT

The ASME Journal of Fluids Engineering is abstracted and indexed in the following:

Applied Science & Technology Index, Chemical Abstracts, Chemical Engineering and Biotechnology Abstracts (Electronic equivalent of Process and Chemical Engineering), Civil Engineering Abstracts, Computer & Information Systems Abstracts, Corrosion Abstracts, Current Contents, Ei EncompassLit, Electronics & Communications Abstracts, Engineered Materials Abstracts, Engineering Index, Environmental Engineering Abstracts, Environmental Science and Pollution Management, Excerpta Medica, Fluidex, Index to Scientific Reviews, INSPEC, International Building Services Abstracts, Mechanical & Transportation Engineering Abstracts, Mechanical Engineering Abstracts, METADEX (The electronic equivalent of Metals Abstracts and Alloys Index), Petroleum Abstracts, Process and Chemical Engineering, Referativnyi Zhurnal, Science Citation Index, SciSearch (The electronic equivalent of Science Citation Index), Shock and Vibration Digest, Solid State and Superconductivity Abstracts, Theoretical Chemical Engineering

Evolution of Liquid Meniscus Shape in a Capillary Tube

Shong-Leih Lee
e-mail: sllee@pme.nthu.edu.tw

Hong-Draw Lee

Department of Power Mechanical Engineering,
National Tsing Hua University,
Hsinchu 30013, Taiwan

There are still many unanswered questions related to the problem of a capillary surface rising in a tube. One of the major questions is the evolution of the liquid meniscus shape. In this paper, a simple geometry method is proposed to solve the force balance equation on the liquid meniscus. Based on a proper model for the macroscopic dynamic contact angle, the evolution of the liquid meniscus, including the moving speed and the shape, is obtained. The wall condition of zero dynamic contact angle is allowed. The resulting slipping velocity at the contact line resolves the stress singularity successfully. Performance of the present method is examined through six well-documented capillary-rise examples. Good agreements between the predictions and the measurements are observable if a reliable model for the dynamic contact angle is available. Although only the capillary-rise problem is demonstrated in this paper, the concept of this method is equally applicable to free surface flow in the vicinity of a contact line where the capillary force dominates the flow. [DOI: 10.1115/1.2746898]

1 Introduction

Capillary-force-dominant flow is encountered in nature and in many modern industrial applications. The water rise in the vessels of a plant, the free surface flow in the vicinity of the moving contact line in a gas/liquid/solid system, and the conducting water flow through the micro-channels inside a fuel cell, are some of the examples. In the past decades, evolution of the liquid meniscus in gas/liquid/solid systems including the shape and the moving contact line has attracted much scientific attention. However, there are still a few fundamental difficulties to resolve. First, use of the classical no-slip boundary condition in various mathematical models has led to a shear-stress singularity at the contact line that is physically unrealistic. Second, the nonlinear force balance equation is not quite easy to solve when the macroscopic dynamic contact angle approaches zero (i.e., the slope of the free surface shape becomes infinite at the contact line). Third, reliable modeling for the macroscopic dynamic contact angle is still lacking.

It is noted that the term "contact angle" has different meanings in the literature, such as the microscopic contact angle, the macroscopic contact angle, the apparent contact angle, and the effective contact angle. The contact angle "observed" on the molecular scale is known as the microscopic contact angle. By contrast, the angle formed at the intersection of the free surface and the solid boundary is called the macroscopic contact angle, if the free surface is treated as a geometrical surface of zero thickness possessing some intrinsic surface properties. It is exactly the one employed in Young's equation. In practice, however, the macroscopic contact angle is not visible because the free surface image near the wall could be lost due to the critical angle of refraction [1]. Thus, the apparent contact angle, i.e., a macroscopic angle formed by the solid wall and the tangent plane to the free surface at a *certain distance* from the contact line, is often used as an auxiliary concept in interpreting the experimental observations. Finally, the effective contact angle is defined as the one over some "effective" smooth and homogeneous boundary, if the solid surface is rough and/or chemically inhomogeneous. In the present study, only the macroscopic dynamic contact angle is considered. For simplicity, the macroscopic dynamic contact angle θ_D will be referred to as the "dynamic contact angle."

To remove the stress singularity at the contact line while simultaneously retaining the Navier-Stokes equation for the fluids, a few particular approaches have been proposed. They include at least the three-region formulation [2–4], the partial-slip boundary condition [5], and the slipping models used by Lowndes [6], Zhou and Sheng [7], and Sheng and Zhou [8]. The three-region formulation [2–4] employs a singularly perturbed technique along with a matching procedure among the three regions. Its implementation on complex flow configuration is not practical. Similarly, the partial-slip boundary condition [5] is rather "artificial" than natural, and thus it is not expected to give satisfactory results for capillary-force-dominant flow. In the use of the slipping models [6–8], a slip boundary condition between the liquid and the solid is postulated to occur at a small region (known as the slipping length l_s) around the contact line. For a solid wall smooth on the molecular scale, the molecular-dynamics simulations show the slipping length to be on the order of a nanometer [9,10]. Thus, an extra-fine grid system is required for the solution procedure [6–8]. The resulting meniscus profile was found very sensitive to the slipping length [6]. The slipping length, however, is very difficult to determine for a given system.

In solving the force balance equation on the meniscus inside a vertical circular capillary tube, Lowndes [6] employed a normal-stress iterative procedure to determine the static meniscus profile. The pressure difference across the meniscus was integrated to yield the slope function of the meniscus. The meniscus profile then was renewed from the slope function. By contrast, Zhou and Sheng [7,8] solved the nonlinear second-order ordinary differential equation directly to determine the meniscus profile. Both numerical procedures ([6] and [7,8]) treat the dynamic contact angle θ_D as a prescribed constant. Moreover, θ_D cannot be zero due to the numerical difficulty in evaluating cot θ_D (slope of the meniscus at the contact line). Hence, applications of the solution procedures [6–8] are restricted to constant capillary number problems with a given nonzero contact angle ($\theta_D \neq 0$).

An alternate way to compute the evolution of the liquid meniscus is the method of molecular dynamics simulation. The molecular dynamics technique could be a very effective tool to study the dynamics of solid/liquid interfaces and wetting processes in Couette and Poiseuille flows [11]. However, 10^6 molecules along with a very small time step (e.g., 0.005 ps) are typically required in the use of the molecular dynamics simulation. This implies the need of large storage space and large CPU time. The purpose of this paper is to propose a simple geometry method for the evolution of the liquid meniscus in the vicinity of a contact line where the capillary force dominates the flow. Variable macroscopic dynamic

Contributed by the Fluids Engineering Division of ASME for publication in the JOURNAL OF FLUIDS ENGINEERING. Manuscript received August 27, 2005; final manuscript received February 2, 2007. Review conducted by Ali Beskok.

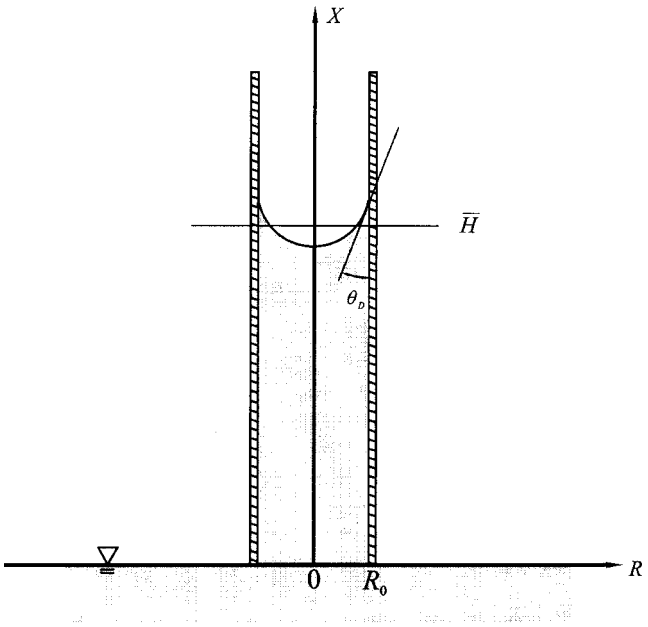

Fig. 1 The coordinate system and geometrical variables appearing in the problem

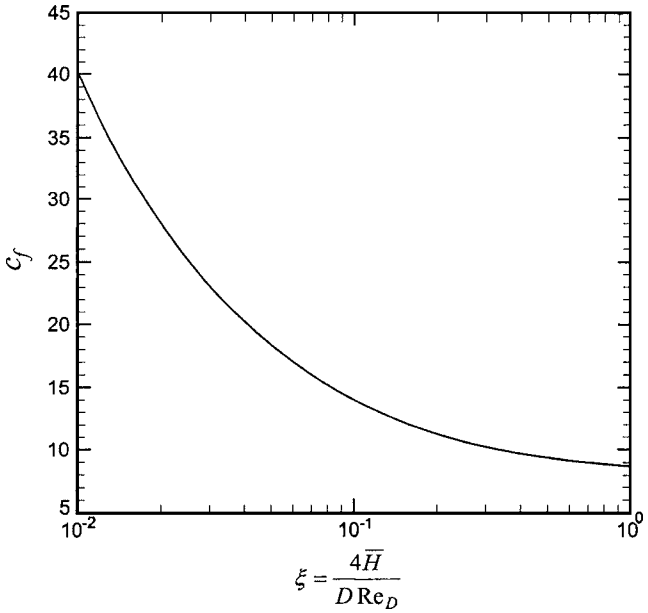

Fig. 2 The average friction factor c_f as a function of ξ for Eq. (1)

contact angle is considered in the computations. Wall condition of zero contact angle ($\theta_D=0$) is allowed. The solution includes the moving speed and the shape of the liquid meniscus. The resulting slipping velocity at the contact line resolves the stress singularity successfully. The performance of the present method will be examined through six well-documented capillary rise problems.

2 One-Dimensional Approach

Consider a liquid rising up in a vertical circular capillary tube, as illustrated in Fig. 1. There are four main forces acting on the liquid, namely, the surface tension on the free surface, the weight of the liquid column, the viscosity force on the inner surface of the tube, and the inertia force. After balancing the four forces, one obtains the well-known Washburn-Lucas equation [11] that governs the mean height of the liquid over the cross section of the tube $\bar{H}(t^*)$:

$$2\pi R_0\gamma\cos\theta_D = \pi R_0^2\rho g\bar{H} + c_f\pi\mu\bar{H}\frac{d\bar{H}}{dt^*} + \pi R_0^2\rho\frac{d}{dt^*}\left(\bar{H}\frac{d\bar{H}}{dt^*}\right) \tag{1}$$

where t^* is the time measured in seconds, g is the gravity, R_0 is the inner radius of the tube, and θ_D is the dynamic contact angle. All of the physical properties, including the liquid density ρ, the viscosity of the liquid μ, and the surface tension γ, are assumed constant. The term on the LHS of Eq. (1) stands for the surface tension force, while the other three terms on the RHS of Eq. (1) are the gravity force, the viscosity force, and the inertia force, respectively. For simplicity, the average friction factor c_f over the liquid column is estimated from the wall shear stress in the entrance region of a steady laminar flow through a circular tube. The result is shown in Fig. 2 as a function of the conventional dimensionless axial coordinate

$$\xi = \frac{4\bar{H}}{\mathrm{Re}_D D} \quad \mathrm{Re}_D = \frac{\rho\bar{U}D}{\mu} \tag{2}$$

where $\bar{U}$ is the mean velocity and D is inner diameter of the tube ($D=2R_0$). When the liquid column is sufficiently long, c_f approaches 8. Use of c_f instead of the conventional value 8 in Eq. (1) is to examine the entrance effect. In equilibrium, both viscous force and inertia force vanish and thus Eq. (1) reduces to

$$2\pi R_0\gamma\cos\theta_e = \pi R_0^2\rho g\bar{H}_\infty \tag{3a}$$

or

$$\bar{H}_\infty = \frac{2\gamma\cos\theta_e}{R_0\rho g} \tag{3b}$$

where θ_e is the equilibrium contact angle, and $\bar{H}_\infty$ is the equilibrium height of the liquid column. Subtraction of Eq. (1) from Eq. (3*a*) yields

$$2\pi R_0\gamma(\cos\theta_e - \cos\theta_D) = \pi R_0^2\rho g(\bar{H}_\infty - \bar{H}) - c_f\pi\mu\bar{H}\frac{d\bar{H}}{dt^*} - \pi R_0^2\rho\frac{d}{dt^*}\left(\bar{H}\frac{d\bar{H}}{dt^*}\right) \tag{4}$$

The quantity $\gamma(\cos\theta_e - \cos\theta_D)$ is known as the out-of-balance Young's force [12]. After introducing the dimensionless transformation

$$\bar{h} = \frac{\bar{H}}{\bar{H}_\infty} \quad t = \frac{t^*}{t_c} \quad t_c = \frac{8\mu\bar{H}_\infty}{\rho g R_0^2} \quad U_c = \frac{\bar{H}_\infty}{t_c} \quad \mathrm{We}_c = \frac{\rho U_c^2 D}{\gamma} \tag{5}$$

Eq. (4) becomes

$$1 - \frac{\cos\theta_D}{\cos\theta_e} = (1-\bar{h}) - \left(\frac{c_f}{8}\right)\bar{h}\frac{d\bar{h}}{dt} - \frac{\mathrm{We}_c}{4\cos\theta_e}\frac{d}{dt}\left(\bar{h}\frac{d\bar{h}}{dt}\right) \tag{6}$$

where the Weber number We_c is based on the reference velocity U_c. For the capillary-rise flow under study, the Weber number is very small (since the tube diameter is very small). Hence, the inertia effect is negligible as demonstrated by Hamraoui et al. [13] if the equilibrium contact angle θ_e is also small. Without the inertia effect, Eq. (6) further reduces to

$$\frac{d(\bar{h}^2)}{dt} = \frac{(\cos\theta_D/\cos\theta_e) - \bar{h}}{c_f/16} \tag{7}$$

It is interesting to note that Eq. (7) needs only one initial condition due to neglect of the inertia term. The initial velocity be-

Table 1 Liquid properties and experimental conditions in cases a–d (Hamraoui et al. [13]) and cases e–f (Fan et al. [20])

	Case a	Case b	Case c	Case d	Case e	Case f
Liquid	Ethanol	Water	Water	Water-ethanol	Engine oil	Engine oil
ρ (kg/m^3)	789	1000	1000	982	849	849
μ (N s/m^2)	0.00117	0.001	0.001	0.001	0.38	0.38
γ (N/m)	0.022	0.072	0.072	0.050	0.0294	0.0294
θ_e (deg)	0	0	0	0	15	15
Glass tube	Dry	Prewetted	Dry	Dry	Dry	Dry
R_0 (mm)	0.295	0.295	0.295	0.295	0.365	0.525
$\bar{H}_0$ (mm)	5.35	11.17	2.17	1.50	0.00	0.00
$\bar{H}_\infty$ (mm)	19.28	49.78	49.78	35.20	18.69	12.99
t_c (s)	0.2680	0.4666	0.4666	0.3360	51.23	17.21
r_0	0.01530	0.005926	0.005926	0.008381	0.01953	0.04042
h_0	0.2775	0.2244	0.04359	0.04261	0.0001	0.0001
Ca_c	0.003825	0.001482	0.001482	0.002095	0.004716	0.009756
Bo	130.7	337.4	337.4	238.7	98.92	47.82
Ca_e	0	0	0	0	0.0003060	0.0003060

comes a part of the solution in case the initial position of the liquid surface has been imposed on the problem. This implies that there is no need to start the calculation of Eq. (7) from the instant when the liquid just enters the entrance of the capillary tube. Use of the "initial" position $h_0 \geq 0$ does not affect the solution, although the time coordinate might shift by a certain period of time. With the "initial" condition $\bar{h}^2(0)=\bar{h}_0^2$, Eq. (7) can be easily solved to yield a solution for $\bar{h}^2$ with the Runge-Kutta method of order 4. However, a numerical model for $\cos\theta_D$ is needed before the solution procedure is performed.

To investigate the dynamic contact angle, Hamraoui et al. [13] studied the capillary rise problem both numerically and experimentally. Four experiments were performed for the problem. The liquid properties and the experimental conditions of the four experiments are shown in Table 1 (i.e., cases a, b, c, and d). Measurements on the mean height of the liquid column with respect to time $\bar{H}(t^*)$ were obtained for all of the four cases. In the numerical work, Hamraoui et al. [13] solved Eq. (1) without the entrance effect (i.e., using $c_f=8$) to obtain the solution $\bar{H}(t^*)$ while the dynamic contact angle assumed the form [14]

$$\cos\theta_D = \cos\theta_e - \frac{\beta}{\gamma}\frac{d\bar{H}}{dt^*} \tag{8}$$

where the parameter β (known as the coefficient of wetting-line friction [11]) was determined such that the experimental data of $\bar{H}(t^*)$ was best fitted. The resulting β values were 0.04, 0.2, 0.45, and 0.14 for cases a, b, c, and d, respectively. Finally, the dynamic contact angle as a function of time $\theta_D(t^*)$ was evaluated from Eq. (8) for three of the four experiments, i.e., cases a, b, and c.

In the present study, the dynamic contact angles θ_D provided by Hamraoui et al. [13] for cases a, b, and c were employed to solve Eq. (7) with and without the entrance effect. The result of the dimensionless mean height of liquid $\bar{h}(t)$ is presented in Fig. 3. It can be converted into the dimensional form with the reference quantities ($\bar{H}_\infty$ and t_c) provided in Table 1. The influence of the entrance effect on the $\bar{h}(t)$ result is less than 0.005 in the very beginning of the process. Thus, only a single curve is used to represent both situations in Fig. 3. The experimental data from Hamraoui et al. [13] are plotted also in Fig. 3 for comparison. Excellent agreements between the numerical results and the experimental data are observed. For a further examination of the viscous effect, the friction factor c_f, and the Reynolds number

$$\mathrm{Re}_D = \frac{\rho\bar{U}D}{\mu} \quad \bar{U} = \frac{d\bar{H}}{dt^*} = \frac{\bar{H}_\infty}{t_c}\frac{d\bar{h}}{dt} = U_c\frac{d\bar{h}}{dt} \tag{9}$$

for cases a, b, and c are shown in Figs. 4 and 5, respectively. From Fig. 4, it is seen that the entrance effect is restricted to very beginning of the capillary-rise flow. Furthermore, it is not significant even in the early time ($t<1$ or $t^*<0.5$ s) of the experiment. Similarly, Fig. 5 reveals that the Reynolds number is not large. This implies that the creeping flow theory ($c_f=8$) would make a good assumption for the capillary-rise flow.

3 Axisymmetric Approach

3.1 The Governing Equations. In the previous section, it has been demonstrated that the Washburn-Lucas equation could produce an excellent result for the mean height of the liquid column $\bar{H}(t^*)$ as long as the modeling of the dynamic contact angle θ_D is sufficiently accurate. However, evolution of the liquid meniscus as a function of radial coordinate and time $H(R,t^*)$ is still not available. To investigate the evolution of the liquid meniscus including the shape and the moving speed, let the axisymmetric flow velocity be represented by (U,V) in a cylindrical coordinate system (X,R). The gravity is in the $-X$ direction.

After making the dimensionless transformation

$$x = X/L \quad r = R/L \quad h = H/L \quad r_0 = R_0/L$$

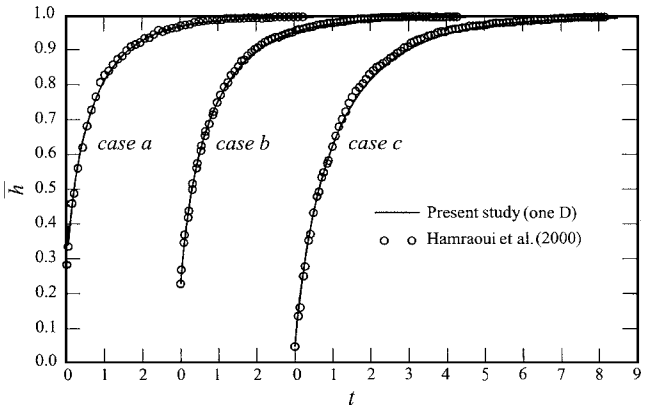

Fig. 3 Comparison of the predicted capillary rise $\bar{h}(t)$ with the existing experiment for cases a, b, and c

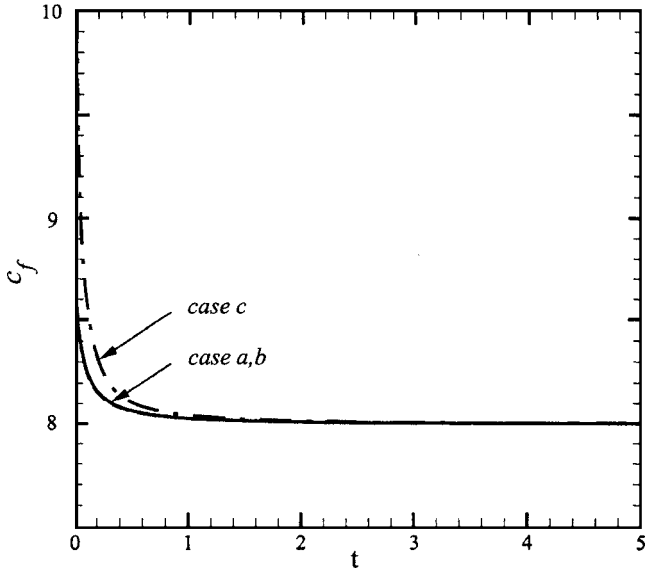

Fig. 4 The average friction factor c_f as a function of t for cases a, b, and c

$$u = U/U_c \quad v = V/U_c \quad t = t^*/t_c \quad t_c = L/U_c \quad p = (P - P_{\text{ref}})/\rho U_c^2$$

$$\text{Re}_c = \rho U_c L/\mu \quad \text{Fr}_c = U_c/\sqrt{gL} \tag{10}$$

the capillary-rise flow inside a vertical circular tube is expressible as

$$\frac{\partial(ru)}{\partial x} + \frac{\partial(rv)}{\partial r} = 0 \tag{11}$$

$$\text{Re}_c\left(\frac{\partial u}{\partial t} + u\frac{\partial u}{\partial x} + v\frac{\partial u}{\partial r}\right) = -\text{Re}\left(\frac{dp}{dx} + \frac{1}{\text{Fr}_c^2}\right) + \frac{1}{r}\frac{\partial}{\partial r}\left(r\frac{\partial u}{\partial r}\right) \tag{12}$$

where the reference length L and the reference velocity U_c are to be assigned. The associated boundary conditions for the axial component of the flow $u(x,r,t)$ are

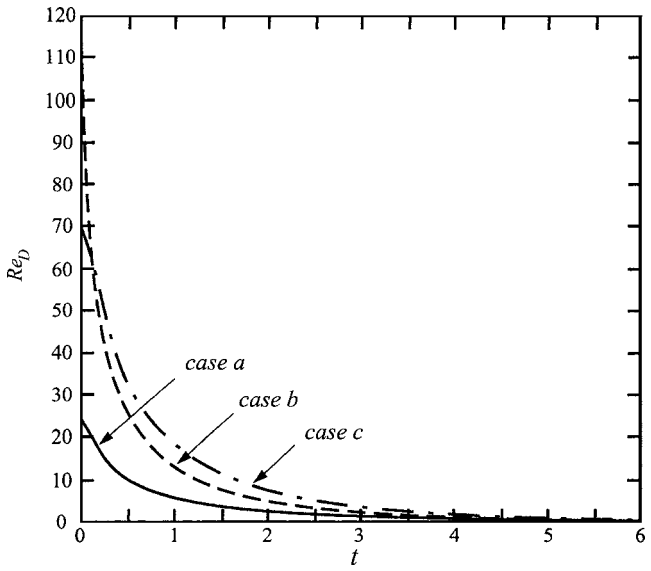

Fig. 5 Variation of the Reynolds numbers for cases a, b, and c

$$u(0,r,t) = f(t) \quad \partial u(x,0,t)/\partial r = 0 \quad u(x,r_0,t) = 0 \tag{13}$$

while the radial component of the flow $v(x,r,t)$ has a nonpermeable condition on the tube wall. It is noteworthy that the formulation (11)–(13) is based on a few assumptions. First, the axial component of the viscosity force ($\partial^2 u/\partial x^2$) in Eq. (12) is negligible as compared to the radial component. Second, the momentum equation in the radial direction is negligible. Third, the inlet velocity has a uniform profile, i.e., $u(0,r,t)=f(t)$. These assumptions are pertinent to the problem under study because the error occurs only when $\bar{h} < 2r_0$. Note also that the no-slip condition $u(x,r_0,t)=0$ is invalid in the vicinity of the contact line. This will be discussed later.

The pressure at the inlet of the tube ($x=0$) is assumed to be uniform and equal to the ambient pressure P_∞. Thus, $p(0,r,t)=0$ if the ambient pressure P_∞ is used as the reference pressure ($P_{\text{ref}}=P_\infty$). On the liquid meniscus $x=h(r,t)$, the force balance equation should be satisfied [15,16]

$$p_\ell = p_a - \frac{1}{\text{Re}_c}\left(\frac{\kappa}{\text{Ca}_c} - (\sigma_{nn})_\ell + \frac{\mu_a}{\mu_\ell}(\sigma_{nn})_a\right) \tag{14a}$$

$$\text{Ca}_c = \mu U_c/\gamma \quad \sigma_{nn} = 2\frac{\partial v_n}{\partial n} \tag{14b}$$

where p_ℓ and p_a, and $(\sigma_{nn})_\ell$ and $(\sigma_{nn})_a$, are the static pressures and the normal stresses on the liquid side and the air side of the liquid meniscus, respectively. The notations v_n and $\partial v_n/\partial n$ stand for the normal velocity and the normal strain rate, respectively. The dimensionless curvature κ normalized by L^{-1} is positive for a concave liquid meniscus. The reference quantities used in the dimensionless transformation (10) are defined by

$$L = \bar{H}_\infty = \frac{2\gamma\cos\theta_e}{R_0\rho g} \quad t_c = \frac{32\mu\bar{H}_\infty}{\rho g D^2} \quad U_c = \frac{L}{t_c} = \frac{\rho g D^2}{32\mu} \tag{15}$$

to achieve a variable and parameter system consistent with that in the previous section. Based on the reference quantities (15), the characteristic parameters Re_c, Fr_c, and Ca_c are not necessarily equal to the respective conventional definitions for the Reynolds number, the Froude number, and the capillary number.

3.2 Liquid Pressure on the Meniscus. When the liquid meniscus reaches a height that is considerably larger than the tube diameter, the flow can be divided into three regions, i.e., the entrance region, the fully developed region, and the fountain flow region. At the tube inlet ($x=0$), the flow is assumed to be uniform with the velocity

$$u(0,r,t) = f(t) = \frac{d\bar{h}(t)}{dt} \tag{16}$$

where

$$\bar{h}(t) = \frac{2}{r_0^2}\int_0^{r_0} rh(r,t)dr \tag{17}$$

is the mean height of the liquid column over the tube cross section. In the entrance region, the radial component of the velocity $v(x,r,t)$ is small as compared to the axial component $u(x,r,t)$. Beyond the entrance region, there is the fully developed region where the radial velocity component even becomes zero, $v(x,r,t)=0$, and thus, the axial velocity component has the fully developed profile

$$u(x,r,t) = 2f(t)\left(1 - \left(\frac{r}{r_0}\right)^2\right) \tag{18}$$

This gives rise to the viscous force

$$\frac{1}{r}\frac{\partial}{\partial r}\left(r\frac{\partial u}{\partial r}\right) = -\frac{8f(t)}{r_0^2} \tag{19}$$

The third region (known as the fountain flow) deals with a particular flow pattern in a small region beneath the liquid meniscus. In a filling process of a viscoelastic liquid inside a tube of small diameter, Sato and Richardson [17] found that the axial flow component in the fountain flow region is essentially independent of both x and r, i.e.,

$$u(x,r,t) \approx f(t) = \frac{d\bar{h}(t)}{dt} \approx \frac{dh_{cl}(t)}{dt} \tag{20}$$

where $h_{cl}(t)$ denotes $h(0,t)$, the height of the liquid column at the *center line* of the tube. If the mean velocity $f(t)$ is subtracted from the original velocity (u,v), the remainder would be a weak circulation flow relative to the moving free surface [17]. This means that there should be a "slipping velocity" at the contact line. Such an important feature of the fountain flow effect occurs also in Newtonian fluid.

Due to the fact that $v(x,r,t)$ is always very small as compared to $u(x,r,t)$, the viscous force (19) makes good approximation in the whole liquid domain $0 \le x \le h_{cl}$ except for the fountain flow region. Fortunately, the fountain flow region is generally very short. It is roughly equal to a tube diameter only. Moreover, the entrance effect is not significant in the capillary-rise problem as verified in the previous section. Thus, Eq. (12) reduces to

$$0 = -\frac{d\hat{p}}{dx} + \frac{1}{r}\frac{\partial}{\partial r}\left(r\frac{\partial u}{\partial r}\right) \tag{21}$$

where

$$\hat{p} = \mathrm{Re}_c\left(p + \frac{x}{\mathrm{Fr}_c^2}\right) \tag{22}$$

is a flow-induced pressure. The pressure level $p(0,r,t)=0$ assigned in Sec. 3.1 leads to

$$\hat{p}(0,r,t) = 0 \tag{23}$$

Note that the flow-induced pressure vanishes in static liquid (when $u=0$) as observable from Eqs. (21) and (23), i.e., $\hat{p}(x,r,t)=\text{const}=0$.

Next, substitute Eqs. (19) and (20) into Eq. (21) to obtain

$$\frac{d\hat{p}}{dx} = -\frac{8}{r_0^2}\frac{dh_{cl}}{dt} \tag{24}$$

Upon integrating Eq. (24) from $x=0$ to $x=h_{cl}(t)$ at time t with the boundary condition (23), one has

$$\hat{p}(h_{cl},r,t) = -\frac{8}{r_0^2}h_{cl}\frac{dh_{cl}}{dt} = -\frac{4}{r_0^2}\frac{d(h_{cl}^2)}{dt} \tag{25}$$

In the fountain flow region, both the flow-induced pressure gradient $(d\hat{p}/dx)$ and the normal stress σ_{nn} could be negligibly small as compared to the "fully developed" region [17]. Hence, the flow-induced pressure gradient is neglected in the "meniscus region" in the present study. This implies a uniform flow-induced pressure $(\hat{p}_\ell=\text{const})$ along the meniscus where it is "free" of stresses; i.e.,

$$\hat{p}_\ell(r,t) = \hat{p}(h,r,t) \approx \hat{p}(h_{cl},r,t) = -\frac{4}{r_0^2}\frac{d(h_{cl}^2)}{dt} \tag{26}$$

3.3 Solution Method for Force Balance Equation. The radius of the capillary tube under study is less than 0.525 mm (see Table 1). Moreover, the capillary number is assumed very small. Thus, the normal stresses on both sides of the liquid meniscus are assumed negligible as compared to the surface tension. In addition, variation of the air pressure along the air side of the meniscus (p_a) is also negligible as compared to the surface tension [17]. Upon imposing these assumptions, the force balance equation (14) on the meniscus $x=h(r,t)$ reduces to

$$p_\ell = -\frac{\kappa}{\mathrm{Re}_c\,\mathrm{Ca}_c} \tag{27}$$

or

$$\frac{\hat{p}_\ell}{\mathrm{Re}_c} - \frac{h}{\mathrm{Fr}_c^2} = -\frac{\kappa}{\mathrm{Re}_c\,\mathrm{Ca}_c} \tag{28}$$

from Eq. (22). Similar assumptions and treatments have been employed in the Washburn-Lucas equation (1). For convenience, Eq. (28) is rewritten as

$$\kappa = \mathrm{Re}_c\,\mathrm{Ca}_c\left(\frac{h}{\mathrm{Fr}_c^2} - \frac{\hat{p}_\ell}{\mathrm{Re}_c}\right) = \mathrm{Bo}\,h - \mathrm{Ca}_c\,\hat{p}_\ell \tag{29}$$

where

$$\mathrm{Bo} = \frac{\rho g L^2}{\gamma} = \frac{\cos^2\theta_e}{2\,\mathrm{Ca}_c} \tag{30}$$

and

$$\mathrm{Ca}_c = \frac{\mu U_c}{\gamma} = \frac{\rho g D^2}{32\gamma} \tag{31}$$

are, respectively, the Bond number and the characteristic capillary number based on the reference quantities (15). Equations (29) indicate that the liquid meniscus profile $h(r,t)$ is governed by the two parameters, Bo and Ca_c. In equilibrium $(\hat{p}_\ell=0)$, the curvature $\kappa(r,t)$ is proportional to $h(r,t)$ with a positive proportional coefficient Bo. In case the equilibrium contact angle θ_e is less than 90 deg, the free surface shape has a positive curvature at the tube wall, i.e., $\kappa(r_0,t)>0$, such that $h(r,t)$ is also positive. The trend is reversed if $\theta_e>90$ deg. This is consistent with the physical meaning.

Geometrically, the liquid meniscus in the present study is an azimuthally symmetric surface generated by rotating the curve $h(r,t)$ about the axis $r=0$ at time t. The principal curvatures at point $P(r,h)$ on the free surface are

$$\kappa_1 = \frac{h''}{(1+h'^2)^{1.5}} \tag{32}$$

$$\kappa_2 = \frac{h'}{r(1+h'^2)^{0.5}} \tag{33}$$

where the primes denote the partial derivatives with respect to r. The subscript 1 and 2 are, respectively, referred to the curvatures on the normal and binormal planes at the tangent point P. The normal curvature κ_1 thus is expressible as

$$\kappa_1 = \kappa - \kappa_2 \tag{34}$$

At the centerline of the tube $(r=0)$, $\kappa_2=\kappa_1$, such that Eq. (34) becomes

$$\kappa_1 = \frac{\kappa}{2} \tag{35}$$

Equation (29) is a nonlinear ordinary differential equation of second order for $h(r,t)$. The associated boundary conditions are

$$h'(0,t) = 0 \tag{36}$$

$$h'(r_0,t) = \cot\theta_D \tag{37}$$

Due to the high nonlinearity, finding an analytical solution to Eq. (29) is not possible. In the present study, a simple geometry method is employed to solve Eq. (29). Let the uniform grid system

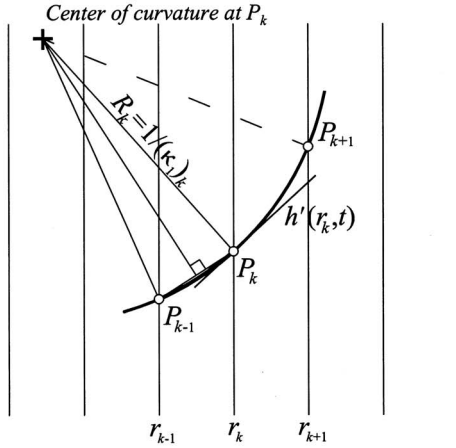

(a)

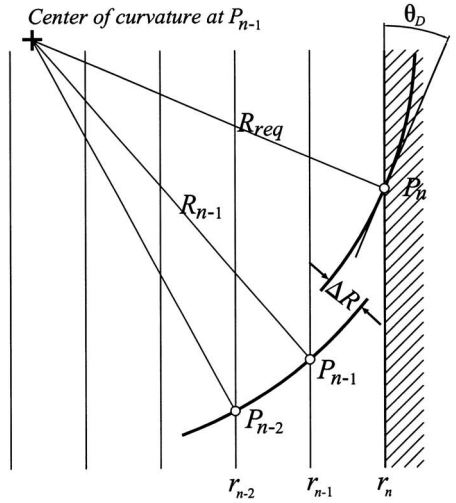

(b)

Fig. 6 A schematic description for the geometry method

$$r_k = (k-1)\Delta r \quad k = 1,2,\ldots,n \tag{38}$$

be defined on the r domain ($0 \le r \le r_0$) with the grid mesh $\Delta r = r_0/(n-1)$, while the time step Δt could be variable. The solution at $r=r_k$ and time level $t=t_j$ is denoted with point $P_k(r_k,h_k,t_j)$ as illustrated in Fig. 6(*a*). In this connection, the curvature at point P_k is represented by $(\kappa)_k$. For convenience, the algorithm for the solution at time level t_j is described as follows in case the solution at the previous time level t_{j-1} has been obtained:

1. Guess a value for $h_{cl}(t_j)$, i.e., the solution at point $P_1(0,h_{cl},t_j)$.
2. Evaluate the flow-induced pressure $\hat{p}_\ell$ from Eq. (26) with a backward difference scheme for the time-derivative term.
3. Evaluate $(\kappa)_1$ from Eq. (29) and then $(\kappa_1)_1$ from Eq. (35). This gives rise to the curvature radius $R_1=1/(\kappa_1)_1$ for point P_1.
4. Locate the center of curvature $(0,h_{cl}+R_1,t_j)$ for point P_1 by using the boundary condition (36).
5. Construct the osculating circle C_1 of the free surface at point P_1 with the curvature center $(0,h_{cl}+R_1,t_j)$ and the curvature radius $|R_1|$.
6. Determine point $P_2(r_2,h_2,t_j)$ by assuming that C_1 goes through the two points P_1 and P_2, i.e., $h_2=h_{cl}+R_1(1-\sqrt{1-(r_2/R_1)^2})$.
7. Suppose that the solutions at the first k points from $P_1(r_1,h_1,t_j)$ to $P_k(r_k,h_k,t_j)$ have been obtained (see Fig. 6(*a*)), where $k \ge 2$.
8. Evaluate the total curvature $(\kappa)_k$ from Eq. (29).
9. Use substeps a–e to determine $(\kappa_1)_k$ and $(\kappa_2)_k$
   a. Guess the value of $(\kappa_2)_k$.
   b. Evaluate the curvature $(\kappa_1)_k$ from (34).
   c. Use the two points P_{k-1} and P_k as well as the curvature radius $R_k=1/(\kappa_1)_k$ to locate the center of curvature at point P_k. The result is (r_k+c,h_k+d,t_j), where
   $$c = -\frac{bR_k}{|b|}\sqrt{1-\left(\frac{d}{R_k}\right)^2} \quad d = -\frac{b}{2} + a\sqrt{\frac{R_k^2}{a^2+b^2}-\frac{1}{4}}$$
   $$a = r_k - r_{k-1} = \Delta r \quad b = h_k - h_{k-1} \tag{39}$$
   d. Compute the tangent of the osculating circle C_k at point P_k, $h'(r_k,t_j)=-c/d$, and then renew $(\kappa_2)_k$ from Eq. (33).
   e. Return to Step 9b and repeat the computations until $(\kappa_2)_k$ converges within a prescribed tolerance. In this connection, a successive over-relaxation factor can be applied to the guessed $(\kappa_2)_k$.
10. Construct the osculating circle C_k of the free surface at point P_k with the curvature center and the curvature radius $|R_k|$. The point P_{k+1} can be estimated by assuming that C_k goes through the three points p_{k-1}, P_k, P_{k+1}. This leads to
    $$h_{k+1} = h_k + d - R_k\sqrt{1-\left(\frac{\Delta r - c}{R_k}\right)^2} \tag{40}$$
11. Go to Step 7 and repeat the computations until the curvature radius R_{n-1} as well as the center of curvature $(r_{n-1}+c,h_{n-1}+d,t_j)$ for point P_{n-1} is obtained (see Fig. 6(*b*)).
12. Compute the required curvature radius R_{req} that yields the desired contact angle θ_D (based on some model for θ_D) at point P_n on the tube wall. The results are
    $$R_{\text{req}} = \frac{r_n - r_{n-1} - c}{\cos\theta_D} = \frac{\Delta r - c}{\cos\theta_D} \tag{41}$$
13. Evaluate the difference $\Delta R=R_{n-1}-R_{\text{req}}$. Note that $\Delta R=0$ is mandatory, because the osculating circle C_{n-1} should go through all of the three points P_{n-2}, P_{n-1}, and P_n.
14. Adjust the value of $h_{cl}(t_j)$ with a shooting method (the bisection method is highly recommended), then go back to Step 2 and repeat the computations until $\Delta R=0$ is satisfied within a prescribed tolerance.
15. After $\Delta R=0$ is satisfied, determine the point P_n from
    $$h_n = h_{n-1} + d - R_{n-1}\sqrt{1-\left(\frac{\Delta r - c}{R_{n-1}}\right)^2} \tag{42}$$

Conventionally, the dynamic contact angle θ_D (see Step 12) is modeled as a function of the capillary number Ca [12,18,19], i.e.,

$$\text{Ca} = \frac{\mu U(R_0,t^*)}{\gamma} = \text{Ca}_c\frac{dh(r_n,t)}{dt} \tag{43}$$

where $U(R_0,t^*)$ is the slipping velocity at the contact line. In the present study, the slipping velocity is estimated from

$$\frac{dh(r_n,t)}{dt} \approx \frac{dh(r_{n-1},t)}{dt} \tag{44}$$

for simplicity. Thus, the dynamic contact angle θ_D at the time level t_j can be updated once the point P_{n-1} is obtained. Note also

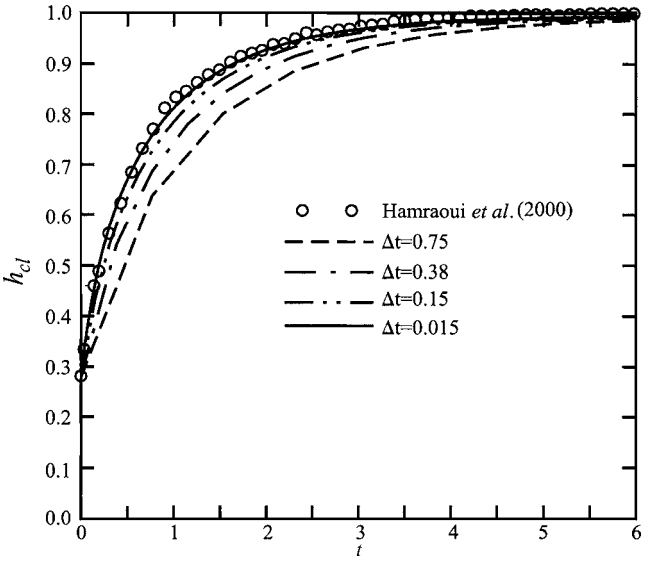

Fig. 7 Influence of the time step on the $h_{cl}(t)$ results for case a

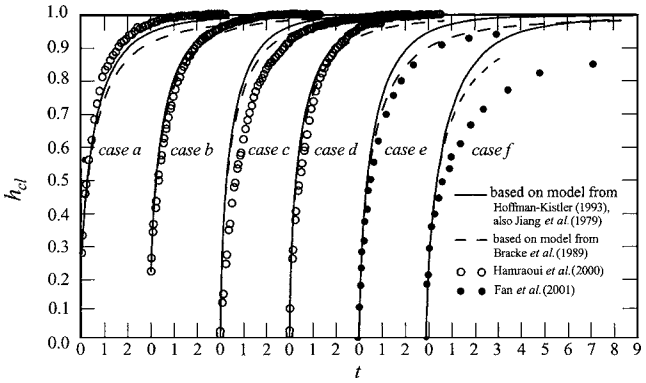

Fig. 8 The resulting $h_{cl}(t)$ functions based on various θ_D models

that another possible shooting procedure is to monitor the required θ_D directly. However, the success is not guaranteed because the curvature radius R_{n-1} of the osculating circle C_{n-1} could be too short to reach the tube wall (and thus point P_n does not exist) during the shooting procedure. Such a numerical difficulty is unavoidable when the dynamic contact angle is zero. Fortunately, the proposed shooting procedure that monitors the requirement $\Delta R=0$ (see Fig. 6(*b*)) poses no such numerical difficulty.

3.4 Results and Discussion. Six cases of the capillary-rise problem are employed to examine the performance of the present method. The liquid properties as well as the problem configurations (including the initial height of the liquid column), the reference length $\bar{H}_\infty$ and time t_c, and the corresponding dimensionless parameters r_0, h_0, Ca_c, and Bo are shown in Table 1. Cases a, b, c, and d are conducted to simulate the capillary rise flow observed by Hamraoui et al. [13], while cases e and f are used to simulate the experiments of Fan et al. [20]. The liquid meniscus in the present flow configuration is nearly spherical. This implies a weak dependence of the numerical result on the grid size when the geometry method is applied. Hence, a uniform grid system with $n=101$ or $\Delta r=r_0/100$ was found adequate for all of the cases.

Figure 7 reveals the resulting $h_{cl}(t)$ based on the dynamic contact angle (8) from Hamraoui et al. [13] for case a at various time steps. The experimental data observed by Hamraoui et al. [13] are plotted also in Fig. 7 for comparison. From Fig. 7, one sees that the present prediction agrees excellently with the experimental data when the time step is sufficiently small. Similar situations occur for cases b and c (not shown here). The mean height of the liquid column is found identical to that from the one-dimensional approach (see Fig. 3). This evidences the accuracy of the present geometry method for the prediction of the moving meniscus as long as a "correct" dynamic contact angle θ_D is available.

There are a few models for advancing dynamic *apparent* contact angle including at least the Hoffman-Kistler's model [12]

$$\cos\theta_D = F(\mathrm{Ca}+\mathrm{Ca}_e) \tag{45a}$$

$$\cos\theta_e = F(\mathrm{Ca}_e) \tag{45b}$$

$$F(\mathrm{Ca}) = 1 - 2\tanh\left(5.16\left(\frac{\mathrm{Ca}}{1+1.31\mathrm{Ca}^{0.99}}\right)^{0.706}\right) \tag{45c}$$

the model of Jiang et al. [18]

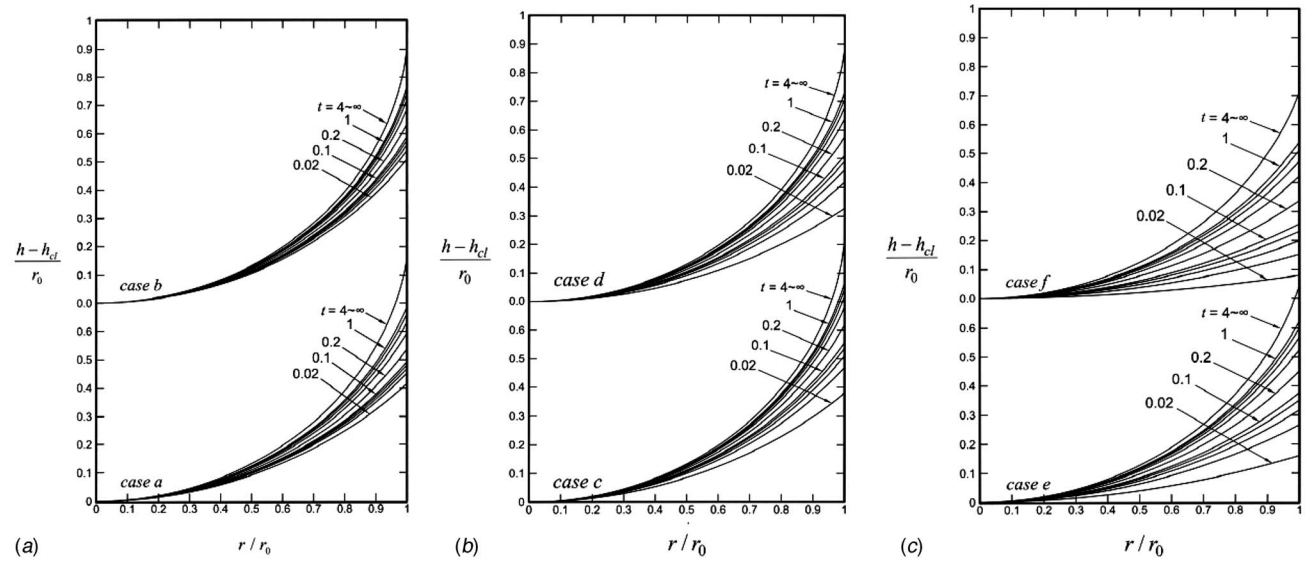

Fig. 9 Evolution of the free surface shape based on Hoffman-Kistler's model [12] for cases a, b, c, d, e, and f

Table 2 Curvature variation $\kappa_1(r_0,t)/\kappa_1(0,t)$ based on Hoffman-Kistler's model [12] for cases a–f

	Case a	Case b	Case c	Case d	Case e	Case f
$t=0.02$	1.013	1.006	1.005	1.007	1.014	1.029
$t=1.00$	1.017	1.007	1.007	1.010	1.020	1.038
$t=2.00$	1.019	1.008	1.008	1.011	1.021	1.042
$t=4.00$	1.020	1.008	1.008	1.011	1.022	1.045
$t=8.00$	1.021	1.008	1.008	1.012	1.023	1.047

$$\cos\theta_D = \cos\theta_e - (1+\cos\theta_e)\tanh(4.96\,\mathrm{Ca}^{0.702}) \tag{46}$$

and that of Bracke et al. [19]

$$\cos\theta_D = \cos\theta_e - 2(1+\cos\theta_e)\mathrm{Ca}^{0.5} \tag{47}$$

In the use of the Hoffman-Kistler's model [12], the value of Ca_e corresponding to the equilibrium contact angle θ_e should be determined from Eq. (45*b*) before the model is applied. For instance, $\mathrm{Ca}_e=0.0003060$ when $\theta_e=15$ deg. Due to the lack of reliable models for macroscopic dynamic contact angle, the apparent dynamic contact angles from Refs. [12,18,19] are regarded as the macroscopic dynamic contact angles in the present study. The resulting $h_{cl}(t)$ functions for cases a, b, c, d, e, and f are depicted in Fig. 8, while the meniscus profiles (based on Hoffman-Kistler's model [12]) are shown in Fig. 9 at some representative times (the time increment is 0.02 in $0.02\le t\le 0.10$, and 0.2 in $0.2\le t\le 1.0$). The experimental observations from Hamraoui et al. [13] for cases a, b, c, and d, and that from Fan et al. [20] for cases e and f are shown also in Fig. 8 for comparison. Satisfactory agreements are found between the predictions and the measurements for some of the six cases. Note that the dimensional quantities can be converted from the reference length $\bar{H}_\infty$ and time t_c given in Table 1. In all of the six cases, the principal curvature $\kappa_1(r,t)$ monotonically increases with the radial coordinator r at any given time. The curvature variation $\kappa_1(r,t)/\kappa_1(0,t)$ at the tube wall $r=r_0$ gradually increases with time as shown in Table 2 for each of the six cases. However, the curvature variation at $r=r_0/2$ seems to be time independent. Their values are 1.003, 1.001, 1.001, 1.002, 1.004, 1.008, respectively, for cases a–f. Similar situation occurs in the curvature $\kappa_2(r,t)$. The curvature ratio κ_2/κ_1 is found to monotonically decrease from unity at the centerline to a minimum at the tube wall that decreases with time. The equilibrium curvature ratio κ_2/κ_1 at the tube wall is 0.9847, 0.9937, 0.9937, 0.9930, 0.9835, and 0.9667 for cases a, b, c, d, e, and f, respectively.

Panchamgam et al. [21] used the image-analyzing interferometry to measure the thickness and curvature profiles of a liquid film in the contact line region in the presence of a precursor film. The curvature of the liquid meniscus was found to be relatively large and constant in the region where the film thickness δ is larger than 1 μm, while the curvature has a sharp decrease toward the liquid front in the thinner part ($\delta<1$ μm). In the presence of a precursor film, therefore, care must be exercised in the use of the present geometry method that assumes a constant curvature in the region $r_{n-2}\le r\le r_n$ (see Step 13). The major difference between cases b and c is that case b has a prewetted tube wall. When a precursor film of liquid at least 0.1 μm thick covers the solid surface ahead of the advancing liquid front, the profile of the advancing meniscus joins smoothly into the pre-existing film that sets the contact angle to $\theta_D\approx 0$ deg [22]. Hence, prewetting the tube would give rise to a faster capillary rising speed. Unfortunately, the existing models [12,18,19] do not consider the influence of the tube condition (prewetted or dry). As a result, the predicted $h_{cl}(t)$ for case b fits the experimental data [13] satisfactorily, while that for case c is considerably larger than the experimental data [13]. Similar situations occur in cases e and f. By contrast, the measured liquid column for the dry tube in case a is slightly faster than the present prediction for $h_{cl}(t)$.

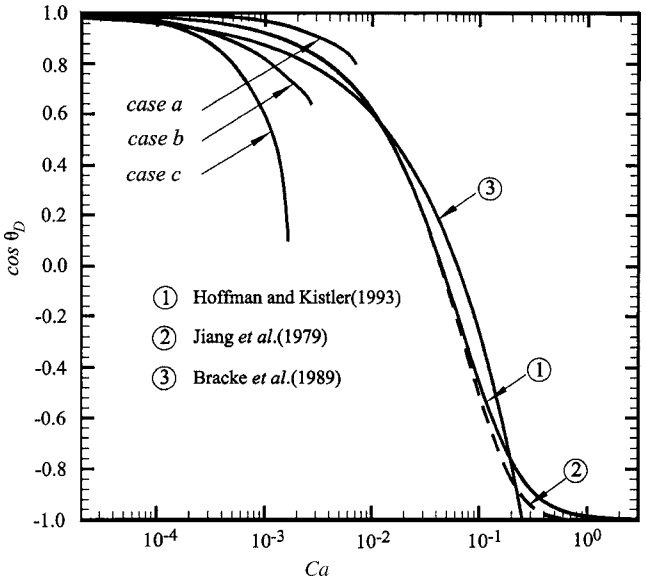

Fig. 10 The "correct" dynamic contact angle for cases a, b, and c

Finally, the "correct" dynamic contact angles (that were determined to fit the experimental data [13]) for cases a, b, and c are compared with the existing models [12,18,19] in Fig. 10. Great discrepancies among the "correct" dynamic contact angles and the existing models are observed. This reflects the need of a more general and more precise modeling for the macroscopic dynamic contact angle. In this connection, influences of tube prewetting, the viscosity ratio of the fluids, and some molecular parameters such as the jump frequency and jump length of the liquid atoms at the triple line should be taken into account. Besides precise experiments (if any), the molecular-kinetic theory [11,22] might be one of the possible techniques that are able to provide a general and accurate model for the coefficient of wetting-line friction (8).

4 Conclusion

A simple geometry method is proposed in this paper to solve the force balance equation on the liquid meniscus. From the six well-documented capillary-rise examples investigated in the present study, the following conclusions are drawn:

a. The geometry method solves the force balance equation for the evolution of the liquid meniscus successfully. The resulting slipping velocity at the contact line resolves the stress singularity issue.
b. The geometry method applies to the wall condition of zero contact angle as well.
c. The advancement of the liquid meniscus predicted by the geometry method agrees with that from the one-dimensional Washburn-Lucas equation excellently.
d. A more general and more precise modeling for the macroscopic dynamic contact angle is needed.

Acknowledgment

The authors wish to express their appreciation to the National Science Council of Taiwan for the financial support of this work through the contract NSC 90-2212-E007-062.

References

[1] Hoffman, R. L., 1975, "A Study of the Advancing Interface I. Interface Shape in Liquid-Gas Systems," J. Colloid Interface Sci., **50**, pp. 228–241.
[2] Dussan, V. E. B., 1976, "The Moving Contact Line: The Slip Boundary Condition," J. Fluid Mech., **77**, pp. 665–684.

[3] Shikhmurzaev, Y. D., 1997, "Moving Contact Lines in Liquid/Liquid/Solid Systems," J. Fluid Mech., **334**, pp. 211–249.
[4] Cox, R. G., 1998, "Inertial and Viscous Effects on Dynamic Contact Angle," J. Fluid Mech., **357**, pp. 249–278.
[5] Lee, S. L., and Sheu, S. R., 2001, "A New Numerical Formulation for Incompressible Viscous Free Surface Flow Without Smearing the Free Surface," Int. J. Heat Mass Transfer, **44**, pp. 1837–1848.
[6] Lowndes, J., 1980, "The Numerical Simulation of the Steady Movement of a Fluid Meniscus in a Capillary Tube," J. Fluid Mech., **101**, pp. 631–646.
[7] Zhou, M. Y., and Sheng, P., 1990, "Dynamics of Immiscible-Fluid Displacement in a Capillary Tube," Phys. Rev. Lett., **64**, pp. 882–885.
[8] Sheng, P., and Zhou, M. Y., 1992, "Immiscible-Fluid Displacement: Contact-Line Dynamics and the Velocity-Dependent Capillary Pressure," Phys. Rev. A, **45**, pp. 5694–5708.
[9] Koplik, J., Banavar, J. R., and Willemsen, J. F., 1988, "Molecular Dynamics of Poiseuille Flow and Moving Contact Angle," Phys. Rev. Lett., **60**, pp. 1282–1285.
[10] Thompson, P. A., and Robbins, M. O., 1989, "Simulation of Contact-Line Motion: Slip and the Dynamic Contact Angle," Phys. Rev. Lett., **63**, pp. 766–769.
[11] Martic, G., Gentner, F., Seveno, D., Coulon, D., De Coninck, J., and Blake, T. D., 2002, "A Molecular Dynamics Simulation of Capillary Imbibition," Langmuir, **18**, pp. 7971–7976.
[12] Kistler, S. F., 1993, "Hydrodynamics of Wetting," in *Wettability*, Berg, J. C., ed., Marcel Dekker, New York, Chap. 6, pp. 311–429.
[13] Hamraoui, A., Thuresson, K., Nylander, T., and Yaminsky, V., 2000, "Can a Dynamic Contact Angle be Understood in Terms of a Friction Coefficient?," J. Colloid Interface Sci., **226**, pp. 199–204.
[14] Blake, T. D., and Haynes, J. M., 1969, "Kinetics of Liquid/Liquid Displacement," J. Colloid Interface Sci., **30**, pp. 421–423.
[15] Sarpkaya, T., 1996, "Vorticity, Free Surface and Surfactants," Annu. Rev. Fluid Mech., **28**, pp. 83–128.
[16] Tsai, W. T., and Yue, D. K. P., 1996, "Computation of Nonlinear Free-Surface Flows," Annu. Rev. Fluid Mech., **28**, pp. 249–278.
[17] Sato, T., and Richardson, S. M., 1995, "Numerical Simulation of the Fountain Flow Problem for Viscoelastic Fluid," Polym. Eng. Sci., **35**, pp. 805–812.
[18] Jiang, T. S., Oh, S. G., and Slattery, J. C., 1979, "Correlation for Dynamic Contact Angle," J. Colloid Interface Sci., **69**, pp. 74–77.
[19] Bracke, M., de Voeght, F., and Joos, P., 1989, "The Kinetics of Wetting: The Dynamic Contact Angle," Prog. Colloid Polym. Sci., **79**, pp. 142–149.
[20] Fan, H., Gao, Y. X., and Huang, X. Y., 2001, "Thermodynamics Modeling for Moving Contact Line in Gas/Liquid/Solid System: Capillary Rise Problem Revisited," Phys. Fluids, **13**, pp. 1615–1623.
[21] Panchamgam, S. S., Gokhale, S. J., Plawsky, J. L., DasGupta, S., and Wayner, P. C., 2005, "Experimental Determination of the Effect of Disjoining Pressure on Shear in the Contact Line Region of a Moving Evaporating Thin Film," ASME J. Heat Transfer, **127**, pp. 231–243.
[22] Blake, T. D., 1993, "Dynamic Contact Angles and Wetting Kinetics," in *Wettability*, Berg, J. C., ed., Marcel Dekker, New York, Chap. 5, pp. 251–309.

Cavitation Influence on von Kármán Vortex Shedding and Induced Hydrofoil Vibrations

Philippe Ausoni

Mohamed Farhat

Laboratory for Hydraulic Machines,
EPFL, Ecole polytechnique fédérale de Lausanne,
Avenue de Cour 33bis,
1007 Lausanne, Switzerland

Xavier Escaler

Eduard Egusquiza

Center for Industrial Diagnostics,
UPC, Universitat Politecnica de Catalunya,
Avenidad Diagonal 647,
08028 Barcelona, Spain

François Avellan

Laboratory for Hydraulic Machines,
EPFL, Ecole polytechnique fédérale de Lausanne,
Avenue de Cour 33bis,
1007 Lausanne, Switzerland
e-mail: francois.avellan@epfl.ch

The present study deals with the shedding process of the von Kármán vortices at the trailing edge of a 2D hydrofoil at high Reynolds number $Re_h=25\times10^3$–65×10^3. This research focuses mainly on the effects of cavitation and fluid-structure interaction on the mechanism of the vortex generation. The vortex shedding frequency, derived from the flow-induced vibration measurement, is found to follow the Strouhal law provided that no hydrofoil resonance frequencies are excited, i.e., lock-off. For such a regime, the von Kármán vortices exhibit strong spanwise 3D instabilities and the cavitation inception index is linearly dependent on the square root of the Reynolds number. In the case of resonance, the vortex shedding frequency is locked onto the hydrofoil eigenfrequency and the spatial coherence is enhanced with a quasi-2D shape. The measurements of the hydrofoil wall velocity amplitude and phase reveal the first torsion eigenmotion. In this case, the cavitation inception index is found to be significantly increased compared to lock-off conditions. It makes clear that the vortex roll-up is amplified by the phase locked vibrations of the trailing edge. For the cavitation inception index, a new correlation relationship that encompasses the entire range of Reynolds numbers, including both the lock-off and the lock-in cases, is proposed and validated. In contrast to the earlier models, the new correlation takes into account the trailing edge displacement velocity. In addition, it is found that the transverse velocity of the trailing edge increases the vortex strength linearly. This effect is important in the context of the fluid-structure interaction, since it implies that the velocity of the hydrofoil trailing edge increases the fluctuating forces on the body. It is also demonstrated that cavitation developing in the vortex street cannot be considered as a passive agent for the turbulent wake flow. In fact, for fully developed cavitation, the vortex shedding frequency increases up to 15%, which is accompanied by the increase of the vortex advection velocity and reduction of the streamwise vortex spacing. In addition, a significant increase of the vortex-induced vibration level is found at cavitation onset. These effects are addressed and thought to be a result of the increase of the vorticity by cavitation. [DOI: 10.1115/1.2746907]

Introduction

Vortex shedding is the dominant feature of two-dimensional (2D) body wakes. Due to its fundamental importance and the wide range of industrial applications including heat exchangers, underwater drilling rig, and electric transmission lines, vortex shedding has been studied intensively for the flow past cylinders and some other bluff bodies. In contrast, the vortex shedding past hydrofoils has been studied to much less extent, particularly for high Reynolds numbers, despite numerous practical applications; for example, in ship propulsion and hydropower generation. The lack of experimental data for hydrofoils becomes particularly evident today, since engineers tend to use materials to their limits, causing structures to be more flexible, so that the vortex-induced vibrations become one of the primary damage mechanisms (Blevins [1]). For instance, it is found that the vibrations caused by von Kármán vortex shedding can cause premature and fatigue cracks in the stay vanes of turbines. Recently, Lockey et al. [2] and Shi [3] report on the damage of runners due to resonance regime, i.e., lock-in. Besides, depending on the pressure level in the flow, cavitation can occur in the shed vortices. However, except for several early studies, the phenomenon of cavitation developing in the shed vortices has been ignored for a long time. The goal of the present work is to investigate the effect of cavitation and fluid-structure interaction on the development of the von Kármán vortex street in the wake of a 2D hydrofoil at high Reynolds numbers. The role of the hydrofoil vibration in the cavitation inception and vortices strength is pointed out.

Placed in a fluid stream, bluff bodies generate separated flow over a substantial proportion of their surface that extends to their wake. The detachment of the boundary layers on both upper and lower surfaces forms two shear layers generating above critical values of Reynolds numbers, a periodic array of discrete vortices termed von Kármán street. In a range of upstream velocity, the vortex shedding frequency is known to follow the Strouhal law. From a hydrodynamic point of view, the instability of the shear layer separating from a circular cylinder has been extensively investigated; see Williamson and Roshko [4] for a comprehensive review. Many authors observe that the wake structure may exhibit a 3D aspect even if the obstacle and the upcoming flow are 2D. Gerrard [5] observed curved vortices and suspected that the cylinder end conditions might be the cause. Tritton [6] and Slaouti and Gerrard [7] report that vortices may be shed at a swept angle from the cylinder axis, which is called oblique shedding. Gerich and Eckelmann [8], Prasad and Williamson [9], and Williamson [10] find that the spanwise end conditions control the primary vortex shedding and significantly affect the stability of the separating shear layer.

Vortex-induced vibration and fluid-structure interaction phenomena have been subjected to much research, which Rockwell [11] and Williamson and Govardhan [12] have reviewed. It is well known that the bodies that shed spanwise vortices may be excited into oscillation by the fluctuating side forces resulting from such vortices. For instance, the resonance occurs when the vortex shed-

Contributed by the Fluids Engineering Division of ASME for publication in the JOURNAL OF FLUIDS ENGINEERING. Manuscript received June 27, 2006; final manuscript received March 16, 2007. Review conducted by Timothy J. O'Hern.

ding frequency coincides with one of the eigenfrequencies of the combined fluid-structure system. In the case where the response amplitude becomes sufficiently large, the structural displacement can control the fluid excitation, leading to the so-called "lock-in" phenomenon. The vortex shedding frequency is therefore "locked" onto the structural eigenfrequency over a rather extended range of free stream velocity magnitudes. With large structural displacement, the vortex strength is increasing as well as the periodic forces. And with the axial correlation of vorticity increasing, the periodic forces are further increased. Therefore, the vibration increases until the energy fed into the structure by the flow equals the energy dissipated per cycle. The response of freely vibrating cylinders is detailed by Feng [13]. For a lightly damped circular cylinder, vibration amplitude hysteresis is observed when reduced velocity is increased over a certain range and then is decreased back over the same range. However, this hysteresis is still to be fully explained. Davies [14] compared the wake structure for stationary and oscillating bluff bodies. The results showed an increase of 35% in the circulation of vortices shed from the oscillating cylinder, compared with those in the wake of a stationary body. Gilbert and Sigurdson [15] investigated the influence of the structural vibration on the vortex street morphology. They visualized hydrogen bubble flow of a self-oscillating cylinder vortex street "void." Interestingly, "voids" did not originate at nodes in the cylinder's vibration; they were seen to appear where the cylinder is vibrating at amplitudes that appear to be a large fraction of the cylinder's diameter.

When the pressure is low enough, bubbles filled with vapor and noncondensable gas are initiated and persist in the center of individual shed vortices. Sridhar and Katz [16] investigated the effect of entrained bubbles on the structure of vortex rings. They demonstrated that few microscopic bubbles are able to fragment the core of the vortex into two regions with peak vorticities that were 20% higher than the original maximum vorticity. Considering a Rankine vortex, Arndt and Keller [17] established that the maximum velocity in the cavitation vortex is $\sqrt{2}$ higher than in the noncavitating vortex. Young and Holl [18] investigated the case of a flow around wedges. They observed that the cavitation development in the wake increased the shedding frequency by up to 25% and therefore affected the dynamics of the von Kármán street. Dupont et al. [19] confirmed these results in the case of a 2D hydrofoil. Models for cavitation inception in the wake of bluff bodies have been presented by Belahadji et al. [20] and Arndt [21]. The models lead to a linear $\sigma_i \sim \sqrt{\mathrm{Re}_h}$ law that correctly predicts the correlation between the cavitation inception index and the Reynolds number for the considered range of upstream velocities. Although remarkably successful in describing the cavitation inception for fixed bluff bodies, none of these studies provides a direct insight into the role of the trailing edge vibration on the cavitation occurrence.

In this paper, the experimental setup and the measuring techniques are first presented. The following section is devoted to the experimental results of the fluid-structure interaction in the cavitation free regime: the vortex shedding frequency and the hydrofoil vibration amplitude are evidenced as well as the lock-in and the corresponding eigenmode. The next section studies the fluid-structure interactions' influence on cavitation inception: a direct insight is provided into the role of the hydrofoil trailing edge vibration. Finally, the cavitation development for both lock-off and lock-in conditions are illustrated through wake visualizations and flow-induced vibration analysis. The paper's conclusions are summarized in the last section.

Experimental Setup

The Ecole polytechnique fédérale de Lausanne (EPFL) high-speed cavitation tunnel, outlined in Fig. 1, is a closed loop with a test section of $150 \times 150 \times 750$ mm (Avellan et al. [22]). The operating flow parameters are the upstream velocity C_{ref} and the cavitation index σ. The incidence angle of the hydrofoil α is kept at 0 deg and the cavitation index is set above 0.2 to allow cavitation occurrence only in the wake and not on the hydrofoil wall.

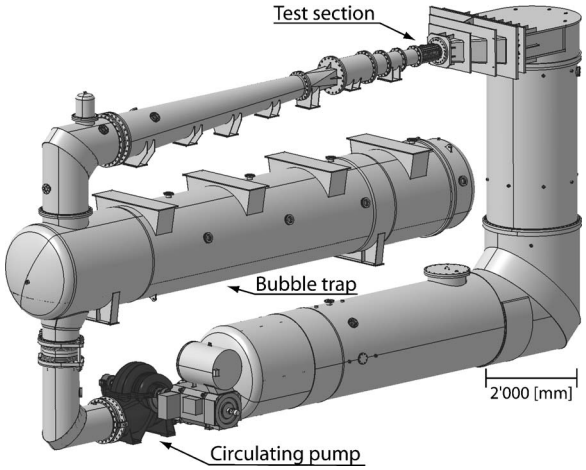

Fig. 1 EPFL high speed cavitation tunnel

The experimental 2D hydrofoil, sketched in Fig. 2, is a blunt truncated NACA 0009 made of stainless steel. The trailing edge thickness h is 3.22 mm and its chord length L and span b are 100 mm and 150 mm, respectively. The hydrofoil mounting in the test section can be considered as a perfect embedding on one side and pivot embedding on the other.

A specific optical probe is developed to investigate the vortex advection velocity, the shedding frequency and the intervortex spacing for different cavitation development. As sketched in Fig. 3, two parallel laser beams, 4 mm apart, which are periodically interrupted by the von Kármán vortex cavitation, are set to cross the wake. Two fast photodiodes are placed to track the light beam intensities modulated by the passing cavities. The probe is mounted on a traversing system, and measurements are performed at different locations in the wake.

The flow-induced vibrations are measured with the help of an accelerometer and a laser vibrometer. The piezoelectric accelerometer whose resonance frequency is 54 kHz is fitted on the profile support and a portable laser vibrometer is used to survey the hydrofoil wall vibrations. The measurement principle of the laser vibrometer is based on the detection of the frequency shift of the reflected laser beam according to the doppler effect; the frequency shift being directly related to the displacement velocity of the wall in the laser direction. The location of the vibration amplitude measurements points is shown in Fig. 4. Hydrofoil vibration measurements are synchronized with the accelerometer signal used as a reference. The amplitude and the phase of the hydrofoil motion for each measurement point are measured and the eigenmode is identified for the detected hydro-elastic coupling. The data acquisition system has 16 bits A/D resolution, 16 inputs, a memory depth of 1 MSamples per channel, and a maximum sampling frequency of 51.2 kHz per channel.

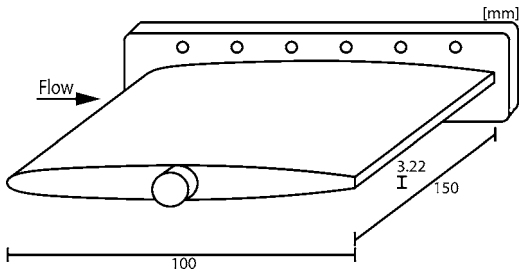

Fig. 2 Blunt truncated NACA 0009 hydrofoil

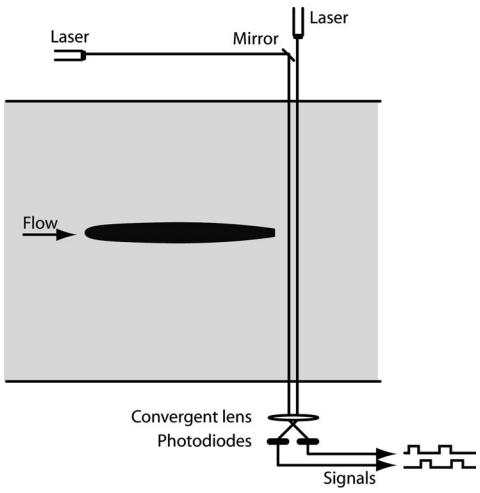

Fig. 3 Sketch of the double laser optical probe

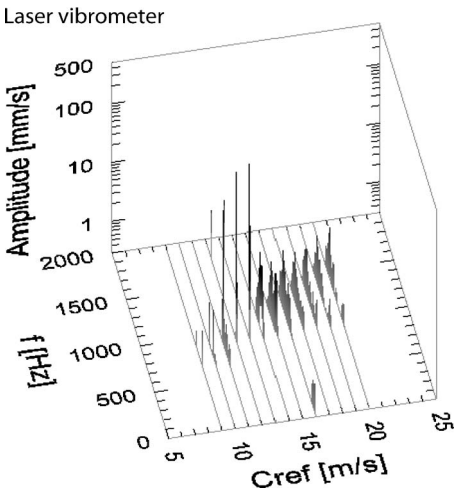

Fig. 5 Waterfall spectra of the laser vibrometer signals for different upstream velocities

The vortical structures in the wake are visualized with the help of a high speed digital camera. The CCD image resolution is 512×192 pixels at 10,000 frames/s, and the exposure time may be adjusted down to 10 μs.

Fluid-Structure Interactions in Cavitation Free Regime

The waterfall spectra of the laser vibrometer signals is presented in Fig. 5 for different upstream velocities. Most of the spectral energy is concentrated around a frequency that increases with the upstream velocity. We have identified this frequency as the shedding frequency of von Kármán vortices. The amplitude of the induced vibration changes according to the upstream velocity: as the vortex-shedding frequency approaches one of the natural frequencies of the combined fluid-structure system, the coupling takes place with a significant increase of noise and vibration levels. The vortex-shedding frequency is "locked" onto the structural eigenfrequency that is 900 Hz for flow velocity ranging from 11 m/s to 13 m/s; i.e., Re_h=35,000 to 42,000. In addition to the energy at the vortex-shedding frequency, all the spectra show energy for this eigenfrequency.

The vortex-shedding frequency normalized by the lock-in frequency and derived from the laser vibrometer and the accelerometer signals is presented in Fig. 6 as a function of the flow velocity. Both measuring techniques provide equivalent signal time history. A linear relationship between the vortex-shedding frequency and the upstream velocity is observed provided that no hydrofoil resonance frequencies are excited. For such a lock-off regime, the generation process of von Kármán vortices occurs at constant Strouhal number, i.e., St=0.24. The hydrofoil trailing edge vibration amplitude at the vortex shedding frequency is also evidenced in Fig. 6.

In lock-in conditions corresponding to 11–13 m/s upstream velocities, we observe the increase and decrease of the vibration amplitude. As the upstream velocity is increased and decreased, neither shedding frequency nor vibration amplitude reveal a hysteresis effect. For the above-mentioned lock-in condition, the hydrofoil wall vibration is surveyed by laser vibrometer measurements. As illustrated in Fig. 7, the modal shape is identified as the first torsion mode. The maximum vibration amplitude of the trailing edge is up to 0.2×10^{-3} m. For this condition, the vibration is found to be large enough to dominate the unsteady flow field and a self-controlled vibration is induced.

Fluid-Structure Interactions' Influence on Cavitation Inception

Bubbles are initiated in the individual vortices' centers, where the minimum pressure is reached. As previously described, models for cavitation inception in the wake of bluff bodies have already been proposed. The method is based on the known pressure distribution for either Rankine or Oseen models. Relating the vor-

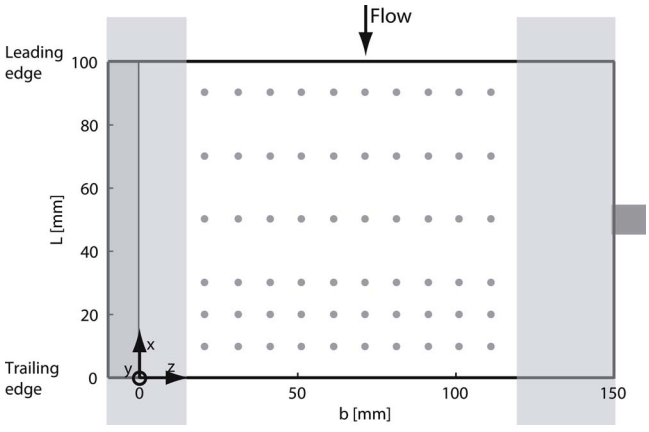

Fig. 4 Location of the hydrofoil vibration amplitude measurement points

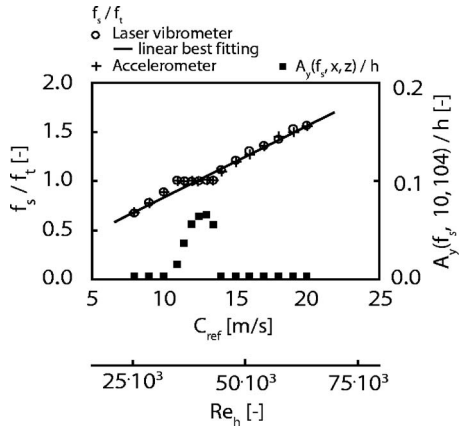

Fig. 6 Shedding frequency of von Kármán vortices and vibration amplitude of the hydrofoil trailing edge for different upstream velocities

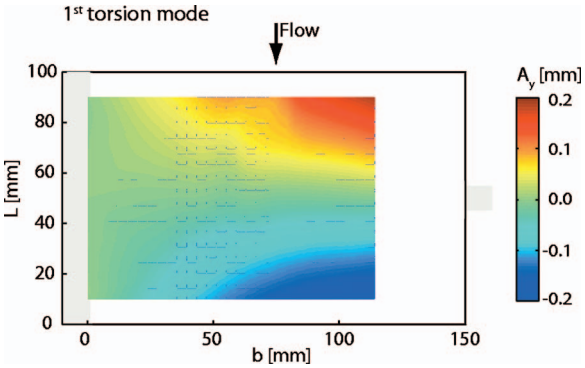

Fig. 7 Survey of the hydrofoil wall vibration amplitude for lock-in condition; C_{ref}=12 m/s

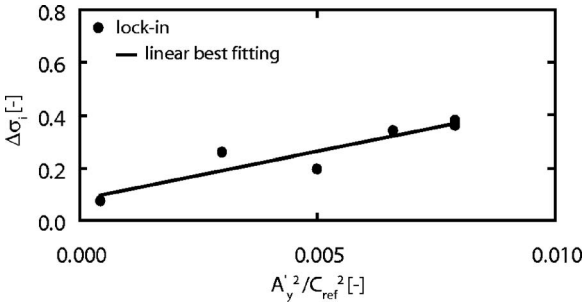

Fig. 9 Difference between the cavitation inception number in lock-in condition and the value derived from the linear regression of the cavitation inception numbers in lock-off condition versus the square of the hydrofoil trailing edge vibration velocity scaled by the upstream velocity

tex core diameter to the boundary-layer thickness, the method leads to a linear $\sigma_i \sim \sqrt{\mathrm{Re}_h}$ law, which correctly predicts the correlation between the cavitation inception index and the Reynolds number for the considered range of upstream velocities. Although successful in describing the cavitation inception for fixed bluff bodies, none of these studies provides a direct insight into the role of the trailing edge vibration on the cavitation occurrence. In the present study, the cavitation index inception values are presented in Fig. 8 as a function of the square root of the Reynolds number. Distinctions are made between lock-in and lock-off conditions.

For lock-off conditions, a linear tendency between the cavitation inception index and the square root of the Reynolds number is evidenced in Fig. 8 and is in accordance with former models. For lock-in conditions corresponding to the torsion mode, the cavitation inception index is significantly higher than for the lock-off conditions. The trailing edge vibration adds dynamic effects in the generation process of von Kármán vortices. The differences ($\Delta\sigma_i$) between the cavitation inception number in lock-in condition and the value derived from the linear regression of the cavitation inception numbers in lock-off condition is calculated and plotted in Fig. 9 as a function of the square of the hydrofoil trailing edge vibration velocity A'_y scaled by the upstream velocity C_{ref}. A clear linear relationship between $\Delta\sigma_i$ and A'^2_y/C^2_{ref} is achieved. The former models for wake cavitation inception have to be extended by taking into account the hydrofoil trailing edge displacement velocity as:

$$\sigma_i = a + b\sqrt{\mathrm{Re}} + c\frac{A'^2_y}{C^2_{ref}} \tag{1}$$

Furthermore, if a cavitation free streamwise vortex is simply modeled as a Rankine vortex, the pressure p_c within the core of diameter a, is given by

$$p_{ref} - p_c = \rho\left(\frac{\Gamma}{2\pi a}\right)^2 \tag{2}$$

At the cavitation inception in the vortex, the core pressure reaches the vapor pressure, i.e., $p_c = p_v$. According to the definition of the cavitation inception index, the relation (2) yields the following expression for the vortex strength Γ:

$$\frac{\Gamma}{a} = \pi C_{ref}\sqrt{2\sigma_i} \tag{3}$$

By using the relation (3), the ratio Γ/a is evaluated for both lock-in and lock-off conditions. The observations of the vapor core size at cavitation inception for different upstream velocities under lock-in conditions and different vibration levels did not show any evidence of significant size changes. Therefore, it is believed that the influence of blade vibratory motion on the viscous core of the vortex is negligible and allows us to assume a constant core diameter. The differences $\Delta\Gamma$ between the calculated strength in lock-in condition and the value derived from the linear regression of the strength in lock-off condition Γ are then derived and plotted in Fig. 10 as a function of the trailing edge vibration velocity scaled by the upstream velocity A'_y/C_{ref}. In Fig. 10, a linear trend for the vortex strength increase in relation to the trailing edge vibratory velocity is observed. We have also presented the corresponding value found from the comparison of the wake structure for a stationary and oscillating cylinder [14] and this value matches remarkably well the linear relationship derived from our measurements. As mentioned by Davies [14], this increase in vortex strength is important in terms of fluid-structure interaction, since it implies that the hydrofoil trailing edge velocity increases the fluctuating forces on the body and this effect is additional to any increased spanwise coherent length, as observed for the resonance condition.

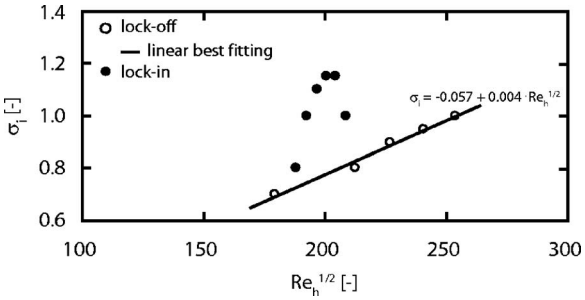

Fig. 8 von Kármán vortices cavitation inception index versus the square root of the Reynolds number

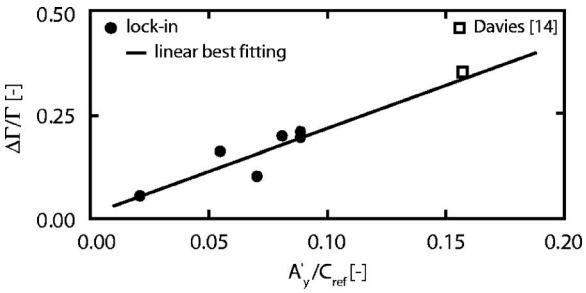

Fig. 10 Relative vortex strength for lock-in condition versus the hydrofoil vibration amplitude

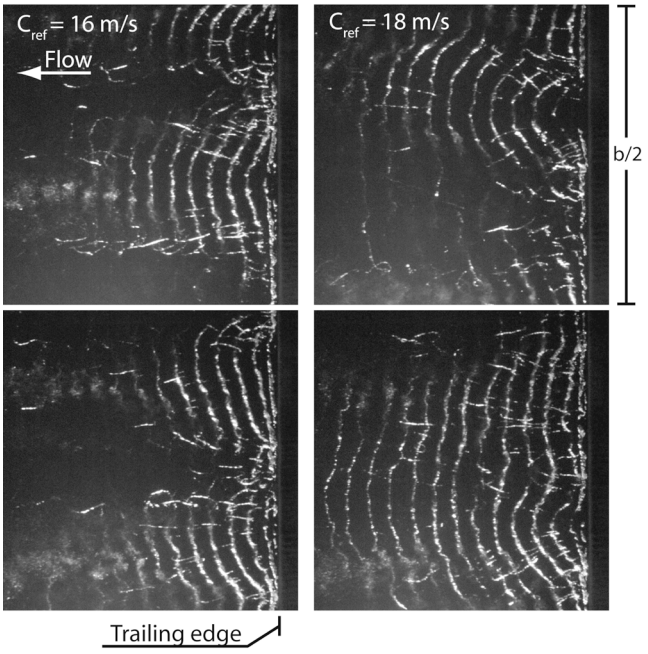

Fig. 11 Top-view photographs of von Kármán vortex street cavitation in lock-off conditions

Cavitation Development in Lock-Off Conditions

Two pairs of top-view photographs of cavitating vortex street in lock-off condition for two upstream velocities are presented in Fig. 11. It is observed that the wake exhibits 3D instabilities. The distortions and the spatial randomness of the vortical structures are evidenced. As already mentioned, the test section walls at both ends of the hydrofoil generate vorticity that can alter the 2D advection of the vortex street. The coherence length is, therefore, shorter as compared to the hydrofoil span.

For different values of cavitation index at 16 m/s upstream velocity, the waterfall spectra of the laser vibrometer signals is presented in Fig. 12, and shows notable influences of cavitation: as soon as the cavitation appears in the core of the von Kármán vortices ($\sigma/\sigma_i=1$), a significant increase of the shedding frequency but also of the structural vibration amplitude is observed. As the cavitation index is further reduced, the shedding frequency keeps increasing in an almost linear way and exceeds by 15% the cavitation free regime value. Although the shedding frequency increase with the development of the cavitation has already been observed in previous research for flow around wedges, the above-

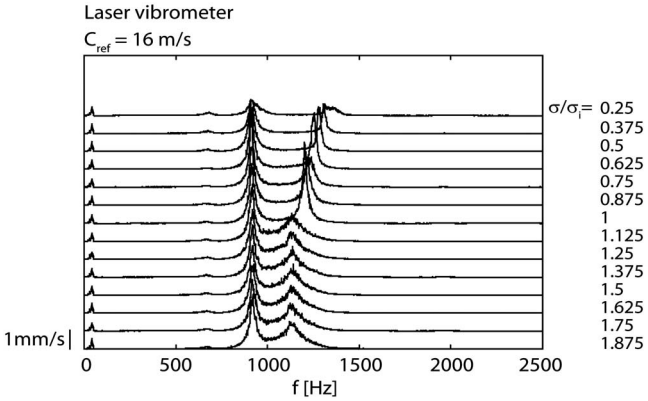

Fig. 12 Waterfall spectra of the laser vibrometer signals for different values of cavitation index and for lock-off condition

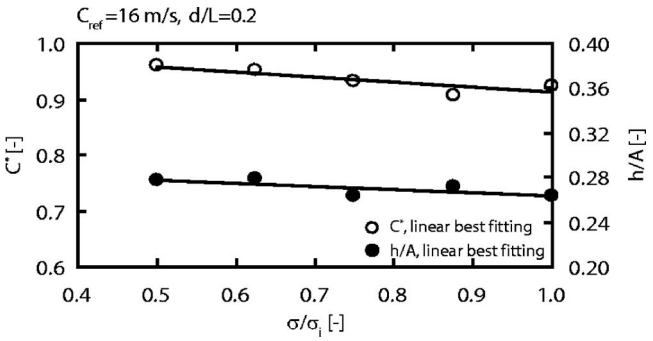

Fig. 13 Reduced advection velocity of the vortices and spacing ratio of the vortex street versus cavitation index for lock-off condition

mentioned increase of the vortex-induced vibration at early stage of cavitation has not been reported earlier. When the cavitation is fully developed ($\sigma/\sigma_i<0.4$), the vibration amplitude drops and the vortex structures merge to form a single vapor cavity at the trailing edge. Moreover, all the spectra show energy at 900 Hz corresponding to the eigenfrequency of the torsion mode.

The cavitation effects on the vortices' reduced advection velocity $C^*=C_{\text{Kármán}}/C_{\text{ref}}$ and the intervortex spacing h/A is presented in Fig. 13. The results correspond to a lock-off condition with an upstream velocity of 16 m/s. The distance from the trailing edge is 0.02 m, which is sufficiently far downstream from the vortex generation zone. It is observed that the vortices' advection velocity increases with the cavitation development as much as 4% for $\Delta\sigma=0.4$. This increase is linear and occurs as soon as the cavitation appears in the wake. By using the measurements of the vortices' advection velocity and their corresponding shedding frequencies, the intervortex spacing is evaluated by

$$A(t)=x(t+T)-x(t)=\int_t^{t+T} C_{\text{Kármán}}(\tau)d\tau \tag{4}$$

where $x(t)$ is the position of a vortex at time t and T is the vortex-shedding period. The ratio h/A is plotted for several cavitation index values in Fig. 13. Since the intervortex spacing is found to decrease for decreasing cavitation index, the ratio h/A increases with the development of the cavitation. h/A can be considered as an approximation of the spacing ratio B/A. In Fig. 13, for cavitation inception, the spacing ratio value reaches 0.27, which is close to the value 0.281 predicted by the von Kármán stability theory.

At the present stage, it becomes obvious that cavitation cannot be considered as a passive agent for the visualization of the turbulent wake flow. It is believed that the shedding frequency increase with the development of the cavitation can be explained by the interpretation of the description of the vortex street formation made by Gerrard [23]. The description postulates that a vortex continues to grow, fed by circulation from its connected shear layer, until it is strong enough to draw the opposing shear layer across the near wake. Sridhar and Katz [16] show that few microscopic bubbles fragment the core of the vortex into two regions with peak vorticities that are 20% higher than the original maximum vorticity. In the cavitating growing vortex, this higher vorticity draws sooner the opposing shear layer across the wake than in the cavitation free vortex. Consequently, the approach of oppositely signed vorticity cuts off sooner the supply of circulation to the growing vortex. The vortex shedding frequency is thus increased. Furthermore, the increase of the hydrofoil vibration at cavitation inception is likely attributed to the above-mentioned vorticity increase. In addition, as the vorticity increases and assuming a constant vortex core diameter, the maximum tangential velocity of the vortices and, therefore, their advection velocities increase. Considering a Rankine vortex, Arndt and Keller [17]

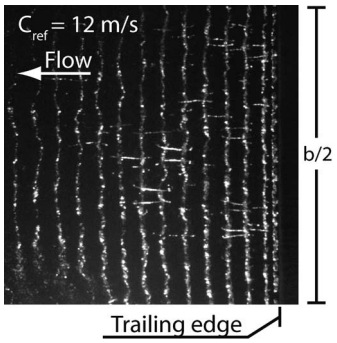

Fig. 14 Top-view photographs of cavitation von Kármán vortex street for lock-in condition (first torsion mode)

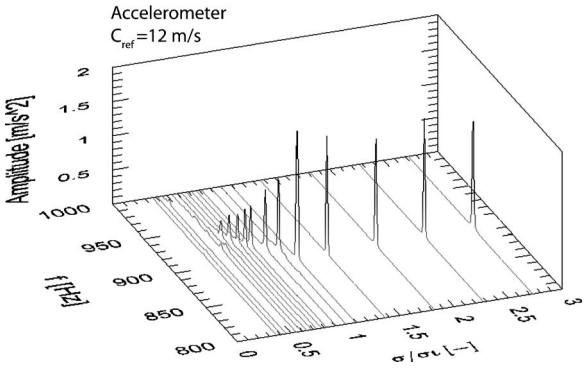

Fig. 16 Waterfall spectra of the acceleration signals for different values of cavitation index at 12 m/s upstream velocity

established that the maximum velocity in the cavitating vortex is $\sqrt{2}$ higher than in the noncavitating vortex and support our claim. As the vortex-shedding frequency and advection velocity increase, the intervortex spacing decreases for stability of the vortex street.

Cavitation Development in Lock-In Conditions

For lock-in, the trailing edge vibration leads to more organized wake structures. When the torsion mode is excited, the transverse motion of the trailing edge significantly increases the coherent length of the vortex street, and parallel vortex shedding takes place as evidenced in Fig. 14.

Frames of high speed visualizations of the von Kármán vortex street for lock-in condition are presented in Fig. 15 for moderated cavitation development (σ/σ_i=0.85), and full cavitation development (0.7). The five frames from top to bottom represent one generation cycle of a pair of von Kármán vortices. It can be observed that during the motion of the trailing edge from its minimum lower to its maximum upper transverse location, the volume of vapor in the recirculation zone increases and starts rolling up without being advected by the mean flow. When the hydrofoil reaches its maximum displacement, the vortex detaches from the trailing edge and accelerates in the hydrofoil wake. As soon as the upper vortex has been detached, the lower one is generated in a similar way during the backward motion of the hydrofoil. Besides the primary von Kármán vortices, the wake also exhibits secondary vortices for the developed cavitation condition σ/σ_i=0.7. According to these visualizations, the roll-up of the separated shear layers takes place precisely at the rear face of the body. Therefore, we conceive that the displacement velocity of the trailing edge strongly acts on the generated vortices' strength, as previously evidenced.

As the vortex-shedding frequency tends to increase with the cavitation development, it is found possible to enable or disable hydro-elastic couplings just by permitting a sufficient cavitation development while keeping the upstream velocity constant. In Figs. 16 and 17, it is shown how the hydrofoil resonance is dis-

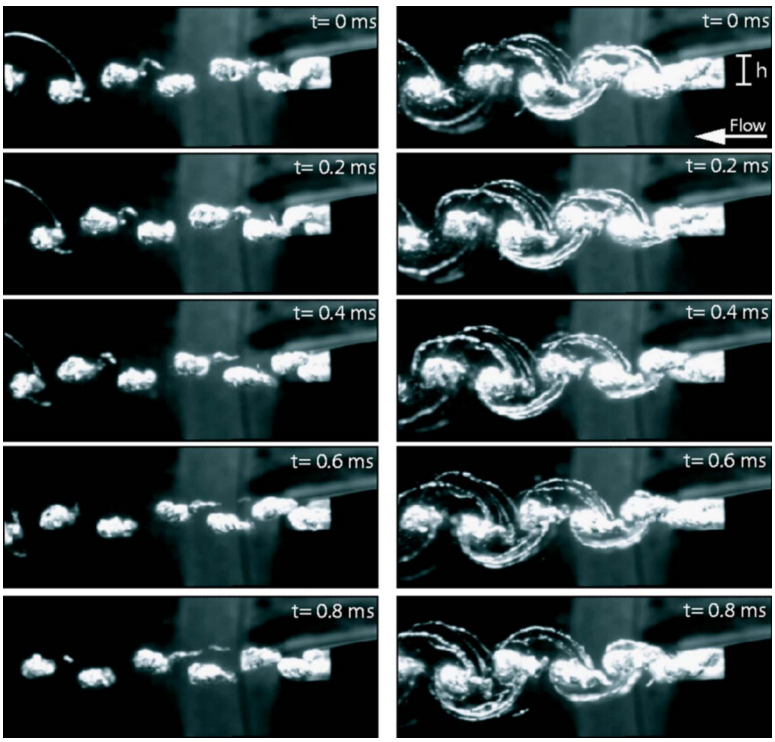

Fig. 15 Frame series of von Kármán vortex street for lock-in condition (first torsion mode; C_{ref}=12 m/s) and for two cavitation indices (left) σ/σ_i=0.85, (right) σ/σ_i=0.7

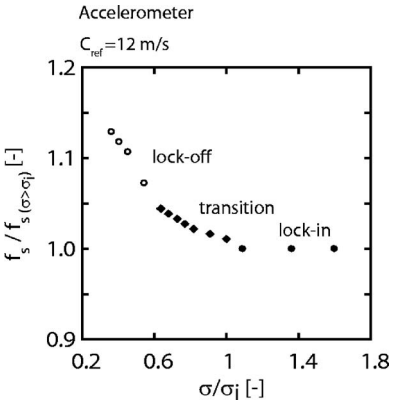

Fig. 17 Shedding frequency of von Kármán vortices versus cavitation index at 12 m/s upstream velocity

abled when the upstream velocity is maintained at 12 m/s, for which the torsion mode is excited in a cavitation free regime. In Fig. 16, waterfall spectra of the accelerometer signals for different values of cavitation index are presented. Figure 17 illustrates the vortex shedding frequency f_s, normalized by its corresponding value for the cavitation free regime $f_s(\sigma > \sigma_i)$ versus the cavitation index. As the cavitation appears in the wake and develops, the vortex-shedding frequency increases, but at a lower rate than in the case out of resonance. Although the amplitude of vibration decreases, the resonance is maintained since the amplitudes remain higher than in the lock-off condition. The structural vibration therefore tends to control the unsteady flow field and forces the vortices to be shed near the eigenfrequency. Upon further decrease of the cavitation index, the coupling is no longer maintained, so that the vortex-shedding frequency increases in a more marked way.

Conclusions

The von Kármán vortex street generated in the wake of a 2D hydrofoil with a truncated trailing edge is investigated in the EPFL high speed cavitation tunnel. The data are obtained for a wide range of cavitation indices and Reynolds numbers; i.e., $\mathrm{Re}_h = 25 \times 10^3 - 65 \times 10^3$. Combination of high speed visualization, laser optical probe, and measurements of flow-induced vibration provides a unique way of analyzing the dynamics of the von Kármán vortex street. The mutual effects of hydrofoil vibration and cavitation development on the mechanism of the vortex generation are pointed out.

In cavitation free regime, the shedding frequency of von Kármán vortices occurs at a constant Strouhal number provided that no hydrofoil resonance frequencies are excited; i.e., lock-off. In the case of resonance (lock-in), the vortex-shedding frequency is locked onto the hydrofoil eigenfrequency and the vortex coherent length is significantly increased. The measurements of the hydrofoil wall velocity amplitude and phase reveal the first torsion eigenmotion.

It is demonstrated that cavitation developing in the vortex street cannot be considered as a passive agent for the turbulent wake flow. In fact, for fully developed cavitation, the vortex-shedding frequency increases up to 15%, accompanied by the increase of the vortex advection velocity and reduction of the streamwise vortex spacing. In addition, a significant increase of the vortex-induced vibration level is found at cavitation onset, which has never before been reported. These effects are addressed and are thought to be a result of the increase of the vorticity by cavitation.

The wake cavitation inception index is linearly dependent on the square root of the Reynolds number in the lock-off regime, which agrees well with the earlier experimental observations. However, in the lock-in regime, the cavitation inception index is significantly higher than in the lock-off case, and it is no longer linearly dependent on the Reynolds number. For the cavitation inception index, a new correlation relationship that encompasses the entire range of Reynolds numbers, including both the lock-off and the lock-in cases, is proposed and validated. In contrast to the earlier models, the new correlation takes into account the trailing edge displacement velocity. In addition, it is found that the transverse velocity of the trailing edge increases the vortex strength linearly. This effect is important in the context of the fluid-structure interaction, since it implies that the velocity of the hydrofoil trailing edge increases the fluctuating forces on the body.

Acknowledgment

The investigation reported in this paper is part of the work carried out for the HYDRODYNA, Eureka Research Project No. 3246, whose partners are ALSTOM Hydro, EDF-CIH, EPFL, GE Hydro, UPC-CDIF, VATECH Hydro, and VOITH-SIEMENS Hydro Power Generation. The project is also financially supported by CTI, the Swiss Federal Commission for Technology and Innovation Grant No. 7045-1 and NSF, the Swiss National Science Foundation Grant No. 2000-068320. The authors are very grateful to the HYDRODYNA Technical Committee for its involvement and constant support to the project. Finally the staff of the EPFL Laboratory for Hydraulic Machines should be thanked for its support in the experimental and numerical work.

Nomenclature

A = vortex row spacing, m
$A_y(f_s,x,z)$ = hydrofoil vibration amplitude for the shedding frequency f_s at coordinates (x,z), m
A'_y = hydrofoil vibration velocity, m/s
b = hydrofoil span, m
B = distance between vortex rows, m
C_{ref} = reference velocity at the test section inlet, m/s
$C_{\mathrm{Kármán}}$ = vortex advection velocity, m/s
C^* = reduced advection velocity, $C^* = C_{\mathrm{Kármán}}/C_{\mathrm{ref}}$
f_s = vortex shedding frequency, Hz
f_t = hydrofoil torsion eigenfrequency, Hz
L = hydrofoil chord length, m
p_{inlet} = reference pressure at the test section inlet, bar
p_v = vapor pressure, bar
Re_h = Reynolds number, $\mathrm{Re}_h = C_{\mathrm{ref}}h/\nu$
St = Strouhal number, $\mathrm{St} = f_s h/C_{\mathrm{ref}}$
h = hydrofoil trailing edge thickness, m
α = incidence angle of the hydrofoil, deg
σ = cavitation index, $\sigma = 2(p_{\mathrm{inlet}} - p_v)/\rho C_{\mathrm{ref}}^2$
σ_i = cavitation inception index
ν = kinematic viscosity, m^2/s

References

[1] Blevins, R. D., 1985, "The Effect of Sound on Vortex Shedding From Cylinders," J. Fluid Mech., **161**, pp. 217–237.
[2] Lockey, K. J., Keller, M., Sick, M., Staehle, M. H., and Gehrer, A., 2006, "Flow-Induced Vibrations at Stay Vanes: Experience on Site and CFD Simulations," Int. J. Hydropow. Dams, **5**, pp. 102–106.
[3] Shi, Q., 2004, "Abnormal Noise and Runner Cracks Caused by von Karman Vortex Shedding: A Case Study in Dachaoshan Hydroelectric Project, Proceedings of the 22nd IAHR Symposium on Hydraulic Machinery and Systems," Stockholm, Sweden, Paper No. A13-2:1–12.
[4] Williamson, C. H. K, and Roshko, A., 1998, "Vortex Formation in the Wake of an Oscillating Cylinder," J. Fluids Struct., **2**, pp. 355–381.
[5] Gerrard, J. H., 1978, "Wakes of Cylindrical Bluff Bodies at Low Reynolds-Number," Philos. Trans. R. Soc. London, Ser. A, **288**(1354), pp. 351–382.
[6] Tritton, D. J., 1959, "Experiments on the Flow Past a Circular Cylinder at Low Reynolds Number," J. Fluid Mech., **6**, pp. 547–567.
[7] Slaouti, A., and Gerrard, J. H., 1981, "An Experimental Investigation of the End Effects on the Wake of a Circular Cylinder Towed Through Water at Low Reynolds Number," J. Fluid Mech., **112**, pp. 297–314.
[8] Gerich, D., and Eckelmann, H., 1982, "Influence of End Plates and Free Ends on the Shedding Frequency of Circular Cylinders," J. Fluid Mech., **122**, pp. 109–122.

[9] Prasad, A., and Williamson, C. H. K., 1997, "The Instability of the Shear Layer Separating From a Bluff Body," J. Fluid Mech., **333**, pp. 375–402.
[10] Williamson, C. H. K., 1988, "Defining a Universal and Continuous Strouhal-Reynolds Number Relationship for the Laminar Vortex Shedding of a Circular Cylinder," Phys. Fluids, **31**, pp. 2742–2744.
[11] Rockwell, D., 1998, "Vortex-Body Interactions," Annu. Rev. Fluid Mech., **30**, pp. 199–229.
[12] Williamson, C. H. K., and Govardhan, R., 2004, "Vortex-Induced Vibrations," Annu. Rev. Fluid Mech., **36**, pp. 413–455.
[13] Feng, C. C., 1968, "The Measurement of Vortex-Induced Effects in Flow Past Stationary and Oscillating Circular and D-Section Cylinders," MS thesis, Univ. Br. Columbia, Vancouver, Canada.
[14] Davies, M. E., 1975, "A Comparison of the Wake Structure of a Stationary and Oscillating Bluff Body, Using a Conditional Averaging Technique," J. Fluid Mech., **75**, pp. 209–231.
[15] Gilbert, S, and Sigurdson, L., 2005, "Hydrogen Bubble Flow Visualization of a Self-Oscillating Cylinder Vortex Street 'Void'," Phys. Fluids, **17** p. 091104.
[16] Sridhar, G., and Katz, J., 1999, "Effect of Entrained Bubbles on the Structure of Vortex Rings," J. Fluid Mech., **397**, pp. 171–202.
[17] Arndt, R. E. A., and Keller, A. P., 1992, "Water Quality Effects on Cavitation Inception in a Trailing Vortex," J. Fluids Eng., **114**, pp. 430–438.
[18] Young, J., and Holl, J., 1966, "Effects of Cavitation on Periodic Wakes Behind Symmetric Wedges," J. Basic Eng., **88**, pp. 163–176.
[19] Dupont, P., Avellan, F., and Wegner, M., 1987, "Wake Flow Analysis for a Hydrofoil With and Without Hydroelastic Lock-In," Proc. Int. Conf. on Flow Induced Vibrations, BHRA, Bowness-on-Windermere, England.
[20] Belahadji, B., Franc, J. P., and Michel, J. M., 1995, "Cavitation in the Rotational Structures of a Turbulent Wake," J. Fluid Mech., **287**, pp. 383–403.
[21] Arndt, R. E. A., 1976, "Semi-Empirical Analysis of Cavitation in the Wake of a Sharp-Edged Disk," ASME J. Fluids Eng., **90**, pp. 560–562.
[22] Avellan, F., Henry, P., and Ryhming, I. L., 1987, "A New High Speed Cavitation Tunnel," ASME Winter Annual Meeting, Boston, MA, Vol. 57, pp. 49–60.
[23] Gerrard, J. H., 1966, "The Mechanics of the Formation Region of Vortices Behind Bluff Bodies," J. Fluid Mech., **25**, pp. 401–413.

Analysis of Thermal Effects in a Cavitating Inducer Using Rayleigh Equation

Jean-Pierre Franc
LEGI, BP 53,
38041 Grenoble Cedex 9, France
e-mail: jean-pierre.franc@hmg.inpg.fr

Christian Pellone
LEGI, BP 53,
38041 Grenoble Cedex 9, France
e-mail: christian.pellone@hmg.inpg.fr

A simple model based on the resolution of Rayleigh equation is used to analyze thermal effects in cavitation. Two different assumptions are considered for the modeling of heat transfer toward the liquid/vapor interface. One is based upon a convective type approach using a convection heat transfer coefficient or the equivalent Nusselt number. The other one is based upon the resolution of the heat diffusion equation in the liquid surrounding the bubble. This conductive-type approach requires one to specify the eddy thermal diffusivity or the equivalent Peclet number. Both models are applied to a cavitating inducer. The basic pressure distribution on the blades is determined from a potential flow computation in a two-dimensional cascade of flat plates. The sheet cavity, which develops from the leading edge, is approximated by the envelope of a hemispherical bubble traveling on the suction side of the blade. Cavity shape and temperature distribution predicted by both models are compared. The evolutions of cavity length with the cavitation number for cold water (without thermal effects) and for Refrigerant 114 at two different temperatures is compared to experimental data. Such a simple model is easy to apply and appears to be quite pertinent for the analysis of thermal effects in a cavitating inducer. [DOI: 10.1115/1.2746919]

1 Introduction

In a number of fluids, the development of cavitation goes with significant thermal effects. The so-called thermodynamic effect has been extensively studied since the early works of Stahl et al. [1] and Stepanoff [2]. The phenomenon is characterized, in particular, by a temperature drop inside two-phase regions. It is due to the latent heat of vaporization, which is taken to the liquid surrounding the cavitating zone whose temperature is then lowered.

The effect is negligible in water at room temperature but may be significant at a higher temperature or in other liquids as, e.g., cryogenic fluids used for the propulsion of space rockets. Several parameters have been introduced to estimate the importance of thermal effects in cavitating flows. Stepanoff [2] defined a characteristic temperature drop by

$$\Delta T^* = \frac{\rho_v L}{\rho_\ell c_{p\ell}} \tag{1}$$

This is the temperature drop to be applied to a unit volume of liquid to supply the latent heat required for the vaporization of a unit volume of vapor. Experiments show that this parameter is a relevant order of magnitude of the temperature drop in cavitating flows. For water at room temperature, it is quite small and equal to 0.01 K, whereas it exceeds 1 K for liquid hydrogen at 22 K. This big difference demonstrates the major influence of the liquid properties on the phenomenon. The well-known B factor of Stepanoff [2] is the nondimensional parameter:

$$B = \frac{\Delta T}{\Delta T^*} \tag{2}$$

where ΔT is the actual temperature drop in the cavitating flow.

Using the slope dp_v/dT of the vapor pressure curve, a characteristic pressure difference can be built on the basis of the previous characteristic temperature difference ΔT^*:

$$\Delta p_v^* = \frac{dp_v}{dT}\Delta T^* \tag{3}$$

This is the drop in vapor pressure associated with the drop in temperature ΔT^*. Since ΔT^* is a relevant order of magnitude of the temperature drop, Δp_v^* can be considered as a relevant order of magnitude of the pressure drop inside the cavities. This is true as long as the thermodynamic equilibrium condition is achieved, which is generally the case. Nonequilibrium is expected only at the very final stage of collapse when the kinetics of phase change can become a limiting factor because of the very high velocity of the interface.

Brennen [3,4] suggests the use of the thermodynamic parameter

$$\Sigma = \frac{\Delta p_v^*}{\rho_\ell \sqrt{\alpha_\ell}} \tag{4}$$

to measure the importance of thermal effects in cavitating flows. The Σ parameter was derived from the analysis of the dynamics of a single bubble with the assumption that heat transfer to the interface is provided by conduction through the surrounding liquid. The thickness of the thermal boundary layer then plays an important role and accounts for the presence of the square root of the liquid thermal diffusivity α_ℓ. The Σ parameter has the units $\mathrm{m/s^{3/2}}$.

Considering the case of a sheet cavity and still assuming heat transfer to the cavity interface by conduction through the neighboring liquid, Kato [5] introduced a similar parameter defined by

$$\alpha = \sqrt{\frac{\rho_\ell}{\rho_v}}\Sigma \tag{5}$$

The importance of thermal effects increases with α and Σ. From a systematic analysis of Hord's experiments [6], Kato [5] showed a good correlation of the nondimensional pressure drop $2\Delta p_v/\rho_\ell V^2$ inside the cavity with the nondimensional parameter $\alpha\sqrt{c/V^3}$, where c and V are a reference length scale and a reference velocity scale of the flow.

It is of major concern to observe that, in such models based on a well-defined interface between the liquid and either a cavitation bubble or a sheet cavity, heat transfer by conduction characterized

Contributed by the Fluids Engineering Division of ASME for publication in the JOURNAL OF FLUIDS ENGINEERING. Manuscript received October 31, 2006; final manuscript received January 31, 2007. Review conducted by Joseph Katz.

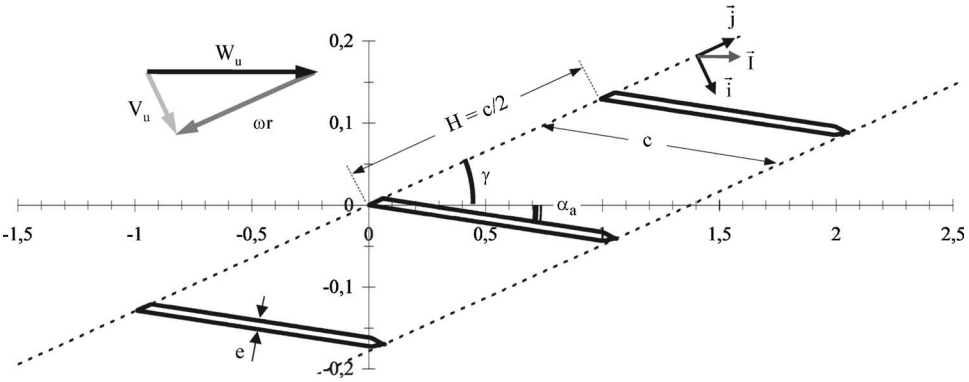

Fig. 1 Scheme of the 2D cascade (vertical scale has been expanded)

by the classical liquid thermal diffusivity α_ℓ is far too small to account for the measured values of the temperature drop. For a correct prediction, Kato [5] and Watanabe et al. [7] have shown that the liquid thermal diffusivity should be multiplied by an amplifying coefficient ε of the order of 8000 [7] up to 10^5 [5]. This large value is supposed to account for the enhancement of heat transfer due to both turbulence and an increase in the interface area probably due to the small-scale instabilities of the interface. The importance of the so-called interface roughness was confirmed by Fruman et al. [8,9] on the basis of Billet's entrainment theory [10–12].

Besides interface models, two-phase models have been developed. The two-phase mixture is generally considered as a pseudofluid, which obeys the Navier–Stokes equations. A suitable constitutive equation for the mixture as the barotropic law can be specified (Rapposelli et d'Agostino [13], Rolland et al. [14]). Another option consists in solving an additional transport equation for the vapor phase with a source term modeling the cavitation phenomenon (see, e.g., Tani and Nagashima [15] and Hosangadi and Ahuja [16–18]). The vaporization or condensation process can be modeled either by ad hoc equations as in Ref. [16] or by seeding the flow field with microbubbles and computing their evolution using the Rayleigh–Plesset equation, as proposed originally by Kubota et al. [19] (see, e.g., Singhal et al. [20]). To address thermal effects, it is necessary to solve the energy equation for the mixture together with the mass and momentum conservation equations. These equations are essentially coupled through the dependence of the vapor pressure with the temperature.

For interface models, the volume of liquid surrounding vapor is almost infinite and heat transfer is supposed to be limited by the growth rate of the thermal boundary layer. Conversely, two-phase models assume an intimate mixing of liquid and vapor and the volume of liquid surrounding a given bubble is naturally limited by the surrounding bubbles. Hence, thermal effects are essentially regulated by the limited volume of liquid able to supply the heat for vaporization and not by heat diffusion as for interface models. Thermal effects are then basically controlled by the evolution of void fraction without any influence of the liquid thermal diffusivity.

The difference between both types of models can easily be demonstrated by comparing basic expressions of the B factor. In the case of a bubble whose radius grows from 0 to R during time t, the B factor is given by (see, e.g., Ref. [21])

$$B \approx \frac{R}{\sqrt{\alpha_\ell t}} \tag{6}$$

On the other hand, for a two-phase mixture of void fraction α_v, the heat conservation equation leads to (see Ref. [22]):

$$B \approx \frac{\alpha_v}{1-\alpha_v} \tag{7}$$

In the case of Eq. (6), thermal effects depend upon the liquid thermal diffusivity, which is obviously not the case for Eq. (7). In addition, Eq. (7) becomes singular when the void fraction approaches unity, which shows that the two-phase model is valid for rather dilute mixtures but fails when the cavitating region becomes pure vapor. If so, it is necessary to switch to interface-type models. Hence, it is of primary importance, in practice, to recognize the type of cavities in order to be able to identify the appropriate physical mechanism, which actually limits the supply of heat necessary for vaporization.

The present paper is devoted to an analysis of thermal effects on the basis of the Rayleigh equation. It belongs to the class of interface models for which heat transfer through the thermal boundary layer is supposed to be the limiting physical phenomenon. The present analysis is very similar to that conducted by Watanabe et al. [7] except that it considers bubble cavitation instead of sheet cavitation. It is also applied to the case of a cavitating inducer of a space rocket turbopump investigated experimentally by Franc et al. [22].

The analysis comprises two successive steps. First, the pressure distribution in a two-dimensional (2D) noncavitating cascade is computed using a boundary element method. Second, the Rayleigh equation is solved using the previous pressure distribution in order to compute the evolution of a cavitation bubble on the blade suction side.

The original aspect of the present contribution essentially lies in the thermal term added to the Rayleigh equation in order to account for thermal aspects. Two different forms based either on a convective- or a conductive-type approach are considered. Both approaches are evaluated by comparison with the experimental results [22]. The main objective is to evaluate whether this kind of simple model is able to account for the trends observed experimentally as the increase of the B factor with the cavity length.

In the present approach, the sheet cavity observed experimentally is compared to the computed envelope of a hemispherical bubble, which grows and collapses on the suction side of the blades. This kind of simple model obviously suffers from limitations. One is the lack of any feedback of cavitation on the pressure distribution since the bubble evolution is computed using the noncavitating pressure distribution. The 2D nature of the computation of the pressure distribution is also a limitation since inducers may be subjected to backflow, which may significantly change angles of attack. Nevertheless, the present work supplies a theoretical support for the physical interpretation and understanding of experimental results.

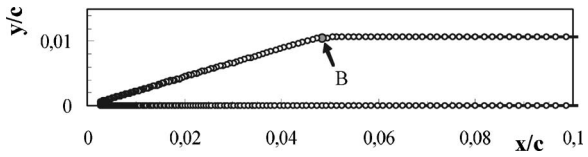

Fig. 2 Close view of the blade leading edge

2 Pressure Distribution Computation

The inducer is represented by a 2D cascade of flat plates, as shown in Fig. 1. This 2D configuration is obtained from a cylindrical section of the inducer at radius r. Enlargements of the leading edge and trailing edge are shown in Figs. 2 and 3. Calculation of the bubble evolution was started at the back end of the bevel, from point B where the pressure is minimum (see also Fig. 4). This location corresponds to the observed point of detachment of cavities. As for the trailing edge, its shape was chosen in order to allow a smooth detachment of the flow in a direction parallel to the blades.

The relative thickness of the blade is about 1% and the solidity c/H is 2. The incidence angle α_a and the stagger angle γ of the cascade are such that the blade bevel is parallel to the **j** direction of the grid. The inlet velocity $V_u\mathbf{i}$ is supposed perpendicular to the grid (no prerotation). At upstream infinity, the reference relative velocity is

$$W_u = \sqrt{V_u^2 + \omega^2 r^2} \tag{8}$$

where ω is the angular speed of rotation. Any radial flow normal to the cylinder surface is ignored and the flow is then supposed to be 2D in the $(\mathbf{i},\mathbf{j})$ plane. In addition, it is assumed incompressible, irrotational, and inviscid. Under these assumptions, the pressure coefficient is given by

$$C_p = 1 - \frac{W^2 - \omega^2 r^2}{W_u^2 - \omega^2 r^2} \tag{9}$$

The pressure distribution on the blade is computed using the boundary element method. A double distribution of sources and vortices (σ^*, γ^*) is distributed on the blade surface with the space periodicity H in the **j** direction to take into account the infinite series of blades. This distribution is chosen so that the relative velocity at upstream infinity is in the **I** direction. The boundary conditions consist in a zero normal velocity on the blade (slip condition) and the continuity of pressure at the trailing edge. Conservation of flowrate through the inducer requires that the component of the relative velocity $\mathbf{W}\cdot\mathbf{i}$ is the same at upstream and downstream infinity. The flow at downstream infinity is deviated with an angle ϕ given by

$$\tan\phi = \frac{(\sin\gamma)\oint_{\text{blade}} \gamma^* dx}{HW_u + (\cos\gamma)\oint_{\text{blade}} \gamma^* dx} \tag{10}$$

The double distribution used here introduces more unknowns than equations to be solved. Additional conditions are imposed in order to minimize the discretization errors. This allows us to compute, with an improved accuracy, the pressure coefficient on blades of small relative thickness.

The computational method has been validated by comparison with the results obtained by Watanabe et al. [7]. Both computations agree fairly well, as shown in Fig. 4. The differences, which are observed particularly at the leading edge near the bevel, are due to the nonlinear nature of the present computation contrary to Ref. [7], which assumes blades of zero thickness.

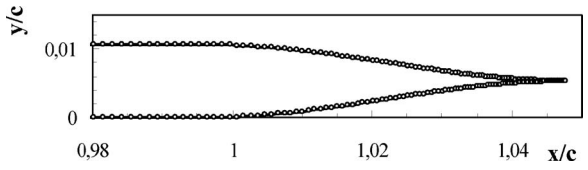

Fig. 3 Close view of the blade trailing edge

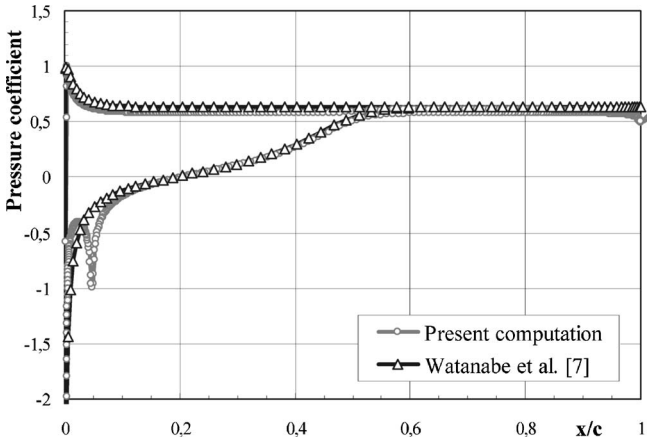

Fig. 4 Pressure distribution on the blades. Comparison between the present results and that of Watanabe et al. (Ref. [7]).

3 Basic Equations

3.1 Nondimensional Form of the Rayleigh Equation. Once the pressure distribution has been computed, Rayleigh equation

$$R\frac{d^2R}{dt^2} + \frac{3}{2}\left(\frac{dR}{dt}\right)^2 = \frac{p_v(T_c) - p(t)}{\rho_\ell} \tag{11}$$

is solved in order to determine the evolution of the radius R of a bubble traveling on the suction side of the blades. $p(t)$ is the time dependent pressure to which the bubble is subjected as it moves along the blades. The effects of viscosity and gas content, which generally become negligible as soon as the original microbubble becomes a macroscopic cavitation bubble, are disregarded and the present work is focused on the thermodynamic effect. To account for thermal effects, it is necessary to consider in Rayleigh equation the vapor pressure corresponding to the actual temperature T_c inside the bubble, which is different from the liquid temperature T_∞ far from the bubble.

Using the pressure coefficient previously calculated

$$C_p = \frac{p - p_u}{(1/2)\rho_\ell W_u^2} \tag{12}$$

and the usual cavitation number defined on the basis of the vapor pressure at the liquid temperature at infinity $p_v(T_\infty)$

$$\sigma_v = \frac{p_u - p_v(T_\infty)}{(1/2)\rho_\ell W_u^2} \tag{13}$$

Rayleigh equation (11) becomes

$$R\frac{d^2R}{dt^2} + \frac{3}{2}\left(\frac{dR}{dt}\right)^2 = \frac{p_v(T_c) - p_v(T_\infty)}{\rho_\ell} - W_u^2\frac{C_p + \sigma_v}{2} \tag{14}$$

The first term on the right hand side accounts for thermal effects.

The bubble is supposed to travel on the blade with the local fluid velocity $W_u\sqrt{1-C_p}$. Time derivatives in the original Rayleigh equation are then transposed into space derivatives using the following equation:

$$\frac{d}{dt} = W_u\sqrt{1-C_p}\frac{d}{dx} \tag{15}$$

In addition, lengths are made nondimensional using the foil chord length c. Then, Eq. (14) takes the following nondimensional form:

$$[1-C_p]\left[\bar{R}\frac{d^2\bar{R}}{d\bar{x}^2}+\frac{3}{2}\left(\frac{d\bar{R}}{d\bar{x}}\right)^2\right]-\frac{1}{2}\frac{dC_p}{d\bar{x}}\bar{R}\frac{d\bar{R}}{d\bar{x}}+\frac{1}{\rho_\ell W_u^2}\frac{dp_v}{dT}(T_\infty-T_c) = -\frac{C_p+\sigma_v}{2}, \tag{16}$$

where bars denote nondimensional variables.

3.2 Convective Approach. The problem is now to estimate the temperature inside the bubble T_c. Two different approaches are considered. In the present section, heat transfer at the bubble wall is supposed to be of convective nature. In other words, the heat flux at the interface is supposed to be proportional to the temperature difference $T_\infty - T_c$:

$$\varphi = h(T_\infty - T_c) \tag{17}$$

where h is the convection heat transfer coefficient. The validity of the convective approach is open to discussion especially when considering that the bubble is traveling at the same velocity as the liquid. From this viewpoint, the conductive approach considered in Sec. 3.3 might appear more appropriate. Nevertheless, the statement that the heat flux at the bubble wall is proportional to the temperature difference appears physically reasonable. In the absence of any validated correlation applicable to cavitating flows, the heat transfer coefficient is considered here as a tuning parameter.

Under this assumption, the heat balance for the bubble is writen as

$$\frac{d}{dt}\left[\frac{4}{3}\pi R^3\rho_v\right]L = 4\pi R^2 h(T_\infty - T_c) \tag{18}$$

This equation allows us to compute the temperature inside the bubble:

$$T_\infty - T_c = \frac{\rho_v L}{h}\frac{dR}{dt} \tag{19}$$

Equation (19) shows that the thermal effect $\Delta T = T_\infty - T_c$ is proportional to dR/dt. In the growing phase, the bubble temperature is then lower than the liquid temperature and is higher during collapse. Using form (19) of the thermal effect, Rayleigh equation (16) becomes

$$[1-C_p]\left[\bar{R}\ddot{\bar{R}}+\frac{3}{2}\dot{\bar{R}}^2\right]-\frac{1}{2}\dot{C}_p\bar{R}\dot{\bar{R}}+\frac{1}{\mathrm{Nu}}\frac{\Delta p_v^*}{\rho_\ell\alpha_\ell}\tau\sqrt{1-C_p}\dot{\bar{R}} = -\frac{C_p+\sigma_v}{2} \tag{20}$$

where Nu is the Nusselt number defined by

$$\mathrm{Nu} = \frac{hc}{\lambda_\ell} \tag{21}$$

and $\tau = c/W_u$ is the transit time.

According to this approach, the thermodynamic effect introduces an additional term in Rayleigh equation, which is proportional to the bubble growth rate $\dot{\bar{R}}$. The magnitude of thermal effects depends upon the factor:

$$\frac{1}{\mathrm{Nu}}\frac{\Delta p_v^*}{\rho_\ell\alpha_\ell}\tau \tag{22}$$

It is the ratio of two characteristic times, the transit time τ and the following time:

$$\tau_T = \mathrm{Nu}\frac{\rho_\ell\alpha_\ell}{\Delta p_v^*} \tag{23}$$

which can be considered as a thermal time since it essentially contains the information on heat transfer at the interface.

If the thermal time is much larger than the transit time, thermal effects are negligible and Eq. (20) reduces to the usual Rayleigh equation. Conversely, if the thermal time is much smaller than the transit time, thermal effects are predominant. A suitable criterion for estimating the magnitude of thermal effects is then based on the comparison of these two characteristic times. Besides the Nusselt number, the thermal time depends on $\Delta p_v^*/\rho_\ell\alpha_\ell$, which is very similar to Brennen's parameter (4). Equation (20) will be solved to compute the bubble evolution with thermal effects. As already mentioned, the convection heat transfer coefficient or the corresponding nondimensional Nusselt number is a free parameter of the model. We can also imagine correlating the Nusselt number with the Reynolds ($\mathrm{Re} = cW_u\rho_\ell/\mu_\ell$) and Prandtl ($\mathrm{Pr} = \mu_\ell/\alpha_\ell\rho_\ell$) numbers as in traditional convection heat transfer theory, but this has not yet been done for cavitating flows.

Let us observe that Eq. (19) takes the following nondimensional form:

$$B = \frac{\mathrm{Pe}\sqrt{1-C_p}}{\mathrm{Nu}}\dot{\bar{R}} \tag{24}$$

where Pe is the Peclet number (see Eq. (27)).

3.3 Conductive Approach. The second approach tested here is the conductive approach. It requires to solve the heat diffusion equation in the liquid surrounding the bubble. An explicit expression of the bubble wall temperature has been proposed by Plesset and Zwick [23–25] (see also Brennen [3]) under the assumption that the thickness of the thermal boundary layer is much smaller than the bubble radius. The validity of this assumption is evaluated at the end of the present section. If so, bubble wall temperature T_c can be calculated at each instant t by the following expression:

$$B = \frac{T_\infty - T_c}{\Delta T^*} = \frac{1}{\sqrt{\pi\varepsilon\alpha_\ell}}\int_{u=0}^{u=t}\frac{R^2(u)(dR/dt)(u)du}{\sqrt{\int_{v=u}^{v=t}R^4(v)dv}} \tag{25}$$

This equation is the solution of the unsteady heat diffusion problem with a moving spherical boundary. It includes the enhancement coefficient ε discussed in Sec. 1. It is similar to some extent to Eq. (19), although more complicated. Both approaches will be compared in detail in Sec. 4.1.

Using the nondimensional procedure given in Sec. 3.1 and switching to a space dependency rather than a time dependency, Eq. (25) becomes

$$B = \frac{T_\infty - T_c}{\Delta T^*} = \sqrt{\frac{\mathrm{Pe}}{\varepsilon}}J(\bar{x}) \tag{26}$$

where Pe is the Peclet number defined by

$$\mathrm{Pe} = \mathrm{Re}\,\mathrm{Pr} = \frac{W_u c}{\alpha_\ell} \tag{27}$$

and J is the integral

$$J(\bar{x}) = \frac{1}{\sqrt{\pi}}\int_{u=0}^{u=\bar{x}}\frac{\bar{R}^2(u)d\bar{R}/d\bar{x}(u)du}{\sqrt{\int_{v=u}^{v=x}\bar{R}^4(v)/\sqrt{1-C_p}dv}} \tag{28}$$

By introducing expression (26) of the interface temperature into Rayleigh equation (16), we get the final following equation:

$$[1-C_p]\left[\bar{R}\ddot{\bar{R}}+\frac{3}{2}\dot{\bar{R}}^2\right]-\frac{1}{2}\dot{C}_p\bar{R}\dot{\bar{R}}+\frac{\Delta p_v^*}{\rho_\ell W_u^2}\sqrt{\frac{\mathrm{Pe}}{\varepsilon}}J=-\frac{C_p+\sigma_v}{2} \tag{29}$$

When using Brennen's parameter Σ defined in Eq. (4), previous equation takes the equivalent form:

$$[1-C_p]\left[\bar{R}\ddot{\bar{R}}+\frac{3}{2}\dot{\bar{R}}^2\right]-\frac{1}{2}\dot{C}_p\bar{R}\dot{\bar{R}}+\Sigma\sqrt{\frac{c}{W_u^3}}\frac{1}{\sqrt{\varepsilon}}J=-\frac{C_p+\sigma_v}{2} \tag{30}$$

Bubble evolution including thermal effects is obtained by solving Eq. (30) together with Eq. (28). The numerical procedure is presented in Sec. 3.4.

As mentioned previously, the consistency of the approach depends upon the relative order of magnitude of the thermal boundary layer thickness compared to bubble size, which is typically of the order of the chord length. The order of magnitude of the boundary layer thickness is

$$\delta\approx\sqrt{\varepsilon\alpha_\ell\tau} \tag{31}$$

so that

$$\frac{\delta}{c}\approx\frac{\sqrt{\varepsilon}}{\sqrt{\mathrm{Pe}}}=\frac{\sqrt{\varepsilon}}{\sqrt{\mathrm{Re\,Pr}}} \tag{32}$$

A typical value of the Reynolds number for rocket turbopump inducers is 10^6. For Refrigerant 114 considered later in this work, we have $\mathrm{Pr}\cong 5$. A typical value for the amplifying coefficient ε is 10^4 (see Sec. 4). Hence, we have $\delta/c\approx 0.04$ so that the hypothesis of a thin thermal boundary layer compared to the characteristic length scale of the cavities appears appropriate. The larger the ε, the larger the effective thermal diffusivity and the less accurate this hypothesis.

In a few cases and particularly when thermal effects become important, the conductive model presented above may lead to an unrealistic shape of the cavity characterized by oscillations. This effect is generally observed around cavity closure when the bubble starts to collapse, i.e., when the local pressure exceeds the vapor pressure. It is due to the fact that the temperature increases because of condensation as well as the corresponding vapor pressure. If thermal effects are large enough, the vapor pressure may exceed the local pressure. The bubble will then grow again so that the cavity interface oscillates.

To avoid this effect, which is not observed experimentally, it is chosen to set the temperature difference T_c-T_∞ to zero as soon as it becomes positive. This is equivalent to assuming that the bubble temperature cannot exceed the liquid temperature. In other words, it is assumed that heat diffusion is considerably enhanced during the collapse phase so that the temperature becomes uniform almost instantaneously. The instability of the spherical shape together with the splitting of the vapor phase into small scale structures during collapse can justify this assumption. The entire growth phase is not affected by this effect. A similar assumption is made by Watanabe et al. [7], who neglected the heat flux due to condensation near the trailing edge of the cavity, assuming that condensation occurs far downstream of the cascade because of the shedding of vapor structures by the cavity.

For coherence and to make relevant comparisons between the conductive and the convective model, the same assumption of a uniform temperature in the condensation zone is also made for the convective model. The consequence on the temperature distribution in the cavity is clearly visible on Fig. 5(*b*), for instance.

3.4 Numerical Aspects. Equation (20) is a nonlinear differential equation of the second order, whereas Eq. (30) is an integrodifferential equation because of integral (28). To solve these equations, a combination of two Runge–Kutta methods of orders 4 and 5, respectively, is used. The first provides the solution, and the second an estimate of the error. This combination, due to Fehlberg and improved by Kash and Carp [26], allows us to control the error during iterations. Indeed, for a specified tolerance, the order of magnitude of the error is calculated and the integration step is modified so that the precision criterion is satisfied: the step value is increased if the error is too small and decreased if the error is too large. Thus, the integration step is variable and the computing time is considerably reduced while keeping an excellent relative precision (10^{-6}). This method is extended to the resolution of a system of two first order differential equations, using R and dR/dx as unknown functions. In this case, the relative error is simply the maximum value of the two relative errors.

The iterative resolution procedure makes it possible to transform the integrodifferential equation (30) into an ordinary differential equation. Indeed, at the current iteration, integral J is calculated using estimates obtained at the previous iteration.

Mechanical and thermal equilibriums are assumed as initial conditions for the bubble. So, the interface velocity $(dR/dx)_0$ and acceleration $(d^2R/dx^2)_0$ are initially zero, and the temperature is equal to T_∞ and $J_0=0$ (Eq. (25)). To correctly initiate the iterative procedure, a nonzero value of R_0 is required. It has been checked that the subsequent behavior of the bubble is insensitive to the value of its initial radius within a very large range of variation.

Under these assumptions, strictly speaking, Eq. (20) or (30) imposes that $C_{p0}+\sigma_v=0$ at the initial time. The cavity starting point being fixed, this last condition is generally not satisfied, except for the very special case $\sigma_v=-C_{p0}$. Nevertheless, for all values of σ_v, the preceding initial conditions are preserved. Hence, the interface velocity presents a discontinuity at the initial time. The numerical results show that this discontinuity does not affect the resolution of the differential equation.

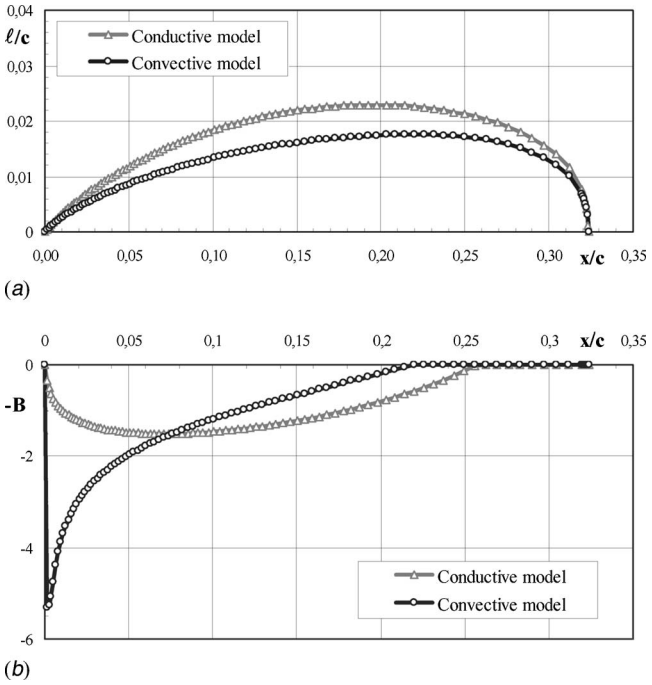

Fig. 5 Comparison between the convective ($\mathrm{Nu}=7.31\times10^6$) and the conductive ($\varepsilon=5\times10^4$) models for the same cavity length. (*a*) cavity shape. (*b*) Temperature distribution (R114 40°C – $\sigma_v=0$).

4 Results and Discussion

4.1 Comparison Between the Convective and the Conductive Model. Cavity shape and temperature distribution obtained by both approaches are compared on Fig. 5. Values of Nusselt number Nu for the convective model and of the ratio ε of the eddy

diffusivity to the molecular one for the conductive model have been chosen so that the cavity length is the same. Figure 5(*b*) shows that temperature distributions are quite different for both cases.

For the convective model, temperature exhibits a sudden drop at the leading edge of the cavity. The temperature depression is maximum there and the temperature increases regularly along the cavity. As shown by Eq. (19), the convective model assumes that the temperature depression is proportional to the bubble growth rate. Since the latter is maximum at the cavity leading edge where pressure is minimum, the temperature depression is also maximum at this location.

For the conductive model, the temperature depression is zero at the cavity leading edge. The temperature inside the cavity first decreases and then increases so that a minimum is observed. This smooth behavior is the consequence of the solution of the heat diffusion equation in the liquid, which does not allow any jump in temperature.

Because of the large temperature drop at the cavity leading edge, the initial bubble growth rate is smaller for the convective approach. In the conductive case, it is the same as that without thermal effects (see Fig. 9), since temperature depression is initially zero. As a consequence, the cavity is somewhat thinner for the convective model.

The maximum cavity thickness is located closer to the cavity trailing edge for the convective approach (see Fig. 5(*a*)). Its location corresponds exactly to the point where the B factor vanishes, still because of the proportionality between B and $\dot{R}$. For the conductive model, the relationship between B and $\dot{R}$ is more complicated (see Eq. (25)), since the cavity temperature at any time depends upon the whole temperature history of the surrounding liquid. As a consequence, the conductive model predicts a shift between the location of maximum cavity thickness and the point where the B factor vanishes, as shown in Fig. 5(*a*).

It is difficult to know which model is more appropriate. On the one hand, the instantaneous initial jump in temperature predicted by the convective model may be considered as unrealistic from a physical viewpoint. On the other hand, experimental results (see Hord [6] and Fruman et al. [8]) tend to prove that the temperature depression is maximum at the cavity leading edge and decreases regularly downstream. However, the maximum observed experimentally is usually not as pronounced as the convective model predicts and measured temperature profiles are generally rather flat just downstream of the cavity detachment. On the whole, the conductive model may be preferred although no definite conclusion can be drawn from the present work. It will be shown in next section that the differences between both models decrease when thermal effects increase and that both models tend toward the same limit for large enough thermal effects.

4.2 Effect of Nu or ε on Thermal Effects. Both models include a free parameter, which controls the amplitude of thermal effects. The tuning parameter is the Nusselt number for the convective approach and the ratio ε for the conductive one. Thermal effects are zero when Nu or ε are infinite and increase with decreasing Nu or ε.

The similar influence of Nu and ε can be understood by comparing both models. The heat flux to the interface is given by

$$q = h \cdot \Delta T \tag{33}$$

for the convective model, and by approximately

$$q \approx \lambda_l \cdot \frac{\Delta T}{\delta} \tag{34}$$

for the conductive one since $\Delta T/\delta$ is the order of magnitude of the temperature gradient.

The identification of forms (33) and (34) of the heat flux together with the estimate (31) of the boundary layer thickness leads to the following nondimensional relation:

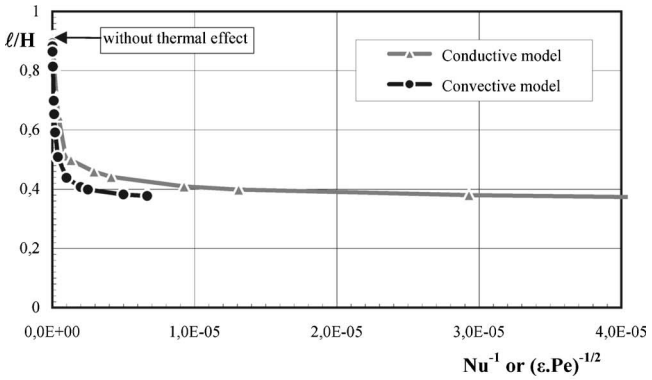

(*a*)

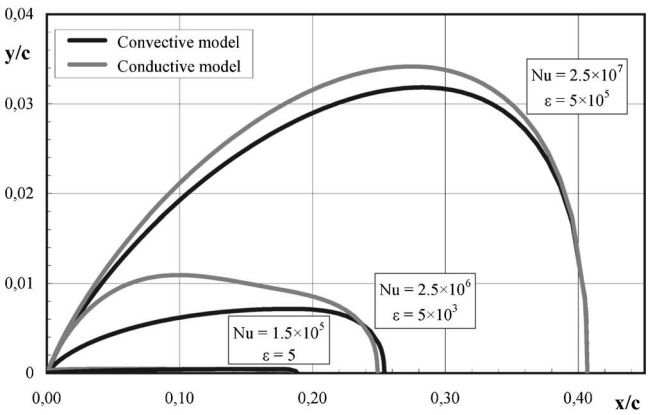

(*b*)

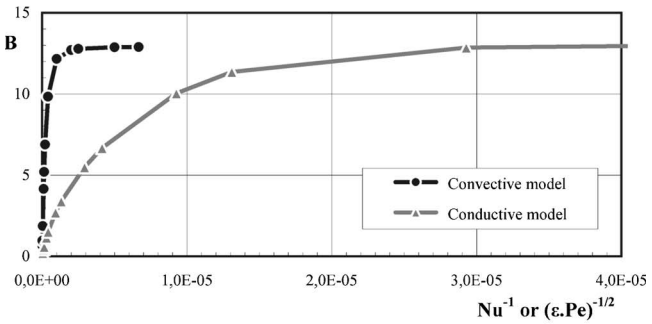

(*c*)

Fig. 6 Effect of Nu (convective model) or ε (conductive model) on (*a*) cavity length, (*b*) cavity shape, and (*c*) maximum B factor (R114 40°C – σ_v=0).

$$\mathrm{Nu} \approx \sqrt{\varepsilon \mathrm{Pe}} \tag{35}$$

This equation suggests a link between the conductive and the convective models. To some extent, it can be expected that the influence of the Nusselt number in the convective model is similar to that of $\sqrt{\varepsilon \mathrm{Pe}}$ for the conductive one. Figure 6(*a*) confirms that the variations of cavity length with Nu and $\sqrt{\varepsilon \mathrm{Pe}}$ for the convective and the conductive model, respectively, are comparable. When thermal effects are increased, i.e., when either Nu or $\sqrt{\varepsilon \mathrm{Pe}}$ are decreased, cavity length decreases in a similar way. Moreover, both models predict the same minimum cavity length for very large thermal effects.

This minimum cavity length is not zero. However, Fig. 6(*b*) indicates, and detailed computations confirm, that the cavity thickness as well as the cavity volume comes to zero when thermal effects are increased. The bubble growth rate $\dot{R}$ together with $\ddot{R}$

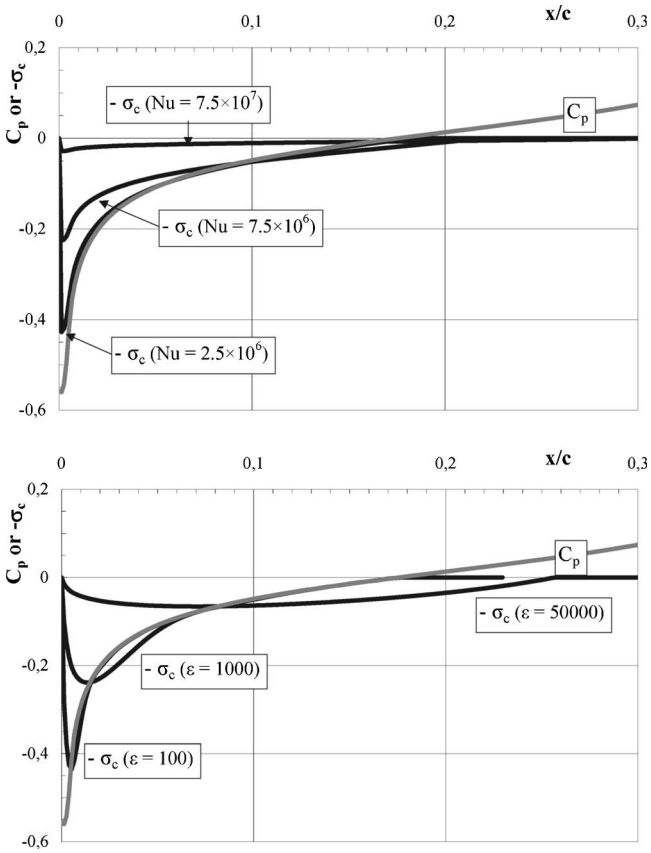

Fig. 7 Effect of increasing thermal effects on the distribution of the cavitation number σ_c based on the vapor pressure at the local cavity temperature $p_v(T_c)$. Comparison with the pressure coefficient distribution (R114 40°C – σ_v=0).

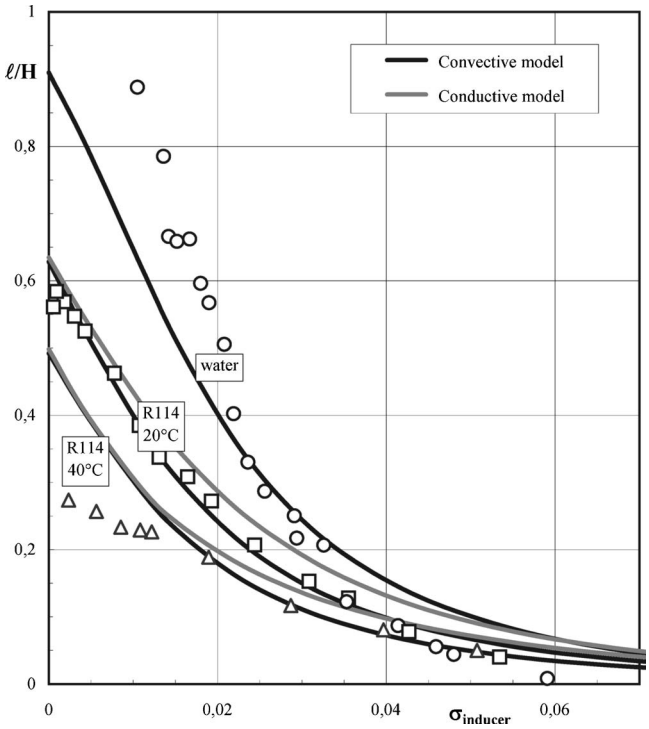

Fig. 8 Cavity length versus cavitation number. Comparison between computation and experiments (Ref. [22]) for cold water and R114 at two different temperatures (20 and 40°C). Cavity length is made nondimensional using blade spacing *H* (convective model, Nu=2.085×10^6; conductive model, ε=5000).

also vanishes. Then, the inertial term on the left hand side of Rayleigh equation (11) tends to zero. As a consequence, the right hand side term should also vanish. This implies that, whatever the thermal model may be the vapor pressure $p_v(T_c)$ based on the actual cavity temperature T_c tends toward the local pressure at any point along the cavity. This is confirmed on Fig. 7, which clearly shows that the opposite of the cavitation number $-\sigma_c$ based on the actual cavity pressure approaches everywhere the pressure coefficient C_p when thermal effects are increased. In the limit case corresponding to the suppression of cavitation by thermal effects, the temperature distribution inside the cavity is determined only by the pressure distribution on the blade and the vapor pressure curve of the fluid. In particular, the maximum value of the *B* factor is independent of the model, as shown by Fig. 6(*c*), and determined by the minimum pressure $p_{\min}$ on the blade. The minimum value of the temperature inside the cavity $T_{c\ \min}$ is determined by $p_v(T_{c\ \min})=p_{\min}$.

The existence of a minimum value of the cavity length when thermal effects become predominant can be qualitatively understood on the basis of the convective model. The limit shape of the cavity is given by the solution of Rayleigh equation (20) in which the inertial terms are neglected as previously mentioned. This simplified equation writes

$$\dot{\bar{R}} \cong -\frac{\tau_T}{\tau}\frac{C_p+\sigma_v}{2\sqrt{1-C_p}} \tag{36}$$

Since

$$\int_0^{\ell} \dot{R}dx = 0 \tag{37}$$

the minimum cavity length ℓ is determined by the following equation:

$$\int_0^{\ell} \frac{C_p+\sigma_v}{\sqrt{1-C_p}}dx = 0 \tag{38}$$

It depends only upon the pressure distribution and the cavitation number. In practice, the situation is more complicated since the B factor is forced to zero in the condensation region, where Eq. (36) is then no longer valid. The situation is even more complex in the conductive case for which equations are much more complicated. Anyway, the previous simplified argument makes the idea of a minimum cavity length quite understandable when thermal effects are increased even though an exact equation for the quantitative prediction of this minimum cavity length could not be derived.

4.3 Comparison With Experiments. Figure 8 presents the evolution of cavity length with the cavitation number for water and Refrigerant 114. The cavitation number plotted here is the inducer cavitation number σ_{inducer}. It is deduced from the cavitation number of the 2D cascade σ defined in Eq. (13) by the following relation:

$$\frac{\sigma_{\text{inducer}}}{\sigma} \cong \frac{1}{2}\left[\frac{r}{R}\right]^2 \tag{39}$$

where r is the local radius between hub and casing where the 2D cascade is considered and R is the inducer peripheral radius used as reference length scale for the computation of the inducer cavitation number.

In the case of water, i.e., without thermal effects, the predicted curve $\ell(\sigma)$ is in reasonable agreement with experiments. Because

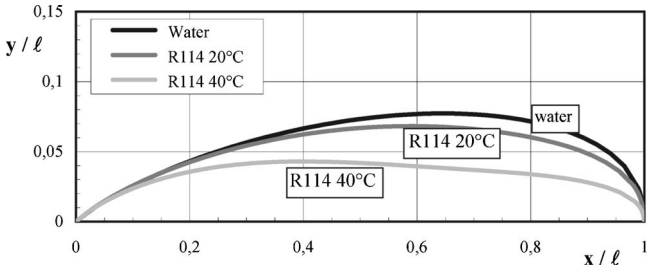

Fig. 9 Influence of thermodynamic effect on the shape of the cavity. Results for water and R114 at two different temperatures (20 and 40°C) are compared. For the three cases, the cavity length is kept constant $\lambda H \equiv 0.5$ (conductive model, $\varepsilon = 5000$).

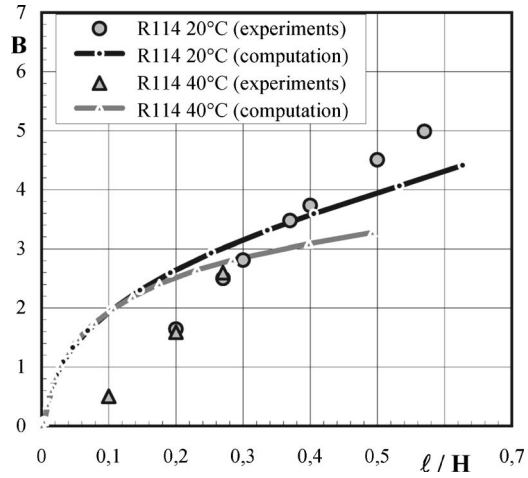

Fig. 10 *B* factor versus cavity length for $\varepsilon = 5000$. Comparison between computation by the conductive model and experiments (Ref. [22]) for R114 at two different temperatures (20 and 40°C). Cavity length is made nondimensional using blade spacing *H*. The plotted value of *B* corresponds to maximum temperature depression.

of several shortcuts in the modeling mentioned in Sec. 1, together with the oversimplification of the real shape of the inducer blades by flat plates, discrepancies are unavoidable. However, they are not prejudicial to the present discussion, which is focused on thermodynamic effect.

The influence of thermal effects computed from both models on cavity length $\ell(\sigma)$ is shown in Fig. 8 for R114 at two different temperatures (20 and 40°C). The computation was conducted with the value $\varepsilon = 5000$ for the conductive model. As for the convective one, the Nusselt number was adjusted to give the same cavity length as the conductive model in the particular case $\sigma_{\text{inducer}} = 0$ for R114 at 20°C. This value of the Nusselt number (2.085×10^6) was then kept constant for all computations including at 40°C.

The comparison of experimental and computational results shows that, with these values of ε and Nu, both models lead to a reduction in cavity length due to the thermal effects of the same order of magnitude as that observed experimentally. Both models can then be considered as acceptable for the modeling of thermal effects although further computations are required for an advanced validation. In particular, the choice of the Nusselt number or the ε parameter remains an open question. The use of a specific correlation between Nusselt number and Reynolds and Prandtl numbers as for classical convection would make the method predictive and give a basis for transposition of experimental results to other fluids and/or other operating conditions.

Figure 9 presents a comparison of cavity shapes obtained with the conductive model, in water (without thermal effects) and in Refrigerant 114 for two different temperatures. For each computation, the σ value was adjusted in order to keep the cavity length approximately constant. As already observed, the cavity becomes thinner as thermal effects increase. This is due to a decrease in the bubble growth rate (and also in the collapse rate). Similarly, Ahuja and Hosangadi [16] noticed differences in the cavity content computed from their two-phase model. They report that the cavity becomes more porous and frothy as thermal effects increase as it can reasonably be expected assuming a smaller growth rate due to thermal effects.

From Fig. 9, it can be concluded that there is no similarity in cavity shape when the amplitude of thermal effects changes. Strictly speaking, cavities with and without thermodynamic effect are not similar as well as cavities for the same fluid but at two different temperatures. If thermal effects are not negligible, exact scaling requires the conservation of an additional parameter, characterizing thermal effects (as $\Sigma\sqrt{c/V^3}$ introduced in Sec. 1) in addition to the usual σ scaling law. Results can be transposed rigorously only if such an additional scaling law is satisfied. The same conclusion holds for the temperature distribution inside the cavity which cannot be transposed from water to R114 neither between two different temperatures in R114.

The computed maximum temperature drop inside the cavity is plotted as a function of cavity length on Fig. 10 and compared to the experimental results. The experimental procedure for computing the *B* factor consisted in determining the equivalent vapor pressure drop (and so the corresponding temperature drop), which would lead to the observed reduction in cavity length in comparison with reference tests in cold water [22]. In the absence of any direct measurement of the temperature distribution inside the cavities, this experimental procedure based on visualizations is the only way to get a practical estimate of the temperature depression in the rotating machinery and make a possible comparison with computational results.

The predicted temperature depression increases with cavity length, as shown by experiments. The conductive approach predicts a rapid increase in the *B* factor for short cavities, whereas the experimental trend is an almost linear increase of the *B* factor with cavity length over the whole range of variation of cavity length investigated experimentally. As for the influence of the fluid temperature on thermal effects, the present approach appears to be in reasonable agreement with experiments, since it predicts a negligible influence of the fluid temperature on the nondimensional temperature depression *B* at least for small enough cavities as observed experimentally.

The conductive model is suitable for a comparison with experimental data in terms of *B* factor since the temperature distribution in the cavity is rather flat (see Fig. 5). The minimum temperature can then be considered as representative of a kind of mean cavity temperature as determined experimentally from visualizations of cavitation extent. This is not the case for the convective approach because of the sudden jump in temperature at the cavity leading edge (see Fig. 5). The temperature is far from being uniform and the comparison with experiments in terms of *B* factor is difficult. The mean cavity temperature, for example, proved to be inadequate for the comparison. Nevertheless, it has to be noticed that the experimental evolution of the *B* factor with cavity length shown in Fig. 10 was deduced from the $\ell(\sigma)$ curves presented in Fig. 8 and then contains basically the same information. Hence, in the absence of direct measurements of temperature inside the cavities, it seems better to base the confrontation of computational and experimental results on the curves $\ell(\sigma)$ rather than $B(\ell)$.

5 Concluding Remarks

The present work is devoted to an analysis of thermal effects in a cavitating inducer. The rotating machinery is modeled by a 2D cascade of flat plates. The potential flow is computed using a

nonlinear approach based on the boundary element method. The development of cavitation is predicted by solving Rayleigh equation using the pressure distribution deduced from the fully wetted flow computation. The interface of the sheet cavity is approximated by the envelope of a hemispherical bubble traveling on the suction side of the blades. Thermal effects in the Rayleigh equation are taken into account by considering the vapor pressure at the actual bubble temperature T_c, which is different from the liquid temperature T_∞ far from the bubble.

Two different approaches are evaluated to model heat transfer at the bubble wall and compute the cavity temperature T_c. In the convective approach, the heat flux is supposed to be proportional to the temperature difference $\Delta T = T_\infty - T_c$. The amplitude of thermal effects is controlled by the magnitude of the convective heat transfer coefficient or the corresponding nondimensional Nusselt number. The second approach is based upon the resolution of the heat diffusion equation in the liquid surrounding the bubble. For this conductive-type model, thermal effects are controlled by the ratio ε of the eddy thermal diffusivity to the liquid molecular thermal diffusivity.

The main conclusions of the present work are the following.

(1) The convective model predicts a sudden drop in temperature at the cavity leading edge followed by a gradual increase up to T_∞. For the conductive model, the temperature decreases smoothly from T_∞ at cavity detachment, and exhibits a minimum before gradually increasing to T_∞. Such differences in temperature distributions induce differences in cavity shapes. The convective approach predicts a thinner cavity and the location of maximum thickness is also different.
(2) Thermal effects are increased by decreasing either the Nusselt number for the convective model or the ε heat transfer enhancement factor for the conductive one. Cavity length decreases and reaches a minimum value, which is the same for both models but which is not zero. The cavity thickness also decreases but tends toward zero. Both models tend toward the same solution when thermal effects are predominant. This solution corresponds to the suppression of cavitation by thermal effects, which is achieved by a local vapor pressure $p_v(T_c)$ equal everywhere to the local pressure on the blade.
(3) The evolution of cavity length with cavitation number is compared to experimental data obtained for an inducer [22] in the case of cold water (i.e., without thermal effect) and R114, which exhibits a significant thermal delay at 20 and 40°C. On the whole, both models lead to an acceptable reduction in cavity length as compared to experiments when the Nusselt number or the eddy thermal diffusivity is kept constant.

Such a simple model based on a 2D potential flow computation coupled to the resolution of the Rayleigh equation presents clear limitations due to simplifying assumptions. However, this work shows that they are easy to run and can supply a support for the interpretation of experimental data relative to thermal delays, in particular, in inducers. They can also help in the prediction of basic trends following changes in fluid, operating conditions and geometry.

Acknowledgment

This research was supported by CNES/SNECMA (Contract No. 2005-015-I). The authors are particularly grateful to H. Horiguchi and Y. Tsujimoto for their help in the validation of the potential flow computation and to B. Chanut for his contribution to this work.

Nomenclature

B = B factor of Stepanoff (Eq. (2))
c = chord length of the blade
C_p = pressure coefficient
$c_{p\ell}$ = liquid heat capacity
e = blade thickness
h = convection heat transfer coefficient
ℓ = cavity length
L = latent heat of vaporization
Nu = Nusselt number based on chord length (Eq. (21))
p = pressure
p_u = reference upstream pressure
p_v = vapor pressure
Pe = Peclet number (Eq. (27))
Pr = Prandtl number
R = bubble radius
$\bar{R}$ = nondimensional bubble radius R/c
Re = Reynolds number based on chord length
t = time
T = temperature
T_c = local temperature in the cavity
T_∞ = liquid temperature at infinity
V = flow velocity
V_u = upstream flow velocity
W = relative flow velocity
W_u = upstream relative flow velocity
x = curvilinear abscissa on the blade
$\bar{x}$ = nondimensional distance x/c
α = Kato's thermodynamic parameter (Eq. (5))
α_a = angle of attack
α_ℓ = thermal diffusivity of the liquid
α_t = turbulent thermal diffusivity
α_v = void fraction
δ = thermal boundary layer thickness
Δp_v^* = characteristic vapor pressure drop (Eq. (3))
ΔT = temperature drop in the cavitating flow $T_\infty - T_c$
ΔT^* = characteristic temperature drop (Eq. (1))
ε = heat transfer enhancement coefficient α_t/α_ℓ or λ_t/λ_ℓ
λ_ℓ = thermal conductivity of the liquid
λ_t = turbulent thermal conductivity
μ_ℓ = water molecular viscosity
ρ_v = vapor density
ρ_ℓ = liquid density
Σ = Brennen's thermodynamic parameter (Eq. (4))
σ_c = local cavitation number based on $p_v(T_c)$
σ_v = cavitation number (Eq. (10))
τ = transit time c/W

References

[1] Stahl, H. A., Stepanoff, A. J., and Phillipsburg, N. J., 1956, "Thermodynamic Aspects of Cavitation in Centrifugal Pumps," ASME J. Basic Eng., November 1956, pp. 1691–1693.
[2] Stepanoff, A. J., 1964, "Cavitation Properties of Liquids," J. Eng. Power, pp. 195–200.
[3] Brennen, C. E., 1995, *Cavitation and Bubble Dynamics*, Oxford University Press, New york.
[4] Brennen, C. E., 1994, *Hydrodynamics of Pumps*, Oxford University Press, New Yark.
[5] Kato, H., 1984, "*Thermodynamic Effect on Incipient and Developed Sheet Cavitation*," International Symposium on Cavitation Inception, New Orleans, Dec. 9–14, Vol. 16, pp. 127–136.
[6] Hord, J., "Cavitation in Liquid Cryogens," NASA Report No. CR-2054; 1972, NASA Report No. CR-2156; 1973, NASA Report No. CR-2242; 1974, NASA Report No. CR-2448.
[7] Watanabe, S., Hidaka, T., Horiguchi, H., Furukawa, A., and Tsujimoto, Y., 2005, "Steady Analysis of Thermodynamic Effect of Partial Cavitation Using Singularity Method," *2005 ASME Fluids Engineering Division Summer Meeting and Exhibition*, Houston, TX, Jun. 19–23.
[8] Fruman, D. H., Benmansour, I., and Sery, R., 1991, "Estimation of the Thermal Effects on Cavitation of Cryogenic Liquids," 1991, *Cavitation and Multiphase Flow Forum*, ASME FED, 109, pp. 93–96.

[9] Fruman, D. H., Reboud, J. L., and Stutz, B., 1999, "Estimation of Thermal Effects in Eavitation of Thermosensible Liquids," Int. J. Heat Mass Transfer, **42**, pp. 3195–3204.
[10] Billet, M. L., 1970, "Thermodynamic Effects on Developed Cavitation in Water and Freon 113," MS thesis, The Pennsylvania State University.
[11] Billet, M. L., Holl, J. W., and Weir, D. S., 1981 "Correlations of Thermodynamic Effects for Developed Cavitation," J. Fluids Eng., **103**, pp. 534–542.
[12] Holl, J. W., Billet, M. L., and Weir, D. S., 1975, "Thermodynamic Effects on Developed Cavitation, J. Fluids Eng., **97**, pp. 507–514.
[13] Rapposelli, E., and d'Agostino, L., 2003, "A Barotropic Cavitation Model with Thermodynamic Effects, *Fifth International Symposium on Cavitation*, Osaka, Japan, Nov. 1–4.
[14] Rolland, J., Boitel, G., Barre, S., Goncalves, E., and Fortes, Patella R., 2006, "Experiments and Modelling of Cavitating Flows in Venturi-Part I: Stable Cavitation," *Sixth International Symposium on Cavitation*, Wageningen, The Netherlands, Sept.
[15] Tani, N., and Nagashima, T., "Numerical Analysis of Cryogenic Cavitating Flow on Hydrofoil: Comparison Between Water and Cryogenic Fluids," *Fourth International Contevence on Launcher Technology*, Liege, Belgium, Dec. 3–6.
[16] Ahuja, V., and Hosangadi, A., 2006, "A Numerical Study of Cavitation in Cryogenic Fluids. Part I: Mean Flow Parametric Studies," *Sixth International Symposium on Cavitation*, Wageningen, The Netherlands, Sept.
[17] Hosangadi, A., and Ahuja, V., 2006, "A Numerical Study of Cavitation in Cryogenic Fluids. Part II: New unsteady Model for Dense Cloud Cavitation," *Sixth International Symposium on Cavitation*, Wageningen, The Netherlands, Sept.
[18] Hosangadi, A., and Ahuja, V., 2005, "Numerical Study of Cavitation in Cryogenic Fluids," J. Fluids Eng., **127**, pp. 267–281.
[19] Kubota, A., Kato, H., and Yamaguchi, H., 1992, "A New Modeling of Cavitating Flows: A Numerical Study of Unsteady Cavitation on a Hydrofoil Section," J. Fluid Mech., **240**, pp. 59–96.
[20] Singhal, A. K., Athavale, M. M., Li, H., and Jiang, Y., 2002, "Mathematical Basis and Validation of the Full Cavitation Model," J. Fluids Eng., **124**, pp. 617–624.
[21] Franc, J. P., and Michel, J. M, 2004, *Fundamentals of Cavitation*, Kluwer Academic, Dordrech; Franc, J. P., Janson, E., Morel, P., Rebattet, C., and Riondet, M., 2001, "Visualizations of Leading Edge Cavitation in an Inducer at Different Temperatures," Fourth International Symposium on Cavitation, Pasadena, CA, Jun. 20–23.
[22] Franc, J. P., Rebattet, C., and Coulon, A., 2004, "An Experimental Investigation of Thermal Effects In a Cavitating Inducer," J. Fluids Eng., **126**, pp. 716–723.
[23] Plesset, M. S., and Zwick, S. A., 1952, "A Nonsteady Heat Diffusion Problem with Spherical Symmetry," J. Appl. Phys., **23**(1), pp. 95–98.
[24] Plesset, M. S., and Zwick, S. A., 1954, "The Growth of Vapour Bubbles in Superheated Liquids," J. Appl. Phys., **25**(4), pp. 493–500.
[25] Zwick, S. A., and Plesset, M. S., 1955, "On the Dynamics of Small Vapour Bubbles in Liquids," J. Math. Phys. (Cambridge, Mass.), **33**, pp. 308–330.
[26] Fortin, A, 2002, *Analyse numérique*, Internationales Polytechniques, Montreal.

PIV Measurements in Square Backward-Facing Step

Mika Piirto
Aku Karvinen
Hannu Ahlstedt
Pentti Saarenrinne
Reijo Karvinen
Institute of Energy and Process Engineering,
Tampere University of Technology,
P.O. Box 589,
FI-33101 Tampere, Finland

Measurements with both two-dimensional (2D) two-component and three-component stereo particle image velocimetry (PIV) and computation in 2D and three-dimensional (3D) using Reynolds stress turbulence model with commercial code are carried out in a square duct backward-facing step (BFS) in a turbulent water flow at three Reynolds numbers of about 12,000, 21,000, and 55,000 based on the step height h and the inlet streamwise maximum mean velocity U_0. The reattachment locations measured at a distance of $\Delta y = 0.0322h$ from the wall are 5.3h, 5.6h, and 5.7h, respectively. The inlet flow condition is fully developed duct flow before the step change with the expansion ratio of 1.2. PIV results show that the mean velocity, root mean square (rms) velocity profiles, and Reynolds shear stress profiles in all the experimental flow cases are almost identical in the separated shear-layer region when they are nondimensionalized by U_0. The sidewall effect of the square BFS flow is analyzed by comparing the experimental statistics with direct numerical simulation (DNS) and Reynolds stress model (RSM) data. For this purpose, the simulation is carried out for both 2D BFS and for square BFS having the same geometry in the 3D case as the experimental case at the lowest Reynolds number. A clear difference is observed in rms and Reynolds shear stress profiles between square BFS experimental results and DNS results in 2D channel in the spanwise direction. The spanwise rms velocity difference is about 30%, with experimental tests showing higher values than DNS, while in contrast, turbulence intensities in streamwise and vertical directions show slightly lower values than DNS. However, with the modeling, the turbulence statistical differences between 2D and 3D RSM cases are very modest. The square BFS indicates $0.5h-1.5h$ smaller reattachment distances than the reattachment lengths of 2D flow cases. [DOI: 10.1115/1.2746896]

1 Introduction

Separation and reattachment of turbulent flow occur in many applications, e.g., in diffusers, combustion chambers, channels with sudden expansion, and flows around airfoils and buildings. In turbulent flow separation, the adverse pressure gradient causes separation of the boundary layer from the wall. Subsequent reattachment of the flow creates a recirculation bubble. A backward-facing step (BFS) is the common flow geometry in studies of separated flows. This is mainly because of the simple geometry and because separation occurs at the sharp corner, so that the separation point is known in advance. For these reasons, considerable work has been done on this flow.

Most previous studies have been concerned with the two-dimensional (2D) case, where the aspect ratio (AR) of the incoming flow is assumed infinite. The AR is defined as the ratio of the channel width to the step height. According to Ref. [1], the flow is primarily 2D away from the sidewalls for an AR greater than 10 in the case of an expansion ratio (the ratio of downstream duct height to upstream duct height) of 1.11. In Ref. [2], AR independency of a reattachment length has been assured when AR is greater than about 10, in the case of an expansion ratio (ER) of 2. Therefore, in the literature, it is usually accepted that the flow can be assumed 2D if AR is greater than 10 regardless of ER and other flow properties. More about the effect of AR can be found in article Ref. [3].

2D experiments have been done, for example, in Ref. [4,5] with ER=1.25 and AR=11.4 (2D). In these articles, the effect of separating shear-layer thickness and shape on the structure of the flow in the reattachment region of a BFS has been examined using (1) wall static-pressure profiles and turbulence data and (2) reattachment length and wall shear stress data. In article Ref. [6], mean velocities, Reynolds stresses, and triple products have been measured using a laser Doppler velocimeter (LDV) in the case of ER=1.25 and AR=12. Also, numerical calculations using the $k-\varepsilon$ turbulence model and algebraic Reynolds stress model (ARSM) have been performed in this article. In their article, Jovic and Driver [7] have used LDV in the case of ER=1.2 and AR=47. In their measurements, the geometry of direct numerical simulation (DNS) in 2D channel of Ref. [8] has been duplicated precisely, except for AR. Measurements for greater Reynolds number have been conducted in Ref. [9]. 2D experiments using a particle image velocimetry (PIV) have been conducted, for example, in Ref. [10] (ER=1.02, AR=62) and Ref. [11] (ER=1.2, AR=10). Experiments and Reynolds averaged Navier Stokes (RANS)-based calculations have been carried out in Ref. [12] (ER=1.94). In Ref. [13], the 2D case has been considered and different RANS models have been compared. RANS turbulence models have been used also in Ref. [14], in which effects of turbulence model constants have been inspected. Large eddy simulation (LES) has been utilized in Ref. [15] for the case of ER=5/3 and AR=10. LES calculations in 2D channel have been carried out in Refs. [16,17] also.

Shih and Ho [18] have used a laser Doppler anemometer (LDA) to measure the case of AR=3, i.e., a three-dimensional (3D) case. Their results reveal that the reattachment and the flow in the recirculation region are highly 3D due to the small AR. The 3D case has been measured using PIV Ref. [19]. LES in the 3D case has been used in Ref. [20], where ER=2 and AR=3. In addition to the DNS of Ref. [8], DNS calculation has been performed also in Ref. [21], where ER=1.1 and the case is considered to be 3D (AR=6). In this article, a swept BFS is investigated also. The third DNS article on BFS found in the literature is [22] (ER=1.2 and AR=6), but the Reynolds number of the flow is not large enough for it to be considered fully turbulent.

In addition to the turbulent flow measurements and calcula-

Contributed by the Fluids Engineering Division of ASME for publication in the JOURNAL OF FLUIDS ENGINEERING. Manuscript received: October 20, 2005; final manuscript received: February 21, 2007. Review conducted by Joseph Katz.

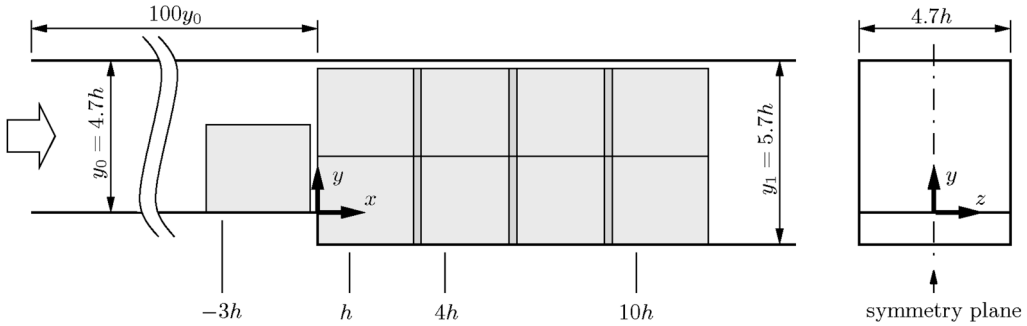

Fig. 1 Square BFS configuration and measurement locations. All measurements were performed in symmetry plane. Step height h=10 mm.

tions, there are a few laminar flow field investigations in the literature, for instance, Ref. [23], in which a time evolution of the 3D flow structure has been examined. A more extensive review of the BFS flow can be found in Ref. [24].

The experimental research in this article concentrates on a BFS flow with fully developed turbulent 3D square duct inlet flow. The measurement results are compared with computational fluid dynamics (CFD) data. The DNS results of Ref. [8] and RSM data for both 2D and 3D flow cases are compared with experiments in order to investigate and understand the sidewall effects on symmetry plane flow characteristics inherent in square BFS flows. ER and Reynolds number both have an effect on turbulent BFS flows and their influence is discussed.

In the DNS of Ref. [8], the computation is carried out in an infinite-width channel. However, these available DNS results are an excellent tool for investigating differences between 2D BFS flows and 3D BFS cases. In the RSM tests carried out here, the modeling is performed both for the 2D flow case (RSM 2D) and the 3D square BFS case (RSM 3D).

Compared to the previous experimental study of Ref. [19], a lot of emphasis has been placed on the design of the BFS duct loop to ensure that the inlet flow before the step is fully developed and that the ER is the same as in the DNS study of Ref. [8]. The duct length is 100 times duct height y_0 (or width) and ER=y_1/y_0 =1.2, where $y_1=y_0+h$. The AR is 4.7. The RSM 3D test has exactly the same geometry as the experimental setup. The inlet flow conditions of the DNS of Ref. [8], the square duct measurements, and both RSM cases are compared with the DNS of Ref. [25]. Three turbulent flows at Reynolds numbers of about Re_h =12,000 (Case A), 21,000 (Case B), and 55,000 (Case C) based on the step height h and the inlet streamwise maximum mean velocity U_0 are measured. The Reynolds number of DNS (Re_h =5,100) is about half the value of the lowest Reynolds number of the measurements, but it is considered fully turbulent.

RSM 2D and RSM 3D tests are performed with the lowest Reynolds number of the experimental setup. The reattachment length with RSM is uncertain because of the limitations of backflow reported in Refs. [26,27], and, in practice, the reattachment length cannot be predicted correctly with the RSM computation results of this study. In spite of these limitations of RSM, results using the RSM simulations have been included in this study because they enable 2D/3D comparison. In addition, RSM is widely used in turbulence modeling of practical applications, and, therefore, it is worthwhile to investigate the quality of RSM results.

For turbulent flow of $\mathrm{Re}_h > 6600$, the reattachment length is relatively constant according to the experiments of Ref. [12]. The reattachment length is measured and a slight difference between flow cases is discovered even though Reynolds number is clearly higher than the limit suggested by Ref. [12]. Typically, reattachment lengths between $6h$ and $7h$ are measured in the previous studies [7,8,28] for fully turbulent 2D BFS flows with ER≈1.2. In the present study, results of square BFS indicate reattachment distances, which are $0.5h-1.5\ h$ smaller than these.

The measurements with both two-component and stereo PIVs are carried out in a square BFS in a turbulent water flow. The discrete window shift (DWS) PIV interrogation method is utilized [29]. Similar PIV measurements for 2D BFS flows are found in Refs. [10,11]. In this work, the emphasis is on the PIV turbulence characterization: The mean velocity, the root mean square (rms), and the Reynolds shear stress estimates are calculated. The results of the lowest Reynolds number case are compared with the results both of the DNS of Ref. [8] and computational data of RSM 2D and RSM 3D. In addition to this, the reattachment length estimation is reported and discussed.

2 Experimental Setup

The setup of a BFS after a square duct is measured with a two-component PIV and with a stereo PIV system at the measurement positions marked in Fig. 1. The dimensions of the square inlet duct are 47×47 mm^2 and the step height is h=10 mm. The origin is situated at the step corner in the duct symmetry plane and the x-coordinate direction downwards from the step is considered positive. The flow characteristics at the positions $x/h=1,4,10$ and inlet flow at $x/h=-3$ are investigated. The flow directions are streamwise, vertical, and spanwise, denoted by x, y, and z, respectively. The corresponding mean velocities are denoted by plain variables U, V, W, and fluctuating velocities by u, v, w (in graphics). The inlet streamwise maximum mean velocities are U_0 ≈1.2 m/s, U_0≈2.1 m/s, and U_0≈5.5 m/s for Cases A, B, and C, respectively.

2.1 PIV System. The PIV system consists of a neodymium-doped yttrium aluminum garnet (Nd:YAG) double cavity laser with light sheet optics and a charge coupled device (CCD) camera of resolution 1280×1024 pixels. Water flow is seeded by hollow sphere glass particles with an average diameter of 10 μm. The seeding density is about ten particles per interrogation area when the laser sheet thickness is about 0.5 mm. The size of the final interrogation area is 32×32 pixels (0.866×0.866 mm^2) and 50% overlap was used. In the computation of the velocity vectors, the DWS method [11,29] is applied. In the computation of the velocity vectors, the correlation peaks are required to be located in the physically acceptable velocity range. With this velocity range limit, there is no need for vector validation in the recirculation region. Only few (10–20) erroneous velocity components conflicting with local median criteria are detected in inlet flow. The spurious velocity vector components are replaced by interpolation. The total rms error of the DWS method is of the order of 0.05 pixel [30]. The velocity random error is verified by a test measurement set with a zero flow, similar to that of Ref. [31], leading to the same order of error estimate of about 0.05 pixel. This test measurement is performed at the inflow measurement

position at $x/h=-3$. The same zero flow test gives an error of 0.15 pixel for the third velocity component of stereo PIV measurements. After nondimensionalizing, the spanwise velocity component rms error is of the order of 0.03. These random errors, after nondimensionalizing by U_0 of Case A, are of the order of $\sigma_u/U_0=\sigma_v/U_0\approx 0.01$ and $\sigma_w/U_0\approx 0.03$.

In the stereo PIV measurements, an angle of 30° is set between the cameras with Scheimpflug adapters and a procedure of Ref. [32] is applied to correct the camera images. The sampling interval between the measurements is 0.25 s, and, thus, statistical independency in time domain can be assumed. The number of measurement samples is 1000 in each location. For the spatial sampling resolution test, 2000 vector fields per location are measured. In all samples, spatial averaging in the streamwise direction over seven lines is used. The distance of seven vectors corresponds to $0.2h$, and, in practice, within this length the values of the estimates do not change, except that the measurement noise decreases. However, the averaging does not increase the number of the statistically independent measurements, i.e., samples.

The results of the 2D/three-component (3C) PIV measurements are fixed with 2D/two-component (2C) PIV measurements in xz plane at levels $y/h=0.1$, 0.3, 0.5, 0.7, 0.9, and 1.1. After the fixing, the stereo PIV streamwise and spanwise rms velocity results and the corresponding PIV measurements in xz plane are the same at the previously mentioned levels at the center of the duct.

2.2 Reynolds Stress Model. Numerical simulations are performed using the commercial CFD software FLUENT 6.1.22 [33] based on the finite volume method. As a turbulence model, a RSM is used [34]. Two different grids are formed for 2D flow in the infinite-width channel. The coarser one consists of 63,400 control volumes. The finer one, which is used in the grid independent test, consists of 280,255 control volumes. The test indicates the grid independency between the cases. In the construction of the 3D grid, the resolution of 63,400 cells is chosen in the symmetry plane of the channel, and a similar resolution is achieved with the 2D lower resolution case. The 3D grid includes 1,723,200 cells, and because of the symmetry, only half of the domain is computed.

All the grids are constructed so that the dimensionless wall unit, $y^+=u_\tau y/\nu$, in which u_τ is the friction velocity, y is the distance from the wall, and ν is the kinematic viscosity, is close to unity at the wall-adjacent cells of all no-slip walls. Flow field is resolved to the wall, and, thus, no wall functions are needed. The near-wall domain is subdivided into two regions, based on $\mathrm{Re}_y=k^{1/2}y/\nu$, in which k is the turbulence kinetic energy. In the fully turbulent region, $\mathrm{Re}_y>200$, the RSM is applied without modifications. In the area where $\mathrm{Re}_y<200$, basic model equations are retained, but the turbulent viscosity ν_t and the dissipation of the turbulent kinetic energy ε are calculated as proposed in Refs. [35,36]. Between the inner ($\mathrm{Re}_y<200$) and outer ($\mathrm{Re}_y>200$) regions, ν_t and ε are blended to ensure a smooth transition. This near-wall region is probably the most challenging part of the BFS modeling, as reported in Refs. [26,27], and at least the mean velocity of the recirculation bubble cannot be predicted properly.

All terms in all equations are discretized in space using second-order central differencing, apart from the convection term, which is discretized using a second-order upwind scheme. Pressure-velocity coupling is done using the traditional SIMPLE algorithm. Calculations are iterated until the scaled residuals approach the machine number. Therefore, it can be assumed that iteration error is negligible.

3 Inlet Flow

Some turbulent boundary layer characteristics for Cases A, B, and C at $x/h=-3$, i.e., before the step, are shown in Table 1. The boundary layer thickness is defined as duct half-height (width) $\delta=y_0/2$. The inlet flow is measured with the same 2D PIV setup as for the other measurements in BFS. Due to the disturbances close to the wall, reliable measurements could not be conducted closer than $0.01h$ to the wall. Thus, a rough estimate of the friction velocity u_τ is solved by fitting the mean inlet velocity profile measured with PIV with Spalding's universal velocity profile for boundary layers [37], using parameters $\kappa=0.41$ and $C=5.0$ instead of the parameters used in the original paper. Errors in the estimated friction velocities are of the order of 1%. The result of fitting Spalding's velocity profile to the PIV profile in flow Case A is shown in Fig. 2. Inlet mean velocity and rms velocity profiles for the streamwise component in $x/h=-3$ are shown in Figs. 3 and 4, respectively. The PIV results are compared with the DNS of Ref. [8], the DNS of Ref. [25] with $\mathrm{Re}_\tau=590$, and with 2D and 3D RSM results. A study similar to that of Ref. [25] is found in Ref. [38], in which the Reynolds number is slightly higher, $\mathrm{Re}_\tau=640$, and the results of these two studies are very similar. Thus,

Table 1 Inlet flow boundary layer properties. $\mathrm{Re}_\tau=u_\tau\delta/\nu$.

	Case A	Case B	Case C
U_0 (m/s)	1.2	2.1	5.5
u_τ (m/s)	0.051	0.085	0.2
Re_τ	1170	2000	4700

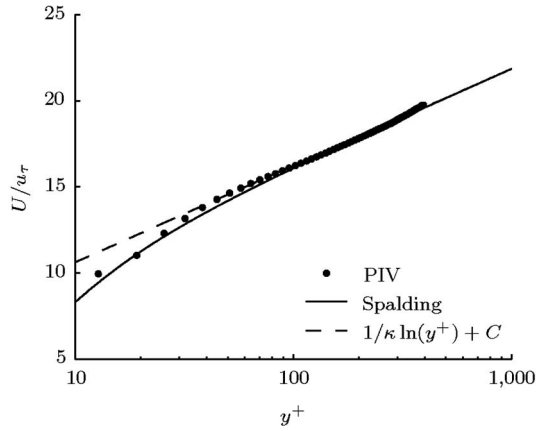

Fig. 2 Fitting of Spalding's velocity profile to PIV mean velocity profile in flow Case A. Spalding and log-law parameters are $\kappa=0.41$ and $C=5.0$.

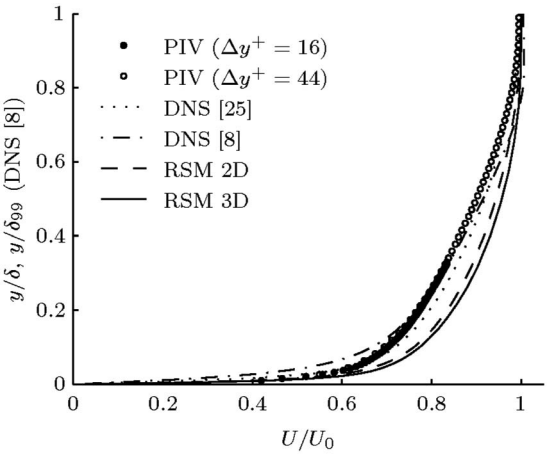

Fig. 3 Inlet mean velocity profiles for PIV Case A, DNS of Ref. [25], DNS of Ref. [8], and RSM 2D and RSM 3D at $x/h=-3$. Boundary layer thickness in DNS of Ref. [8] $\delta_{99}=1.2h$.

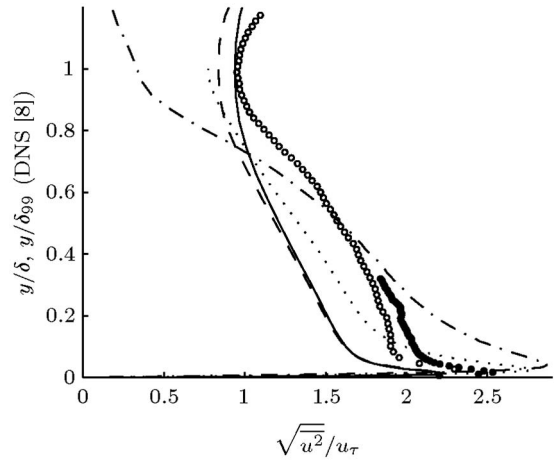

Fig. 4 Inlet streamwise rms velocity profiles for PIV Case A, DNS of Ref. [25], DNS of Ref. [8], and RSM 2D and RSM 3D at $x/h=-3$. Boundary layer thickness in DNS of Ref. [8] $\delta_{99}=1.2h$. Legend see Fig. 3.

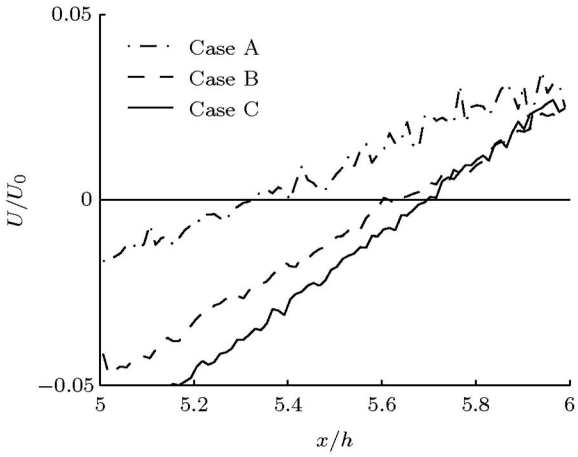

Fig. 5 Streamwise mean velocity and reattachment points with highest spatial sampling resolution $\Delta y=0.0322h$, which is also distance from wall

only one of them is chosen for the comparison. Reynolds number for RSM 2D and RSM 3D cases is $\mathrm{Re}_\tau=1170$. The same Reynolds number is used in PIV Case A. The mean profiles with RSM 2D and RSM 3D results are flatter than the corresponding profiles using PIV and in Ref. [25]. The mean profile of Ref. [8] is clearly not that of the fully developed turbulent channel flow, but close to the wall—which is the most important location in conducting good BFS research—the difference between inlet mean flow profiles is diminutive.

The DNS computations of both Refs. [8,25] are performed in an infinite-width channel. It could be assumed that a bounded duct leads to higher turbulence intensities than the corresponding intensities in infinite-width channels. According to the low Reynolds number results, the DNS study of Ref. [39] at $\mathrm{Re}_\tau=150$ for a straight square duct gives about 10% higher streamwise rms velocity than the infinite-witdh channel DNS of Ref. [25] at $\mathrm{Re}_\tau=180$. Even though the Reynolds number of the DNS study of Gavrilakis is lower than that of studies conducted in recent years and the simulation suffers from certain low Reynolds number effects, the result is in rather good agreement with the present study, in which the streamwise rms velocity of PIV is about 15% higher than the rms of DNS results in Ref. [25] between $y/\delta=0.2$ and 1.0, as can be noticed in Fig. 4. The upper boundary conditions limit the results of Ref. [8] especially between $y/\delta=0.2$ and 1.0, but closer to the wall than $y/\delta=0.2$ the streamwise velocity mean and rms profiles are in fairly good agreement with those of the DNS of Ref. [25]. RSM 2D and RSM 3D streamwise rms velocity profiles are almost identical, but, in general, they are lower than DNS and PIV results.

The maximum streamwise rms velocity of PIV is slightly lower than in the DNS of Ref. [25]. In addition to this, in the PIV results, the higher measurement resolution $\Delta y=0.0322h$ ($\Delta y^+=16$) gives slightly higher turbulence intensity than the lower resolution of $\Delta y=0.0866h$ ($\Delta y^+=44$), which is the spatial distance between two independent measurement samples and also the side length of the interrogation area. With the higher resolution, the measurements are conducted closer to the wall, and, thus, also the turbulence intensity peak is found, which is about $(\overline{u^2})^{1/2}/u_\tau=2.5$. For 2D simulations, i.e., the DNS of Ref. [8] and the DNS of Ref. [25], it is about 2.7 and for both the RSM 2D and RSM 3D cases it is about 2.25.

4 Reattachment Length

The ER effect on the reattachment length is investigated, e.g., in Ref. [28], in which the developed low Reynolds number k-ε turbulence model is used to predict the reattachment length of fully turbulent flows ($\mathrm{Re}_h \geqslant 28{,}000$) and the results are compared with five experimental data sets having different ERs; if ER ≈ 1.2 (1.125 and 1.25), the reattachment length is between $6h-7h$ ($6.21h$ and $6.67h$), while in contrast when ER $\geqslant 1.5$, the reattachment length is about $7h-8h$. According to the experimental study with laser Doppler velocimetry of Ref. [7] with ER=1.2, the reattachment length is about 6, which is in good agreement with these. In all these above-mentioned studies, flows are considered to be 2D.

Measured reattachment lengths after the step change in flow Cases A, B, and C are $5.3h$, $5.6h$, and $5.7h$, respectively. The reattachment distance is estimated using the change in mean velocity direction as close as possible to the wall. In Fig. 5, streamwise mean velocity and the location at which the direction of flow changes are shown. The distance from the wall is approximately the highest spatial resolution $\Delta y=0.0322h$, which corresponds to a distance of about 0.322 mm. In wall units, it is $\Delta y^+=16$ for Case A, $\Delta y^+=27$ for Case B, and $\Delta y^+=64$ for Case C. The total error of the measured reattachment length is of the order of $0.1h$ and it consists of an error in fixing the origo, an error in velocity measurements and an error in reading Fig. 5. In the previous study of Ref. [19], the reattachment distance is $6.2h$, but the flow geometry is slightly different and the inlet flow is not fully developed. According to the DNS of Ref. [8], the reattachment distance is $6.3h$, but again the upper symmetry boundary condition may have an increasing effect on it. However, compared with these and the experimental studies of ER ≈ 1.2 mentioned above, it seems that the reattachment lengths of square duct BFS turbulent flows are shorter than the corresponding reattachment lengths with infinite-width BFS turbulent flows. In addition to this, there is a clear increase in reattachment length of about $0.3h$ between flow Cases A and B, when the Reynolds number increases from $\mathrm{Re}_h=12{,}000$ to $\mathrm{Re}_h=21{,}000$. After that, the increase in reattachment length between Cases B and C is minuscule.

5 Turbulence Profiles

The measured nondimensionalized mean velocity, rms velocity, and Reynolds shear stress profiles are compared with corresponding profiles of the DNS of Ref. [8], RSM 2D, and RSM 3D at $x/h=1$, $x/h=4$, and $x/h=10$ in Figs. 6–9. In Fig. 10, spanwise rms velocity results are shown. Unfortunately, only the location at $x/h=4$ is measured with stereo PIV for spanwise rms velocity, but this is probably the most important location in the separated shear-layer region and most of the published results include at least this position. DNS profiles at $x/h=1$ are not available either in the

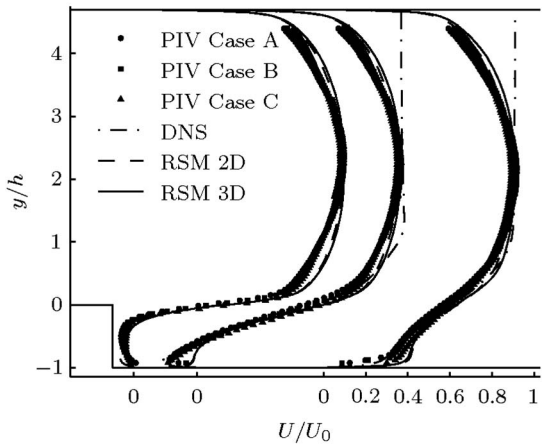

Fig. 6 Mean velocity profiles for PIV cases, DNS of Ref. [8], RSM 2D, and RSM 3D at $x/h=1$, $x/h=4$, and $x/h=10$

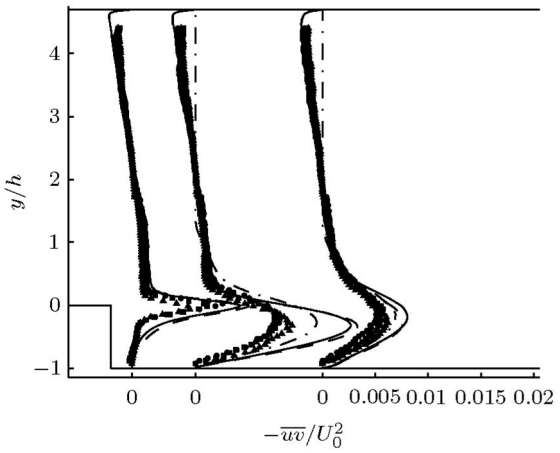

Fig. 9 Reynolds shear stress profiles for PIV cases, DNS of Ref. [8], and RSM 2D and RSM 3D at $x/h=1$, $x/h=4$, and $x/h=10$. Legend see Fig. 6.

European Research Community on Flow, Turbulence and Combustion (ERCOFTAC) database. Generally, the mean velocity and turbulence intensity profiles are almost identical to the experimental Cases A–C, and, in practice, turbulence statistic results are Reynolds number independent of this Reynolds number range. Only a slight decrease of about 0.02 in streamwise rms velocity peak is found at $x/h=1$ when Reynolds number increases, while in contrast at $x/h=4$, this rms peak increases about 0.01 with the higher Reynolds number cases.

The shapes of the profiles for streamwise mean velocity are very close to those of the profiles of DNS in the separated shear-layer part of flow, but outside that area between $y/h=0.5\cdots5.0$, the results are not comparable with each other because of the DNS boundary conditions. With PIV and DNS backward streamwise mean velocity, the peak is about $U/U_0=-0.15$. There is a sudden change in RSM velocity mean by the wall after about $x/h=3.5$, and the peak is too low, as also noted in Ref. [26]. At the position $x/h=1$, RSM 2D and RSM 3D backward streamwise mean velocities agree well with those of the PIV cases. Differences between mean profiles of the different PIV cases are very modest. Only a very modest tendency toward flat velocity profile in the main stream region is noticed with higher Reynolds number Cases B and C compared with Case A.

rms in streamwise and vertical directions and Reynolds shear stress profiles of PIV are very similar, showing slightly lower values than DNS in the recirculation bubble area, i.e., in the region $y/h<0.5\cdots1$. Streamwise rms velocity maximum at x/h

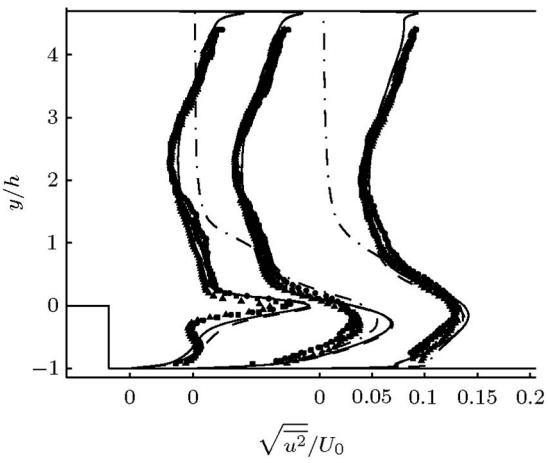

Fig. 7 Streamwise rms velocity profiles for PIV cases, DNS of Ref. [8], and RSM 2D and RSM 3D at $x/h=1$, $x/h=4$, and $x/h=10$. Legend see Fig. 6.

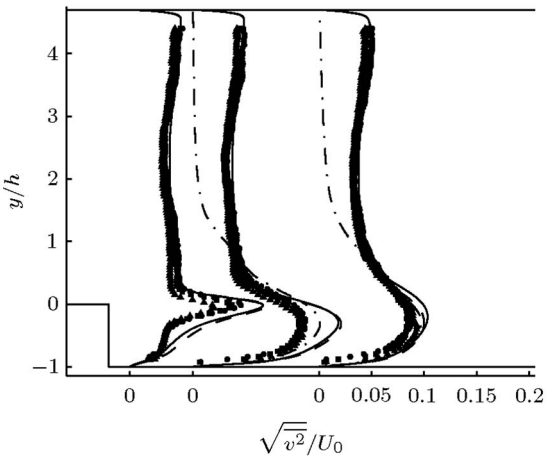

Fig. 8 Vertical rms velocity profiles for PIV cases, DNS of Ref. [8], RSM 2D and RSM 3D at $x/h=1$, $x/h=4$, and $x/h=10$. Legend see Fig. 6.

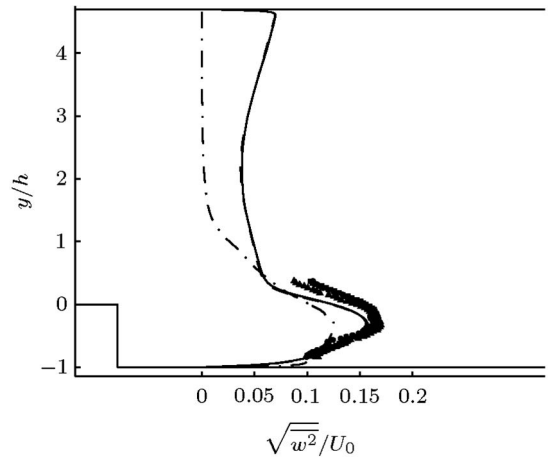

Fig. 10 Spanwise rms velocity profiles for PIV cases, DNS of Ref. [8], and RSM 2D and RSM 3D at $x/h=4$. Legend see Fig. 6.

=4, after nondimensionalization with U_0, is u_0=0.151 for PIV, u_0=0.175 for DNS, and u_0=0.188 for RSM 2D and RSM 3D. A similar difference between PIV, DNS, and RSM cases is noticed for vertical rms velocity maxima. In contrast with this, the measured spanwise turbulence intensity is clearly higher than with the DNS. The measured rms peak value is about 30% higher than the rms peak value of DNS. This means that the difference is the opposite, and the higher estimates of PIV than of DNS can be explained by the sidewall effects of the square duct.

With RSM, the shapes of the profiles are close to those from PIV and DNS, but especially the Reynolds shear stress maximum is considerably higher at x/h=4 than the corresponding PIV and DNS maxima, which was also found by Ref. [26]. In addition to this, the maxima of streamwise velocity rms are slightly closer to the wall, especially at x/h=4 and x/h=10, than corresponding PIV and DNS profiles. However, RSM 2D and RSM 3D results, when U_0 is used for the nondimensionalizing, do not differ significantly, and, thus, the sidewall effect is not found. This result is in contradiction with PIV and DNS results.

6 Spatial Sampling Resolution and rms Error

The PIV spatial sampling resolution used in the results of the previous section is Δy=0.0866h. The increased spatial sampling resolution and the measurement rms error are important factors as they have an increasing effect on turbulence intensity. In turbulence intensity estimation, the effect of the spatial sampling resolution is considerable. In the case of velocity gradient estimation, the effect of the spatial sampling resolution is even more significant [40]. In this study, the focus is on turbulence intensity estimation, and, thus, only the relation between the spatial sampling resolution and turbulence intensities is analyzed. If the resolution is high, the smaller turbulence scales are included in the estimates and the results are more realistic. However, if the measurement spatial resolution passes the capacity of the PIV system and there are too few particles in a particular interrogation area, this also has an increasing effect on the estimates due to the measurement error. Because of this fact, it is important to prove that the data sets are stationary at least in the rms sense [41] and also verify that the measurement rms error does not increase when the spatial resolution increases. This is verified using a special test to ensure that the average velocity and the rms velocity satisfy the following criteria [19]: If the instantaneous vector data of Δy=0.0322h are averaged with a 2×2 filter, the average velocity and rms are the same as with the vector data of Δy=0.0644h, having a margin of error less than 3%. The same criterion with the vector data from Δy=0.0644h to Δy=0.1288h and from Δy=0.1288h to Δy=0.2576h yields a margin of error of about 4%.

After a satisfactory stationary test, the effect of the spatial resolution can be analyzed and the results are plotted in Figs. 11 and 12 for streamwise rms velocity and Reynolds shear stress maxima. According to this test, the effect of the spatial sampling resolution is about 5–10% for streamwise rms velocity with Cases A–C, and about 5% for Reynolds shear stress. A similar increase as in streamwise direction rms velocity is noticed in vertical direction rms velocity. The resolution increases from Δy=0.1288h to Δy=0.2576h. The corresponding integral length scales are order of $L_{x,\max}$=1.12h and $L_{x,\min}$=0.85h in streamwise direction and $L_{y,\max}$=0.42h and $L_{y,\min}$=0.25h in vertical direction. These values are estimated as averaged of different image areas. As mentioned above, the resolution Δy=0.1288h is used with 2D/2C and 2D/3C measurements. This increased spatial resolution will bring the PIV turbulence intensity results in streamwise and vertical directions even closer to the corresponding DNS turbulence intensity results shown in the previous section. In addition to this, in spanwise direction, the difference between PIV and DNS turbulence intensity results slightly increases.

It should be noted that all turbulence results include the rms error estimated in Sec. 2.1. One kind of estimate of the uncertainty is obtained if these rms errors are divided by rms maxima. In location x/h=4, these maxima are about 1.4, 1.4, and 2.3 pixels for streamwise, vertical, and spanwise rms velocity estimates, leading to an uncertainty error of about 4%, 4%, and 15%, respectively. Because of the fixing procedure explained in Sec. 2.1, the spanwise velocity rms error of stereo PIV experiments is of the same order of magnitude as the streamwise and vertical errors. In practice, the rms error increases turbulence rms. In conclusion, the increased spatial resolution recovers slightly more turbulence energy than that lost due to the rms error in these measurement cases.

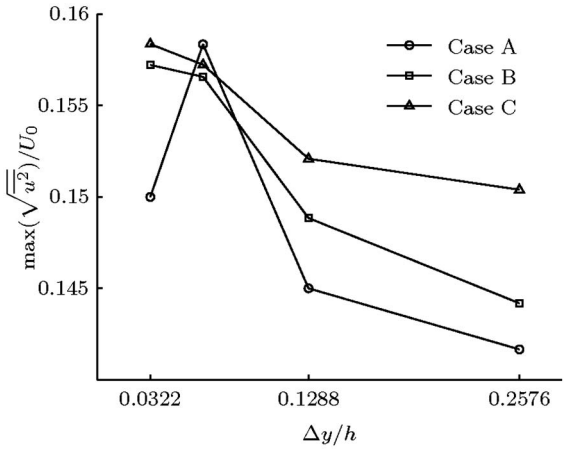

Fig. 11 Streamwise rms velocity maxima at x/h=4 with PIV test data sets of different spatial sampling resolutions

7 Conclusions

Turbulent BFS flow of a square duct is measured by a conventional PIV system and stereo PIV system at three Reynolds numbers of about 12,000 (Case A), 21,000 (Case B), and 55,000 (Case C), based on the step height h and the inlet streamwise maximum mean velocity U_0. The inlet duct flow before the step is fully developed and the ER of the step is 1.2. The AR is 4.4. The mean velocity and turbulence intensity profiles are almost identical to the experimental cases at different Reynolds numbers, and only a slight decrease of about 0.02 in streamwise rms velocity peak is found at x/h=1 when Reynolds number increases. Even though these tests are considered to be fully turbulent, the reattachment

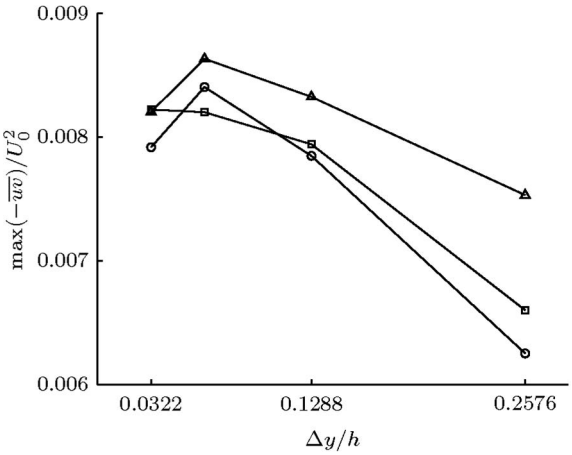

Fig. 12 Reynolds shear stress maxima at x/h=4 with PIV test data sets of different spatial sampling resolutions. Legend see Fig. 11.

length still increases, especially in Cases A and B, and they are $5.3h$, $5.6h$, and $5.7h$ for Cases A, B, and C, respectively.

The square BFS PIV results of Case A are compared with the DNS of Ref. [8] and a RSM of infinite-width channel, which have a Reynolds number similar to that in Case A. The shapes of the profiles are very similar to each other in the separated shear-layer part $y/h < 0.5 \cdots 1.5$. The most significant difference is the spanwise rms velocity maximum, which is 30% higher with PIV than in DNS, and turbulence intensity seems to depend more on the sidewalls than turbulence intensities in the other directions. Typically, the reattachment lengths between $6h$ and $7h$ are measured in earlier studies for fully turbulent 2D flows, and, thus, the present 3D results are about $0.5h-1.5h$ smaller. With the DNS of Ref. [8], the reattachment length is $6.3h$, whereas for RSM, the shapes of the mean profiles are not appropriate for reattachment length estimation.

Turbulence statistics of the RSM of an infinite-width channel are compared with the statistics of RSM for square BFS having the same geometry and Reynolds number as Case A. No significant differences between turbulence intensity profiles were observed, and this fact is in contradiction with PIV and DNS results. The effect of the PIV spatial sampling resolution is analyzed using the four test data sets. The PIV rms error, which increases turbulence quantities, is of the order of 0.01 after nondimensionalizing by inlet mean maximum velocity for Case A, and is even smaller for Cases B and C. When the effect of spatial sampling resolution and rms error is taken into account, the turbulence maxima between PIV and DNS are almost the same for streamwise and vertical velocity fluctuations, and the PIV rms peak is at least 30% higher than the DNS peak in spanwise direction.

References

[1] de Brederode, V., and Bradshaw, P., 1972, "Three-Dimensional Flow in Nominally Two-Dimensional Separation Bubbles," Imperial College of Science and Technology, Technical Aero Report No. 72-19.

[2] Papadopoulos, G., and Ötugen, M. V., 1995, "Separation and Reattaching Flow Structure in a Suddenly Expanding Rectangular Duct," ASME J. Fluids Eng., **117**, pp. 17–23.

[3] Berbee, J. G., and Ellzey, J. L., 1989, "The Effect of Aspect Ratio on the Flow Over a Rearward-Facing Step," Exp. Fluids, **7**, pp. 447–452.

[4] Adams, E. W., and Johnston, J. P., 1988, "Effects of the Separating Shear Layer on the Reattachment Flow Structure, Part 1: Pressure and Turbulence Quantities," Exp. Fluids, **6**, pp. 400–408.

[5] Adams, E. W., and Johnston, J. P., 1988, "Effects of the Separating Shear Layer on the Reattachment Flow Structure, Part 2: Reattachment Length and Wall Shear Stress," Exp. Fluids, **6**, pp. 493–499.

[6] Driver, D. M., and Seegmiller, H. L., 1985, "Features of a Reattaching Turbulent Shear Layer in Divergent Channel Flow," AIAA J., **23**, pp. 163–171.

[7] Jovic, S., and Driver, D. M., 1994, "Backward-Facing Step Measurements at Low Reynolds Number, $Re_h=5000$," NASA, Technical Report No. TM-108807.

[8] Le, H., Moin, P., and Kim, J., 1997, "Direct Numerical Simulation of Turbulent Flow Over a Backward-Facing Step," J. Fluid Mech., **330**, pp. 349–374.

[9] Jovic, S., 1996, "An Experimental Study of a Separated/Reattached Flow Behind a Backward-Facing Step, $Re_h=37{,}000$," NASA, Technical Report No. TM-110384.

[10] Kostas, J., Soria, J., and Chong, M. S., 2002, "Particle Image Velocimetry Measurements of a Backward-Facing Step Flow," Exp. Fluids, **33**, pp. 838–853.

[11] Scarano, F., and Riethmuller, M. L., 1999, "Iterative Multigrid Approach in PIV Image Processing With Discrete Window Offset," Exp. Fluids, **26**, pp. 513–523.

[12] Armaly, B. F., Durst, F., Pereira, J. C. F., and Schönung, B., 1983, "Experimental and Theoretical Investigation of Backward-Facing Step," J. Fluid Mech., **127**, pp. 473–496.

[13] So, R. M. C., and Yuan, S. P., 1998, "Near-Wall Two-Equation and Reynolds-Stress Modeling of Backstep Flow," Int. J. Eng. Sci., **36**, pp. 283–298.

[14] Bischof, C. H., Bücker, H. M., and Rasch, A., 2004, "Sensitivity Analysis of Turbulence Models Using Automatic Differentiation," SIAM J. Sci. Comput. (USA), **20**, pp. 510–522.

[15] Wang, B., Zhang, H.-Q., and Wang, X.-L., 2004, "Large Eddy Simulation of SGS Turbulent Kinetic Energy and SGS Turbulent Dissipation in a Backward-Facing Step Turbulent Flow," Chin. Phys. Lett., **21**, pp. 1773–1776.

[16] Delcayre, F., 1999, "Etude Par Simulation Des Grandes échelles d'un écoulement Décollé; la Marche Descendante," Ph.D. thesis, Grenoble.

[17] Dubief, Y., and Delcayre, F., 2000, "On Coherent-Vortex Identification in Turbulence," J. Turbul., **1**, pp. 1–22.

[18] Shih, C., and Ho, C.-M., 1994, "Three-Dimensional Recirculation Flow in a Backward-Facing Step," ASME J. Fluids Eng., **116**, pp. 228–232.

[19] Piirto, M., Saarenrinne, P., Eloranta, H., and Karvinen, R., 2003, "Measuring Turbulence Energy With PIV in a Backward-Facing Step Flow," Exp. Fluids, **35**, pp. 219–236.

[20] Fureby, C., 1999, "Large Eddy Simulation of Rearward-Facing Step Flow," AIAA J., **37**, pp. 1401–1410.

[21] Kaltenbach, H.-J., and Janke, G., 2000, "Direct Numerical Simulation of Flow Separation Behind a Swept, Rearward-Facing Step at $Re_H=3000$," Phys. Fluids, **12**, pp. 2320–2337.

[22] Bärwolff, G., Wengle, H., and Jeggle, H., 1996, "Direct Numerical Simulation of Transitional Backward-Facing Step Flow Manipulated By Oscillating Blowing/Suction," *Engineering Turbulence Modelling and Experiments 3*, W. Rodi, and G. Bergeles, eds., Elsevier, Amsterdam, pp. 219–228.

[23] Chiang, T. P., and Sheu, T. W. S., 1999, "Time Evolution of Laminar Flow Over a Three-Dimensional Backward-Facing Step," Int. J. Numer. Methods Fluids, **31**, pp. 721–745.

[24] Eaton, J. K., and Johnston, J. P., 1981, "A Review of Research on Subsonic Turbulent Flow Reattachment," AIAA J., **19**, pp. 1093–1100.

[25] Moser, R. D., Kim, J., and Mansour, N. N., 1999, "Direct Numerical Simulation of Turbulent Channel Flow Up to $Re_\tau=590$," Phys. Fluids, **11**, pp. 943–945.

[26] Parneix, S., Laurence, D., and Durpin, P. A., 1998, "A Procedure for Using DNS Databases," ASME J. Fluids Eng., **120**, pp. 40–47.

[27] Pope, S. B., 2000, *Turbulent Flows*, Cambridge University Press, Cambridge, England.

[28] Abe, K., Kondoh, T., and Nagano, Y., 1994, "A New Turbulence Model for Predicting Fluid Flow and Heat Transfer in Separating and Reattaching Flow. I. Flow Field Calculations," Int. J. Heat Mass Transfer, **37**, pp. 139–151.

[29] Piirto, M., Eloranta, H., Saarenrinne, P., and Karvinen, R., 2005, "A Comparative Study of Five Different PIV Interrogation Algorithms," Exp. Fluids, **39**, pp. 573–590.

[30] Westerweel, J., Dabiri, D., and Gharib, M., 1997, "The Effect of a Discrete Window Offset on the Accuracy of Cross-Correlation Analysis of Digital PIV Recordings," Exp. Fluids, **23**, pp. 20–28.

[31] Forliti, D. J., Strykowski, P. J., and Depatin, K., 2000, "Bias and Precision Errors of Digital Particle Image Velocimetry," Exp. Fluids, **28**, pp. 436–447.

[32] Soloff, S. M., Adrian, R. J., and Liu, Z.-C., 1997, "Distortion Compensation for Generalized Stereoscopic Particle Image Velocimetry," Meas. Sci. Technol., **8**, pp. 1441–1454.

[33] Fluent Inc., 2005, FLUENT 6.2 user's guide, Lebanon.

[34] Gibson, M. M., and Launder, B. E., 1978, "Ground Effects on Pressure Fluctuations in the Atmospheric Boundary Layer," J. Fluid Mech., **86**, pp. 491–511.

[35] Wolfshtein, M., 1969, "The Velocity and Temperature Distribution of One-Dimensional Flow With Turbulence Augmentation and Pressure Gradient," Int. J. Heat Mass Transfer, **12**, pp. 301–318.

[36] Chen, H. C., and Patel, V. C., 1988, "Near-Wall Turbulence Models for Complex Flows Including Separation," AIAA J., **26**, pp. 641–648.

[37] Spalding, D. B., 1961, "A Single Formula for the Law of the Wall," ASME J. Appl. Mech., **28**, pp. 455–458.

[38] Abe, H., Kawamura, H., and Matsuo, Y., 2001, "Direct Numerical Simulation of a Fully Developed Turbulent Channel Flow With Respect To Reynolds Number Dependency," ASME J. Fluids Eng., **123**, pp. 382–393.

[39] Gavrilakis, S., 1992, "Numerical Simulation of Low-Reynolds-Number Turbulent Flow Through a Straight Square Duct," J. Fluid Mech., **244**, pp. 101–129.

[40] Fouras, A., and Soria, J., 1998, "Accuracy of Out-Of-Plane Vorticity Measurements Derived From In-Plane Velocity Field Data," Exp. Fluids, **25**, pp. 409–430.

[41] Piirto, M., Ihalainen, H., Eloranta, H., and Saarenrinne, P., 2001, "2D Spectral and Turbulence Length Scale Estimation With PIV," J. Vision, **4**, pp. 39–49.

Surface Tension Measurement at High Temperatures by Using Dynamics of Melt Flow

A. Moradian[1]

J. Mostaghimi

Centre for Advanced Coating Technologies,
Department of Mechanical & Industrial Engineering,
University of Toronto,
Toronto, ON, M5S 3G8, Canada

Surface tension of melts at high temperature has significant effects on different industrial processes. In a new containerless method for surface tension measurement, an atmospheric radio-frequency inductively coupled plasma melts metallic or ceramic rods and a high-speed charge-coupled device records the drop formation caused by melting. Pendant drops produced by the melt flow are compared with the theoretical Young–Laplace (YL) profiles. Moreover, the dynamics of the melt flow is mimicked by using numerical simulations of drop injection from a nozzle. The numerical model solves the axisymmetric Navier–Stokes equations for both the melt and the surrounding gas by using the finite volume method. Since the YL equations provide theoretical pendant drop profiles based on an inviscid quasiequilibrium condition, a detailed study of the differences between experimental, numerical, and theoretical profiles demonstrates some of the hydrodynamic effects influencing the surface tension measurement methods, which are based on drop profiles. Results from this surface tension measurement method, in addition to a discussion on the hydrodynamic effects, are presented. [DOI: 10.1115/1.2746918]

1 Introduction

Many industrial processes at high temperature are controlled by surface tension. The most direct applications are in thermal spray coating, metal soldering, brazing, sintering, and welding. From a modeling prospective, computational based mathematical models used in industrial simulations are highly developed in terms of the mathematical equations; however, they rely on the accuracy of the physical and the physicochemical materials property data they are modeling. In many cases, these data are not available, and this is particularly true in the case of surface tension and viscosity of high-melting-point materials. These properties are the critical factors in modeling processes in any fluid flow problem. Moreover, the dynamics of a moving free interface between two fluids is mainly governed not only by the characteristics of external force fields imposed on the bulk of fluid, but also by the viscosity and the surface tension. For instance, because of the surface tension force, a static bulk of fluid gets a final or an equilibrium shape with the minimum value of the total free energy.

The measurements of viscosity and surface tension at high temperatures are currently prone to large errors, and the literature data for absolute values for even pure liquid metals show a scatter between 20% and 100% [1]. For many materials, the data for the property relationship with temperature are even less accurate, and there is a paucity of any form of data for alloys used in the industry. Because of various technical difficulties, the regular surface tension measurement methods [2,3] are not applicable at high temperatures. Eliminating containers from the measurement techniques reduces some of the problems that are related to the melting point of a container, contaminations, and chemical reactions. Therefore, among the common measurement methods, some containerless methods (such as the pendant drop (PD) method [4], the drop weight (DW) method [5], and the drop levitation method [6]) were implemented in the past. Allen [7] and Passerone and Ricci [8] reviewed a number of the surface tension measurement methods that have been used for high temperatures. However, even these methods are limited in terms of accuracy at very high temperatures.

In essence, all of the containerless methods require a separate bulk of fluid. This can be a bubble or a drop, hanging (or detached) from the tip of a nozzle. Regarding the general studies conducted on drop formation, growth, and detachment, Peregrine et al. (1990) [9] did a comprehensive experimental study on the evolution and the pinch-off of a liquid thread. His qualitative investigation motivated Zhang and Basaran (1995) [10] to investigate the drop evolution as a function of flow rate, viscosity, surface tension, thickness of the tube wall, and radii of the orifice. Drop formation is usually described by fluid ejection from a nozzle. Dynamics of flow injection from a nozzle of diameter d is controlled by Reynolds and Weber numbers defined as

$$\mathrm{Re} = \frac{\rho V d}{\mu} \tag{1}$$

$$We = \frac{\rho d V^2}{\sigma} \tag{2}$$

where ρ, V, μ, and σ are the density, velocity, viscosity, and surface tension. At low Weber numbers, the melt appears as discrete drops that detach because of its weight; this constant-frequency dripping is called the periodic dripping mode. This mode is the basis for a number of the well-known surface tension measurement methods [11]. For instance, the measurement of surface tension can be undertaken through both the PD and the DW methods. In the first case, the surface tension is given by

$$\sigma = g\rho L^2 \tag{3}$$

where g and L^2 are the acceleration due to gravity and a capillary constant (based on geometrical parameters of a suspended drop), respectively [12].

Surface tension of fluids can also be measured by using the theoretical Young (1805) [13] and Laplace (1839) [14] relations for an axisymmetric profile of a PD. The earliest efforts in the analysis of axisymmetric drops were those of Bashford and Adams (1883) [15]. Furthermore, based on drop profiles, Maze and Burnet (1969) presented a nonlinear regression calculation procedure for contact angle and surface tension from sessile drops. In

[1]Corresponding author.

Contributed by the Fluids Engineering Division of ASME for publication in the JOURNAL OF FLUIDS ENGINEERING. Manuscript received September 29, 2006; final manuscript received January 25, 2007. Review conducted by Timothy J. O'Hern. Paper presented at the 2005 ASME International Mechanical Engineering Congress (IMECG2005), Orlando, FL, Nov. 5–11, 2005.

their approach, the initial estimates of the drop shape and the size parameters had to be made close enough to the true values so that the computations will converge [16]. Then, they modified their method by eliminating the errors caused by an improper location of the drop apex [17]. Hartland and Hartley (1976) [18] also investigated the interfacial tension measurement of axisymmetric fluid-fluid menisci. Based on their pioneering approach, Lahooti et al. (1996) [19] developed a technique called axisymmetric drop shape analysis profile (ADSA-P). The ADSA-P technique fits the measured profile of a drop to a Laplacian curve. Recently, Hoorfar and Neumann reviewed the recent progress in the ADSA method. They defined a new parameter, shape factor, and they discussed the range of applicability of ADSA [20].

In addition to using drop profiles, DW (or volume) is also used to measure surface tension. Tate (1864) presented the DW method based on a simple force balance [5]. However, Harkins and Brown (1919) [21] suggested a correction factor to Tate's relation. This correction is because of a part of liquid remaining on the nozzle after a drop is detached. Wilkinson (1972) [22] extended the range of applicability of the correction factor introduced by Harkins and Brown. Taking into account the remaining liquid and the necking diameter (minimum diameter of the liquid ligament), Garandet et al. (1994) [23] showed that these corrections can be defined by a momentum balance just before the release.

Moreover, Miller et al. (1994) studied the relation between the geometry of a nozzle and the properties of a liquid to the detachment time. According to their study, for each capillary, the relation between the drop detachment time and the dimensionless parameter r_{cap}/a (where $a=\sqrt{2\sigma/\Delta\rho g}$) was linear; the longer the drop detachment time, the smaller the r_{cap}/a [24]. Later, they considered hydrodynamic effects on this detachment time. They discussed that during the period of time necessary for the act of detachment itself, a certain amount of liquid flows additionally into the detaching drop; as a result, they presented a relation for detachment time as a function of viscosity [25].

In this paper, we propose a new method for measuring the surface tension of high-melting-point materials. This method is based on the dynamics of melting. The flow of melts due to gravity results in drop formation at the tip of the samples that are heated by a radio-frequency inductively coupled plasma (rf-ICP) [26]. The drop profiles are reproduced by solving the Young-Laplace (YL) equations; the value of surface tension, which produces profiles similar to the experimental drop profiles, is the surface tension of the material. The results are validated with some popular methods (PD and DW methods). The drop formation is modeled numerically by solving the full Navier–Stokes (NS) equations. Comparing the modeling results and the YL profiles illustrates the deviation of the dynamic surface tension values from the static value used as the input data at instances when hydrodynamic effects are significant.

A detailed study of the hydrodynamic effects on surface tension measurement methods is in progress.

2 Surface Tension Measurement Methodology

Samples, in the form of rods, were axially aligned with a plasma torch, and a high-speed camera recorded the melting process. In addition to observing the qualitative aspects of the phenomenon, a precise and quantitative analysis was also required to facilitate the comparison between the experiments and the simulations. This was performed by an image analysis [27,28]. Matching the theoretical profiles on the experimental ones resulted in a value for the surface tension. To validate the measurements, the surface tension of the samples used in the present study was measured using different experimental methods, which were completely independent of the proposed procedure (e.g., DW and PD).

To validate the accuracy of this method, we simulated a dripping nozzle in which the feeding rate of the liquid corresponded to the melting rates obtained from the experiments. The simulations required physical properties (e.g., surface tension and viscosity) as input. The input values, which result in dynamics similar to the experimental dynamics (drop profiles during the process of drop formation), correspond to the melt properties. To simplify the comparison, we used theoretical PD profiles based on the YL equations. Applying the same procedure used for the experimental profiles on the profiles that resulted from the numerical modeling provided surface tension values based on the shape of the drops.

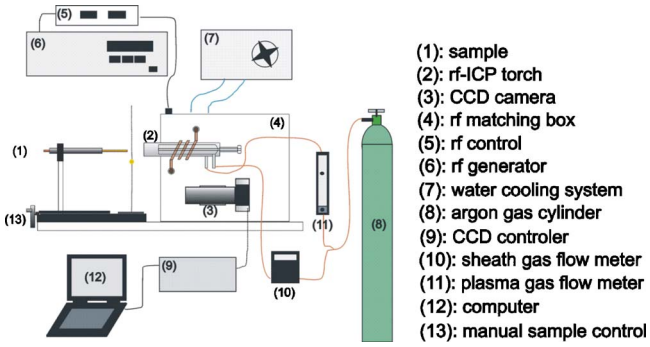

Fig. 1 Schematic of the experimental setup

Primary experiments were conducted on copper samples to establish the method, and the application of the method for ceramics or alloys is similar. It is noteworthy that in the case of ceramic samples, the oxidation effects are eliminated; however, other issues, such as uniform heating and optical filtering (ceramics have higher emissivities compared to liquid metals), are more challenging.

3 Experimental Setup

Figure 1 shows the schematic of the experimental setup. An atmospheric 40 MHz argon rf-ICP plasma with a maximum power of 1 kW was used to melt the samples. Rods were aligned with the axis of symmetry of the torch. Argon flows were 1.2 SLPM (standard liters per minute) and 7.6 SLPM for the plasma and the sheath gases, respectively. Initial studies were conducted with copper rods (99.8%) of 1.6 mm diameter with a melting point of 1084 °C. The argon rf-ICP produced the required high temperatures for melting the rods. In addition, the flow of argon prevented the samples from oxidations. The rf quartz torch (Delta Scientific Laboratories, Mississauga) had an internal diameter of 18 mm. The schematic of the rf-ICP torch and the location of the sample is shown in Fig. 2. The rf power supply (Advanced Energy Industries, Inc., CO) generates up to 1 kW forward power at 40 MHz. The dynamics of melting was recorded by a high-speed camera (Photron Fastcam ultima 1024, Corporation Ltd., Kitchener, ON) equipped with a 90 mm macrolens at 1000 frames/s. The speed was adjusted based on the diameter and material of the samples. A lower frame per second was more appropriate for larger diameters (or materials with higher melting point) since in such cases the process of interest happens in a relatively longer period. Details of the dimensions and other characteristics of the plasma system and

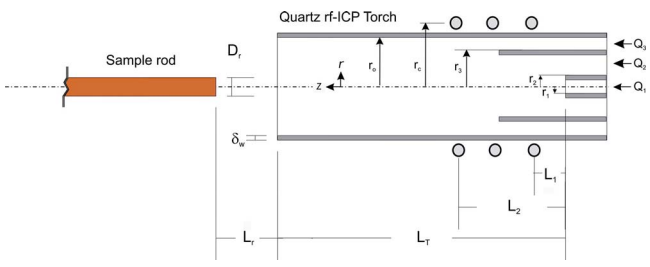

Fig. 2 Schematic of the rf-ICP torch and the relative situation of samples

Table 1 Characteristics of the rf-ICP and the sample

Plasma	Generator	Power Frequency	~400 W 40 MHz	
	Gas	Argon, 99.999%	Sheath (Q_3) Plasma (Q_2) Center (Q_1)	15.0 SLPM 1.2 SLPM 0.0 SLPM
	Torch dimensions	r_1=0.5 mm r_2=2.0 mm r_3=7.5 mm	R_o=9.0 mm R_c=14.5 mm δ_w=1.0 mm	L_1=1.0 mm L_2=14.0 mm L_T=25.0 mm
Rod	Material Size Distance		Copper D_r=1.6 mm L_r=15 mm	

the sample are shown in Table 1. Figure 3 shows a copper sample being heated axially by the rf-ICP torch. In order to maintain the heat flux constant, for a constant power of the rf generator, the rod was moved constantly toward the torch so that the distance between the tip of the sample and the torch was constant. A detailed evolution of the drop is shown in Fig. 4.

4 Theoretical Profiles

Geometry of an axisymmetric pendant (or sessile) drop can be represented with a set of ordinary differential equations, which include different parameters: arc length (s), slope angle of a tangent to a point of the profile (φ), and curvature at the apex (b) (see Fig. 5). The YL equation [13,14] presents the profiles as a function of the curvatures on two perpendicular planes at each point. A set of three simultaneous nonlinear, nonhomogeneous, and first order ordinary differential equations can be solved simultaneously to calculate three unknowns (φ, X, and Z) while s is the independent variable measured from the apex:

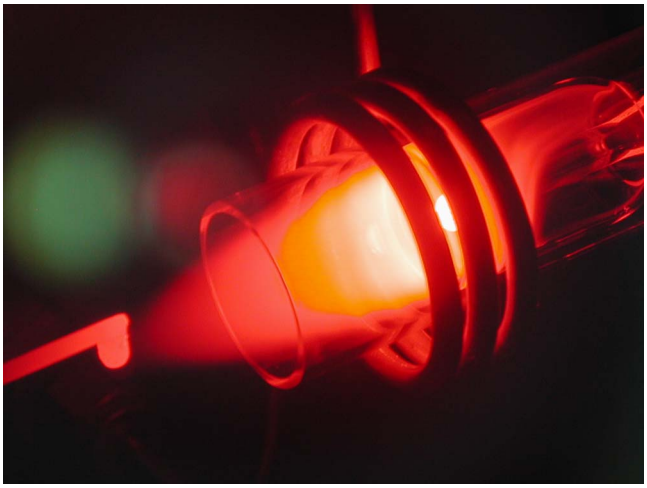

Fig. 3 Axial heating of a copper rod by rf-ICP

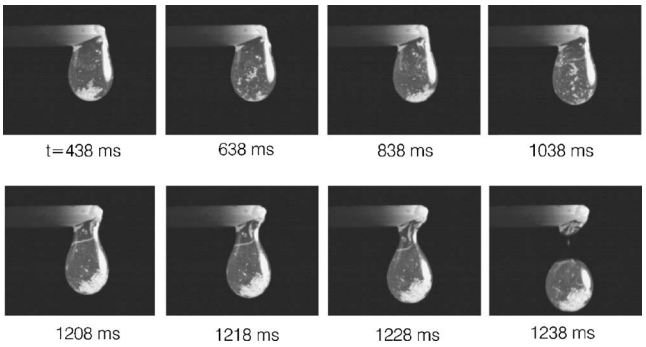

Fig. 4 Evolution of a PD of copper during the melting process

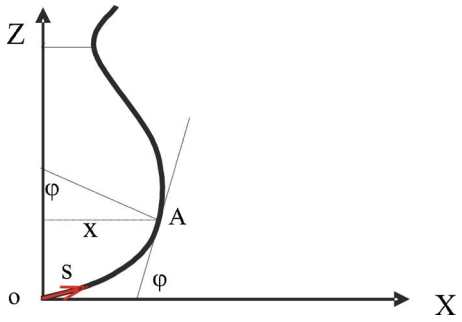

Fig. 5 Parameters for determining the profile of a PD

$$\frac{d\varphi}{dS} = \frac{2}{B} - Z - \frac{\sin\varphi}{|X|} \tag{4}$$

$$\frac{dX}{dS} = \cos\varphi \tag{5}$$

$$\frac{dZ}{dS} = \sin\varphi \tag{6}$$

where S, X, Z, and B are dimensionless parameters for (s, x, z, b) based on the characteristic length $\sqrt{\Delta\rho g/\sigma}$.

In order to calculate the surface tension, the theoretical profiles can be fitted onto the experimental profiles of the PD. Based on the governing equations, there are two adjustable parameters for matching the profiles. A change in B results in different profiles, which resemble the evolution of the shape of a drop during the growth process. Moreover, a theoretical profile (dimensionless) should be scaled to fit onto an experimental one. Therefore, the scale factor (or length scale) provides a value for surface tension.

5 Image Analysis

In order to investigate the dynamic behavior of the PDs formed because of melting, the evolution of the melt is photographed at a rate of 1000 frames/s. Such a frame rate made it possible to capture the complete phenomena of growing, necking, and detachment of a primary drop and a secondary (satellite) droplet. In order to study the drop evolution cycle from formation to detachment, we developed an image analysis program [27] based on MATLAB. Images were digitized, and the detailed information about the evolving drop, such as volume, necking rate, growth rate, and interfacial flow, were obtained.

The melting rate for the experiments was approximately 0.06 g/s. Drop profiles produced in such melting rate were fitted well by the YL profiles. Surface tensions calculated based on comparing the experimental and the theoretical profiles were presented in Ref. [29]. The method of matching the theoretical profiles on the experimental profiles was applied with another automated image analysis program, which finds the best fit, i.e., the corresponding surface tension, based on the YL equations [29]. The iterative procedure of matching the theoretical profiles on the experimental profiles was controlled by a relative error defined as

$$e_{\text{exp-YL}} = \max\left(\frac{R_{\text{exp},i=1} - R_{\text{YL},i=1}}{R_{\text{exp},i=1}}, \frac{R_{\text{exp},i=2} - R_{\text{YL},i=2}}{R_{\text{exp},i=2}}\right) \times 100\% \tag{7}$$

where $i=1$ and $i=2$ correspond to the maximum diameter (equator) and the minimum diameter (neck), respectively. R_{expt} and R_{YL} are the radial lengths based on the experimental and the theoretical results. The definition of errors based on the difference be-

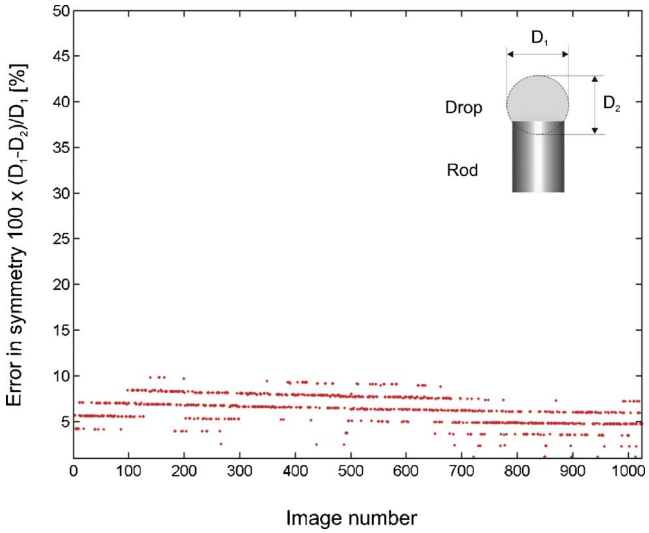

Fig. 6 Investigation of the symmetry for the drop during the formation

tween theoretical and experimental profiles at two critical—vertical—locations (Eq. (7)) was the most efficient approach among different criteria. For instance, an error based on three different diameters was more time consuming and resulted in a similar accuracy.

6 Experimental Results

Images in Fig. 4 show a PD formed at the tip of a copper rod. The PD accelerates after the neck is formed; therefore, higher frame rates were required to capture the process. As Fig. 4 shows, detachment of the primary drop and the satellite droplet happened almost 40 ms after the neck was formed. Images in the first row (200 ms interval) show the growth of a PD. During this period, the drop moves very slowly; however, as it gets closer to the detachment time, the dynamics of the droplet becomes much faster. Therefore, images close to the detachment have been shown at a shorter time interval. In some cases, small oxide layers appeared as white spots on the surface of drops; we used these particles to study the interfacial flow.

A rf-ICP torch provides a reliable and a containerless heating source at high temperature, which does not introduce combustion byproducts or contact contaminations (as in conduction heating equipments). In addition, the high temperature gas, flowing from the rf-ICP torch at velocities in the order of 15 m/s, has very low density. Figure 6 illustrates diameters of an evolving drop in two perpendicular directions. As is shown, the flow of plasma gas does not have enough momentum to affect the symmetry of the liquid ligament.

The surface tension of the samples was measured initially based on fitting the theoretical profiles on the experimental profiles. Figure 7 shows four theoretical profiles matched with the corresponding experimental profiles at four different instants of time. Based on the figure, the quasiequilibrium condition was a reasonable assumption, and the Laplacian profiles predicted the melt shape accurately. The surface tension of the samples—in the current condition—was calculated by different methods independent of the profiles. For instance, results calculated by the DW method based on the data collected from different detached drops are given in Table 2. The DW method uses the weight of detached drops and applies a correction factor suggested by Harkins and Brown [21] to calculate the surface tension. The dynamic surface tension values are shown in Fig. 8. Results from the DW and PD methods are also depicted in this figure. The Geometry of drops determines a parameter that is used in the PD method.

The effect of rod diameter was investigated for three different diameters. It was observed that melting samples with larger diameters required higher powers, i.e., higher gas flows. This higher gas momentum introduced more errors in the measurements. It should be noted that, based on Fig. 9, for time periods before necking, the larger the diameter of samples, the more difficult it is to match the theoretical profiles on the experimental profiles. This was the case for the rod with a diameter of 5.0 mm. In terms of purity, the 5.0 mm rod had the highest purity. Although the higher purity corresponds to higher surface tension values, the difference in the purities of the samples of different diameters is unlikely to be responsible for the scatter in values calculated for different samples.

According to the literature, surface tension values for liquid copper near the melting point range between 1.038 N/m and 1.355 N/m [7]. These values were reported for pure copper in vacuum. Since the results from different methods used in our study were consistent, deviation from the literature is due to the oxidation, the purity of the samples, and less likely, the choice of liquid density.

6.1 Discussion and Error Analysis. The systematic errors involved in the study of surface tension are of two kinds; one is associated with the methods used and the other is related to the heating method. Since the neck (where the drop detaches) is close to the solid-liquid interface, the temperature must be close to the melting point of the sample; therefore, any probable temperature gradient in the PDs is ignored. This is more meaningful in the case of molten metals because of their high thermal conductivity.

The samples were cleaned chemically and mechanically; hence, probable oxidation plays the most significant role rather than the contamination. However, for the case of ceramics, this will not introduce much difficulty. Estimating the effect of contaminations and impurities is complicated because some impurities are highly surface active and some are not. Due to the effect of possible active impurities, higher values of the measurements are preferred in this field on the argument that they shall be closer to the true value for totally pure metals [30]. This argument should be taken with great caution because the existence of systematic errors should be ruled out by careful calibration experiments. Nevertheless, quantifying the possible oxidations or determining the precision in heating the samples at such temperatures is difficult.

The distortion of the drop shape due to the gas flow is negligible, while the pressure of the plasma gas and its momentum cannot affect the symmetry of drop profiles for samples with small diameter (see Fig. 6). The interfacial flow is due to three major reasons: shear force of the gas flow, melting rate, and the Marangoni effect, although the shear force contributes more than the others.

Regarding the PD method, the errors introduced due to the empirical correction factors remain. Fitting the profiles in order to measure the surface tension does not depend on an empirical factor; however, it requires relatively high-resolution images with an accurate postprocessing. The accuracy of the image analysis for the present study was 0.02 mm. Uncertainties due to the blurry edges at high temperature, the accuracy in the profile fitting process, and the mechanical oscillations, which affect the equilibrium state of a PD, are the major concerns in this method. The vibration of a drop may cause the drop to depart prematurely, resulting in an underestimation of the surface tension. According to Peterson et al. (1958) [31], small low-frequency vertical oscillations before falling can be a cause of random errors. Therefore, it is recommended that a low melting rate be maintained just before detachment. For the case of liquid metals (also metal oxides), the Rayleigh instability causes the drop to detach from the neck when the ratio of the length to the equator diameter exceeds a critical value ($\approx 1.5-2.5$).

Moreover, the errors due to the liquid density affect most of the surface tension measurement techniques. Considering the sources of uncertainty indicated above, difficulties in an accurate tempera-

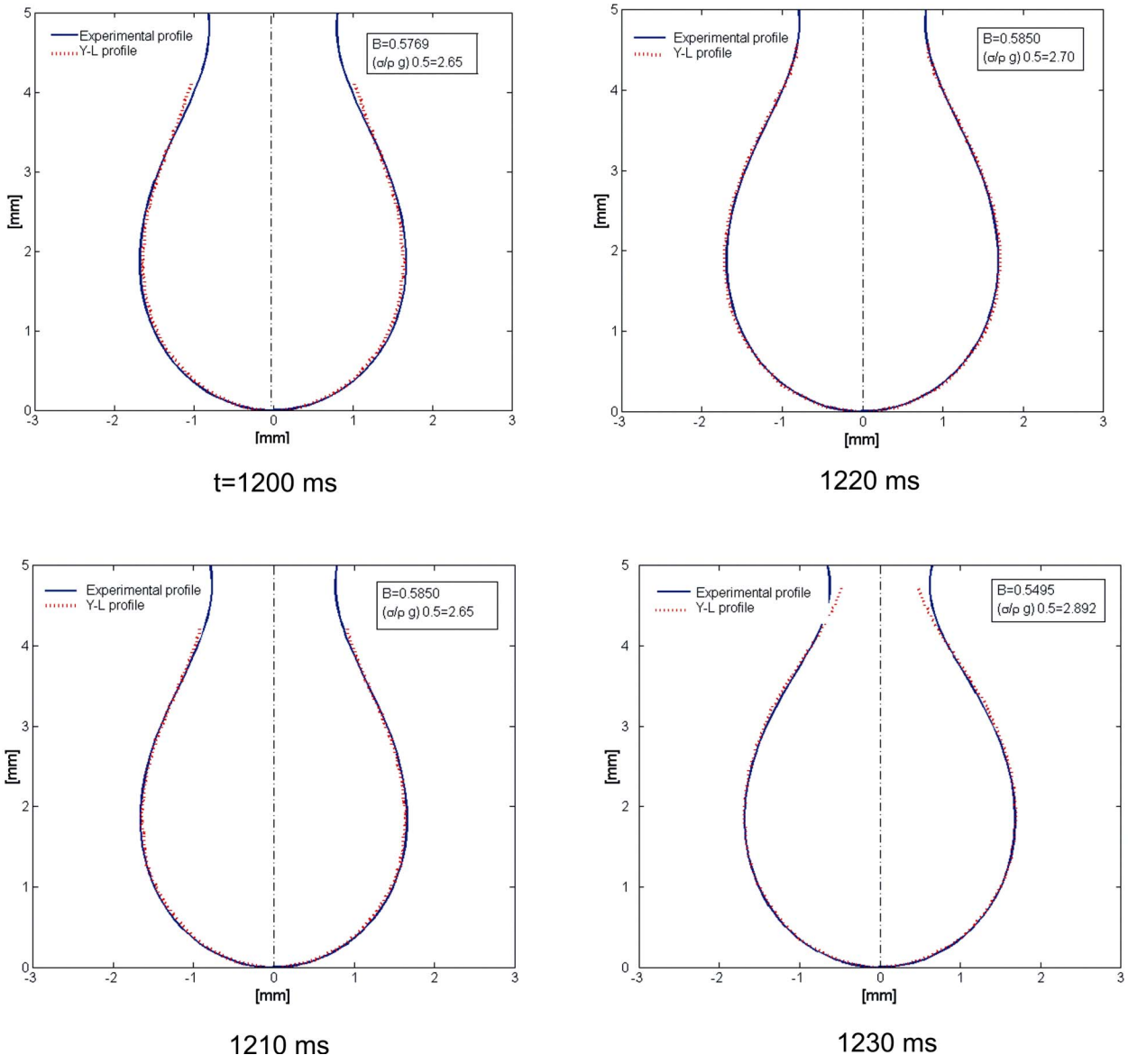

Fig. 7 Experimental and theoretical profiles of copper drop at different instances of time

Table 2 Surface tension of the 1.6 mm copper sample calculated based on the DW method based on correction factors suggested by Harkins et al.

Mass (g)	Drop diameter (mm)	Correction factor	Surface tension (N/m)
0.3401	4.3302	0.7698	0.86
0.3272	4.2748	0.7677	0.83
0.4072	4.5981	0.7794	1.02
0.313	4.212	0.7653	0.8
0.3331	4.3003	0.7687	0.85
0.2986	4.1464	0.7628	0.76
0.2709	4.014	0.7575	0.7
0.2954	4.1316	0.7622	0.76
0.2926	4.1184	0.7618	0.75
0.3111	4.2035	0.765	0.79
0.3131	4.2125	0.7653	0.8
0.2601	3.9599	0.7553	0.67
0.3057	4.179	0.764	0.78

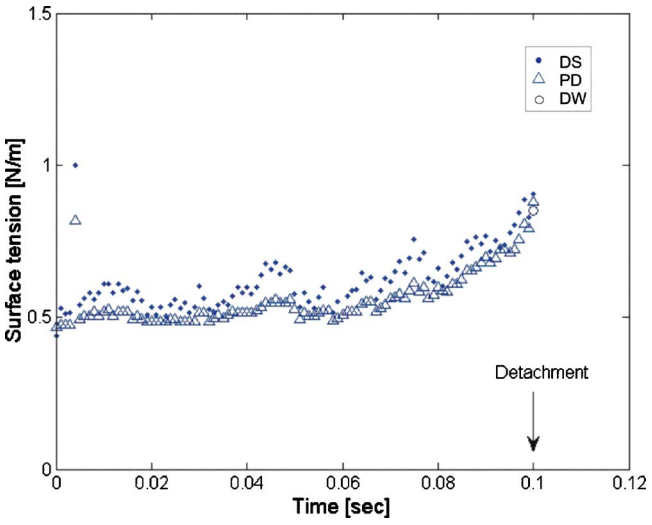

Fig. 8 Surface tension calculated based on experimental profiles, results from DS, PD, and DW methods

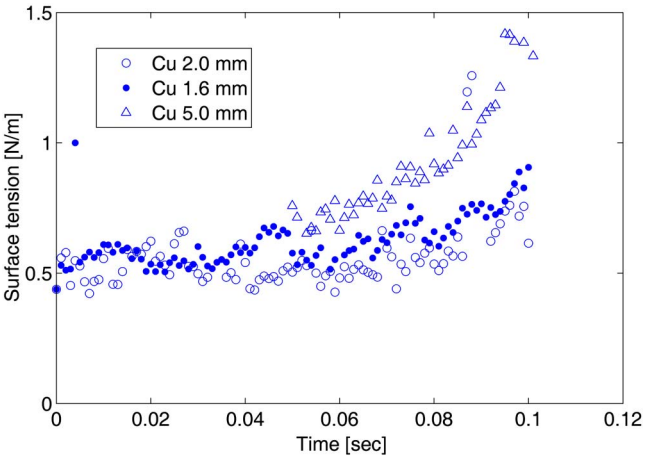

Fig. 9 Surface tension of samples with different diameters calculated based on drop profiles

ture measurement or in obtaining data as a function of temperature are the major drawbacks of this method. In the case of the samples with very low thermal conductivity, such as ceramics, the existence of a temperature gradient increases the uncertainties in the measurements.

7 Numerical Modeling

An alternative approach to investigate the validity of the method described is to simulate the process of drop formation and to apply the profile matching procedure on the numerical profiles. In order to model the process numerically, the fluid properties, including surface tension, are required. Therefore, if the results from this reverse engineering approach recover the input value of the surface tension, the numerical model is reliable and the method is valid.

The process of melting was mimicked by a continuous injection of liquid from a nozzle with a diameter equal to the diameter of the rod. The injecting flow rate was changed during the process to decrease the inertial forces acting on the motion of the PD. In order to decrease the CPU time of the simulation and to obtain a quasiequilibrium condition, the velocity was defined by a step function,

$$V_i = \begin{cases} V_{i1} & t < t_c \\ V_{i2} & t > t_c \end{cases} \qquad V_{i2} < V_{i1} \quad V_{i2} < V_{i1} \tag{8}$$

Reducing the velocity after the time t_c decreases the inertia forces; this facilitates the comparison between the resulting profiles with the YL profiles. Reducing the inertial forces also decreases the oscillations due to the momentum of the injected liquid and the restoring surface tension forces. Therefore, the PD will be closer to the quasiequilibrium state presumed for the YL profiles. The higher the flow rate (or the viscosity), the greater the overestimation in the volume of the detached drop (i.e., surface tension) [32]. In addition, the flow rate has a larger effect on increasing the volume of the satellite than that of the primary drops [10].

7.1 Mathematical Formulation. The fluid mechanics equations governing the process of injection of a Newtonian fluid from a nozzle, the continuity and the momentum equations, are as follows:

$$\nabla \cdot \mathbf{V} = 0 \tag{9}$$

$$\frac{\partial(\rho \mathbf{V})}{\partial t} + \nabla \cdot (\rho \mathbf{V}\mathbf{V}) = -\nabla P + \nabla \cdot \tau + \mathbf{F}_b \tag{10}$$

We implemented the volume of fluid (VOF) method to track free surfaces. According to this method, volume fraction f is a scalar function, which is 1 or zero for the cells containing the denser fluid or lighter fluid, respectively; for the interfacial cells, it assumes a value between zero and 1 [33]. Advection of the volume fraction is governed by

$$\frac{\partial f}{\partial t} + \mathbf{V} \cdot \nabla f = 0 \tag{11}$$

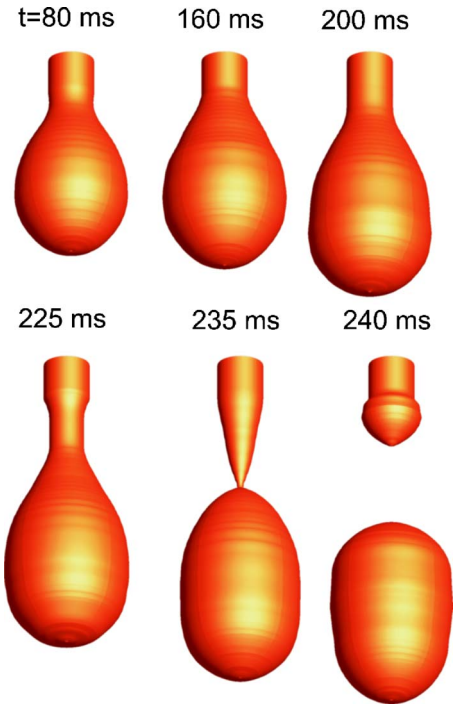

Fig. 10 Axisymmetric simulation of drop formation, results from numerical solution of full NS equations in cylindrical coordinates

7.2 Numerical Model. An axisymmetric two-fluid model [33] based on the finite volume method (FVM) is used to solve the full NS equations. The incompressible interfacial flows in such two immiscible fluids (the melt and the surrounding gas) are separated by an interface. The present numerical model uses a one-field VOF tracking method based on the one fluid VOF method modified by Youngs [34]. The numerical code is based on RIPPLE [35] with a modified volume tracking algorithm. The surface tension force is applied by using the continuum surface force (CSF) method [36]. This method applies the surface tension force as a body force on a limited region around the interfacial cells. In the one-field method, the concept of mixed properties is used to represent cells containing multiple fluids [33].

8 Numerical Results and Discussion

Numerical modeling of the process was performed for a nozzle diameter of 1.6 mm. The dynamics of the drop formation and detachment is shown in Fig. 10. Profiles of a drop during its evolution are shown in Fig. 11. The density, surface tension, and viscosity of the melt were 8000 kg/m, 0.85 N/m, and 5.3×10^{-7} m^2/s, respectively, and the velocity was reduced at 60 ms from 0.35 m/s to 0.1 m/s. The input value of the surface tension was selected based on the results obtained from the DW method and the profile fitting on the experimental images. The instant at which the velocity is changed, t_c, was obtained from a simulation with a constant velocity of V_{i1}. The second velocity V_{i2} was a small velocity used to increase the volume (weight) of the droplet gently reach a gradual detachment. In a simulation with a constant uniform velocity of 0.35 m/s, the detachment happened at

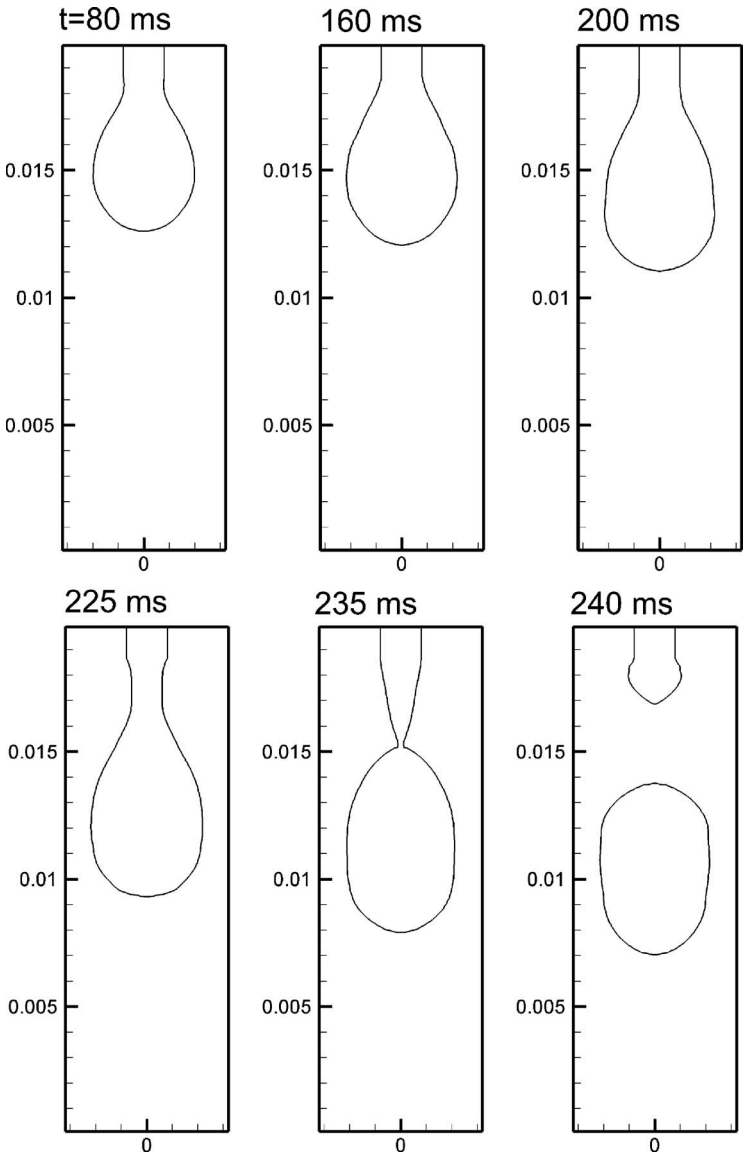

Fig. 11 Profiles of the numerical drop

230 ms. Setting a simulation with the same condition but with a step function for injection velocity changing from 0.35 m/s to 0.1 m/s at t_c=60 ms resulted in the detachment at 237 ms. The density and the kinetic viscosity of the surrounding gas were 1.0 kg/m and 1.54×10^{-4} kg/m s, respectively.

Figure 12 shows the velocity and pressure distribution 60 ms after the start of the injection (almost 177 ms to the detachment). The interface of the liquid is continuously under oscillation during the growth period. The oscillation (capillary waves) is the result of the interaction between the injected momentum and the restoring surface tension force. The outflow of the melt from the nozzle generated a doughnut shape circulation in the surrounding gas; this is illustrated as two circulations in the vertical section shown in Fig. 12(*a*). As the drop grows, a number of circulations move toward the interface of the profile. A portion of these circulations is due to some spurious currents [37] in the numerical implementation of the surface tension force.

Spurious currents are currently the major challenge in modeling free surface flows. This study was started with a (3D) simulation of the process. However, because of spurious currents, the dynamics of the simulations were not accurate enough for our measurements. Therefore, we implemented this axisymmetric model. In this two-fluid model, spurious currents are not as much to affect the dynamics of drops within the size range of our interest. It will be shown that the model predicts drop profiles in the current surface tension dominant flow very accurately. In the case of high spurious currents, these nonphysical velocities deform the profiles and make it impossible to fit a theoretical profile (i.e., YL profile) on the simulations.

According to the pressure contour (Fig. 12(*b*)), there is a jump in pressure across the interface of the drop, which is due to the surface tension. The size of the domain is selected so that the effect of boundaries on the flow is negligible.

Such numerically produced profiles were compared with the theoretical profiles resulting from the YL equations. Therefore, by optimizing the value of the capillary length (characteristic length) and the curvature at the apex, the surface tension value was calculated at any instant of time. The semiexperimental correlation presented by Huh and Reed [38] was used for the initial value for the curvature at the apex. This value and a corresponding capillary length were iteratively changed, and the set (curvature at the apex and capillary length) corresponding to the minimum error (relative difference between the numerical profile and the Laplacian curve) was chosen.

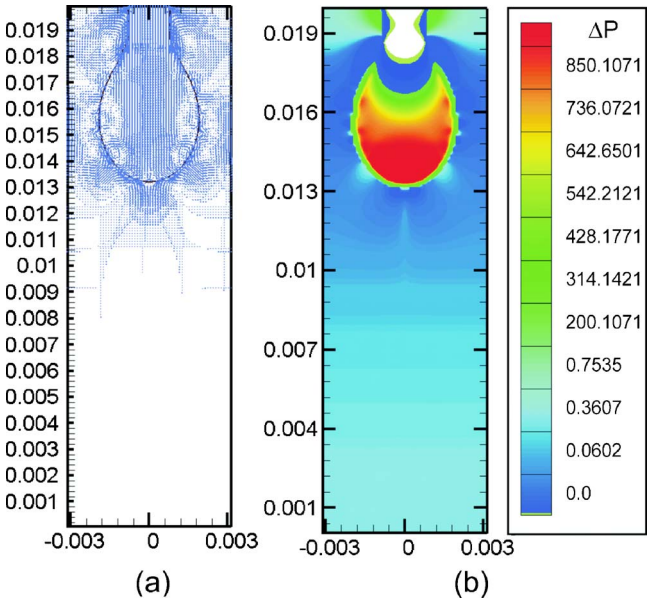

Fig. 12 Velocity field (*a*) and pressure contour (*b*) for a drop close to detachment time

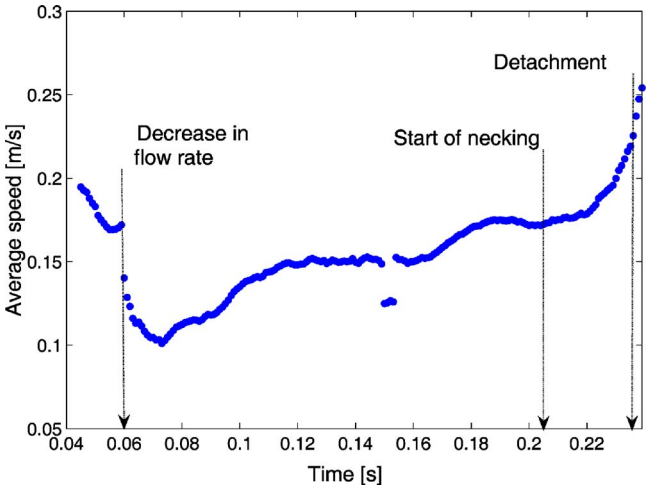

Fig. 13 Average speed of the numerical drop. The speed includes the speed of all numerical cells containing the drop (defined in Eq. (12)).

Since the major differences between the YL profiles and the profiles that resulted from the numerical solution of the NS equations are because of inertial and viscous effects, these variations can be interpreted based on an overall quantity representing flow convection, for instance, kinetic energy or an average speed for each instant of time. Such a speed can be defined as

$$\bar{V} = \frac{\sum_{i=1}^{i\,\max}\sum_{j=1}^{j\,\max}(u_{ij}^2 + v_{ij}^2)^{1/2} f_{ij}}{\sum_{i=1}^{i\,\max}\sum_{j=1}^{j\,\max} f_{ij}} \tag{12}$$

where u and v are components of the velocity field, and f is the VOF function. The VOF function is unity in the domain where there is a denser fluid. Therefore, such a definition of the average speed for each profile during the evolution process considers the flow field inside the denser liquid (the drop) rather than the flow field in the surrounding fluid. The average speed for the profiles is shown in Fig. 13. As indicated in Fig. 13, the drop formation process was divided into three stages. The first stage started from the beginning of injection until $t=60$ ms. During this period the fluid formed a pendant ligament at the tip of the nozzle. Then, the drop grew until it was heavy enough to start moving downward. The last stage began when the drop started to move, and the speed (i.e., kinetic energy) started to increase.

By initiating a neck, the shape became closer to a sphere. As a result, the kinetic energy started to increase, and the surface energy started to decrease. The gradual increase became faster when the gravitational force overcame the surface tension force. In this third stage, the neck diameter decreased very fast (in about 30 ms). The necking stage was longer when the injection velocity (i.e., the inertial forces) was lower. A similar trend was observed for the other sets with different injection functions; the faster the drop grew, the shorter the necking period was.

Figure 14 shows the relative deviation of the profiles from the quasiequilibrium profiles predicted by the YL equations. This deviation (or error in the matching process) is defined by Eq. (13), where N is the number of numerical cells on the height of the growing drop at each instant of time. This definition depicts the average of the relative errors in terms of distances between the numerically produced profiles and the YL profiles. This error was defined based on all the diameters corresponding to the number of the numerical cells capturing the drop in the vertical direction,

$$\mathrm{Dev}_{\text{Num-YL}} = \frac{1}{N}\sum_{i=1}^{N}\left|\frac{R_{\text{Num},i} - R_{\text{YL},i}}{R_{\text{Num},i}}\right| \times 100\% \tag{13}$$

Figure 15 shows the corresponding calculated surface tensions based on a simulation with a surface tension input value of 0.85 N/m. According to the average speed of the profiles during the drop formation, after the initial stages with a relatively higher speed, the calculated surface tension was in good agreement with the input value. It shows that for time intervals in which the speed is not increasing, the surface tension is calculated with an acceptable accuracy. Generally, since the quasiequilibrium assumption of the YL equation does not consider the presence of inertial and viscous forces, the error increases with speed. Figures 13 and 14 show that the error is increased as the average speed is increased; however, the calculated dynamic surface tension (shown in Fig. 15) agrees with the input value of the model. The scatter in the surface tension values that resulted from the measurement at some certain instants of time is reasonable since the profiles for a dynamic and a viscous flow ejection are fitted by the static-inviscid profiles. In addition, the measured values are the dynamic surface

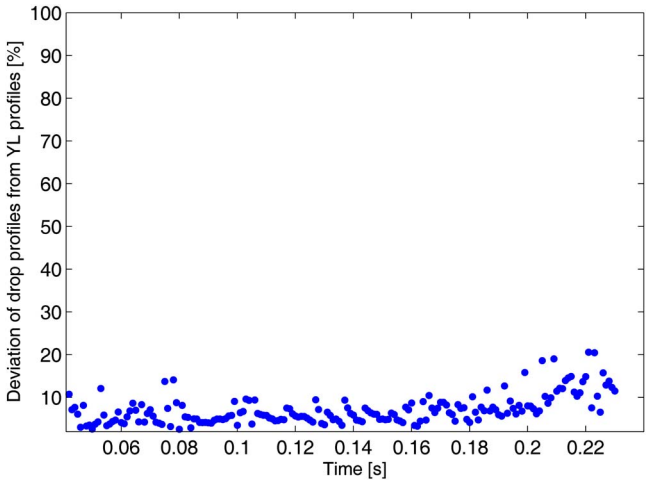

Fig. 14 Deviation of the numerical profile from quasiequilibrium condition during the drop formation

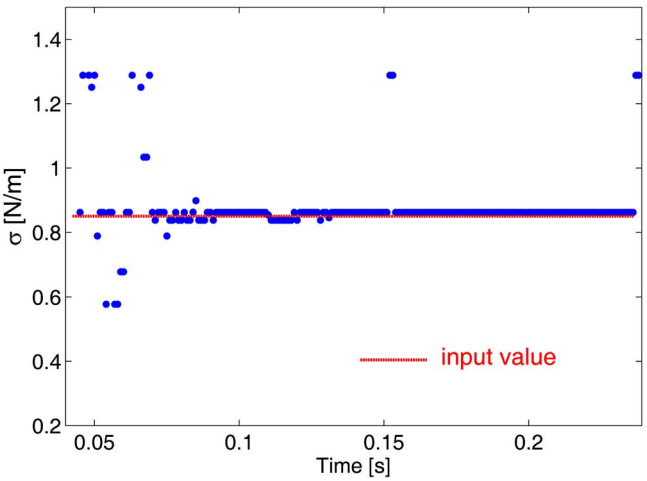

Fig. 15 Surface tension values based on fitting the YL and simulation profiles. Line: the input value for the simulation.

tension values and the input value is the static surface tension, valid for the instants when the drop comes to a complete equilibrium.

The ratio of the kinetic energy to the surface energy determines at which instants, during the drop formation, the inertial forces become important as compared to the surface forces. Figure 16 shows this ratio for the process of drop formation. Accordingly, for the periods in which the ratio remained almost constant, the surface tension values calculated in Fig. 15 did not change, and the results were in a very good agreement with the input data. However, as the ratio of the kinetic energy to the surface energy changes in time, higher deviations between the model and the input value are observed. These deviations occur in two separate periods: one in the initial stage of injection when the velocity is higher, and the other when the weight of PDs pulls down the drop quickly.

The results show the possibility of estimating the dynamic surface tension for the viscous process of the drop injection by using the YL equation. The scatter in the results, which happened at about 150 ms, was investigated in more detail. The reason for this jump in calculating surface tension (which is consistent with the jump in Fig. 16) was a ripple that happened on the surface of the profile. The ripple started from the apex and ended adjacent to the nozzle.

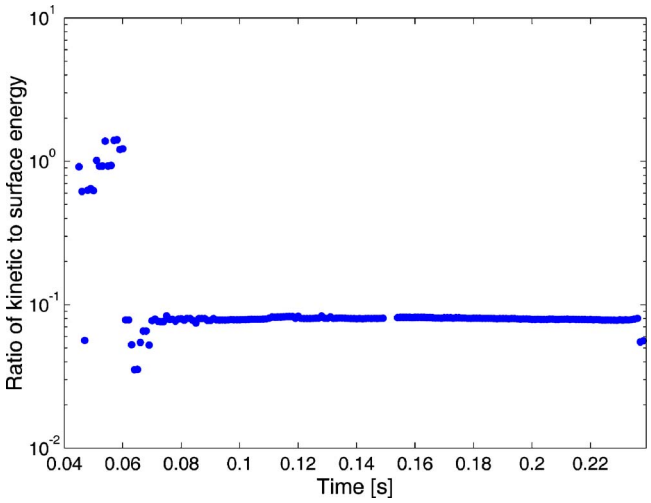

Fig. 16 Ratio of kinetic energy to surface energy for a numerical drop from formation to detachment. The kinetic energy was calculated based on the injection velocity.

The effect of oscillations introduced by measurements was recently studied by Leser et al. (2005) [39]. Their study suggests that the hydrodynamic effects cause a deviation of drop and bubble profiles from a Laplacian shape. They analyzed the oscillation behavior of drops and bubbles for water/air and oil/air systems to estimate the limiting frequency up to which the shape tensiometry was valid. Based on that study, for frequencies higher than 3 Hz, a certain dilatational elasticity modulus (which cannot exist for a pure water/air interface) was observed. This apparent modulus was mimicked by the deviation of the drop/bubble shape from that given by the YL equation. The higher the surface tension, the higher the critical frequency (threshold) above which the errors are considerable. Since the surface tension values used in our study were those of liquid metals (or even metal oxides), with at least one order of magnitude higher than water, the expected threshold value for frequency should have been much higher. However, density and viscosity also affect the inertial forces, i.e., the critical frequency as well [40].

The effects of two different types of injection velocity function were investigated in Figs. 17 and 18. Fig. 17 corresponds to linear—decaying—functions for injection with different slopes, whereas Fig. 18 corresponds to different step functions for injection velocity. Figures 17(*a*) and 18(*a*) show the injection functions. Kinetic energies, defined based on the injection velocity, are illustrated in Figs. 17(*b*) and 18(*b*), and surface energies are shown in Figs. 17(*c*) and 18(*c*). The volume of the drops at each instant of time was calculated based on the numerical profiles. The surface energy was defined based on the free surface of drops and the input value of surface tension. Among all the cases, the linear function with the slope of −1.75 resulted in a uniform drop formation. Therefore, errors in fitting the YL profiles remained less than 2% for the majority of the points. For cases with slopes −1.3460 and −0.8974, the inertia affects the drop formation and results in more deviations from the quasiequilibrium. The same trend was observed in the set with a step injection. The case in which the fluid was injected for a longer period with an initial velocity of −0.35 m/s resulted in more deviations. At certain instants of time, the inertial effects deformed the growing profile so quickly that the surface forces could not restrain the Laplacian shape. Therefore, the shape tensiometry resulted in inaccurate values. In addition, such cases with higher velocities in inaccurate values (see Figs. 17(*d*) and 18(*d*)) resulted in a faster detachment and a smaller primary drop.

9 Conclusion

The surface tension of molten copper was calculated based on the YL equations. The measurement procedure consisted in melting copper rods with a rf-ICP torch and recording the melting dynamics. The melting of the samples was simulated numerically, and the resulting profiles were compared against the theoretical YL equations. The agreement between the input value of the surface tension and the dynamic values calculated based on the profiles validated the accuracy of the model.

Deviations between the theoretical and the numerical profiles were due to hydrodynamic effects. These hydrodynamic effects, which influence the accuracy of the surface tension measurement methods based on drop profiles, were discussed. The proposed method is applicable for higher melting point alloys and ceramics, and the discussions on the hydrodynamic effects are valid for any material.

Nomenclature

b = curvature at the apex
B = dimensionless curvature at the apex
CCD = charge-coupled device

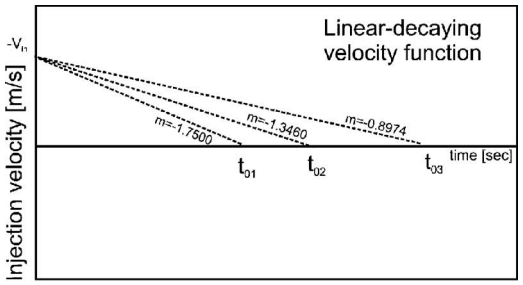

(a) Linear injection

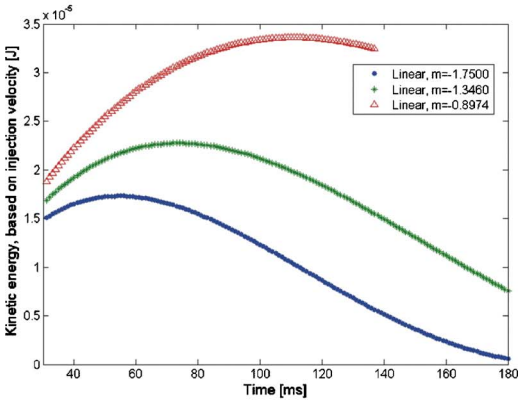

(b) Kinetic energy

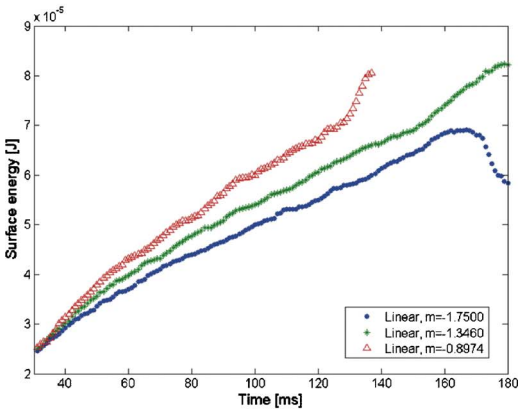

(c) Surface energy

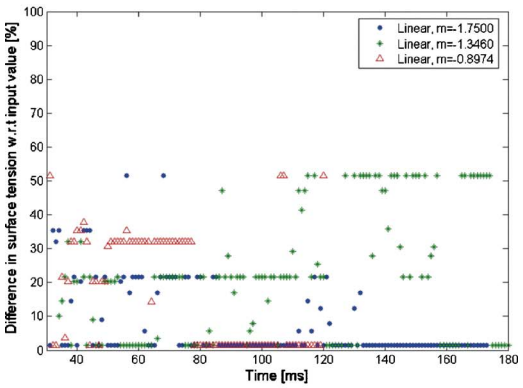

(d) Deviation from the input value

Fig. 17 Effect of injecting flow on drop formation and surface tension measurement based on drop profiles, linear injection

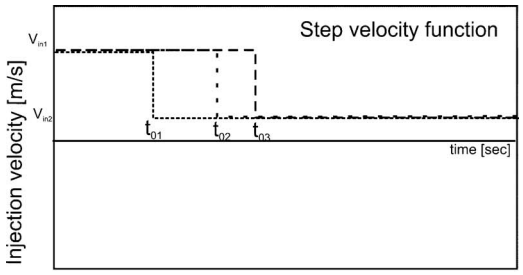

(a) Step injection

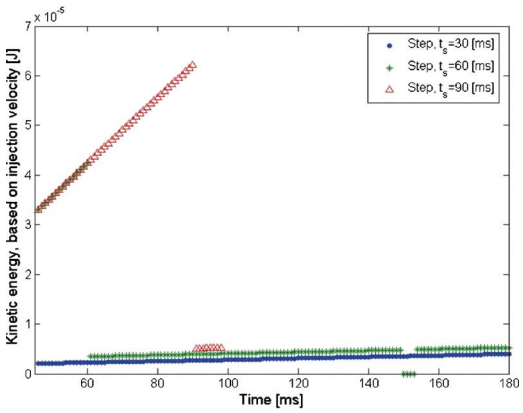

(b) Kinetic energy

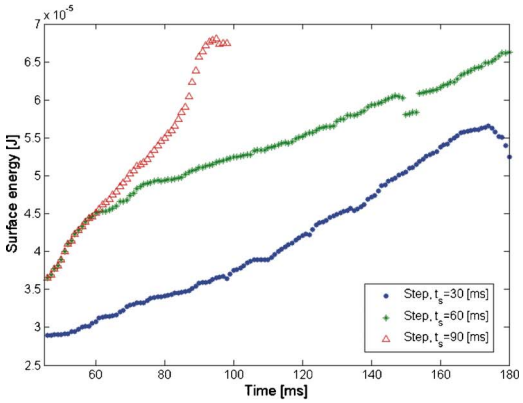

(c) Surface energy

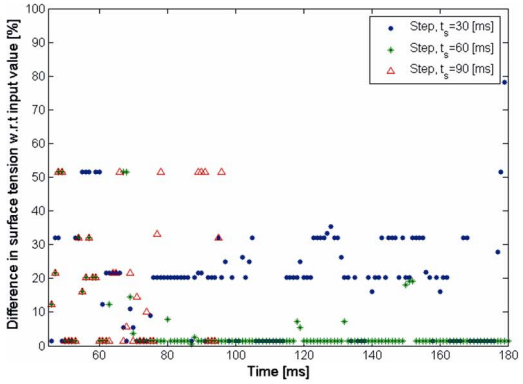

(d) Deviation in measured surface tension from the input

Fig. 18 Effect of injecting flow on drop formation and surface tension measurement based on drop profiles, step injection

CSF = continuum surface force
d = diameter of rod
DW = drop weight
$\mathrm{Dev}_{\mathrm{Num\text{-}YL}}$ = error of numerical profiles versus Young-Laplace profiles
$e_{\mathrm{Expt\text{-}YL}}$ = deviation in experimental profiles versus Young-Laplace profiles
F_b = body forces per unit volume
FVM = finite volume method
f = volume of fluid function
g = gravitational acceleration
L = capillary constant
P = pressure field
PD = pendant drop
rf-ICP = radio-frequency inductively coupled plasma
r_{cap} = radius of capillary
R = radial distance of profiles from the central axis
t_c = critical time
u, v = components of velocity field
V = velocity vector
$\bar{V}$ = average speed
VOF = volume of fluid
YL = Young-Laplace
τ = stress tensor
σ = surface tension
ρ = density
μ = kinematic viscosity
φ = component of polar coordinate

References

[1] Brooks, R. F., Egry, I., Seetharaman, S., and Grant, D., 2001, "Reliable Data for High Temperature Viscosity and Surface Tension: Results From a European Project," High Temp. - High Press., **33**(6), pp. 631–637.

[2] Drelich, J., Fang, C., and White, C. L., 2003, "Measurement of Interfacial Tension in Fluid-Fluid Systems," in *Encyclopedia of Surface and Colloid Science*, Marcel Dekker, New York.

[3] Rusanov, A. I., and Prokhorov, V. A., 1996, "Interfacial Tensiometry," in *Studies of Interface Science*, D. Mobius, and R. Miller, eds., Elsevier, Amsterdam.

[4] Andreas, J., Hauser, A., and Tucker, W. B., 1938, "Boundary Tension by Pendant Drops," J. Phys. Chem., **42**, pp. 1001–1019.

[5] Tate, T., 1864, "On the Magnitude of a Drop of Liquid Formed Under Different Circumstances," Philos. Mag., **27**, pp. 176–180.

[6] Egry, I., Lohoefer, G., and Jacobs, G., 1995, "Surface Tension of Liquid Metals: Results From Measurement on Ground and in Space," Phys. Rev. Lett., **75**, pp. 4043–4046.

[7] Allen, B. C., 1972, "The Surface Tension of Liquid Metals," in *Liquid Metals: Chemistry and Physics*, S. Z. Beer, ed., Marcel Dekker, New York, pp. 161–212.

[8] Passerone, A., and Ricci, E., 1998, "High Temperature Tensiometry," in *Drops and Bubbles in Interfacial Research*, D. Mobius and R. Miller, eds, Elsevier Science, New York, pp. 475–524.

[9] Peregrine, D. H., Shoker, G., and Symon, A., 1990, "The Bifurcation of Liquid Bridges," J. Fluid Mech., **212**, pp. 25–39.

[10] Zhang, X., and Basaran, O. A., 1995, "An Experimental Study of Dynamics of Drop Formation," Phys. Fluids, **7**, pp. 1184–1203.

[11] Clanet, C., and Lasheras, J. C., 1999, "Transition From Dripping to Jetting," J. Fluid Mech., **383**, pp. 307–326.

[12] Rayleigh, L., 1899, "Investigations in Capillarity," Philos. Mag., **48**, pp. 321–327.

[13] Young, T., 1805, "An Essay on the Cohesion of Fluids," Philos. Trans. R. Soc. London, **95**, pp. 65–87.

[14] Laplace, P. S., 1839, "Traite de Mecanique Celeste," in *Supplement to Book 10*, Gauthier-Villars, Paris.

[15] Bashford, F., and Adams, J. C., 1883, *An Attempt to Test the Theory of Capillary Action*, Cambridge University Press and Deighton Bell&Co., Cambridge.

[16] Maze, C., and Burnet, G., 1969, "A Nonlinear Regression Method for Calculating Surface Tension and Contact Angle From the Shape of a Sessile Drop," Surf. Sci., **13**, pp. 451–470.

[17] Maze, C., and Burnet, G., 1971, "Modifications of a Nonlinear Regression Technique Used to Calculate Surface Tension From Sessile Drops," Surf. Sci., **24**, pp. 335–342.

[18] Hartland, S., and Hartley, R. W., 1976, *Axisymmetric Fluid-Liquid Interfaces*, Elsevier Scientific, Amsterdam.

[19] Lahooti, S., Del Rio, O. I., Neumann, A. W., and Cheng, P., 1996, "Axisymmetric Drop Shape Analysis (ADSA)," in *Applied Surface Thermodynamics*, A. W. Neumann and J. K. Spelt, eds., Marcel Dekker, New York, pp. 441–509.

[20] Hoorfar, M., and Neumann, A. W., 2006, "Recent Progress in Axisymmetric Drop Shape Analysis (ADSA)," Adv. Colloid Interface Sci., **121**(1–3), pp. 25–49.

[21] Harkins, W. D., and Brown, F. E., 1919, "The Determination of Surface Tension (Free Surface Energy) and the Weight of Falling Drop," J. Am. Chem. Soc., **41**, pp. 499–524.

[22] Wilkinson, M. C., 1972, "Extended Use of, and Comments on, the Drop-Weight (Drop-Volume) Technique for the Determination of Surface and Interfacial Tensions," J. Colloid Interface Sci., **40**, pp. 14–26.

[23] Garandet, J. P., Vinet, B., and Gros, P., 1994, "Considerations on Pendant Drop Method: A New Look at Tate's Law and Harkins' Correction Factor," J. Colloid Interface Sci., **165**, pp. 351–354.

[24] Miller, R., Schano, K.-H., and Hofmann, A., 1994, "Hydrodynamic Effects in Measurements With the Drop Volume Technique at Small Drop Times I. Surface Tensions of Pure Liquids and Mixtures," Colloids Surf., A, **92**, pp. 189–196.

[25] Miller, R., Bree, M., and Fainerman, V. B., 1998, "Hydrodynamic Effects in Measurements With the Drop Volume Technique at Small Drop Times III. Surface Tensions of Viscous Liquids," Colloids Surf., A, **142**, pp. 237–242.

[26] Montaser, A., and Golightly, D. W., 1992, *Inductively Coupled Plasmas in Analytical Atomic Spectrometry*, 2nd ed., VCH, New York.

[27] Moradian, A., and Mostaghimi, J., 2005, "High Temperature Tensiometry by a Coupled Modeling and Experimental Approach," Proceedings of the International Thermal Spray Conference, Basel, Switzerland, proceedings on DVD.

[28] Moradian, A., and Mostaghimi, J., 2005, "High Temperature Surface Tension Measurement," IEEE Trans. Plasma Sci., **33**(2), pp. 410–411.

[29] Moradian, A., and Mostaghimi, J., 2005, "A New Surface Tension Measurement Technique for High-Melting-Point-Materials," Proceedings of the International Symposium Plasma Chemistry, Toronto, Canada, pp. 939–940.

[30] Vinet, B., Garandet, J. P., Marie, B., Domergue, L., and Drevet, B., 2004, "Surface Tension Measurements on Industrial Alloys by the Drop-Weight Method," Int. J. Thermophys., **25**, pp. 869–883.

[31] Peterson, A. W., Kedesdy, H., Keck, P. H., and Schwartz, E., 1958, "Surface Tension of Titanium, Zirconium, and Hafnium," J. Appl. Phys., **29**, pp. 213–216.

[32] Henderson, D. C., and Micale, F. J., 1993, "Dynamic Surface Tension Measurement with the Drop Mass Technique," J. Colloid Interface Sci., **158**, pp. 289–294.

[33] Mehdi-Nejad, V., 2004, "Modeling Flow and Heat Transfer in Two-Fluid Interfacial Flows with Applications to Drops and Jets," Ph.D. thesis, University of Toronto, Canada.

[34] Youngs, D. L., 1984, "An Interface Tracking Method for a 3D Eulerian Hydrodynamics Code," AWRE Technical Report No. 44/92/35.

[35] Kothe, D. B., Mjolsness, R. C., and Torrey, M. D., 1991, "RIPPLE: A Computer Program for Incompressible Flows with Free Surfaces," Technical Report LA-12007-MS.

[36] Brackbill, J. U., Kothe, D. B., and Zamach, C., 1992, "A Continuum Method for Modeling Surface Tension," J. Comput. Phys., **100**, pp. 335–354.

[37] Francois, M. M., Cummins, S. J., Dendy, E. D., Kothe, D. B., Sicilian, J. M., and Williams, M. W., 2006, "A Balanced-Force Algorithm for Continuous and Sharp Interfacial Surface Tension Models Within a Volume Tracking Framework," J. Comput. Phys., **213**(1), pp. 141–173.

[38] Huh, C., and Reed, R. L., 1983, "A Method for Estimating Interfacial Tension and Contact Angles From Sessile and Pendant Drop Shapes," J. Colloid Interface Sci., **91**, pp. 472–484.

[39] Leser, M. E., Acquistapace, S., Cagna, A., Makievski, A. V., and Miller, R., 2005, "Limits of Oscillation Frequencies in Drop and Bubble Shape Tensiometry," Colloids Surf., A, **261**, pp. 25–28.

[40] Miller, R., 2006, Max-Planck Institute of Colloids and Interfaces, personal communication.

Donghyun You[1]
Center for Turbulence Research,
Stanford University,
Stanford, CA 94305
e-mail: dyou@stanford.edu

Meng Wang
Department of Aerospace and Mechanical Engineering,
University of Notre Dame,
Notre Dame, IN 46556

Parviz Moin
Center for Turbulence Research,
Stanford University,
Stanford, CA 94305

Rajat Mittal
Department of Mechanical and Aerospace Engineering,
George Washington University,
Washington, DC 20052

Vortex Dynamics and Low-Pressure Fluctuations in the Tip-Clearance Flow

The tip-clearance flow in axial turbomachines is studied using large-eddy simulation with particular emphasis on understanding the unsteady characteristics of the tip-leakage vortical structures and the underlying mechanisms for cavitation-inducing low-pressure fluctuations. A systematic and detailed analysis of the velocity and pressure fields has been made in a linear cascade with a moving end-wall. The generation and evolution of the tip-leakage vortical structures have been investigated throughout the cascade using mean streamlines and λ_2 contours. An analysis of the energy spectra and space-time correlations of the velocity fluctuations suggests that the tip-leakage vortex is subject to a pitchwise low frequency wandering motion. Detailed statistics of the pressure fields has been analyzed to draw inferences on cavitation. The regions of low pressure relative to the mean values coincide with regions of strong pressure fluctuations, and the regions are found to be highly correlated with the vortical structures in the tip-leakage flow, particularly in the tip-leakage and tip-separation vortices. [DOI: 10.1115/1.2746911]

Keywords: tip-clearance flow, tip-leakage vortex, cavitation, turbomachinery, large-eddy simulation, vortex dynamics

1 Introduction

The radial clearance between a rotor-blade tip and casing wall in a turbomachine is indispensable for its operation. However, its existence has been a major source of unfavorable flow phenomena. Complicated vortical structures are generated by the tip-clearance flow and its interactions with the end-wall boundary layer, the blade wake, and the neighboring blade. The tip-clearance vortical structures often induce rotating instabilities and blockage in the flow passage, which result in severe performance loss and subsequent stall of axial compressors [1,2]. In addition, in a transonic compressor, the interaction between passage shock and tip-clearance flow is implicated in the degradation of efficiency as well as vibrations and noise generation [3]. These issues have motivated a number of experimental and computational investigations of the compressor tip-clearance flow, and some basic understanding has been achieved (e.g., [4–11]).

On the other hand, in hydraulic turbomachines such as submarine propulsors and liquid pumps, the existence of tip clearance is considered to be a cause for cavitation, which can result in loud acoustic noise, performance deterioration, and the erosion of blades and casing wall (e.g., [8,9,12–14]). In order to understand the mechanisms for cavitation, it is necessary to study the detailed vortex dynamics in the rotor-blade wake and tip-clearance region and the associated low-pressure events.

In the 1950s, Rains [12] investigated cavitation phenomenon in an axial flow pump and observed that the tip-leakage vortex forms from the leading edge of the blade, and convects downstream across the passage for a range of tip-gaps of 0.2–5.2% chord. Later, in an axial pump, Zierke et al. [13] showed the existence of a trailing-edge tip-separation vortex that migrates radially upward along the trailing edge. This trailing-edge tip-separation vortex then moves along the circumferential direction near the casing and in the opposite direction of blade rotation. They also established the trajectory of the tip-leakage vortex core with the observation of the unsteadiness of the vortex, subject to wandering and kinking motions in the passage and downstream. Similar unsteadiness is also discussed in the work of Goto [9]. Pressure fluctuation and turbulence measurements made adjacent to the casing wall show the track of developing tip-leakage vortex as a strip of high turbulence levels, which grows across the passage [8]. The pressure frequency spectra of Goto [9] showed a general rise in high-frequency spectral levels in the vicinity of the casing, suggesting the presence of small scale turbulence in the region containing the tip-leakage vortex. Although these and other earlier investigations have revealed gross features of the tip-leakage vortical structures and related flow phenomena, the detailed dynamics of the vortical structures such as the tip-leakage vortex and tip-separation and induced vortices, and influence of the end-wall vortical structures on the low pressure, pressure fluctuations, and cavitation are poorly understood.

In recent years, a series of experiments has been performed at Virginia Tech. to make detailed measurements of the flow field in a low speed linear compressor cascade with stationary and moving end-walls [15–20]. Mean velocity, vorticity, turbulent kinetic energy, and frequency energy spectra were measured downstream of the rotor blades. Wang and Devenport [16] employed a moving end-wall and found noticeable difference in the mean velocity and Reynolds stress distributions from the experiments that utilized a stationary end-wall [15]. Kuhl [18] and Ma [20] examined the effects of upstream vortex pairs on the downstream tip-leakage vortex. Employing a stationary end-wall, Wenger et al. [17] performed two-point measurements of the turbulent fluctuations in the downstream tip-leakage flow, and showed conclusively that the tip-leakage vortex is not subject to low-frequency pitchwise "wandering" motions. On the other hand, an experiment employing a moving end-wall showed a noticeable low-frequency spectral peak in the pitchwise velocity energy spectra [16]. However, no further investigation regarding the origin and mechanism of this low-frequency peak were made.

These experiments [15,16,18,20] have provided useful information regarding the flow as well as valuable data for validating computational techniques. However, since the measurements were limited to the flow field at least one-and-a-half chord lengths downstream from the trailing edge, they could not shed light on

[1]Corresponding author.

Contributed by the Fluids Engineering Division of ASME for publication in the JOURNAL OF FLUIDS ENGINEERING. Manuscript received May 22, 2006; final manuscript received January 24, 2007. Review conducted by Paul Durbin.

the upstream flow features, which are critically important. In addition, these experiments could not provide information regarding the mean pressure and pressure fluctuations in the cascade passage region. Ma [20] performed pressure measurements in the far downstream planes using microphones but indicated that the measured mean pressure and pressure fluctuations could be affected by the noise in the cascade tunnel, probe interference, and wind induced noise inside the microphone.

Experimental measurements of the tip-leakage flow in the vicinity of the tip-gap very close to the end-wall are generally difficult due to technical and safety issues. In addition, the strong unsteadiness of the tip-leakage flow limits the applicability of conventional Reynolds-averaged Navier-Stokes approaches in a computational study. These difficulties have been major obstacles to a detailed understanding of the tip-leakage flow physics leading to cavitation. Although the gross feature of the tip-leakage vortex has been known for some time, a deeper quantitative understanding of the dynamics of the tip-leakage vortical structures and their interaction with the end-wall boundary layer is needed to elucidate the tip-leakage cavitation mechanisms.

In this study, the tip-leakage flow, particularly in regions not studied experimentally, is investigated using data generated by large-eddy simulation (LES). The objective is to gain an improved understanding of the unsteady characteristics of the vortical structures present in the typical tip-clearance configuration, and the cavitation-inducing low-pressure fluctuations associated with the tip-leakage vortical structures. In order to gain such an understanding, it is necessary to study the detailed turbulence dynamics in the rotor-blade wake and the tip-clearance region and to examine the space-time correlations of the coherent turbulence structures present in the end-wall tip-leakage flow. A detailed investigation regarding mean pressure and pressure fluctuations is also carried out to understand tip-leakage cavitation in hydraulic turbomachines.

The computational methodology is described in Sec. 2. Details of the vortex dynamics, velocity and pressure fluctuations, and cavitation inception are discussed in Sec. 3, followed by conclusions in Sec. 4.

2 Computational Methodology

2.1 Numerical Method. The numerical algorithm and solution method are described in detail in Ref. [21]. Here, we summarize the main features of the methodology. The three-dimensional, unsteady, incompressible Navier-Stokes equations are solved in a generalized coordinate system on a structured grid in conjunction with a Smagorinsky type dynamic subgrid-scale (SGS) model. Given the fully inhomogeneous nature of the flow, a Lagrangian dynamic SGS model, which averages the model coefficient along the flow pathlines [22], is employed.

The integration method used to solve the governing equations is based on a fully implicit fractional-step method, which avoids the severe time-step restriction in the tip-clearance region. All terms including cross-derivative diffusion terms are advanced in time using the Crank-Nicolson method and are discretized in space by energy-conserving second-order central-differencing. A Newton iterative method is used to solve the discretized nonlinear equations. For the pressure Poisson equation, an efficient multigrid procedure, which is a combination of the line and red-black Gauss-Seidel multigrid method, is used. This method is particularly appropriate for parallelization. The simulation code is parallelized using OpenMP.

2.2 Computational Setup. The flow configuration, coordinate definition, and measurement planes for investigating the flow field are schematically shown in Fig. 1. The present study is focused on a linear cascade with a moving end-wall at the bottom of the tip gap that matches the experimental setup of Wang and Devenport [16]. A single blade passage is considered, with periodic boundary conditions in the y-direction to mimic the flow in the interior of a cascade. The computational domain is of size $L_x \times L_y \times L_z = 1.8C \times 0.929C \times 0.5C$, where C is the blade chord. The mesh size used for the final simulation is $449 \times 351 \times 129$.

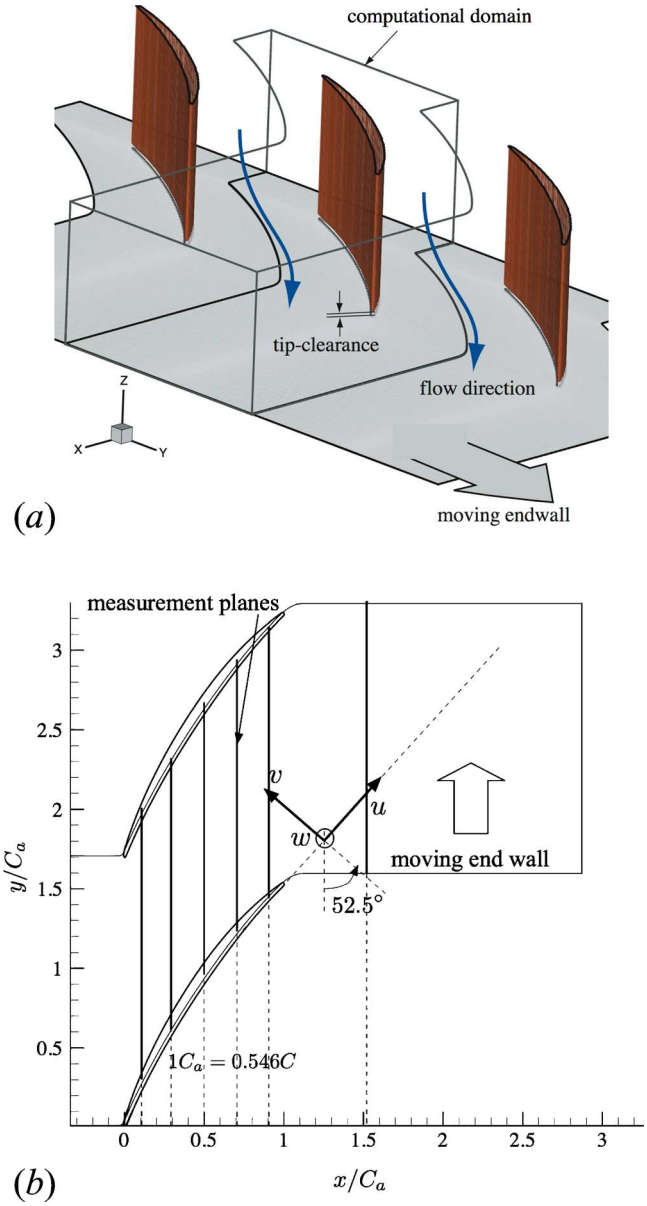

Fig. 1 (*a*) Flow configuration and coordinate system for the tip-clearance flow and (*b*) measurement planes for investigating the flow field and definitions of velocity coordinates

The important parameters for the simulation are as follows: The size of the tip clearance is $0.0165C$, the blade pitch is $0.9C$, and the blade span is $0.5C$. The blade has a relatively high stagger-angle of about 57 deg. The Reynolds number of this flow is 400,000 based on the chord and inflow free-stream velocity, and the inflow turbulent boundary layer has a Reynolds number of 780 based on the momentum thickness. The momentum thickness of the inflow is 11.8% of the tip-gap size. The speed of moving end-wall is 90.8% of the inflow free-stream velocity. The coordinate variables are normalized using the blade axial chord C_a $(=0.546C)$.

The inflow turbulent boundary-layer data are provided using the method of Lund et al. [23], modified to account for the fact that the mean flow direction is not perpendicular to the inflow/outflow

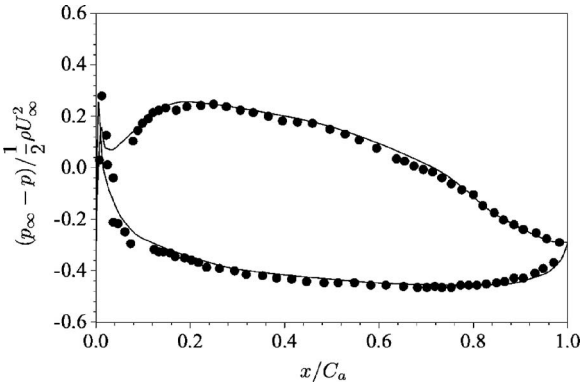

Fig. 2 Surface pressure coefficient at z/C_a=0.916. —, LES; •, experiment [15]

plane. No-slip boundary conditions are applied along the rotor blade and moving end-wall, and the convective boundary condition is applied at the exit boundary.

The difficulty with grid topology in the tip-clearance region is overcome by an approach that combines an immersed boundary technique [24] with a structured grid in a generalized coordinate system. The advantage of using a curvilinear mesh with an immersed-boundary method is that we can generate grid lines almost parallel to the blade surface. This ensures an adequate resolution on the boundary layers, and allows periodic boundary conditions to be applied on the curved upper and lower boundaries. The immersed boundary method, when used with the curvilinear mesh, obviates a complex mesh topology and allows us to use a simple single-block mesh [21]. In addition to this, the high stagger angle in the experimental setup necessitates the use of very skewed mesh, which requires fine control of mesh parameters such as the stretching ratio and the aspect ratio, and an adequate formulation of nonlinear convection terms to avoid numerical instability (see Refs. [25,26] for more details).

3 Results and Discussion

3.1 Effects of Resolution and SGS Model. In general, the grid resolution on the blade surface is reasonable compared to previous LES studies of wall bounded turbulent flows using similar numerical methods [27]. The grid spacings based on the chord in the streamwise, pitchwise, and spanwise directions are $9.9\times10^{-4}\le\Delta x/C\le1.4\times10^{-2}$, $9.8\times10^{-4}\le\Delta y/C\le6.5\times10^{-3}$, and $4.6\times10^{-4}\le\Delta z/C\le1.2\times10^{-2}$, respectively. In wall units, the blade-surface resolution in the region of primary interest is within the range $\Delta x^+\le50$, $\Delta y^+\le3$, and $\Delta z^+\le30$ (Δz^+ increases up to 90 far from the tip-gap region). As seen in Fig. 2, the pressure distribution over the blade surface is generally comparable with that of experiment with stationary end-wall [15] and indicates that the current mesh topology is capable of resolving the gross features of the flow. The grid resolution normal to the end-wall is in the range of $0.3\le\Delta z^+\le2.1$. In the directions parallel to the end-wall, Δx^+ and Δy^+ are generally less than 50, except in a small end-wall region where the maximum values reach 90–100 because of the strong effect of the tip-leakage vortex on the boundary layer. In the y-z plane at x/C_a=0.6, more than 50 grid points in the pitchwise and spanwise directions are allocated across the tip-leakage vortex core. The grid spacing based on the chord and the resolution in wall units in the important regions are presented in Tables 1 and 2. The resolution in Kolmogorov units (η), which is estimated by an evaluation of the production and assuming equilibrium, is in the range of $\Delta x/\eta, \Delta y/\eta\le40$, and $\Delta z/\eta\le10$ in the end-wall region, while $\Delta z/\eta$ increases up to 110 far from the end-wall. Figure 3 shows that ratios of the grid spacing to the Kolmogorov lengthscale in the end-wall parallel directions are relatively high underneath the blade-tip and around the tip-leakage vortex core (Figs. 3(a) and 3(b)), while the ratio of the spanwise grid spacing to the Kolmogorov lengthscale is relatively high on the suction surface boundary layer far from the end-wall (Fig. 3(c)).

Prior to this simulation, coarser grid simulations had been carried out to determine the resolution requirements, and the final mesh was subsequently constructed using this information. To investigate the grid sensitivity, simulations of flow through the cascade without tip-gap, which are less expensive than the present simulation, were performed with refined meshes in all three directions, and it was confirmed that results are relatively insensitive to the grid resolution. Figure 4 is an example of the study which shows reasonable robustness of the mean velocity with respect to the grid resolution. Further details of the grid resolution study and comparisons with experimental data were reported in [21].

The simulation is advanced in time with the maximum Courant-Friedrichs-Lewy (CFL) number equal to 4, which corresponds to $\Delta tU_\infty/C\approx0.73\times10^{-3}$, where U_∞ is the incoming free-stream ve-

Table 1 Grid spacing and resolution along the blade suction (pressure) surface at z/C_a=0.2

x/C_a	$\Delta x/C$	Δx^+	$\Delta y/C$	Δy^+	$\Delta z/C$	Δz^+
0.2	0.0025	8.074 (9.341)	0.0004	1.29 (1.50)	0.0045	14.53 (16.81)
0.4	0.0031	10.09 (16.02)	0.0004	1.30 (2.07)	0.0045	14.65 (23.25)
0.6	0.0032	10.73 (18.23)	0.0004	1.34 (2.28)	0.0045	15.09 (25.64)
0.8	0.0045	12.60 (28.13)	0.0004	1.12 (2.50)	0.0045	12.60 (28.13)

Table 2 Grid spacing and resolution on the end-wall

$\Delta x/C$	Δx^+	$\Delta y/C$	Δy^+	$\Delta z/C$	Δz^+
0.001–0.0138	1.82–95	0.0009–0.0066	1.2–100	0.000046	0.3–2.1

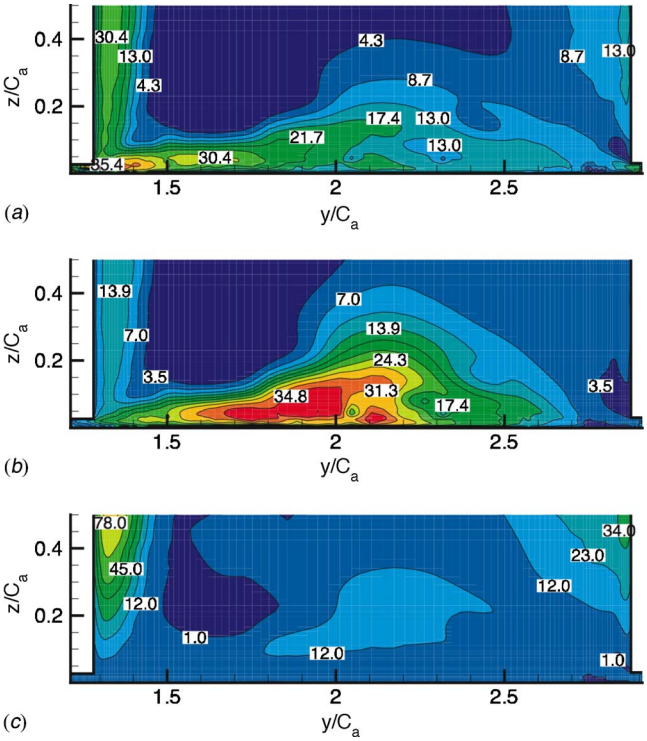

Fig. 3 Resolution in Kolmogorov units (η) in a y-z plane at x/C_a=0.7. (a) $\Delta x/\eta$; (b) $\Delta y/\eta$; (c) $\Delta z/\eta$

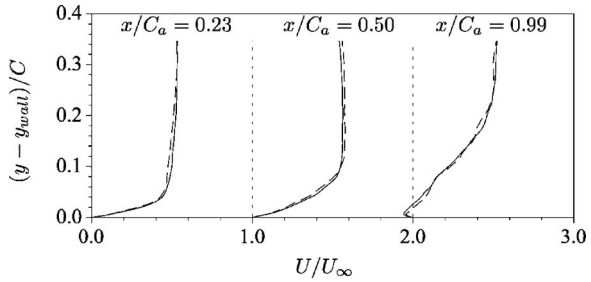

Fig. 4 Mean velocity U/U_∞ profiles on the suction surface. —, 897×701×16 mesh; - - - -, 449×351×8 mesh. The profiles at x/C_a=0.50 and 0.99 are shifted by 1 and 2, respectively.

locity. The effect of CFL number on the instantaneous solution has been examined in simulations performed with CFL numbers of 1.5, 2.5, 4, and 5. As seen in Fig. 5, in terms of the amplitude and phase, the variation of the streamwise velocity is reasonably robust up to the CFL number of 4. The maximum CFL number occurs near the pressure side of the blade tip where the strong downward flow passes across the dense mesh region aligned parallel to the blade tip and to the blade surface as seen in Fig. 6, and except for this location, the CFL number is much less than 1. The severe time-step restriction in the dense mesh region is avoided by employing a fully implicit integration method. In wall units, the time-step ($\Delta t^+ = \Delta t u_\tau^2/\nu$) is generally far less than 0.8. Each time-step requires a wall-clock time of about 200 s when 128 CPUs of an SGI Origin 3800 are used. The results discussed below are obtained by integrating the governing equations over a time interval of about $30C/U_\infty$.

The flow field near the suction surface necessitates enhanced eddy viscosity compared to the pressure side where the eddy-viscosity becomes negligible because of very low level of turbulence activity. Except for the relatively coarse mesh region in the blade wake far from the end-wall, the peak mean eddy viscosity is usually less than ten times the value of the molecular viscosity, which is similar to the magnitude observed in the LES study of backward facing step flow [27]. Figure 7 shows the resolved and total Reynolds shear stress profiles along the spanwise direction at x/C_a=0.6 and y/C_a=1.51, and apparently indicates that the contribution of the subgrid-scale shear stress to the total Reynolds shear stress is reasonably small.

3.2 Development of End-Wall Vortical Structures. The pressure difference between the pressure and suction sides of the blade tip generates a strong jet flow through the blade tip-gap. The tip-leakage jet produces the tip-leakage vortex, tip-separation vortices, and several other secondary vortices such as induced vortices. Although many aspects of the tip-leakage vortex have been reported in the literature, details regarding the evolutionary features of the tip-leakage vortex and other secondary vortices have not been well understood. This understanding is crucial in predicting and eventually controlling the cavitation phenomena in hydraulic tip-clearance configurations since the behavior and pattern of tip-leakage cavitation are closely related to those of the end-wall vortical structures.

In this section, streamlines are utilized to visualize the end-wall vortical structures and investigate their behaviors along their evolutionary paths as shown in Fig. 8. Figure 9 shows mean streamlines in the end-wall normal cross-sectional planes shown in Fig. 8 as viewed by an observer looking upstream. In this plot, a pitchwise velocity that corresponds to the moving end-wall velocity is subtracted from the mean flow field to elucidate the end-wall vortices. Among the distinct vortical structures, the tip-leakage vortex which is found near the suction side of the blade dominates the field. To the right of the tip-leakage vortex, induced vortices are

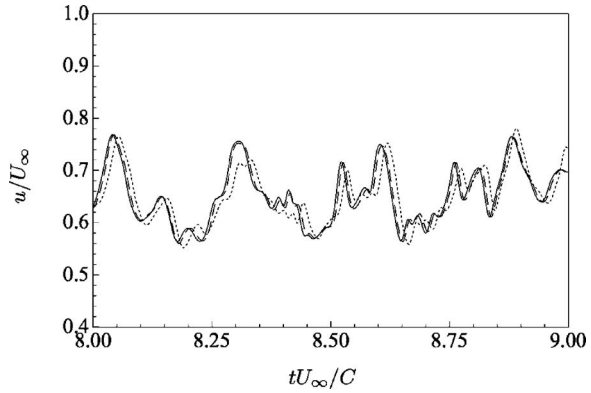

Fig. 5 Time-histories of the streamwise velocity at x/C_a=0.7, y/C_a=1.3, and z/C_a=0.1 using different CFL numbers. —, CFL=1.5; - - - -, CFL=4; ·····, CFL=5.

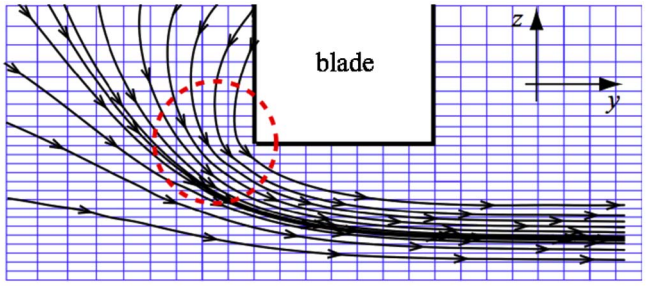

(*a*)

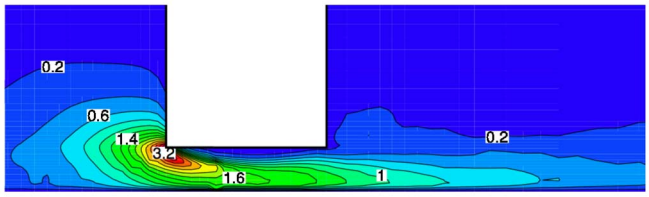

(*b*)

Fig. 6 (*a*) Mean streamlines and (*b*) contour plot of CFL number distribution in a *y*-*z* plane at x/C_a=0.7. In (*a*), every third and second points are shown in *y*- and *z*-directions, respectively.

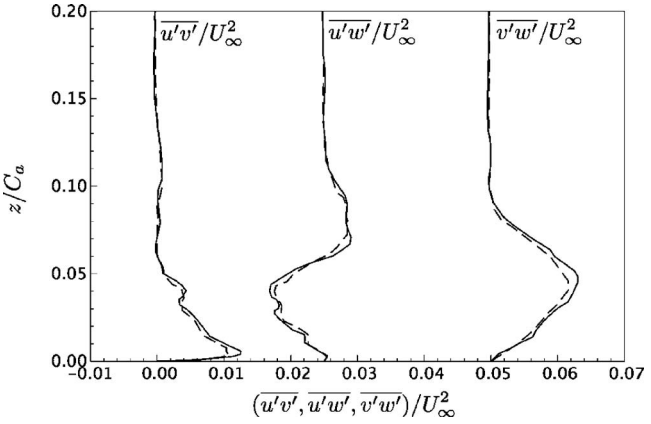

Fig. 7 Profiles of Reynolds shear stresses along the spanwise direction at $(x/C_a, y/C_a)$=(0.6,1.51). —, total stress; - - - -, resolved stress. The profiles of $\overline{u'w'}/U_\infty^2$ and $\overline{v'w'}/U_\infty^2$ are shifted by 0.025 and 0.05, respectively.

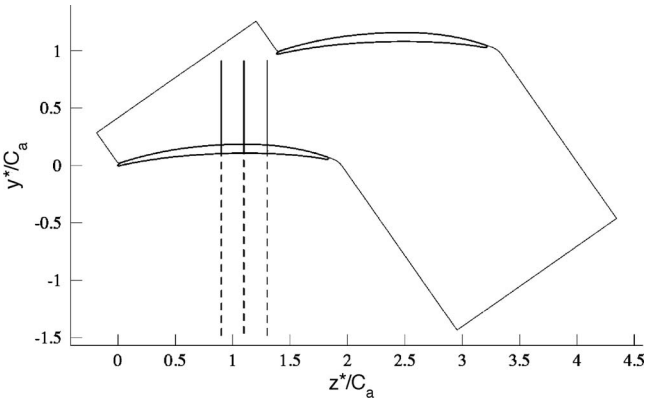

Fig. 8 Locations of the end-wall normal planes in which the mean streamlines in Fig. 9 are visualized

noticed. A pitchwise stretched recirculating region is also observed underneath the blade tip. This circulation is closely related to the tip-separation vortices near the trailing edge.

The generation and evolution of the end-wall vortical structures observed in Fig. 9 are more extensively discussed along with Fig. 10, which shows λ_2 contours representing vortices in a series of y-z planes along the streamwise direction as viewed by an observer looking upstream. It is generally difficult to identify various vortical structures with different convection speeds embedded in the tip-leakage flow using streamlines. The λ_2 vortex identification method makes it easier to clearly identify the vortical structures in

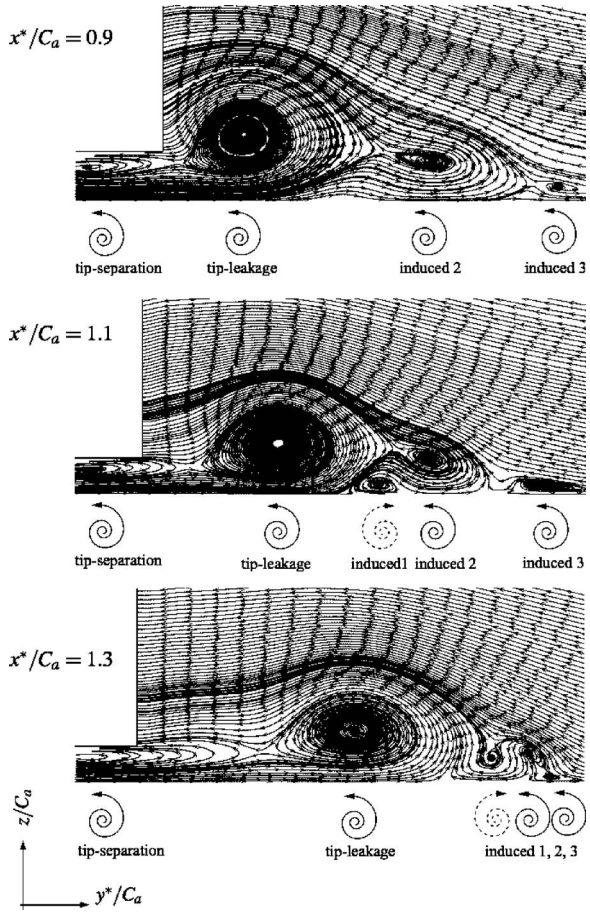

Fig. 9 Mean streamlines showing vortical structures in the end-wall region in y^*-z planes

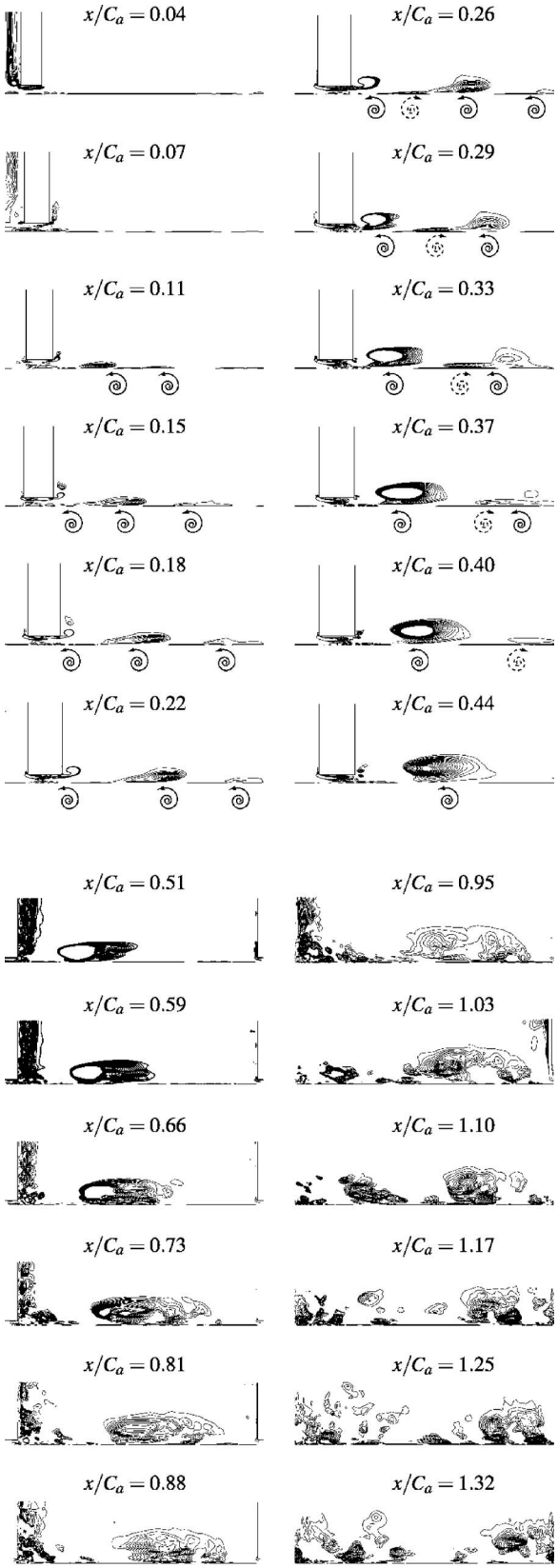

Fig. 10 Generation and evolution of end-wall vortical structures along the streamwise direction visualized using the λ_2 vortex identification method [31]

the end-wall normal planes at various streamwise locations. Since the λ_2 contours cannot provide the rotational direction of a vortex, the rotational direction for each end-wall vortex is determined using streamlines as shown in Fig. 9. At about 7% axial chord, a secondary vortex is induced by the tip separation and by the moving end-wall. This secondary vortex rotates in a counter-clock wise direction and corresponds to the induced vortex 2 in Fig. 9. The tip-leakage vortex begins to be identified at around $x/C_a = 11-20\%$ axial chord. In this range of axial chord, a small secondary vortex is also observed slightly above the tip-leakage vortex near the blade suction surface. However, the strength of the secondary vortex is weak and is not observed in further downstream locations. At 26% axial chord, the strong tip-leakage vortex and the induced vortex 2 which is generated in the upstream induce another secondary vortex (induced vortex 1 at $x^*/C_a = 1.1$ and 1.3 in Fig. 9) between them. The induced vortex 1 is found to rotate in the opposite direction of the other vortices and its rotational strength increases with the strength of the tip-leakage vortex. During the course of its evolution, the strength of the first induced vortex decreases rapidly after 30% axial chord. The mechanism for generation of the third secondary vortex (induced vortex 3 in Fig. 9) is unclear. It is observable from the plane at 11% axial chord location, but its rotational strength is much weaker than those of the other vortices. It may be induced by the end-wall motion which drags the inflow turbulent boundary layer in the positive pitchwise direction.

The strength of the induced vortices is significantly reduced at about 37% axial chord, where the rotational strength of the tip-leakage vortex reaches its maximum. Then, the strength of the tip-leakage vortex decreases with axial chord and pitchwise stretching of the vortex becomes significant ($x/C_a = 0.40$ and 0.44). As seen at 51% and 59% axial chords, the induced vortices are still identifiable near the pressure side of the neighboring blade, but their strengths are much reduced and they eventually dissipate. Muthanna and Devenport [15] and Wang and Devenport [16] also observed the induced vortices, but they could not clarify the mechanisms for their generation, propagation, and decay. In their experiments, it was assumed that the induced vortices disappear from the end-wall by being engulfed by the tip-leakage vortex, not by dissipation.

From 51% axial chord location, another noticeable vortical structure is found on the blade suction surface that corresponds to the blade boundary layer separation. The tip-separation vortices become significant near the suction side of the blade tip after the mid-chord. Unlike the tip-leakage vortex which is formed by the roll-up of the tip-leakage jet, the tip-separation vortices are generated by the circulating region, which is dragged by the tip-leakage jet (Fig. 9).

An interesting development of the tip-leakage vortex is found at about 73% axial chord. At this location, the pitchwise stretched tip-leakage vortex breaks up near the end-wall and its shape becomes more complicated. However, even at further downstream locations ($x/C_a \geq 0.81$), the core of the main part of the tip-leakage vortex is still well defined. Near the trailing edge ($x/C_a = 0.95$), the end-wall vortical field becomes highly complicated due to the tip-leakage vortex separation, the tip-separation vortices, and the blade wake near the blade tip. The end-wall region further downstream is characterized by the interaction of these vortical structures.

3.3 Two-Point Correlations of Velocity Fluctuations. In this section, the spatial and temporal behaviors of the coherent structures present in the tip-leakage flow are examined more quantitatively. Two-point correlations of velocity fluctuations are computed to elucidate the coherent structures embedded in the end-wall tip-leakage flow. Figure 11 shows the mean streamwise velocity contour in a y-z plane at $x/C_a = 1.51$ as seen by an observer looking upstream and the location (**A**) where the two-point correlations of velocity fluctuations are computed. Vertical

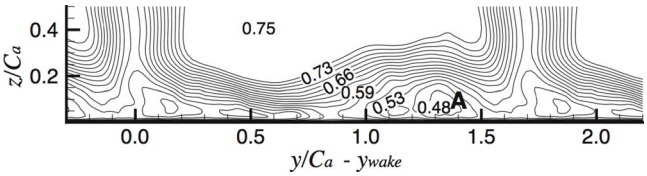

Fig. 11 Contour plot of the mean streamwise velocity in a y-z plane at $x/C_a = 1.51$ and location where the energy spectra in Fig. 13 and space-time correlations in Fig. 15 are measured. y_{wake} denotes the location of peak deficit in the blade wake.

bundles of the mean streamwise velocity contour are present in the wakes of rotor blades, and the tip-leakage vortices are found as velocity deficits near the end-wall. In this plane, the mean streamwise velocity and turbulence intensity profiles are compared with the experimental data along the spanwise direction at $y/C_a = 1.35$, and are shown in Fig. 12. Considering the experimental difficulty in measuring near wall flow quantities on a moving end-wall and the mass leakage in the experiment (see Refs. [21,28] for more detailed discussion on this issue), the agreement is favorable.

In order to obtain energy spectra of velocity fluctuations and space-time correlations, which will be discussed later in this section, about 15,000 samples of the streamwise, pitchwise, and spanwise velocity components were collected over a time interval $TU_\infty/C \sim 20$. The Lomb periodogram technique [29] with an oversampling factor of 4 was used to perform the spectral analysis of unevenly sampled data. Note that the time step is not constant because the filtered Navier-Stokes equations are integrated in time using a fully implicit method with a fixed CFL number.

Figure 13 shows normalized energy spectra of velocity fluctuations computed in the core of the tip-leakage vortex (see Fig. 11 for the location). The spectral density and frequency are normalized using the inflow free-stream velocity (U_∞) and blade chord (C). Energy spectra for the three velocity components show broadband characteristics of the turbulent fluctuations present in the end-wall tip-leakage flow. Energy spectra in all three velocity components predict an inertial subrange that is typically described with the slope of $-5/3$. In addition, the present results at $x/C_a = 1.51$ show favorable agreement with the experimental data provided by Wang and Devenport [16].

In the core of the tip-leakage vortex inside the cascade passage ($x/C_a = 1.51$), noticeable spectral peaks are observed in the energy

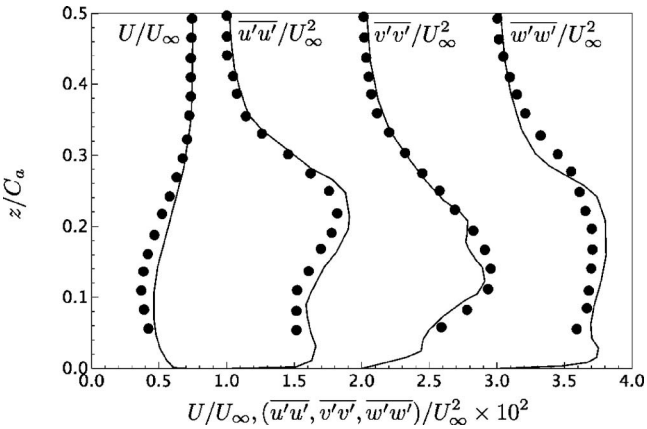

Fig. 12 Profiles of the mean streamwise velocity (U/U_∞) and Reynolds normal stresses ($(\overline{u'u'}, \overline{v'v'}, \overline{w'w'})/U_\infty^2 \times 10^2$) along the spanwise direction at $(x/C_a, y/C_a) = (1.51, 1.35)$. —, LES; •, experiment [16]. The profiles of $\overline{u'u'}/U_\infty^2 \times 10^2$, $\overline{v'v'}/U_\infty^2 \times 10^2$, and $\overline{w'w'}/U_\infty^2 \times 10^2$ are shifted by 1, 2, and 3, respectively.

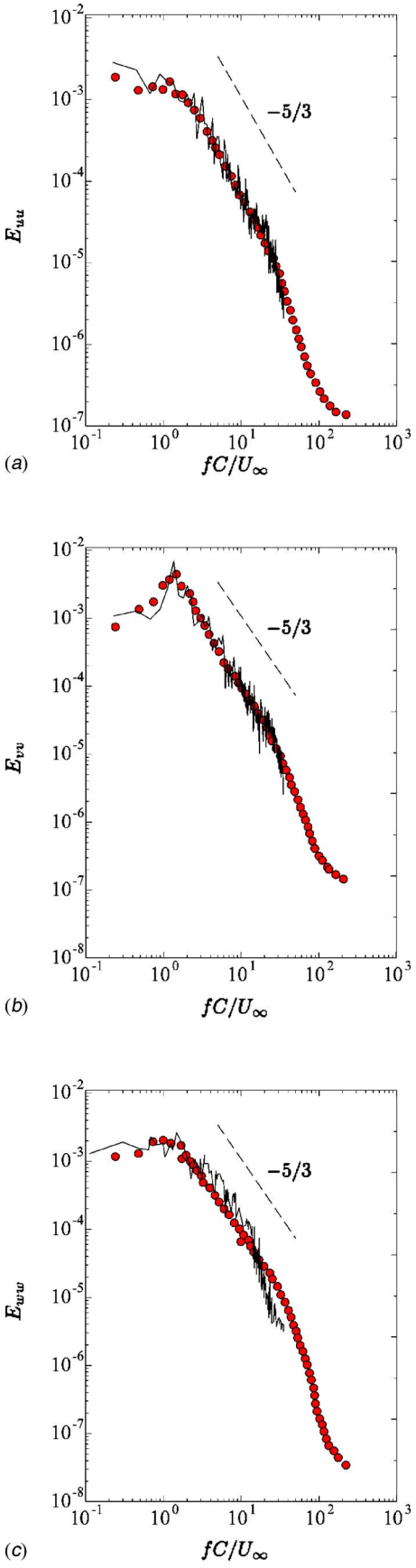

Fig. 13 One-dimensional frequency spectra of velocity fluctuations at the location A in Fig. 11. (*a*) E_{uu}; (*b*) E_{vv}; (*c*) E_{ww}. —, LES; •, experiment [16].

spectra of the pitchwise velocity component, while no indications of significant low-frequency coherent structures are found in the energy spectra of other velocity components. The spectral peaks are observed to be concentrated in the non-dimensional frequency of 1.5. The existence of the spectral peak in the pitchwise velocity fluctuations has also been reported by Wang and Devenport [16]. However, it was unclear in this experiment as to what caused the low-frequency spectral peak. This finding was not in accordance with the observations in the experiments employing a stationary end-wall [15] where low-frequency spectral peaks were not observed except for the peak found in the blade wake. By analyzing two-point correlations of the velocity fluctuations in the end-wall tip-leakage flow, Wenger et al. [17] concluded that the low-frequency coherent (or wandering) motion of the tip-leakage vortex is not present in the experiments employing a stationary end-wall.

In order to investigate the possibility that the blade wake causes the observed low-frequency coherent motion, the energy spectra of velocity fluctuations in the blade wake at a location of $x/C_a = 1.51$, $y/C_a = 2.2$, and $z/C_a = 0.9$, which is far from the end-wall, are computed. In Fig. 14, the present LES results are also compared with the experimental data [15]. The LES results show earlier drops of energy in the high-frequency region, especially of the spanwise velocity component. This is related to the relatively coarse resolution along the span far away from the end-wall (see Fig. 3(*c*)). Energy spectra for the pitchwise velocity fluctuations show a prominent spectral peak, which indicates existence of periodic shedding of the blade wake. However, in both the present LES and experiment [16], the measured frequency for the wake shedding is found to be around $fC/U_\infty = 5-6$, which is quite different from the peak frequency ($fC/U_\infty = 1.5$) measured in the end-wall tip-leakage vortex. Therefore, the shedding of the blade wake does not directly influence the pitchwise coherent motion in the end-wall tip-leakage flow.

Energy spectra of velocity fluctuations are processed by an inverse Fourier transform to obtain the normalized space-time correlation coefficients,

$$R_{u_i u_i}(y, \Delta y, z, \Delta z, \Delta\tau) = \frac{\sum_\omega E_{u_i u_i}(y, \Delta y, z, \Delta z, \omega) e^{-i\omega t}}{\overline{u_i^2(y,z)}} \qquad (1)$$

where Δy, Δz, and $\Delta\tau$ represent spatial separations in the pitchwise and spanwise directions, and the temporal separation, respectively. $i = 1, 2$, and 3 correspond to the streamwise, pitchwise, and spanwise directions, respectively.

Considering that the spectral peak appears only in the pitchwise velocity fluctuations, the space-time correlation coefficients for velocity fluctuations are computed as a function of pitchwise and temporal separations. Figure 15 shows the space-time correlations of the pitchwise velocity fluctuations at the same location as for Fig. 13. The space-time correlations show sign changes along the pitchwise separation axis indicating the existence of a large-scale coherent structure. The pitchwise extent of the correlation is roughly equal to the pitchwise extent of the tip-leakage vortex. In the present study, for small values of pitchwise separation, the major axis of the correlation contours is found to be nearly parallel to the time separation axis. This reflects the existence of a coherent motion of the large-scale structure corresponding to the long time delay.

The present correlations are different from those found by Wenger et al. [17] in the stationary end-wall case. They found that the correlations are concentrated in an elliptical region whose major axis extends diagonally in the pitchwise-temporal separation plane. The major axis of the ellipse extends five to six times farther than its minor axis, and no noticeable correlations along the time separation axis are observed for zero pitchwise separation. They concluded that the coherent motions responsible for these correlations are not wandering.

Figure 16 shows the oscillatory feature of the tip-leakage vortex

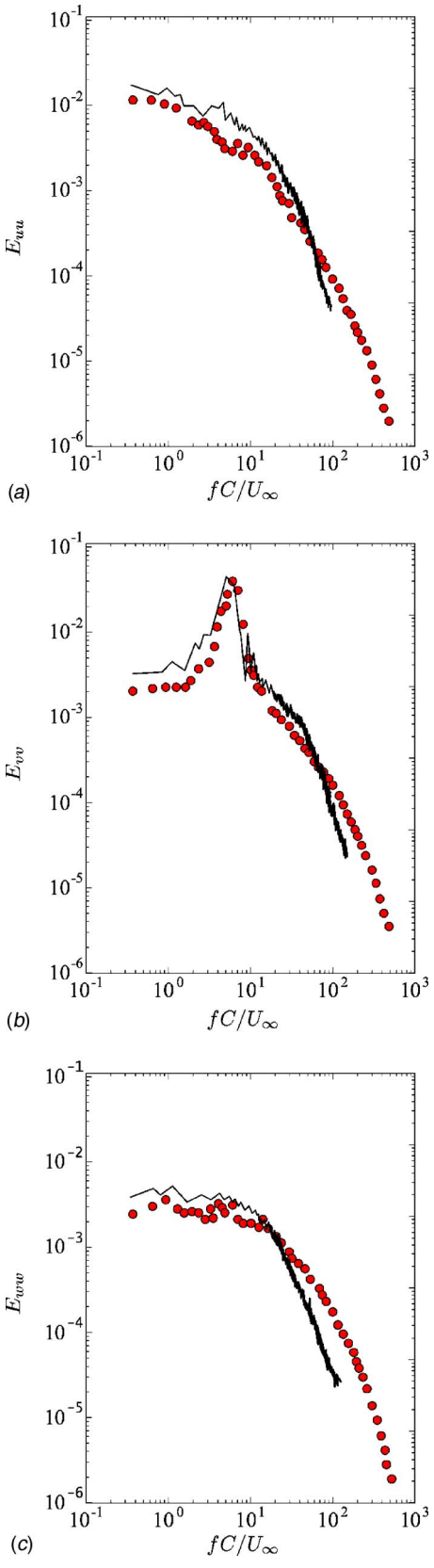

Fig. 14 One-dimensional frequency spectra of velocity fluctuations in the blade wake at x/C_a=1.51, y/C_a=2.2 and z/C_a=0.9. (*a*) E_{uu}; (*b*) E_{vv}; (*c*) E_{ww}. —, LES; •, experiment [15].

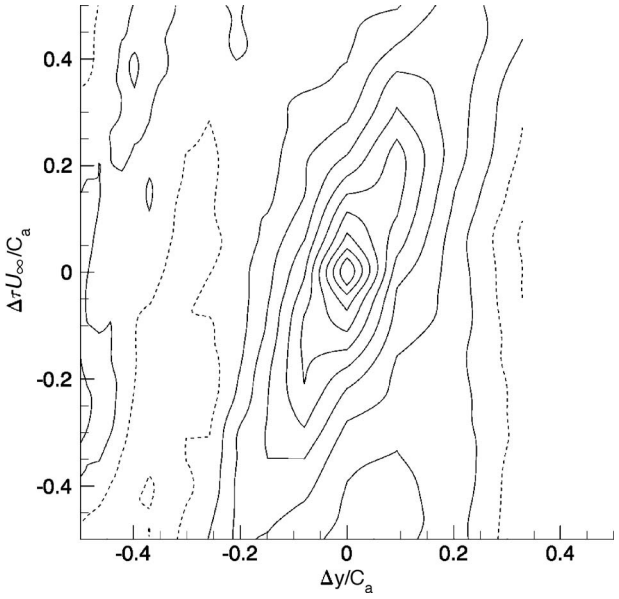

Fig. 15 Contour plot of two-point correlations of the pitchwise velocity fluctuations as a function of the pitchwise spatial and temporal separations in the location A in Fig. 11. Contours are from –1 to 1 with increments of 0.1.

in terms of the instantaneous low pressure iso-surfaces at two different times separated by the half-period of the pitchwise oscillation. It is found that the frequency of the oscillatory motion of the tip-leakage vortex corresponds to the frequency observed in the energy spectra. The exact source of the low-frequency spectral peak is not clearly identified. Considering that the frequency is much lower than the typical wake shedding frequencies observed

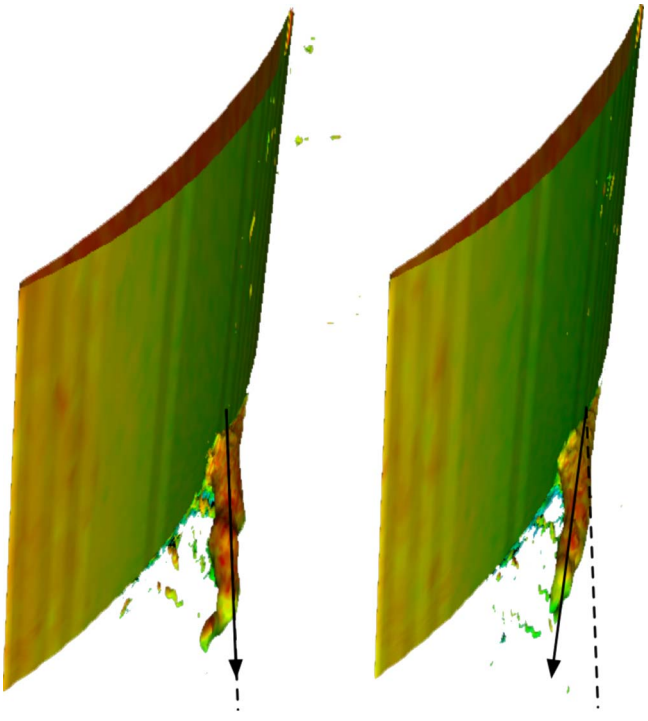

Fig. 16 Instantaneous low-pressure ($p/\rho U_\infty^2$=–0.2) iso-surfaces showing a low-frequency wandering motion of the tip-leakage vortex. (*a*) t_0; (*b*) $t_0+0.33C/U_\infty$.

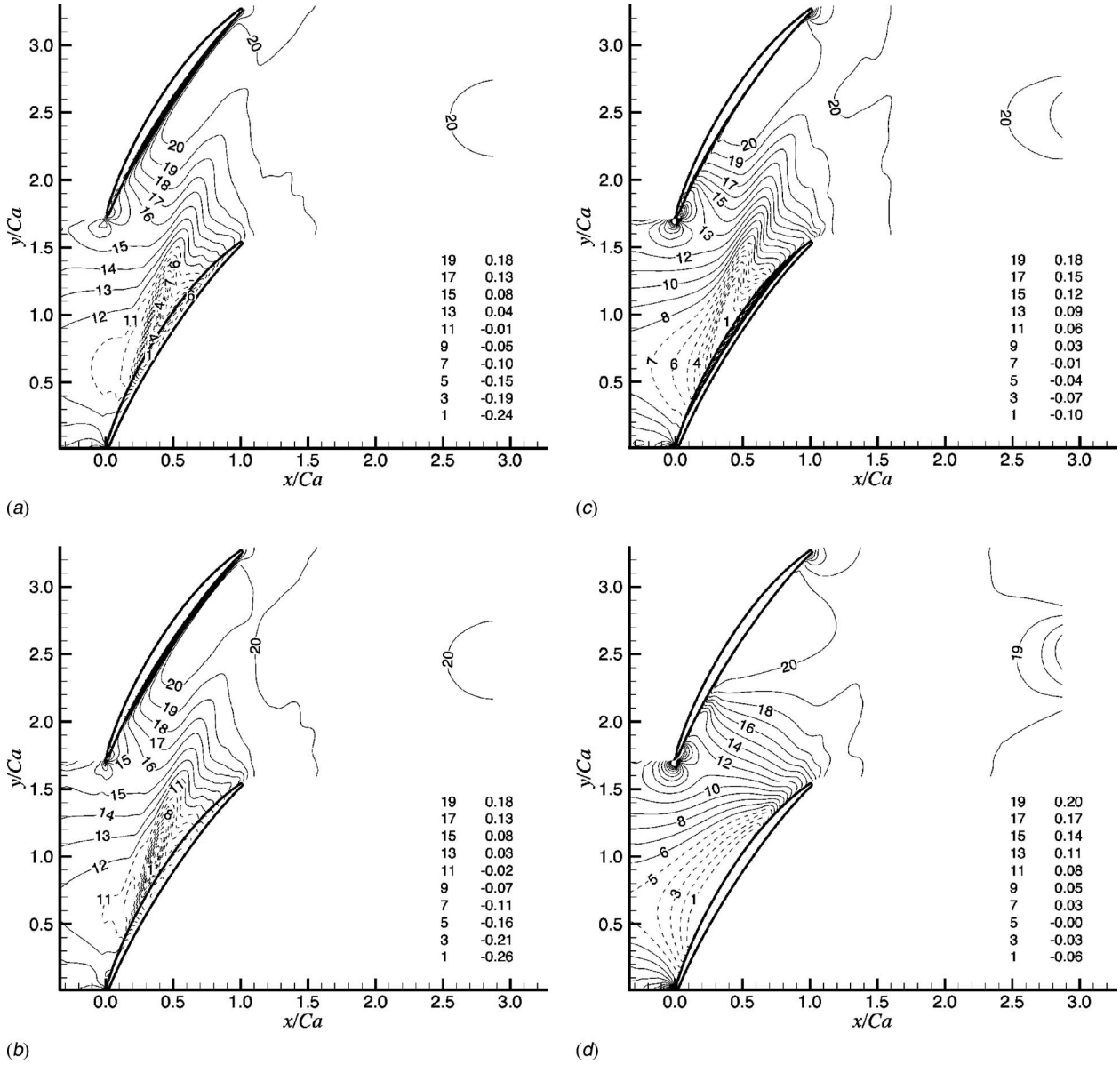

Fig. 17 Contour plots of mean pressure in *x-y* planes along the *z*-direction. (*a*) z/C_a=0.01; (*b*) z/C_a=0.025; (*c*) z/C_a=0.1; (*d*) z/C_a=0.5.

in the blade trailing-edge and the blade tip, the shear layer instability in the tip-leakage jet flow is considered as the most probable cause for the low-frequency spectral peak.

3.4 Mean Pressure and Pressure Fluctuations. The dynamic behaviors of the end-wall vortical structures are also reflected in the distributions of mean pressure and pressure fluctuations. As already discussed in Sec. 3.1, an insight regarding the end-wall vortical structures will be useful in predicting the pattern of tip-leakage cavitation. In the single phase flow approach employed here, the resulting pressure field is most relevant to the cavitation inception. The mean pressure fields obtained from the present LES are shown in Fig. 17 in the *x-y* planes along the span. In the plane very close to the end-wall (z/C_a=0.01), low pressure is observed in the upstream portion of the tip-leakage vortex and underneath the blade tip. The existence of the tip-leakage vortex is reflected in the pressure iso-contour lines in further downstream locations as well. Comparisons of the contour lines of mean pressure distribution in planes z/C_a=0.01 and 0.025 suggest that the mean pressure distributions across the blade tip are qualitatively and quantitatively similar. It is also noted that the mean pressure on the pressure side of the blade tip near the end-wall is significantly higher while that on the suction side of the blade tip is relatively low. The pressure difference is the driving force for the tip-leakage jet across the tip-gap.

At z/C_a=0.1, negative mean pressure (or of which levels are smaller than the mean pressure) is found on the blade suction surface as well as along the tip-leakage vortex. Further away from the end-wall (z/C_a=0.5), only the blade suction surface and its vicinity attain negative pressure. The magnitude of the negative pressure is significantly smaller than that of the end-wall tip-leakage vortex. From this perspective, it is most likely that cavitation occurs in the upstream portion of the tip-leakage vortex and underneath the tip-gap.

The intensity of the pressure fluctuations is also an important factor in triggering cavitation, especially in the region where the mean pressure is close to the vapor pressure. Due to the pressure fluctuations, the instantaneously observed extent of the cavitation is usually more significant. The intensity of pressure fluctuations

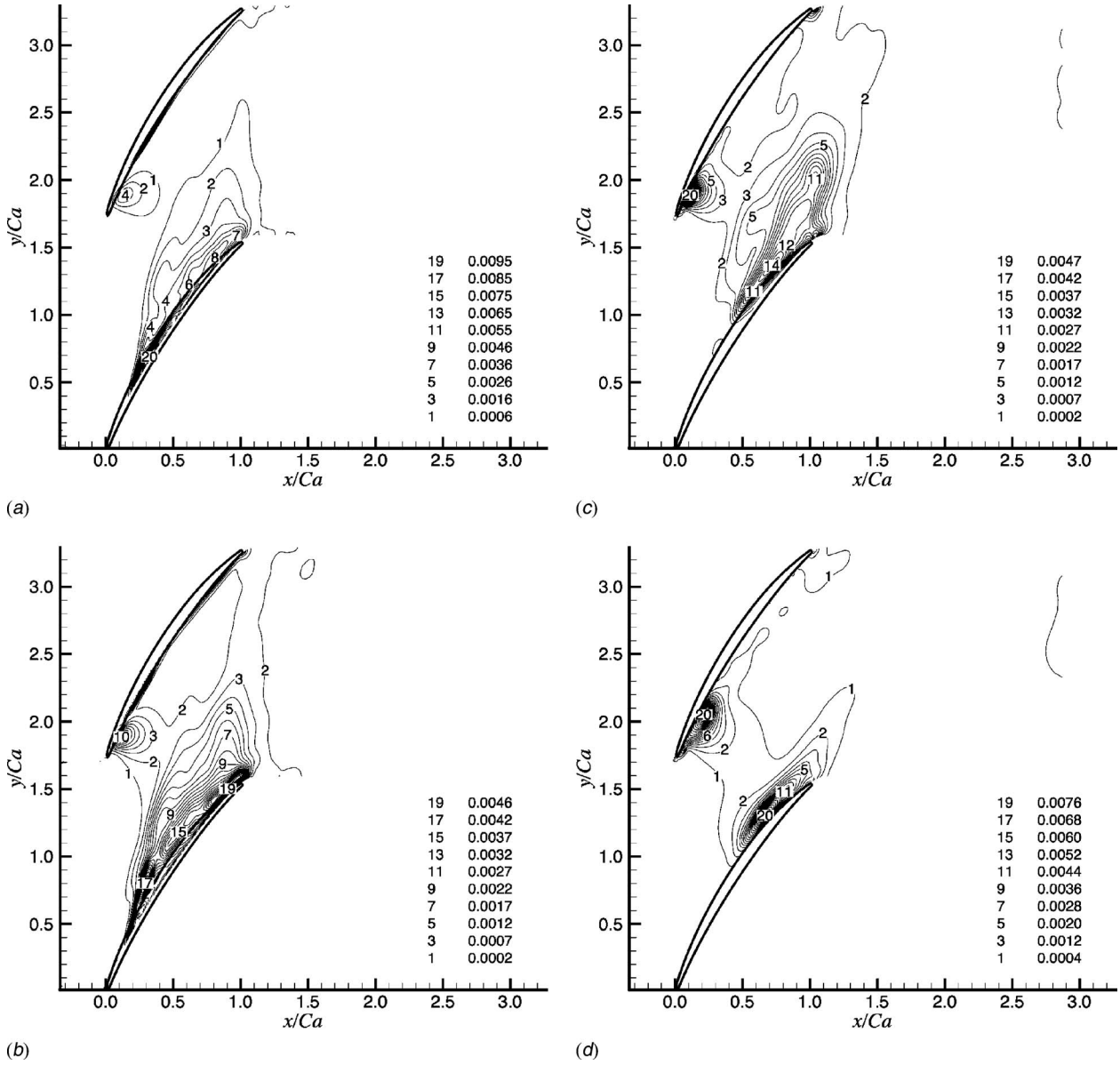

Fig. 18 Contour plots of $\overline{p'p'}$ in *x-y* planes along the *z*-direction. (*a*) $z/C_a=0.01$; (*b*) $z/C_a=0.025$; (*c*) $z/C_a=0.1$; (*d*) $z/C_a=0.5$.

is shown in Fig. 18 at four *x-y* planes along the span. High levels of pressure fluctuations are found in the tip-leakage vortex and underneath the blade tip. In addition, a small region near the leading edge on the pressure side of the blade shows fluctuations due to the separation near the leading edge ($z/C_a=0.01$ and 0.025). The intensity of pressure fluctuations on the pressure surface near the leading edge and on the suction surface near the trailing edge become significant in planes further away from the end-wall ($z/C_a \geq 0.1$). Compared to the pressure fluctuations in those regions, the pressure fluctuations along the blade wake appear to be small.

The mean pressure and pressure fluctuations are also examined in a number of *y-z* planes along the streamwise direction as shown in Figs. 19 and 20. At 10% axial chord location (Fig. 19(*a*)), no significant low-pressure region is found near the end-wall since no significant vortical structures are generated. Although a small-scale weak induced vortex is observed at this location, its strength is insufficient to produce a noticeable pressure drop in the vortex core (see Fig. 10). A significant pressure drop due to the formation of the tip-leakage vortex is observed at about 30–40% axial chord (Fig. 19(*b*)) where the minimum pressure is located exactly in the core of the tip-leakage vortex (also see Fig. 10).

At 50% axial chord (Fig. 19(*c*)), the tip-leakage vortex core corresponds to the low-pressure region as well defined by the pressure iso-contours. At a downstream plane ($x/C_a=0.7$, Fig. 19(*d*)), the core of the tip-leakage vortex is not a region of negative pressure, while the region underneath the blade tip still attains negative pressure but with significantly reduced magnitude. At a *y-z* plane near the trailing edge ($x/C_a=0.9$, Fig. 19(*e*)), the pressure contours still reflect the existence of the tip-leakage vortex. However, the pressure in this location has already increased above the free-stream value.

Figure 20 shows the intensity of the pressure fluctuations in *y-z* planes along the streamwise direction. The intensity of pressure fluctuations appears to be the maximum at about 30% axial chord (Fig. 20(*b*)). In the upstream location at 10% axial chord (Fig. 20(*a*)), significant levels of pressure fluctuations due to boundary layer separation on the blade pressure surface are observed. At

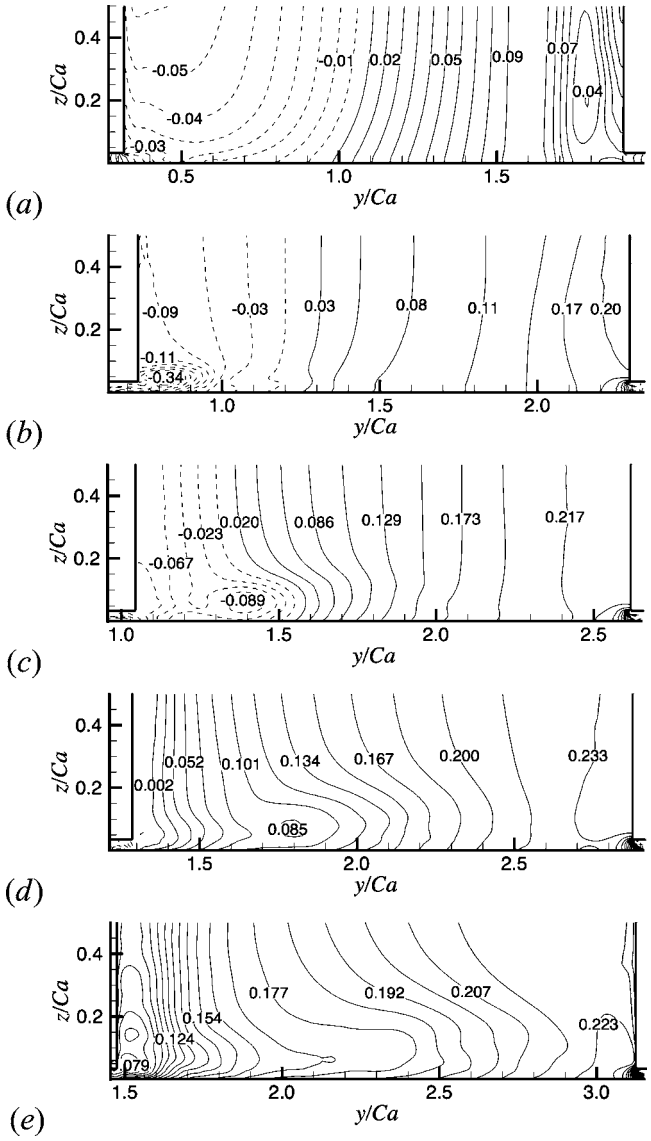

Fig. 19 Contour plots of mean pressure in *y-z* planes along the *x*-direction. (*a*) $x/C_a=0.1$; (*b*) $x/C_a=0.3$; (*c*) $x/C_a=0.5$; (*d*) $x/C_a=0.7$; (*e*) $x/C_a=0.9$.

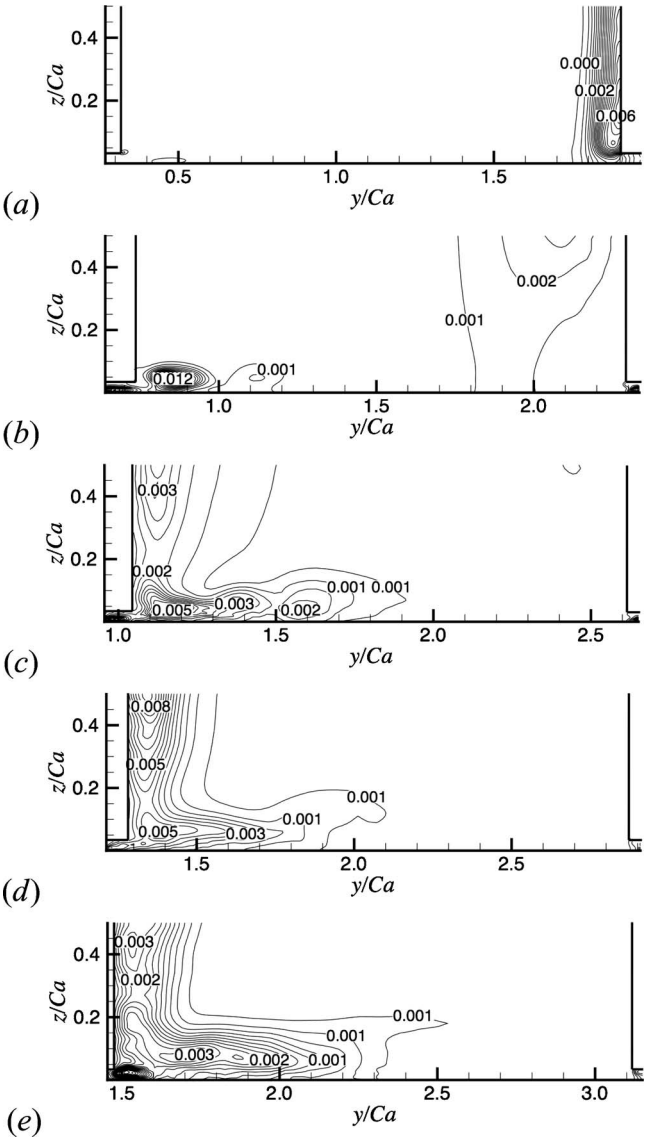

Fig. 20 Contour plots of $\overline{p'p'}$ in *y-z* planes along the *x*-direction. (*a*) $x/C_a=0.1$; (*b*) $x/C_a=0.3$; (*c*) $x/C_a=0.5$; (*d*) $x/C_a=0.7$; (*e*) $x/C_a=0.9$.

50% axial chord (Fig. 20(*c*)), the tip-leakage vortex is still well defined as a region of high levels of pressure fluctuations, but the region between the tip-leakage vortex and the suction side of the blade tip generates enhanced pressure fluctuations. This may be caused by the strong turbulence and vorticity productions in the tip-leakage jet as discussed in detail in Ref. [25]. The high level of pressure fluctuations in these regions may cause vibration of the blade and casing, as well as significant noise. In Figs. 17–20, it is obvious that the region of upstream tip-leakage vortex, especially at around 30–40% axial chord, is most susceptible to cavitation and generates the most significant pressure fluctuations. Therefore, in the present configuration, cavitation can be best mitigated by diminishing the strength and coherency of the tip-leakage vortex at around 30–40% axial chord.

3.5 Cavitation Inception. The low-pressure regions are known to be susceptible to cavitation. Figure 21 shows an example of cavitation inception analysis in a plane parallel to the end-wall inside the tip gap using the minimum tension criterion proposed by Joseph [30].

This criterion is based on the normal stress of the fluid and the critical vapor pressure:

$$B_{ii} = \tau_{ii} - p + p_c > 0 \tag{2}$$

where τ_{ii} is the normal stress, p is local pressure, and p_c is the pressure in the cavity. Only the resolved normal-stress components defined as $\tau_{ii}=2\mu\partial\bar{u}_i/\partial x_i$, where $\bar{u}_i$ is the filtered velocity, are considered while the filtered pressure is corrected to account for the trace of the subgrid stress. For this example, p_c of 0.01 is used, assuming the cavitation number of 0.02 based on the cascade inlet pressure. If all three components of the stress B_{11}, B_{22}, and B_{33} are positive, a cavity will open.

Instantaneous and time-averaged contours of $B=1/3(B_{11}+B_{22}+B_{33})$ are plotted in Figs. 21(*a*) and 21(*b*), respectively, in regions where all three components are positive. High levels of B in both the instantaneous and time-averaged contours are concentrated in the tip-leakage region. In particular, the tip-leakage vortex appears as the dominant source of cavitation. The tip-separation vortex is less important even though it involves comparable low pressure

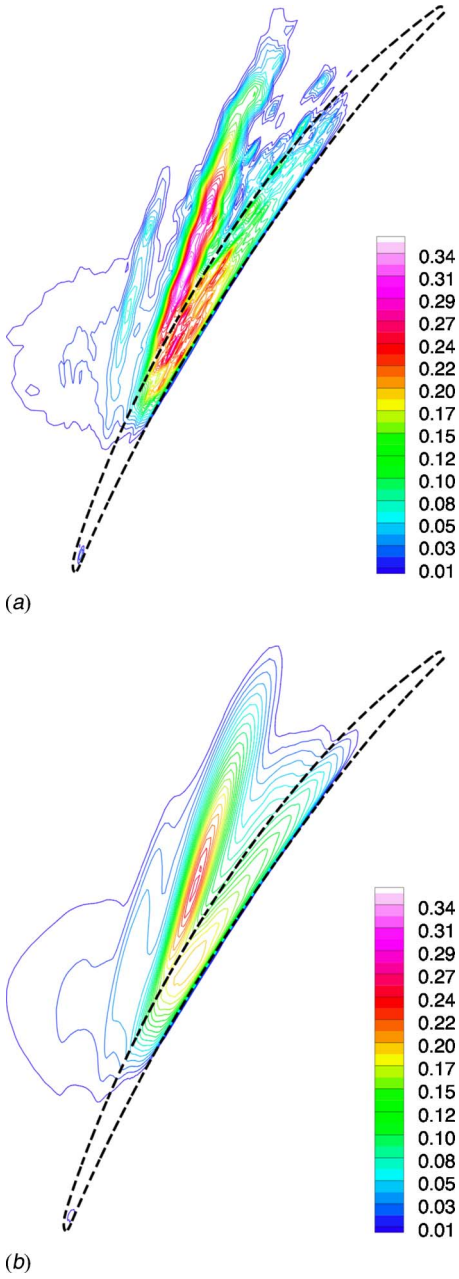

Fig. 21 Contours of (*a*) instantaneous and (*b*) time-averaged cavitation criterion, $B=1/3(B_{11}+B_{22}+B_{33})$, in a plane inside the tip-gap at $z/C_a=0.01$

(see Figs. 17(*a*) and 17(*b*)). This is due to the high positive values of the normal stress τ_{ii} in addition to the strong low pressure found in the tip-leakage vortex.

4 Conclusions

The tip-clearance flow in axial turbomachines has been studied using large-eddy simulation with an emphasis on understanding the unsteady characteristics of the tip-leakage vortical structures and the underlying mechanisms for cavitation-inducing low-pressure fluctuations in the vicinity of the tip-gap. The generation and evolution of the tip-leakage vortical structures have been investigated throughout the cascade using mean streamlines and λ_2 contours. Among the distinct vortical structures, the tip-leakage vortex dominates the end-wall region. The induced vortices are active in the upstream end-wall region while the tip-separation vortices become significant near the suction side of the blade tip after the mid-chord. In the present configuration, the tip-leakage vortex is initiated at around 15–20% axial chord, and the evolution of the tip-leakage vortex is found to be closely related to the generation and decay of the induced vortices. Interestingly, the tip-leakage vortex is observed to spin off a part of it at about 73% axial chord due to the pitchwise end-wall motion. Although this feature of the tip-leakage vortex was not seriously considered in the literature, the tip-leakage vortex separation and its interaction with other end-wall vortices makes the downstream end-wall vortical region extremely active and complex.

To examine the spatial and temporal characteristics of the coherent structures present in the tip-leakage flow, two-point correlations of the velocity fluctuations were computed. In general, the energy spectra of the three velocity components show broadband characteristics, while a noticeable spectral peak is particularly observed in the energy spectra of the pitchwise velocity fluctuations. Analysis of the vortex shedding frequency in the blade wake and space-time correlations of the velocity fluctuations in the end-wall tip-leakage flow suggest that a pitchwise wandering motion of the tip-leakage vortex is the cause for the low-frequency spectral peak.

The dynamic behaviors of the end-wall vortical structures are also reflected in the distributions of mean pressure and pressure fluctuations. Detailed examination of the mean pressure field revealed that cavitation is most likely in the upstream portion of the tip-leakage vortex and underneath the tip-gap. A significant pressure drop due to the formation of the tip-leakage vortex is observed at about 30–40% axial chord where the minimum pressure coincides with the core of the tip-leakage vortex, and the intensity of pressure fluctuations appears to be at the maximum. The 30–40% axial chord is also found to be the location of the strongest portion of the tip-leakage vortex in terms of the λ_2 contours.

Based on the characteristics of the mean and fluctuating pressure, it is obvious that the region of the upstream tip-leakage vortex, especially at around 30–40% axial chord, is most susceptible to cavitation. The high activity of the pressure fluctuations in these regions may also appear as a source of strong vibration of the blade and casing as well as significant levels of noise. Therefore, it is expected that a control device which can effectively diminish the strength and coherence of the tip-leakage vortex at around 30% axial chord location may also lead to reduced the cavitation, noise, and vibration.

Acknowledgment

The authors acknowledge the support of the Office of Naval Research under Grant No. N00014-99-1-0389, with Dr. Ki-Han Kim as program manager. Computer time was provided by a Challenge Project Grant (C82) from the U.S. Department of Defense (DoD) High Performance Computing Modernization Program (HPCMP) through Army Research Laboratory (ARL) and Aeronautical Systems Center (ASC) Major Shared Resource Centers (MSRC). The authors would also like to thank Professor William Devenport of VPI for providing experimental data and helpful discussions.

Nomenclature

C = chord length
C_a = axial chord length
f = frequency
p = pressure
Re = Reynolds number
t = time
U = time-averaged streamwise velocity
U_∞ = inflow free-stream velocity
u_i = x_i component of velocity
u_τ = wall-shear velocity
u = streamwise velocity
v = pitchwise velocity

w = spanwise velocity
x_i = Cartesian coordinates
x = streamwise coordinate
y = pitchwise coordinate
z = spanwise coordinate
ν = kinematic viscosity
Δ = grid spacing
ω = angular frequency
$()^+$ = quantity in wall-unit
$()'$ = fluctuation component

References

[1] Furukawa, M., Saiki, K., Nagayoshi, K., Kuroumaru, M., and Inoue, M., 1998, "Effects of Stream Surface Inclination on Tip Leakage Flow Fields in Compressor Rotors," ASME J. Turbomach., **120**(4), pp. 683–694.

[2] Mailach, R., Lehmann, I., and Vogeler, K., 2001, "Rotating Instabilities in an Axial Compressor Originating From the Fluctuating Blade Tip Vortex," ASME J. Turbomach., **123**(3), pp. 453–463.

[3] Suder, K. L., 1998, "Blockage Development in a Transonic, Axial Compressor Rotor," ASME J. Turbomach., **120**(3), pp. 465–476.

[4] Lakshminarayana, B., and Ravindranath, A., 1982, "Interaction of Compressor-Rotor Blade Wake With Wall Region/Vortex in the End-Wall Boundary Layer," ASME J. Eng. Power, **104**(2), pp. 467–478.

[5] Lakshminarayana, B., Pouagare, M., and Davino, R., 1982, "Three-Dimensional Flow-Field in the Tip Region of a Compressor Rotor Passage, Part 1: Mean Velocity Profiles and Annulus Wall Boundary Layer," ASME J. Eng. Power, **104**(4), pp. 760–771.

[6] Pandya, A., and Lakshminarayana, B., 1983, "Investigation of the Tip-Clearance Flow Inside and at the Exit of a Compressor Rotor Passage. Part 1: Mean Velocity Field," ASME J. Eng. Power, **105**(1), pp. 1–12.

[7] Lakshminarayana, B., Sitaram, N., and Zhang, J., 1986, "End-Wall and Profile Losses in a Low-Speed Axial Flow Compressor Rotor," ASME J. Eng. Gas Turbines Power, **108**(1), pp. 22–31.

[8] Inoue, M., Kuroumaru, M., and Fukuhara, M., 1986, "Behavior of Tip-Leakage Flow Behind an Axial Compressor Rotor," ASME J. Eng. Gas Turbines Power, **108**(1), pp. 7–14.

[9] Goto, A., 1992, "Three-Dimensional Flow and Mixing in an Axial Flow Compressor With Different Rotor Tip Clearances," ASME J. Turbomach., **114**(3), pp. 675–685.

[10] Stauter, R. C., 1993, "Measurement of the Three-Dimensional Tip Region Flow Field in an Axial Compressor," ASME J. Turbomach., **115**(3), pp. 468–476.

[11] Lakshminarayana, B., Zaccaria, M., and Marathe, B., 1995, "The Structure of Tip Clearance Flow in Axial Flow Compressors," ASME J. Turbomach., **117**(3), pp. 336–347.

[12] Rains, D. A., 1954, "Tip Clearance Flows in Axial Compressors and Pumps," Ph.D. thesis, Division of Engineering and Applied Science, California Institute of Technology, Pasadena, California.

[13] Zierke, W. C., Farrell, K. J., and Straka, W. A., 1995, "Measurement of the Tip Clearance Flow for a High-Reynolds-Number Axial-Flow Rotor," ASME J. Turbomach., **117**(4), pp. 522–532.

[14] Laborde, R., Chantrel, P., and Mory, M., 1997, "Tip Clearance and Tip Vortex Cavitation in an Axial Flow Pump," ASME J. Fluids Eng., **119**(3), pp. 680–685.

[15] Muthanna, C., and Devenport, W. J., 2004, "Wake of a Compressor Cascade With Tip Gap. Part 1. Mean Flow and Turbulence Structure," AIAA J., **42**(11), pp. 2320–2331.

[16] Wang, Y., and Devenport, W. J., 2004, "Wake of a Compressor Cascade With Tip Gap. Part 2. Effects of Endwall Motion," AIAA J., **42**(11), pp. 2332–2340.

[17] Wenger, C. W., Devenport, W. J., Wittmer, K. S., and Muthanna, C., 2004, "Wake of a Compressor Cascade With Tip Gap. Part 3. Two-Point Statistics," AIAA J., **42**(11), pp. 2341–2346.

[18] Kuhl, D. D., 2001, "Near Wall Investigation of Three Dimensional Turbulent Boundary Layers," Master's thesis, Department of Aerospace and Ocean Engineering, Virginia Polytechnic Institute and State University, Blacksburg, Virginia.

[19] de la Riva, D. H., 2001, "Turbulence Interaction in a Highly Staggered Cascade-Propulsor Configuration," Master's thesis, Department of Aerospace and Ocean Engineering, Virginia Polytechnic Institute and State University, Blacksburg, Virginia.

[20] Ma, R., 2003, "Unsteady Turbulence Interaction in a Tip Leakage Flow Downstream of a Simulated Axial Compressor Rotor," Ph.D. thesis, Department of Aerospace and Ocean Engineering, Virginia Polytechnic Institute and State University, Blacksburg, Virginia.

[21] You, D., Mittal, R., Wang, M., and Moin, P., 2004, "Computational Methodology for Large-Eddy Simulation of Tip-Clearance Flows," AIAA J., **42**(2), pp. 271–279.

[22] Meneveau, C., Lund, T. S., and Cabot, W. H., 1996, "A Lagrangian Dynamic Subgrid-Scale Model of Turbulence," J. Fluid Mech., **319**, pp. 353–385.

[23] Lund, T. S., Wu, X., and Squires, K. D., 1998, "Generation of Turbulent Inflow Data for Spatially-Developing Boundary Layer Simulations," J. Comput. Phys., **140**(2), pp. 233–258.

[24] Fadlun, E. A., Verzicco, R., Orlandi, P., and Mohd-Yusof, J., 2000, "Combined Immersed-Boundary Finite-Difference Methods for Three-Dimensional Complex Flow Simulations," J. Comput. Phys., **161**(1), pp. 35–60.

[25] You, D., Moin, P., Wang, M., and Mittal, R., 2004, "Study of Tip Clearance Flow in a Turbomachinery Cascade Using Large Eddy Simulation," Report TF-86, Department of Mechanical Engineering, Stanford University, Stanford, California.

[26] You, D., Mittal, R., Wang, M., and Moin, P., 2006, "Analysis of Stability and Accuracy of Finite-Difference Schemes on a Skewed Mesh," J. Comput. Phys., **213**(1), pp. 184–204.

[27] Akselvoll, K., and Moin, P., 1995, "Large Eddy Simulation of Turbulent Confined Coannular Jets and Turbulent Flow Over a Backward Facing Step," Report TF-63, Department of Mechanical Engineering, Stanford University, Stanford, California.

[28] Khorrami, M. R., Li, F., and Choudhan, M., 2002, "Novel Approach for Reducing Rotor Tip-Clearance-Induced Noise in Turbofan Engines," AIAA J., **40**(8), pp. 1518–1528.

[29] Press, W. H., Teukolsky, S. A., Vetterling, W. T., and Flannery, B. P., 1992, *Numerical Recipes*, Cambridge University Press, Cambridge.

[30] Joseph, D. D., 1998, "Cavitation and the State of Stress in a Flowing Liquid," J. Fluid Mech., **366**, pp. 367–378.

[31] Jeong, J., and Hussain, F., 1995, "On the Identification of a Vortex," J. Fluid Mech., **285**, pp. 69–94.

Unsteady Flow and Wake Transport in a Low-Speed Axial Fan With Inlet Guide Vanes

Jesús Manuel Fernández Oro
e-mail: jesusfo@uniovi.es

Katia María Argüelles Díaz

Carlos Santolaria Morros

Eduardo Blanco Marigorta

Área de Mecánica de Fluidos,
Universidad de Oviedo,
Campus de Viesques,
33271, Gijón (Asturias), Spain

The present study is focused on the analysis of the dynamic and periodic interaction between both fixed and rotating blade rows in a single stage, low-speed axial fan with inlet guide vanes. The main goal is placed on the characterization of the unsteady flow structures involved in an axial flow fan of high reaction degree, relating them to working point variations and axial gap modifications. For that purpose, an experimental open-loop facility has been developed to obtain a physical description of the flow across the turbomachine. Using hot-wire anemometry, measurements of axial and tangential velocities were carried out in two transversal sectors: one between the rows and the other downstream of the rotor, covering the whole span of the stage for a complete stator pitch. Ensemble- and time-averaging techniques were introduced to extract deterministic fluctuations from raw data, both of which are essential to understand flow mechanisms related to the blade passing frequency. An exhaustive analysis of the measured wakes has provided a comprehensive description of the underlying mechanisms in both wake-transport phenomena and stator-rotor interaction. In addition, unmixed stator wakes, observed at the rotor exit, have been treated in terms of dispersion and angular displacement to indicate the influence of the blades loading on the transport of the stator wake fluid. The final aim of the paper is to highlight a complete picture of the unsteady flow patterns inside industrial axial fans. [DOI: 10.1115/1.2746920]

Introduction

The unsteady behavior of any turbomachine is based on the appearance of unsteady flow patterns due to the relative motion of blade surfaces. In fact, the existence of a steady relative flow, with a tangential velocity gradient in the blade passages, produces an unsteady flow when observed from an absolute frame of reference (Lyman [1]). On the other hand, the periodic shedding of boundary layers from the blade surfaces generates avenues of wakes that will be mixed and transported throughout the machine, establishing new unsteady phenomena. All these unsteady features are also responsible for the energy exchange in the flow, so an accurate description of the unsteadiness may be very important when predicting the turbomachine performance (Greitzer et al. [2]). As a consequence, two basic mechanisms related to the flow unsteadiness, but with different nature, have to be considered in the case of subsonic turbomachinery. First, the row interaction, characterized as a potential effect due to the relative motion of the blades at the rotational speed, and secondly, the wake-blade interaction, a viscous mechanism caused by the impinging of the incoming wakes onto the blades.

Any velocity trace measured in an axial-flow multistage environment presents a broad range of scales. In particular, the length scales range from the machine circumference to the Kolmogorov length scale of a turbulent eddy, while the time scales range from a fraction of the shaft speed to the inner scales of the smallest dissipative eddies (Adamczyk [3]). The contribution of all this unsteadiness produces a velocity signal composed by all-range fluctuations. Since their origin and nature are diverse, it is necessary to introduce a filtering (frequency domain) or an averaging (time domain) procedure to segregate and identify every source of unsteadiness. Three different averaging operators are usually employed for that purpose (Uzol et al. [4]). Every one is associated with a characteristic time scale, so all the unsteadiness with a higher frequency than the inverse of such a scale is filtered out. The first one, an "ensemble averaging" (or "phase averaging"), accounts for the turbulence and is used also in unsteady RANS. In essence, it is a Reynolds averaging, but applied to every rotor phase independently. The second operator is a "time averaging" (or "passage averaging") that covers time scales that are of the order of the shaft period (typically, the blade passing frequency). It removes the deterministic unsteady flow, including phase-dependent variations in the flow structure, that is, all the unsteadiness associated with the rotating blade row. The third operator is a "passage-to-passage averaging," applied in the case of turbomachinery with a varying number of rotors and stators on consecutive stages. It accounts for the effect of circumferential spatial distortions with length scales unrelated to the pitch of the blade row of interest (Adamczyk [5]). In the case of a single-stage, low-speed axial fan, it has no relevance in addressing unsteady features of the flow. Therefore, both ensemble- and time-averaging techniques provide all the necessary framework to understand the underlying mechanisms of the unsteady flow inside single-staged turbomachinery.

The measurement of raw velocity traces in multistage turbomachines can be achieved using both intrusive and non-intrusive methods. In particular, intrusive methods have always played an important role when carrying out experimental investigations of unsteady flows. Thus, five-hole probes, high-frequency response transducers (Cherret et al. [6]), hot-wire anemometry (i.e., Goto [7], with a single slanted hot-wire, or Senkter et al. [8,9], with dual hot-wire probes), or hot-film anemometry have generally been employed using both single and multipoint measurements between blade rows. Recently, non-intrusive methods such as PIV systems are being introduced as a powerful tool to obtain blade-to-blade 2D images of the flow ([4], Soranna et al. [10]), despite being more expensive and requiring special transparent characteristics in the test sections. In addition, stereo-PIV (3D) or LDV systems (Ciocan et al. [11]) are also being employed by other

Contributed by the Fluids Engineering Division of ASME for publication in the JOURNAL OF FLUIDS ENGINEERING. Manuscript received December 5, 2006; final manuscript received March 15, 2007. Review conducted by Chunill Hah. Paper presented at the 2005 ASME Fluids Engineering Division Summer Meeting and Exhibition (FEDSM2005), Houston, Texas, June 19–23, 2005.

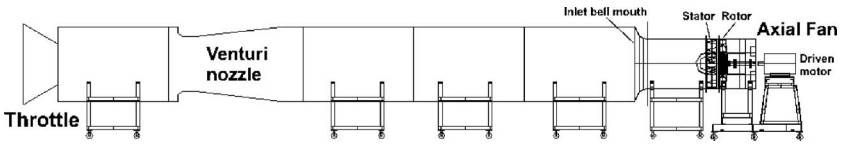

Fig. 1 Test facility

researchers as useful optical techniques to obtain complete maps of the flow. However, hot-wire anemometry can still provide valuable information if used intensively.

In this paper, mechanisms involved in stator-rotor interaction, such as blade blockage and wake transport, are shown in detail. First of all, a brief description of the machine and the experimental facility will lead to the presentation of the measuring probes and test sections. Thereafter, averaging techniques will be defined properly in order to obtain both instantaneous and time-averaged flow patterns. Results and discussion will be focused on the time-averaged impact of unsteady mechanisms. The effect of the unsteady inflow conditions for the rotor, the transport and dispersion of unmixed stator wakes, and the influence of the working point and the axial gap configuration in the throughflow distributions will provide insight on the complete picture of the unsteady flow.

Experimental Setup and Procedures

Experimental Facility. Low-Speed Axial Fan With IGVs. The experimental measurements of the unsteady flow field have been conducted on a single-stage, low-speed axial fan with inlet guide vanes. It is operated in an open-loop facility that includes a throttle at the inlet to modify the operating conditions. A Venturi nozzle (developed according to standard normative BS848) is included far upstream to measure the volumetric flow rate. Figure 1 shows a sketch of the experimental facility that includes a long duct (20 fan diameters length) between the control valve and the fan bell-mouth inlet to assure uniform inlet flow.

The fan analyzed presents a nine-blade rotor based on the NACA 65 family and designed to provide a free-vortex distribution of the absolute tangential velocity. The flow is previously guided by a 13-vane stator, based on the British circular family C1. The hub and tip diameters are 380 mm and 820 mm, respectively, giving a hub-to-tip ratio of 0.46. The tip clearance is 2.3% of the blade height. Figure 2 shows both stator and rotor profiles at hub, midspan, and tip sections. Some geometrical parameters are also given in the figure.

The facility has been constructed with the possibility of changing the axial gap between the rows. The stator-rotor separation is modifiable through a set of annular rings that can be removed or added in the fan shroud to increase or decrease the gap. In these experiments, two axial gap configurations were tested: a larger, nominal gap of 50% of the blade chord, and a lower gap of a 37% of the blade chord, both at the hub section. The rotor is directly coupled to a 37 kW AC motor via a long shaft. The power is supplied by an industrial frequency converter that also controls the rotational speed of the fan, 2400 rpm, with maximum deviations of ±2 rpm. At nominal conditions, the volumetric flow rate is 16.5 m^3/s, with a total pressure increment of 1150 Pa.

Figure 3 represents total-to-total pressure coefficient, $\psi=(P_2-P_1)/(0.5\rho U_t^2)$, and overall efficiency against the flow coefficient, i.e., $\phi=\bar{U}/U_t$, where U_t denotes the blade tip velocity. Static and dynamic pressure coefficients are also included in the figure. The overall efficiency indicates a relationship between the power transferred into the air stream and the power supply of the frequency converter. The three operating points that were studied, defined as "nominal" (Q_n), "partial load" ($0.85Q_n$) and "near stall" ($0.7Q_n$), are shown in the figure. The nominal point corresponds to the peak efficiency of the fan performance, at $\phi=0.38$. The uncertainty of the curves has been estimated in ± 2% for the flow rate and ± 1.4% for the total pressure. With this level of accuracy, no relevant differences have been observed in the performance curves for both gap configurations.

Measurement Techniques. Dual Hot-Wire Anemometry. The experimental data have been obtained using hot-wire anemometry. In particular, dual hot-wire techniques were employed to measure both axial and tangential velocity fields across the stage. This technique gives a relatively high frequency response to velocity fluctuations, so flow disturbances at BPF (360 Hz) can be perfectly captured. The anemometric probe was composed of two tungsten filament wires of 5 μm diameter, in a 120 deg crossed layout, with output signals connected to a TSI IFA100 constant temperature anemometer (Fig. 4). The angular uncertainty has been estimated at 1 deg in the center of the measurement range and 3 deg at the borders. Consequently, the uncertainty of the absolute velocity value has reached up to 1.3% in the center and up to 3% near the borders. More details about the probe and the calibration setup can be found in Blanco et al. [12].

Figure 5 shows the measurement locations used in the experiments. The first sector (D) was placed 15 mm behind the stator TE to capture flow patterns between the rows. In addition, a second sector (R) was located 50 mm downstream of the rotor TE to analyze the rotor wake velocity deficit. Since there are no clocking effects of additional stages, all the periodic unsteadiness is observable inside a circular sector covering the whole span of the machine over one stator pitch. For the spatial discretization, 15 single points were adopted over the span in both sectors, with a progressive separation, according to an equal subtended area criterion. On the other hand, another 15 angular positions—every

	STATOR			ROTOR		
	Hub	Midspan	Tip	Hub	Midspan	Tip
Radius (mm)	190	300	410	190	300	410
Chord length (mm)	157.0	165.3	170.8	179.0	165.8	157.4
Solidity	1.71	1.14	0.86	1.35	0.792	0.55
Stagger angle (°)	18.11	12.97	10.77	48.64	59.70	66.45
Camber angle (°)	37.1	27.8	23.3	13.76	7.42	5.74
Thickness/Chord (%)	3.0	3.0	3.0	12	9.43	8
Pitch (mm)	91.8	145	198.1	132.6	209.4	286.2
Inlet flow angle (°)	0.0	0.0	0.0	59.61	64.7	69.36
Outlet flow angle (°)	31.17	20.73	15.68	47.73	60.07	67.16

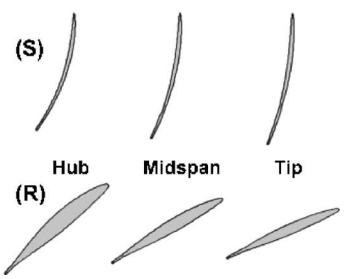

Fig. 2 Characteristics of vanes and blades

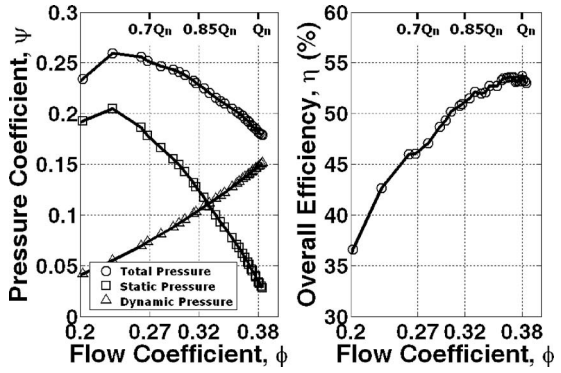

Fig. 3 Fan performance curves

1.8 deg—were used to complete the vane's passage definition in the tangential direction. Therefore, two grids of 225 measuring points were finally defined in both sectors (Fig. 5).

To avoid aliasing of the signals, the data sampling rate was fixed at 36 kHz, that is, a temporal resolution of 100 samples per blade passing period. For every velocity trace, 100 rotor blade passing periods were approximately recorded, so a total number of 10^4 samples were stored at each measuring point of the 15×15 sector grid. A continuous recording trigger (Fig. 4) enables to distinguish every rotor revolution. As a result, it is possible to identify every rotor phase, and accurate data sets can be rearranged from every velocity trace in order to phase average the instantaneous signals.

Data Processing Techniques

Ensemble and Time Averaging. The hot-wire traces have been processed in order to segregate periodic fluctuations from random unsteadiness. Since the velocity fluctuations are considered to have a random (turbulent) component and a deterministic component, the instantaneous velocity can be decomposed into a periodic, deterministic velocity and a stochastic function as follows:

$$u(\boldsymbol{r}, \vartheta) = \tilde{U}(\boldsymbol{r}, \varphi) + u'(\boldsymbol{r}, \vartheta) \tag{1}$$

The deterministic velocity is obtained through the definition of the *ensemble averaging*:

$$\tilde{U}(\boldsymbol{r}, \varphi) = \frac{1}{M} \sum_{m=1}^{M} u\,(\boldsymbol{r}, \vartheta)\big|_m \quad \vartheta = \varphi + \frac{2\pi}{B}(m-1) \tag{2}$$

In this case, this operator has been applied for one hundred passages recorded for every velocity trace ($M = 100$ rotor blades periods stored). The variable $\boldsymbol{r}$ represents the spatial coordinates and φ is the phase angle of the rotor passage. B is the number of blades and ϑ is the total angular displacement. A temporal resolution of 100 samples per blade passing period was defined, so a single phase-locked position of the rotor pitch (40 deg) is obtained every 0.4 deg. This phase-averaged flow leads to the final

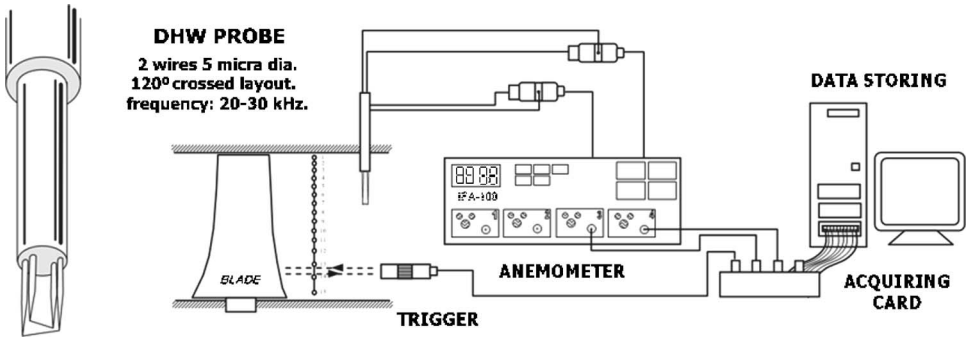

Fig. 4 Sketch of the dual hot-wire probe. Measurement chain.

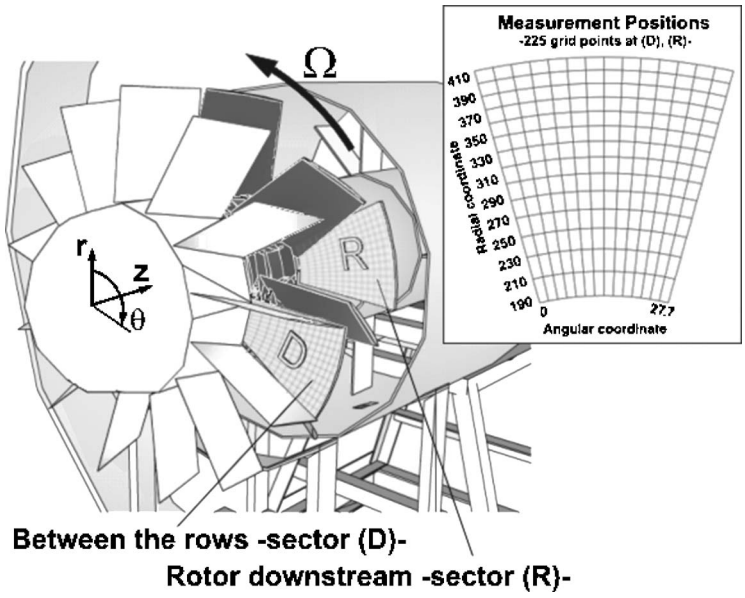

Fig. 5 Measuring sectors D (at stator exit) and R (at rotor exit)

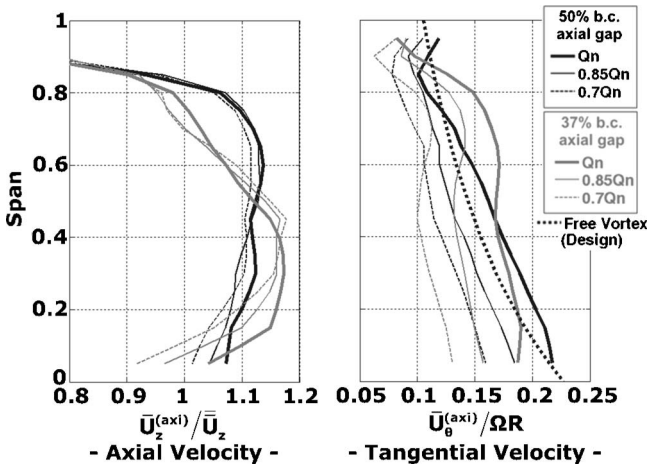

Fig. 6 Throughflow at stator exit

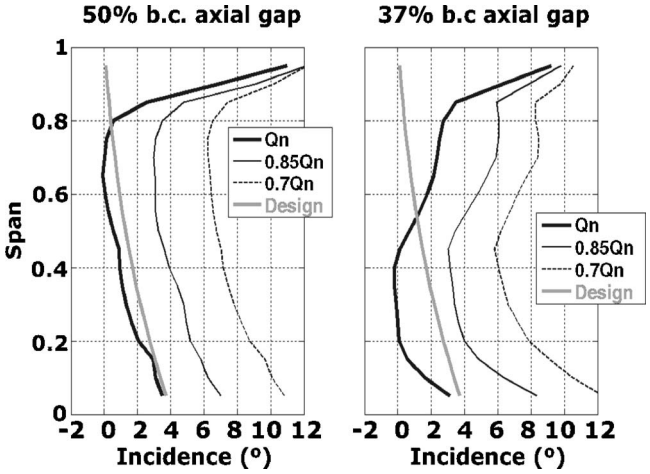

Fig. 7 Throughflow incidence

passage-averaged flow if the deterministic velocity is further decomposed into a mean value and a deterministic fluctuation.

$$\tilde{U}(\boldsymbol{r},\varphi) = \bar{U}(\boldsymbol{r}) + U(\boldsymbol{r},\varphi) \tag{3}$$

Considering that the deterministic fluctuations occur on large time scales, they can be easily identified by *time averaging* (or passage averaging) the deterministic velocity, according to:

$$\bar{U}(\boldsymbol{r}) = \frac{1}{N}\sum_{n=1}^{N} \tilde{U}\,(\boldsymbol{r},\varphi)|_n \tag{4}$$

where n represents every phase-averaged realization that covers an entire passage ($N=100$). Notice that the phase φ is removed in the time-averaged velocity $\bar{U}$, so passage-averaged variables are phase-rotor independent values (steady maps). Equation (5) gives the final decomposition of the instantaneous velocity in its more compact form, as the contribution of a mean value $\bar{U}$, a deterministic fluctuation or "unsteadiness" U, and a pure chaotic randomness or "turbulence" u':

$$u(\boldsymbol{r},\vartheta) = \bar{U}(\boldsymbol{r}) + U(\boldsymbol{r},\varphi) + u'(\boldsymbol{r},\vartheta) \tag{5}$$

Experimental Results and Discussion

Throughflow. Averaged blade-to-blade variations are filtered out when the passage-averaged flow is additionally pitch-averaged. The resulting flow field (usually known as *throughflow*) describes an axisymmetric flow, assuming that each blade row has an infinite number of thin blades. As a consequence, only radial distributions of the flow are obtained, with a core (inviscid) region and two endwall (viscous) regions describing the hub and tip boundary layers. Though quite simple, the throughflow analysis provides a first approach to the underlying physics inside the fan stage.

Figure 6 shows the radial distribution of both axial and tangential velocities at the stator exit after pitch averaging. The axial component has been normalized with the overall mean axial velocity in each particular test condition, while the tangential velocity has been made non-dimensional with the tip blade velocity. The definition of the cylindrical coordinates is included in Fig. 5, with the axial coordinate following the flow sense and the tangential coordinate opposite to the rotation axis. In the case of the larger axial gap (black lines), the axial component is quite uniform, even at lower flow rates (dashed line). On the contrary, when the axial gap is reduced, an important blockage is observed from midspan to tip sections, thus concentrating the flow near the hub region. This blockage, induced by the proximity of the rotor blades, is developed by the aerodynamic loadings of the suction sides, overturning the flow streamlines. Since the rotor blades are practically perpendicular to the stator passage from midspan to tip sections (Fig. 2), the pressure conditions on the blade surfaces easily penetrate into the stator passage, establishing the flow blockage. (Fernandez Oro et al. [13]).

In the design of the rotor blades, a free vortex distribution was adopted to ensure radial equilibrium flow. Therefore, due to the stator-rotor configuration, there must be a swirl velocity at the stator exit giving a spanwise vortex-free pre-rotation (design line in the right graph). Effectively, at larger axial gap (black lines), the experimental tend to follow the pattern as expected. In any case, in the core region, the swirl velocity shows a linear distribution, instead of a hyperbolic law with the radius. The theory of radial equilibrium holds that this deviation must be balanced by the axial velocity, as stated by the equation for the radial variation of the total pressure (Dixon [14], Chap. 6). Consequently, the axial component cannot be perfectly uniform spanwise, as shown in the black lines of the graph on the left. On the other hand, in the case of a lower axial gap, the axial blockage is balanced by the tangential velocity, which is increased from midspan to tip regions, overturning the flow (gray lines in the graph on the right).

Figure 7 introduces the flow incidence in respect to the rotor blades from both axial gap configurations. It has been computed as the difference between the relative velocity angle and the blade angle at the leading edge. Common characteristics for both gaps are an increment of the incidence in the casing boundary layer (over 80% of the span) and also an overall displacement to higher incidence values because of a reduction in the flow rate.

In the case of the nominal gap, experimental data show a good agreement with the design incidence. The design incidence has been calculated using Lieblein's correlations ([15]), which assures minor profile losses for the NACA 65 family. On the contrary, the axial blockage developed for the lower gap is responsible for the establishment of an inverted incidence distribution, i.e., from hub to midspan, the axial velocity concentration reduces the nominal incidence, whereas from midspan to tip, the blockage increases the incidence. This behavior, which is reproduced in the case of lower flow rate, reveals a major disorder of the rotor inflow patterns and higher cascade losses.

In order to complete the description of the throughflow, Fig. 8 shows the radial distributions of both axial and tangential velocities at the rotor exit for all the cases tested in the measurements. The analysis of the axial component describes three important characteristics of the mean throughflow in the rotor passage. Firstly, the results obtained for both axial gaps are very similar at every operating point. Differences in the distribution for both axial gaps are only observable near the casing boundary layer.

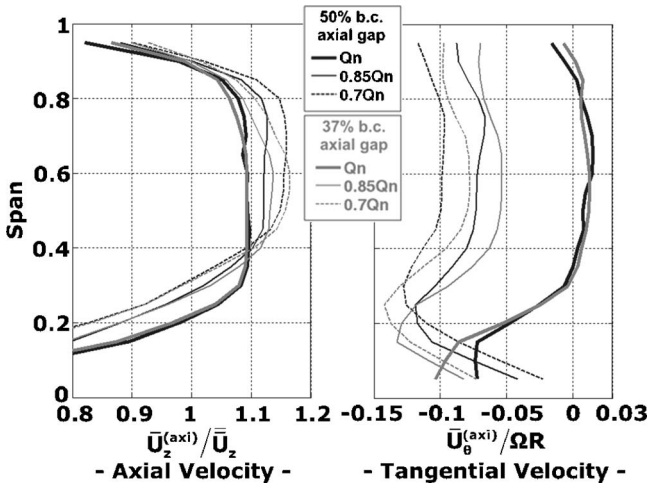

Fig. 8 Throughflow at rotor exit

Secondly, these differences clearly recall the axial blockage at the stator exit, increasing as the flow rate is reduced. Since the distribution from the midspan to the hub boundary layer is now practically uniform, it implies that the flow inside the rotor passage is reorganized. Thirdly, the width of the hub boundary layer is clearly increased when the flow coefficient is reduced. This effect is a direct consequence of the application of the radial equilibrium inside the rotor passage: when the flow rate is reduced, the incidence is increased and the relative size of the product of the radius times the tangential velocity increases towards the tip region. As a consequence, the radial equilibrium equation is balanced with a higher reduction of the axial velocity, especially near the hub (Cumptsy [16]), thus increasing the thickness of the boundary layer. This radial imbalance of the hub region is also observed moving radially towards the midspan as the flow rate is reduced in the distribution of the tangential velocity (right-hand graph). Outside the hub region, the tangential distributions are always nearly uniform, with zero values in the case of nominal conditions.

Finally, a simplified sketch of the throughflow streamlines is introduced in Fig. 9 to illustrate some of the basic ideas that were explained above. In particular, it represents the lower axial gap configuration in case of a reduced flow rate. Under these conditions, both rotor blockage in the tip region and radial imbalance near the hub were identified as the basic mechanisms modifying the uniform flow conditions across the stage: the flow concentrates near the hub at the rotor inlet, decreasing its relative incidence there and favoring a major separation on the suction side of the blades. In addition, the radial disequilibrium forces the flow to move out spanwise in the rotor passage, thickening the hub boundary layer and rearranging the flow deficit previously induced by the blockage near the tip.

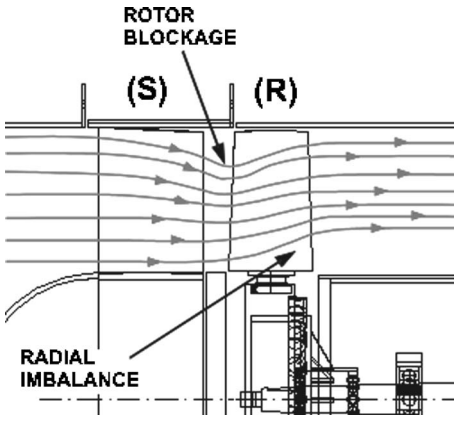

Fig. 9 Sketch of streamlines in the throughflow

Unsteadiness at Stator Exit. The unsteadiness at the stator exit is generated by the potential effect of the rotating blade surfaces, which is felt as a periodic blockage on the phase-averaged flow (Fernández Oro [17]). The impact of the unsteady rotor blockage on the time-averaged flow is summarized in Fig. 10, which also analyzes the influence of the gap configuration and the operating point on the axial velocity distribution. The results have been redrawn over a second stator passage in the tangential coordinate, since the flow is periodic in the pitchwise direction. The axial velocity has been normalized by the overall mean value as usual. In the case of a larger axial gap (left-hand column), the results show a clear uniformity in both tangential and radial directions, independently of the flow rate. The stator wakes exhibit a greater mixed-out state than in the case of the lower axial gap, because of the higher axial distance between the rows, which facilitates the convection of the wakes. On the contrary, the wakes introduce a considerable discontinuity into the velocity field for the lower gap (right-hand column). At nominal conditions, there is a tangential fluctuation in the blockage structure, suggesting a clear interaction between the stator wakes and the periodic blockage of the rotor. Moreover, when the flow rate is reduced, the axial velocity is more concentrated between the wakes, and the rotor blockage masks all the stator pitch periodicity from midspan to tip sections, becoming the predominant flow structure. In any case, the reduction of the flow rate influences the shape of the wakes, thickening them, especially at the hub region.

Figure 11 analyzes in detail the interaction that is established between the stator wakes and the periodic blockage of the rotor blades. Temporal variations of the axial velocity distribution for nominal conditions and operation near stall are shown in the case of the lower axial gap. Only the shape and intensity of the stator wakes are shown in five snapshots during a complete rotor blade passing period. In both cases the deficit in the stator wakes is clearly increased when the blockage passes along the wake path ($t/T_r=0.00$), while the wake becomes narrower when the blade has already passed by ($t/T_r=0.40$). Because of the relative transversal position of the vane's TE and the blade's LE, a radial migration of the wake-rotor interaction is developed during the rotor passing period. Notice how the wake structure is clearly modified over time by the rotor blockage from midspan to tip sections. At $0.7Q_n$, the stator wake is even broken by the effect of the rotor blockage when $t/T_r=0.60$. On the contrary, in the hub sections, the wake deficit remains practically unaffected by the pressure propagation of the rotor blades.

Finally, in order to demonstrate how the axial gap modifies the convection of the stator wakes, Fig. 12 is shown here to compare the sharpness of the wakes in both configurations. These results show temporal distributions of tangential velocity (normalized by the tip blade velocity) along the stator pitch at the midspan, considering nominal (top) and near stall (bottom) conditions for a comparison between larger (left-hand column) and lower (right-hand column) axial gaps. The vertical axis shows time, nondimensionalized by the rotor blade passing period, while the horizontal axis corresponds to the stator pitch (plotted twice for clarity). Vertical bands of low velocity correspond to the stator wakes, fixed at a particular tangential position in the plots; transversal bands running diagonally to the plots represent the rotor blockage. Obviously, they are diagonal because they are moving tangentially over time. The slope of these bands depends on the relative number of vanes and blades. As a consequence, the blockage is displaced along 13/9 of the stator pitch in every rotor blade passing period. At nominal conditions, differences between the wakes of both axial gaps are definitive: in the case of the lower axial gap, they appear chopping the blockage effect, clearly unmixed and embedded in the potential fluctuation coming from the rotor.

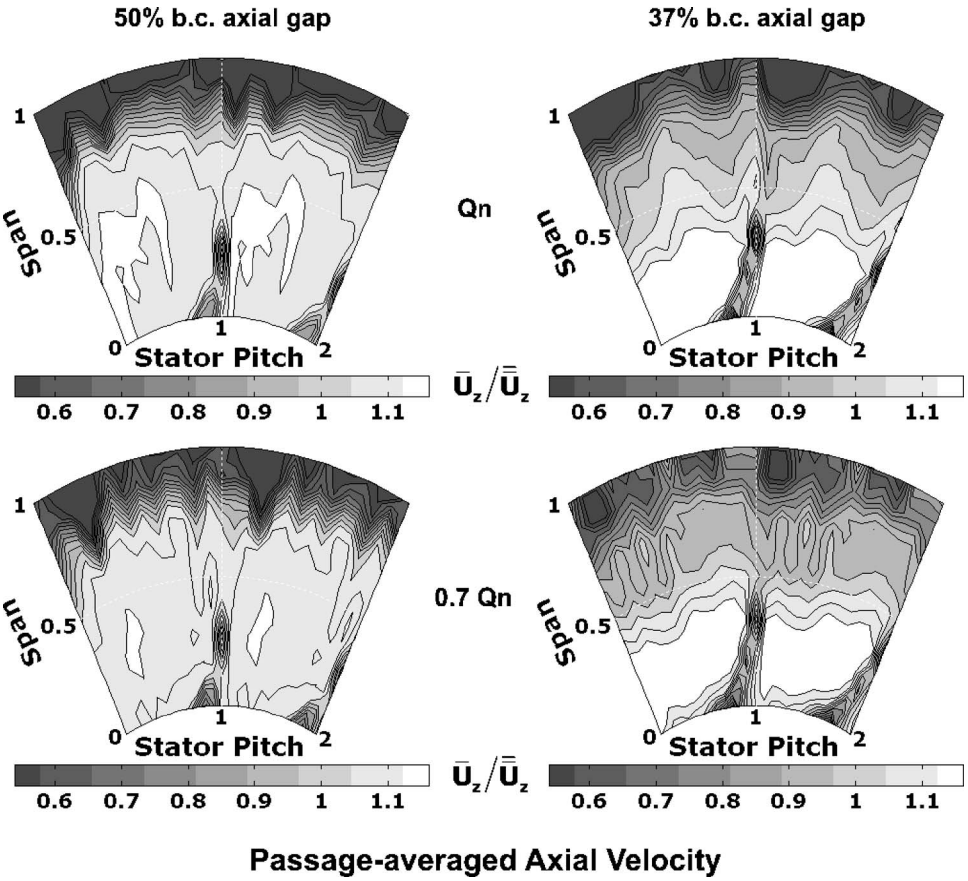

Fig. 10 Influence of the rotor blockage on the time-averaged flow at different operating conditions

When the gap is increased, the wakes are more diffused, modulating the rotor blockage rather than chopping it. On the other hand, at near-stall conditions, major differences between both axial gaps are now placed on the intensity of the rotor blockage. In addition, the presence of the stator wakes has been reduced practically to a low-velocity spot, generated in the intersection of the wake velocity deficit and the rotor blockage when leaving the wake path. Once again, it is observed how the blockage increases the tangential velocity, overturning the flow (white regions in the maps) and weakening the stator wakes' structure. When the blade has already passed by, the tangential velocity is reduced, strengthening the wake structure by means of the establishment of low-velocity spots.

Unsteadiness at the Rotor Exit. The transport of wake velocity deficits is the basic mechanism responsible for the existence of an unsteady scenario inside multistage turbomachinery. Since its convection across the machine is established according to different deterministic variables (such as the number of vanes and blades, the flow coefficient, or the rotational speed), the velocity variations due to the wakes' streets can be described as periodic flow fluctuations. Specifically, the present paper focuses on the analysis of the rotor wakes' structures—periodic flow disturbances—and the interaction of unmixed stator wakes with time-averaged flow patterns derived from such unsteady structures.

Figure 13 shows the structure of the rotor wakes at different radial positions from hub to tip. For that purpose, normalized axial and tangential velocity components are plotted over time at nominal, partial, and near-stall conditions. In order to isolate the tangential variations caused by the blades loadings from any other effect (i.e., rotor blockage), only results of the larger axial gap are represented here (Fig. 8 showed uniform outflow for this gap). Additionally, these results have been obtained by pitch averaging, that is, filtering any possible contribution with stator pitch periodicity. Bearing in mind this constraint, the temporal evolution in the absolute frame of reference is directly related to the circumferential gradients in the relative frame of reference, in agreement with (see [1])

$$\frac{\partial}{\partial t} = -\Omega \frac{\partial}{\partial \theta} \tag{6}$$

In other words, the temporal fluctuations captured by the anemometric probe are the tangential gradients of the velocity components in the rotor passage. At nominal flow rate (thick lines), the axial velocity distribution presents an inversion on the deficits of both SS and PS shear layers from hub to tip. In particular, from 65% of the span to the tip, velocity on the SS (from $t/T_r=0.5$ on) is progressively reduced, while from 35% of the span to the hub the velocity value is increased. At midspan, the blade-to-blade distribution becomes flat outside the wake region.

This trend in the axial velocity distribution from hub to tip is also observed at other operating conditions, with a spanwise displacement of the radial position in which the inversion takes place. In these cases, at 25% of the span, the wake-core structure is also completely lost due to the thickening of the hub boundary layer (combined effects of radial imbalance and flow separation). Finally, the graph of the tangential velocity reveals a uniform radial distribution of this component. Since no differences are appreciable between PS and SS, the tangential deficit can be viewed as symmetric. At partial load, the flow is underturned inside the rotor passage, while at nominal conditions the designed

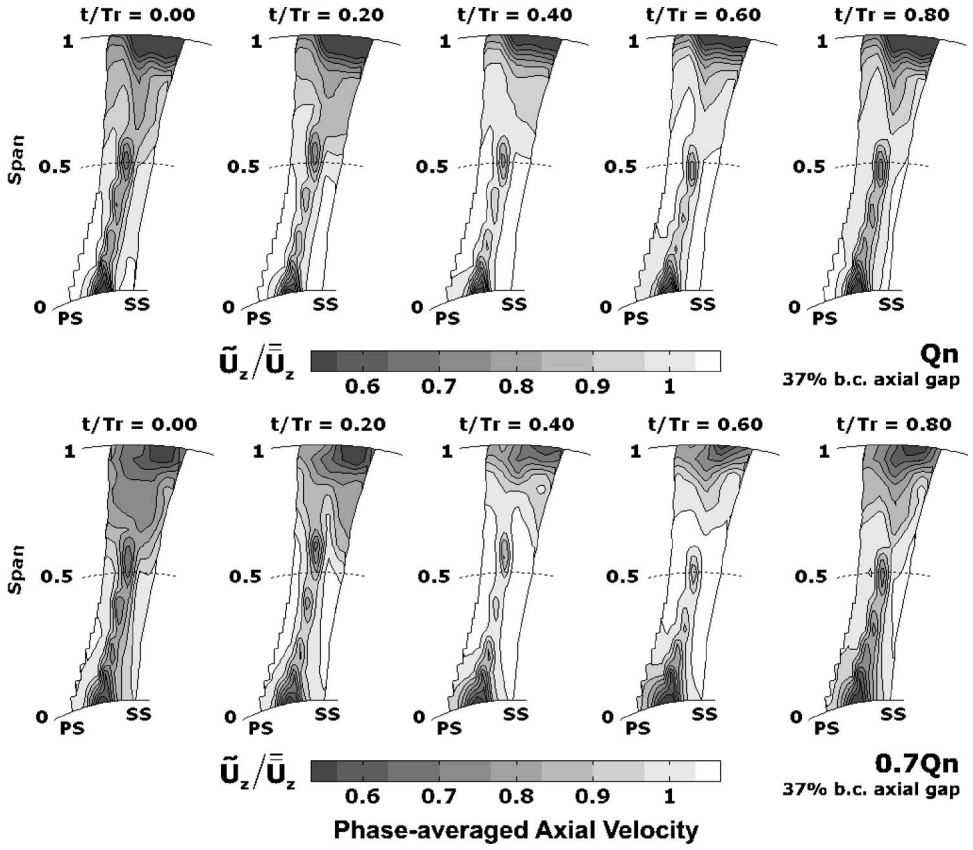

Fig. 11 Influence of the operating conditions on the radial migration of the stator wake-rotor blockage interaction

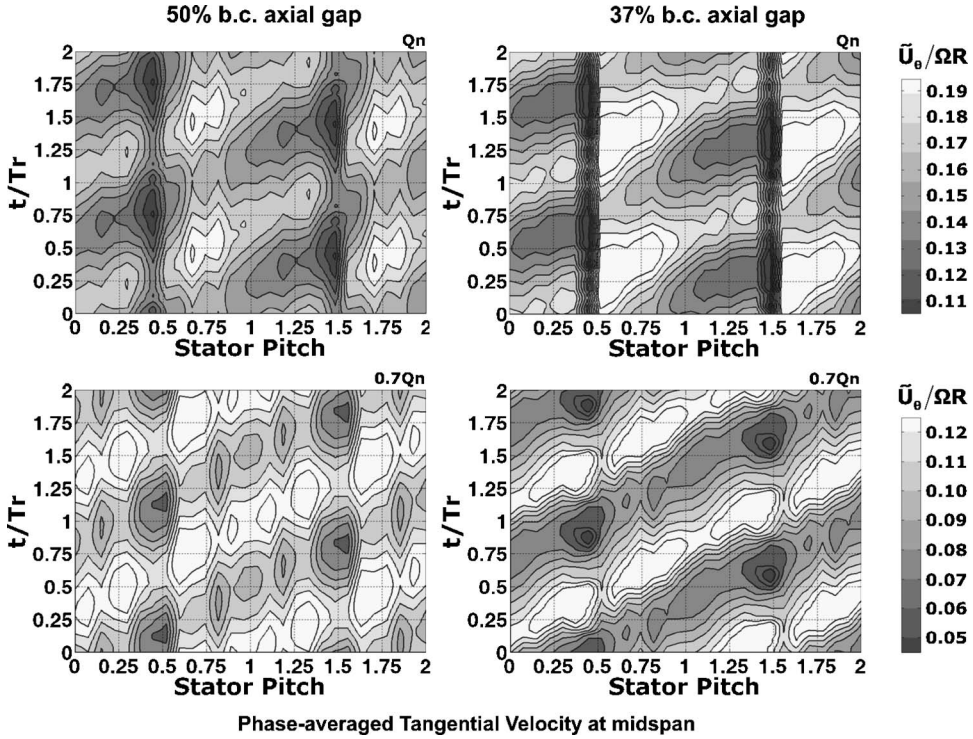

Fig. 12 Influence of the axial gap in the dispersion of stator wakes at different operating conditions for the midspan

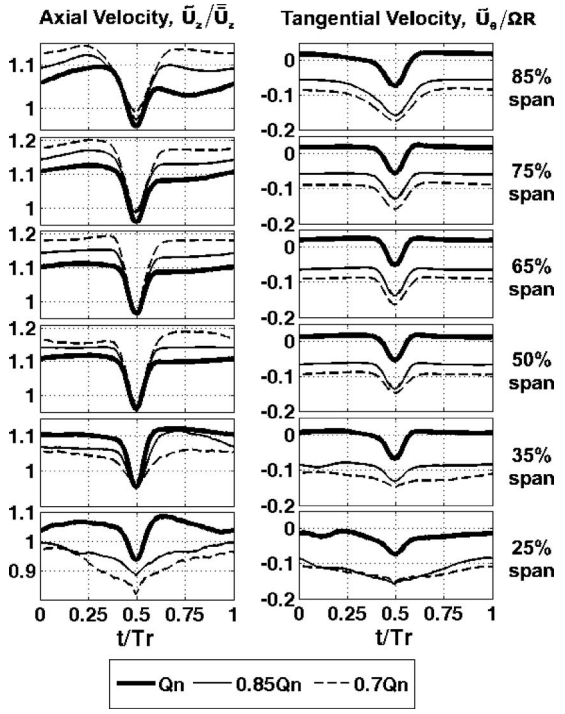

Fig. 13 Radial evolution of the rotor wake structure

zero swirl velocity is achieved.

More detailed information about the measured rotor wakes is now presented. Typical parameters such as the displacement thickness and the shape factor will be introduced here to characterize the shear layers. Radial distributions will also be shown to analyze the influence of the operating point on the wakes structure. Figure 14 illustrates how the shear layers are identified in the blade-to-blade velocity distributions (shaded regions). Basically, the beginning of the shear layers in both sides is associated with a sudden reduction of the velocity. Thus, the point where the velocity gradient exceeds the mean gradient in the core region is defined as the limit of the shear layer on each side. Next, according to the boundary layer theory, the displacement thickness is obtained for both suction and pressure sides by evaluating the area under the distribution as follows:

$$\delta_S^* = \delta_S - \frac{A_S}{(U_S - U_D)} \quad \delta_P^* = \delta_P - \frac{A_P}{(U_P - U_D)} \tag{7}$$

where U_S and U_P are the free-stream velocities for every side and U_D is the velocity deficit of the wake. Other important parameters of the wakes, such as the momentum thickness θ or the kinetic

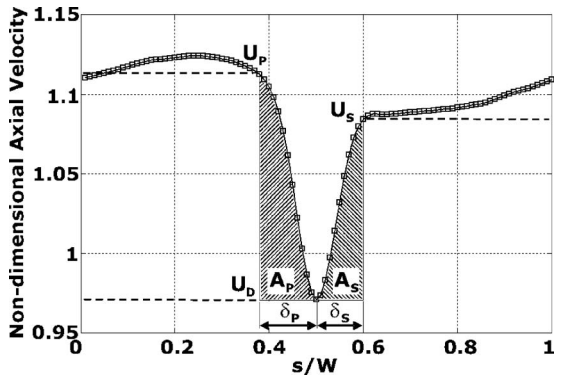

Fig. 14 Identification of the rotor wakes' shear layers

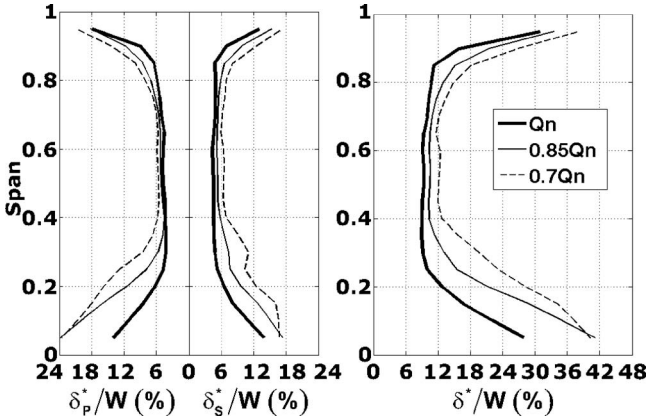

Fig. 15 Radial distribution of the rotor wakes' displacement thickness

energy thickness θ^* were also determined using analogous geometric considerations. Finally, non-dimensional parameters, like the shape factor H and the energy factor K were obtained as the ratio of different shear layer thickness, according to Vavra, [18]:

$$H = \frac{\delta^*}{\theta} \quad K = \frac{\theta^*}{\theta} \tag{8}$$

The radial distribution of the displacement thickness is shown in Fig. 15 after applying (7) to all the spanwise measurements. It has been divided by the rotor pitch W to compare the wakes' thickness in respect to the width of the rotor passage. Both pressure and suction sides have been represented independently in the graph on the left, whereas the total value is drawn in the right-hand plot. From 25% to 85% of the span, the rotor wakes exhibit a clear radial uniformity, with similar thickness for both shear layers. At nominal conditions, the total displacement thickness is about an 8%. When the flow rate is reduced, the rotor wakes broaden, reaching 10% for $0.85Q_n$ and even 12% for $0.7Q_n$ (relative increments of 25% and 50% in the wakes' thickness, respectively). In addition, around the midspan, the thickening of the shear layer in the suction side is more influenced by the reduction in the flow rate than on the pressure side (see the plot on the left). As expected, lower flow rates induce thicker boundary layers on the SS and major flow separation. Results outside the range of 25% and 85% of the span cannot be considered as fully representative of the wakes thickness on the viscous boundary layers. In those regions, where three-dimensional effects are predominant in the flow patterns, the wake-core structure is lost (previously showed in Fig. 13), so a two-dimensional analysis of the wakes becomes unrealistic.

Additional parameters of the rotor wakes are summarized in Table 1. In particular, high-order thicknesses at midspan are listed for all the flow rates tested in the experiments. Besides, the radial distributions of momentum and kinetic energy thickness (not shown here) reveal similar radial evolutions as in the case of the displacement thickness.

The characterization of the rotor wakes concludes with the rep-

Table 1 Parameters of the rotor wakes' shear layers at midspan

	Momentum thickness θ/W (%)	Kinetic energy thickness θ^*/W (%)
Nominal, Q_n	2.5	3.8
Partial load, $0.85Q_n$	3.0	4.6
Near-stall, $0.7Q_n$	3.6	5.4

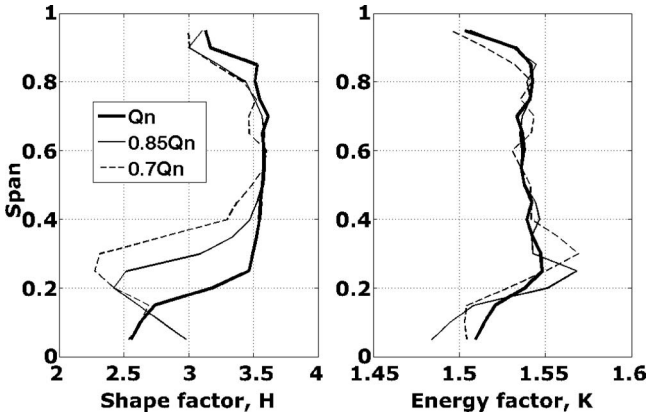

Fig. 16 Radial distribution of the rotor wakes' shape and energy factors

resentation of both shape and energy factors in Fig. 16, obtained according to (8). Around the midspan region, the shape factor is radially uniform, with a characteristic value of 3.5. Notice that this parameter is not influenced by operating point variations. In the hub boundary layer, the shape factor is also independent of the flow rate conditions because all the distributions present the same slope (in fact, the radial position in which the shape factor begins to be reduced varies due to the growth of the viscous boundary layer as the flow rate is reduced). Similar independence of the flow rate is encountered for the energy factor, which also presents a uniform distribution around 1.54. In this case, two abrupt peaks appear at 25% and 30% of the span for partial load and near-stall conditions, respectively. Their origin may be related to the existence of separated flow at off-design conditions, especially in the suction side, which modifies the pattern of the rotor wake.

In order to analyze the relative importance of the casing boundary layers and the wakes shear layers, the vortical structure of the flow at the rotor exit is outlined in Fig. 17. Since the experiments provide only axial and tangential components of the velocity inside a transverse sector, only in-plane radial and tangential derivatives can be computed to obtain the vorticity distribution. Therefore, all the streamwise variations of the velocity components are neglected in (9).

$$\frac{\omega_r}{|\mathbf{\Omega}|} = \frac{1}{\Omega}\left(\frac{1}{r}\frac{\partial V_{\mathrm{ax}}}{\partial \theta} - \frac{\partial V_\theta}{\partial z}\right) \quad \frac{\omega_\theta}{|\mathbf{\Omega}|} = \frac{1}{\Omega}\left(\frac{\partial V_r}{\partial z} - \frac{\partial V_{\mathrm{ax}}}{\partial r}\right) \tag{9}$$

Of course, this is an important restriction because out-of-plane (3D) effects may have an important impact on these terms, especially at hub and tip sections. However, valuable information is still obtained from both radial and circumferential variations of the axial velocity. Thus, the plot on the left shows circumferential vorticity of the passage-averaged flow, normalized by the rotational speed. The contribution of the rotor wakes is filtered out and only the effects of viscous boundary layers in both hub and tip zones are observed. From mid to 80% of the span, the flow behaves inviscidly at any flow rate value.

Between the midspan and the hub, the flow exhibits a progressive generation of vorticity as the mass flow rate is reduced. Complementarily, vorticity associated to the rotor wakes is presented at three particular radial positions on the right plot: 15%, 50% and 85% of the span. These vorticity distributions, obtained from the phase-averaged flow, are periodically superimposed on the previous hub-to-tip pattern, resulting in a more complex, three-dimensional vortical field. Positive oscillations indicate an increment of the vorticity when moving tangentially (entering in the wake), while negative oscillations show the change in the vorticity sign (leaving the wake). Once again, at 15% of the span, the wake-core structure is lost. At mid and 85% of the span, the reduction of the flow rate produces thicker shear layers. In any case, the orders of magnitude of both tangential and radial distributions are similar, so unsteady shear layers are as important as endwall viscous layers. Therefore, unsteady sources play a major role in describing vortical dynamics.

A complete picture of the unsteady flow downstream of the rotor is shown in Fig. 18. A particular snapshot of both phase-averaged axial and tangential velocities is represented in the case of the larger axial gap at nominal conditions. This temporal map, redrawn over a second stator pitch to obtain a better representation, illustrates the whole spatial distribution (radial and tangential) of the unsteadiness in sector R. Towards the center of both stator passages, bands of low axial velocity confirm the presence of unmixed stator wakes rotor downstream. In this particular moment in time, i.e., $t/T_r=0.80$, the rotor wake (rotating counterclockwise) begins to interact with the stator wake fluid at the hub

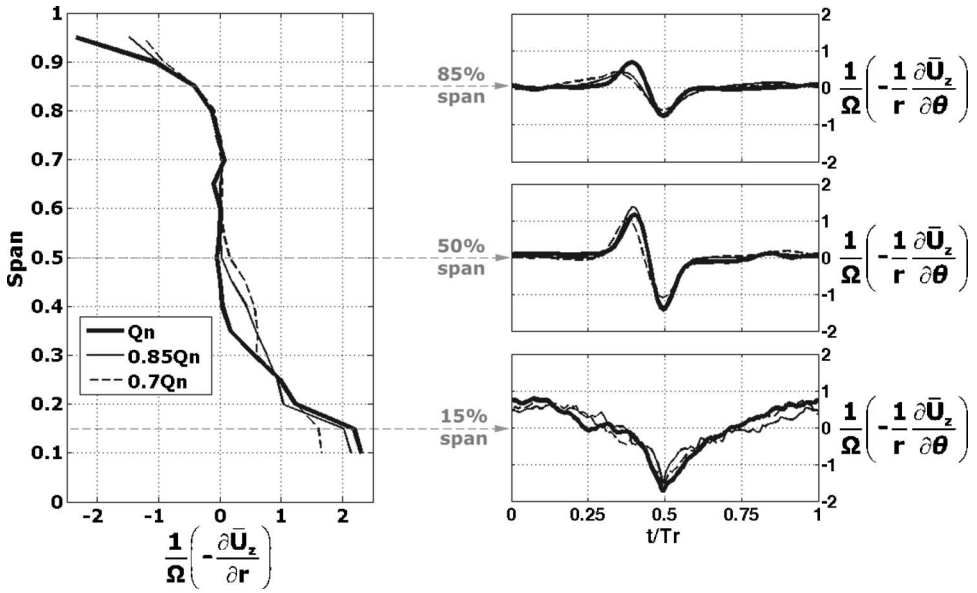

Fig. 17 Vorticity structure of boundary layers: casing viscous regions and wakes' shear layers at rotor exit

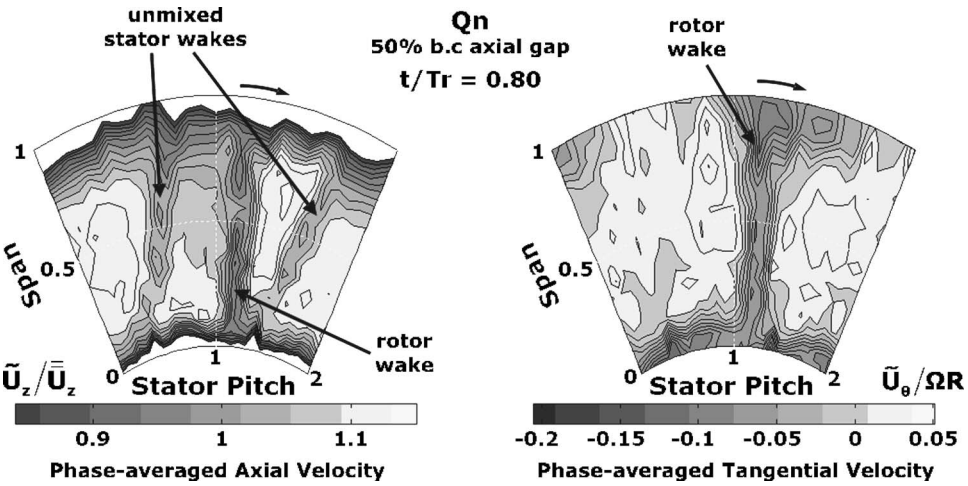

Fig. 18 Unsteady flow patterns in axial and tangential velocity distributions at rotor exit

while it is still stretching the first stator wake from midspan to tip. High background levels of axial velocity are encountered at midspan and central positions. These levels gradually decrease spanwise towards both hub and casing boundary layers. Nonetheless, viscous boundaries give no valuable information about the transport of unsteady wakes, so they have been removed from all the drawings to enhance the midspan colormap. On the other hand, the phase-averaged tangential velocity presents an excellent uniformity, only broken by the rotor wakes. The unmixed stator wakes are not observable in this velocity component.

Figure 19 analyzes the influence of the operating conditions in the transport of unmixed stator wakes in the case of the lower axial gap. In addition, other unsteady mechanisms, developed due to the stator-rotor interaction, will be shown. The three operating points are reproduced in the same instantaneous realization to facilitate their comparison (t/T_r=0.12). In this snapshot, two rotor wakes are exhibited in the drawings. This is possible because two stator pitches cover 55.4 deg and there are only 40 deg between the rotor wakes. Notice that different flow structures are manifested depending on the velocity component that is studied. In the axial velocity, a wake-wake interaction, the existence of a turbulent spot and the periodic interaction between the rotor wake and the spot it can be observed. In the tangential distributions, flow separation and leakage flow are identified. At nominal conditions (top left), a wake-wake interaction is established when the second stator wake is masked by the second rotor wake. This mechanism will be presented later in more detail in Figs. 20 and 21. Additionally, a new turbulent structure appears at the relative stator pitch position of 1.1. This vortical disturbance suggests the existence of separated flow in the stator vanes. This turbulent spot is stationary linked to that particular angular coordinate, instead of being transported tangentially (not shown here). Therefore, its origin is in the stator row, though it is induced by the rotor blockage. In addition, if this phenomenon is simply developed in the stator and then convected across the stage by the mean throughflow, its velocity deficit should be of the order of the unmixed stator wakes. On the contrary, it presents similar levels to those observed in the rotor wakes, suggesting that this vortical structure is intensified when interacting with rotor passage structures. Both partial load (middle left) and near stall conditions (bottom left) exhibit similar trends, even though the turbulent spot enlarges its size and reduces its deficit, especially when interacting with the rotor wake. Alternatively, maps of tangential velocity on the right column show the presence of separated flow in the inner half of the rotor passage, rotating counter-clockwise and developed on the suction side of the blades. As expected, a progressive enlargement of the flow separation occurs when the mass flow rate is reduced. In addition, the flow field in the outer half of the passage is dominated by tip leakage flow. At low flow rates, the rotor wakes are significantly broadened in the tip region, and as a result, the leakage flow gets embedded in the wake fluid, and the overall flow structure becomes more disordered.

Unsteady Wake Transport. The paper concludes with the analysis of the unsteadiness caused by the periodic interaction of unmixed stator wakes with downstream rotor blades. It is well known that the incoming wakes are chopped by the rotor blades, producing new unsteady phenomena, which modifies the wake pattern. In order to improve this description, the influence of different parameters in this mechanism is presented in the case of low-speed axial fans. Hence, the impact of the operating point or the effect of the radial position is introduced to facilitate the detailed understanding of the transport of the unmixed stator wakes through the rotor passage. Figure 20 shows the temporal pitchwise distribution of the axial velocity deficit (in percentage, respect to the mean value) at the rotor exit, in the case of partial load ($0.85Q_n$) at three different radial positions: 35%, 50%, and 65% of the span. Though the tangential discretization (15 points per vane passage) was not enough to obtain a smooth trace of both stator and rotor wakes, overall trends can be identified in the present results. Velocity distributions, corresponding to ten intermediate instants of the blade passing period, are stacked for every radial position, in order to trace the displacement of the rotor wake (marked with gray lines) and the position of the unmixed stator wakes (marked with dashed lines). The interpretation of this figure reveals two mechanisms affecting the stator wakes chopping. On the one hand, the position of the unmixed stator wakes is progressively shifted over time, suggesting that the blade passage modifies the stator wake characteristics. On the other hand, between t/T_r=0.6 and t/T_r=0.7, a discontinuity arises in the stator wake position in order to correct that shift, just when the rotor wake passes from PS to SS. Moreover, this periodic disturbance of the stator wake position becomes more severe towards the hub. Notice how the total shift of the IGV wakes evolves from less than a quarter of the pitch at 65% of the span to more than a quarter of the pitch at 35% of the span.

This radial decrease of the stator wake displacement is a direct consequence of the spanwise reduction of the blade camber (Fig. 2). Actually, it is well known that when a wake segment is convected through a blade passage, large differences on both suction and pressure sides induce a stretching process, tilting the wakes. In the temporal distributions of Fig. 20, the tilting process is manifested as a tangential shift of the stator wake fluid, whereas the discontinuity reveals the stretching developed by the blade load-

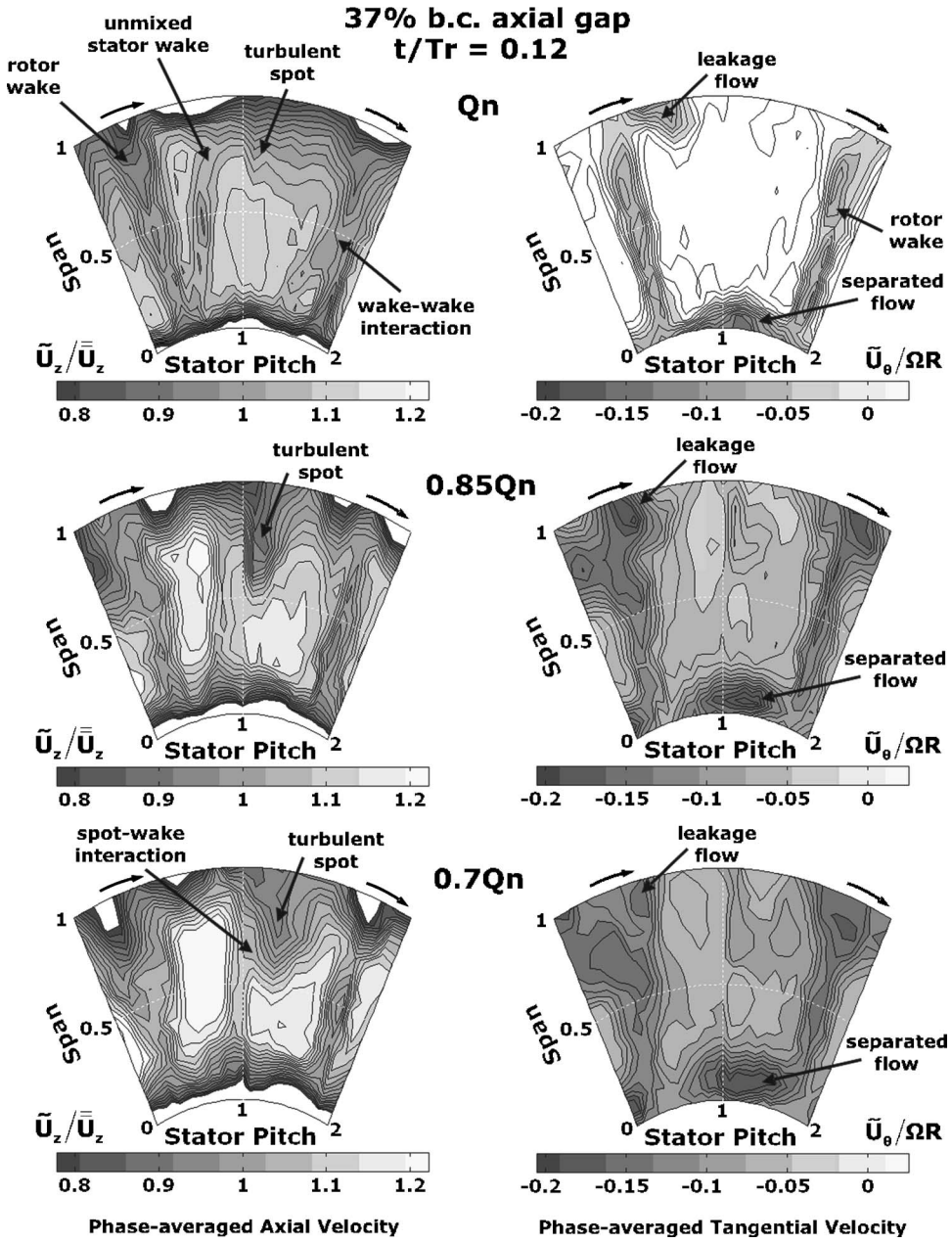

Fig. 19 Unsteady flow patterns at rotor exit as a function of the operating point in the case of reduced axial gap

ing. Thus, the lower the camber (tip zones), the lesser the stretching of the wake patterns. In order to illustrate these mechanisms, Fig. 21 reproduces a sketch of the transport of the wake segments chopped by the rotor blades. The pitchwise distribution of the axial velocity deficit downstream of the rotor is also included. Once the wake has passed the LE of the blades, the wake structure is exposed to a non-uniform velocity distribution. As a result, the wake segment is stretched at the SS, becoming wider (from $t/T_r = 0.4$ to $t/T_r = 0.6$), and developing a phase gap between both leading and trailing wake segments. Consequently, the stator wake, though narrowed at the PS of the blade TE, presents a phase lag that causes a discontinuity in the axial velocity. (See also Soranna et al. [9], for an excellent analysis of the vortical mechanism involved in the impingement of IGV wakes in rotor blades.) Being transported rotor downstream, this discontinuity of the wake segments derives in a tangential disturbance in the stator wake position, measured when the wake fluid reaches the probe ($t/T_r = 0.6$ *to* 0.7).

The impact of the mass flow rate conditions in the wake transport is finally analyzed in Fig. 22. Temporal distributions of axial velocity along the stator pitch are considered at midspan for nominal (top), partial load (middle), and near-stall (bottom) conditions. Transversal bands of low velocity represent the rotor wakes, increasing their width as the flow rate decreases. In addition, stator wake segments (gray zones), resulting from rotor blade chopping, are increasingly rotated as the rotor blade loading increases. In fact, a wake passing through a passage is tilted and stretched due to the blades circulation, i.e., loading (Van Zante et al. [19]). As a consequence, when the flow rate is reduced, higher loading is responsible for more tilted wake segments, enlarging the length of the wake segment. Following a 2D inviscid mechanism, according to Kelvin's theorem, when the length of a wake segment is increased, its velocity deficit is reduced, leading to a reduction in the wake mixing loss (Adamczyk [5]). Hence, when a wake suf-

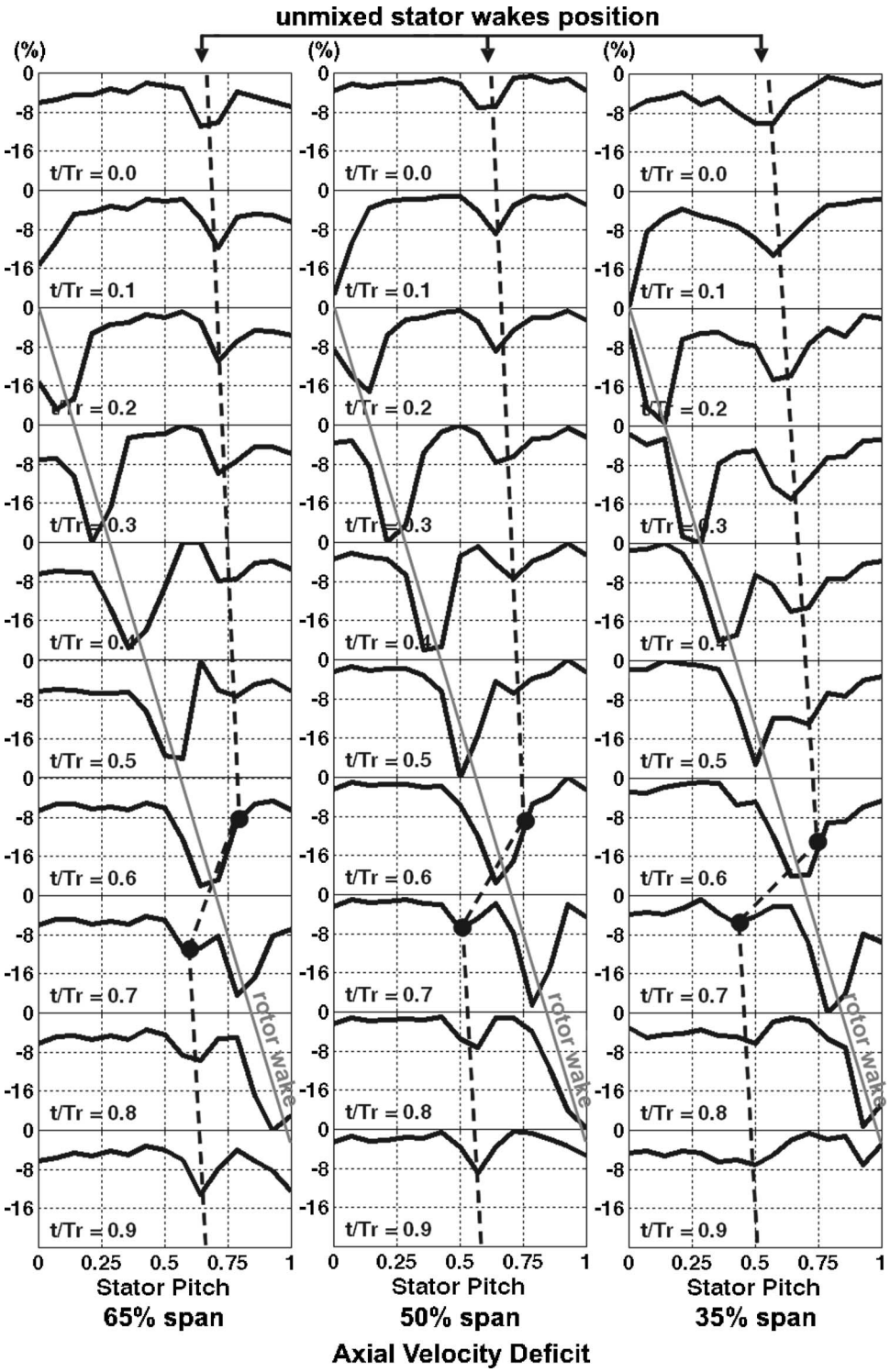

Fig. 20 Temporal pitchwise distribution of axial velocity at the rotor exit for nominal conditions

fers a stretching process, the velocity decay decreases and the wake segment becomes thinner (derived from kinematic arguments). Therefore, higher blade loadings (lower flow rate) produce more narrowed segments and a higher phase lag between the leading and the trailing part of the wake. These considerations are confirmed in the figure if the evolution of the stator wake segments is analyzed: from nominal to near stall conditions, the wakes are narrowed and the discontinuity between segments increases.

Figure 20 showed the affection of the blade camber in the transport of the stator wakes as an enhancement of the wake stretching towards the hub. Now, the spanwise influence of the passage geometry will also be analyzed in Fig. 23 in the case of nominal conditions. This figure is a three-dimensional view of the stator wake transport over time at the rotor exit. To obtain this spanwise evolution, temporal distributions of axial velocity along the stator

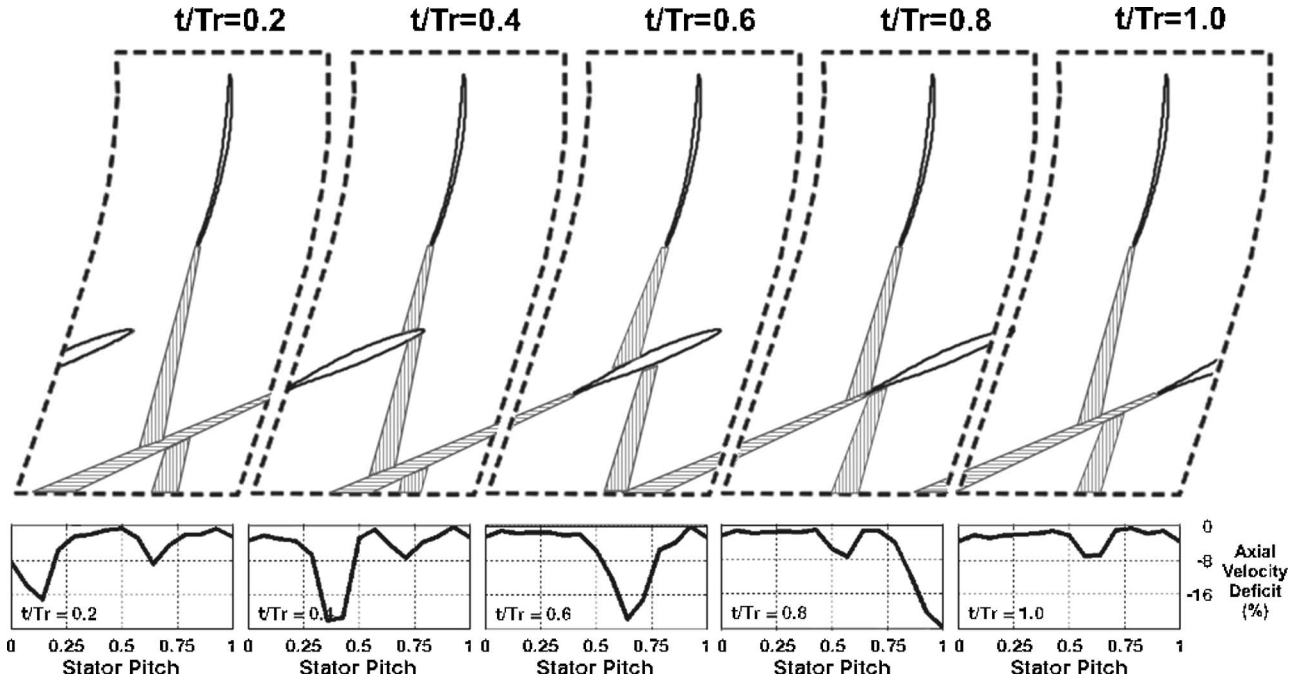

Fig. 21 Sketch of the transport and convection of an IGV wake through a rotor passage

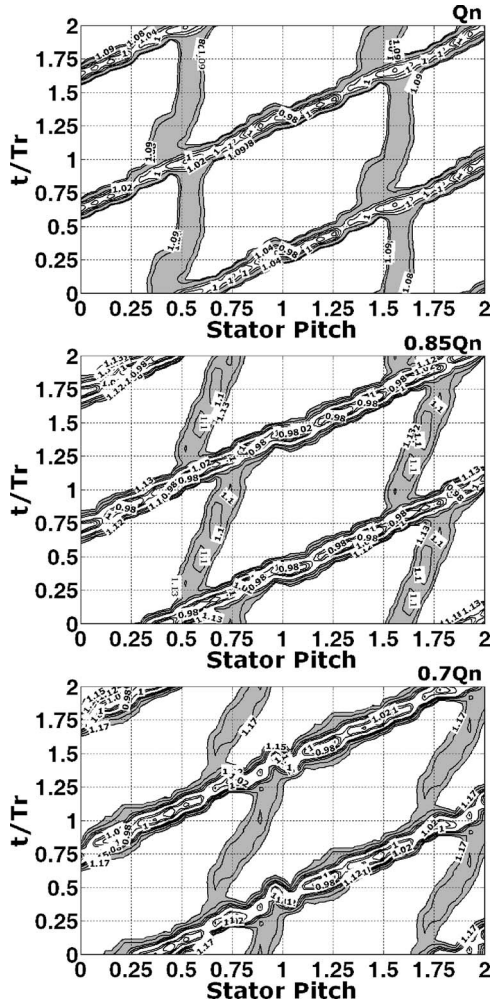

Fig. 22 Influence of the operating conditions in the wake transport at midspan

pitch were stacked along the z-axis. Both casing and hub boundary layers were removed to be clearly focused on the wakes shape. As expected, the effect of the blade camber appears in the figure once again, increasingly rotating the wake segment, especially towards the inner radial positions. Additionally, however, near both hub and tip sections, the wake segment begins to separate from the shear layers of the rotor wakes. In particular, in the tip region, the wake segment is separated from the pressure side, while in the hub region it is separated from the suction side of the wakes. Following the direction of the rotor wakes (drawn in four contour slices with gray background), relative velocity patterns are observed in the cross section of the blade passage. This section is highly twisted due to the differences in the stagger angle of the blades from hub to tip (Fig. 2), leading to an important distortion of the section, especially beneath both SS and PS in hub and tip zones. Thus, this effect contributes the modification of the wake transport, overturning the wake segments according to this geometrical distortion of the blade passage. As a result, the unmixed wakes are progressively aligned to the relative flow direction towards the endwalls.

Finally, Fig. 24 analyzes the impact of unmixed wakes on the time-mean flow structure downstream of the rotor. A comparison between vane-to-vane non-uniformities upstream and downstream of the rotor gives a precise idea of the dispersion and angular displacement of the wake transport through the blade passage. In order to highlight the unmixed wake structure, the pitch-averaged distribution of the mean flow (i.e., the throughflow) has been subtracted from the time-averaged flow. As a result, the periodic effect of the rotor wakes is completely filtered out and the endwall viscous layers removed from the maps. Hence, this procedure emphasizes the mean time spatial disturbances (periodic with the stator pitch), scaled in the figure as a percentage of the overall mean value. In the case of the larger axial gap, between the rows the velocity deficit of the IGV wakes reaches 30% of the free-stream velocity in the test section. When convected through the rotor passage, this deficit is reduced to 6% in the measuring location at the rotor exit. Besides, the unmixed wakes are dispersed and displaced tangentially as a result of all the unsteady mechanisms previously discussed. Dashed lines joining upstream and downstream sectors allow us to observe the angular displacement of the wakes. Results in case of nominal (left) and near stall

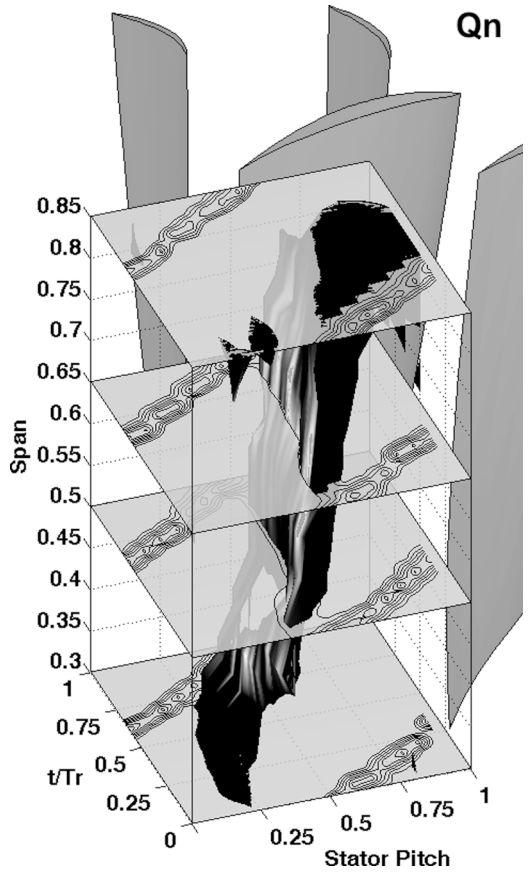

Fig. 23 Three-dimensional view of the stator wake transport downstream of the rotor

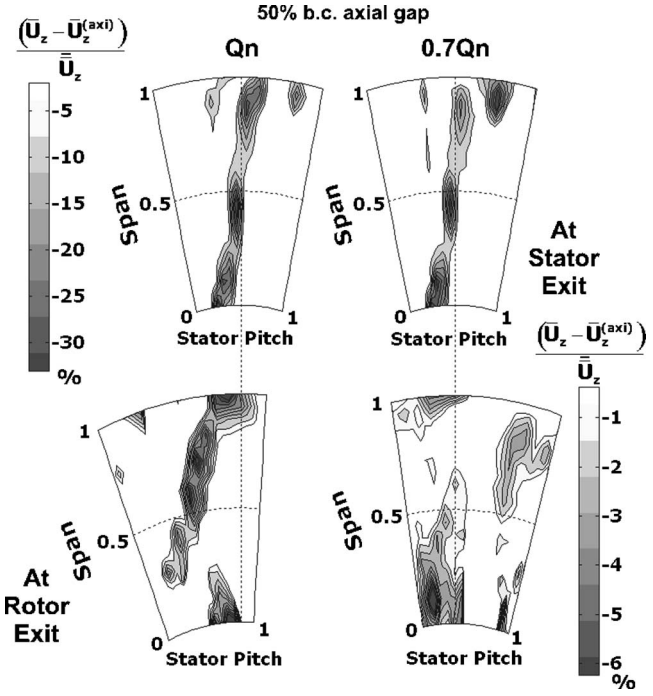

Fig. 24 Dispersion and angular displacement of unmixed stator wakes

conditions (right column) are represented in the figure. At the stator exit, no differences are observed in the wake structure of both situations. On the contrary, they become completely different after being convected through the rotor passage. In any case, the wakes always get thicker after the transport because of their diffusion on the mean flow structures, due mainly to the averaged effect of the shifting process shown in Fig. 20. At nominal conditions, the wake is broken down at 25% of the midspan, though it preserves much of its original shape from there to the tip. Besides, the wake is increasingly tilted towards the hub, because of the averaged contribution of the wake stretching process. At near-stall conditions, high loading of the blades leads to a major dispersion of the wakes. In addition, the effect of the distortion of the blade passage (overtilting the wake in the viscous layers) facilitates the breaking of the wake at midspan.

Conclusions

Unsteady flow structures and wake transport in a single-stage, low-speed axial with inlet guide vanes have been analyzed in detail. Dynamic and periodic interaction between both fixed and rotating blade rows have been described across the stage using hot-wire anemometry techniques intensively. For that purpose, deterministic fluctuations and their impact on the time-mean flow patterns were determined using a well-established averaging framework. The influence of different operational parameters, such as the variation in the flow rate, or the impact of the axial gap configuration were studied in addition to the effect of geometrical characteristics of the stage in order to obtain a complete picture of the unsteady flow inside an industrial axial fan.

The analysis of the rotor blockage on the vane-to-vane flow structures has revealed the significance of the axial gap on the propagation of this potential mechanism. Major interaction is generated in the tip region, because of the clear disturbance of the blade loading on the stator vanes passage. Furthermore, not only is the effect of the rotor blockage observed as a periodic perturbation, but it even becomes the predominant structure in the time-mean flow patterns at the stator exit, especially at reduced flow rate conditions in the case of reduced axial gap. Moreover, a radial migration of stator wake fluid is shown to be a consequence of the wake-blockage interaction, with major diffusion of the stator wakes in the case of higher axial gap (less affection of the rotor blockage on the wakes).

Unsteadiness at the rotor exit has been described with the characterization of the rotor wakes and the transport of unmixed stator wakes. Different parameters were employed to give detailed information about the wakes measured, including vorticity distributions of the shear layers. In addition, phase-averaged velocity maps were included to illustrate all the unsteady mechanisms involved in the rotor-stator interaction. The influence of the operating conditions and the axial gap configuration revealed significant trends about the origin and intensity of turbulent spots and separated regions.

Finally, mechanisms involved in the transport of unmixed wakes through the rotor passage were discussed in the paper. The reduction of mass flow rate was shown to have a significant influence on the wake chopping process. In addition, geometrical characteristics, such as the blade camber and the stagger angle, were found to have an impact on the wake stretching. Both parameters are responsible for a spanwise twisting of the wake segments, because of high blade circulation and distortion of the passage crossed area, respectively. To conclude, overall dispersion and angular displacement of the stator wakes after being convected through the rotor were analyzed in the time-mean flow structures. It was observed that lower flow rates lead to a major disorder in the convection of the stator wakes. On the contrary, the wake structure at nominal conditions is preserved from excessive diffusion, reducing the mixing losses. Future research will be focused on these aspects of the deterministic unsteady flow, relating mixing losses (and recovery) at different operating points with both generation and transport of deterministic stresses.

Acknowledgment

This work was supported by the Research Project "Modeling of Deterministic Stresses in Axial Turbomachinery," ref. DPI2003-09712, CICYT.

Nomenclature

BPF = blade passing frequency, s^{-1}
LE = leading edge
H = shape factor
IGV = inlet Guide Vane
K = energy factor
LDV = laser Doppler velocimetry
M = total number of stored rotor blades periods
N = number of samples per blade passing period
P = pressure, Pa
PIV = particle image velocimetry
PS = pressure side
Q, Q_n = flow rate and nominal flow rate, m^3/s
R = rotor radius, m
RANS = Reynolds-averaged Navier-Stokes
$\boldsymbol{r}$ = spatial position in cylindrical coordinates
r = radial coordinate, m
SS = suction side
t = time, s
T_r = Rotor blade passing period, s
TE = trailing edge
u = instantaneous velocity, m/s
u' = random velocity fluctuation, m/s
$\tilde{U}$ = deterministic velocity component, m/s
U = deterministic velocity fluctuation, m/s
$\bar{U}$ = mean velocity, m/s
$\bar{\bar{U}}$ = overall mean velocity, m/s
W = width of the rotor passage, m
z = axial coordinate, m

Greek Letters

δ = wake width, m
δ^* = displacement thickness, m
ϕ = flow coefficient
φ = rotor blade phase, deg
η = overall efficiency
θ = angular coordinate, rad = Momentum thickness, m
θ^* = kinetic energy thickness, m
ϑ = rotor phase, deg
ρ = density, kg/m^3
τ = Time lag, s
ψ = pressure coefficient
ω = vorticity, s^{-1}
Ω = rotational speed, rad/s

Superscripts and Subscripts

$\tilde{\_}$ = ensemble-averaging
$\bar{\_}$ = time-averaging
(axi) = pitch-averaging
t = tip
1,2 = inlet and outlet

References

[1] Lyman, F. A., 1993, "On the Conservation of Rothalpy in Turbomachines," ASME J. Turbomach., **115**, pp. 520–526.
[2] Greitzer, E. M., Tan, C. S., and Graf, M. B., 2004, *Internal Flow: Concepts and Applications*, Cambridge University Press, Cambridge.
[3] Adamczyk, J. J., 1996, "Modeling the Effect of Unsteady Flows on the Time Average Flow Field of a Blade Row Embedded in an Axial Flow Multistage Turbomachine," VKI Lecture Series, 1996–05.
[4] Uzol, O., Chow, Y-C., Katz, J., and Meneveau, C., 2002, "Experimental Investigation of Unsteady Flow Field Within a Two-Stage Axial Turbomachine Using Particle Image Velocimetry," ASME J. Turbomach., **124**, pp. 542–552.
[5] Adamczyk, J. J., 2000, "Aerodynamic Analysis of Multistage Turbomachinery Flows in Support of Aerodynamic Design," ASME J. Turbomach., **122**, pp. 189–217.
[6] Cherret, M. A., and Bryce, J. D., 1992, "Unsteady Viscous Flow in High-Speed Core Compressor," ASME J. Turbomach., **114**, pp. 287–294.
[7] Goto, A., 1992, "Three-Dimensional Flow and Mixing in an Axial Flow Compressor With Different Rotor Tip Clearances," ASME J. Turbomach., **114**, pp. 675–685.
[8] Senkter, A., and Reiss, W., 1998, "Measurement of Unsteady Flow and Turbulence in a Low Speed Axial Compressor," Exp. Therm. Fluid Sci., **17**, pp. 124–131.
[9] Senkter, A., and Reiss, W., 2000, "Experimental Investigation of Turbulent Wake-Blade Interaction in Axial Compressors," Int. J. Heat Fluid Flow, **21**, pp. 285–290.
[10] Soranna, F., Chow, Y-C., Uzol, O., and Katz, J., 2006, "The Effect of Inlet Guide Vanes Wake Impingement on the Flow Structure and Turbulence Around a Rotor Blade," ASME J. Turbomach., **128**, pp. 82–95.
[11] Ciocan, G. D., Avellan, F., and Kueny, J. L., 2000, "Optical Measurement Techniques for Experimental Analysis of Hydraulic Turbines Rotor-Stator Interaction," ASME-FEDSM2000-11056, Proceedings of ASME Fluids Engineering Division Summer Meeting and Exhibition 2000, Boston, MA.
[12] Blanco, E., Ballesteros, R., and Santolaria, C., 1998, "Angular Range and Uncertainty Análisis of Non-Orthogonal Crossed Hot Wire Probes," ASME J. Fluids Eng., **123**, pp. 90–94.
[13] Fernández Oro, J. M., Argüelles Díaz, K. M., Santolaria Morros, C., and Ballesteros Tajadura, R., 2006, "Upstream Potential Propagation Effects of Unsteady Rotor-Stator Interaction in an Axial Flow Blower," ASME-FEDSM2006-98244, Proceedings of ASME Fluids Engineering Division Summer Meeting and Exhibition 2006, Miami, FL.
[14] Dixon, S. L., 1998, *Fluid Mechanics and Thermodynamics of Turbomachinery*, 4th ed., Butterworth-Heinemann, Boston.
[15] Lieblein, S., 1960, "Incidence and Deviation-Angle Correlations for Compressor Cascades," ASME J. Basic Eng., **82**, pp. 575–587.
[16] Cumptsy, N. A., 1989, *Compressor Aerodynamics*, Longman Scientific & Technical, London.
[17] Fernández Oro, J. M., 2005, "Unsteady Rotor-Stator Interaction in an Axial Turbomachine," Ph.D. thesis (in Spanish), University of Oviedo, Spain.
[18] Vavra, M. H., 1974, *Aero-Thermodynamics and Flow in Turbomachines*, Robert E. Krieger Publishing Company, New York.
[19] Van Zante, D. E., Adamczyk, J. J., Strazisar, A. J., and Okiishi, T. H., 2002, "Wake Recovery Performance Benefit in a High-Speed Axial Compressor," ASME J. Turbomach., **124**, pp. 275–284.

Influence of Passive Flow-Control Devices on the Pressure Fluctuations at Wing-Body Junction Flows

Semih M. Ölçmen
Associate Professor
The University of Alabama,
Aerospace Engineering and Mechanics Department,
P.O. Box 870280,
Tuscaloosa, AL 35487-0280
e-mail: solcmen@eng.ua.edu

Roger L. Simpson
Professor
Virginia Polytechnic Institute and State University,
Aerospace and Ocean Engineering Department,
215 Randolph Hall,
Blacksburg, VA 24061
e-mail: simpson@aoe.vt.edu

The effectiveness of passive flow-control devices in eliminating high surface rms pressure fluctuations at the junction of several idealized wing/body junction flows was studied. Wall-pressure fluctuation measurements were made using microphones along the line of symmetry at the wing/body junction of six different wing shapes. The wings were mounted on the wind tunnel floor at a zero degree angle-of-attack. The six wing shapes tested were: a 3:2 semi-elliptical-nosed NACA 0020 tailed generic body shape (Rood wing), a parallel center-body model, a tear-drop model, a Sandia 1850 model, and NACA 0015 and NACA 0012 airfoil shapes. Eight different fence configurations were tested with the Rood wing. The two double-fence configurations were found to be the most effective in reducing the pressure fluctuations. Two of the single fence types were nearly as effective and were simpler to manufacture and test. For this reason one of these single fence types was selected for testing with all of the other wing models. The best fence flow-control devices were found to reduce rms wall-pressure fluctuations by at least 61% relative to the baseline cases. [DOI: 10.1115/1.2746917]

1 Introduction

The interaction of the boundary layer flow forming on a surface and an object protruding from the surface results in a limiting-streamline picture on the surface resembling a horse-shoe vortex (Baker [1], Rood and Keller [2], Simpson [3]). The boundary layer approaching the object separates from the surface due to the adverse pressure gradient generated by the presence of the wing, rolls inwards towards the wing/wall junction, and forms a vortical structure. The vortical structure next stretches and wraps itself around the object to form the horse-shoe vortex. The legs of the vortices can extend many chord lengths beyond the trailing edge before decaying. The presence of the vortical structure increases the heat transfer rate, wall-shear stress, Reynolds stresses in the flow, and the pressure fluctuations around the wing near the wing-wall junction. Many examples of such flows can be observed in engineering and in nature; for example, wing/fuselage junctions on airplanes, bridge pier/river junctions, sail/hull junctions on submarines, and blade/hub junctions in turbomachinery. A schematic of wing-body junction flow and the microphone placement used in this study is shown in Fig. 1.

Much previous work has been done by Simpson and his coworkers at Virginia Tech to define the physics of wing/body junction flows. A recent review by Simpson [4] describes in detail the latest research accomplished with respect to junction flows. The time dependent shape and size of the vortical structure at the symmetry plane was studied by Devenport and Simpson [5,6]. Their study showed that the vortical structure changes its shape in a chaotic fashion, resulting in a velocity histogram with two distinct peaks (bimodal histogram). Bimodal histograms were also obtained for wall-pressure signals measured along the symmetry plane (Ölçmen and Simpson [7]). Using a water tunnel, Kim et al. [8] documented a sequence of events within the symmetry plane that showed the vortical flow field to be highly unsteady. Formation of multiple vortical structures leap-frogging over one another was observed. Ölçmen and Simpson [7] measured rms wall-pressure fluctuations near the nose of the wing that were about ten times larger than the rms pressure fluctuations under the approaching turbulent boundary layer. In other studies, it has been shown that the vortical flow formation increases mixing at the wing-nose/body junction resulting in large velocity and pressure fluctuations, as well as increased heat transfer rates (Lewis and Simpson [9]). Descriptions of the physics of the 3-D turbulent boundary layer forming on the wall around the wing can be found in papers by Ölçmen and Simpson [10–13].

The aim of the current study was to reduce pressure fluctuations at the wing/body junction, specifically in the vicinity of the nose, using passive flow-control devices. It was presumed that breaking up the horse-shoe vortex where it initiates at the nose would result in reduced wall-pressure fluctuation amplitudes. Wall-pressure measurements were made along the line of symmetry ahead of the wing with and without the flow-control devices to test the effectiveness of various flow-control devices. The flow-control devices tested were fence type devices (crescent shaped sheet metal) that were attached to the leading edge of the wings. The sizes of the fences and the height locations where to attach the fences on the wing nose were determined using the previous velocity field data obtained by Devenport and Simpson [5] on the symmetry plane ahead of the wing. The study indicated that the wing thickness is an appropriate length scale in this region and that the flow field near the nose region is dominated by the horse-shoe vortex. Different approaches in controlling the flow field near the nose can be found in the literature, such as the use of a strake or a fillet near the nose tested by Devenport et al. [14,15] or the flow suction scheme used by Barberis et al. [16].

In the study, six different wing shapes and several configurations of flow-control devices were tested. Wings were individually placed on the flat wind-tunnel floor and subjected to an identical high Reynolds number incoming boundary layer. The approach boundary layer had a Reynolds number based on momentum thickness of $\mathrm{Re}_\theta = 4450$; the free-stream velocity was $U_{\mathrm{ref}} = 32.5$ m/s. The measurement techniques employed included the surface-microphone pressure measurement technique, hot-wire

Contributed by the Fluids Engineering Division of ASME for publication in the JOURNAL OF FLUIDS ENGINEERING. Manuscript received June 6, 2006; final manuscript received February 23, 2007. Review conducted by Joseph Katz. Paper presented at the 22nd Southeastern Conference on Theoretical and Applied Mechanics (SECTAM XXII), 2004.

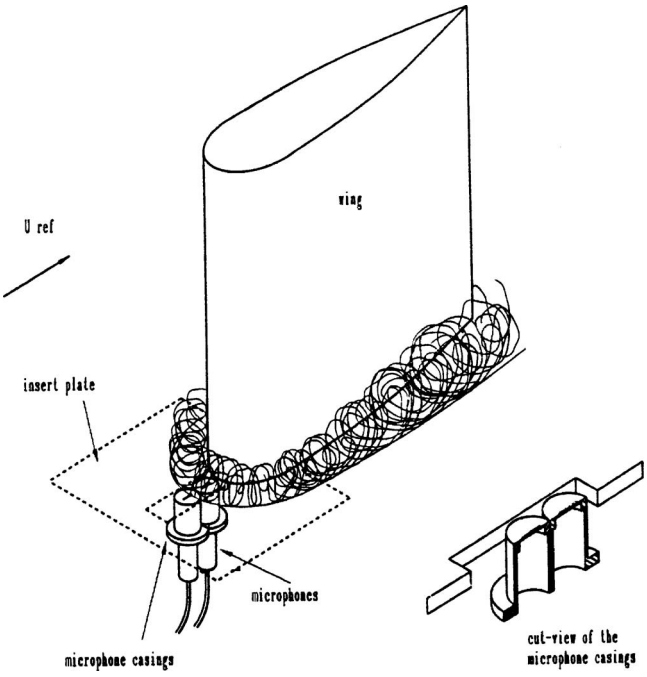

Fig. 1 Schematic drawing of wing/body junction flow and the placement of microphones

anemometry, and oil-flow surface flow visualization. A single-wire hot wire was used to measure the mean and fluctuating velocity components in the axial direction of the approach boundary layer. Oil-flow visualization was used to observe the details of the horse-shoe vortex footprint on the wall with and without the use of the fences. Presence of the fences do not grossly alter the horse-shoe vortex footprint and some of the oil-flow pictures for the baseline models can be found in the paper by Ölçmen and Simpson [7].

2 Experimental Apparatus and Techniques

Details on the experimental techniques, wind-tunnel characteristics, data-reduction methods, wing models, and the boundary-layer flow upstream of the wing can be found in the paper by Ölçmen and Simpson [7]. The tunnel characteristics, experimental and data reduction methods are briefly repeated here for completeness.

2.1 Description of the Tunnel and Flow Conditions. Measurements were made in the Boundary Layer Tunnel at Virginia Polytechnic Institute and State University. In this tunnel, air is filtered before entering a blower where its pressure is increased. The air then passes through a honeycomb and a series of seven screens used to remove swirl and turbulence. Next, the flow is accelerated through a rectangular four-to-one contraction nozzle before entering the 8 m long test section. In this study, the boundary layer on the tunnel floor was controlled so that 0.655 m upstream of the wing leading edge Re_θ was approximately 4450. This was achieved by "scooping out" the boundary layer flow ahead of the test article (at 1.73 m from the tunnel entrance) to allow development of a new boundary layer on a false floor raised 2.54 cm above the actual tunnel floor and located just downstream of the scoop. Each wing was placed in the tunnel with its leading edge approximately 1.18 m downstream of the scoop, to make sure that the incoming boundary layer was the same for each model. The mean static pressure along the axis of the tunnel on the false floor was kept constant with a trailing-edge flap attached to the false floor oriented 7 deg up. The flap was located approximately 3 m downstream of the scoop.

The mean and fluctuating streamwise velocity components in the boundary layer were measured with a single hot wire 0.655 m upstream of the wing leading edge (~0.525 m downstream of the scoop) with and without the wing in the tunnel. Results showed that the approaching boundary layer was a canonical turbulent boundary layer and that the presence of the wing did not alter its properties. The freestream velocity was, $U_{\mathrm{ref}}=32.5$ m/s. For a wing thickness t of 71.7 mm, dimensionless characteristic boundary layer scales at 0.655 m upstream of the wing leading edge were: momentum thickness, $\theta/t=0.031$, boundary layer thickness $\delta/t=0.2613$, and displacement thickness, $\delta^*/t=0.0425$. Additional measurements showed that at 27 m/s the tunnel turbulence intensity was 0.1% and the potential core was uniform within 0.5% in the spanwise and 1% in the vertical directions, respectively.

2.2 Wing and Flow Control Device (Fence) Shapes

Wing Shapes. The wing shapes used in the investigation were: Model 0, a 3:2 semi-elliptical-nosed NACA-0020-tailed wing; Model 1, a parallel centerbody model; Model 2, a tear drop shaped model; Model 3, a Sand 1850 model; Model 4, a NACA 0015 profile wing; and Model 5, a NACA 0012 profile wing (see Fig. 2). The important characteristics of each wing are given in Table 1. Each model was 22.9 cm high. The boundary layer was tripped at the leading edge of the model using 120-grit sandpaper to ensure that the wing boundary layer was turbulent. The shapes of the NACA profiles may be found in Abbott and Von Doenhoff [17]. The tear-drop body had a circular nose with a diameter $D=12.7$ cm; the tail of the body after $x/c=0.235$ consists of planar surfaces. The shape of the Model 688 and Sand 1850 are given in a paper by Olcmen and Simpson [18].

Fences. The fences were made out of 0.84 mm thick stainless steel. Fence shapes were obtained as the difference area between the wing and the wing translated along the symmetry plane by the fence width at the nose region. Figure 2 provides reduced size pictures of the fences. Table 2 summarizes the heights above the tunnel floor, YF, at which the fences were attached and the centerline widths of the fences, XF (Fig. 3). The fences were fixed in place with super glue.

Eight fences were used with Model 0. Fence designations for this wing model are as follows:

- Fences 1, 2, and 3: For these fences, XF/t was 0.10623, 0.17705, and 0.24788, respectively. These fences were tested at the heights above the tunnel floor given in Table 2. The five test configurations for Fence 1 are designated Fence 11 to fence 15, in order of increasing height. Test configurations for fences-2 and -3 are similarly named.
- P20: This was the same as fence 2, except the lower side of the fence leading edge was filed to an angle of 20 deg.
- M20: The same as fence 2, but with the top of the fence leading edge filed to 20 deg.
- R175: Unlike the other fences, this fence was not planar but was arced. First, the fence was made identical to fence 2, then it was bent to fit on a cylinder of diameter of 44.5 cm (17.5 in.). This fence was glued on the wing such that the fence touched the wing nose at YF=0.10623 and the tail of the fence was parallel to the floor. This allowed the fence to smoothly deflect the flow. The tangent to the fence at the leading edge was at an angle of 20 deg to the freestream flow.
- Double-fences 23 and 33: For both of these fences, one fence 3 was placed at YF/t=0.24788. Then, a second fence was placed at half of this height off the floor. For double fence 23, the second fence was a fence 2; for double-fence 33, the second fence was a fence 3.

Tests with the NACA-0020-tailed model data showed that the

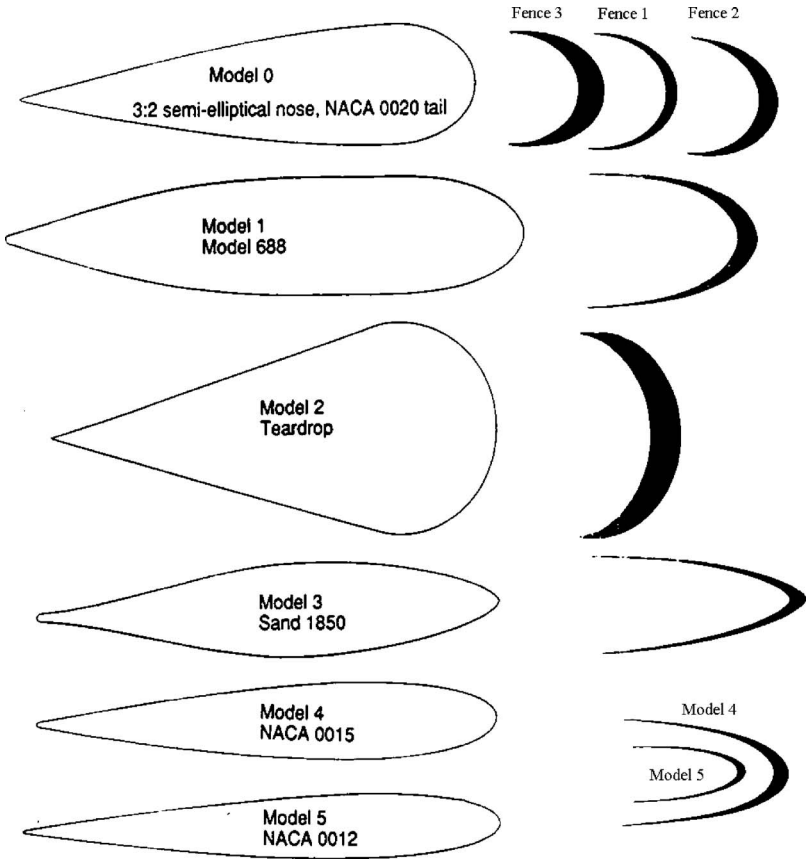

Fig. 2 Models and the fences used in the current investigation. Figure does not reflect the relative sizes. Model details are given in Table 1.

double-fences 23 and 33 fences were the most effective in reducing the wall-pressure fluctuations, as will be shown later in this paper. Fences 2 and 3 were the next best fences, the two being equally effective. Fence 2 was chosen for further testing on Models 1 through 5, since it required less material for almost the same benefit as the double fences and fence 3. The normalized fence width XF/t was maintained at 0.17705 for Models 1 through 5. Fence 2 was tested at three different YF/t heights for these models.

2.3 Pressure Fluctuation Measurements and Data Reduction. Wall-pressure fluctuations were measured with two Sennheiser MKH 110 microphones. The two pressure measurements were simultaneously sampled at 10 kHz using a universal wave form analyzer DATA 6000 (Model 611 Data Precision Corporation, Analogic Corporation) that had the memory to store long data samples in 1991. Data taken simultaneously from the microphones were stored in an IBM PC-AT computer through a GPIB cable with the use of a Tecmar Inc. A/D board. Thirty separate loads of data, each taken with 16,384 consecutive measurement points, resulted in a 491,520 data points for each of the microphones in 49.512 s. The data were stored on an optical disk (Panasonic 940). The reduction of the data was carried out in an IBM PC-RT and the results were again saved to optical disks.

The two plexiglass microphone casings, each 22.5 mm in diameter and placed adjacent to each other were held in a fixed configuration by an aluminum fixture mounted under the tunnel floor. The top of the casings were flush with the tunnel floor in the positions along the symmetry line shown in Fig. 1. The gaps around the tops of the casings were covered with tape. The top of each casing had five 0.75 mm diameter holes spaced 2.1 mm apart along the centerline, with the center hole placed at the center of the casing. Only one hole on the top of each casing was left open during the measurements in order to increase the spatial resolution of the measurements. Once a set of measurements (ten measure-

Table 1 Important characteristics of the models used

Model name	Model number	Chord length c (cm)	Maximum thickness t (cm)	x-location of maximum thickness/c	L.E. radius/t	Maximum velocity location/ chord length	trip location/c (circumferentially)	trip length/c
3:2 semi-elliptical nose. NACA-0020 tail	0	30.5	7.17	0.1983	0.333	0.1262	0.1406	0.0208
Model 688 parallel centerbody	1	44.2	8.89	0.3559	0.127	0.1423	0.158	0.0216
Tear drop	2	29.9	12.7	0.2156	0.5	0.1907	0.2542	0.0374
Sand 1850	3	61.0	11	0.4256	0.0496	0.4256	0.1372	0.0375
NACA 0015	4	60.8	9.21	0.3036	0.1638	0.1327	0.1152	0.0376
NACA 0012	5	40.6	4.9	0.3079	0.131	0.1198	0.0918	0.0375

Table 2 Description of the fences and the height locations of the fences

Model name and number	Fence name	XF/t (fence width on the center line)	YF/t (height locations where each fence was placed individually for the measurements, except for the double fence cases where there were two fences on the wing). YF/δ values are given in parenthesis. δ=18.74 mm.
Model 0: 3:2 semi-elliptical nose NACA 0020 tail	Fence 1	0.10623	YF_1=0.03541, YF_2=0.07082, YF_3=0.10623, YF_4 =0.14164, YF_5=0.17705
	Fence 2	0.17705	0.03541, 0.07082, 0.10623, 0.14164, 0.17705 (YF/δ =0.136, 0.271, 0.407, 0.542, 0.678)
	Fence 3	0.24788	0.03541, 0.07082, 0.10623, 0.14164, 0.17705
	P20	0.17705	0.10623 and leading edge of the fence is filed to be at 20E
	M20	0.17705	0.10623 and the leading edge is filed to be at −20E
	R175	0.17705	0.10623 where touching the wing. Fence is curved as to be an arc of a 17.5 in. diameter circle
	Double-Fence 23	0.17705 and 0.24788	Fence 2 at 0.05312, fence 3 at 0.10623.
	Double-Fence 33	0.24788 and 0.24788	Fence 3 at 0.05312, fence 3 at 0.10623
Model 1: Parallel centerbody	Fence 2	0.17705	0.07082, 0.10623, and 0.14164 correspond to fences 22, 23, and 24, respectively. (YF/δ=0.336, 0.504,0.671)
Model 2: Tear drop body	Fence 2	0.17705	0.07082, 0.10623, 0.14164 (YF/δ=0.480, 0.720, 0.960)
Model 3: Sand 1850	Fence 2	0.17705	0.07082, 0.10623, 0.14164 (YF/δ=0.416, 0.624, 0.832)
Model 4: NACA 0015	Fence 2	0.17705	0.07082, 0.10623, 0.14164 (YF/δ=0.348, 0.522, 0.696)
Model 5:NACA 0012	Fence 2	0.17705	0.07082, 0.10623, 0.14164 (YF/δ=0.185, 0.277, 0.370)

ments) were completed as described, the microphones were moved to more downstream locations (by about 10 mm every move) and the measurements were repeated to obtain closely spaced data along the symmetry line.

Histograms of the normalized pressure fluctuations, p_{rms}/q_{ref}, the skewness coefficient, the flatness (kurtosis) coefficient, and the power spectra were calculated from the recorded data. Each power spectrum was adjusted to correct for extraneous vibration and acoustical content using the technique described by Agarwal and Simpson [19], (also, see Ölçmen and Simpson [7]); then corrections for the microphone and casing response (Simpson et al. [20]) were applied. Thirty spectral averages were used to define each power spectrum. rms pressure fluctuations were calculated from the corrected spectra. The uncertainties in the measured mean square pressure $\overline{p^2}$ were estimated to be $(\overline{\delta p^2}/\overline{p^2})_{random}$=0.0164, and $(\overline{\delta p^2}/\overline{p^2})_{bias}$=0.086, resulting in about 3.2% uncertainty in the presented p_{rms}/q_{ref} values [7]. Comparison of the p_{rms}/q_{ref} using adjusted and unadjusted spectra below 1.5 kHz showed that the difference between the values is minimal except around the peak p_{rms}/q_{ref} value, where a difference of 20% was observed.

The histograms, skewness, and flatness of the pressure fluctuation data were calculated using the time-series data. Histograms were computed by dividing the measurement range (in Pa) into 2048 bins and finding the number of samples falling into each bin. The probability density function was estimated by dividing the number of data points in each bin by the total number of data points in the calculation; the sum of the resulting percentages over all bins is then 1. The flatness and skewness of the pressure distribution were computed as:

$$\text{skewness} = \frac{\overline{p^3}}{(\overline{p^2})^{3/2}} \quad \text{flatness} = \frac{\overline{p^4}}{(\overline{p^2})^2} \tag{1}$$

The skewness and flatness of a data set can be used to indicate the deviation of the data from having a Gaussian distribution. The uncertainties in the skewness and flatness values were estimated as, ΔSkewness/Skewness=0.21, ΔFlatness/Flatness=0.28 [7]. Although the time-series data were not corrected for the tunnel noise and the microphone casing response, the skewness and the flatness values are qualitatively accurate since the pressure fluctuations in the region of interest are dominated by the horse-shoe vortex near the nose.

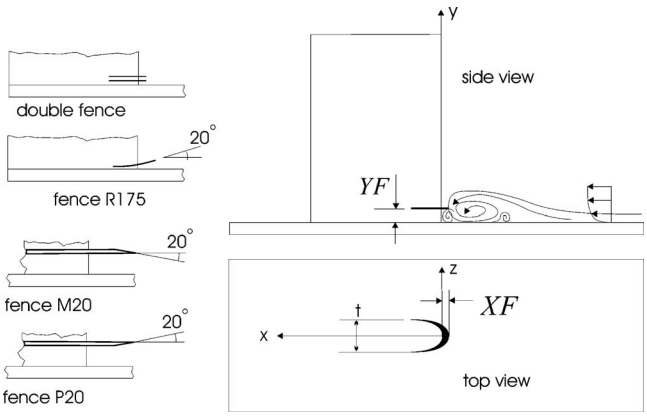

Fig. 3 Schematic describing fence configurations. The fence of width XF is placed at height of YF from the tunnel floor.

3 Experimental Results

In this section, measured pressure fluctuations, normalized by q_{ref}, are compared to the baseline condition (no fence) for each wing model. Skewness and flatness coefficients are also compared. Note that pressure fluctuations under the approaching boundary layer are smaller by an order of magnitude when there is no wing present. A reduction in pressure fluctuation levels under the horse-shoe vortex by a factor of 10, therefore, would result in surface pressure fluctuations comparable to those that exist under the turbulent boundary in the absence of the wing/body junction. Although not plotted, baseline pressure fluctuation histograms show bimodal (double peaked) distributions for Model 0, between x/t=−0.12 to −0.319, for Model 1 between x/t=−0.153 to −0.226, for Model 2 slight bimodal distribution between x/t= −0.135 to −0.191 and strong bimodal distribution between x/t= −0.207 to −0.311, and for Model 4 slight bimodal distribution at x/t=−0.178. For Models 3 and 5, no bimodal pressure fluctuation histograms were observed. Each of the fences discussed in the current paper was observed to eliminate the bimodality of the histograms [21], thus affecting the natural development of the structure of the horse-shoe vortex near the nose of the wing.

3.1 Results for Model 0. The same baseline p_{rms}/q_{ref} results are shown in Figs. 4–6 for comparison. It can be seen that for the

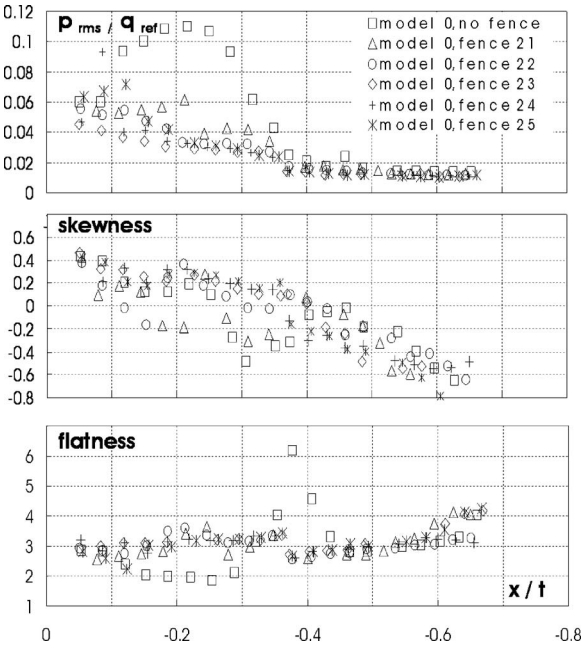

Fig. 4 p_{rms}/q_{ref}, **skewness, and flatness profiles obtained for Model 0 using fence 2. Approach boundary layer separates at** $x/t=-0.45$, -0.41, -0.45, -0.436, -0.49, -0.433, **for no fence, fences 21, 22, 23, 24, and 25, respectively.**

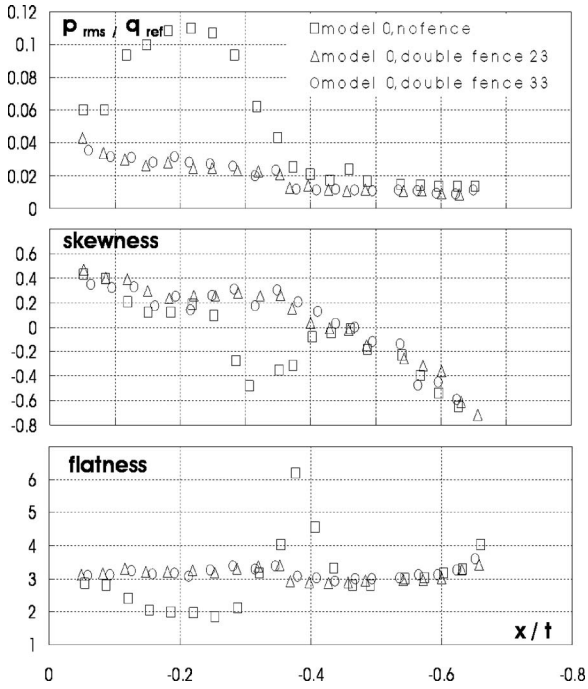

Fig. 6 p_{rms}/q_{ref}, **skewness, and flatness profiles obtained for Model 0 using double fences. Approach boundary layer separates at** $x/t=-0.45$, -0.475, -0.458, **for no fence, double fences 23 and 33, respectively.**

baseline case, the normalized pressure fluctuation reaches a maximum of ~ 0.11 at $x/t \sim -0.22$. Further upstream, far away from the wing/body junction, normalized pressure fluctuation levels decrease to 0.011. Figure 4 shows the results obtained with fence 2 at the five heights shown in Table 2. The results obtained for fences M20, P20, and R175 are shown in Fig. 5, and those for the double fences in Fig. 6. The results obtained for fence 1 and fence 3 were similar to those obtained for fence 2, therefore they are not reproduced here. The findings for fence 2, for fences M20, P20, and R175, and for the double fences are discussed in more detail below. All of the fences studied reduce the peak rms pressure at $x/t \sim -0.22$ by at least 45% and in some cases more than 75%.

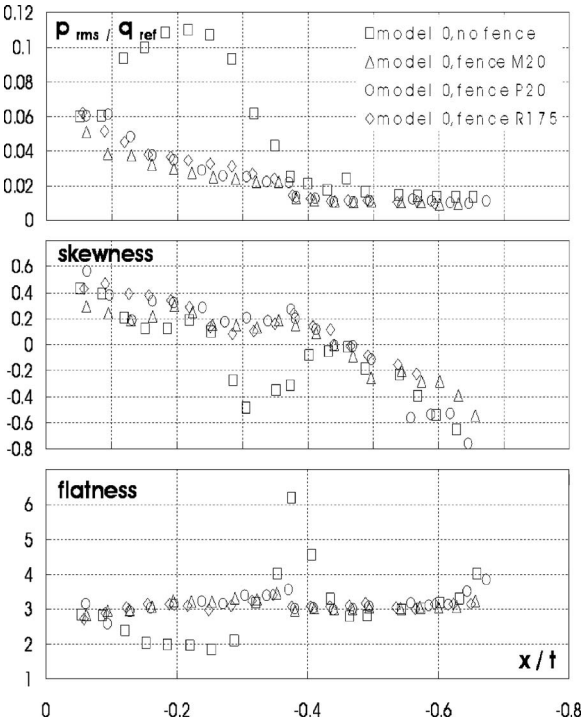

Fig. 5 p_{rms}/q_{ref}, **skewness, and flatness profiles obtained for Model 0 using fences M20, P20 and R175. Approach boundary layer separates at** $x/t=-0.45$, -0.451, -0.398, -0.535, **for no fence, fences M20, P20, and R175, respectively.**

Fence 2. The results for fence 2 are shown in Fig. 4. Configuration 23 (YF/t=0.10623, approximately 40% of the height of the approaching boundary layer thickness) was the most effective at reducing the rms surface pressures, resulting in a 73% reduction at $x/t \sim -0.22$. This effectively moves the position of peak pressure fluctuation closer to the nose/body junction. For almost all fence heights, p_{rms}/q_{ref} gradually decreases from a value of ~ 0.047 near the nose to ~ 0.013 at the most upstream measurement point. Even the least effective height for fence 2, configuration 21, results in a $\sim$45% reduction in the rms pressure fluctuation at $x/t \sim -0.22$ relative to the baseline.

Skewness coefficients for the baseline case decrease from approximately +0.4 to −0.6 from $x/t=-0.05$ to −0.6, i.e., in the upstream direction, away from the nose. Under baseline conditions, this decrease is oscillatory. It was expected that the fences would break up the orderly structure of the horse-shoe vortex and, thereby, make the pressure fluctuations more random or Gaussian. Gaussian data has a skewness of 0. Consistent with this, the skewness values were expected to move closer to 0. While at all heights fence 2 did reduce the wave-like pattern in the skewness, overall, skewness values did not move closer to zero.

The value of the flatness for Gaussian data is 3. It can be seen from the bottom plot in Fig. 4 that under baseline conditions the flatness deviates substantially from 3 in some locations, taking on a minimum value of 2 in the vicinity of $x/t \sim 0.22$ (where the rms pressure is a maximum) and a maximum value of about 6 at $x/t \sim -0.38$. Overall, the effect of fence 2 at all of the heights tested is to smooth out the variations in flatness values, bringing the extremes closer to the Gaussian value of 3.

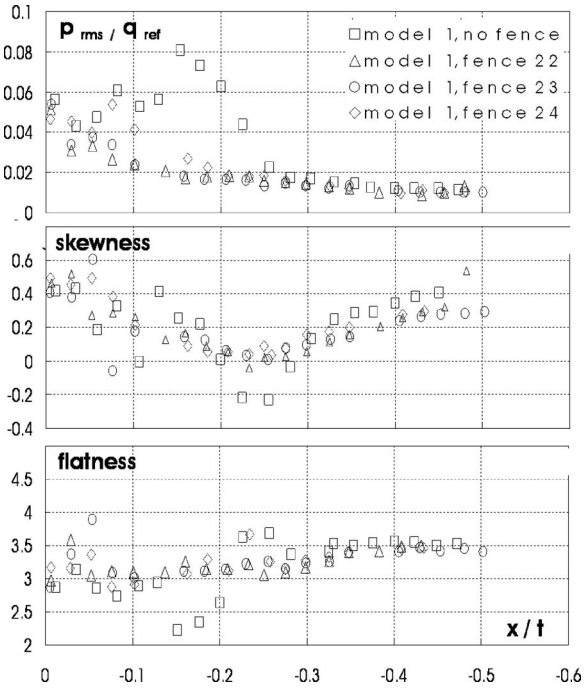

Fig. 7 p_{rms}/q_{ref}, skewness, and flatness profiles obtained for Model 1 using different fences. Approach boundary layer separates at $x/t=-0.393$, -0.308, -0.376, -0.435, for no fence, fences 22, 23 and 24, respectively.

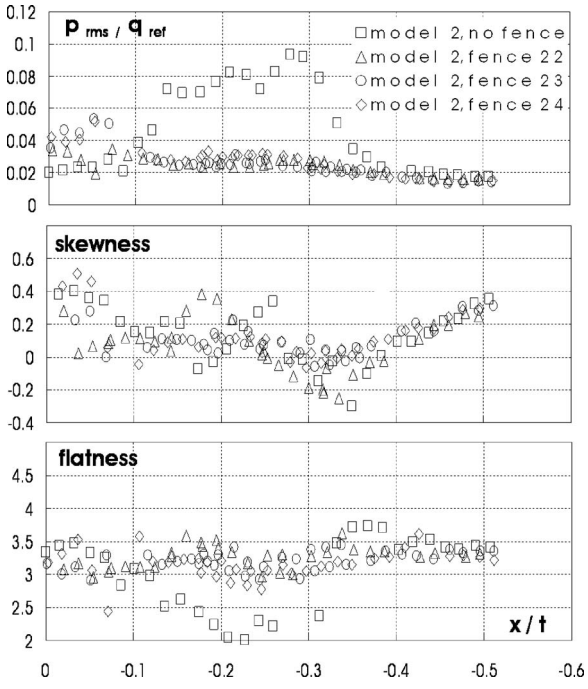

Fig. 8 p_{rms}/q_{ref}, skewness, and flatness profiles obtained for Model 2 using different fences. Approach boundary layer separates at $x/t=-0.518$, -0.443, -0.439, -0.445, for no fence, fences 22, 23, and 24, respectively.

Fences M20, P20, and R175. Figure 5 shows the rms pressure, skewness, and flatness results obtained for Fences M20, P20, and R175. None of these fences was more effective than the best fence 2 in reducing the pressure fluctuations and bringing the skewness and flatness values closer to Gaussian values, but of the three fences, M20 was the most effective, reducing the rms pressure by as much as 73% relative to the baseline case. Pressure fluctuation values for all of these fences decrease smoothly from p_{rms}/q_{ref} ~ 0.06 near the wing nose to 0.012 at the last upstream measurement point. The skewness values range from positive 0.3 to 0.6 near the nose, approach 0 near $x/t=-0.45$, and then become increasingly negative moving further upstream. At $x/t=-0.65$, the skewness values are all close to -0.5. Only over $x/t\sim-0.27$ to -0.37 are the levels of skewness more nearly Gaussian compared to baseline conditions. As was the case for fence 2, the flatness values with these fences remain close to 3 over the x/t range studied.

Double-fences 23 and 33. As can be seen from Fig. 6, these fences were the most effective at reducing the rms pressure fluctuations relative to baseline conditions, resulting in $\sim$77% reduction of p_{rms}/q_{ref} at $x/t\sim-0.22$ versus a reduction of $\sim$73% for single fence 2 at height 3. The trend in the skewness values is similar to those is Figs. 4 and 5, except that the skewness initially decreases from ~ 0.4 then varies around 0.2 before continuing through 0 and reaching a value of ~ -0.7 at the most upstream measurement location. The flatness values stay close to 3, similar to fences M20, P20, and R175, but then begin increasing slowly upstream of $x/t\sim-58$.

3.2 Results for Other Models. While the tests with Model 0 showed that the double-fence 23 and double-fence 33 were the most effective in reducing the wall-pressure fluctuations, fence 2 was nearly as effective. Because fence 2 was less complex and required less material, only this fence (XF=0.17705t) was used for the later tests on Models 1 through 5. Three fence heights were used (Table 2). As previously noted, these configurations are designated Fences 22, 23, and 24. Note that in all cases, peak rms pressures on the centerline upstream of the wing tip were lower for the baseline wing Models 1 through 5 relative to the baseline condition for Model 0. The baseline flow for these wing models was characterized by Ölçmen and Simpson [7].

Model 1. Normalized rms pressure fluctuations, skewness, and flatness for Model 1 are shown in Fig. 7. The maximum normalized pressure fluctuation under baseline conditions is ~ 0.08 at $x/t\sim-0.15$. Fence 2 resulted in reduced rms pressure fluctuations at $x/t\sim-0.15$ at all three heights. The most reduction of $\sim$77% was obtained by fence 23. The skewness values measured with the fences are not, overall, closer to 0. Unlike all of the Model 0 cases and the Model 1 baseline case, the skewness values measured with fences 22, 23, and 24 are always positive. This means that pressure histograms are positively skewed at all of the measurement locations. The baseline flatness values vary around a value of 3 downstream of $x/t\sim-0.2$, then increase and settle down to a value close to 3.5. The effect of all fences is to reduce the large variations and, overall, bring the flatness values closer to the value of 3.0 expected for Gaussian random pressure fluctuations.

Model 2. The baseline pressure fluctuations reach their maximum at $x/t=-0.275$ with a value of $p_{rms}/q_{ref}=0.0925$ for Model 2 (Fig. 8). All of the fences tested eliminate the relatively extended region of high level pressure fluctuations from $x/t\sim-0.13$ to -0.35. The skewness values measured for the three different fence configurations tend closer to the value of 0, but still show significant variations. The flatness values show less variation than the baseline configuration and are uniformly closer to the value of 3.

Model 3. The results for Model 3 are given in Fig. 9. It can be seen that this model had the lowest baseline pressure fluctuations. Fences 22 and 23 reduce the region of increased pressure fluctuations centered on $x/t\sim-0.75$ in the baseline case, so that the rms pressure fluctuations show a monotonic decrease from 0.05 near the nose to an asymptotic value close to 0.01 upstream of $x/t\sim-0.2$. With the exception of one measurement location with fence 23, all of the skewness values measured with the fences 22, 23,

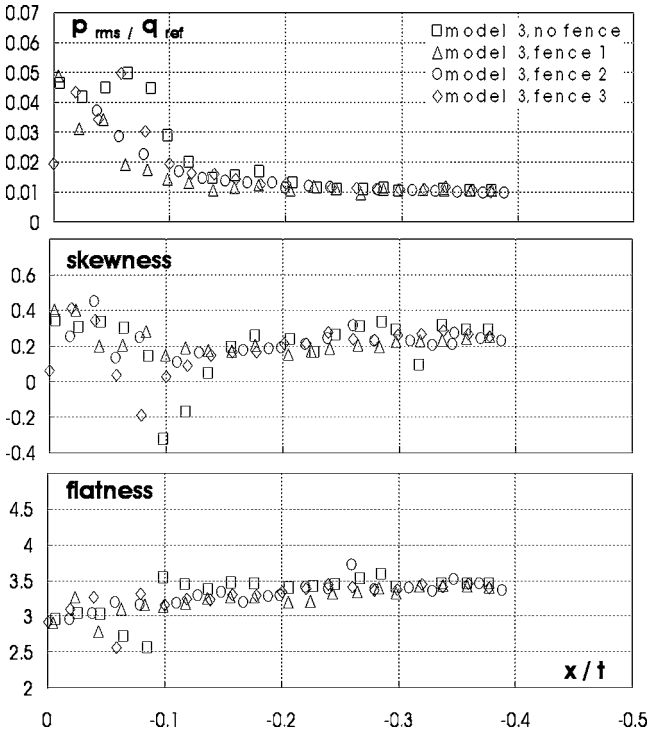

Fig. 9 p_{rms}/q_{ref}, skewness, and flatness profiles obtained for Model 3 using different fences. Approach boundary layer separates at $x/t=-0.157$, -0.208, -0.197, -0.203, for no fence, fences 22, 23, and 24, respectively.

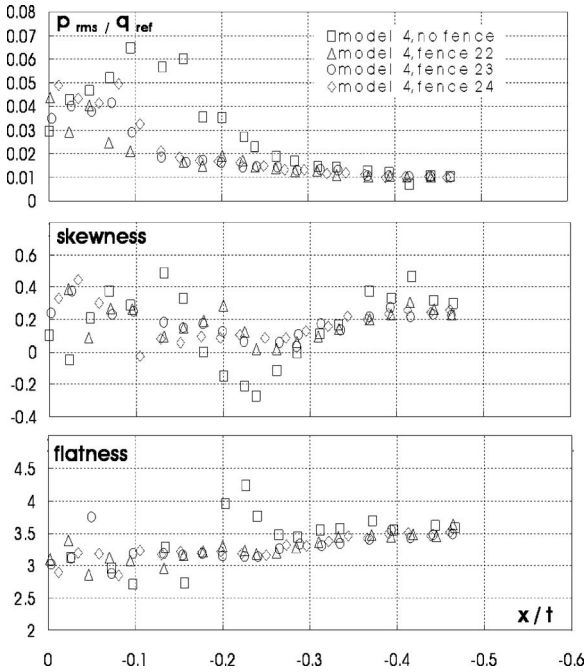

Fig. 10 p_{rms}/q_{ref}, skewness, and flatness profiles obtained for Model 4 using different fences. Approach boundary layer separates at $x/t=-0.294$, -0.258, -0.295, -0.299, for no fence, fences 22, 23, and 24, respectively.

and 24 are positive. The variations in the skewness values are small relative to the baseline case. The flatness values also vary less relative to the baseline.

Model 4. Baseline rms pressure fluctuations for Model 4 are shown in Fig. 10. There is a pronounced double peak in the rms pressure, and the baseline skewness and flatness display a pattern of relatively orderly variations. The effect of fences 22 to 24 is to preserve the first peak in the rms pressure near $x/t\sim-0.09$, but eliminate the second peak near -0.14. Variations in the skewness and kurtosis near the nose remain, but the fences reduce the pressure fluctuations and bring the skewness and kurtosis slightly closer to the Gaussian values at distances upstream of $x/t\sim-0.1$.

Model 5. Next to Model 3, Model 5 had the lowest peak rms pressure under baseline conditions (Fig. 11), and the physical lengths of the regions of elevated rms pressures both for the baseline Models 5 and for 3 are practically the same. The effect of fence 2 at all the three tested heights is to virtually eliminate the region of elevated rms pressures. There is almost no notable effect on the skewness and flatness distributions, except, oddly enough, at the furthest upstream measurement locations (beyond $x/t\sim-0.18$).

4 Conclusions

Fence-type passive flow-control devices were tested for six different models. Results for Model 0 show that among all fences tested double-fences 23 and 33, and additionally, fences 2 and 3 at YF_3 were seen to result in most reduction of the pressure fluctuations. All of the fences studied for Model-0 reduce the p_{rms} peak value by between 45% to 77% at the baseline peak x/t location.

For the Models 1 through 5, the fences reduce the p_{rms} very effectively by at least 61% at the baseline peak x/t location for each model. The fences located at the first fence height location ($YF/t=0.07082$) work best for the Models 1 through 4, but for Model 5, the second fence height location ($YF/t=0.10623$) works slightly better.

Fences not only reduce the pressure fluctuations beneath the fence but also upstream of the fence, indicating that the fences

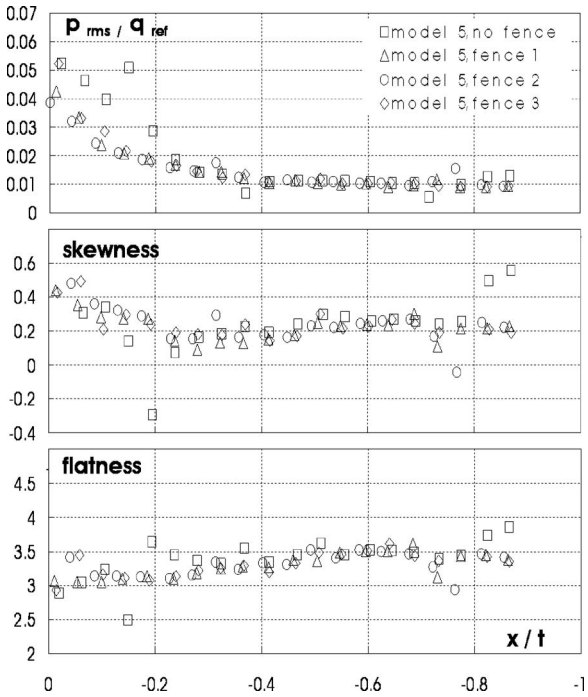

Fig. 11 p_{rms}/q_{ref}, skewness, and flatness profiles obtained for Model 5 using different fences. Approach boundary layer separates at $x/t=-0.339$, -0.283, -0.333, -0.281, for no fence, fences 22, 23, and 24, respectively.

change the mechanism of the formation of the vortical structure near the nose region. For all the models and fence cases tested the skewness and flatness profiles show that the fences result in histograms closer to a Gaussian distribution, indicating that breaking up the chaotic horse-shoe vortex structure results in smaller vortices where the fluctuating velocity field and the fluctuating pressure field become more random resulting in values closer to Gaussian values than obtained for the baseline cases. However, the skewness and flatness values are different than zero and three, respectively, indicating that the distributions are not truly Gaussian.

Acknowledgment

This work was supported by the Office of Naval Research under Contract Nos. N00014-88-C-0291 and N00014-90-J-1909 and monitored by J. A. Fein. The authors gratefully acknowledge this support and the gifts of the Sand 1850 and NACA 0015 (Sandia Corp.) and the NACA 0012 (Sikorsky Aircrafty) wing sections. The authors would also like to thank to Dr. Sally McInery of the UA-AEM Department for reading the manuscript and making very valuable suggestions.

Nomenclature

c = chord length
f = frequency
p = fluctuating pressure
p_{rms} = square root of the averaged pressure fluctuations
q_{ref} = $(1/2)\rho U_{\mathrm{ref}}^2$, reference dynamic pressure
t = wing maximum thickness
U_{ref} = reference velocity
x, y, z = Cartesian coordinate system axes
XF = fence centerline width
YF = fence height above the tunnel floor
δ = boundary layer thickness
θ = momentum thickness
δ^* = displacement thickness
Re_θ = Reynolds number based on momentum thickness
$\overline{()}$ = mean quantity

References

[1] Baker, C. J., 1980, "The Turbulent Horseshoe Vortex," J. Wind. Eng. Ind. Aerodyn., **6**, pp. 9–23.
[2] Rood, E. P., and Keller, J. E., 1984, "Evidence of Large Scale Time Dependent Flow in the Wingwall Interaction Wake," in *Unsteady Turbulent Boundary Layers and Friction, FGD*, Am. Soc. Mech. Eng., Fluids Eng. Div., New York, Vol. 12, pp. 39–44.
[3] Simpson, R. L., 1996, "Aspects of Turbulent Boundary Layer Separation," Prog. Aerosp. Sci., **32**, pp. 457–521.
[4] Simpson, R. L., 2001, "Junction Flows," Annu. Rev. Fluid Mech., **33**, pp. 415–443.
[5] Devenport, W. J., and Simpson, R. L., 1990, "Time-Dependent and Time-Averaged Turbulence Structure Near the Nose of a Wing-Body Junction," J. Fluid Mech., **210**, pp. 23–55.
[6] Devenport, W. J., and Simpson, R. L., 1992, "Flow Past a Wing-Body Junction: Experimental Evaluation of Turbulence Models," AIAA J., **30**, pp. 873–881.
[7] Ölçmen, M. S., and Simpson, R. L., 1994, "Influence of Wing Shapes on Surface Pressure Fluctuations at Wing-Body Junctions," AIAA J., **32**, pp. 6–15.
[8] Kim, S. A., Walker, D. A., and Simpson, R. L., 1991, "Observation and Measurements of Flow Structures in the Stagnation Region of a Wing-Body Junction," *VPI&SU Rep. VPI-E-91-20*, Va. Polytech. Inst. State Univ., Blacksburg.
[9] Lewis, D. J., Simpson, R. L., and Diller, T. E., 1993, "Time-resolved Surface Heat Flux Measurements in the Wing/Body Junction Vortex," J. Thermophys. Heat Transfer, **8**, pp. 656–663.
[10] Ölçmen, M. S., and Simpson, R. L., 1995, "An Experimental Study of Three-Dimensional Pressure-Driven Turbulent Boundary Layer," J. Fluid Mech., **290**, pp. 225–262.
[11] Ölçmen, M. S., and Simpson, R. L., 1996, "Experimental Transport-Rate Budgets in Complex Three-Dimensional Turbulent Flows at a Wing/Body Junction," *27th Am. Inst. Aeronaut. Astronaut. Fluid Dyn. Conf.*, New Orleans, AIAA-96-2035.
[12] Ölçmen, M. S., and Simpson, R. L., 1997, "Experimental Evaluation of Turbulence Diffusion Models in Complex 3-D Flow Near a Wing/Body Junction," *35th Am. Inst. Aeronaut. Astronaut. Aerosp. Sci. Meet.*, Reno, NV, AIAA-97-0650.
[13] Ölçmen, M. S., and Simpson, R. L., 1997, "Some Features of a Turbulent Wing-Body Junction Vortical Flow," *AIAA-97-0651, 35th AIAA, Aerosp. Sci. Meet.*, Reno, NV.
[14] Devenport, W. J., Agarwal, N. K., Dewitz, M. B., Simpson, R. L., and Poddar, K., 1990, "Effects of a Fillet on the Flow Past a Wing-Body Junction," AIAA J., **28**, pp. 2017–2024.
[15] Devenport, W. J., Dewitz, M. B., Agarwal, N. K., and Simpson, R. L., 1992, "Effects of a Leading-Edge Fillet on the Flow Past an Appendage-Body Junction," AIAA J., **30**, pp. 2177–2183.
[16] Barberis, D., Molton, P., and Malaterre, T., 1998, "Control of 3D Turbulent Boundary Layer Separation Caused by a Wing-Body Junction," Exp. Therm. Fluid Sci., **16**, pp. 54–63.
[17] Abbott, I. H., and von Doenhoff, A. E., 1949, *Theory of Wing Sections: Including a Summary of Airfoil Data*, McGraw Hill.
[18] Ölçmen, M. S., and Simpson, R. L., 1992, "Influence of Wing Shapes on the Surface Pressure Fluctuations of a Wing-Body Junction," *Aerosp. Sci. Meet., 30th*, Reno., NV, AIAA-92-0433.
[19] Agarwal, N. K., and Simpson, R. L., 1989, "A New Technique for Obtaining the Turbulent Pressure Spectrum From the Surface Pressure Spectrum," J. Sound Vib., **135**(2), pp. 346–350.
[20] Simpson, R. L., Ghodbane, M., and McGrath, B. E., 1987, "An Experimental Study of Surface Pressure Fluctuations in a Separating Turbulent Boundary Layer," NASA CR-178309.
[21] Ölçmen, M. S., Simpson, R. L., Kim, S., and Ha, S. M., 1991, "Some Effects of Appendage Shape and a Fence Control Device on Appendage/Hull Junction Flows," VPI-AOE-183, Aerospace and Ocean Engineering Department, VPI&SU.

Evolution and Turbulence Properties of Self-Sustained Transversely Oscillating Flow Induced by Fluidic Oscillator

Rong Fung Huang[1]
National Taiwan University of Science and Technology,
Taipei, Taiwan 10672, Republic of China
e-mail: rfhuang@mail.ntust.edu

Kuo Tong Chang
Mingchi University of Technology,
Taipei, Taiwan 24306, Republic of China

The evolution process and turbulence properties of a transversely oscillating flow induced by a fluidic oscillator are studied in a gravity-driven water tunnel. A planar jet is guided to impinge a specially designed crescent surface of a target blockage that is enclosed in a cavity of a fluidic oscillator. The geometric configuration of the cavity transforms the inherent stability characteristics of the jet from convective instability to absolute instability, so that the jet precedes the persistent back and forth swinging in the cavity. The swinging jet is subsequently directed through two passages and issued alternatively out of the fluidic oscillator. Two short plates are installed near the exits of the alternatively issuing pulsatile jets to deflect the jets toward the central axis. The deflected jets impinge with each other and form a pair of counter-rotating vortices in the near wake of the oscillator with a stagnation point at the impingement point. The stagnation point of the counter-rotating vortex pair moves back and forth transversely because of the phase difference existing between the two issued jets. The merged flow evolving from the counter-rotating vortices formed by the impingement of the two pulsatile jets therefore presents complex behavior of transverse oscillation. The topological models corresponding to the flow evolution are constructed to illustrate the oscillation process of the oscillating flow. Significant momentum dispersion and large turbulence intensity are induced by the transverse oscillation of the merged flow. The statistical turbulence properties show that the Lagrangian integral time and length scales of the turbulence eddies (the fine-scale structure) produced in the oscillating flow are drastically reduced.
[DOI: 10.1115/1.2746905]

1 Introduction

Jet flows have been widely studied by many investigators [1–3] over many decades due to the inherent natures of both the fundamental and application characteristics. The temporal evolution and spatial distribution of the physical flow properties, such as momentum, coherent structure, entrainment, mixing, vorticity transport, heat dissipation, combustion, noise generation, hydrodynamic stability, etc., of a jet issued from a slot, a tube, an orifice, or a nozzle provide standard test benchmarks for research on classical flow field. After decades of studies on the characteristics of natural jets, investigators' interests diverted to issues surrounding the control or manipulation of the jet properties. One of the most attractive subjects is control of the frequency and/or amplitude of the coherent structures generated along the mixing layer due to their dominant roles in the mixing rates [4]. Considerable efforts have been devoted to understanding and controlling the interaction of the organized structure and the characteristics of mixing, entrainment, and noise production [5–7]. Although it has been proven that manipulating the coherent structures through acoustic excitation, pulsating, geometric modification of the nozzle at the jet exit, etc., can enhance the turbulence fluctuation, entrainment, and mixing rate of a jet, practical application cases were still limited because a homogeneous jet is a pure, convectively unstable flow [8]. In these cases, the effects induced by these jet-control methods seem not to be overly significant because the impulse response induced by the transient disturbance will diminish to zero over long periods of time at all points in the flow with convectively unstable characteristics [9].

In many applications such as mixing, heat transfer, combustion, etc., the jet flow plays an important role. The natural jet usually requires modifications to enhance its transport properties in momentum, heat, and mass transfers [10]. If a natural jet can be guided to pass through a specially designed device that can induce transverse jet oscillation, i.e., transform the inherent jet instability characteristics from a condition of being convectively unstable to absolutely unstable, it would be possible to modify the flow characteristics such as the transient large-scale flow structures and the turbulence properties for applications. This is because the impulse response induced by the transient disturbance will become unbounded over large periods of time at all points in a flow with absolute unstable characteristics [8,9].

A variety of devices with cavity configurations for inducing effective jet oscillation have been developed by investigators. The fluidic flowmeter uses feedback pressure as the driving force to induce self-sustaining oscillation of the jet, and is widely used and studied [11–14]. Rockwell and Naudascher [15] grouped the unstable flow past cavities into fluid-dynamic, fluid-resonant, and fluid-elastic categories. Analytical analysis of Lalanne et al. [16] revealed that the physical mechanism of inducing the flow oscillation is the Hopf bifurcation, and a periodic asymmetric state can be attained when the Reynolds number exceeds a critical value of 51. This state of equilibrium defines a limit cycle that is characterized with an oscillation frequency and saturated amplitude. In general, the jet flow going through the cavity of the fluidic oscillator presents an axially pulsatile property at the outlet.

In order to transform the inherent jet instability characteristics from convective instability to absolute instability, a cavity-driven

[1]Corresponding author.

Contributed by the Fluids Engineering Division of ASME for publication in the JOURNAL OF FLUIDS ENGINEERING. Manuscript received April 4, 2006; final manuscript received February 3, 2007. Review conducted by James A. Liburdy.

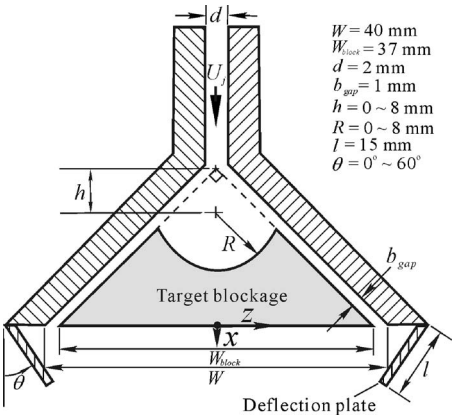

Fig. 1 Fluidic oscillator developed for inducing transversely oscillating flow

fluidic oscillator that can induce transverse jet oscillation is adopted in this study. The goal is to develop a planar fluidic oscillator through the use of the characteristics of jet-impingement instability [17]. The planar natural jet is converted to large transverse oscillation motion by a special geometric design. Explorations on the evolutionary process of the large-scale flow structure and the turbulence properties of the oscillating flow generated by the developed fluidic oscillator are subsequently performed. The oscillating flow is expected to combine with the wake flow in the future to develop further complicated flow control methods for practical application.

2 Development of Fluidic Oscillator

A specially designed fluidic oscillator that can induce transverse jet oscillation is developed, as shown in Fig. 1. The flow is supplied through a narrow channel with a width d, and injected into a cavity enclosed by two plates configured in the shape of an inverse-Y and containing a target blockage. The aspect ratio of the channel cross section is 20 so that the jet can be treated as almost planar. The target blockage has a specially designed crescent surface facing the inlet of the oscillator. The plates next to the target blockage are made of high transparency Plexiglas® so that laser light can penetrate them during the flow visualization experiment and particle image velocimetry (PIV) measurement. The thickness of the flat plates is 3 mm. The inverse-Y arrangement has an angle of 90 deg, a cross-stream span length L of 400 mm, and a downstream width W of 40 mm. The blockage is a triangular aluminum block with the vertex part removed so that the upper surface is concave. The characteristic geometric parameters for the design of the blockage, h, b_{gap}, R, and W_{block}, are shown in Fig. 1. The crescent profile is a concave arc with a radius R originating from the point located on the symmetry axis at a distance h from the virtual vertex of the triangular target blockage. Experiments are conducted to optimize the geometric parameters so that the transverse oscillation of the jet in the cavity appears due to the Hopf bifurcation [16]. With the optimized design, the jet impinging the crescent surface can swing back-and-forth transversely in the cavity and eject out of the alternate exits of the side passages on the bottom plane of the device. Two *deflection plates*, shown in Fig. 1, are installed at the side ends of the inverse-Y device in order to merge the pulsing jets that issue alternately out of the bottom exits to form a transversely oscillating flow. The deflection angle θ is measured from the vertical axis. The length of the deflection plates is 15 mm.

3 Experimental Apparatus and Method

3.1 Apparatus. The experiments are conducted in a vertically aligned, gravity driven water circulation system, as shown in Fig. 2. The fluidic oscillator is immersed in water contained in a large tank (indicated as the "inner tank" in Fig. 2). Because the water jets issuing out of the fluidic oscillator bear the downward momentum, the environmental fluid in the water tank is inevitably disturbed, and the water level rises. In order to reduce the influence of the environmental fluid fluctuations on the oscillating flow and keep the water level constant, a square cylinder with open ends is placed in the inner water tank to serve as a shield. The flow visualization of the whole flow field shows that a shielding window of $500\times500\times800$ mm^3 in width, length, and height, respectively, can effectively cancel the effects of the disturbances induced by the up-flowing excess water. Further, the maximum lateral spread of the oscillating flow at $x/W\approx4$ is about $\pm2z/W$, and therefore the flow in the domain of the experiment is not subjected to the influence of the side walls of the shield, which are located about $\pm6W$ away from the fluidic oscillator. The water tanks and the shielding window are all made of high transparency Plexiglas® so that the flow visualization is possible. The thickness of the Plexiglas® is 5 mm. The excess water goes up through the gap between the shielding window and the inner tank and flows out of the inner tank so that a constant water level is maintained. The overflow from the inner tank is collected in an outer tank and recirculated via a water supply system to be used by the jet flow of the fluidic oscillator. The water supply system consists of a pump, a metering valve, a calibrated rotameter, a distributor, a buffer tank, three layers of polymer-fiber filters, and a configured nozzle with a contraction ratio (inlet to exit area ratio) of 30:1. Using an on-line weighting-and-timing calibration procedure, the uncertainty of the measurement of the volumetric flow rate of the water flow is estimated to be as large as 1.5% of the full scale of the rotameter. The connecting narrow channel from the exit of the nozzle tothe inlet of the fluidic oscillator has a length of 1 m to ensure a fully developed flow before going into the fluidic oscillator [18]. The flow rate of the water jet is controlled by the height of the buffer tank and the needle valve.

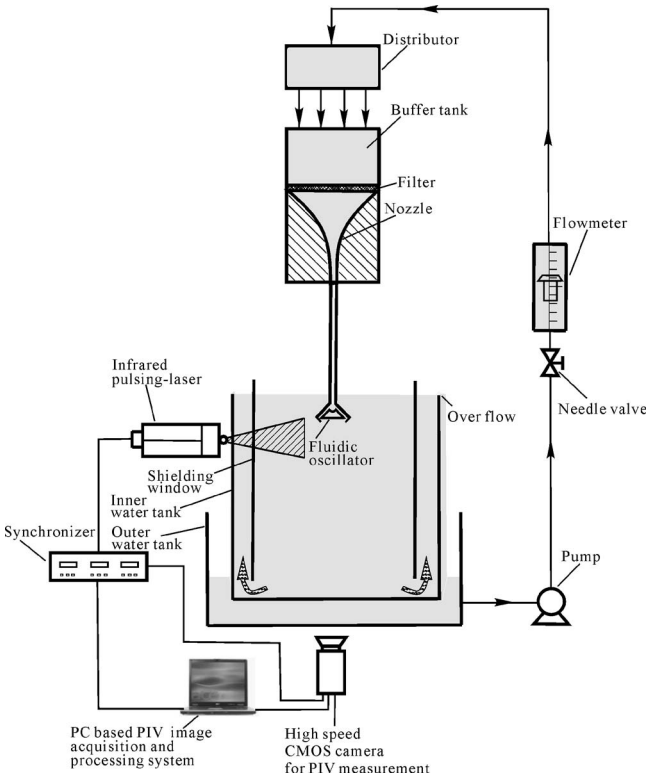

Fig. 2 Experimental setup

3.2 Flow Visualization. The particle tracking flow visualiza-

tion method is employed to understand characteristic flow evolution processes. Plastic particles made of polyamide are seeded in the water tank to scatter the laser light. The diameters of the particles are between 30 μm and 70 μm and the specific weight is 1.03 at 25°C. Ignoring the effect of the turbulent diffusion, the relaxation time constant is estimated to be less than 6×10^{-5} s and the Stokes number is lower than the order of 10^{-5} within the range of the experiment [19]. Because the Stokes number and the relaxation time are negligibly small, the slip between the flow and the particles could be ignored [20]. The laser beams emitted from two 120 mW Nd:YAG lasers (Onset Electronic Optics, Inc.) with a wave length of 532 nm are transmitted through 20 deg laser-light sheet expanders, adjusted to a thickness of about 0.5 mm, collimated, and shot into the water tank across the middle span of the fluidic oscillator to illuminate a two-dimensional plane in the flow field.

The streak images of both short and long exposures are recorded and stored in the computer memory by using a Redlake MotionScope® PCI 2000S CCD camera. The camera is mounted on a firm steel frame and faces the y direction. The framing rate of the camera is 60–2000 frames per second (fps). The shutter speed can be adjusted between 1/60 s and 1/40,000 s. The zoom lens for close-up photographing has a focal length and lowest f-stop of 50 mm and 1.2, respectively. Identification and analysis of formation and evolution processes of the jet oscillation and/or vortex system are conducted either by replaying the movies of the particle images on a computer monitor or by tracing the long-exposure streak pictures.

3.3 PIV Measurement. A high-speed PIV system (Model ProVision-XS, Integrated Design Tools, Inc.) is used for measuring the unsteady flow structure. The system consists of an infrared pulsing laser, a high speed complementary metal oxide semiconductor (CMOS) camera, an electronic synchronizer, and a notebook computer installed with the sequence control, image acquiring, and PIV analysis software.

A 10 W diode pumped solid state laser (Model XS-IR-10, Integrated Design Tools, Inc.) that can be externally triggered to emit pulsing infrared laser light at the wave length of 795 nm is used as the illumination light source. A laser-light sheet expander is mounted at the exit of the laser head so that the laser beam is expanded to a triangular light sheet with a thickness smaller than 0.5 mm. The maximum pulsing rate is 10,000 pulses per second. A single pulsing mode is used in this study because the required pulse separation is long enough to make the double pulse unnecessary. The particle images are recorded by a CMOS camera (Model X-stream XS-4, Integrated Design Tools, Inc.). The light-sensing array of the camera possesses 512×512 pixels with a pixel size of 16×16 μm. The maximum framing rate is 5145 fps at the highest image resolution of 512×512 pixels. The external trigger mode with single exposure is selected in this study. The pixel array is zoomed and mapped to a physical region of approximately 40–80 mm in this study so that the spatial resolution is about 79–156 μm/pixel. The seeding particles used in the PIV measurements are the same as those used for the flow visualization.

Two consecutive image frames are analyzed by using the cross-correlation technique [21] imbedded in the PIV analysis software. The software calculates the average displacement of local groups of particles in consecutive images. The minimum particle displacement that can be analyzed by the software is 0.05 pixels. Corresponding to the physical space, therefore, the resolution for displacement in this study is about 4–8 μm. The number of vectors (the grids) predetermined for the PIV analysis results is set to 6084. Error checks and interpolation are used to identify outliers and then regenerate interpolated values to replace any identified outliers. In general, less than 3% of spurious vectors per instantaneous field are obtained in this study.

In this study, the instantaneous velocities downstream of the fluidic oscillator are generally lower than approximately 0.2 m/s except for the region closest the jet exits. The pulse separation and pulse width of the laser operation are set at 2.5 ms and 50 μs, respectively. The frame rate and exposure time of the camera are 400 fps and 1/400 s, respectively. With these arrangements, the displacements of particles between two consecutive images will be between about 3–6 pixels. The interrogation window is set to 24×24 pixels in this study in order to optimize the measurement results. It is about four times the estimated maximum displacement and is a proper setting according to the suggestion of previous investigators [21].

The uncertainty estimates for each variable in the graphs are based on the method of Abernethy et al. [22]. The total uncertainty $E$of the variables can be found by combining systematic and random errors as $E=[B^2+(tS_D)^2]^{1/2}$, where B is the systematic uncertainty, S_D is the standard deviation of the mean, and the degrees of freedom t set at 2 for a 95% confidence level. The systematic uncertainty B is estimated based on the calibration data and previous test experience, and the standard deviation of the mean S_D is computed from the raw measurement data. For instance, $B=0.007$ and $S_D=0.01$ for the frequency measurements, and thus the uncertainty of the frequency therefore is about ±1.06% of the local value. The uncertainties of the measured axial velocities and velocity fluctuations are estimated to be about ±2.15% and ±3.21%, respectively, of the local values. The uncertainties of the measured lateral velocities and velocity fluctuations are about ±3.18% and ±4.26%, respectively, of the local values.

4 Results and Discussion

4.1 Periodic Jet Swing in Cavity. The optimized b_{gap} is between 1 mm and 2 mm. By selecting $b_{gap}=1$ mm and properly adjusting the geometric parameters and the Reynolds number Re_d, the jet injected into the cavity can oscillate. Figure 3 shows the process of the oscillating motion of the flow in the cavity. In Fig. 3(a), the jet impinges at approximately the midpoint of the crescent surface of the target blockage. As time progresses, the jet swings to the right and induces a pair of counter-rotating vortices, as shown in Fig. 3(b). The left vortex rotates clockwise and the right one rotates counter-clockwise. In Fig. 3(c) the rightward-swinging jet attaches to the right wing of the inverse-Y and issues out of the oscillator through the right passage. At the instant the left clockwise-rotating vortex grows and occupies the whole space of the cavity. In Fig. 3(d) the jet swings back and nearly reaches the central position again. The jet subsequently swings to the left, induces counter-rotating vortices, attaches to the left wing of the inverse-Y, and issues out of the oscillator through the left passage, as shown in Figs. 3(e) and 3(f). The jet persists in periodically swinging back and forth in the cavity. At the exits of the side passages, the jets are issued alternatively into the downstream region with inverse phase angles. A map for the operation range of the jet swing is obtained, as shown in Fig. 4. The jet can swing periodically only on the right side of the tongue-shaped curves. The higher the Reynolds number is, the larger the operation range becomes.

The periodic swing frequency of the jet in the cavity can be estimated by observing the consecutive images of the flow in the cavity recorded by the high-speed camera. In order to reduce the estimation deviation, the elapse time over 200 oscillation periods is used to calculate the average swing frequency. The results show that the frequency of fluidic oscillation (f_f) increases linearly with the increase of the average jet velocity U_j. At the low Reynolds number regime, the Strouhal number $\mathrm{St}_{d,f}$ based on width d and the average jet velocity U_j increases nonlinearly with the increase in the Reynolds number Re_d and the values of the Strouhal number are smaller than the order of magnitude of 10^{-2} when Re_d is less than 2500. Lalanne et al. [16] and Camci and Herr [10] reported the performance of some specially designed fluidic flowmeters: the Strouhal numbers they attained were 0.009 and 0.007,

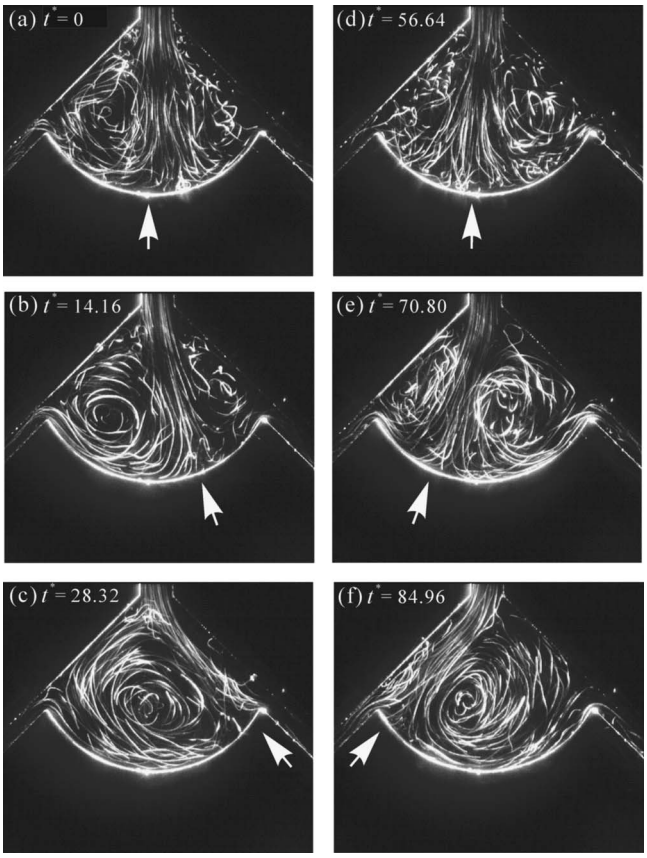

Fig. 3 Oscillation process of jet in cavity of fluidic oscillator. $t^* = t \times U_j/d$, $\mathrm{Re}_d = 1667$, $R/d = 4$, $h/d = 1.5$. Frame rate = 60 fps. Exposure time = 1/60 s.

respectively, at $\mathrm{Re}_d = 5000$. In the present study, the Strouhal numbers attained were 0.009 and 0.007 at $\mathrm{Re}_d = 2250$ and 1700, respectively. It seems that at the same Reynolds numbers the presently developed oscillator can induce a higher oscillation frequency.

4.2 Transverse Oscillation of Merged Flow. As discussed in the previous section, the jet swings back and forth in the cavity and issues alternately into the exits of the side passages and eventually the region downstream. If the deflection plates (Fig. 1) are

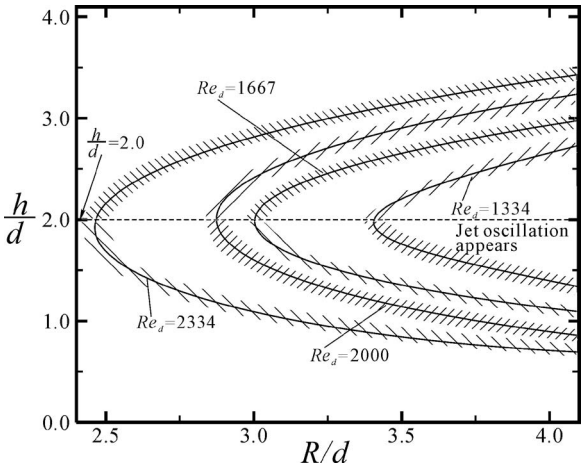

Fig. 4 Instability domain of jet oscillation. Deflection plates not installed.

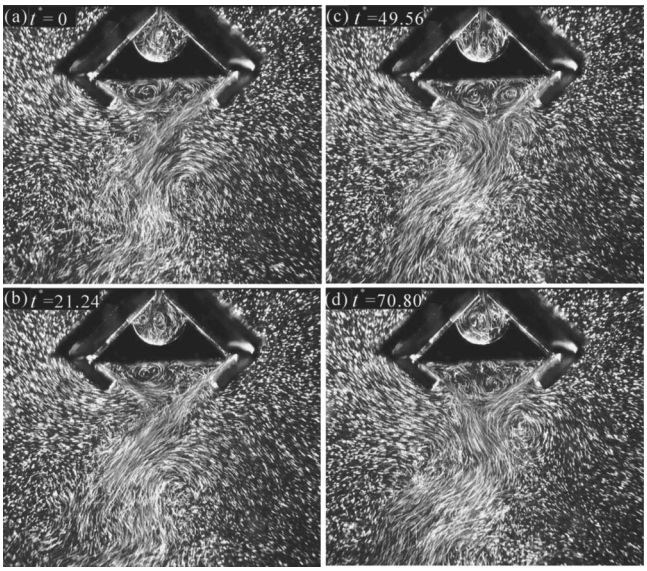

Fig. 5 Instantaneous flow visualization picture of fluidic oscillator. Deflection plates installed, deflection angle $\theta = 60$ deg. $\mathrm{Re}_d = 2000$, $R/d = 3.5$, $h/d = 2.5$. Frame rate = 60 fps. Exposure time = 1/60 s.

not installed, the jets would inject diversely. However, as the deflection plates are installed, the diversely issued jets impinge on the deflection plates, turn around to interact with each other, and merge as a transversely oscillating flow. Figure 5 shows the instantaneous pictures of the oscillation process of the oscillating flow at the deflection angle $\theta = 60$ deg and the Reynolds number $\mathrm{Re}_d = 2000$. The framing rate is 60 fps and the exposure time of each picture is 1/60 s. At the instant of Fig. 5(*a*), the jet in the cavity is swinging towards the left and impinging on the crescent surface a little left of the central position. The jets going out of the passages are deflected by the deflection plates and directed towards the central axis. These two jets impinge around the central area, merge together, and go downstream with transverse oscillation. The oscillating flow at this instant resembles an "S." Along the sides of the oscillating flow, vortices are accompanied where the "S"-shaped jet concaves. Above the oscillating flow and just beneath the target blockage, the shear effects developed by the impinging jets induce two counter-rotating vortices. At the instant depicted in Fig. 5(*b*), the jet in the cavity swings to far left of the central axis. Since the momentum of the jet issuing out of the left passage becomes stronger than that issuing from the right at this instant, the impinging point of these two jets is pushed to the right far of the central axis. When the jet in the cavity swings from left to right and almost reaches the centerline, as shown in Fig. 5(*c*), the shape of the oscillating flow becomes an *inverse* "S" because the swing direction of the jet in the cavity is reversed as compared to the situation in Fig. 5(*a*). In Fig. 5(*d*), the jet in the cavity swings further to the right so that the momentum of the jet issuing out of the right passage becomes stronger than that swinging from the left one. The impinging point of these two jets is pushed to the left off the central axis. Although the variation of the vortex size of the counter-rotating vortex pair is difficult to identify in Fig. 5, it is very clear upon observing the recorded animation. When the impingement point moves to the right, the left vortex of the counter-rotating vortex pair becomes larger and vice versa.

The instability frequencies f of the oscillating flow downstream from the oscillator and the fluidic oscillation in the cavity always coincide with each other. In Fig. 6, at small or medium deflection angles (e.g., $\theta = 0$, 30, and 45 deg), the instability frequencies f of the merged oscillating flow increase linearly with the increase of U_j and have the same values as the fluidic oscillation frequencies

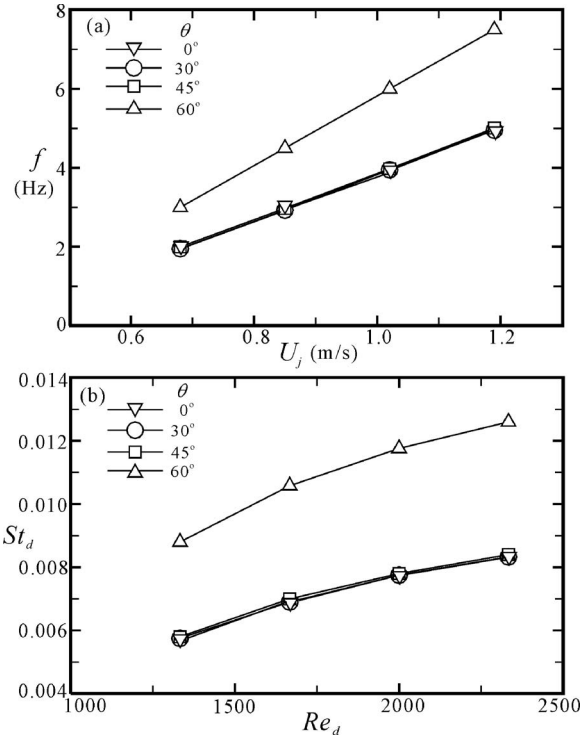

Fig. 6 Frequencies (a) and Strouhal numbers (b) of oscillating flow. Deflection plates installed. $R/d=3.5$, $h/d=2.5$.

f_f corresponding to the case when the deflection plates are not installed. However, at a high deflection angle (e.g., $\theta=60$ deg), the oscillation frequency f of the merged oscillating flow increases by almost 50% as compared to the cases of low or medium deflection angles. The physical mechanism of inducing such an increase in the instability frequencies is unclear. Still, the increased back-pressure at the exit of the passages due to the blockage effect of the deflection plate, as well as the disturbance and natural frequency of the standing vortices beneath the oscillator may lead to the modification in the oscillation frequency.

4.3 Topological Evolution Process of Jet Oscillation. Hand sketches of the topological flow structures are shown in Fig. 7 to assist the illustration of the flow oscillation process. The topological sketches are obtained by employing the critical point theory (usually termed the "phase plane analysis" mathematically) [23]. Using the critical point theory, the sectional streamline patterns including nodes (foci or centers), saddles, bifurcation lines, and their combinations can be identified by depicting the separatrices, critical points, and alleyways. This technique can assist in revealing the features in the flow field of either the steady flow structures or the evolutionary process of unsteady vortical motions. Hunt et al. [24] obtained a general formula for the relationship between the numbers of nodes (including four-way nodes N and three-way nodes N') and saddles (including four-way saddles S and three-way saddles S') for the flows around surface obstacles: $(\Sigma N+\frac{1}{2}\Sigma N')-(\Sigma S+\frac{1}{2}\Sigma S')=1-n$, in which n is the connectivity of the section of the flow under consideration. In the present case, $n=2$ if only the flow surrounding the target blockage is under consideration. This formula can be used to examine the correctness of the topological model.

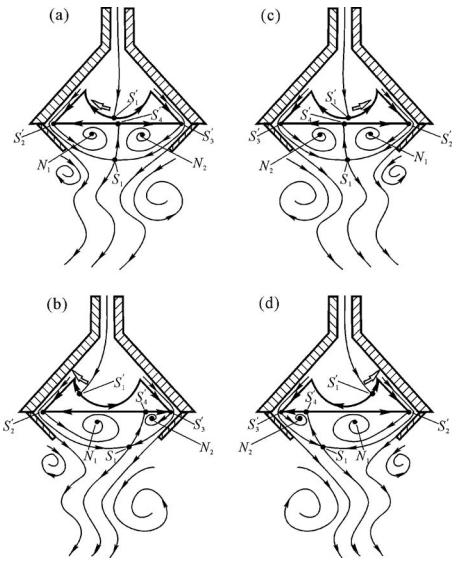

Fig. 7 Hand sketches of topological flow evolution process

Figure 7(*a*) shows the topological model at an instant when the leftward swinging jet comes down from the narrow channel and impinges on the crescent surface a little to the left of the central axis. Several critical points are identified on the proposed topological model: two nodes denoted by N_1 and N_2, one four-way saddle denoted by S_1, as well as four three-way saddles denoted by $S_1'-S_4'$. The jet impinges on the crescent surface at the three-way stagnation point S_1', then bifurcates to the left and right along the contour of the target blockage. Two three-way saddles, i.e., S_2' and S_3', are denoted at the lower tips of the target blockage since the separatrices bifurcating from S_1' meet the separatrices from the three-way saddle S_4' along the bottom surface of the target blockage and leave the tips. The separatrices leave the three-way saddles S_2' and S_3' and are wrapped around to form the counter-rotating standing vortices around the nodes N_1 andN_2. The separatrices along the passages merge at the stagnation point, i.e., the four-way saddle S_1, and subsequently bifurcate up and down. The upper bifurcated separatrix proceeds to the three-way saddle S_4' and the lower bifurcated separatrix proceeds downstream due to transverse oscillation. The evolved separatrices in the downstream area at this instant are in an "S" shape to represent the oscillation direction of the merged flow.

When the jet coming from the channel swings further to the left, the momentum issuing out of the left passage overwhelms that issuing out of the right passage so that the stagnation point (the four-way saddle S_1) moves away from the central axis towards the right, as shown in Fig. 7(*b*). The left standing vortex N_1 therefore becomes larger than the right vortex N_2. When the jet coming from the channel swings to the right, the situation is a mirror-reflection about the central axis, as shown in Figs. 7(*a*) and 7(*b*). The evolved separatrices in the downstream area during this "swinging rightwards" process are each in the shape of an *inverse* "S." In short, the movement of the stagnation point at the vertex of the counter-rotating standing vortices is always opposite to that of the swinging jet in the cavity. When the jet in the cavity swings to the left, the stagnation point moves to the right, and vice versa. When the jet in the cavity is on the left side of the cavity, the stagnation point is located on the right side of the central axis and the shape of the oscillating flow downstream from the stagnation point appears to be an "S." When the situation is reversed, the oscillating flow downstream from the stagnation point appears to be an inverse "S."

By counting the numbers of the critical points in Fig. 7, i.e., $\Sigma N=2$, $\Sigma N'=0$, $\Sigma S=1$, and $\Sigma S'=4$, the expression $(\Sigma N+\frac{1}{2}\Sigma N')-(\Sigma S+\frac{1}{2}\Sigma S')$ becomes -1, which satisfies the topological rule of Hunt et al. [24].

4.4 Averaged Flow Patterns. By averaging 2000 frames of the instantaneous velocity vector maps, the time-averaged velocity vector field and the streamline patterns are obtained, as shown in

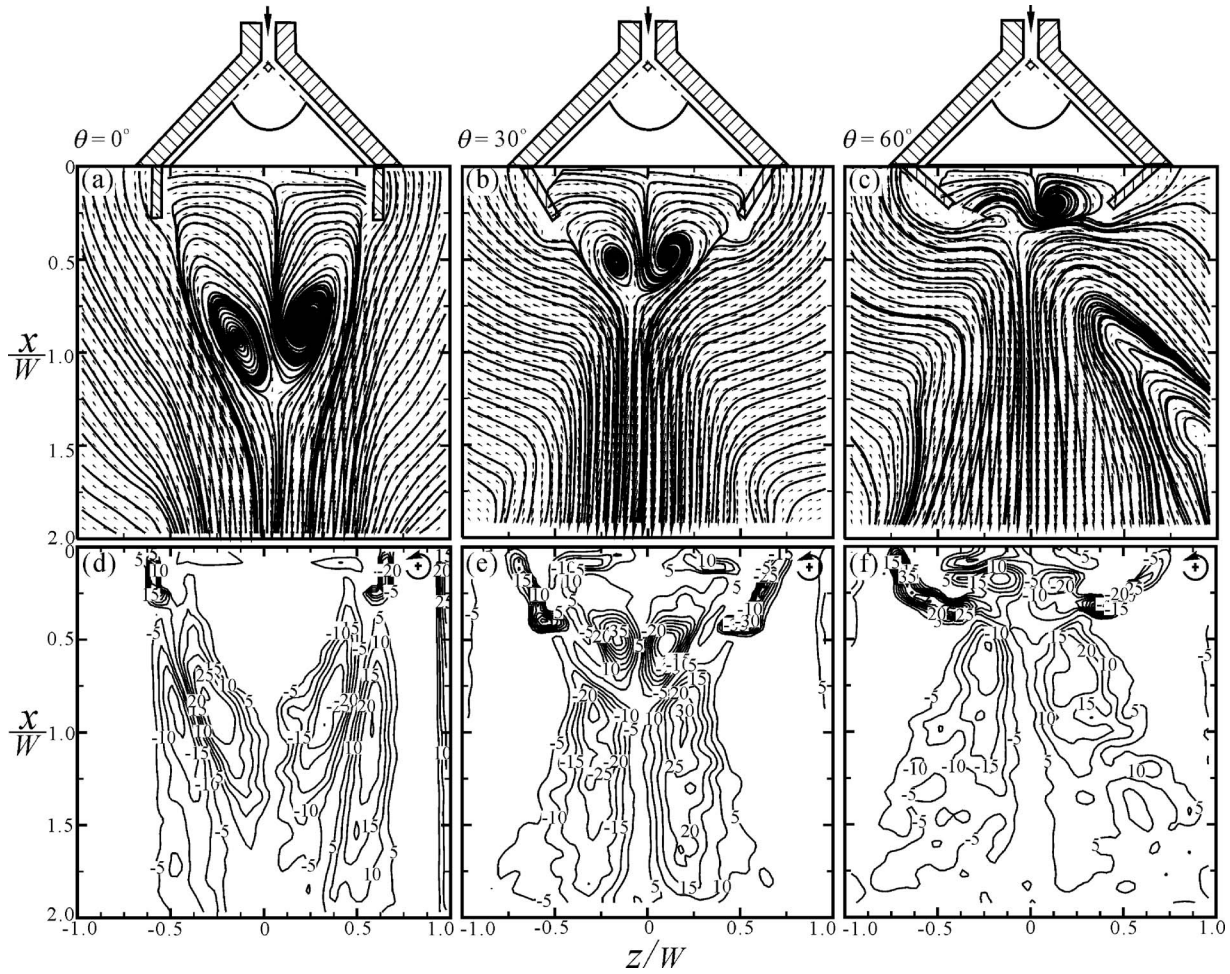

Fig. 8 Time-averaged velocity vector maps and streamline patterns (*a*, *b*, *c*) and corresponding vorticity contours (*d*, *e*, *f*) of oscillating flow. Deflection plates installed. Re_d=2000, *R*/*d*=3.5, *h*/*d*=2.5.

Figs. 8(*a*)–8(*c*). The corresponding vorticity contours are shown in Figs. 8(*d*)–8(*f*). The flow patterns are slightly asymmetric about the centerline because the alignment of the blockages is difficult to install at the exact symmetric position. At all deflection angles, the time-averaged flow patterns of the oscillating flow in the near field look similar to the time-averaged flow pattern commonly observed in a bluff-body wake [25]—a counter-rotating vortex pair exists behind the bluff body when a parallel flow passes over. In the case of the bluff-body wake, the time-averaged counter-rotating vortex pair is obtained from the time-varying phenomenon of vortex shedding. However, the time-averaged counter-rotating vortex pair in the flow field of the present flow is obtained from the standing, size-varying, counter-rotating vortices. The streamline patterns of Figs. 8(*a*)–8(*c*) appear to resemble a "point jet" [26]. However, the details of the time-averaged flow characteristics are not similar because the flow evolves from an unsteady wake other than a point source. The vorticity contours, as shown in Figs. 8(*d*)–8(*f*), show concentration of vorticity in the regions around the stagnation point. The core regions of the counter-rotating vortices have largest vorticity values induced by the rotation motion of fluids. Aside the centerline, just a little downstream from the stagnation point, the vorticity also imparts large values because the side fluids are entrained towards the center region and make a turn of relatively small radius of curvature there.

The length of the bubble l_{bubble}, i.e., the axial position of the stagnation point of the counter-rotating vortex pair, shortens with the increase of the deflection angle, as shown in Fig. 9. At θ =0 deg, the bubble length attains almost 1.2 W. At θ=60 deg, the bubble length reduces drastically to about 0.28 W. The time-averaged flow pattern of the oscillating flow at θ=0 deg looks comparative to that of two parallel plane jets separated by a distance [27,28]. The bubble length generated by two parallel turbulent air jets with a separation of 40 jet widths at the Reynolds number 7600 is about 1.1 W [27], which is quite close to that

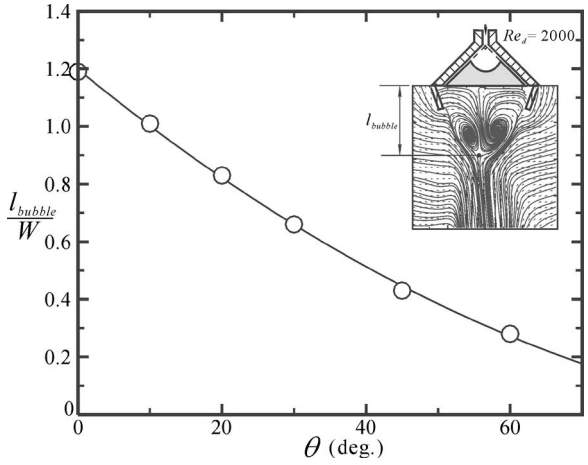

Fig. 9 Axial length of stagnation point of counter-rotating vortex pair. Re_d=2000, *R*/*d*=3.5, *h*/*d*=2.5.

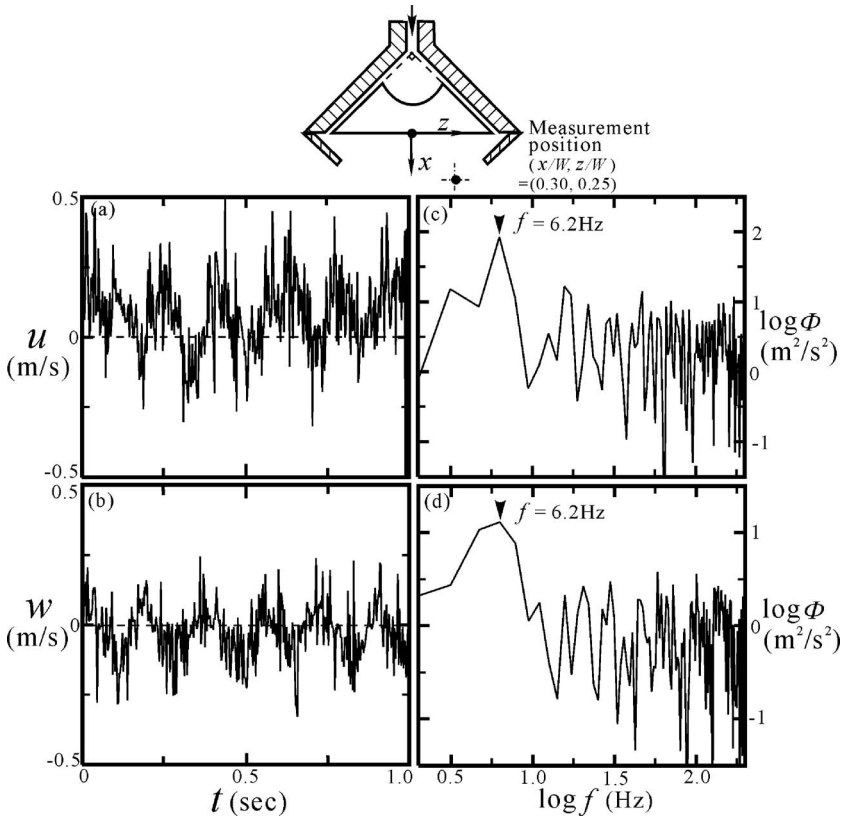

Fig. 10 Time histories (*a*, *b*) and corresponding power spectrum density functions (*c*, *d*) of *u* and *w* velocity components. Deflection plates installed, deflection angle θ=60 deg. Re_d=2000, R/d=3.5, h/d=2.5.

(1.2 W) of the present study at θ=0 deg with 43 jet widths separation. The bubble length generated by two turbulent air jets with a small separation of 4.25 W at the Reynolds number 11,000 is decreased to about 8 W [28]. If the fluidic oscillator developed in this study is reduced in size, it might lead to a shortened bubble length.

4.5 Power Spectrum and Turbulence Scales. By processing the PIV measured instantaneous data, some turbulence properties in the shear layer can be extracted. Figure 10 shows the typical time series of the instantaneous velocities u and w in the x and z directions, respectively, and their corresponding power spectrum density functions Φ at the location $(x/W, z/W)=(0.30, 0.25)$ at Re_d=2000 and θ=60 deg. The reasoning behind choosing this location to illustrate of the velocity and power spectrum peak is because the fluctuation signals are most apparent in the region near the exit of the defected jets. The power spectrum density functions are converted from the time series of the instantaneous velocity data by using the discrete fast Fourier transform [29]. Both the instantaneous velocities u and w have periodical harmonics superimposed by large fluctuations. The average values of the u and w velocity components (Figs. 10(a) and 10(b)) are positive and negative, respectively, because the measurement location is on the right side near the jet exit. The power spectrum density functions corresponding to the u and w velocity components, as shown in Figs. 10(c) and 10(d) respectively, present the same peak values at 6.2 Hz, which is almost the same as the values taken from the flow visualization method (Fig. 6).

Figures 11(a) and 11(b) show the autocorrelation coefficients $R_{\tau,u}$ and $R_{\tau,w}$ of the fluctuation velocities of the u and w components, respectively, at $(x/W, z/W)=(0.30, 0.25)$. The symbol τ denotes the shifting time in doing convolution calculation [29]. The autocorrelation coefficients of u and w fluctuations decrease from unity at τ=0 to null over a short period of time, which is then followed by periodic wave forms with a period of about 0.161 s (the continuous periodic wave forms at large τ are not shown here). This is typical behavior for the autocorrelation coefficient when the time series of signals present periodical harmonics and are superimposed by fluctuations. The period 0.161 s (corresponding to the 6.2 Hz frequency) can be taken as the statistical time scale of the large-scale oscillating flow passing over the point of measurement.

The autocorrelation coefficients shown in Figs. 11(a) and 11(b) also provide a Lagrangian integral time scale [30] τ_t of about 17 ms and 15 ms for the u and w velocity fluctuations, respectively. The Lagrangian integral time scale obtained from the autocorrelation coefficient is roughly a measure of the statistical time interval that the large-scale turbulent eddies may have. Although the Lagrangian integral time scale is not a quantity representing real physical time in the flow, it can provide an estimate for the comparative basis of time scales of turbulent fluctuations of large eddies. The normalized Lagrangian integral time scale, τ_t/T_f, where T_f is the period of the fluidic oscillation, is shown in Fig. 11(c) for various values of deflection angle θ. The value of τ_t/T_f decreases from 0.35 at θ=0 deg to 0.1 at θ=60 deg. Apparently, installing the deflection plates can shorten the time scales of large-scale turbulent fluctuations. Further, the larger the deflection angle, the smaller the required time scale, i.e., the higher the fluctuating frequency of the turbulence eddies. Operating the jet oscillator at large deflection-plate installation angles is beneficial to increasing the turbulence disturbance. By employing Taylor's frozen flowfield hypothesis [31], the length scale of the large turbulence eddies can be estimated by multiplying the local average velocity to the correspondingLagrangian time scale. Figure 11(d) shows the normalized length scales of u and w fluctuations $l_{t,u}/W$

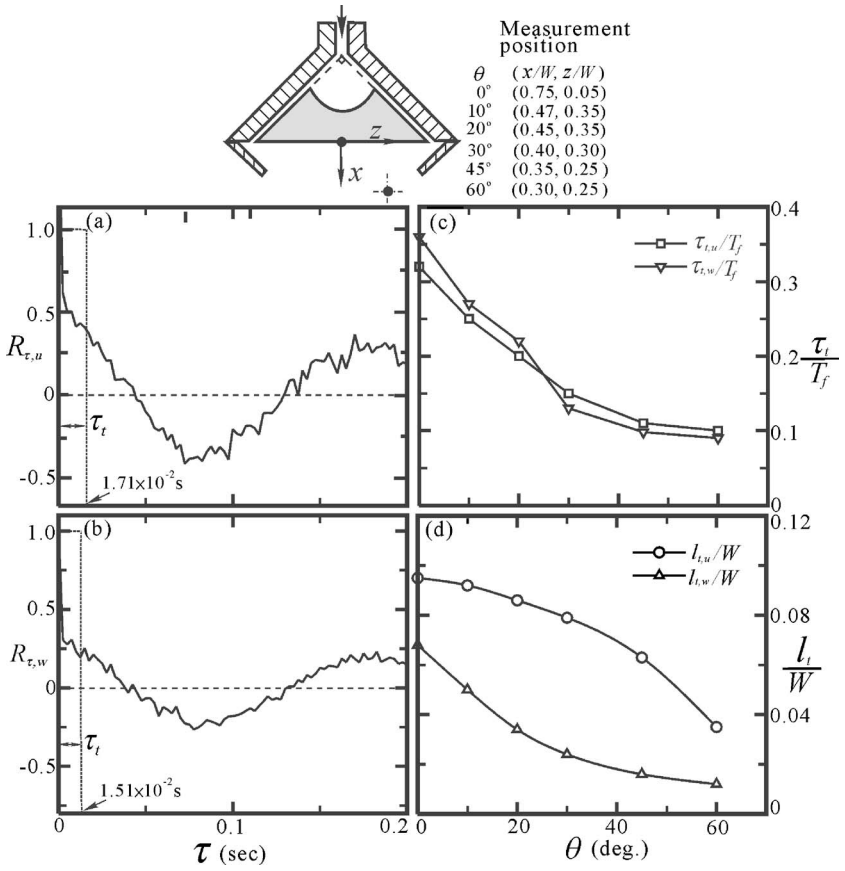

Fig. 11 Autocorrelation coefficients (*a*, *b*) and normalized Lagrangian time and length scales (*c*, *d*). Re_d=2000, R/d=3.5, h/d=2.5.

and $l_{t,w}/W$, respectively. The integral length scales of the turbulence eddies decreases with the increase of θ, which corresponds to the behavior of τ_t. In addition, the eddy size in the x direction is much larger than that in the z direction. This may be induced by the effect of vortex stretching which is provided by the main stream in the x direction.

It has been acknowledged that the mixing is related to the size of the contact surface between the species to be mixed. Good mixing is achieved when the contact surface is maximized, which is the case at small turbulent scales. Control of mixing therefore has to aim at controlling the small scale structure of turbulence, which is typically possible only by indirect means via a forced breakup of the controllable large scales. The reduction of the large-scale turbulence eddies by using the present flow control method could be beneficial to increase the mixing capability if the turbulence intensities are also enhanced.

4.6 Velocity Distribution and Turbulence Intensity. The distributions of the normalized average velocity and turbulence intensities along the central axis are shown in Fig. 12. The average velocity $\bar{u}$ and $\bar{w}$ are the arithmetic averages of 2000 instantaneous velocity components u and w, respectively. The values of $\bar{w}$ along the central axis are not shown here because they are almost zero. The turbulence intensities are defined as u'/U_j and w'/U_j, where u' and w' are the root mean square values of the fluctuations of the velocity components$u$ and w, respectively.

As shown in Fig. 12(*a*), for the case lacking deflection plates, the normalized axial velocity appears to be slightly negative because of the recirculation occurring there. In the downstream region about $x/W>1.5$, the reverse flow on the central axis almost vanishes. When the deflection plates are installed, the axial velocities in the bubble region present negative values because of the flow reversal there. Downstream from the stagnation points, the axial velocity increases with the increase in the axial distance. The axial velocity decreases abruptly in the near field at $x/W\approx1.5$ when θ=0 deg and at $x/W\approx1.8$ when θ=20 deg and 60 deg. It is apparent that the transverse oscillation motion of the merged flow presented in this study induces significant lateral momentum dispersion so that the axial momentum is hardly maintained in areas far downstream.

Figures 12(*b*) and 12(*c*) show the axial and lateral turbulence intensities, respectively. The axial and lateral turbulence intensities with deflection plates installed are much larger than those without deflection plates. The turbulence intensities at θ=60 deg are on average about twice those at θ=0 deg and 20 deg. At θ=60 deg, the values of u'/U_j and w'/U_j may attain values as high as 11% and 17%, respectively. If the normalization factor U_j is replaced by the local velocities, the turbulence intensities may even attain ten times the present values. The present transversely oscillating flow can apparently induce a drastic increase in the turbulence fluctuations. This property could be of much benefit to the momentum exchange, mixing, and combustion if further polishing can be performed for applications.

The axial velocity in the near field along the centerline of two parallel plane jets separated by a distance [28] behaves quite similarly to that in the present case. However, the induced turbulence intensities along the centerline of the parallel jets do not remain as high in areas far downstream as those induced by the oscillating flow described in this study. They decrease to low values shortly after passing the recirculation bubble [28]. The transverse agitation effect induced by the oscillation motion of the merged flow of this study seems to be dramatic (as compared to the induced turbulence intensities).

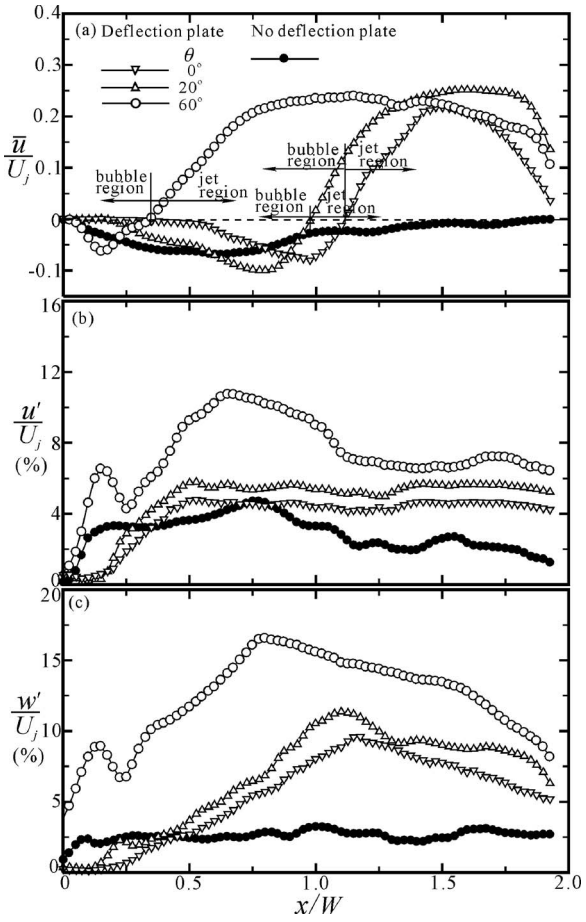

Fig. 12 Distributions of normalized velocity properties along central axis. (*a*) axial velocity, (*b*) axial turbulence intensities, (*c*) lateral turbulence intensity. Re_d=2000, *R*/*d*=3.5, *h*/*d*=2.5.

5 Conclusions

An innovative fluidic oscillator is developed to induce transversely oscillating flow. The dynamic behaviors of the periodic flow oscillation and the turbulence properties are investigated experimentally. By properly designing the fluidic oscillator, the swinging jet can be guided through passages to issue alternatively as two pulsatile jets with inverse phase angles. The alternatively issued pulsatile jets can be deflected by plates to impinge upon each other and thereby form a counter-rotating vortex pair. The stagnation point of the vortex pair oscillates transversely and periodically and therefore causes a merged flow, which originates from the stagnation point to oscillate transversely. The oscillation frequency is increased proportionally to the increase of the Reynolds number. The oscillating flow causes large lateral dispersion of the axial momentum so that the width of the merged flow expands very fast over a short distance. The statistical time and length scales of the large turbulence eddies are reduced and the turbulence intensities are drastically increased by the transverse oscillation of the merged flow. Therefore, it appears to be beneficial to apply the presently developed jet oscillator to situations that require large momentum, mass, and energy dispersions over a short distance.

Acknowledgment

This research was supported by the National Science Council of the Republic of China under grant number NSC 93-2212-E011-014.

Nomenclature

l_{bubble} = axial length of counter-rotating vortex pair
d = jet width at inlet of fluidic oscillator
f = oscillation frequency of merged flow, Hz
f_f = fluidic oscillation frequency induced in cavity, Hz
h = offset distance from crescent origin to virtual vertex of target blockage
L = length of fluidic oscillator in span direction
$l_{t,u}$ = length scale of fluctuations of u component
$l_{t,w}$ = length scale of fluctuations of w component
R = radius of crescent profile of target blockage
$R_{\tau,u}$ = autocorrelation coefficient of fluctuations of u component
$R_{\tau,w}$ = autocorrelation coefficient of fluctuations of w component
Re_d = Reynolds number based on width d and U_j ($=U_j d/\nu$)
$St_{d,f}$ = Strouhal number of fluidic oscillation based on width d ($=f_f d/U_j$)
St_d = Strouhal number of oscillating merged flow based on width d ($=fd/U_j$)
T_f = period of fluidic oscillation
U_j = average velocity at inlet of fluidic oscillator
u = local instantaneous velocity in x direction
$\bar{u}$ = local time-averaged velocity in x direction
u' = root mean square of fluctuating velocity of u component
W = cross-stream width of fluidic oscillator
w = local instantaneous velocity in z direction
$\bar{w}$ = local time-averaged velocity in z direction
w' = root mean square of fluctuating velocity of w component
x = coordinate in jet injection direction
z = cross-stream coordinate

Greek Symbols

τ_t = Lagrangian integral time scale
θ = deflection angle measured from vertical axis
Φ = power spectrum density function of fluctuation velocity
ν = kinetic viscosity of air stream

References

[1] Yule, A. J., 1978, "Large-Scale Structure in the Mixing Layer of a Round Jet," J. Fluid Mech., **89**, pp. 413–432.
[2] Brown, G. L., and Roshko, A., 1974, "On Density Effects and Large Structure in Turbulent Mixing Layers," J. Fluid Mech., **64**, pp. 775–816.
[3] Tritton, D. J., 1988, *Physical Fluid Dynamics*, Oxford University Press, Oxford, pp. 123–151.
[4] Coles, D., 1985, "The Uses of Coherent Structure," AIAA Paper 85-0506.
[5] Laufer, J., and Ta-Chun, Y., 1983, "Noise Generation by a Low Mach Number Jet," J. Fluid Mech., **134**, pp. 1–31.
[6] Fiedler, H. E., and Mensing, P., 1985, "The Plane Turbulent Shear Layer With Periodic Excitation," J. Fluid Mech., **150**, pp. 281–309.
[7] Schadow, K. C., and Gutmark, E., 1992, "Combustion Instability Related to Vortex Shedding in Dump Combustors and Their Passive Control," Prog. Energy Combust. Sci., **18**, pp. 117–132.
[8] Huerre, P., and Monkewitz, P. A., 1985, "Absolute and Convective Instabilities in Free Shear Layers," J. Fluid Mech., **159**, pp. 151–168.
[9] Gad-el-Hak, M., 1998, *Flow Control - Fundamentals and Practices*, M. Gad-el-Hak, A. Pollard and J.-P. Bonnet, eds., Springer-Verlag, Berlin, pp. 335–429.
[10] Camci, C., and Herr, F., 2002, "Forced Convection Heat Transfer Using a Self-Oscillating Impinging Planar Jet," ASME J. Heat Transfer, **120**, pp. 770–782.
[11] Tippetts, J. R., Ng, H. K., and Royle, J. K., 1973, "An Oscillating Bi-Stable Fluid Amplifier for Use as a Flowmeter," J. Fluid Control, **5**, pp. 28–42.
[12] Yamasaki, H., and Honda, S., 1981, "A Unified Approach to Hydrodynamic Oscillator Type Flowmeters," J. Fluid Control, **13**, pp. 1–17.
[13] Wang, H., Beck, S. B. M., Priestman, G. H., and Boucher, R. F., 1998, "A Remote Measuring Flow Meter for Petroleum and Other Industrial Applications," Meas. Sci. Technol., **9**, pp. 779–789.

[14] Yamamoto, K., Hiroki, F., and Huodo, K., 1999, "Self-Sustained Oscillation Phenomena of Fluidic Flowmeters," J. Visualization, **1**, pp. 387–396.
[15] Rockwell, D., and Naudascher, E., 1978, "Review—Self-Sustaining Oscillations of Flow Past Cavities," ASME J. Fluids Eng., **100**, pp. 152–165.
[16] Lalanne, L., Le Guer, Y., and Creff, R., 2001, "Dynamics of a Bifurcating Flow Within an Open Heated Cavity," Int. J. Therm. Sci., **40**, pp. 1–10.
[17] Lin, J.-C., and Rockwell, D., 2001, "Oscillations of a Turbulent Jet Incident Upon an Edge," J. Fluids Struct., **15**, pp. 791–829.
[18] Potter, M. C., 2002, *Mechanics of Fluids*, Prentice-Hall, New York.
[19] Flagan, R. C., and Seinfeld, J. H., 1988, *Fundamentals of Air Pollution Engineering*, Prentice-Hall, Englewood Cliffs, NJ, pp. 290–307.
[20] Richard, C. F., and John, H. S., 1988, *Fundamentals of Air Pollution Engineering*, Prentice Hall, NJ, pp. 290–357.
[21] Keane, R. D., and Adrian, R. J., 1992, "Theory of Cross-Correlation Analysis of PIV Images," Appl. Sci. Res., **49**, pp. 191–215.
[22] Abernethy, R. B., Benedict, R. P., and Doedell, R. B., 1985, "ASME Measurement Uncertainty," ASME J. Fluids Eng., **107**, pp. 161–164.
[23] Lighthill, M. J., 1963, *Laminar Boundary Layers*, Oxford University Press, Cambridge, pp. 48–88.
[24] Hunt, J. C. R., Abell, C. J., Peterka, J. A., and Woo, H., 1978, "Kinematical Studies of the Flows Around Free or Surface-Mounted Obstacles: Applying Topology to Flow Visualization," J. Fluid Mech., **86**, pp. 299–446.
[25] Zdravkovich, M. M., 1997, *Flow Around Circular Cylinder*, Oxford University Press, Oxford, UK.
[26] Batchelor, G. K., 2000, *An Introduction to Fluid Dynamics*, Cambridge University Press, Cambridge, UK, 3rd ed., pp. 205–216.
[27] Lin, Y. F., and Sheu, M. J., 1991, "Interaction of Parallel Plane Jets," AIAA J., **29**, pp. 1372–1373.
[28] Nasr, A., and Lai, J. C. S., 1997, "Comparison of Flow Characteristics in the Near Field of Two Parallel Plane Jets and an Offset Plane Jet," Phys. Fluids, **9**, pp. 2919–2931.
[29] McGillem, C. D., and Cooper, G. R., 1984, *Continuous and Discrete Signal and System Analysis*, 2nd ed., Holt, Rinehart and Winston, NY, pp. 168–197.
[30] Tennekes, H., and Lumley, J. L., 1972, *A First Course in Turbulence*, MIT Press, Cambridge, pp. 248–261.
[31] Zaman, K. B. M. Q., and Hussain, A. K. M. F., 1981, "Taylor Hypothesis and Large-Scale Coherent Structures," J. Fluid Mech., **112**, pp. 379–396.

Clarisse Fournier

Marc Michard

Centre de Thermique de Lyon,
UMR CNRS 5008,
INSA de Lyon,
Bat Sadi Carnot, 20 av. Albert Einstein,
69621 Villeurbanne Cedex, France
e-mail: clarisse.fournier@insa-lyon.fr

Françoise Bataille

PROMES,
UPR CNRS 8521,
Rambla de la thermodynamique, Tecnosud,
66100 Perpignan, France

Heat Transfer in a Laminar Channel Flow Generated by Injection Through Porous Walls

Steady state similarity solutions are computed to determine the temperature profiles in a laminar channel flow driven by uniform fluid injection at one or two porous walls. The temperature boundary conditions are non-symmetric. The numerical solution of the governing equations permit to analyze the influence of the governing parameters, the Reynolds and Péclet numbers. For both geometries, we deduce a scaling law for the boundary layer thickness as a function of the Péclet number. We also compare the numerical solutions with asymptotic expansions in the limit of large Péclet numbers. Finally, for non-symmetric injection, we derive from the computed temperature profile a relationship between the Nusselt and Péclet numbers. [DOI: 10.1115/1.2746908]

Keywords: blowing, laminar channel flow, heat transfer, boundary layer, asymptotic expansions

1 Introduction

Flows induced by blowing through permeable walls have been the subject of many isothermal studies due to their importance in various engineering applications. These include, for example, flow filtration process [1] or diffuse separation of gaseous isotopes [2]. There are many geometries found in the literature that model the combustion in solid propellant rocket motors. In these cases, the fluid is normally injected through the porous wall [3,4]. This type of channel flow presents some characteristics quite different from that observed in a pipe or in a boundary layer flow with impermeable walls: curvature of the streamlines, accelerated flow, and intrinsic instability of the flow [5–7].

The case of the laminar, steady, incompressible, and two-dimensional channel flow perturbed by symmetric injection or suction on both walls has been first examined by Berman [2]. With the assumption of an uniform injection or suction velocity V_{in}, Berman proposed a similarity solution for the velocity field using a stream ϕ function of a form $\phi(x,y)=-V_{in}xf(y/e)$, where e represents the half-height of the channel. The Navier-Stokes equations are reduced to a fourth-order non-linear ordinary differential equation for the similarity function f with suitable boundary conditions at the walls. Berman constructed a series solution for small values of Re_{in}, where the Reynolds number Re_{in} is based on the injection velocity V_{in} and the half-height e of the channel. Many authors were interested in the analytical solutions of the Berman's equations and their stability [8–10], or their extension to appreciably different cases: non-symmetric suction/injection [11] or one impermeable wall [12]. For very large Reynolds numbers and a semi-infinite plane channel with symmetric injection, Taylor [1] and Culick [13] proposed a solution of Berman's problems by using a harmonic function for f. The corresponding velocity profile verify Euler's equations, while satisfying a no-slip condition at the walls where injection takes place; this solution is in excellent agreement withthe numerical solution of Berman's equations if the Reynolds number Re_{in} is greater than a few hundreds. Taylor solution was tested in experiment [14] and velocities measurements were found to be in agreement with laminar theory. The transition of the Berman's flow to a fully turbulent one has been numerically investigated by several authors [4,15–18].

The number of papers related to flows generated by wall injection led to an increasingly detailed knowledge of the velocity field in laminar or turbulent regimes. Nevertheless, the temperature field is much less analyzed in the literature. Ferro and Gnavi [19] studied the influence on the structure of the Berman's flow of dynamic viscosity variations due to temperature for both symmetric injection and suction. These authors use also a similarity solution f to describe the velocity field; because of invariance of the normal velocity with respect to the streamwise coordinate, the temperature field is only a function of the normal coordinate. These authors are mainly focused on the stability of the flow, and they do not provide any results concerning temperature in the case of non-symmetric injection.

The objective of this work is to investigate the characteristics of the temperature field of a flow induced by blowing through two or one porous wall (symmetric or non-symmetric injection). We consider, at first, a geometry, hereafter denoted case a, with two permeable walls (see Fig. 1(*a*)). The distance between the walls is $2e$; the fluid is normally injected with an uniform velocity $V_{in}>0$ at the lower wall and $-V_{in}$ at the upper wall, while the wall temperatures are uniform and, respectively, equal to T_1 and T_2 ($T_2>T_1$). Therefore, an internal thermal boundary layer develops along the channel centerline far from the walls. In the second geometry (Fig. 1(*b*)), thereafter denoted case b, the fluid is injected at the lower wall with an uniform positive velocity V_{in} and a no-slip condition is fixed at the upper impermeable wall at a distance e. The fluid temperature at the lower wall is T_1, while an uniform heat flux q_w is imposed on the upper impermeable wall. In that case, the boundary conditions give rise to both dynamic and thermal boundary layers along the upper impermeable wall. A plane Cartesian coordinate system (x,y) is used, with the origin placed on the centerline for case a, and on the lower wall for case b. In both cases, the length of the walls is large compared to the distance between walls and the end effects are therefore neglected.

The flow is supposed to be two dimensional, steady, and laminar. Temperature variations are sufficiently small to consider constant properties of the fluid (viscosity, thermal diffusivity, etc.). Moreover, the density is supposed to be uniform. As is usually done, we neglect the dissipation and pressure terms in the energy equation. The following analysis is valid both for gases and liquids. Most of numerical results are presented for a Prandtl number $\mathrm{Pr}=1$ but Péclet number effects on heat exchanges are also studied.

Contributed by the Fluids Engineering Division of ASME for publication in the JOURNAL OF FLUIDS ENGINEERING. Manuscript received March 17, 2006; final manuscript received March 18, 2007. Review conducted by Subrata Roy.

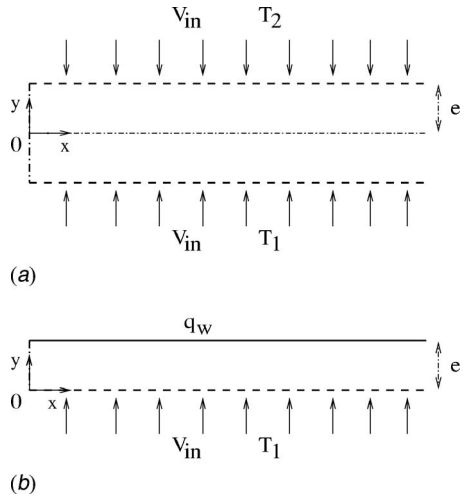

Fig. 1 Flow geometry (*a*) case a and (*b*) case b

In Sec. 2 we derive results concerning the bulk velocity and bulk temperature in both configurations. We present in Sec. 3 the non-dimensional basic equations. The influence of the Reynolds and Péclet numbers on the velocity, pressure, and temperature profiles, and on the scaling law of the thermal boundary layer thickness, are discussed in Sec. 4. Asymptotic expansions of the temperature profile are proposed in Sec. 5. We finally determine in Sec. 6 for case b, a correlation giving the heat transfer coefficient as a function of $\mathrm{Re}_{\mathrm{in}}$ and $\mathrm{Pe}_{\mathrm{in}}$.

2 Bulk Velocity and Temperature

Before solving the equations giving the local velocity and temperature fields in both geometries, we derive some results concerning bulk, or global quantities. We define a bulk velocity U_b and a bulk temperature T_b in any cross section S of the flow according to usual relations [20]:

$$U_b = \frac{1}{S}\int_S U(x,y)dS \tag{1}$$

$$T_b = \frac{1}{SU_b(x)}\int_S U(x,y)T(x,y)dS \tag{2}$$

In both geometries, surface integrals reduce to a simple integral. For case a (symmetric injection), the lower and upper bounds of integration are $-e$ and e, while the bounds are 0 and e for case b (non-symmetric injection).

2.1 Case a: Two Porous Walls. We now consider the control volume, shown in Fig. 2, delimited by cross sections S_x and S_{x+dx} located at x and $x+dx$, by surface elements S_1 and S_2 at the walls, and with a unit length in the spanwise direction. Using the assumption of uniform density, the mass conservation applied to this control volume gives the streamwise gradient of U_b:

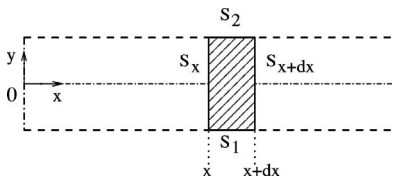

Fig. 2 Sketch of the control volume

$$\frac{dU_b}{dx} = \frac{V_{\mathrm{in}}(x)}{e} \tag{3}$$

Since V_{in} is supposed to be uniform in this work, integration of Eq. (3) gives the relation between $U_b(x)$, V_{in}, and x:

$$U_b(x) = V_{\mathrm{in}}\frac{x}{e} \tag{4}$$

We now apply the first law of thermodynamics to the same control volume. Due to the symmetric injection conditions, the heat fluxes through S_1 and S_2 are opposite and the enthalpy outflow is equal to the enthalpy inflow:

$$\int_{S_{x+dx}} \rho U i dS - \left(\int_{S_x} \rho U i dS + \rho_{\mathrm{in}} V_{\mathrm{in}} i(x, y=-e) S_1 + \rho_{\mathrm{in}} V_{\mathrm{in}} i(x, y=e) S_2\right) = 0 \tag{5}$$

where i denotes the specific enthalpy of the fluid. Assuming an uniform density and applying the law of an ideal perfect gas relating i to T ($i=C_pT$), the preceding equation can be written in the following form:

$$\frac{d(U_bT_b)}{dx} = \frac{V_{\mathrm{in}}}{e}\frac{T_1+T_2}{2} \tag{6}$$

Finally, combining Eqs. (4) and (6) and integrating between 0 and x, we conclude that the bulk temperature is independent of x and given by the following relation:

$$T_b(x) = T_b = \frac{T_1+T_2}{2} \tag{7}$$

The fact that the bulk temperature is equal to the arithmetic mean of T_1 and T_2 results of course from the symmetric injection conditions.

2.2 Case b: One Porous Wall and One Impermeable Wall. Equations (3) and (4) for the bulk velocity are always valid, whatever the shape of the streamwise velocity profile. Applying the first law of thermodynamics to the control volume, the contribution of the imposed heat flux at the upper wall needs now to be taken into account in the balance between inflow and outflow enthalpy:

$$\int_{S_{x+dx}} \rho U i dS - \left(\int_{S_x} \rho U i dS + \rho_{\mathrm{in}} V_{\mathrm{in}} i(x, y=0) S_1\right) = q_w S_2 \tag{8}$$

With the same assumptions, we derive the governing equation for the bulk temperature in the second geometry:

$$\frac{d(U_bT_b)}{dx} = \frac{V_{\mathrm{in}}}{e}T_1 + \frac{q_w}{e\rho_{\mathrm{in}}C_p} \tag{9}$$

One more time, combining Eqs. (4) and (9) gives the bulk temperature, which is independent of the streamwise coordinate x:

$$T_b(x) = T_b = T_1 + T_f \tag{10}$$

The quantity T_f in Eq. (10) which is called the friction temperature, by reference to the usual friction velocity used in fluid mechanics, is given by:

$$T_f = \frac{q_w}{\rho C_p V_{\mathrm{in}}} \tag{11}$$

We note that Eqs. (3), (6), and (9) are valid even if the injection velocity is not uniform. We pay attention to the fact that in case b, we neglected the heat flux at the porous walls in the application of the first law of thermodynamics to the control volume. This assumption is justified because the heat flux at the porous wall remains small compared to the imposed heat flux at the imperme-

able wall. It is shown in Sec. 6 that this condition is verified even for moderate Péclet numbers.

3 Model Equations

Non-dimensional spatial coordinates x^* and y^* are expressed in units of e, while velocity and pressure are normalized respectively, by V_{in} and $\rho_{in}V_{in}^2$. A non-dimensional temperature T^* is defined as $T^*=(T-T_1)/(T_b-T_1)$, where the bulk temperature T_b has been derived in Sec. 2. Therefore, $T_b-T_1 \sim T_2-T_1$ for case a, and $T_b-T_1 \sim T_f$ for case b.

Under the assumptions given in Sec. 1, the non-dimensional momentum and energy equations are:

$$U^*\frac{\partial U^*}{\partial x^*}+V^*\frac{\partial U^*}{\partial y^*}=-\frac{\partial P^*}{\partial x^*}+\frac{1}{\mathrm{Re}_{in}}\left(\frac{\partial^2 U^*}{\partial x^{*2}}+\frac{\partial^2 U^*}{\partial y^{*2}}\right) \tag{12}$$

$$U^*\frac{\partial V^*}{\partial x^*}+V^*\frac{\partial V^*}{\partial y^*}=-\frac{\partial P^*}{\partial y^*}+\frac{1}{\mathrm{Re}_{in}}\left(\frac{\partial^2 V^*}{\partial x^{*2}}+\frac{\partial^2 V^*}{\partial y^{*2}}\right) \tag{13}$$

$$U^*\frac{\partial T^*}{\partial x^*}+V^*\frac{\partial T^*}{\partial y^*}=\frac{1}{\mathrm{Pe}_{in}}\left(\frac{\partial^2 T^*}{\partial x^{*2}}+\frac{\partial^2 T^*}{\partial y^{*2}}\right) \tag{14}$$

where $\mathrm{Re}_{in}=V_{in}e/\nu$ and $\mathrm{Pe}_{in}=V_{in}e/\alpha$ are, respectively, the Reynolds and Péclet numbers based on the injection velocity, the length scale e, the kinematic viscosity ν and the thermal diffusivity α.

Following the previous works [2,19], as a consequence of the uniform injection velocity, we express the non-dimensional velocity and temperature fields in terms of self-similarity functions f and θ:

$$U^*(x^*,y^*)=x^*\cdot f'(y^*) \tag{15a}$$

$$V^*(x^*,y^*)=-f(y^*) \tag{15b}$$

$$T^*(x^*,y^*)=\theta(y^*) \tag{15c}$$

The self-similarity linear evolution with x^* of the streamwise velocity U^* is justified by the linear variation of the bulk velocity with x. We remark that both normal velocity V^* and temperature θ are functions of y^* only. With this similarity hypothesis, the governing equations for f and θ are deduced from Eqs. (12)–(14):

$$f^{(4)}+\mathrm{Re}_{in}(ff'''-f'f'')=0 \tag{16a}$$

$$\theta''+\mathrm{Pe}_{in}f\theta'=0 \tag{16b}$$

where "′" denotes differentiation with respect to y^*. For case a, the boundary conditions are:

$$f(-1)=-1 \quad f(1)=1 \quad f'(-1)=f'(1)=0 \quad \theta(-1)=0 \quad \theta(1)=1 \tag{17}$$

and for case b:

$$f(0)=-1 \quad f(1)=0 \quad f'(0)=f'(1)=0 \quad \theta(0)=0 \quad \theta'(1)=\mathrm{Pe}_{in} \tag{18}$$

The boundary conditions $f'(\pm 1)=0$ for case a and $f'(0)=0$ for case b express the no-slip condition at the porous walls, an assumption that is justified if the permeability of the porous material is high enough to prevent streamwise flow inside the porous wall. Moreover, the boundary conditions are different by considering the solutions for a coupled flow both through and above the porous wall [21].

The main differences between symmetric and non-symmetric injections rely on the different values imposed at the upper wall for $f(1)$, $\theta(1)$, or $\theta'(1)$. Equations (16)–(18) show that the key parameters governing the behavior of velocity and temperature fields are Re_{in} and Pe_{in}. Of course, the velocity field is explicitly a function of the Reynolds number through the value of Re_{in} in Eq. (16*a*) for f. The temperature field is an explicit function of Pe_{in} through Eq. (16*b*) for θ and the corresponding boundary condition in Eq. (18) for case b. It is an implicit function of Re_{in} (or of the normal velocity) through f in Eq. (16*b*) for θ.

Let us define $F=(f,f',f'',f''')$ and $G=(\theta,\theta')$. The set of Eqs. (16*a*) and (16*b*) can be rewritten as: $dF/dy^*=\xi(F,\mathrm{Re}_{in})$ and $dG/dy^*=\zeta(F,G,\mathrm{Pe}_{in})$. The numerical resolution of these first-order ordinary differential equations is performed by using a two-point boundary value algorithm developed in the Matlab® package. All the results shown in this paper are obtained with a relative tolerance for the residuals fixed to a constant value of 10^{-12}. More details on the numerical resolution are given in the Appendix.

4 Velocity, Pressure, and Temperature Profiles

4.1 Velocity Profiles. Our primary purpose is to compare the influence of the Reynolds number on the velocity profiles in both cases a and b. We derive in a first step the expression of f for two limiting cases: $\mathrm{Re}_{in}\to 0$ and $\mathrm{Re}_{in}\to\infty$. If $\mathrm{Re}_{in}\to 0$, Eq. (16*a*) reduces to $f^{(4)}=0$, whose solutions with boundary conditions (Eqs. (17) and (18)) are, respectively:

$$f_0(y^*)=-\frac{1}{2}y^{*3}+\frac{3}{2}y^*(\text{case a}) \quad f_0(y^*)=-2y^{*3}+3y^{*2}-1(\text{case b}) \tag{19}$$

On the other hand, when $\mathrm{Re}_{in}\to\infty$, the corresponding solution for case a is the Taylor flow:

$$f_\infty(y^*)=\sin\left(\frac{\pi y^*}{2}\right) \tag{20}$$

For case b, the solution given by Eq. (21) is valid for an inviscid fluid. Nevertheless, the actual no-slip condition $f'(1)=0$ at the upper wall is not consistent with the cosine profile,

$$f_\infty(y^*)=-\cos\left(\frac{\pi y^*}{2}\right) \tag{21}$$

The non-dimensional streamwise velocity profile $f'(y^*)=U^*(x^*,y^*)/x^*$ is shown in Fig. 3 for case a and case b, as a function of the Reynolds number. For the first flow configuration (Fig. 3(*a*)), profiles are shown only for the lower half-channel, between the lower porous wall ($y^*=-1$) and the channel centerline ($y^*=0$). This figure shows that the streamwise velocity profile for any finite and positive value of the Reynolds number is bounded between f_0' and f_∞', and that these two functions are very near each other. In particular, the maximum value of $f'(0)$, the normal velocity gradient on the centerline, is bounded between $f_0'(0)=1.5$ and $f_\infty'(0)=\pi/2\approx 1.57$. As a consequence, between the two asymptotic cases $\mathrm{Re}_{in}\to 0$ and $\mathrm{Re}_{in}\to\infty$, the variations of $f'(0)$ do not exceed 5%. Examining now Fig. 3(*b*) for case b, the results clearly show the influence of the no-slip condition at the upper wall. Profiles look somewhat like those obtained in a wall jet, with a maximum of streamwise velocity at some distance of the wall. The location of this maximum shifts towards the upper wall for increasing Reynolds numbers. This result is of course in accordance with the expected decrease of the dynamic boundary layer thickness with increasing values of Re_{in}.

Non-dimensional normal velocity profiles $-f(y^*)=V^*(x^*,y^*)$ are shown in Fig. 4. While the normal velocity profile is nearly insensitive to the Reynolds number for symmetric injection (Fig. 4(*a*)), its shape is clearly a function of Re_{in} for non-symmetric injection (Fig. 4(*b*)). The basic difference between case b compared to case a is that the velocity gradient at the upper wall $|dV^*/dy^*|_{y^*=1}=-f'(1)$ is always equal to zero, a consequence of the imposed no-slip condition. In conjunction with the other imposed boundary conditions $f(0)=-1$, $f'(0)=0$ and $f'(1)=0$, this implies the existence of an inflexion point somewhere between $y^*=0$ and $y^*=1$. The distance between the location of this inflection point and the upper wall, which can be defined as the dynamic boundary layer

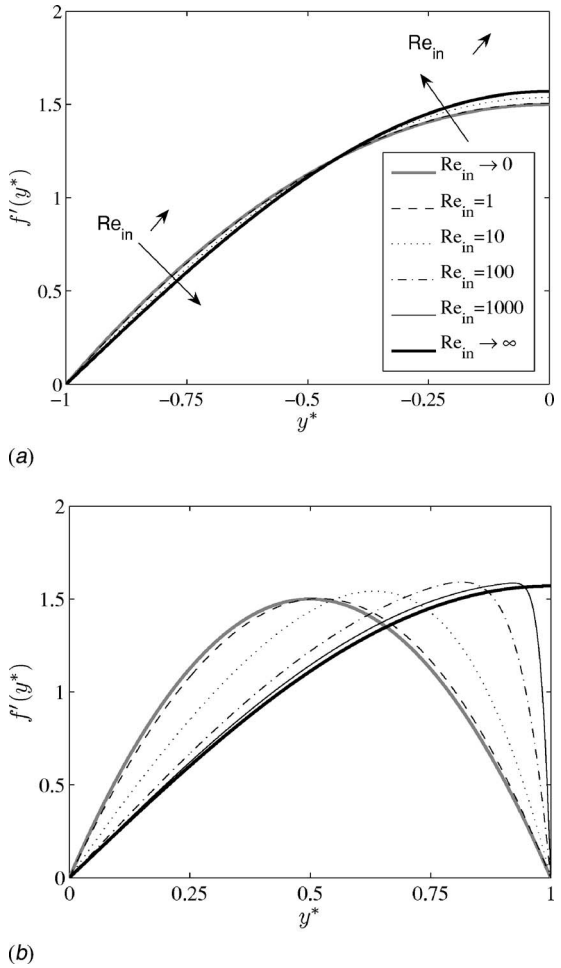

Fig. 3 Non-dimensional streamwise velocity profiles (*a*) case a and (*b*) case b

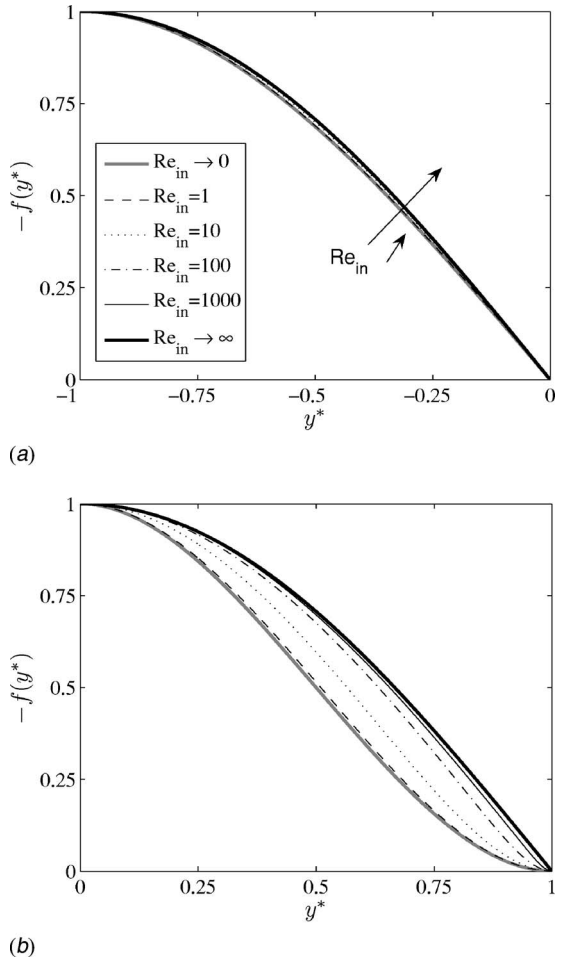

Fig. 4 Non-dimensional normal velocity profiles (*a*) case a and (*b*) case b

thickness, is therefore a measure of the spatial extent of viscous effects. In the near-wall region inside the dynamic boundary layer, f is a quadratic function of the distance to the wall, and its variations are dictated by the second derivative $f''(1)$, whose value is clearly in Fig. 4(*b*) an increasing function of the Reynolds number. We plotted in Fig. 5 the streamlines in both geometries for low and high Reynolds numbers ($\mathrm{Re_{in}}=1$ and 1000). The influence of viscous effects on the curvature of the streamlines at low Reynolds number is clearly shown in Fig. 5(*b*).

We summarize the main results concerning the effect of the Reynolds number on the velocity profile in both geometries. For symmetric injection (case a), the similarity function f, as well as its gradient f', is weakly dependant on the value of the Reynolds number. Near the centerline, the normal velocity profile is a linear function of the spatial coordinate y^*. For non-symmetric injection (case b), the streamwise velocity profile is different from the profile encountered in a usual boundary layer developing along a flat plate; it is similar to a wall-jet velocity profile. The shape of f is strongly dependant on the value of $\mathrm{Re_{in}}$, and exhibits an inflection point. In the near-wall region inside the boundary layer, the normal velocity profile is a quadratic function of the distance to the wall, and its radius of curvature $f''(1)$ increases with $\mathrm{Re_{in}}$. For a fixed $\mathrm{Re_{in}}$, the values of the normal velocity in case b are always smaller than in case a.

4.2 Pressure Profiles. We derive in this part the value of the pressure field. By combining Eqs. (12), (13), (15), and (16*a*), one obtains the following expression for the pressure:

$$P^*(x^*,y^*) = -K\frac{x^{*2}}{2} + \pi(y^*) \tag{22}$$

with

$$\pi(y^*) = -\frac{f^2}{2} - \frac{1}{\mathrm{Re_{in}}}f' \tag{23}$$

In order to analyze the mechanisms fixing the value of the axial pressure gradient, we applied the momentum theorem to the control volume described in Fig. 2 for the case a. We obtain the following expression:

$$\int_{S_{x+dx}} \rho U^2 dS - \int_{S_x} \rho U^2 dS = -|\tau_e| \,.\, e \,.\, dx - \tau_{-e} \,.\, e \,.\, dx - \int_{S_{x+dx}} P dS + \int_{S_x} P dS \tag{24}$$

where τ_e (τ_{-e}) is the wall shear stress at $y=e$ ($y=-e$). Using the fact that $\tau_e^*=-\tau_{-e}^*$ due to the symmetry of the flow, we derive the following equation:

$$\rho\frac{d}{dx}\left[\int_{-1}^{1} U^2(x,y)dy\right] = -2|\tau_e| - \frac{d}{dx}\left[\int_{-e}^{e} P(x,y)dy\right] \tag{25}$$

In non-dimensional form and by using (22), we obtain the value of the constant K involved in the axial pressure gradient:

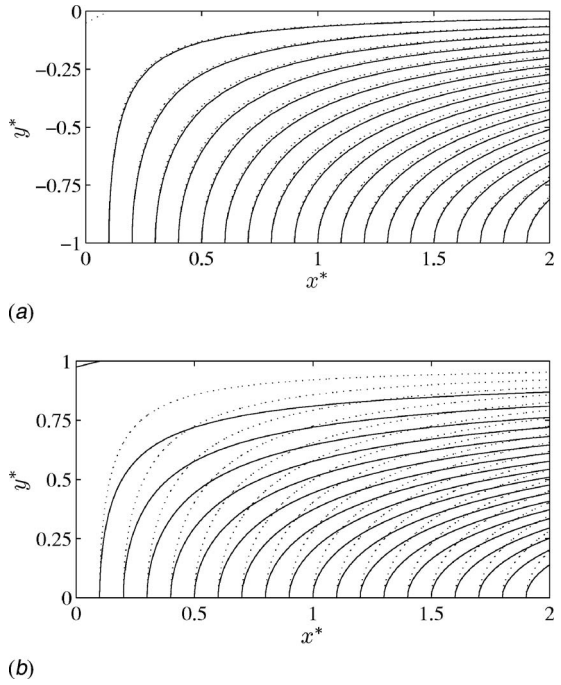

Fig. 5 Streamlines: – –: $Re_{in}=1$ and —: $Re_{in}=1000$ (*a*) case a and (*b*) case b

$$K = \int_{-1}^{1} f'^2(y)dy - \frac{1}{\mathrm{Re}_{\mathrm{in}}} f''(1) \tag{26}$$

Both terms of the right-hand side are positive; therefore, we conclude that the axial pressure gradient is always negative and that its value results from a balance between the acceleration of the flow and the viscous friction at the wall.

The value of K for case b is obtained in the same manner:

$$K = 2\int_{0}^{1} f'^2(y)dy - \frac{1}{\mathrm{Re}_{\mathrm{in}}}[f''(1) - f''(0)] \tag{27}$$

The evolution of K with $\mathrm{Re}_{\mathrm{in}}$ is shown in Fig. 6 for case a and case b. It clearly appears that the viscous part in K is decreasing with $\mathrm{Re}_{\mathrm{in}}$ very quickly in case a (it is negligible at $\mathrm{Re}_{\mathrm{in}}=10$), while it remains more important in case b at the same Reynolds number.

4.3 Temperature Profiles. The temperature profile $\theta(y^*)$ is shown in Fig. 7 for different values of the Reynolds and Péclet numbers. Since the wall temperature $\theta_w=\theta(y^*=1)$ is increasing with $\mathrm{Re}_{\mathrm{in}}$ for non-symmetric injection (imposed heat flux at the upper wall), we stretched the vertical scale by showing in Fig. 7(*b*) the normalized profile $\theta(y^*)/\theta_w$ in order to facilitate the comparisons with case a. For a given Péclet number, as the Reynolds number is increasing from 0 to infinity, the temperature profile is evolving in both cases from a linear one (pure diffusive profile) to a more classical thermal boundary layer type, whose thickness is decreasing with increasing values of $\mathrm{Re}_{\mathrm{in}}$. The effect of the Péclet number is also shown. For a low fixed value of the Reynolds number, the ratio between velocity and thermal boundary layer thickness is strongly decreased when the Prandtl (or Péclet) number is multiplied by seven.

We compare in Fig. 8 for two values of the Reynolds number the computed temperature profiles for both geometries. For a fixed position inside the thermal boundary layer and a given Reynolds number, the temperature is smaller in case b than in case a. Reminding that normal velocities are always smaller for non-symmetric injection, the balance between advection and diffusion implies a thicker thermal boundary layer than for symmetric injection.

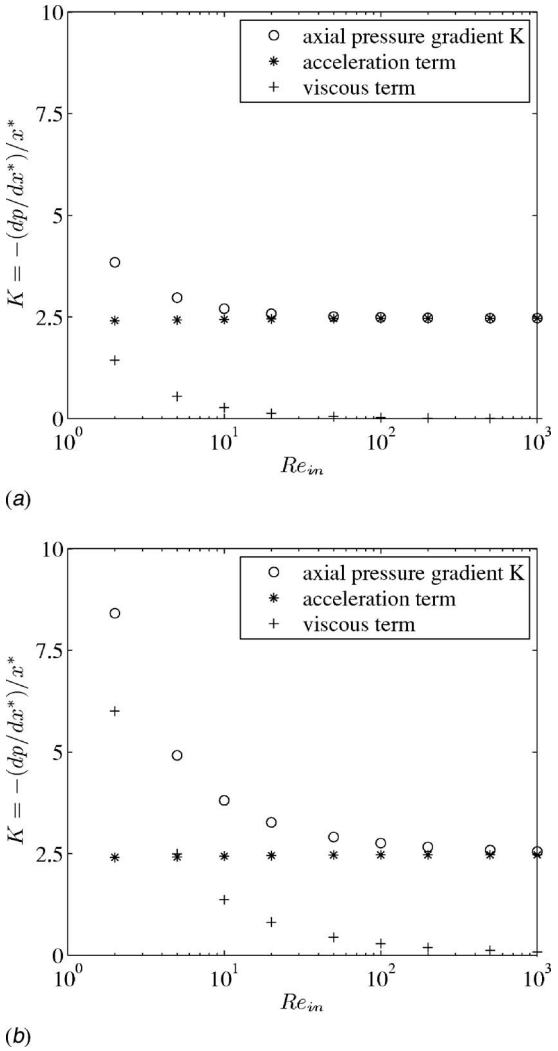

Fig. 6 Evolution of *K* with the Reynolds number (*a*) case a and (*b*) case b

4.4 Thermal Boundary Layer Thickness. In this section, we derive results concerning the scaling law of the thermal boundary layer thickness with the governing parameter of the problem, i.e., $\mathrm{Pe}_{\mathrm{in}}$. We first show in Fig. 9 the evolution with $\mathrm{Pe}_{\mathrm{in}}$ of the two parameters $f'(0)$ (case a) and $f''(1)$ (case b) governing the shape of the normal velocity profile inside the thermal boundary layer. While $f'(0)$ is nearly independent of $\mathrm{Re}_{\mathrm{in}}$, the radius of curvature $f''(1)$, which is also representative of the friction at the upper wall, presents a scaling law of the type: $f''(1)\sim \mathrm{Pe}_{\mathrm{in}}^{1/2}$.

If we now turn back to the original energy equation which in the present case reduces to an ordinary differential equation, we can write:

$$V\frac{dT}{dy} = \alpha\frac{d^2T}{dy^2} \tag{28}$$

Let us define the thermal boundary layer thickness δ_t as the distance in which T varies of an order ΔT, and let V be the order of magnitude of the normal velocity variation on a distance δ_t from the centerline (case a) or from the upper wall (case b). The order of magnitude of the right-hand side of Eq. (28) is $\alpha\Delta T/\delta_t^2$; the order of magnitude of the left-hand side is $V\Delta T/\delta_t$; therefore,

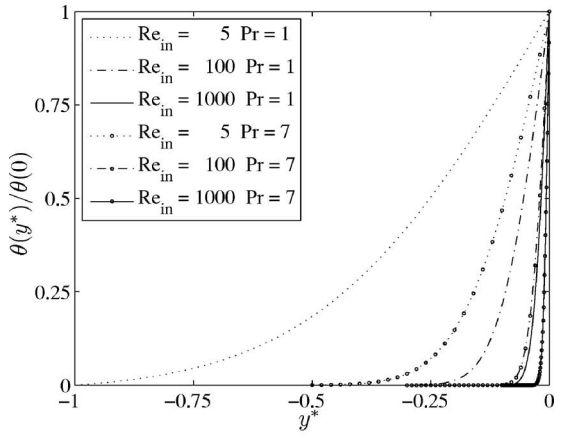

(*a*)

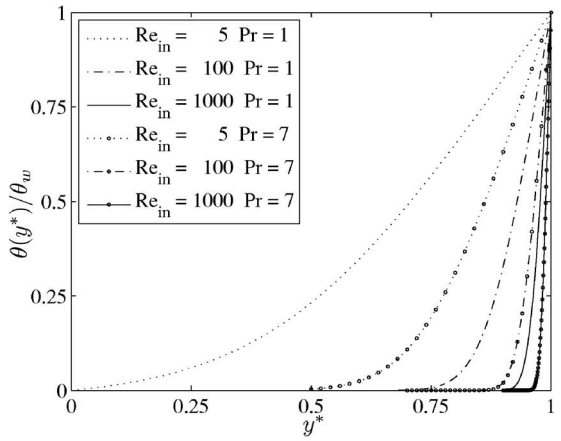

(*b*)

Fig. 7 Non-dimensional temperature profiles (*a*) case a and (*b*) case b

$\delta_t/e \sim \alpha/Ve$. Cases a and b differ in the estimate of the magnitude of V. We will now deduce these values from a Taylor expansion of f.

Scaling Law for Case a. In the vicinity of the centerline, we can write: $V \sim f'(0)V_{\text{in}}\delta_t/e$. Using this value for V, we obtain: $(\delta_t/e)^2 \sim [\text{Pe}_{\text{in}} f'(0)]^{-1}$. Since $f'(0)$ is nearly independent of Re_{in} (or Pe_{in}), we finally obtain the scaling law:

$$\left(\frac{\delta_t}{e}\right) \sim \text{Pe}_{\text{in}}^{-1/2} \tag{29}$$

Scaling Law for Case b. As seen previously, near the upper wall, f is a quadratic function (since $f(1)=f'(1)=0$) and a Taylor expansion of the velocity field gives: $V \sim f''(1)V_{\text{in}}/2(\delta_t/e)^2$. Using this estimate of V, we deduce the relation: $(\delta_t/e)^3 \sim (\text{Pe}_{\text{in}} f''(1))^{-1}$. Since $f''(1) \sim \text{Re}_{\text{in}}^{1/2} \sim \text{Pe}_{\text{in}}^{1/2}$, we derive:

$$\left(\frac{\delta_t}{e}\right) \sim \text{Pe}_{\text{in}}^{-1/2} \tag{30}$$

As a conclusion, although the normal velocity profiles have a quite different behavior in case a and case b, the scaling law predicting the variation of the thermal boundary layer thickness with the Péclet number is a power law with a −0.5 exponent in both cases. This scaling is quite different from that obtained for the suction case studied by Ferro and Gnavi [19]. For the case of symmetric suction, thermal boundary layers are attached to the lower and upper porous walls, and the authors found that the scaling law for δ_t with Pe_{in} is $(\delta_t/e) \sim \text{Pe}_{\text{in}}^{-1}$. According to the −0.5 exponent, the thermal boundary layer thickness for injection decreases much more slowly with increasing Pe_{in}, compared to the suction case. This explains the stiffness of the numerical solution appears for higher values of Pe_{in}, in the case of injection compared to suction.

The preceding results are derived from definitions of the thermal boundary layer thickness δ_t based on a Taylor expansion of f in the vicinity of the centerline for symmetric injection and in the vicinity of the upper wall for non-symmetric injection. We can now detail the values of the thermal boundary layer thickness in each case. If we define a new variable z by the following relations: $z=\sqrt{\text{Pe}_{\text{in}} f'(0)}\,y$ ($z=[\text{Pe}_{\text{in}} f''(1)/2]^{1/3}(1-y^*)$ for case b), the Taylor expansion of the velocity field leads to a simplified equation for the temperature (where the symbol "′" now denotes differentiation with respect to z):

$$\theta'' + z\theta' = 0 \text{ (case a)} \quad \theta'' - z^2\theta' = 0 \text{ (case b)} \tag{31}$$

With these change of variables, we introduce mathematically for each case a characteristic length scale δ_t, defined as the thermal boundary layer thickness, by the following relations:

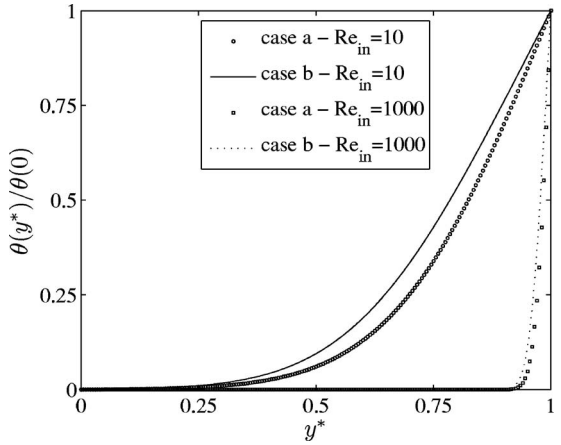

Fig. 8 Non-dimensional temperature profiles: $\text{Re}_{\text{in}}=10$ and $\text{Re}_{\text{in}}=1000$

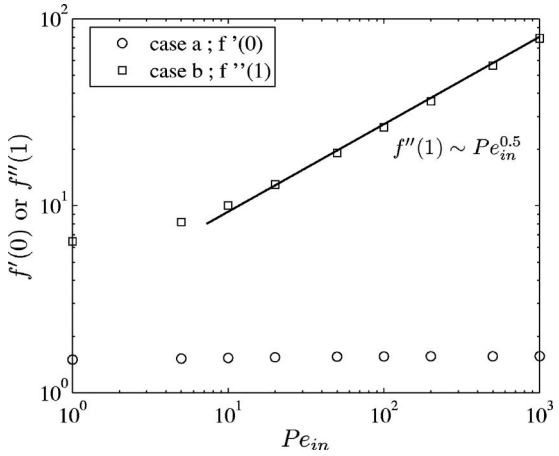

Fig. 9 Scaling laws for $f'(0)$ and $f'(1)$

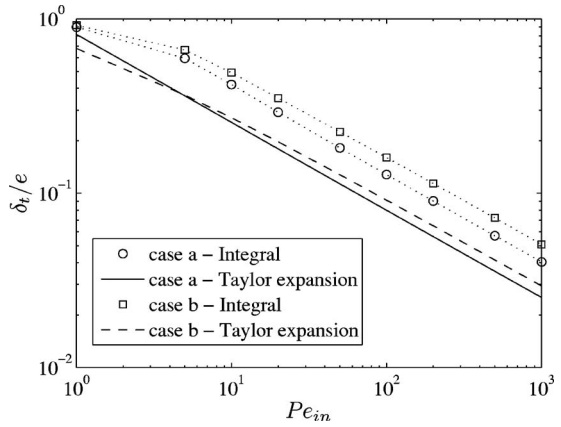

Fig. 10 Scaling laws for the thermal boundary layer thickness (Eqs. (32) and (33))

$$\frac{\delta_t}{e} = [\mathrm{Pe_{in}} f'(0)]^{-1/2} \text{ (case a)} \quad \frac{\delta_t}{e} = \left[\frac{\mathrm{Pe_{in}} f''(1)}{2}\right]^{-1/3} \text{ (case b)} \tag{32}$$

These definitions are consistent with those derived from dimensional analysis.

We can also define the thermal boundary layer thickness in a more classical and global way with a quantity explicitly related to the overall shape of the computed temperature profile. We thus consider the following expressions:

$$\frac{\delta_t}{e} = 4\int_{-1}^{0} \theta^*(y)dy \text{ (case a)} \quad \frac{\delta_t}{e} = 2\int_{0}^{1} \frac{\theta^*(y)}{\theta_w}dy \text{ (case b)} \tag{33}$$

The constants in Eq. (33) have been chosen to arbitrarily obtain $\delta_t/e=1$ for $\mathrm{Pe_{in}}\to 0$.

We compare in Fig. 10 the values of the thermal boundary layer thickness deduced from Eq. (32) and (33), respectively. For a given geometry and Péclet number, the value of the boundary layer thickness deduced from Eq. (33) is somewhat larger than this given by Eq. (32). Moreover, for a fixed Péclet number and in the non-symmetric case, the thermal boundary layer is thicker with both definitions of δ_t than for a symmetric case, as already noted in Sec. 4.2. As expected, all definitions give the same scaling law with the Péclet number: $(\delta_t/e)\sim \mathrm{Pe_{in}}^{-1/2}$, except for small values of the Péclet number.

5 Asymptotic Expansions and Simplified Models for the Thermal Field

In the case of suction through porous walls, Ferro and Gnavi [19] noted that the numerical solution is stiff even for small values of Reynolds number, typically about 10. In the case of injection, the numerical solution of the set equations is stiff with standard techniques for higher values of the Reynolds number, $\mathrm{Re_{in}}\sim 1000$ typically. Nevertheless, it is suitable to derive asymptotic or approximate expansions for f or θ. In this section, we derive two different approximate of the temperature field, and we compare these asymptotic expressions with the computed one.

5.1 Asymptotic Expansions. Ferro and Gnavi [19] used an asymptotic expansion of the temperature profile θ in the limit of large values of $\mathrm{Pe_{in}}$ (large thermal diffusivity). Integrating Eq. (31), Ferro and Gnavi obtained the following approximate expression θ_a for the temperature near the channel centerline:

$$\theta_a(y^*) = \sqrt{\frac{f'(0)\mathrm{Pe_{in}}}{2\pi}}\int_{-1}^{y^*} \exp\left(\frac{-\mathrm{Pe_{in}} f'(0)\,\eta^2}{2}\right)d\eta \tag{34}$$

With the same approach for the case of non-symmetric injection (case b), we use a Taylor expansion of the velocity field near the upper wall. We derive the following simplified equation for the temperature:

$$\theta_a'' + \frac{\mathrm{Pe_{in}} f''(1)}{2}(1-y^*)^2\theta_a' = 0 \tag{35}$$

whose solution is:

$$\theta_a(y^*) = \mathrm{Pe_{in}}\int_{0}^{y^*} \exp\left(\frac{\mathrm{Pe_{in}} f''(1)(1-\eta)^3}{6}\right)d\eta \tag{36}$$

5.2 Simplified Models. We now derive an other approximate solution θ_m for the temperature profile θ. Let us assume that the velocity field is always independent of $\mathrm{Re_{in}}$, and is equal to the similarity function given by Eqs. (20) and (21) in the limit of very large Reynolds numbers (Taylor flow). Combining Eqs. (20), (21), and (31), we derive the following solutions for the temperature gradient θ_m':

$$\theta_m'(y^*) = \theta'(0)\exp\left[\frac{2}{\pi}\mathrm{Pe_{in}}\left(\cos\left(\frac{\pi y^*}{2}\right)-1\right)\right] \text{ (case a)} \tag{37}$$

and

$$\theta_m'(y^*) = \theta'(0)\exp\left[\frac{2}{\pi}\mathrm{Pe_{in}}\sin\left(\frac{\pi y^*}{2}\right)\right] \text{ (case b)} \tag{38}$$

Integrating one more time, and using the specified boundary conditions, we finally obtain after some algebra the temperature profiles:

$$\theta_m(y^*) = \frac{I(y^*)}{I(1)} \text{ where } I(y^*) = \int_0^{y^*} \exp\left\{\frac{2}{\pi}\mathrm{Pe_{in}}\left[\cos\left(\frac{\pi\eta}{2}\right)-1\right]\right\}d\eta \text{ (case a)} \tag{39}$$

$$\theta_m(y^*) = \mathrm{Pe_{in}}\int_0^{y^*} \exp\left\{-\frac{2}{\pi}\mathrm{Pe_{in}}\left[1-\sin\left(\frac{\pi\eta}{2}\right)\right]\right\}d\eta \text{ (case b)} \tag{40}$$

We now turn back to the assumption performed in Sec. 2 when applying the first law of thermodynamics to the control volume. In the balance between outcome and income enthalpy fluxes, we neglect the heat flux at the lower porous wall, compared to the heat flux q_w imposed at the upper impermeable wall. Such an assumption is justified if the ratio between these two fluxes, which in non-dimensional form is equal to $\theta'(1)/\theta'(0)$, is large enough. Eq. (38) with $y^*=1$, in conjunction with the boundary condition $\theta'(1)=\mathrm{Pe_{in}}$, gives a crude estimate of this ratio: $\theta_m'(1)/\theta_m'(0) = \exp(2\mathrm{Pe_{in}}/\pi)$. We conclude that even for a moderate value of the Péclet number, e.g., $\mathrm{Pe_{in}}=5$, the ratio between the two fluxes is equal to 24, and that the assumption was justified.

5.3 Comparisons With Computed Solutions. The temperature computed with Eq. (16*b*) is compared in Figs. 11 and 12 to the asymptotic (Eqs. (34) and (36)) and modeled temperatures (Eqs. (39) and (40)). For a wide range of Reynolds and Péclet numbers in the case of symmetric injection, the actual temperature profile is accurately approximated both by modeled θ_m and asymptotic θ_a temperatures. Results shown for non-symmetric injection shows that the agreement is poor between actual and both asymptotic and modeled temperatures, even if θ_m is in better agreement with the computed temperature θ far from the upper wall. Even if asymptotic and modeled temperatures remain always

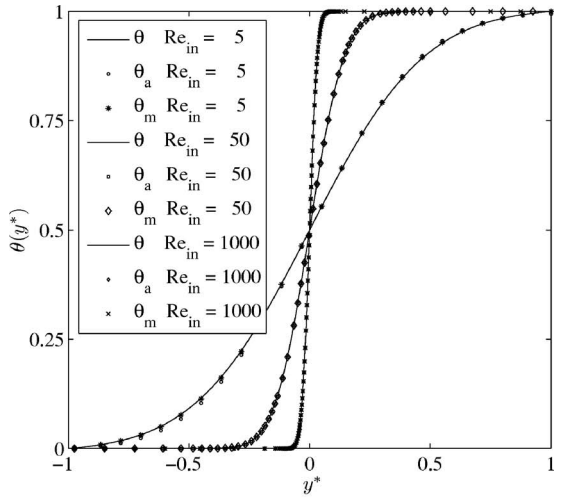

(*a*)

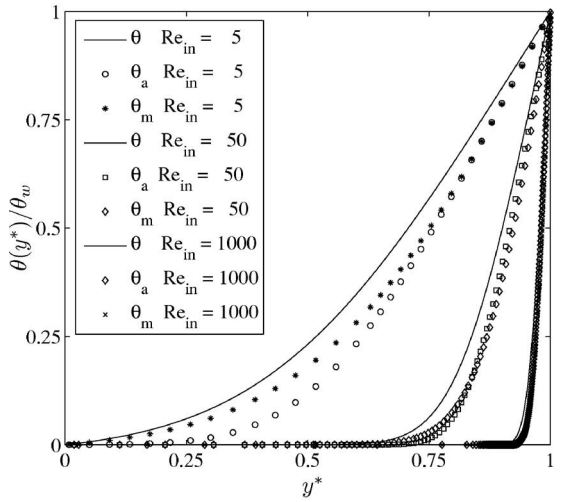

(*b*)

Fig. 11 Computed, asymptotic, and modeled temperature profiles, Pr=1 (*a*) case a and (*b*) case b

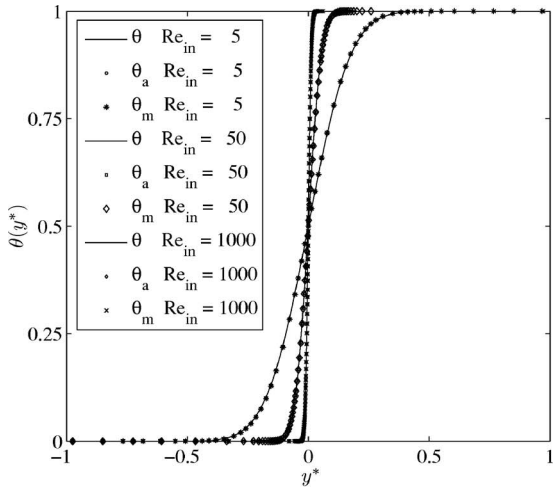

(*a*)

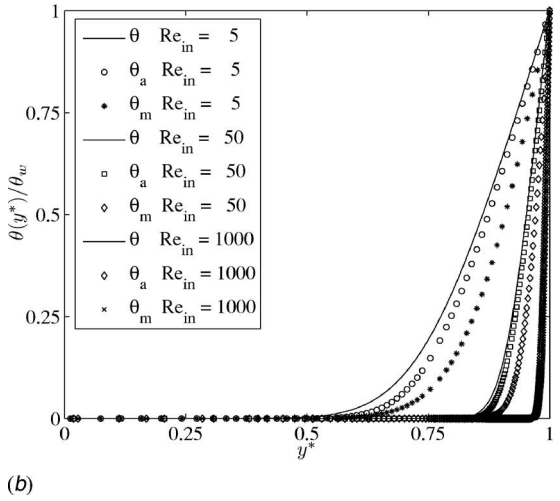

(*b*)

Fig. 12 Computed, asymptotic, and modeled temperature profiles, Pr=7 (*a*) case a and (*b*) case b

overpredicted, the agreement is better if the Péclet number is increased for a fixed value of the Reynolds number. As expected, for non-symmetric injection, neither Eq. (36) nor Eq. (40) are able to reproduce accurately the actual value of the temperature profile in a large range of Péclet numbers, because the proposed expansions for the velocity fields are too far from the actual one with an inflexion point. The agreement between computed and asymptotic temperatures is satisfactory only if the Prandtl number is increased at a fixed value of the Reynolds number, since temperature gradients are located in a thin region where the approximate of f by a quadratic function of the upper-wall distance would be very accurate. However, as shown by Ferro and Gnavi, for higher values of the Prandtl number representative of liquids, viscosity variations with temperature need to be taken into account in that case.

6 Correlation for the Heat Transfer Coefficient

For engineering applications, one important issue in heat transfer problems is the value of the heat transfer coefficient, and its dependence with Reynolds and Prandtl numbers. In this section, we derive an expression of this coefficient in case b. The heat transfer coefficient h characterizing the overall heat transfer efficiency between the upper wall and the flow is defined as $q_w = h(T_w - T_b)$. Since both q_w and $T_w - T_b$ are independent of x, h is also uniform with x. Recalling that by definition: $\theta_w = (T_w - T_1)/T_f$, we can express $T_w - T_b$ as: $T_w - T_b = T_f\theta_w + T_1 - T_b$. Using Eq. (10) for the relation between T_b, T_1 and T_f, we obtain $T_w - T_b = T_f(\theta_w - 1)$. Finally, the value of h is $h = q_w/T_f(\theta_w - 1)$, and using Eq. (11) for T_f, the Nusselt number $\mathrm{Nu} = he/\lambda$ can be written:

$$\mathrm{Nu} = V_{\mathrm{in}} e \frac{\rho C_p}{\lambda} \frac{1}{\theta_w - 1}$$

Introducing the Reynolds and Péclet numbers, we finally obtain the correlations among Nu, $\mathrm{Re_{in}}$ and $\mathrm{Pe_{in}}$:

$$\mathrm{Nu} = \frac{\mathrm{Pe_{in}}}{\theta_w(\mathrm{Re_{in}}, \mathrm{Pe_{in}}) - 1} \tag{41}$$

The computed values of θ_w are shown in Fig. 13 as a function of $\mathrm{Re_{in}}$ for Pr=1 and Pr=7. The results show that for large Reynolds numbers, θ_w scales as $\mathrm{Re_{in}^{-1/2}}$. Therefore, using Eq. (41), we conclude that for large Reynolds numbers, the scaling law of Nu should be: $\mathrm{Nu} \sim \mathrm{Re_{in}^{1/2}}$. This result is shown in Fig. 14, where the Nusselt number is plotted as a function of the Reynolds number.

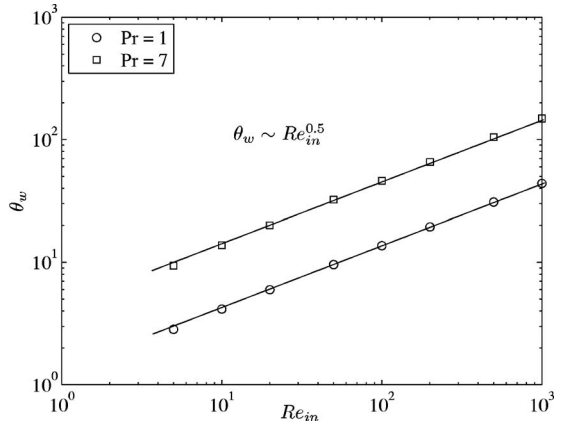

Fig. 13 Evolution of the wall temperature with the Reynolds number (case b)

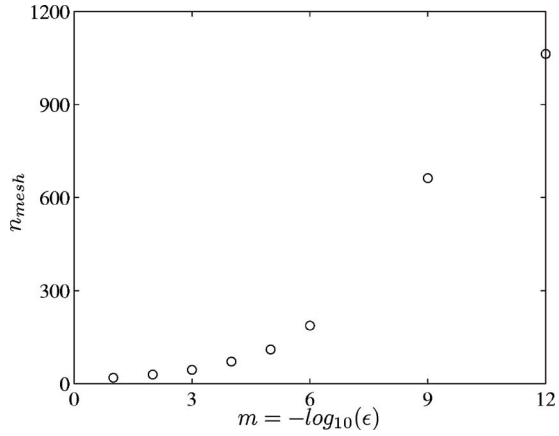

Fig. 15 Evolution of the number of mesh points with the tolerance $\epsilon = 10^{-m}$ ($Re_{in} = 1000$ and $Pe_{in} = 1$)

7 Conclusion

The behavior of velocity and temperature fields of a symmetric or non-symmetric laminar channel flow generated by blowing is compared. The first law of thermodynamics permits to conclude in both cases on the independence of bulk temperature with streamwise coordinate and to compute its value as a function of the imposed temperatures and heat flux. Under the assumption of steady similarity solutions, we resolve the governing equations of the flow for a wide region of the governing parameter Re_{in}. For the symmetric case, the velocity profile is weakly dependent on the value of the Reynolds number whereas for the non-symmetric case, the quadratic variation of the similarity function near the upper wall is very sensitive to Re_{in}. Temperature profiles evolve significantly with the value of Pe_{in}. The thermal boundary layer thickness δ_t is estimated by various methods which all give the following relationship between δ_t and Pe_{in} for the two cases, i.e., $(\delta_t/e) \sim Pe_{in}^{-1/2}$, except for small values of the Péclet number. Nevertheless the thermal boundary layer thickness deduced from the computed temperature profile is thicker for non-symmetric injection than for symmetric case. The actual, asymptotic and modeled values of the temperature are very similar for the symmetric case over a wide range of Re_{in} and Pe_{in}. Significant discrepancies are visible for the non-symmetric case, but the improvement is better if the Péclet number is increasing. The proposed expansions used for the velocity field fail to reproduce the inflexion point of the normal velocity profile. Finally, we compute the value of the heat coefficient transfer between the channel wall and the stream. We obtain for large Reynolds number a scaling law of the Nusselt number according to the following relation: $Nu \sim Re_{in}^{1/2}$.It would be interesting to extend this analysis to a closed head end channel, which corresponds to a more realistic engineering configuration, in order to analyze the impact of the boundary layer attached to this wall on the velocity and temperature fields.

Nomenclature

e = distance between walls, m
f = non-dimensional similarity function for velocity
h = heat transfer coefficient, W m^{-2} K^{-1}
i = specific enthalpy, J kg^{-1} K^{-1}
U = streamwise velocity, m s^{-1}
V = normal velocity, m s^{-1}
Nu = Nusselt number
Pe = Péclet number
Re = Reynolds number
T = temperature, K
x = streamwise direction, m
y = normal direction, m
α = thermal diffusivity, m^2 s^{-1}
δ_t = thermal boundary layer thickness, m
λ = thermal conductivity, W m^{-1} K^{-1}
ν = kinematic viscosity, m^2 s^{-1}
ϕ = stream function, m^2 s^{-1}
θ = non-dimensional similarity function for temperature

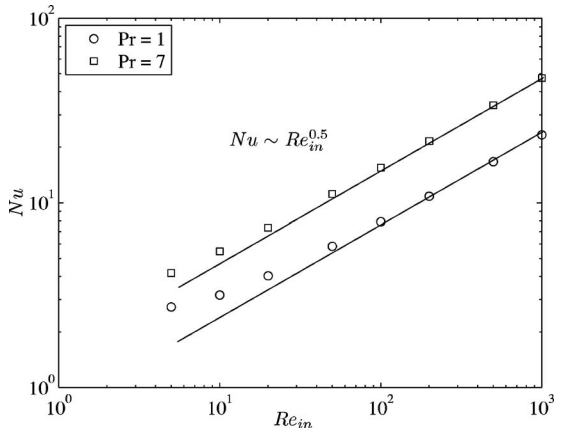

Fig. 14 Nusselt number as a function of Reynolds number

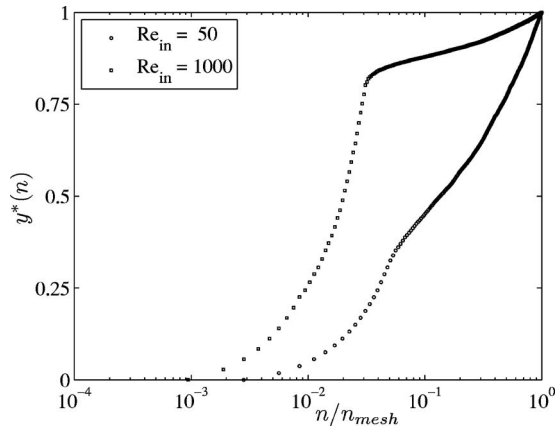

Fig. 16 Location of the mesh points for $Re_{in} = 50$ and 100 and $Pr = 1$ ($\epsilon = 10^{-12}$)

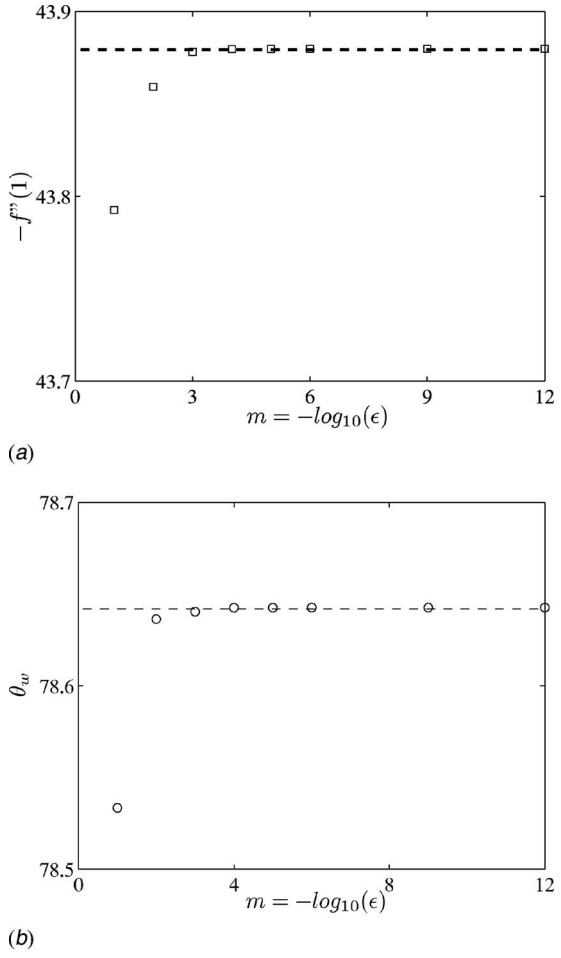

Fig. 17 Evolution of the computed functions with the tolerance $\epsilon = 10^{-m}$ ($Re_{in} = 1000$ and $Pe_{in} = 1$)

Subscripts

b = bulk mean quantity
in = condition at injection surface
w = upper wall

Superscripts

$*$ = non-dimensional variable

Appendix: Numerical Resolution of the Boundary Value Problem

Since boundary conditions (17) and (18) are defined at both ends of the interval y^*, the set of differential equations is a boundary value problem (BVP). In general, a BVP may have a solution, or several solutions. Fortunately, [22] has shown that the problem has one unique solution for the injection case. We solved simultaneously the coupled set of equations for $F=(f,f',f'',f''')$ and $G=(\theta,\theta')$ by using the bvp4c solver in Matlab®. This function implements a collocation method based on the approximation of the solution by a cubic polynomial on each subinterval $[y_n^*, y_{n+1}^*]$ of the mesh, and by imposing the differential equations at both ends and at the midpoint of each subinterval. These conditions result in a system of nonlinear algebraic equations for the coefficients of the approximate solution. These equations are solved iteratively by linearization. This is the reason that it is necessary to supply a guess solution to initialize the iterative process whose convergence is strongly dependent upon the quality of this guess solution. Therefore, we solved the set of differential equations for each integer value of the Reynolds number in the range $Re_{in}=1$ to $Re_{in}=1000$. We used a continuation technique, i.e., for the Reynolds number $Re_{in}=n+1$, we supply as guess functions the solutions f_n and θ_n calculated for the previous value $Re_{in}=n$. For the firstReynolds number ($Re_{in}=1$), the guess function for f is the asymptotic function f_0 given by Eq. (19) and it is a linear function for θ (pure diffusion).

The total number and location of mesh points are defined by the relative tolerance ϵ for the residuals. We show in Fig. 15 the evolution of the total number of mesh points n_{mesh} as a function of ϵ, and in Fig. 16 in a semilog graphic the spatial location of the mesh points for case b (for $Re_{in}=50$ and $Re_{in}=1000$ and with $\epsilon = 10^{-12}$). It is clear that the largest part of the mesh is located inside the boundary layer for large Reynolds numbers. We checked that the computed f and θ functions are independent of the mesh. As an example, we give in Fig. 17 the evolution of two important quantities, the wall friction $-f''(1)$ and the wall temperature $\theta(1)$ as a function of m, where the imposed relative tolerance ϵ is written as $\epsilon=10^{-m}$; both quantities are weakly dependent upon m, provided that $m>5$.

References

[1] Taylor, G. I., 1956, "Fluid Flow in Regions Bounded by Porous Surfaces," Proc. R. Soc. London, Ser. A, **234**(1199), pp. 456–475.
[2] Berman, A., 1953, "Laminar Flow in Channels With Porous Wall," J. Appl. Phys., **24**(9), pp. 1232-1235.
[3] Dunlap, R., Willoughby, P. G., and Hermsen, R. W., 1974, "Flowfield in the Combustion of a Solid Propellant Rocket Motor," AIAA J., **12**(12), pp. 1440–1442.
[4] Beddini, R. A., 1986, "Injection-Induced Flows in Porous-Walled Duct," AIAA J., **24**(11), pp. 1766–1773.
[5] Fournier, C., Bataille, F., and Michard, M., 2005, "Transition Characteristics of Flowfield in a Non-isothermal Duct With Wall Injection," *Proceedings of 4th International Conference on Computational Heat and Mass Transfer*, R. Bennacer et al.., Tec & Doc, Paris, Vol. 2, pp. 899–904.
[6] Fournier, C., 2005, "Study of Heat and Mass Transfer in a Channel Flow Generated by Blowing Through a Porous Wall," Ph.D. thesis, National Institut of Applied Sciences, France.
[7] Casalis, G., Avalon, G., and Pineau, J. P., 1998, "Spatial Instability of Planar Channel Flow With Fluid Injection Through Porous Walls," Phys. Fluids, **10**(10), pp. 2558–2568.
[8] Terrill, R. M., 1964, "Laminar Flow in a Uniformly Porous Channel," Aeronaut. Q., **15**, pp. 299–310.
[9] Durlofsky, L., and Brady, J. F., 1984, "The Spatial Stability of a Class of Similarity Solutions," Phys. Fluids, **27**, pp. 1068–1076.
[10] Ferro, S., and Gnavi, G., 2000, "Spatial Stability of Similarity Solutions for Viscous Flows in Channels with Porous Walls," Phys. Fluids, **12**, pp. 797–802.
[11] Terrill, R. M., and Shrestha, G. M., 1965, "Laminar Flow through Parallel and Uniformly Porous Walls of Different Permeability," Z. Angew. Math. Phys., **16**, pp. 470–482.
[12] Cox, S., 1991, "Two-Dimensional Flow of a Viscous Fluid in a Channel With Porous Walls," J. Fluid Mech., **227**, pp. 1–33.
[13] Culick, F. E. C., 1966, "Rotational Axisymmetric Mean Flow and Damping of Acoustic Waves in Solid Propellant Rocket Motors," AIAA J., **4**(8), pp. 1462–1464.
[14] Traineau, J. C., Hervat, P., and Kuentzmann, P., 1986, "Cold-Flow Simulation of a Two-Dimensional Nozzleless Solid-Rocket Motor", AIAA Paper 1986-1447.
[15] Liou, T. M., Lien, W. Y., and Hwang, P. W., 1998, "Transition Characteristics of Flowfield in a Simulated Solid-Rocket Motor," J. Propul. Power, **14**(3), pp. 282-289.
[16] Chaouat, B., 2002, "Numerical Predictions of Channel Flows With Fluid Injection Using Reynolds-Stress Model," J. Propul. Power, **18**(2), pp. 295–303.
[17] Apte, S., and Yang, V., 2000, "Large Eddy Simulation of Internal Flowfield in Porous Chamber With Surface Mass Injection," AIAA Paper 2000-0709.
[18] Fournier, C., Michard, M., and Bataille, F., 2006, "Numerical Simulations of a Confined Channel Flow Driven by Non Isothermal Wall Injection," Prog. Comput. Fluid Dyn., **6**(1/2/3), pp. 129-136.
[19] Ferro, S., and Gnavi, G., 2002, "Effects of Temperature-Dependent Viscosity in Channels With Porous Walls," Phys. Fluids, **14**(2), pp. 839–849.
[20] Bejan, A., 1993, *Heat Transfer*, Wiley & Sons, New York, 6.
[21] Deng, C., and Martinez, D. M., 2005, "Linear Stability of a Berman Flow in a Channel Partially Filled With a Porous Media," Phys. Fluids, **17**(2), 024102.
[22] Lu, C., 1997, "On the Existence of Steady Flow in a Channel with One Porous Wall or Two Accelerating Walls," *Proceedings of the Third Mississippi State Conference on Differential Equations and Computational Simulations*, Electron. J. Differ. Equations, Conference 01, 1997, pp. 159–170.

PIV Study of Shallow Open Channel Flow Over *d*- and *k*-Type Transverse Ribs

M. F. Tachie
e-mail: tachiemf@cc.umanitoba.ca

K. K. Adane

Department of Mechanical and Manufacturing Engineering,
University of Manitoba,
Winnipeg, Manitoba, R3T 5V6, Canada

A particle image velocimetry was used to study shallow open channel turbulent flow over d-type and k-type transverse ribs of square, circular, and semi-circular cross sections. The ratio of boundary layer thickness to depth of flow varied from 50% to 90%. The mean velocities and turbulent quantities were evaluated at the top plane of the ribs to characterize interaction between the cavities and overlying boundary layer. It was found that the overlying boundary layer interacts more strongly with k-type cavities than observed for d-type cavities. The profiles of the mean velocities and turbulent statistics were then spatially averaged over a pitch, and these profiles were used to study the effects of rib type and cross section on the flow field. The mean velocity gradients were found to be non-negligible across the boundary layer, and the implications of this observation for momentum transport, eddy viscosity, and mixing length distributions are discussed. The results show that the skin friction coefficient, Reynolds stresses and mixing length distributions are independent of rib cross section for d-type. For the k-type ribs, significant variations in skin friction coefficient values, mean flow, and turbulence fields are observed between square ribs and circular/semi-circular ribs. [DOI: 10.1115/1.2746910]

1 Introduction

Two-dimensional transverse ribs are employed in many engineering applications to augment heat transfer rates. They are also often used to study the effects of surface roughness on momentum transport. It is customary to classify these types of rib/roughness into *d*-type and *k*-type based on pitch-to-height-ratio λ/k (Perry et al. [1]; Tani [2]). In this study, $\lambda/k \leqslant 4$ is characterized as *d*-type and $\lambda/k > 4$ as *k*-type ribs. Numerous experiments in turbulent flow over transverse ribs have been made in zero-pressure-gradient boundary layers and fully developed channels. Sato et al. [3] conducted laser Doppler anemometry (LDA) measurements in a channel with both top and bottom walls roughened with square ribs arranged to produce $\lambda/k=7$. Okamoto et al. [4] studied boundary layer flow over square ribs for $2 \leqslant \lambda/k \leqslant 17$. Agelinchaab and Tachie [5] employed a particle image velocimetry (PIV) to measure the mean velocities and turbulent statistics in open channel turbulent flow over three-dimensional hemispherical ribs. A number of direct numerical simulations (DNS) and large eddy simulations (LES) over transverse ribs in two-dimensional channels have also been made in the recent past. Cui et al. [6] performed LES in a channel with the bottom wall roughened with square ribs arranged to yield $\lambda/k=2$, 5, and 10. Leonardi et al. [7] performed DNS in a channel with the bottom wall roughened by square and circular ribs for $2 \leqslant \lambda/k \leqslant 20$ while DNS of channel flow with bottom and top walls roughened by transverse square ribs with $\lambda/k=8$ was performed by Krogstad et al. [8].

The above summary demonstrates that most of the prior experimental and numerical studies over transverse ribs were performed in fully developed channel and zero-pressure gradient turbulent boundary layers. It should be remarked that the characteristics of a shallow open channel flow are quite different from those of canonical turbulent boundary layers. In a shallow open channel flow, for example, the boundary layer thickness is a significant fraction of the depth of flow. The background turbulence level in the outer region of an open channel flow is also substantially higher than in canonical turbulent boundary layers. In this paper, a PIV was used to study the characteristics of a shallow open channel flow developing underneath a free surface flow over transverse ribs of square, circular, and semi-circular cross sections. For each of the three different rib cross sections, the pitch-to-height ratio was varied to produce a *d*-type and a *k*-type rib. As noted by Raupach et al. [9], experimental study of rough-wall turbulent flows is complicated by the characteristic high local turbulence intensities close to the roughness elements. Furthermore, the flow in the vicinity of the roughness is spatially heterogeneous so that spatial averaging is required. Because PIV is a whole-field velocity measurement technique, it was possible to spatially average the profiles along the ribs. In the present study, the spatial averaging was performed over a pitch λ; i.e., from one rib center to the next. Profile averaging has been carried out in prior LES and DNS studies (Cui et al. [6]). The data reported in the present study include spatially averaged mean velocities and Reynolds stresses, distributions of eddy viscosity and mixing length, and the various terms the Reynolds-averaged Navier-Stokes (RANS) equations.

2 Experimental Setup and Preliminary Measurements

2.1 Experimental Setup and Measurement Procedure. The experiments were performed in an open channel with test section that was 2500 mm long, 200 mm wide, and 200 mm deep. The bottom and side walls of the test section were constructed using clear Plexiglas® to facilitate optical access. The ribs comprised transverse acrylic rods of square, circular, and semi-circular cross sections, and the average height of the ribs (or diameter of the circular ribs) was $k=6$ mm. The diameter of the semi-circular ribs was $D=12$ mm. The spacing between corresponding points on adjacent ribs was kept at $\lambda=12$ mm for *d*-type ribs ($\lambda/k=2$) and $\lambda=48$ mm for *k*-type ribs ($\lambda/k=8$). The ribs were glued onto a 4 mm thick Plexiglas® sheet that spanned the width and length of the test section. The sheet was screwed onto the bottom wall of the channel. A 40 mm wide strip of 1 mm sand grains spanning the width of the channel was placed 100 mm from the entrance of the test section to enhance a rapid development of the approach boundary layer. A schematic diagram of the experimental setup showing the test section, light source, and CCD camera, sketches of the ribs and coordinate system is shown in Fig. 1. Here, the

Contributed by the Fluids Engineering Division of ASME for publication in the JOURNAL OF FLUIDS ENGINEERING. Manuscript received November 16, 2006; final manuscript received March 13, 2007. Review conducted by Juergen Kompenhans.

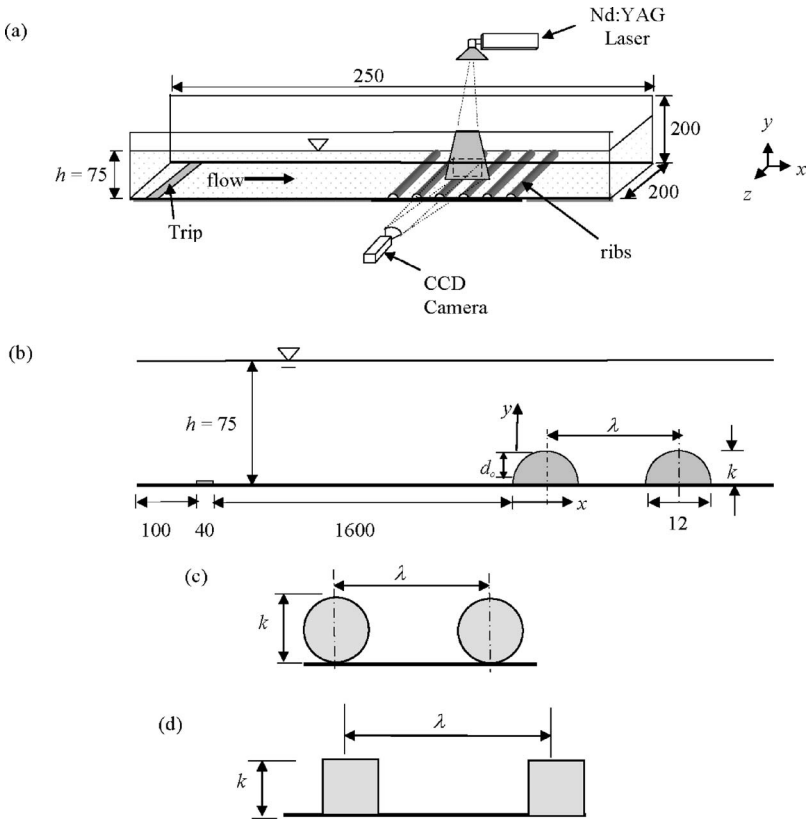

Fig. 1 (*a*) A schematic of experimental setup and coordinate system; (*b*) side view of test section and semi-circular ribs, d_o denotes the virtual origin; (*c*) circular ribs; (*d*) square ribs. All dimensions are in mm; *k*(=6 mm) is rib height and λ is the pitch.

streamwise, wall-normal, and the spanwise directions are denoted by x, y, and z, respectively; $x=0$ corresponds to the upstream edge of the first rib; $y=0$ corresponds to the top plane of the ribs; and $z=0$ corresponds to the middle plane of the channel.

The flow was seeded with polyamide particles having mean diameter of 5 μm and specific gravity of 1.03. A 120 mJ/pulse Nd-YAG laser was used to illuminate the flow. The laser sheet was shot from the top, that is, through the free surface (as shown in Fig. 1), for the closely packed *d*-type ribs. The rationale for this arrangement was to avoid shadows that would otherwise be cast by the *d*-type ribs if the laser were shot from the bottom of the channel. It should be noted that the *d*-type ribs were painted black in order to minimize reflection of laser light, which would otherwise deteriorate the quality of the PIV images close to the ribs. In the case of the more sparsely packed *k*-type ribs, the laser sheet was shot from the bottom. A set of cylindrical lenses converted the laser light into a thin sheet. The laser sheet was located at the mid-plane ($z=0$) of the channel. A 12-bit camera (Dantec® Dynamic HiSense 4M camera) that uses a CCD with 2048 pixel $\times$2048 pixel chip and a pitch of 7.4 μm was used to image the flow. The field of view was typically 59 mm$\times$59 mm for the *d*-type ribs, and 89 mm$\times$89 mm for the *k*-type ribs. The time interval between pulses was chosen such that the maximum particle displacement was smaller than 25% of the interrogation area side. The particle image was estimated to be $d_p=2.4$ and 2.2 pixels, respectively, for the *d*-type and *k*-type experiments. These values are very close to the recommended value of $d_p \approx 2$ pixels required to minimize peak locking. In fact, the histograms of the raw velocity vectors confirmed that there was no observable peak locking.

The PIV images were post-processed using the adaptive-correlation option of FlowManager 4.50.17 (Dantec Dynamics) to obtain the instantaneous velocity vectors. Each image was subdivided into 32 pixel$\times$32 pixel with 50% overlap. The adequacy of 32 pixel$\times$32 pixel to analyze the present data will be discussed in Sec. 2.2. A MaTLAB® script written in our laboratory was used to compute the mean and turbulent statistics from 2500 image pairs or instantaneous vector maps. The data reported subsequently were obtained between the 11th and 12th *d*-type and 9th and 10th *k*-type ribs. The flow rate and water level ($h=75$ mm) were kept constant in all the experiments. The rationale was to keep the upstream conditions similar so that differences observed in the flow over the ribs could be attributed to rib type and/or cross section. Measurement uncertainty analysis was performed following the methodologies proposed and explained by Coleman and Steele [10] and Forliti et al. [11]. The uncertainty estimates at 95% confidence level are represented by error bars in the figures that follow.

Measurements were made at $x=-300$ mm from the first rib on the smooth floor to characterize the approach boundary layer. The Reynolds number based on the upstream freestream velocity ($U_e=0.318$ m/s) and water level was $\mathrm{Re}_h=24{,}000$. The Froude number ($F^2=U^2/gh$) was 0.14, so the flow is in sub-critical regime. At this flow condition, the free surface was fairly calm, and no waves were observed at the free surface. The profiles of the mean velocity and turbulent quantities for the approach boundary layer are shown in Fig. 2. As expected, the measured data follow the log law: $U^+=2.44 \ln y^+ + 5.0$, where $U^+=U/U_\tau$, $y^+=yU_\tau/\nu$, U_τ is friction velocity. The small wake observed in Fig. 2(*b*) is probably due to effects of low Reynolds number and elevated background turbulence. The LDA data of u, v, and $-\overline{uv}$ obtained by Tachie et al. [12] in an open channel are shown in Figs. 2(*c*) and 2(*d*) for comparison. Agreement between the present and previous data

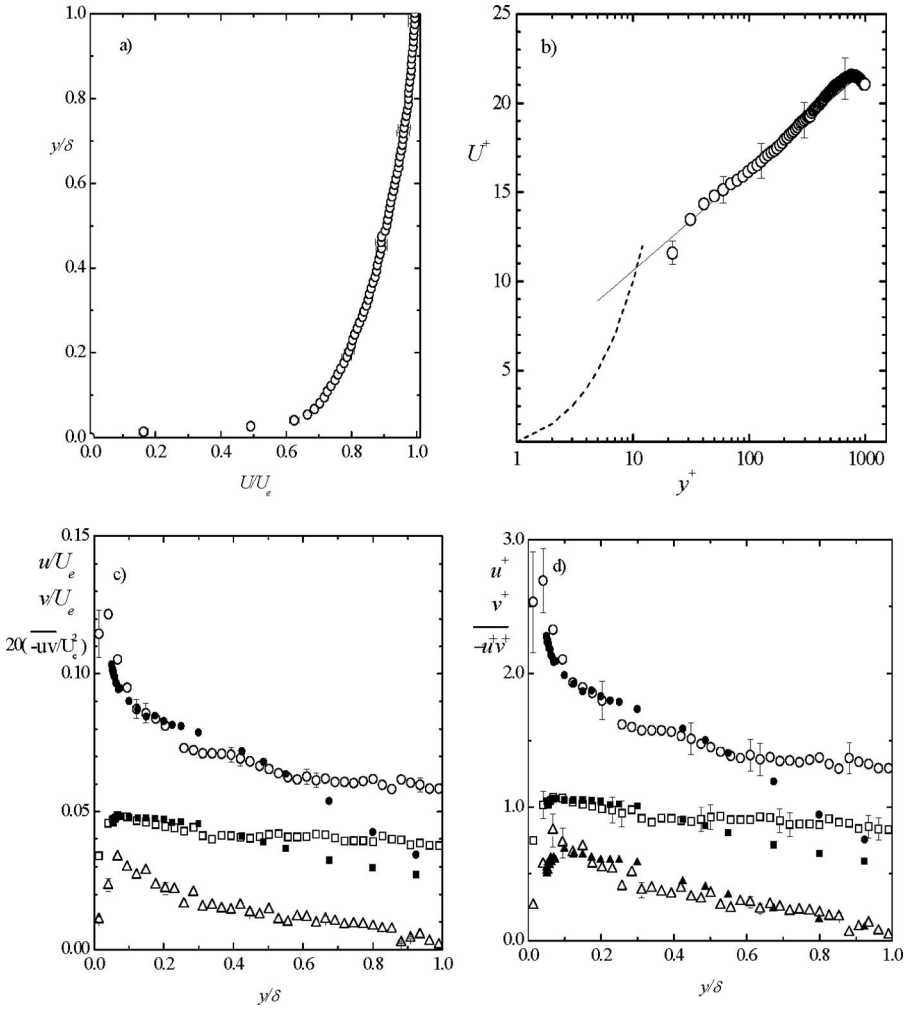

Fig. 2 (*a*) and (*b*) are, respectively, mean velocity profiles in outer and inner coordinates; (*c*) and (*d*) are turbulent intensities and Reynolds shear stress normalized by freestream velocity and friction velocity. Error bars in this and subsequent figures represent measurement uncertainty at 95% confidence level. In (*b*) dashed line: $U^+=y^+$; solid line: $U^+=2.44y^+ +5.0$. Symbols in (*c*) and (*d*) are ○: *u*; □: *v*; and △: $-\overline{uv}$. Open symbols represent present data and solid symbols represent previous LDA data from [12].

sets is reasonable in the region $y/\delta<0.5$. Close to the free surface, however, the present u and v values are higher and more flat due to the higher background turbulence level in the channel. The present value of $(-\overline{uv}^+)_{\max}$ is 0.8 compared to 0.65 in the LDA study.

2.2 The Effects of Spatial Resolution. Prior measurements in near-wall turbulent flows revealed that the magnitude of measured values may depend on probe volume size. The hot-wire measurements by Johansson and Alfredsson [13], for example, showed that $u^+_{\max}$ decreased from 2.9 to 2.1 as the length of the probe in wall units increased from $l^+=2.5$ to 100. Johnson and Barlow [14] also concluded that a larger probe volume of a LDA underestimated $-\overline{uv}$. Saikrishnan et al. [15] compared profiles of turbulent intensities and Reynolds shear stress obtained in a boundary layer with various interrogation window (IW) sides to DNS data. They found that when the IW side in wall units is 20 or less, the ratios of the measured stresses in the buffer region to the DNS values are higher than 0.92. In the present work, the effects of spatial resolution was studied by analyzing the data with 32 pixels $\times$ 32 pixels with 50% overlap, and 32 pixels $\times$ 16 pixels with 50% overlap. These typically correspond, respectively, to $\Delta x=0.46$ mm $\times \Delta y=0.46$ mm, and $\Delta x=0.46$ mm $\times \Delta y=0.23$ mm. Based on the friction velocity determined from the approach boundary layer, it was found that the spacing between vectors or data points in the y-direction (in wall units) were $\Delta y^+=6.5$ and $\Delta y^+=3.3$, respectively. Selected data obtained on rib center/crest and cavity center for *d*-type square ribs are shown in Fig. 3. It should be noted that in all cases every fourth data point is plotted for improved clarity. The profiles obtained using both interrogation window sides compare reasonably well. Based on this observation, and the fact that $\Delta y^+=3.3$ and 6.5, we conclude that both interrogation window sides provide adequate resolution for the present test conditions.

2.3 The Boundary Layer Parameters. For each rib type and cross section, the spatially averaged mean velocity profile was used to determine the boundary layer characteristics over the ribs. As mentioned in Sec. 1, the spatial averaging was performed over a pitch λ. For a given y-location, spatially averaged data is defined as the average of the individual time-averaged quantities along x starting from the center of the 11th rib to the center of the 12th rib for *d*-type ribs, and from the center of the 9th rib to the center of the 10th rib for *k*-type ribs. The number of individual quantities used in computing the spatially averaged data was 26 for the *d*-type ribs and 104 for the *k*-type ribs.

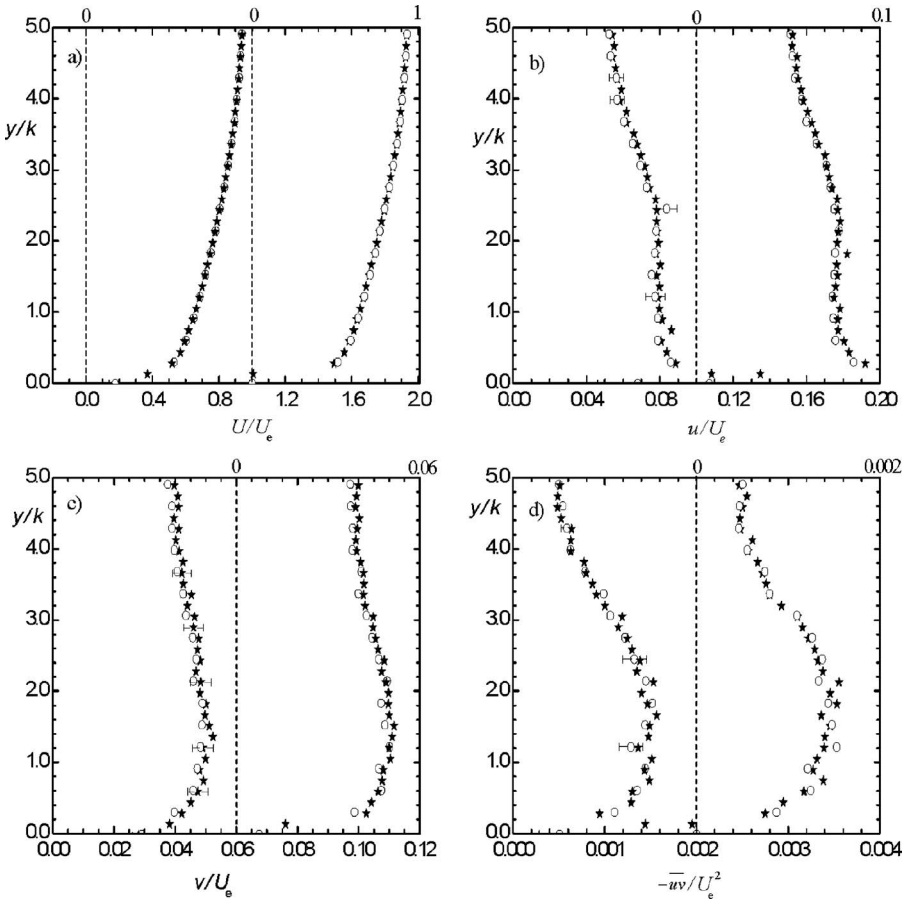

Fig. 3 Mean and turbulent quantities obtained over *d*-type square ribs using different interrogation area sides in pixels: 32×32: ○; 32×16 ★. Note that the horizontal axes are staggered.

The pertinent boundary layer parameters obtained from the upstream boundary layer (hereafter referred to as "smooth") and the spatially averaged mean velocity profiles over the ribs are summarized in Table 1, where U_e is freestream velocity, δ is boundary layer thickness, δ^* is displacement thickness, θ is momentum thickness, H $(=\delta^*/\theta)$ is shape factor, Re_θ $(=U_e\theta/\nu)$ is Reynolds number based on momentum thickness. The spatially averaged mean velocity profiles that were used to calculate the boundary layer parameters will be discussed subsequently. Since the boundary layer thickness covers 50% to 90% of the water depth, the flow is characterized as shallow. Such flow conditions are not uncommon in nature. When the flow is shallow and the background turbulence level at the free surface is high (as in the present study), one would expect the outer layer to be somewhat modified in comparison to canonical turbulent boundary layers. In the present study, $0.09<k/\delta<0.16$ so that the roughness sublayer (defined as distance from rib top to five rib heights) extends up to 50% to 80% of the boundary layer. The present k/δ values, although fairly large, are comparable to $k/\delta=0.15$ to 0.19 in the boundary layer study by Kameda et al. [16] and values of $k/h=0.1$ and 0.2 (where h is half channel height) used in many previous LES and DNS study in fully developed channel. The data shown in Table 1 indicate that the values of U_e over the ribs are higher than for the upstream boundary layer. This is partly explained by flow blockage by the ribs and the higher boundary layer growth over the ribs. The values of δ^*, θ, and H for the *d*-type ribs are only marginally higher than the corresponding

Table 1 Summary of boundary layer parameters for the smooth and rib roughness. For the ribs, the boundary layer parameters were determined using the streamwise mean velocity profiles averaged over a pitch

		Semi-circular		Circular		Square	
Cross-section Pitch ratio	Smooth —	$\lambda/k=2$	$\lambda/k=8$	$\lambda/k=2$	$\lambda/k=8$	$\lambda/k=2$	$\lambda/k=8$
U_e (m/s)	0.318	0.357	0.396	0.369	0.401	0.367	0.407
δ (mm)	37	36	63	36	61	37	69
δ^* (mm)	6.42	8.04	19.92	8.61	20.22	8.97	25.20
θ (mm)	4.45	5.02	9.21	4.85	9.20	5.11	10.91
H	1.51	1.61	2.16	1.77	2.19	1.76	2.41
Re_θ	1420	1790	3640	1790	3690	1870	4440

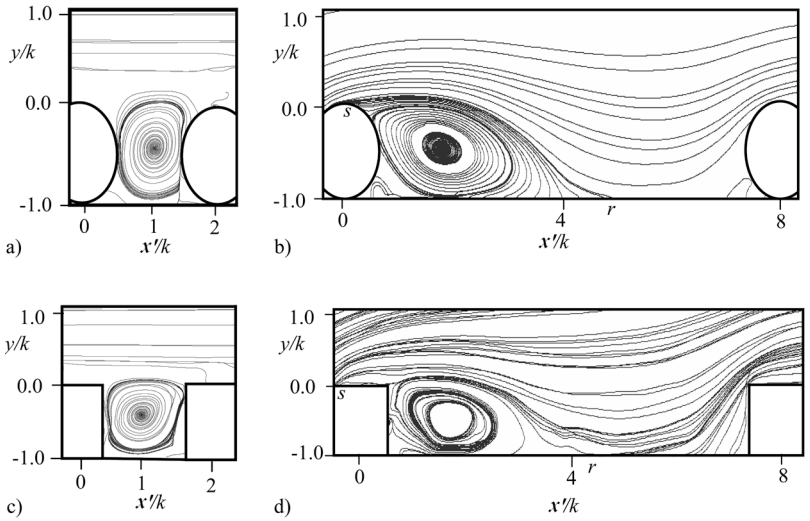

Fig. 4 Streamlines inside cavities and immediately above ribs. (*a*) *d*-type circular; (*b*) *k*-type circular; (*c*) *d*-type square; (*d*) *k*-type square. In (*b*) and (*d*), *s* and *r*, respectively, denote separation point and reattachment point.

smooth-wall values. For the *k*-type ribs, on the other hand, values of δ^* are approximately three to four times as high as the smooth-wall value, while values of θ are about twice as high as the smooth-wall value. The significantly higher values of δ^* and θ obtained for the *k*-type ribs can be explained by the enhanced mass and momentum deficit associated with the higher drag characteristics over the *k*-type ribs. The table also reveals that the boundary layer parameters for *d*-type ribs do not vary significantly with rib cross section. For *k*-type rib, values for circular and semi-circular ribs are similar; however, these values are smaller than those obtained over the square ribs.

3 Results and Discussion

3.1 Streamlines and Velocity Field in the Cavity. The streamlines inside the cavities and immediately above the circular and square ribs are shown in Fig. 4. The approximate locations of the ribs are also shown. The goal is to show qualitatively how the mean flow patterns vary with rib type and rib cross section. It is observed that the cavities of *d*-type ribs (Figs. 4(*a*) and 4(*c*)) are filled by recirculation bubbles. The separating streamlines isolate the outer flow from the flow within the cavities, so the streamlines for the *d*-type ribs are nearly parallel right from the top plane of the ribs. Because the semi-circular ribs touch each other at the base and occupy most of the cavity, their recirculation bubbles (not shown) are smaller and shallower compared to those observed in the cavities of the square and circular ribs. Unlike the *d*-type ribs, the flow reattached on to the floor in the *k*-type cavities (Figs. 4(*b*) and 4(*d*)). Flow separation occurred at the upstream top corner of the square rib, but downstream of the rib center for the circular and semi-circular ribs. The separation points are denoted by *s* on the ribs in the plots. The reattachment point (denoted by *r* on the cavity floor) occurred at $x'/k \approx 5$ for the circular rib and $x'/k \approx 4.3$ for the square rib (where $x'=0$ at the center of the upstream rib). It should be noted that the reattachment length, defined as the distance between the separation and reattachment points, is approximately $5k$ for all *k*-type ribs. The region bounded by the separating streamline, the upstream rib, and the floor is occupied by a relatively larger separation bubble. A smaller corner recirculation bubble was observed below the larger recirculation bubble and downstream of each upstream *k*-type rib, and another recirculation bubble was found just upstream of the downstream rib. These smaller bubbles would have been more distinct in Figs. 4(*b*) and 4(*d*) if the number of streamlines was increased.

3.2 Mean Velocities, Turbulent Intensities, and Momentum Fluxes at the Top-plane of Ribs. Figure 5 shows the mean velocities (U/U_e, V/U_e), the turbulent intensities (u/U_e, v/U_e) and the mean and turbulent momentum fluxes ($-UV/U_e^2$, $-\overline{uv}/U_e^2$) at the top plane of the ribs ($y/k=0$). Data are shown over a pitch (i.e., $0 \leqslant x'/\lambda \leqslant 1.0$, where $x'=0$ and $x'=\lambda$ correspond, respectively, to the upstream and downstream rib center). Note that x'/λ values for each rib type varied from 0 to 1 and the horizontal axis is staggered. Kameda et al. [16] reported similar data sets over square ribs in a zero pressure gradient turbulent boundary layer. Their measurements were obtained using LDA and the pitch-to-height ratios studied were $\lambda/k=3$, 4, and 8. As stated earlier, their values of k/δ varied from 0.15 to 0.19, which are comparable to k/δ values in the present study. In Fig. 5, the LDA data obtained for $\lambda/k=3$ and $\lambda/k=8$ are plotted, respectively, alongside the present *d*-type ($\lambda/k=2$) and *k*-type ($\lambda/k=8$) ribs. The present and previous LDA datasets show similar trends. The agreement between the present and previous mean quantities over the *k*-type ribs is excellent. However, the present turbulent quantities are lower than in the previous study. Over the *d*-type ribs, the magnitude of the previous data sets is generally higher than in the present study. This is partly explained by the higher λ/k value studied in the previous work ($\lambda/k=3$) in comparison to $\lambda/k=2$ in the present study.

For the present measurements, the mean velocity distribution along the *d*-type ribs is nearly independent of rib cross-section. For the *k*-type ribs, on the other hand, the square ribs significantly reduced the values of *U* compared to those measured along the circular and semi-circular ribs. It is clear from Fig. 5(*a*) that the mean flow accelerated ($\partial U/\partial x > 0$) in the region adjacent to the upstream rib and then decelerated ($\partial U/\partial x < 0$) as the downstream rib is approached. It was observed that the mean velocity grows more rapidly across the *d*-type ribs than across the *k*-type ribs. This observation is based on the premise that $\partial U/\partial y$ is typically larger across the *d*-type top-plane than measured across the *k*-type ribs. Across the *d*-type circular ribs, for example, U/U_e at the cavity center ($x'/\lambda=0.5$) increased from nearly 0 at $y/k=-0.33$ to 0.5 at $y/k=0.33$. Over the same *y*-range and at cavity

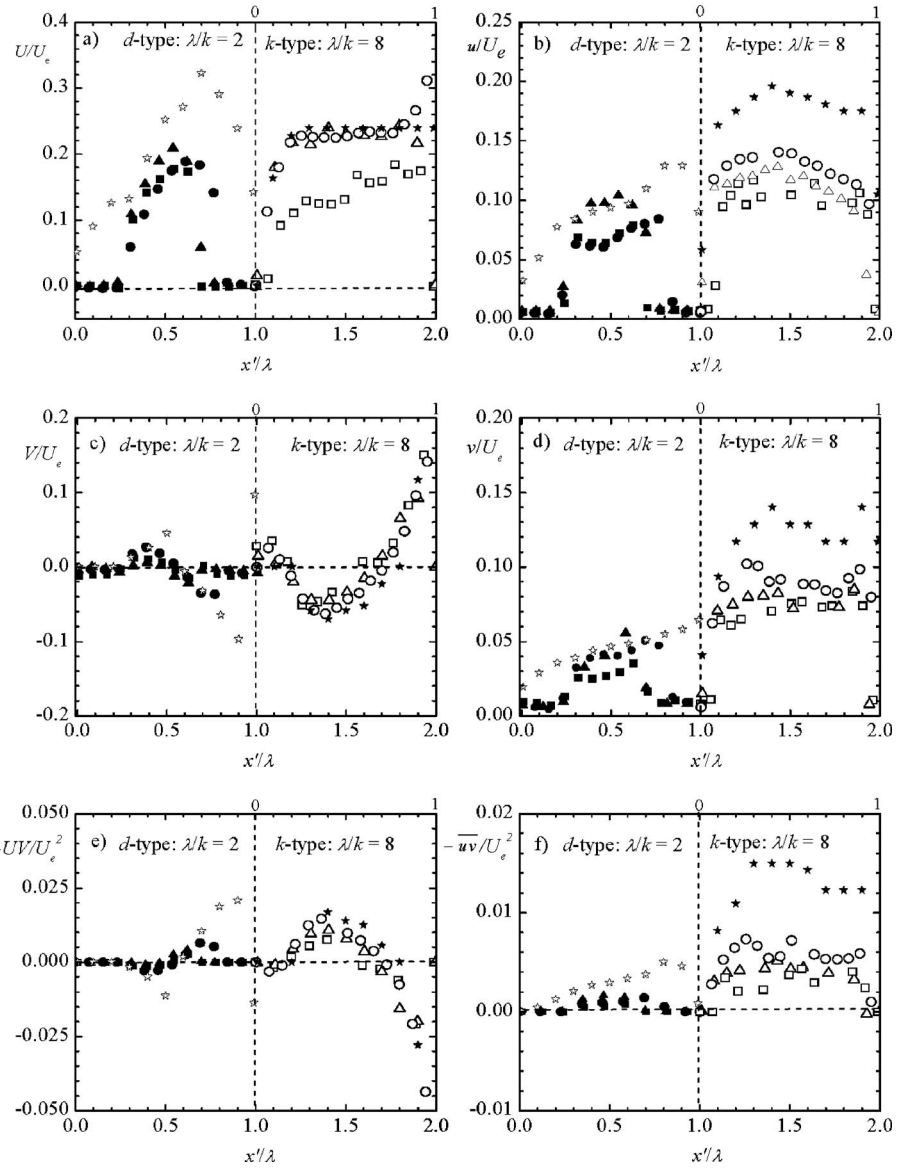

Fig. 5 Variation of mean velocities (*a*, *c*), turbulent intensities (*b*, *d*) and momentum fluxes (*e*, *f*) at the top plane of ribs ($y/k=0$). *d*-type: semi-circular (SC): ▲; circular (RD): ●; square (SQ): ■; Kameda et al.: ☆. *k*-type: SC: △; RD: ○; SQ: □; Kameda et al.: ★. Note that the horizontal axes are staggered.

center, U/U_e increased from 0.16 to 0.3 across the *k*-type circular ribs. The distribution of V (Fig. 5(*c*)) is independent of rib cross section, but it varies significantly with rib type. For *d*-type ribs, V is positive in the region $0<x'/\lambda<0.5$ and negative in the region $0.5<x'/\lambda<1.0$. In this case, the profiles are nearly anti-symmetric with respect to the cavity center. Along the *k*-type ribs, on the other hand, V is positive in a narrow region immediately downstream of the upstream rib followed by a wider region of negative V ($0.15<x'/\lambda<0.70$) and then positive values of V as the flow accelerates over the downstream ribs. The magnitude of V is significantly higher along the *k*-type ribs than the *d*-type ribs. The implication is that vertical motion across the *k*-type top-plane is substantially higher than for the *d*-type ribs. This will likely produce a stronger interaction between the *k*-type cavities and the overlying boundary layer.

The streamwise and wall-normal turbulent intensities (u and v, respectively) increase immediately downstream of the upstream ribs to a maximum value and then decrease to no-slip value on the downstream rib. The values of u and v are also substantially higher along the *k*-type ribs in comparison to the *d*-type ribs. The higher turbulence level along the *k*-type ribs (compared to the *d*-type ribs) can be attributed to the enhanced vertical motion (Fig. 5(*c*)) and stronger interaction between the overlying boundary layer and the *k*-type cavities. The turbulence level along the *k*-type ribs is also lower for the square ribs than the circular and semi-circular ribs. These differences (and also those observed in Fig. 5(*a*)) between the *k*-type square ribs and *k*-type circular/semi-circular ribs may be attributed to the specific differences in flow separation and reattachment. The mean and turbulent momentum fluxes are shown in Figs. 5(*e*) and 5(*f*). The momentum flux ($-UV$) by the mean flow is produced by the curvature of the streamline, Kameda et al. [16]. The non-zero values of $-UV$ and $-\overline{uv}$ at the top-plane are indicative of momentum exchange between the cavities and the overlying shear layer. The absolute values of $-UV$ and $-\overline{uv}$ are higher over the *k*-type ribs than the *d*-type ribs.

3.3 Mean Velocity Profiles. In turbulent flows over trans-

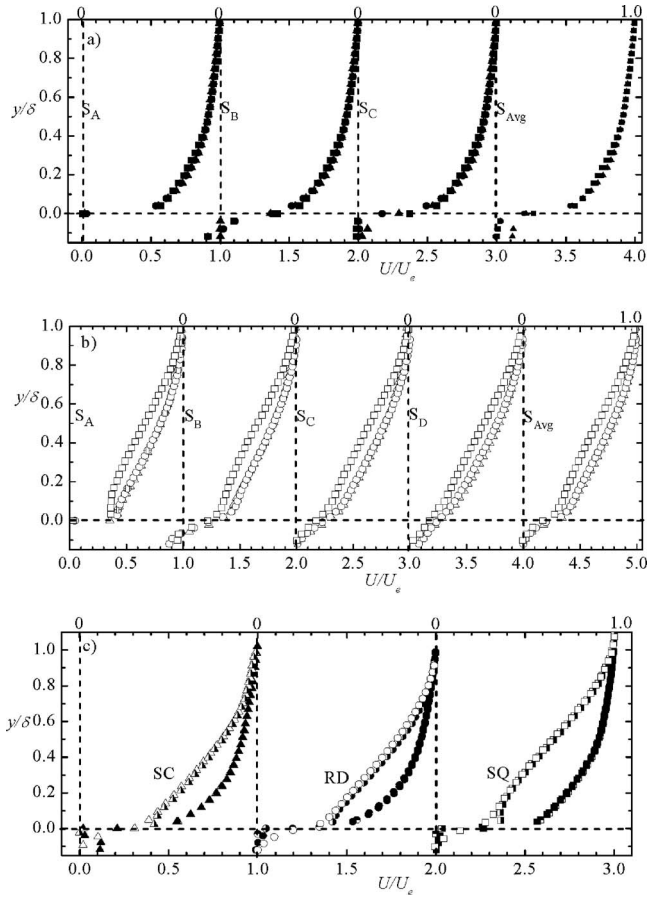

Fig. 6 Mean velocity profiles at rib centers, various *x*-locations in the cavity and spatial averaged profiles (S_{Avg}). (*a*) comparison among *d*-type; (*b*) among *k*-type; (*c*) between *d*-type and *k*-type. For *d*-type profiles, SC: ▲; RD: ●; SQ: ■ and S_A, S_B and S_C, respectively, correspond to $x'/\lambda=0$, 0.50 and 0.75. For *k*-type profiles, SC: △; RD: ○; SQ: □ and S_A, S_B, S_C and S_D, respectively, correspond to $x'/\lambda=0$, 0.25, 0.50 and 0.75. Symbols in (*c*) are: *d*-type SC (averaged: ▲, rib center: half-closed triangle); *k*-type SC (averaged: △, rib center: right-filled triangle); *d*-type RD (averaged: ●, rib center: ◓); *k*-type RD (averaged: ○, rib center: ◑); *d*-type SQ (averaged: ■, rib center: half-closed square); *k*-type SQ (averaged: □, rib center: ◨). Note that the horizontal axes are staggered.

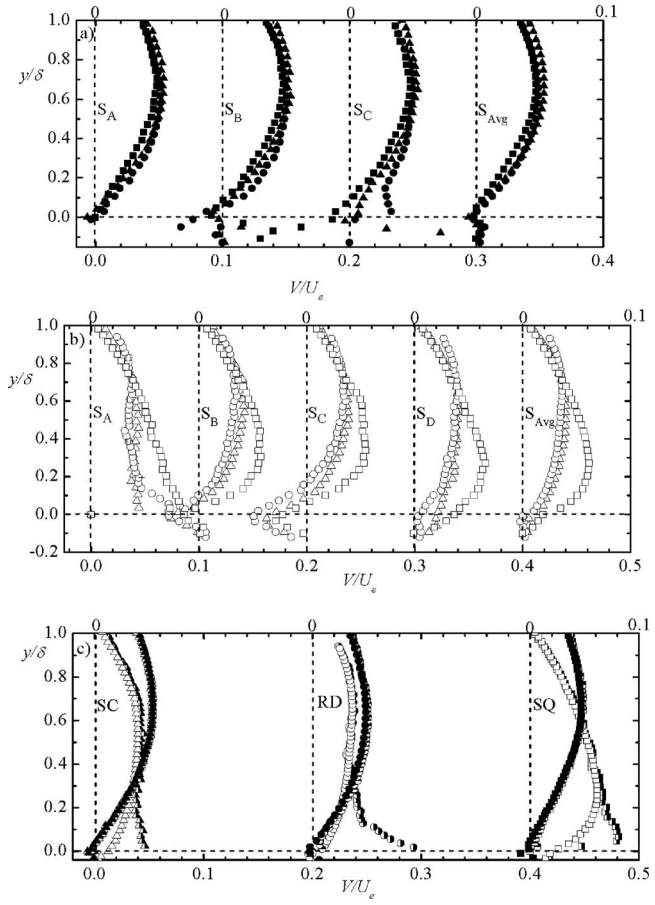

Fig. 7 Wall-normal mean velocity profiles at rib centers, various *x*-locations in the cavity and averaged profiles (S_{Avg}). (*a*) comparison among *d*-type; (*b*) among *k*-type; (*c*) between *d*-type and *k*-type. Symbols and notations are as in Fig. 6. Note that the horizontal axes are staggered.

verse ribs, it is customary to plot profiles at various x-locations inside the cavity and rib center. In the present work, data are presented at $x'/\lambda=0$, 0.50, and 0.75 for the d-type ribs and $x'/\lambda=0$, 0.25, 0.50, and 0.75 for the k-type ribs. As noted earlier, $x'/\lambda=0$ corresponds to the upstream rib center. In addition to these selected individual profiles, the spatially averaged profiles are plotted. For convenience, profiles obtained at $x'/\lambda=0$, 0.50, and 0.75 over d-type ribs will be denoted, respectively, by S_A, S_B, and S_C. Similarly, S_A, S_B, S_C, and S_D will denote profiles at $x'/\lambda=0$, 0.25, 0.50, and 0.75 over k-type ribs. In all cases, S_{Avg} will denote averaged profiles. Because separation occurred at the upstream edge of the square rib ($x'/k=-0.5$), S_A is located downstream of the separating point for the square ribs. For the circular and semi-circular ribs, separation occurred downstream of the crest so that S_A is located downstream of the separation point.

The individual and spatially averaged profiles of the streamwise component of the mean velocity (U) are shown in Fig. 6 using outer scaling (U_e, δ). It should be noted that U/U_e varied from 0 to 1, and the horizontal axis is staggered. In this and subsequent figures, SC, RD, and SQ, respectively, denote semi-circular, circular (or round), and square ribs. Furthermore, adequate data points are skipped for improved clarity. Figure 6(a) compares profiles at corresponding x-locations for the circular, semi-circular and square cross-section d-type ribs. The profiles are almost indistinguishable suggesting that U profiles over d-type ribs are independent of rib cross section. Figure 6(b) shows that U profiles over the k-type ribs are markedly different from those obtained over the d-type ribs. For example, inside the cavities, the profiles varied nearly linearly. The profile obtained at square rib center (S_A) exhibits an overshoot close to the rib. There is a reasonable agreement between the profiles over circular and semi-circular ribs, but these profiles deviate significantly from those obtained over the square ribs across the boundary layer. The latter is also "less full," and this may be attributed to the relatively higher drag characteristics of the square rib compared to the circular and semi-circular ribs. The magnitude of maximum backflow velocity inside the cavities of d-type and k-type roughness is about 10% of the freestream velocity. Figure 6(c) compares profiles at rib center (S_A) and averaged profiles (S_{Avg}) for d-type and k-type ribs. Since the goal is to show the effects of rib type (and not cross section), profiles obtained over similar rib cross section are plotted together. Irrespective of rib cross-section, the d-type profiles are more full than k-type profiles due to higher drag associated with k-type ribs in comparison to d-type ribs. The profiles over d-type ribs vary only slightly with distance in the region $y/\delta>0.4$; however, significant variation is observed in the k-type profiles up to the edge of the boundary layer. For d-type ribs, the spatially averaged profiles are similar to those obtained at rib center right from the top plane of the ribs ($y=0$); however, differences are

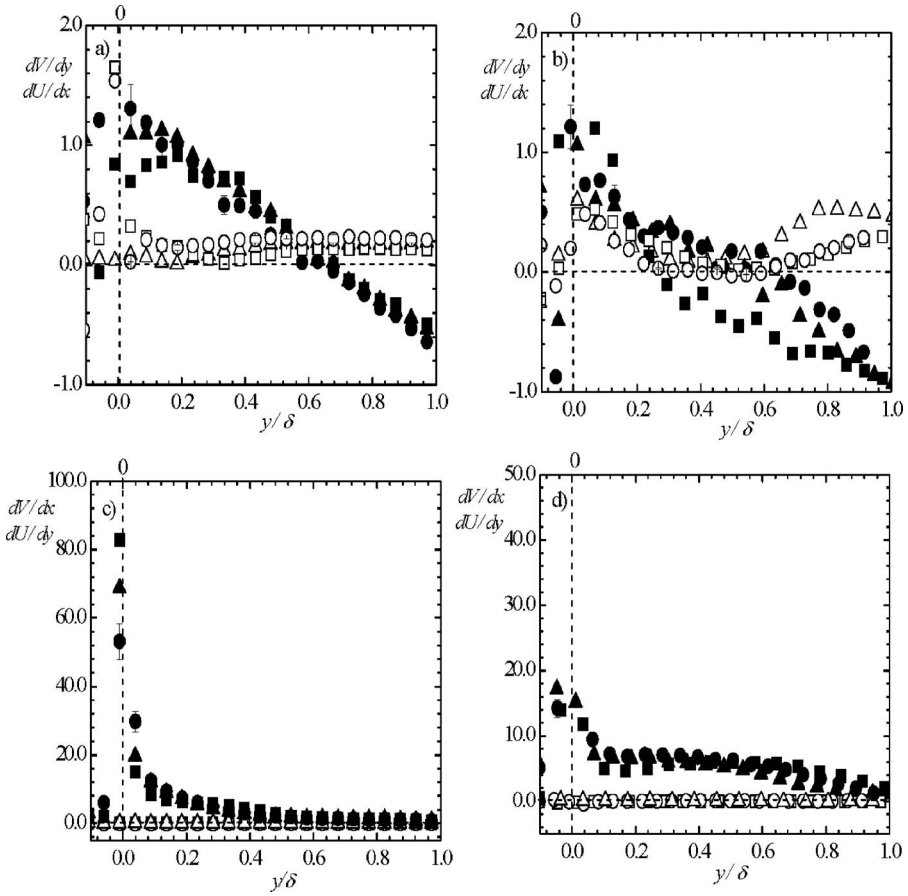

Fig. 8 Averaged velocity gradients across the boundary layer. (*a*) $\partial V/\partial y$ [SC: ▲; RD: ●; SQ: ■] and $\partial U/\partial x$ [SC: △; RD: ○; SQ: □] across *d*-type; (*b*) $\partial V/\partial y$ and $\partial U/\partial x$ across *k*-type, symbols are as in (*a*); (*c*) $\partial U/\partial y$ [SC: ▲; RD: ●; SQ: ■] and $\partial V/\partial x$ [SC: △; RD: ○; SQ: □] across *d*-type; (*d*) $\partial U/\partial y$ and $\partial V/\partial x$ across *k*-type, symbols are as in (*c*).

observed in the *k*-type profiles close to the ribs. This is further evidence that the flow over *d*-type ribs is homogeneous in x right from the rib top. As noted earlier, the boundary layer parameters (Table 1) for the rib roughness were calculated from the spatially averaged streamwise mean velocity profiles. It is evident from Fig. 6 that, although some of the individual profiles have negative values within the cavities, the spatially averaged values are positive within and outside the cavities.

Because of the shallow nature of the flow under investigation and the significant blockage by the ribs, the characteristics of the wall-normal component of the mean velocity V across the boundary layer are also examined. Figure 7(*a*) shows that V profiles close to the *d*-type ribs are more sensitive to rib cross section than observed for U. The low values of V in the immediate vicinity of the *d*-type ribs suggest limited vertical motion over these ribs. The relatively higher values for *k*-type ribs in the inner region are indicative of higher flow angles over *k*-type ribs. Because the mean flow separates upstream of the square rib and is initially deflected outwards, substantially higher V values were observed over the *k*-type square ribs (Fig. 7(*b*)). The maximum value of V is about 5% to 10% of the freestream velocity. The values of V are significantly larger than in canonical turbulent boundary layers. More importantly, V varies considerably with y so that $\partial V/\partial y$ is not negligible. The LES results of Cui et al. [6] also show high values of V close to *k*-type square ribs. Their maximum value for the averaged V profile is about 6% of the bulk velocity, which is similar to $V_{max}/U_e=0.06$ for our *k*-type square ribs.

From the PIV data, the following spatially averaged velocity gradients were computed: $\partial U/\partial x$, $\partial V/\partial y$, $\partial U/\partial y$, and $\partial V/\partial x$, and the results are plotted in Fig. 8. These gradients play significant role in the transport of mean momentum, and also in the production of turbulent kinetic energy and Reynolds stresses. The derivatives shown in Fig. 8 and subsequent sections were obtained using second-order central difference scheme. The positive values of $\partial U/\partial x$ across the boundary layer indicate that the bulk flow accelerates over the ribs due to flow blockage by the ribs. The values of $\partial U/\partial x$ are fairly constant across the boundary layer for *d*-type ribs, and in the region $y/\delta>0.2$ for *k*-type ribs. For a given rib type, $\partial U/\partial$x is nearly independent of rib cross section (except for *k*-type semi-circular ribs). The acceleration parameter $K=\nu U_e^{-2}dU_e/dx$ was estimated to be 1.2×10^{-6} and 1.6×10^{-6} for the *d*-type and *k*-type (square and circular) ribs, respectively. Unlike canonical smooth-wall turbulent flows, values of $\partial V/\partial y$ are large (larger than $\partial U/\partial x$). In the region $y/\delta<0.5$, both $\partial U/\partial x$ and $\partial V/\partial y$ are positive. Therefore, the basic assumption that $\partial U/\partial x \approx -\partial V/\partial y$ is not valid across the boundary layer. This observation also implies that, for the shallow open channel flow studied in this work, the mean flow is three dimensional (i.e., $\partial W/\partial z\neq 0$, from continuity consideration). Figure 8 shows that $\partial U/\partial y>\partial V/\partial x$, $\partial U/\partial y>\partial U/\partial x$ and $\partial V/\partial y>\partial V/\partial x$ across the boundary layer.

3.4 The Friction Velocity and Skin Friction Coefficient. Traditionally, the friction velocity for turbulent flows over smooth and rough surfaces is determined by fitting the classical log law to the overlap region of the mean velocity profile. The difficulties in applying the log law to rough-wall turbulent flows are well known. In the recent past, various researchers (see, for example, Barenblatt [17]; George and Castillo [18]) have proposed different

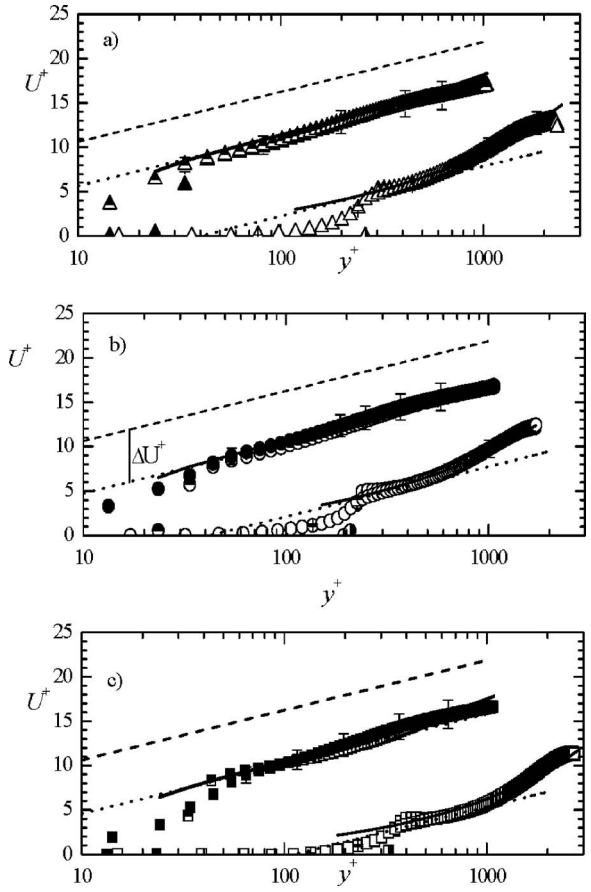

Fig. 9 Mean velocity profiles at rib centers and spatial averaged profiles in inner coordinates. Symbols are as in Fig. 6. Solid lines are power law fits (Eq. (2)); dashed lines are log law for a smooth surface ($U^+=2.44\ln y^+ + 5$), dotted lines are $U^+ = 2.44\ln y^+ + 5 - \Delta U^+$, where ΔU^+ is the roughness shift.

power laws as alternate formulation to model the mean velocity profile of near-wall turbulent flows. As noted by Buschmann and Gad-el-Hak [19], entire sections of AIAA, American Physical Society and American Society of Mechanical Engineers Meetings were devoted to debate the controversy surrounding the validity of the log law and power laws. Sreenivasan [20] argued that even though the power law originally used by engineers to describe the mean velocity profile has been discredited by scientists since the log law was derived from asymptotic arguments, the basis for the power law formulation is a priori as sound as that for the log law particularly at low Reynolds numbers. Buschmann and Gad-el-Hak [19] provided a vivid summary of the various power law formulations. They also applied the log law and the power law formulations to analyze numerous smooth-wall data sets obtained from a variety of research groups. The Reynolds numbers (Re_θ) for the data varied from 500 to 27,000. Among others, they concluded that there is no statistically significant preference toward either the log law or the power laws. However, they noted that power law described a wider range of the profile than the log law. In this study, the power law proposed by George and Castillo [18] is used to model the mean velocity profile and to determine the friction velocity. This power law has been used extensively by the authors to model ZPG turbulent boundary layers, Kotey et al. [21], and open channel flows (Tachie et al. [22]; Bergstrom et al. [23]) over diverse roughness elements. Similar to the observations made by Buschmann and Gad-el-Hak [19], the rough-wall studies revealed that the power law described a wider range of the mean velocity profile compared to the classical log law. This is particularly true for low Reynolds number turbulent flows over rough walls where the classical overlap region is narrow.

The power law formulations in outer and inner coordinates are given, respectively, by:

$$U/U_e = C_o[(y+a)/\delta]^\gamma \tag{1}$$

$$U^+ = C_i[(y^+ + a^+)]^\gamma \tag{2}$$

where the power law constants C_o, C_i, and γ are weak functions of Reynolds number ($\delta^+ = \delta U_\tau/\nu$), and a^+ ($=-16$) represents a shift in origin for measuring y associated with the growth of the mesolayer region ($30 \leqslant y^+ \leqslant 300$). In our previous studies, C_o was found to be close to unity for a smooth surface but tends to decrease slightly for a rougher surface. As the roughness effects increase, C_i decreases and γ increases substantially. It was argued that the increase in γ is due to the characteristic higher drag and wake component for rough surfaces. George and Castillo [18] showed that the friction law is given by:

$$U_\tau/U_e = (C_o/c_i)^{1/(1+\gamma)}(U_e\delta/\nu)^{-\gamma/(1+\gamma)} \tag{3}$$

Because the power law in outer coordinates does not contain U_τ, Eq. (1) was first fitted to the measured data to determine C_o and γ. With these values of C_o and γ, Eqs. (2) and (3) were used iteratively to determine C_i and U_τ. Figure 9 shows the measured data (symbols) and power law fits (solid lines) in inner coordinates. A value of $a^+=-16$ was used in fitting the profiles. The dotted lines in Fig. 9 represent the log law fits obtained when U_τ values determined from the power law were used together with appropriate roughness shifts: $U^+ = 2.44\ln y^+ + 5.0 - \Delta U^+$, where ΔU^+ is the roughness shift representing the downward shift associated with roughness in the overlap region. The values of the power law constants (C_o, C_i, and γ) and U_τ used to obtain the fits shown in Fig. 9 are summarized in Table 2. With the exception of the k-type square ribs, $0.98 \leqslant C_o \leqslant = 1.03$. It is observed that the data over the k-type ribs deviate from the smooth-wall log-law profile (dash lines) more than the d-type profiles do. This is an indication that the flow experiences more resistance or drag over k-type ribs than over d-type ribs. The strength of the wake (i.e., departure of mea-

Table 2 Summary of power law constants and drag characteristics for the various ribs

Cross-section	Semi-circular		Circular		Square	
Pitch ratio	$\lambda/k=2$	$\lambda/k=8$	$\lambda/k=2$	$\lambda/k=8$	$\lambda/k=2$	$\lambda/k=8$
C_o	1.02	0.98	1.02	0.98	1.03	0.94
C_i	5.00	0.30	4.40	0.30	4.10	0.10
γ	0.19	0.50	0.20	0.50	0.21	0.60
U_τ/U_e	0.058	0.075	0.061	0.076	0.061	0.087
C_f	0.007	0.011	0.007	0.012	0.007	0.015
U_τ (m/s)	0.021	0.030	0.022	0.030	0.022	0.035
ΔU^+	5.0	14.0	5.9	14.0	6.0	16.5

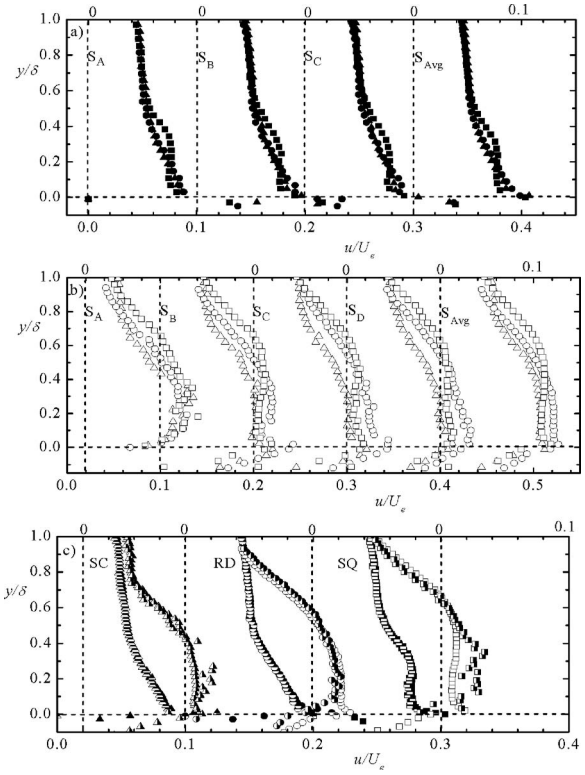

Fig. 10 Profiles of streamwise turbulent intensity at rib centers, various *x*-locations in the cavity and spatial averaged profiles (S_{Avg}). (*a*) comparison among *d*-type; (*b*) among *k*-type; (*c*) between *d*-type and *k*-type. Symbols and notations are as in Fig. 6. Note that the horizontal axes are staggered.

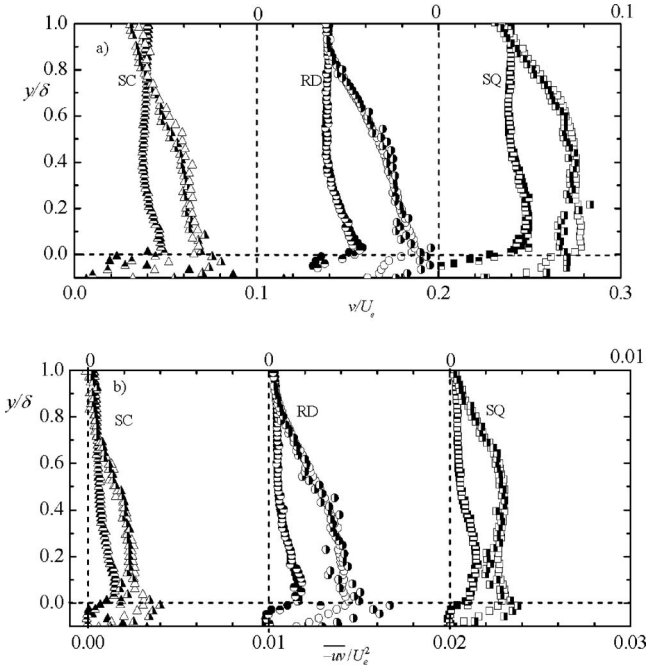

Fig. 11 Profiles of (*a*) wall-normal turbulent intensity and (*b*) Reynolds shear stress at rib centers and averaged profiles. Symbols and notations are as in Fig. 6. Note that the horizontal axes are staggered.

sured data from the log law in the outer region) is stronger for *k*-type than for *d*-type ribs. From Table 2, it is observed that values of C_i decrease and values of γ increase as the roughness effect (ΔU^+) increases. The lower values of C_i and higher values of γ are consistent with the mean velocity over a rougher surface being "less full" due to higher drag and concomitant increase in the strength of the wake component. It is noteworthy that the log law describes only a limited region of the measured data compared to the power law. This provides additional evidence that the power law has some important practical advantages over the log law for relatively low Reynolds number turbulent flows over rough surfaces.

Table 2 shows that the values of U_τ and ΔU^+ are similar for all the *d*-type ribs. The C_f values for the *d*-type ribs are 75% higher than the (upstream) smooth-wall value, and it appears that the potential of *d*-type ribs to augment flow resistance is independent of rib cross section. For the *k*-type ribs, ΔU^+ values are similar for the circular and semi-circular ribs but these values are somewhat lower than for square ribs. The C_f values for the *k*-type ribs are substantially higher than the values obtained over the *d*-type ribs and the smooth wall. The higher C_f values over the ribs are due to pressure-induced drag. The C_f values demonstrate that, for *k*-type ribs, the square rib is more effective than the circular and semi-circular cross sections in augmenting flow resistance. This may be due to the manner in which the pressure field close to the ribs is modified by flow separation (which in the case of *k*-type square ribs occurred at the upstream edge of the rib) and reattachment onto the cavity floor. The present values of $U_\tau/U_e \approx 0.06$ for *d*-type ribs compare reasonably well with values of $U_\tau/U_e \approx 0.050-0.058$ for circular and square ribs in the DNS study of Leonardi et al. [7]. For *k*-type, the present values of U_τ/U_e varied from 0.075 to 0.087 compared with $U_\tau/U_e \approx 0.09$ for square and circular ribs in the DNS study.

3.5 Turbulent Intensities and Reynolds Stresses. Figure 10 shows profiles of streamwise turbulent intensity u. For *d*-type ribs, profiles obtained over the circular and semi-circular ribs collapse reasonably well. The profiles over the square ribs are nearly uniform close to the ribs ($y/\delta < 0.3$) but those over circular and semi-circular ribs fall rapidly with increasing y. For *k*-type ribs (Fig. 10(*b*)), the effects of rib cross-section on the profiles are evident up to the edge of the boundary layer. The *k*-type profiles are more uniform and significantly higher than those obtained over the *d*-type ribs (Fig. 10(*c*)). The profiles of v and $-\overline{uv}$ (Fig. 11) are qualitatively similar to the u profiles. It was found that values of v and $-\overline{uv}$ are small inside the *d*-type cavities. As noted earlier, the separating streamlines isolate the *d*-type cavities from the overlying outer flow, and momentum fluxes at the top plane are low. As a result, there is a limited interaction between the outer flow and flow inside the *d*-type cavities.

The spatially averaged turbulent intensities and Reynolds shear stress normalized by the friction velocity are shown in Figs. 12(*a*)–12(*c*). The figures also show data obtained by Tachie et al. [12] over sand grain roughness in an open channel using LDA. For the sand grain experiment, $\mathrm{Re}_\theta = 2180$ and $k_s^+ = 20$, well in the transitionally rough regime. The profiles for *d*-type ribs fall rapidly and in the region $0.1 < y/\delta < 0.8$, they are consistently lower than *k*-type profiles. For each rib type, profiles for circular and semi-circular ribs are similar. These profiles are quite different from those obtained over the square ribs. The more uniform profiles for the square ribs are probably a result of more intensive mixing of the shear layer that separated upstream of the rib. Over most of the boundary layer, values of v^+ and $-\overline{u^+v^+}$ are higher for the *k*-type ribs than for *d*-type ribs. The profiles obtained in the present study are significantly lower than typical profiles over a smooth surface and in the previous study over transitionally rough sand grain shown in the figures. For example, the spike in u^+ very close to a smooth wall is absent in the rib data. Possible reasons

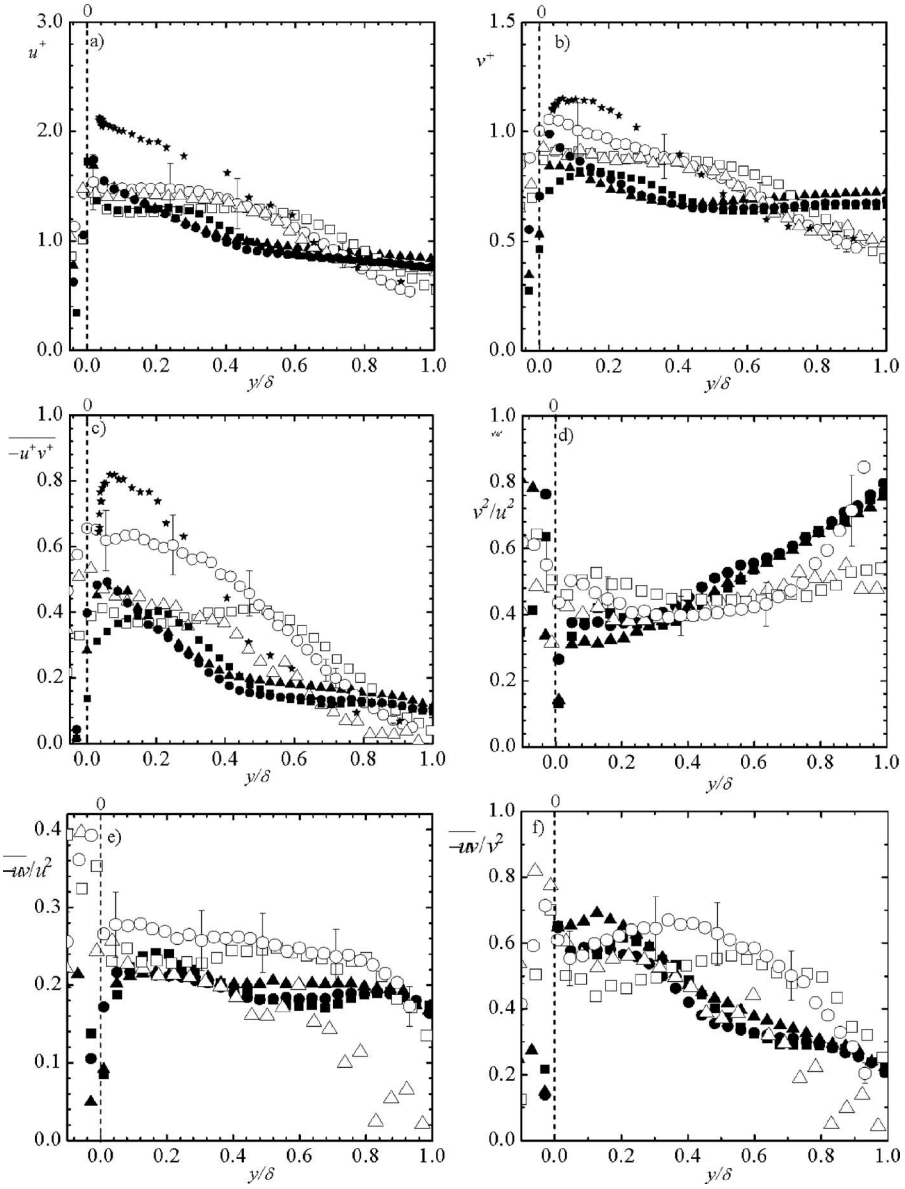

Fig. 12 (*a*) Profiles of turbulent intensities: (*a*), (*b*); and Reynolds shear stress (*c*) in inner coordinates. Distribution of stress ratios: (*d*), (*e*), (*f*). Symbols as in Fig. 6, ★ denotes previous LDA data from [12].

for the lower values may be due to the specific nature of the open flow and surface conditions, as explained below. In a smooth wall, the peak in u^+ is due to viscous effects (Krogstad et al. [8]). They suggested that significant reduction in u^+ close to rough walls is due to break-up of the streamwise vortices. In the present experiments, the rib height in wall units ($k^+=kU_\tau/\nu$) is 120 for the *d*-type ribs and 200 for *k*-type ribs. Thus, the ribs extend well into the logarithmic layer of the approach flow. As noted earlier, pressure-induced drag is large compared with viscous drag, and it appears that the low values of u^+ close to the ribs are partly due to break-up of streamwise vortices by the ribs and minimal viscous influence. It was observed in Fig. 8 that $\partial U/\partial x>0$ across the boundary layer and $\partial V/\partial y>0$ in the region $y/\delta<0.5$. As a consequence, the normal stress production terms in the u^2- and v^2-Reynolds stress equations ($u^2\partial U/\partial x$ and $v^2\partial V/\partial y$) and turbulence kinetic energy equation ($u^2\partial U/\partial x+v^2\partial V/\partial y$) are positive (loss). It is likely that the low turbulence levels in the inner region are, in part, a consequence of reduced production of turbulence as energy is transferred from the turbulence field to the mean flow. A reduction in the levels of u and v will also produce lower values of -uv because previous studies showed that roughness may reduce the correlation coefficient. Indeed, the gradual variation of U with y close to the ribs (see Fig. 6) compared to the near-wall region of a smooth surface, and reduced v^2 values will attenuate production of $-uv$: $P_{uv}=v^2\partial U/\partial y$. It should also be noted that, unlike classical near-wall turbulent flows for which V (and UV) are negligible, these quantities are not negligible in the present flow. Therefore, their dynamic role in the overall momentum balance (and therefore distribution of $-uv$) cannot be ignored.

The higher values of v^2/u^2 close to the *k*-type ribs (Fig. 12(*d*)) are a consequence of the stronger interaction between the outer flow and flow in the cavities of the *k*-type ribs. Further, profiles of v^2/u^2 are fairly uniform for the *k*-type ribs. For the *d*-type ribs, the profiles increase monotonically toward the edge of the boundary layer. The figure demonstrates that $-\overline{uv}/u^2$ (Fig. 12(*e*)) and $-\overline{uv}/v^2$ (Fig. 12(*f*)) are generally higher for the *k*-type than for *d*-type except close to the ribs where $-\overline{uv}/v^2$ does not reveal any

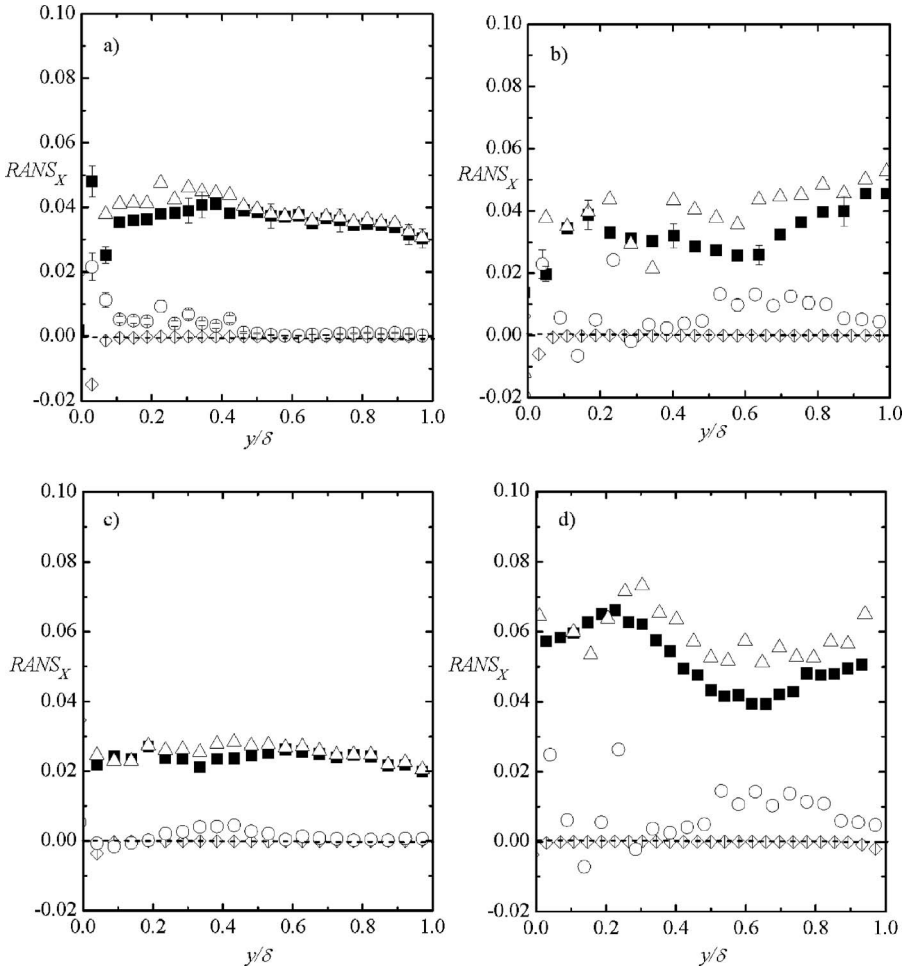

Fig. 13 Various terms in the *x*-momentum equations. (*a*) *d*-type circular ribs; (*b*) *k*-type circular ribs; (*c*) *d*-type square ribs; (*d*) *k*-type square ribs. Symbols are as follows: Convective: ■; Reynolds stress: ○; Viscous: barred diamond; Pressure: △.

systematic trend. It appears production or enhancement of Reynolds shear stress relative to the Reynolds normal stresses is generally higher for *k*-type than *d*-type ribs.

3.6 The Momentum Equation. As noted earlier, the mean flow is three-dimensional across the boundary layer. In this section, we evaluate the implications of this observation for the various transport terms in the mean momentum equations. Because a planar PIV was used in the present study, only the transport terms in the *x*-*y* plane could be evaluated. The *x* and *y* components of the RANS equations may be rearranged as follows:

$$[U\partial U/\partial x + V\partial U/\partial y] + [\partial u^2/\partial x + \partial \overline{uv}/\partial y] - [\nu(\partial^2 U/\partial x^2 + \partial^2 U/\partial y^2)] = -\rho^{-1}\partial P/\partial x \quad (4)$$

$$[U\partial V/\partial x + V\partial V/\partial y] + [\partial \overline{uv}/\partial x + \partial v^2/\partial y] - [\nu(\partial^2 V/\partial x^2 + \partial^2 V/\partial y^2)] = -\rho^{-1}\partial P/\partial y \quad (5)$$

In each of the above equations, the terms on the left hand-side are the convective, Reynolds stress and viscous term, while the term of the right-hand side is the pressure gradient. All the terms on the left were evaluated from measured data and the pressure gradient was obtained by difference. The various terms in the above equations for *d*-type and *k*-type circular and square ribs are shown in Figs. 13 and 14. The viscous term in the *x*-equation is negligible across the boundary layer except in the immediate vicinity of the ribs. In the region $y/\delta < 0.5$, the Reynolds stress gradient term is lower for *k*-type than *d*-type circular ribs because $-\overline{uv}$ is fairly uniform close to *k*-type ribs. Although not negligible, the Reynolds stress term is smaller than the convective term so that the *x*-momentum equation approximately simplifies to a balance between convective and pressure gradient terms. Figure 13 also demonstrates that $\partial P/\partial x$ is nearly constant (independent of *y*) across the boundary layer for *d*-type ribs. The convective term is important across the boundary layer because of non-negligible values of *V* and $\partial U/\partial y$ (producing large $V\partial U/\partial y$) in the inner layer and finite values of *U* and $\partial U/\partial x$ (producing large $U\partial U/\partial x$) in outer region where $\partial U/\partial y \approx 0$. It was found that $\partial(\overline{uv})/\partial y > \partial u^2/\partial x$ as in turbulent boundary layers.

The viscous term in the *y*-equation (Fig. 14) is also negligible across the boundary layer. Unlike classical turbulent boundary layers, the convective term in the *y*-equation is important so that the pressure gradient is not exactly balanced by the Reynolds stress term. The non-negligible convective term in this case is due to large values of $\partial V/\partial y$ across the boundary layer (Fig. 8) and non-negligible values of $U\partial V/\partial x$ close to the ribs where *V* is small. A comparison between the various terms in the *x*- and *y*-RANS equations shows that convective and pressure gradient terms in the *x*-equation are at least an order of magnitude higher than in the *y*-equation. The Reynolds stress gradient terms in both equations are of the same order.

3.7 Eddy Viscosity and Mixing Length. Distributions of the eddy viscosity, i.e., $\nu_t = -\overline{uv}/\partial U/\partial y$, and mixing length, i.e., $l_m = (-\overline{uv})^{1/2}/\partial U/\partial y$, are shown in Fig. 15. The values of l_m are

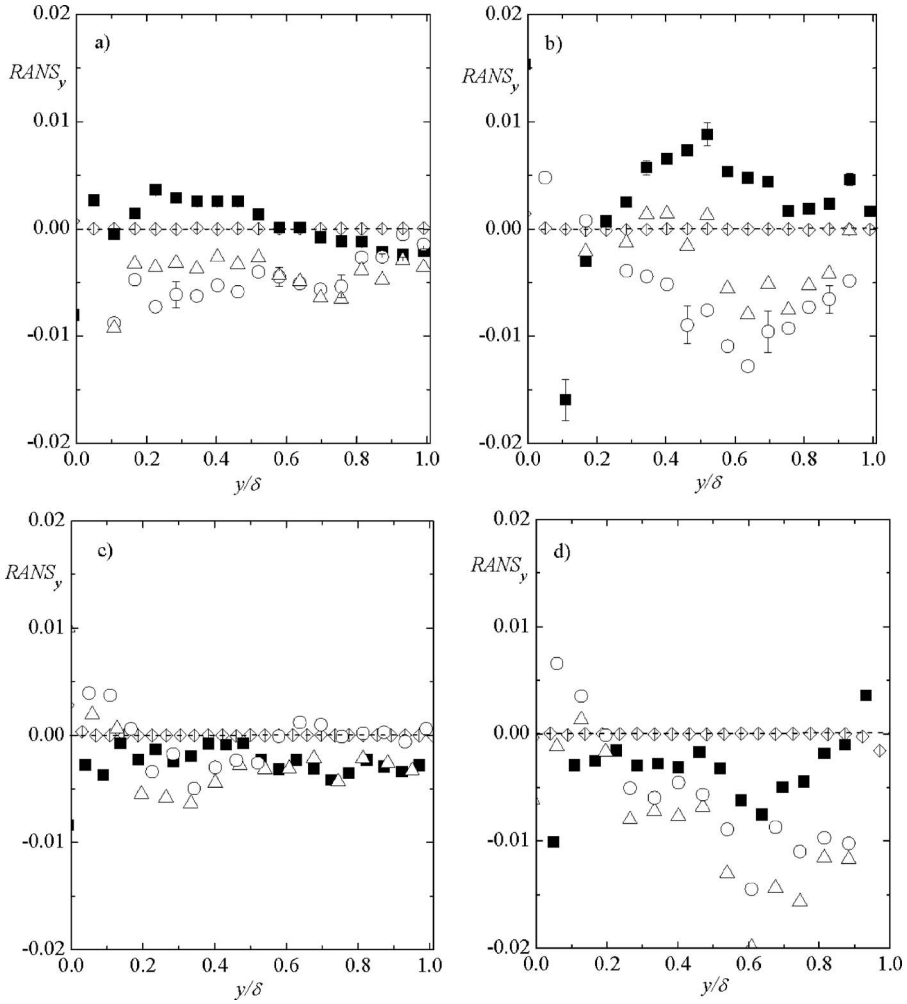

Fig. 14 Various terms in the *y*-momentum equations. (*a*) *d*-type circular ribs; (*b*) *k*-type circular ribs; (*c*) *d*-type square ribs; (*d*) *k*-type square ribs. Symbols are as follows: Convective: ■; Reynolds stress: ○; Viscous: barred diamond; Pressure: △.

made dimensionless using both inner (ν/U_τ) and outer (δ) length scales. The values of ν_τ and l_m are nearly zero at the top plane ($y=0$) of the *d*-type ribs (due to the low levels of $-\overline{uv}$ in the cavities) but not negligible at the top plane of the *k*-type ribs. The profiles over *k*-type ribs increase dramatically in the rib region to a maximum value at $y/\delta=0.15$, followed by a steady decline as the edge of the boundary layer is approached. For *d*-type ribs, the eddy viscosity increases steadily across the boundary layer. The eddy viscosity and mixing length do not depend strongly on rib type. However, the *k*-type profiles are higher close to the ribs (because of their high levels of $-\overline{uv}$) and lower in the outer region where their $\partial U/\partial y$ values become much larger than for the *d*-type ribs. Evidence for larger values of $\partial U/\partial y$ in the outer region of the *k*-type ribs is provided in Fig. 8, and also by the larger wake for the *k*-type profiles in Fig. 9. It is clear that the magnitude and trend of the eddy viscosity and mixing length in the outer layer depend very strongly on the mean velocity gradient. Figure 15(*b*) also shows the eddy viscosity over sand grain and wire mesh roughness in an open channel, Tachie et al. [12]. The values of the Reynolds shear stress obtained over the sand grain and wire mesh roughness are higher than in the present study. It is, therefore, not surprising that their ν_τ values are also higher than those obtained over the *k*-type ribs. The trends in the previous experiments and present *k*-type ribs are similar because relatively higher values of the wake parameter were observed for those surfaces. The mixing length over the *d*-type ribs, previous measurements over sand grain and wire mesh in open channel, and over wire mesh in a zero pressure gradient turbulent boundary layer varies according to $l_m=\kappa y$ in the region $y/\delta<0.1$ (Fig. 15(*c*)). The values of l_m over the *k*-type ribs also vary linearly with a similar slope, however, the expression $l_m=\kappa y$ is not valid because l_m is non-zero at the top-plane of the *k*-type ribs. In this case, the mixing length distributions close to the ribs may be approximated by $l_m=\kappa(y+y_o)$, where $y_o\approx 0.06\delta$. In the region $y/\delta>0.2$, the mixing length is nearly constant over the *k*-type ribs ($l_m=0.057\delta$) and previous zero pressure gradient data over wire mesh ($l_m=0.07\delta$).

4 Conclusions

The data reported in this paper demonstrate that the wall-normal mean velocity, turbulent intensities, and the mean and turbulent momentum fluxes at the top-plane of the ribs are substantially higher for the *k*-type ribs than for the *d*-type ribs. This produces a stronger interaction between the *k*-type cavities and the overlying boundary layer, and also a more uniform Reynolds stress profiles close to the *k*-type ribs than observed over the *d*-type ribs.

The flow is shallow and the ratio of rib height to boundary layer thickness is fairly high in the present study causing roughness effects to be felt across most of the boundary layer. This produces significant blockage and three-dimensional effects, and large values of wall-normal mean velocity. As a result, the contribution of

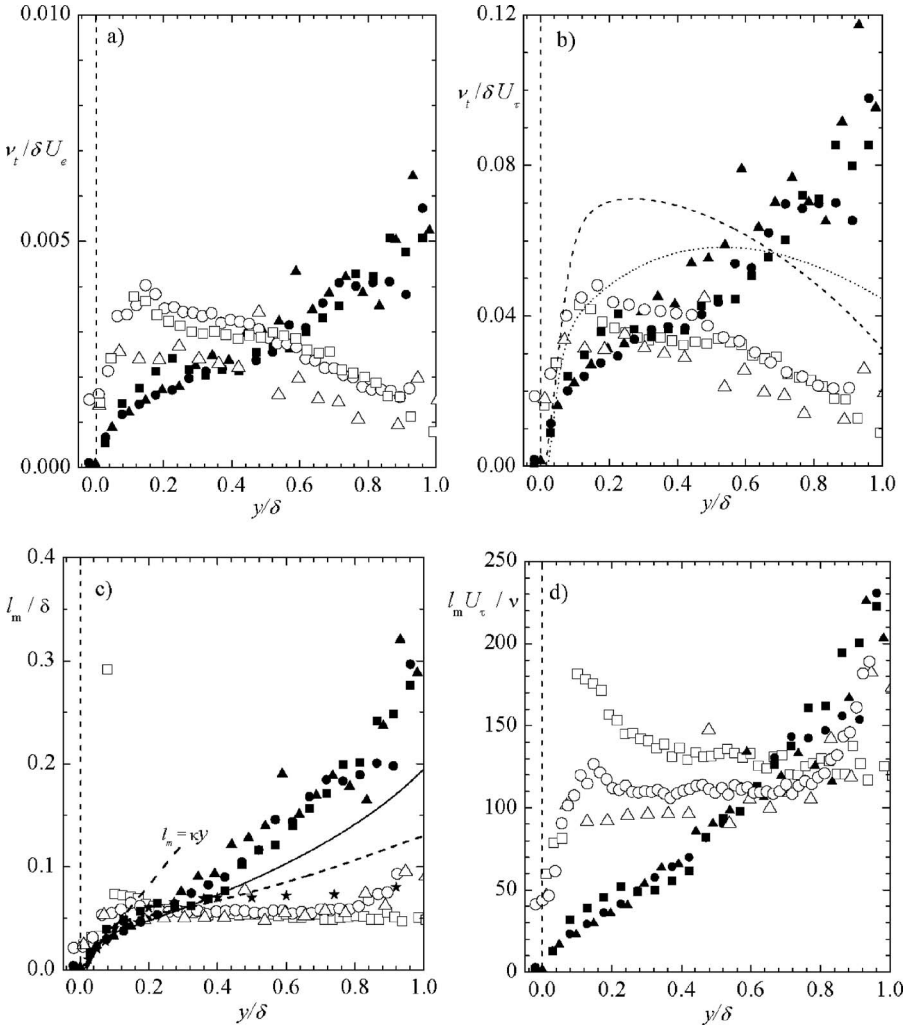

Fig. 15 Distribution of eddy viscosity (*a*, *b*) and mixing length (*c*, *d*) across the boundary layer. Symbols and notations are as in Fig. 6. ★ in (*c*) represents previous boundary layer data over wire mesh; solid and dash lines in (*b*) and (*c*) represent, respectively, previous open channel data over wire mesh and sand grains.

convective terms in the momentum equation is significantly higher than in classical near-wall turbulent flows. The pressure gradient term in the *x*-momentum equation is nearly balanced by the convective term while contributions of convective and Reynolds stress gradient terms in the *y*-equation are nearly the same. The results also demonstrate that distributions of eddy viscosity and mixing length vary with rib type but nearly independent of rib cross-section.

The values of skin friction coefficient for *k*-type ribs are significantly higher than for *d*-type ribs. For the flow conditions and the rib cross sections studied in this work, it was found that the skin friction coefficient for *d*-type roughness is nearly independent of rib cross-section. For *k*-type, however, the square ribs are more effective in augmenting flow resistance than circular and semi-circular ribs. The differences observed in flow resistance and turbulence quantities over *k*-type square ribs and circular/semi-circular ribs may be partly due to the manner in which the various cross sections influence flow separation, reattachment, and the concomitant pressure field in the immediate vicinity of the ribs.

Acknowledgment

The financial support provided by Canada Foundation for Innovation, Natural Sciences and Engineering Research Council of Canada, and Manitoba Hydro is gratefully acknowledged.

References

[1] Perry, A. E., Schofield, W. H., and Joubert, P. N., 1969, "Rough Wall Turbulent Boundary Layers," J. Fluid Mech., **37**, pp. 383–413.
[2] Tani, I., 1987, "Equilibrium, or Nonequilibrium, of Turbulent Boundary Layer Flows," Proc. Jpn. Acad., Ser. B: Phys. Biol. Sci., **63**, pp. 96–100.
[3] Sato, H., Hishida, K., and Maeda, M., 1989, "Turbulent Flow Characteristics in a Rectangular Channel with Repeated Rib Roughness," Heat Transfer in Convective Flows, National Heat Conference HTD, Vol. 107, pp. 191–196.
[4] Okamoto, S., Seo, S., Nakaso, K., and Kawai, I., 1993, "Turbulent Shear Flow and Heat Transfer Over the Repeated Two Dimensional Square Ribs on Ground Plane," J. Fluids Eng., **115**, pp. 631–637.
[5] Agelinchaab, M., and Tachie, M. F., 2006, "Open Channel Turbulent Flow Over Hemispherical Ribs," Int. J. Heat Fluid Flow, **27**(6), pp. 1010–1027.
[6] Cui, J., Patel, V. C., and Lin, C. L., 2003, "Large-Eddy Simulation of Turbulent Flow in a Channel With Rib Roughness," Int. J. Heat Fluid Flow, **24**, pp. 372–388.
[7] Leonardi, S., Orlandi, P., and Antonia, R. A., 2005, "A Method for Determining the Frictional Velocity in a Turbulent Channel Flow With Roughness on One Wall," Exp. Fluids, **38**(6), pp. 796–800.
[8] Krogstad, P. Å., Andersson, H. I., Bakken, O. M., and Ashrafian, A., 2005, "An Experimental and Numerical Study of Channel Flow With Rough Walls," J. Fluid Mech., **530**, pp. 327–352.
[9] Raupach, M. R., Antonia, R. A., and Rajagopalan, S., 1991, "Rough-Wall Turbulent Boundary Layers," Appl. Mech. Rev., **44**, pp. 1–25.
[10] Coleman, H. W., and Steele, W. G., 1995, "Engineering Application of Experimental Uncertainty Analysis," AIAA J., **33**, pp. 1888–1896.
[11] Forliti, D. J., Strykowski, P. J., and Debatin, K., 2000, "Bias and Precision Errors of Digital Particle Image Velocimetry," Exp. Fluids, **28**, pp. 436–447.
[12] Tachie, M. F., Bergstrom, D. J., and Balachandar, R., 2004, "Roughness Effects on the Mixing Properties in Open Channel Turbulent Boundary Layers,"

J. Fluids Eng., **126**, pp. 1025–1032.
[13] Johansson, A. V., and Alfredsson, P. H., 1983, "Effects of Imperfect Spatial Resolution on Measurements of Wall-Bounded Turbulent Shear Flow," J. Fluid Mech., **137**, pp. 411–423.
[14] Johnson, P. L., and Barlow, R. S., 1990, "Effect of Measuring Volume Length on Two-Component Laser Velocimeter Measurements in a Turbulent Boundary Layer," Exp. Fluids, **8**, pp. 137–144.
[15] Saikrishnan, N., Marusic, I., and Longmire, E. K., 2006, "Assessment of Dual Plane PIV Measurements in Wall Turbulence Using DNS Data," Exp. Fluids, **46**, pp. 265–278.
[16] Kameda, T., Mochizuki, S., and Osaka, H., 2004, "LDA Measurement in Roughness Sub-Layer Beneath Turbulent Boundary Layer Developed Over Two-Dimensional Square Rough Surface," 12th International Symposium on Applications of Laser Techniques to Fluid Mechanics, Lisbon, Portugal.
[17] Barenblatt, G. I., 1993, "Scaling Laws for Fully Developed Turbulent Shear Flows: Part I—Basic Hypotheses and Analysis," J. Fluid Mech., **248**, pp. 513–520.
[18] George, W. K., and Castillo, L., 1997, "Zero-Pressure Gradient Turbulent Boundary Layer," Appl. Mech. Rev., **50**(12), pp. 689–729.
[19] Buschmann, M. H., and Gad-el-Hak, M., 2003, "Debate Concerning the Mean-Velocity Profile of a Turbulent Boundary Layer," AIAA J., **41**(4), pp. 565–572.
[20] Sreenivasan, K. R., 1989, "The Turbulent Boundary Layer," *Frontiers in Exp. Fluid Mech.*, M. Gad-el-Hak, ed., Springer-Verlag, Berlin, pp. 159–209.
[21] Kotey, N. A., Bergstrom, D. J., and Tachie, M. F., 2003, "Power Laws for Rough Wall Turbulent Boundary Layers," Phys. Fluids, **15**(6), pp. 3277–1404.
[22] Tachie, M. F., Bergstrom, D. J., and Balachandar, R., 2000, "Use of Power Law Velocity Profiles in Turbulent Boundary Layers," Proc. 3rd International Symposium on Turbulence, Heat and Mass Transfer, Nagoya, Japan, pp. 183–189.
[23] Bergstrom, D. J., Tachie, M. F., and Balachandar, R., 2001, "Application of Power Laws to Low Reynolds Number Boundary Layers on Smooth and Rough Surfaces," Phys. Fluids, **13**, pp. 3277–3284.

New Model for Compressible Vortices

Yasser Aboelkassem[1]
Department of Mechanical Engineering,
McGill University,
817 Sherbrooke Street West,
Montreal, Quebec, H3A-2K6, Canada
e-mail: yasser.aboelkassem@mail.mcgill.ca

Georgios H. Vatistas
Department of Mechanical and Industrial Engineering,
Concordia University,
Montreal, Quebec H3G 1M8, Canada
e-mail: vatistas@encs.concordia.ca

A new analytical solution for self-similar compressible vortices is derived in this paper. Based on the previous incompressible formulation of intense vortices, we derived a theoretical model that includes density and temperature variations. The governing equations are simplified assuming strong vortex conditions. Part of the hydrodynamic problem (mass and momentum) is shown to be analogous to the incompressible kind and as such the velocity is obtained through a straightforward variable transformation. Since all the velocity components are bounded in the radial direction, the density and pressure are then determined by standard numerical integration without the usual stringent simplification for the radial velocity. While compressibility is shown not to affect the tangential velocity, it influences only the meridional flow (radial and axial velocities). The temperature, pressure, and density are found to decrease along the converging flow direction. The traditional homentropic flow hypothesis, often employed in vortex stability and optical studies, is shown to undervalue the density and greatly overestimate the temperature. Comparable to vorticity diffusion balance for the incompressible case, the incoming flow carries the required energy to offset the contributions of conduction, viscous dissipation, and material expansion, thus keeping the temperature steady. This model is general and can be used to obtain a compressible version for all classical previous incompressible analysis from the literature such as Rankine, Burgers, Taylor, and Sullivan vortices.
[DOI: 10.1115/1.2746897]

1 Introduction

Research on incompressible vortices goes back to the times of Rankine [1] and Helmholtz [2]. Since then, the accumulated large scale of knowledge has led to a finer understanding of the phenomenon. Comparatively less is, however, known when density variations are included. This apparent asymmetry is due to two facts. By far, the majority of naturally occurring and industrially produced vortices are of the incompressible type. Furthermore, compressible vortices are theoretically and experimentally more cumbersome.

The seeds of compressible vortex research appeared in the early 1930s with Taylor's [3] theoretical paper on the isentropic potential vortex. Work on the same subject re-emerged again in the mid-1950's in connection with studies on the vortex/shockwave interaction, Hollingsworth and Richards [4] and Howard and Matthews [5], and has continued ever since. Contributions to the confined type were mainly the result of NASA's gaseous nuclear rocket motor project, Ragsdale [6], and the refrigeration effect due to the temperature drop in a Ranque-Hilsh tube, Sibulking [7]. In another front, Meager [8] explored an approximate solution of isentropic swirling flow through a nozzle. Rott [9] discussed the temperature profile in a steady Burger's vortex under rather restrictive conditions. Mack [10] analytically examined the compressible, viscous, and heat-conducting vortex, created by a rotating cylinder in a domain of infinite extend. Later on, Bellamy-Knights [11] extended Mack's solution to take into account the radial flow. Sibulking [12] analyzed the decay of Taylor's vortex for low Mach number conditions. Brown [13] advanced Hall [14] theory on three-dimensional vortices including density variations. Colonius et al. [15] examined the compressibility effects of decaying unconfined vortices, taking into consideration the contributions of viscosity and heat transfer. Bagai and Leishman [16] visualized, via the density gradient technique, helicopter blade vortex structures stipulating isentropic flow conditions. Chiocchia [17] and Ardalan et al. [18] obtained solutions to ideal compressible vortices using hodograph plane transformations. Ellenrieder and Cantwell [19] studied the self-similarity of slightly compressible free vortices. Perez-Saborid et al. [20] investigated the evolution of unconfined vortices including the thermal aspects, while Rusak and Lee [21] looked at the compressibility effects of vortex flows inside pipes. Observations on compressible vortices are due to Mandella [22], Kalkhoran and Smart [23], and Cattafesta and Settles [24].

Future fundamental contributions in this area are relevant to a variety of industrial applications. The need is also expected to intensify in some particular areas. The recent AIRBUS paradigm reveals a market appetite toward larger (heavier) fixed wing aircrafts. As the incompressible wing tip vortex threshold is surpassed, it will also require an in-depth understanding of compressible vortices. In another sector, noise control in rotary wing aircrafts, which will conveniently transport passengers between nearby city centers, also calls for a better understanding of the phenomenon. Furthermore, vortex stability and vortex refrigeration studies will also benefit from any refinement in compressible flow descriptions.

This paper aimed to propose a theoretical analysis that is capable to extend the classical incompressible vortices into compressible version. The foundation of this formulation is the same as that, which produced the celebrated incompressible vortices of Rankine [1], Taylor [25], Burgers [26], and Sullivan [27]. As is customary, the compressibility effects will be included via the equation of energy and the ideal gas law. Based on order of magnitude arguments, the governing equations are brought into a form, amenable to further mathematical treatment. The shared analogy between the incompressible and compressible hydrodynamic parts of the problem makes all the previously known velocity solutions applicable to the present problem. Under the assumption that the Prandtl number is equal to 2/3, the energy equation provides an exact solution for the temperature. The density and the pressure are then determined from the radial momentum and the equation of state, respectively, using standard numerical integration techniques. Although the general methodology is appropriate to all previously known steady vortex formulations of

[1]Corresponding author.

Contributed by Fluids Engineering Division of ASME for publication in the JOURNAL OF FLUIDS ENGINEERING. Manuscript received March 30, 2006. final manuscript received February 26, 2007. Review conducted by Subrata Roy.

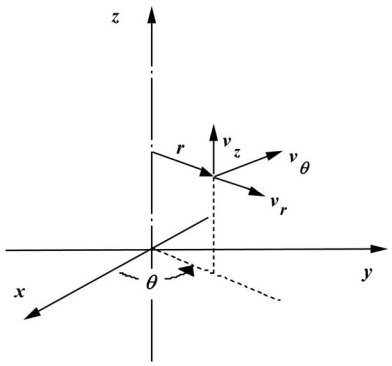

Fig. 1 The problem coordinate system

this kind, we only consider here the $n=2$ member from the n family of vortices proposed by Vatistas et al. [28] for two reasons. First, the $n=2$ is known to provide reasonable approximations to real incompressible problems, see, for example, Han et al. [29], Jeng-Lih et al. [30], Leishman [31], Coton et al. [32], Neuwerth and Jacob [33], Leishman [34], Lan [35], Mcalister [36], Dumitrescu and Frunzulica [37], Malovrh and Gandhi [38], and several others. Second, it provides for the incompressible case an explicit solution for the pressure, and makes a closed form solution for the temperature possible for Prandtl number is equal to 2/3 as mentioned before. The present analysis is an extension and generalization to the short article given by Vatistas and Aboelkassem [39].

2 Problem Formulation

Consider the motion of a steady, compressible and axisymmetric intense vortex flow. We are interested here in solutions of the particular type where the velocity has the general form

$$\mathbf{V} = [u(\xi), V(\xi), w(\xi)]$$

where $\boldsymbol{V}$ is the total velocity vector, V_r, V_θ, V_z are the radial, tangential, and axial velocity components, r, θ, z, are the radial, azimuthal, and axial coordinates, $\xi=r/r_c$ $\zeta=z/r_c$, $\beta(\xi)=\rho(\xi)/\rho_\infty$, ρ is the density, $u(\xi)=V_r/V_{\theta c}$, $w(\xi)=V_z/V_{\theta c}=\zeta h(\xi)$, $V(\xi)=V_\theta/V_{\theta c}$, r_c is the core size, $V_{\theta c}=\kappa/r_c$, $\kappa=\Gamma_\infty/2\pi$, and Γ_∞ is the vortex circulation. The subscript c denotes the value of the parameters at the core (defined as the radius where the tangential velocity attains its maximum). The coordinate system used is illustrated in Fig. 1. The starting points for the subsequent theoretical development are the simplified equations of continuity, Navier-Stokes, energy, and the equation of state of a calorically perfect gas in nondimensional form.

Conservation of mass,

$$\frac{1}{\xi}\frac{\partial}{\partial\xi}([\beta u]\xi) + [\beta h] = 0 \qquad (1)$$

Radial momentum,

$$R_e\beta\left(u\frac{\partial u}{\partial\xi} - \frac{V^2}{\xi}\right) = -R_e\frac{\partial\Pi}{\partial\xi} + \frac{4}{3}\left[\frac{\partial}{\partial\xi}\left(\frac{1}{\xi}\frac{\partial}{\partial\xi}(u\xi)\right) + \frac{1}{4}\frac{\partial}{\partial\xi}(h)\right] = 0 \qquad (2)$$

Tangential momentum,

$$R_e\beta\left(\frac{u}{\xi}\frac{\partial}{\partial\xi}(V\xi)\right) = \frac{\partial}{\partial\xi}\left(\frac{1}{\xi}\frac{\partial}{\partial\xi}(V\xi)\right) \qquad (3)$$

Axial momentum,

Table 1 Typical values of the vortex Reynolds numbers (Ref. [40])

Type of vortex	r_c (m)	$V_{\theta\max}$ (m/s)	Re	δ
Tornadoes	10.0	60.0	$4.0\ 10^7$	o (10^{-7})
Dust devils	3.0	10.0	$5.0\ 10^6$	o (10^{-6})
Whirl pools	15.0	5.0	$7.5\ 10^7$	o (10^{-7})
Cyclone chamber and wing tip vortices	0.2	0.5	$6.7\ 10^5$	o (10^{-5})
Bath tub vortices	0.2	0.1	$2.0\ 10^4$	o (10^{-4})
Aerodynamic	1.0	10.0	$6.7\ 10^5$	o (10^{-5})

$$R_e\beta\left(u\frac{\partial h}{\partial\xi}\right) = -\frac{R_e}{\zeta}\frac{\partial\Pi}{\partial\zeta} + \left[\frac{\partial^2 h}{\partial\zeta^2} + \frac{1}{\zeta}\frac{\partial h}{\partial\zeta}\right] = 0 \qquad (4)$$

Energy,

$$\frac{1}{\xi}\frac{\partial}{\partial\xi}\left(\xi\frac{\partial\Theta}{\partial\xi}\right) + \frac{\partial^2\Theta}{\partial\zeta^2} + \Pr(\gamma-1)M_o^2 f = \beta\,\Pr\mathrm{Re}\left\{u\frac{\partial\Theta}{\partial\xi} + w\frac{\partial\Theta}{\partial\zeta}\right\} - \Pr\mathrm{Re}(\gamma-1)M_o^2\left\{u\frac{\partial\Pi}{\partial\xi} + w\frac{\partial\Pi}{\partial\zeta}\right\} \qquad (5)$$

where

$$f = 2\left\{\left[\frac{\partial u}{\partial\xi}\right]^2 + \left[\frac{u}{\xi}\right]^2 + h^2 + \frac{1}{2}\left[\frac{\partial V}{\partial\xi} - \frac{V}{\xi}\right]^2 + \frac{1}{2}\left[\frac{\partial u}{\partial\zeta} + \zeta\frac{\partial h}{\partial\xi}\right]^2 - \frac{1}{3}\left(\frac{\partial u}{\partial\xi} + \frac{u}{\xi} + h\right)^2 + \frac{1}{3}\left[\frac{1}{\xi}\frac{d\beta u\xi}{d\xi} + \beta h\right]^2\right\}$$

Equation of state,

$$\Pi = \frac{\beta\Theta}{\gamma M_o^2} \qquad (6)$$

where $\Pi=p/\rho_\infty V_{\theta c}^2$, p is the static pressure, $\mathrm{Re}=\rho_\infty V_{\theta c} r_c/\mu$ is the vortex Reynolds number, μ is the viscosity, $\Theta=T/T_\infty$, T is the temperature, T_∞ is the temperature far from the vortex center, f is the viscous dissipation function, $\Pr=\mu c_p/k$ is the Prandtl number, k is the thermal conductivity, c_p is the heat capacity constant pressure, R is the gas constant, M_o is the vortex Mach number $(V_{\theta c}/\sqrt{\gamma RT_\infty})$, γ is the specific heat ratio (c_p/c_v), c_v is the heat capacity constant pressure volume, and δ indicates a small number.

Because we are dealing with strong vortices, the traditional assumption requiring that u and $h \ll V$ is implemented. In terms of order of magnitude, if V is assumed to be of order 1 and in order to establish intense (strong) conditions, u and h could be taken as of order δ, where $\delta\sim 1/\mathrm{Re}$ (for example, in aerodynamically produced vortices, $\mathrm{Re}\sim 10^5$) see Table 1, Vatistas [40]. Based on an order of magnitude argument, one can bring the above system of equations into a simpler form. All terms in Eqs. (1) and (3) are of the same order of magnitude and for this reason both equations remain as they are.

Neglecting the terms in Eq. (2) of order δ and higher, we obtain

$$\frac{\beta V^2}{\xi} = \frac{\partial \Pi}{\partial \xi} \tag{7}$$

The axial momentum equation (4) suggests that the static pressure should not vary appreciably in the ζ direction:

$$\mathrm{Re}\frac{\partial \Pi}{\partial \zeta} \sim \delta \quad \text{or} \quad \frac{\partial \Pi}{\partial \zeta} \sim \delta^2 \rightarrow \frac{\partial \Pi}{\partial \zeta} \approx 0$$

In other words, the pressure should be a sole function of ξ. It is almost trivial to establish, from the radial momentum and state equation, that both the density and temperature must also be functions of ξ alone. Therefore, the energy equation simplifies into

$$\frac{1}{\xi}\frac{d}{d\xi}\left(\xi\frac{d\Theta}{d\xi}\right) + \mathrm{Pr}(\gamma-1)M_o^2 f = \beta\,\mathrm{Pr}\,\mathrm{Re}\,u\frac{d\Theta}{d\xi} - \mathrm{Pr}\,\mathrm{Re}(\gamma-1)M_o^2 u\frac{d\Pi}{d\xi} \tag{8}$$

where

$$f = \xi^2\left\{\frac{d}{d\xi}\left[\frac{V}{\xi}\right]\right\}^2$$

Now, by letting $U=\beta\,\mathrm{Re}\,u$ and $H=\beta\,\mathrm{Re}\,h$, and replacing the pressure gradient by its equivalent $\beta V^2/\xi$, the governing equations transform into the following:

Continuity,

$$\frac{1}{\xi}\frac{dU\xi}{d\xi} + H = 0 \tag{9}$$

Radial momentum,

$$\frac{\beta V^2}{\xi} = \frac{d\Pi}{d\xi} \tag{10}$$

Tangential momentum,

$$\frac{U}{\xi}\frac{dV\xi}{d\xi} = \frac{d}{d\xi}\left\{\frac{1}{\xi}\frac{dV\xi}{d\xi}\right\} \tag{11}$$

Energy,

$$\frac{1}{\xi}\frac{d}{d\xi}\left(\xi d\frac{d\Theta}{d\xi}\right) - \mathrm{Pr}U\frac{d\Theta}{d\xi} = -\mathrm{Pr}(\gamma-1)M_o^2\left\{U\frac{V^2}{\xi} + \xi^2\left\{\frac{d}{d\xi}\left[\frac{V}{\xi}\right]\right\}^2\right\} \tag{12}$$

Equation of state,

$$\Pi = \frac{\beta\Theta}{\gamma M_o^2} \tag{13}$$

The required boundary conditions are as follows:

(i) $\xi=0$, $V(\xi)=U(\xi)=0$, and $dH(\xi)/d\xi=d\Theta(\xi)/d\xi=0$.
(ii) $\xi\rightarrow\infty$, $V(\xi)\xi$, $\Theta(\xi)$, $\gamma M_o\Pi$, and $\beta(\xi)\rightarrow 1$.

The hydrodynamic portion, which consists of Eqs. (9)–(11), has now exactly the same form as its incompressible counterpart; see Vatistas et al. [28] or Vatistas [40]. By analogy, the known solution for these equations when using the $n=2$ vortex is

$$U = -\frac{6\xi}{1+\xi^4} \tag{14}$$

$$H = \frac{24\xi^2}{(1+\xi^4)^2} \tag{15}$$

$$V = \frac{\xi}{\sqrt{1+\xi^4}} \tag{16}$$

One should appreciate that all the above velocity components of this particular solution reduces asymptotically to zero as $\xi\rightarrow\infty$.

$$u = -\frac{6\xi^3}{\mathrm{Re}\,\beta(1+\xi^4)} \quad \text{and} \quad w/\zeta = \frac{24\xi^2}{\mathrm{Re}\,\beta(1+\xi^4)^2} \tag{17}$$

Because the actual radial and axial velocity components involve the density, both will be affected by compressibility. On the other hand, the tangential velocity will not be affected. It is important to note at this point that for the incompressible case, if the radial and axial velocity components are neglected, the emerging incompressible system is mathematically closed since there are an equal number of equations as unknown.

Continuity,

$$\frac{1}{\xi}\frac{du\xi}{d\xi} + h = 0 \tag{18}$$

ξ momentum,

$$\frac{V^2}{\xi} = \frac{d\Pi}{d\xi} \tag{19}$$

θ momentum,

$$\frac{\mathrm{Re}\,u}{\xi}\frac{dV\xi}{d\xi} = \frac{d}{d\xi}\left\{\frac{1}{\xi}\frac{dV\xi}{d\xi}\right\} \tag{20}$$

When, however, the radial and axial velocity components are to be considered, the system is underdetermined, since there are more unknowns than available equations. The problem is thus open and as such there exists an infinite number of solutions. It appears that this detail has been omitted in the technical literature. It is, nevertheless, a significant feature of the formulation because it supports the following argument; if Burger's, Sullivan, and other classical vortex models are accepted to be exact solutions to the Navier–Stokes equations, so must be the previous "empirical" vortex formulations such as those of Scully [41], Vatistas et al. [28], and others. After all, they satisfy the same equations. The last property is also the reason behind the past proliferation of intense vortex formulations.

3 Model Solution

Solutions for ideal conditions such as for an isentropic flow are often useful because they provide a point of reference, furnish a sense of direction, and sometimes yield acceptable approximations to real problems. Here, we will first deal with the isentropic compressible vortex hypothesis. After that, we will derive a solution for the most general case that the present formulation can provide. Under the constant entropy flow assumption, all the processes must be reversible and adiabatic. The last assumption must be respected by all material elements that constitute the field. This flow idealization will emerge if the gas is frictionless and nonheat conducting ($\mu=k=0$). In order for the θ momentum to be respected for any velocity (V) profile, the radial component (and consequently the axial) must be zero. Alternatively, the velocity field should be of the form $[0, V(\xi), 0]$. Based on these constraints, continuity will be identically satisfied, while the ξ- and ζ-momentum equations will also be respected regardless of the tangential velocity form and yield they are given, respectively, as

$$\beta\frac{V^2}{\xi} = \frac{d\Pi}{d\xi}$$

and

$$0 = \frac{\partial \Pi}{\partial \zeta}$$

The θ momentum,

$$\frac{\beta u}{\xi}\frac{\partial V\xi}{\partial \xi}=0 \tag{21}$$

Since the energy equation is automatically satisfied, Gibbs' equation for a calorically perfect gas will provide the necessary additional relation to close the system,

$$\Pi=\frac{\beta^{\gamma}}{\gamma M_o^2} \tag{22}$$

Based on the above equation (23) along with the ξ momentum and the equation of state, taking the azimuthally velocity to be that of an $n=2$ vortex yields the pressure, density, and temperature:

$$\Pi=\frac{1}{\gamma M_o^2}\left\{1-\frac{\gamma-1}{2}M_o^2\left(\frac{\pi}{2}-\arctan\xi^2\right)\right\}^{\gamma/\gamma-1} \tag{23}$$

$$\beta=\left\{1-\frac{\gamma-1}{2}M_o^2\left(\frac{\pi}{2}-\arctan\xi^2\right)\right\}^{1/\gamma-1} \tag{24}$$

and

$$\Theta=1-\frac{\gamma-1}{2}M_o^2\left(\frac{\pi}{2}-\arctan\xi^2\right) \tag{25}$$

The present density expression, Eq. (24), is equivalent to the one derived by Bagai and Leishman [16] in order to visualize vortex structures using the density gradient technique. The most general solution for this class of compressible vortices can be obtained if the homentropic constraint is lifted, thus allowing the flow to be adiabatic and irreversible. Solving the energy equation (12) and applying the temperature derivative boundary condition at $\xi=0$ gives

$$\Theta(\xi)=(\gamma-1)\mathrm{Pr}\,M_o^2\int_0^{\xi}\frac{1}{\vartheta(1+\vartheta^4)^{3/2\mathrm{Pr}}}\left\{\int_0^{\vartheta}\frac{6t^5+2t^9}{(1+t^4)^{3-3/2\mathrm{Pr}}}dt\right\}d\vartheta + c_a \tag{26}$$

From the second temperature boundary condition, we have

$$c_o=1-(\gamma-1)\mathrm{Pr}\,M_o^2\lim_{L\to\infty}\int_0^{L}\frac{1}{\vartheta(1+\vartheta^4)^{3/2\mathrm{Pr}}}\left\{\int_0^{\vartheta}\frac{6t^5+2t^9}{(1+t^4)^{3-3/2\mathrm{Pr}}}dt\right\}d\vartheta$$

The above integrals, and those to come, are easily evaluated by any of the standard numerical methods, say, Romberg's, or better the application of mathematical software such as MATHEMATICA, MAPLE, or MATLAB. The equation of state (13) and the radial momentum (10) yield

$$\frac{d}{d\xi}\ln(\beta\Theta)=\gamma M_o^2\frac{V^2}{\xi\Theta} \tag{27}$$

Integration of the above equation and application of the boundary condition for the density when $\xi\to\infty$ give

$$\beta=\frac{c_1}{\Theta}\exp\left(\gamma M_o^2\int_0^{\xi}\frac{V^2}{\xi\Theta}d\xi\right) \tag{28}$$

where

$$c_1=\frac{1}{\exp\left(\gamma M_o^2\lim_{L\to\infty}\int_0^{L}\frac{V^2}{\xi\Theta}d\xi\right)}$$

The pressure is then determined using the equation of state given by Eq. (13). Burger's vortex formulations do not allow for a similar analytical treatment (without any further simplifications see, for example, Rott [9]) because the radial velocity component grows without bounds in ξ. For the specific case where Pr=2/3, integrating once the energy equation and application of the temperature boundary condition for $\xi=0$ gives

$$\frac{d\Theta}{d\xi}=\frac{2}{3}(\gamma-1)M_o^2\frac{\xi^5}{(1+\xi^4)^2}$$

The above solution can be easily achieved using the standard integrating factor concept. A second integration along with the condition at $\xi\to\infty$ provides the exact solution for the temperature,

$$\Theta(\xi)=1+\frac{(\gamma-1)M_o^2}{6}\left\{\arctan(\xi^2)-\frac{\xi^2}{1+\xi^4}-\frac{\pi}{2}\right\} \tag{29}$$

Since an exact solution for the temperature is now available, we should use it to validate the numerical integration. The results for vortex Mach numbers of 0.4 and 0.8 are shown in Table 2. The exact Θ corresponds to the values produced by Eq. (29), while the approximate ones are the values obtained solving Eq. (28) numerically. It is clear from the same table that the approximate and exact Θ values are the same up to the sixth decimal. Therefore, numerical integration provides a reasonable approximation to the problem.

Next, the sensitivity of the results to the value of the Pr number is examined. It can be seen from Table 3 that in one atmosphere and 300° K, the values of Prandtl number for most of the common gases range from 0.680 for oxygen to 0.716 for nitrogen. For a Mach number of 0.8, a maximum deviation of less than 0.1% will occur if one takes Pr to be 2/3 for nitrogen instead of the actual of 0.716. It is customary under standard conditions to assume a Pr =0.7. As expected, there is an insignificantly small difference (less than 0.02%) between the exact (Pr=2/3) and the numerically obtained (Pr=0.700) results for a Mach number of 0.8. For this reason, the exact temperature formula will be used for the present calculations.

Table 2 Exact and approximate values for the temperature (Pr=2/3, L=1000)

	M_o=0.4		M_o=0.8	
ξ	Θ_{exact}	Θ_{approx}	Θ_{exact}	Θ_{approx}
0.0	0.983 245	0.983 245	0.932 979	0.932 979
0.5	0.983 348	0.983 348	0.933 393	0.933 393
1.0	0.986 289	0.986 289	0.945 156	0.945 156
1.5	0.991 580	0.991 580	0.966 321	0.966 321
2.0	0.994 877	0.994 877	0.979 508	0.979 508
2.5	0.996 644	0.996 644	0.986 574	0.986 574
3.0	0.997 649	0.997 649	0.990 596	0.990 596

4 Results

The analysis assumes a perfect gas, which implies that all the material properties are constant. In reality, however, the properties c_p, c_p, k, and μ do depend on the temperature. In order to be pragmatic, the applicability of the solution should be limited to small temperature variations, say, around 300 K. According to the theoretical treatment in Sec. 2, the tangential velocity should retain the shape of the incompressible vortex. The present theoreti-

Table 3 Prandtl number of different gases at one atmosphere and 300° K

Gas	Pr
Air	0.707
Helium	0.680
Hydrogen	0.701
Nitrogen	0.716
Oxygen	0.711

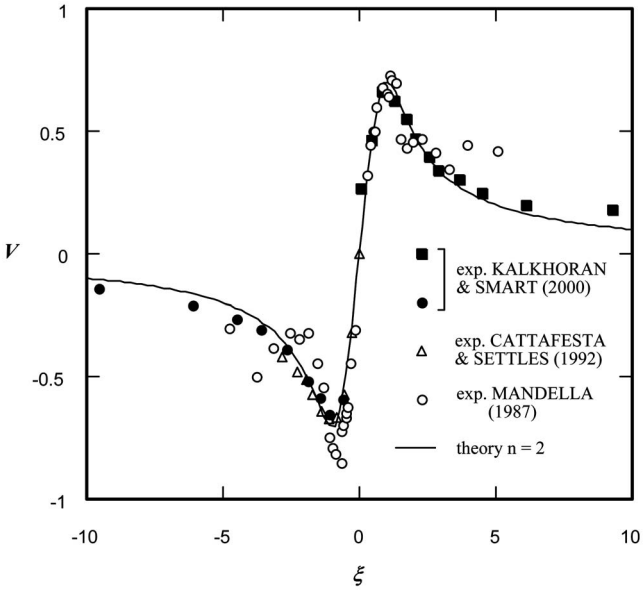

Fig. 2 Correlations of the *n*=2 vortex with the experimental data

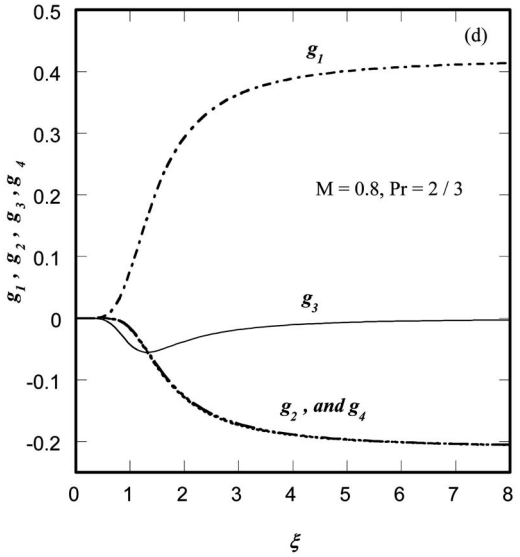

Fig. 3 The magnitude of the different terms in the energy equation (15)

cal deduction is reasonably supported by the observations of Mandella [22], Kalkhoran and Smart [23], and Cattafesta and Settles [24], shown in Fig. 2.

The experimental tangential velocity data were treated via the least squares described by Vatistas [42]. Furthermore, properties such as vorticity and circulation should remain the same as those of the incompressible case. Since the mechanical dissipation does not involve the density, the total frictional losses per unit height will be also equal to the incompressible $n=2$ vortex. Multiplying Eq. (12) by ξ and then integrating once followed by the application of the temperature derivative at $\xi=0$, we obtain

$$-\xi\frac{d\Theta}{d\xi}+\Pr\int_0^{\xi}U\xi\frac{d\Theta}{d\xi}d\xi-\Pr(\gamma-1)M_o^2\int_0^{\xi}[UV^2+\xi f]d\xi=0$$

$$g_1 \quad g_2 \quad g_3 \quad g_4 \tag{30}$$

where g_1, g_2, g_3, and g_4 represent the heat conduction, convection, cooling of fluid element due to expansion, and the heat generated by viscous action, respectively. The magnitudes of the different terms in the Eq. (30) are shown in Fig. 3. There are four processes in action. In order for the flow to balance the centrifugal force, the pressure must increase with the radius. Material elements carried by the converging field (g_3) in the direction of decreasing pressure dilate and, therefore, their temperature ought to drop, attaining a minimum at the center where the temperature must obey the symmetry boundary condition. The effects of heat conduction (g_1) and heat generation (g_4) due to friction are not sufficient to compensate for the temperature dive. Finally, the converging flow carries with it the energy (g_2) required to balance the three other effects and, thus, keeping the temperature steady.

The pressure, density, and temperature profiles for a range of Mach numbers are given in Fig. 4(*a*), 4(*b*), and 4(*c*). It is evident that all three properties decrease along the flow direction attaining minimum values at the vortex center. The present results are in accord with the observations of Mandella [22], and the experimental temperature profiles of Kalkhoran and Smart [23] and Cattafesta and Settles [24]. From this figure, we also see that the isentropic flow condition can only approximate the more realistic flow asymptotically, as $\xi\to\infty$.

The meridional flow velocity components retain the shapes of the incompressible vortex but increase in magnitude, see Fig. 5. As the fluid approaches the center, the fluid elements expand and, thus, the density drops. In order to conserve mass, the fluid compensates for by a velocity increase.

The converging flow, which carries the required vorticity,

$$\beta\,\mathrm{Re}\,u\Omega=\frac{d\Omega}{d\xi}$$

to keep the vortex steady is amply evident from the radial velocity profiles. The last effect is also present in the observations of Cattafesta and Settles [24] and Kalkhoran and Smart [23], where the radial velocity is seen to increase inwards, attaining a maximum, and then reducing gradually to zero at the origin. Both the radial and axial velocity components intensify with the vortex Mach number. The larger the vortex Mach number is, the sharper the density reduction, leading into a more profound adjustment by the velocity.

As mentioned earlier, isentropic flow condition can only approximate the more realistic flow asymptotically as $\xi\to\infty$. This utopian flow will be approached by the general solution (say, to degree $\delta=10^{-5}$), beyond ~35 and ~65 core radii from the center, for M_o values of 0.4 and 0.8, respectively. In addition to the previously treated conservation laws, every mathematical representation of reality must respect the entropy axiom. Using Oswatitsch [43] entropy theorem, it is not difficult to show that the entropy of the general case rises along the flow direction,

$$\Theta\,\Pr U\frac{d\Delta S}{d\xi}=\frac{1}{\xi}\frac{d}{d\xi}\left(\xi\frac{d\Theta}{d\xi}\right)+\Pr(\gamma-1)M_o^2 f$$

$$=\Pr U\frac{d\Theta}{d\xi}-\Pr(\gamma-1)M_o^2U\frac{V^2}{\xi}$$

where $\Delta S=(s-s_\infty)/c_p$, and s is the specific entropy. Integrating once the above equation and applying the boundary condition, $\xi\to\infty$, $\Delta S\to 0$ give

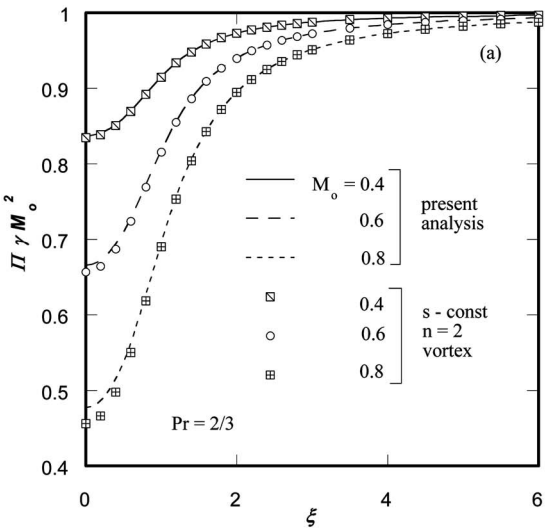

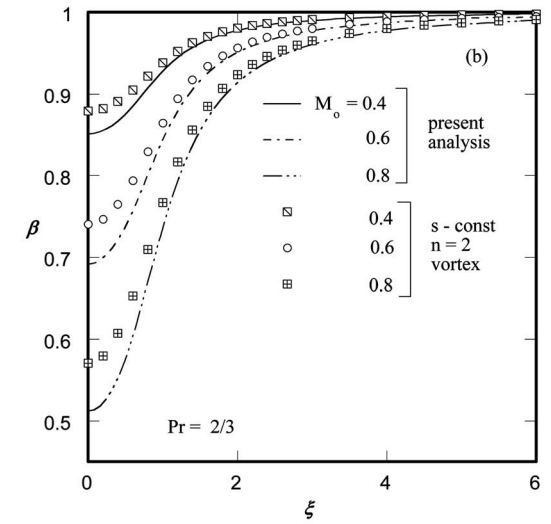

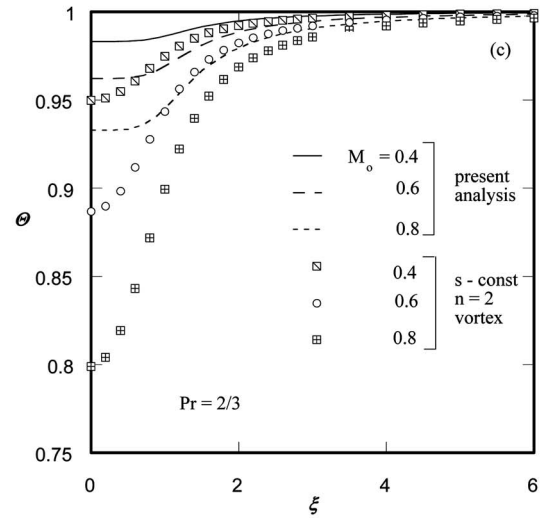

Fig. 4 The static pressure (*a*), density (*b*), and temperature (*c*). (The isentropic curves in (*a*)–(*c*) are calculated using Eq. (16).

$$\Delta S = -\frac{1}{3}(\gamma-1)M_o^2\int_0^{\xi}\frac{(\vartheta^4+3)\vartheta}{\Theta(1+\vartheta^4)^2}d\vartheta + c_2$$

where

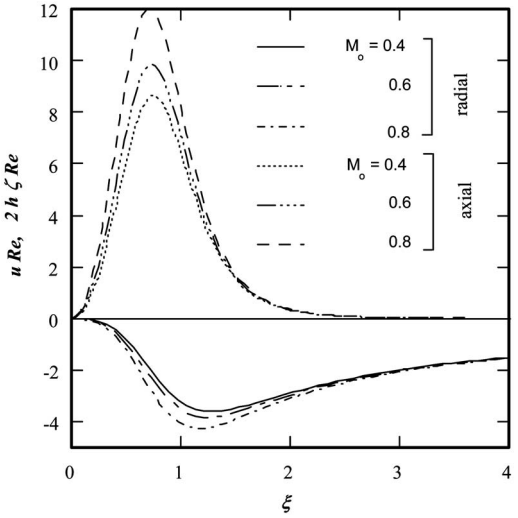

Fig. 5 The radial and axial velocity components of the meridional flow

$$c_2 = -\frac{1}{3}(\gamma-1)M_o^2\lim_{L\to\infty}\int_0^{L}\frac{(\vartheta^4+3)\vartheta}{\Theta(1+\vartheta^4)^2}d\vartheta$$

The results for M_o=0.8, 0.6, and 0.4 for Pr=2/3 are shown in Fig. 6, where the entropy is seen to rise along the flow direction confirming that the present mathematical formulation of the problem is consistent with the second law of thermodynamics.

5 Conclusions

A novel theoretical analysis that is capable of extending the incompressible vortex models into compressible counterpart is derived in this article. The analysis indicated and was confirmed by previous experiments that the density variations affect only both radial and axial velocity components unlike the tangential velocity. The significant increase in the radial and axial velocity components near the core was attributed to the thinning out of the material elements. Similar to the vorticity diffusion balance, it is concluded here that the converging flow carries the needed energy inwards to offset the effects of conduction, viscous dissipation, and material expansion. The results were confirmed qualitatively using the outcome of past experiments. Although we only consid-

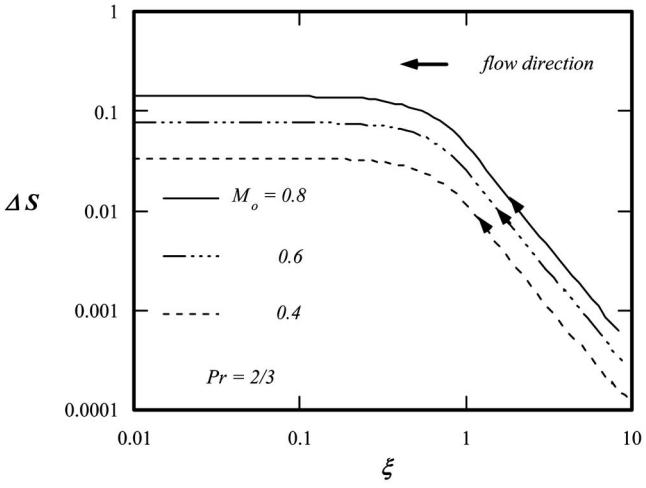

Fig. 6 Entropy increase along the flow direction

ered the $n=2$ vortex, the basic methodology can also be employed to extend other incompressible steady vortex formulations of the same kind.

Acknowledgment

The present work was supported by the Natural Science and Engineering Research Council (NSERC) of Canada.

References

[1] Rankine, W. J. M., 1858, *Manual of Applied Mechanics*, C. Griffen Co., London, England.
[2] Helmholtz, H., 1858, "Uber die Integrale der Hydrodynamischen Gleichungen, Welche den Wirbelbewegungen Entsprechen," J. Reine Angew. Math., **55**, pp. 25–55.
[3] Taylor, G. I., 1930, "Recent Work on the Flow of Compressible Fluids," J. Lond. Math. Soc., **5**, pp. 224–240.
[4] Hollingsworth, M. A., and Richards, E. J., 1955, "A Schlieren Study of the Interaction Between a Vortex and a Shockwave in a Shock Tube," Aeronautical Research Council Technical Report No. 17985.
[5] Howard, L. N., and Matthews, D. L., 1956, "On the Vortices Produced in Shock Diffraction," J. Appl. Phys., **27**, pp. 223–231.
[6] Ragsdale, R. G., 1960, "NASA Research on the Hydrodynamics of the Gaseous Vortex Reactor," NASA Technical Report No. D-288.
[7] Sibulking, M., 1962, "Unsteady, Viscous, Circular Flow Part 3: Application to the Ranque-Hilsh Vortex Tube," J. Fluid Mech., **12**, pp. 289–298.
[8] Meager, A., 1961, "Approximate Solution of Isentropic Swirling Flow Through a Nozzle," ARS Journal, **32**, pp. 1140–1148.
[9] Rott, N., 1959, "On The Viscous Core of a Line Vortex," Z. Angew. Math. Phys., **10**, pp. 73–81.
[10] Mack, L. M., 1960, "The Compressible Viscous Heat-Conducting Vortex," J. Fluid Mech., **8**, pp. 284–292.
[11] Bellamy-Knights, P. G., 1980, "Viscous Compressible Heat Conducting Spiraling Flow," Q. J. Mech. Appl. Math., **33**, pp. 321–336.
[12] Sibulking, M., 1962, "Unsteady, Viscous, Circular Flow Part 3: Application to the Ranque-Hilsh Vortex Tube," J. Fluid Mech., **12**, pp. 289–298.
[13] Brown, S. N., 1965, "The Compressible Inviscid Leading Edge Vortex," J. Fluid Mech., **22**, pp. 17–32.
[14] Hall, M. G., 1965, "The Structure of Concentrated Vortex Cores," Prog. Aeronaut. Sci., **7**, pp. 53–100.
[15] Colonius, T., Lele, S. K., and Moin, P., 1991, "The Free Compressible Viscous Vortex," J. Fluid Mech., **230**, pp. 45–73.
[16] Bagai, A., and Leishman, J. G., 1993, "Flow Visualization of Compressible Vortex Structures Using Density Gradient Techniques," Exp. Fluids, **15**, pp. 431–442.
[17] Chiocchia, G., 1989, "A Hodograph Approach to the Rotational Compressible Flow of an Ideal Fluid," Q. Appl. Math., **47**, pp. 513–528.
[18] Ardalan, K., Meiron, D. I., and Pullin, D. I., 1995, "Steady Compressible Vortex Flows: The Hollow-Core Vortex Array," J. Fluid Mech., **301**, pp. 1–17.
[19] von Ellenrieder, K., and Cantwell, B. J., 2000, "Self-Similar Slightly Compressible Free Vortices," J. Fluid Mech., **423**, pp. 293–315.
[20] Perez-Saborid, M., Herrada, M. A., Gomez-Barea, A., and Barrero, A., 2002, "Downstream Evolution of Unconfined Vortices: Mechanical and Thermal Aspects," J. Fluid Mech., **471**, pp. 51–70.
[21] Rusak, Z., and Lee, J. H., 2002, "The Effects of Compressibility on the Critical Swirl of Vortex Flows in a Pipe," J. Fluid Mech., **461**, pp. 301–319.
[22] Mandella, M. J., 1987, "Experimental and Analytical Studies of Compressible Vortices," Ph.D. thesis, Department of Applied Physics, Stanford University.
[23] Kalkhoran, I. M., and Smart, M. K., 2000, "Aspects of Shock Wave-induced Vortex Breakdown," Prog. Aerosp. Sci., **36**, pp. 63–95.
[24] Cattafesta, L. N., and Settles, G. S., 1992, "Experiments on Shock/Vortex Interaction," AIAA Paper No. 92-0315.
[25] Taylor, G. I., 1918, "On the Dissipation of Eddies," *The Scientific Papers of Sir Geoffrey Ingram Taylor* (Meteorology, Oceanography and Turbulent Flow), G. K. Batchelor, ed., Cambridge University Press, Cambridge, Vol. 2, pp. 96–101.
[26] Burgers, J. M., 1948, "A Mathematical Model Illustrating the Theory of Turbulence," Adv. Appl. Mech., **1**, pp. 171–199.
[27] Sullivan, R. D., 1959, "A Two-Cell Vortex Solution of the Navier-Stokes Equations," J. Aerosp. Sci., **26**(11), pp. 767–768.
[28] Vatistas, G. H., Kozel, V., and Minh, W., 1991, "A Simpler Model for Concentrated Vortices," Exp. Fluids, **11**, pp. 73–76.
[29] Han, Y. Q., Leishman, J. G., and Coyone, A. J., 1997, "Measurements of the Velocity and Turbulence Structure of a Rotor Rip Vortex," AIAA J., **35**(3), pp. 477–485.
[30] Jeng-Lih, H., Jing-Fa, T., Chye-Horng, C., and Cheng-Tsair, Y., 1999, "Measurements of Propeller Tip Vortices Around Near Wake Zone," Ship Technology Research, **46**(2), pp. 93–110.
[31] Leishman, J. G., 1998, "Measurements of a Periodic Wake of a Hovering Rotor," Exp. Fluids, **125**, pp. 252–361.
[32] Coton, F. N., Copland, C. M., and Galbraith, A. D., 1998, "An Experimental Study of the Idealized Vortex System on a Novel Rotor Blade Tip," Aeronaut. J., **102**, pp. 385–392.
[33] Neuwerth, S. B., and Jacob, D., 2000, "The Inlet-Vortex System of Jet Engines Operating Near the Ground," *18th AIAA Applied Aerodynamics Conference*, Denver, CO, Aug. Paper No. AIAA-2000-3998, pp. 14–17.
[34] Leishman, J. G., 2002, *Principles of Helicopter Aerodynamics*, Cambridge University Press, Cambridge, U.K.
[35] Lan, N., 2003, "Mathematical Analysis of Dust Devils," M.S. thesis School of Engineering, Cranfield University.
[36] Mcalister, K. W., 2004, "Rotor Wake Development During the First Revolution," J. Am. Helicopter Soc., **49**(4), pp. 371–390.
[37] Dumitrescu, H., and Frunzulica, F. A., 2004, "Free-Wake Aerodynamic Model for Helicopter Rotors," Proceedings of the Romanian Academy, **5**(3), pp. 1–9.
[38] Malovrh, B., and Gandhi, F., 2005, "Sensitivity of Helicopter Blade-Vortex-Interaction Noise and Interaction Parameters," J. Aircr., **42**(3), pp. 685–697.
[39] Vatistas, G. H., and Aboelkassem, Y., 2006, "Extension of the Incompressible n_2 Vortex Into Compressible," AIAA J., **44**(8), 1912–1915.
[40] Vatistas, G. H., 1998, "New Model for Intense Self-Similar Vortices," J. Propul. Power, **14**(4), pp. 462–469.
[41] Scully, M. P., 1975, "Computation of Helicopter Rotor Wake Geometry and Its Influence on Rotor Harmonic Airloads," Aeroelastic and Structures Research Laboratory, Massachusetts Institute of Technology, Report No. ASRL TR 178–1.
[42] Vatistas, G. H., 2004, "The Fundamental Properties of the $n=2$ Vortex Model," Transactions CSME, **28**(1), pp. 53–58.
[43] Oswatitsch, K., 1945, "Der Luftwiderstand als Integral des Entropiestromes," Nachr. Ges. Wiss. Goettingen, Math.-Phys. Kl., pp. 88–90.

Force Stream Function Method Applied to Classical Griffith's Crack Problem

Xiang Wu[1]
WXY Investments,
4764 Washtenaw Ave., Suite B4,
Ann Arbor, MI 48108

Joseph Genin
Department of Mechanical Engineering,
New Mexico State University,
Las Cruces, NM 88003

*In a previous paper (Wu, X., and Genin, J., 2003, J. Strain Anal. Eng. Des., **38**(2), pp. 181–185), we presented a new stress analysis procedure, the force stream function method. It established a general relationship between a fluid stream function and a force stream function through pure elasticity examples. Here, we expand its applications to the field of linear fracture. A brief review of the new method is provided at the paper's beginning. When applied to the classical Griffith's crack problem, the corresponding fluid stream function of a flow past a normal plate is conveniently used as an analog for the crack problem. Numerical results are employed to verify the general relation in this particular case. The significance of the new force stream function method and some difficulties of its applications are discussed in the paper's conclusion.*
[DOI: 10.1115/1.2746899]

Keywords: stress function, Griffith's crack, stress field, fluid stream function

Introduction

In Wu and Genin [1], a new stress function method, called the force stream function method, was introduced using two classic elasticity problems: torsion and a hole in an infinite plate under tension. Hence, it may be deduced that the force stream function method will apply to general elasticity problems. Then, one may wonder if the new method will apply to fracture problems. Here, one classical linear fracture example, namely, Griffith's crack problem, is successfully solved using the new method without any fundamental modification to the proposed subtle relationship equations. A numerical verification is used since a closed-form verification is unlikely. Even with the new success, the difficulties of new applications of the method are noted in the Conclusion and Discussion section. We begin with a review of the new method.

Review of Force Stream Function Method

The governing equations for the force stream function Ψ are

$$\sigma_x + \tau_{xy} + \tau_{xz} = F_x$$

$$\tau_{xy} + \sigma_y + \tau_{yz} = F_y$$

$$\tau_{xz} + \tau_{yz} + \sigma_z = F_z$$

and

$$F_x = \frac{\partial \Psi}{\partial y}, \quad F_y = -\frac{\partial \Psi}{\partial x}$$

in which σ_{ij} is a stress tensor. For two-dimensional plane stress or plane strain problems, where $\tau_{xz} = \tau_{yz} = 0$, the governing equations reduce to

$$\sigma_x + \tau_{xy} = \frac{\partial \Psi}{\partial y} \tag{1}$$

$$\tau_{xy} + \sigma_y = -\frac{\partial \Psi}{\partial x} \tag{2}$$

Since the force stream function is closely related to the fluid stream function, the relations between the force stream function and the corresponding fluid stream function ψ or fluid potential function ϕ are

$$\Psi = \Psi_I + \Psi_{II}$$

and

$$\Psi_I = \frac{\sigma}{U}\psi \tag{3}$$

$$\frac{\partial^2 \Psi_{II}}{\partial x^2} + \frac{\partial^2 \Psi_{II}}{\partial y^2} = 2\frac{\sigma}{U}\frac{\partial}{\partial n}\left(\frac{\partial \phi}{\partial x} + \frac{\partial \phi}{\partial y}\right) \tag{4}$$

where σ/U is the dimensional factor and n is the nominal direction normal to the flow. When ψ is a harmonic function, Eqs. (3) and (4) become

$$\frac{\partial^2 \Psi}{\partial x^2} + \frac{\partial^2 \Psi}{\partial y^2} = 2\frac{\sigma}{U}\frac{\partial}{\partial n}\left(\frac{\partial \phi}{\partial x} + \frac{\partial \phi}{\partial y}\right)$$

or for two-dimensional cases

$$-\frac{\partial}{\partial x}(\tau_{xy} + \sigma_y) + \frac{\partial}{\partial y}(\sigma_x + \tau_{xy}) = 2\frac{\sigma}{U}\frac{\partial}{\partial n}\left(\frac{\partial \psi}{\partial y} - \frac{\partial \psi}{\partial x}\right) \tag{5}$$

The relation between a force stream function and an Airy stress function Φ is

$$\Psi = \frac{\partial \Phi}{\partial y} - \frac{\partial \Phi}{\partial x}$$

Torsional problems and the stress distribution around a circular hole are two classes of problems that were solved by the force stream function method in [1]. For torsional examples, it was shown that Prandtl's stress function is mathematically equivalent to a force stream function. It was also shown that the force stream function is related to the fluid stream function of corresponding rotational flow. In the stress around a circular hole example, where flow past a cylinder is the corresponding fluid problem, the general relation between the force stream function and fluid stream function in the form of Eq. (5) was proven correct in closed form.

[1]Corresponding author.

Contributed by the Fluids Engineering Division of ASME for publication in the JOURNAL OF FLUIDS ENGINEERING. Manuscript received November 30, 2005; final manuscript received February 25, 2007. Review conducted by Subrata Roy.

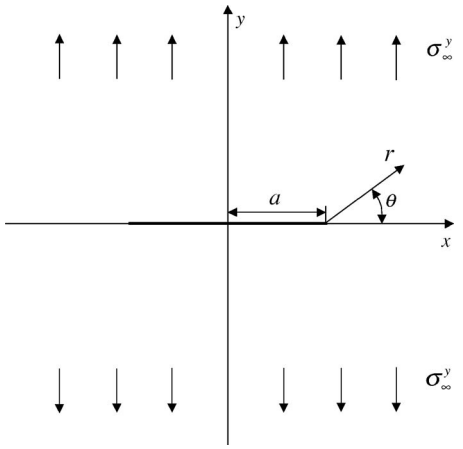

Fig. 1 Griffith's problem

To expand the examples into linear fracture mechanics, in the section that follows, the force stream function method is applied to the classical Griffith's crack problem.

Griffith's Crack Problem

Griffith's problem is the study of a crack in an infinite planar body under uniform tension as depicted in Fig. 1 (solved in [2]). The planar stresses are found to be [3]

$$\sigma_x = \mathrm{Re}\, Z - y\, \mathrm{Im}\, Z' + A$$

$$\sigma_y = \mathrm{Re}\, Z - y\, \mathrm{Im}\, Z' - A$$

$$\tau_{xy} = -y\, \mathrm{Re}\, Z'$$

where A is a real constant that is used to compensate the far field stresses and Z' is the derivative of Z. For this problem, the complex function Z is found to be

$$Z = \frac{\sigma_\infty^y z}{\sqrt{z^2 - a^2}} - \frac{\sigma_\infty^y}{2}$$

where

$$z = x + iy, \quad A = -\frac{\sigma_\infty^y}{2}$$

Now, the full field stress equations around the crack are found to be

$$\sigma_x = \frac{K_I}{\sqrt{2\pi r}} \cos\frac{\theta}{2}\left(1 - \sin\frac{\theta}{2}\sin\frac{3\theta}{2}\right) + \frac{3}{4\sqrt{2}}\left(\frac{r}{a}\right)^{1/2} \times \cos\frac{\theta}{2}\left(1 + \sin^2\frac{\theta}{2}\right)\sigma_\infty^y + \left(\frac{r}{2a}\right)^{1/2} \times \left\{\sum_{n=1}^{\infty}(-1)^n \frac{[1\times 3\times 5\times\cdots\times(2n-1)](2n+3)}{2^{2(n+1)}(n+1)!} \times \left(\frac{r}{a}\right)^n \left[\cos\frac{(2n+1)\theta}{2} - \frac{(2n+1)}{2}\sin \times \frac{(2n-1)\theta}{2}\sin\theta\right]\right\}\sigma_\infty^y - \sigma_\infty^y \tag{6}$$

$$\sigma_y = \frac{K_I}{\sqrt{2\pi r}} \cos\frac{\theta}{2}\left(1 + \sin\frac{\theta}{2}\sin\frac{3\theta}{2}\right) + \frac{3}{4\sqrt{2}}\left(\frac{r}{a}\right)^{1/2} \times \cos\frac{\theta}{2}\left(1 - \sin^2\frac{\theta}{2}\right)\sigma_\infty^y + \left(\frac{r}{2a}\right)^{1/2} \times \left\{\sum_{n=1}^{\infty}(-1)^n \frac{[1\times 3\times 5\times\cdots\times(2n-1)](2n+3)}{2^{2(n+1)}(n+1)!} \times \left(\frac{r}{a}\right)^n \left[\cos\frac{(2n+1)\theta}{2} + \frac{(2n+1)}{2}\sin \times \frac{(2n-1)\theta}{2}\sin\theta\right]\right\}\sigma_\infty^y \tag{7}$$

$$\tau_{xy} = \frac{K_I}{\sqrt{2\pi r}} \cos\frac{\theta}{2}\sin\frac{\theta}{2}\cos\frac{3\theta}{2} - \frac{3}{4\sqrt{2}}\left(\frac{r}{a}\right)^{1/2}\left(\cos^2\frac{\theta}{2}\sin\frac{\theta}{2}\right)\sigma_\infty^y + \left(\frac{r}{2a}\right)^{1/2}\sum_{n=1}^{\infty}(-1)^{n+1}\frac{1\times 3\times 5\times\cdots\times(2n+3)}{2^{(2n+3)}(n+1)!} \times \left(\frac{r}{a}\right)^n \left[\cos\frac{(2n-1)\theta}{2}\sin\theta\right]\sigma_\infty^y \tag{8}$$

where K_I is the stress intensity factor (Broek [4]), and $K_I = \sigma_\infty^y\sqrt{\pi a}$.

An analogous situation in fluid mechanics is flow past a normal plate, as shown in Fig. 2. For this problem, a complex function w is found to be [5]

$$w = iU_\infty^y\sqrt{z^2 - a^2} \quad \text{and} \quad w = \phi + i\psi$$

Thus, the fluid stream and potential functions for this flow are

$$\psi = \frac{\sqrt{2}}{2}U_\infty^y\sqrt{\sqrt{(y^2 - x^2 + a^2)^2 + 4x^2y^2} - (y^2 - x^2 + a^2)}$$

and

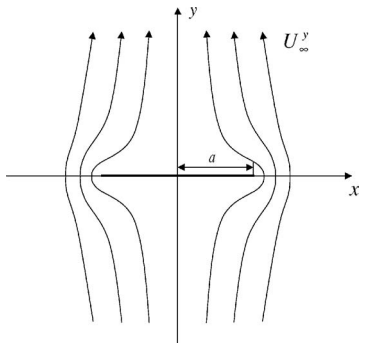

Fig. 2 Flow past a normal plate

Table 1 Excerpt results from the first grid of points

12	0.000817667	0.0000780167	−0.000491678	−0.000748582	−0.000759258
8	0.00212396	−0.00123597	−0.00256866	−0.00229417	−0.00159613
4	0.00310131	−0.019673	−0.0103369	−0.00386698	−0.0013764
0	701.836	0.0874016	0.0169045	0.00598783	0.00278567
$^{y}\uparrow_{\rightarrow x}$	1.01	3.01	5.01	7.01	9.01

Table 2 Excerpt results from the refined grid of points

0.012	−751.143	−679.155	−561.018	−430.533	−311.721
0.008	−1357.9	−1088.65	−732.216	−433.971	−229.698
0.004	−3526.38	−1613.29	−442.721	5.0699	156.962
0	22343.9	4293.65	1992.52	1201.05	822.614
$y\uparrow_{\rightarrow x}$	1.001	1.003	1.005	1.007	1.009

$$\phi = -\frac{(U_\infty^y)^2 xy}{\psi}$$

For this example, the relation between the force stream function Ψ and fluid stream function ψ should also obey the general relation in the form of Eq. (5). Specifically, Eq. (5) is now

$$-\frac{\partial}{\partial x}(\tau_{xy}+\sigma_y)+\frac{\partial}{\partial y}(\sigma_x+\tau_{xy})=2\frac{\sigma_\infty^y}{U_\infty^y}\frac{\partial}{\partial x}\left(\frac{\partial \psi}{\partial y}-\frac{\partial \psi}{\partial x}\right) \tag{9}$$

Theoretically, it seems easy to obtain a verification of Eq. (9). Since all the stress components and the fluid stream function ψ are precisely known, one merely has to duplicate the procedure presented in [1] for the example of a stress distribution around a circular hole. Unfortunately, it is extremely difficult to perform an analytical check on the crack problem solution represented by Eq. (9). Hence, the verification was accomplished using MATHEMATICA with numerical results. The details of the computation are given in Appendix B of Wu [6].

Numerical Results

Here, we shall present an overview of the setup and results. Without loss of generality, let $\sigma_\infty^y=1.0$ and $U_\infty^y=1.0$, where both have appropriate dimensions. That is, either metric, Newtons per square meter and meters per second or pounds per square inch and inches per second depending on the chosen units. Fortunately, it is possible to input stress components into MATHEMATICA in closed form. Since the stress components in Eqs. (6)–(8) are based on the origin being placed at the crack tip, a transformation back to the middle of the crack, changing from polar to rectangular coordinates is used here before differentiation. MATHEMATICA has the ability to do symbolic differentiation; thus, closed-form expressions are obtained from each side of Eq. (9). But these two expressions are very long and look very different. As mentioned in the previous section, numerical results have to be used. We set $a=1.0$, where a is the half crack length or half width of the plate. Given a specified point in the region, two values are calculated from these two expressions. Now it is no longer difficult to compare. There is no surprise that a singularity occurs at the crack tip (which is also the result obtained from linear fracture mechanics theory).

A series of points was taken to establish the comparison. Since both sides of Eq. (9) give the same numerical value for any given point, with no error, it is only necessary to present one value for each point of interest. Here, we shall focus on a few key numbers. An excerpt of the results from each of the two chosen grids of points is shown in Tables 1 and 2. For the first grid, a total of 84 points, the spacings in the x, y directions are 0.5, 4, respectively, and the x range is from 1.01 to 11.01 while y is from 0 to 12. Near the crack tip, where $x=1$ and $y=0$ are the tip coordinates, when $x=1.01$, $y=0$, the value is 701.836 N/m^3 or (701.836 lb/in^3).For remote distances, we selected the following points (which are not all shown in the excerpt): $(x,y)=(11.01,0)$, $(1.01,12)$, and $(11.01,12)$. The corresponding numerical values obtained were 0.00151728, 0.000817667, and −0.000648593. In a refined grid, a total of 76 points, where the spacings are now 0.0005 in x, 0.004 in y, and the x range is from 1.001 to 1.01 while y is from 0 to 0.012, a set of points closer to the crack tip was used. The numerical value calculated is 22343.9 at (1.001,0). It was also noted that the same value from both sides of the comparison equation were obtained using any tested point with different values for a. Except for validating the comparison equation (9), the physical meaning of those values is not clear.

Conclusion and Discussion

In conclusion, the force stream function was successfully applied to the classic linear fracture mechanics problem, Griffith's crack problem. This specific example, along with the governing equations (3) and (4), can provide some theoretical insights to the experimental data shown in Küntz et al. [7]. It may again be deduced that the force stream function method will apply to general linear fracture mechanics problems. It is also clear that one difficulty in using the new method is finding the corresponding fluid stream function.

Even though an effort was made in [1,6] and this paper to show that the new method will embrace not only previously known analogies between fluid and solid mechanics but also some other stress functions, one may still have a tendency to overlook the importance of the force stream function method since a new problem has yet to be addressed. It is also undeniable that, in some cases, fluid and solid mechanics are somehow connected through certain complex functions, such as occurs in Griffith's problem, but it should not be confused with the new development put forth by Eqs. (3) and (4). This might serve as a quantifying link between fluid and solid mechanics. Since the method is new, improvements should come with time. And yet with the general relations between the force stream function and fluid stream function firmly established through the verification of Eq. (5) by the solutions to the stress around a circular hole and Griffith's problem, new applications of the new method will come in time.

One possibility is to solve boundary value problems that have finite regions with the force stream function governing equations (1) and (2), and the equilibrium equations (with no body force)

$$\frac{\partial \sigma_x}{\partial x}+\frac{\partial \tau_{xy}}{\partial y}=0$$

$$\frac{\partial \tau_{xy}}{\partial x}+\frac{\partial \sigma_y}{\partial y}=0$$

along with the appropriate boundary conditions

$$\sigma_x n_x+\tau_{xy}n_y=p_x$$

$$\tau_{xy}n_x+\sigma_y n_y=p_y$$

where p_x and p_y are boundary tractions, n_x and n_y are direction cosines. The resulting boundary value problems will probably require numerical solutions.

References

[1] Wu, X., and Genin, J., 2003, "Force Stream Function Method," J. Strain Anal. Eng. Des., **38**(2), pp. 181–185.

[2] Westergaard, H. M., 1939, "Bearing Pressures and Cracks," ASME J. Appl. Mech., **6**, pp. 49–53.

[3] Gdoutos, E. E., 1990, *Fracture Mechanics Criteria and Applications*, Kluwer, Dordrecht.

[4] Broek, D., 1989, *The Practical Use of Fracture Mechanics*, Kluwer, Dordrecht.

[5] Vallentine, H. R., 1967, *Applied Hydrodynamics*, Butterworths, London.

[6] Wu, X., 1999, "Force Stream Function Method," Ph.D. thesis, New Mexico State University, Las Cruces.

[7] Küntz, M., Lavallée, P., and Mareschal, J. C., 1998, "Steady-State Flow Experiments to Visualise the Stress Field and Potential Crack Trajectories in 2D Elastic-Brittle Cracked Media in Uniaxial Compression," Int. J. Fract., **92**, pp. 349–357.

Power Law Velocity Profile in the Turbulent Boundary Layer on Transitional Rough Surfaces

Noor Afzal
Faculty of Engineering,
Aligarh University,
Aligarh 202002, India
e-mail: noor.afzal@yahoo.com

A new approach to scaling of transitional wall roughness in turbulent flow is introduced by a new nondimensional roughness scale ϕ. This scale gives rise to an inner viscous length scale $\phi\nu/u_\tau$, inner wall transitional variable, roughness friction Reynolds number, and roughness Reynolds number. The velocity distribution, just above the roughness level, turns out to be a universal relationship for all kinds of roughness (transitional, fully smooth, and fully rough surfaces), but depends implicitly on roughness scale. The open turbulent boundary layer equations, without any closure model, have been analyzed in the inner wall and outer wake layers, and matching by the Izakson-Millikan-Kolmogorov hypothesis leads to an open functional equation. An alternate open functional equation is obtained from the ratio of two successive derivatives of the basic functional equation of Izakson and Millikan, which admits two functional solutions: the power law velocity profile and the log law velocity profile. The envelope of the skin friction power law gives the log law, as well as the power law index and prefactor as the functions of roughness friction Reynolds number or skin friction coefficient as appropriate. All the results for power law and log law velocity and skin friction distributions, as well as power law constants are explicitly independent of the transitional wall roughness. The universality of these relations is supported very well by extensive experimental data from transitional rough walls for various different types of roughnesses. On the other hand, there are no universal scalings in traditional variables, and different expressions are needed for various types of roughness, such as inflectional roughness, monotonic roughness, and others. To the lowest order, the outer layer flow is governed by the nonlinear turbulent wake equations that match with the power law theory as well as log law theory, in the overlap region. These outer equations are in equilibrium for constant value of m, the pressure gradient parameter, and under constant eddy viscosity closure model, the analytical and numerical solutions are presented. [DOI: 10.1115/1.2746902]

1 Introduction

The power law velocity profile in a wall-bounded turbulent shear flow is

$$u_+ = Cy_+^\gamma \tag{1}$$

where $u_+ = u/u_\tau$ and $y_+ = yu_\tau/\nu$. Further, u is the velocity along the stream in the x-direction, $u_\tau = \sqrt{\tau_w/\rho}$ is the friction velocity, τ_w is the skin friction, ρ is the fluid density, and ν is the molecular kinematic viscosity of fluid. In fully developed turbulent smooth pipe flow, the power law constants γ and C are estimated as a function of the Reynolds number Re by Nikuradse [1]. Barenblatt [2] proposed expressions for the power law constants α and C as a function of Reynolds number Re. Alternate correlations have been proposed in terms of Re (by Kailasnath [3], Zagarola et al. [4], and McKeon et al. [5]), and R_τ (by Afzal [6]),where $Re = 2\delta U_b/\nu$ is the Reynolds number based on U_b the averaged velocity, $R_\tau = \delta u_\tau/\nu$ is the frictional Reynolds number, and δ is the boundary layer thickness, pipe radius, or semidepth of the channel, as the case may be. For fully rough pipes, Nikuradse [7] estimated the power index γ of Eq. (1), as a function of roughness parameter h/δ, where δ is the pipe radius. For the data of Nikuradse [7] in smooth, traditional, and fully rough regions, Porporato and Sordo [8] estimated the power law constants $\gamma = \gamma(\mathrm{Re}, h/\delta)$ and $C = C(\mathrm{Re}, h/\delta)$, shown in Fig. 1 of their paper, but no correlations were proposed. Afzal et al. [9] presented an alternate treatment for pipe roughness in turbulent pipe flow.

Barenblatt et al. [10] extended the above analysis to the turbulent boundary layer flow, and proposed two power laws (in the inner and outer power law layers), in contrast to one power law in pipe flow. It has been shown by Panton [11] that the prediction based on this theory [10] does not closely describe the data of Osterlund [12]. For a turbulent boundary layer on a rough wall, Balachandar et al. [13], Bergstrom et al. [14], Kotey et al. [15], and Seo and Castillo [16] have extended the smooth wall work of George and Castillo [17]. The outer velocity with a shift in the origin as $y_+ + j_+$ is adopted as

$$\frac{u}{U_\infty} = C_0 E_0 (Y + j)^{\gamma_S + \gamma_R} \tag{2}$$

where $Y = y/\delta$, C_0 and γ_S are smooth wall constants and E_0 and γ_R are rough wall constants [9,18], and the outer layer slip velocity on wall becomes $u(Y=0) \equiv U_S(x) = C_0 E_0 j^{\gamma_S + \gamma_R}$. The outer velocity (Eq. (2)) violates the Townsend's similarity hypothesis on rough walls [19] as E_0 and γ_R depend on roughness of the wall. The initial work of George et al. [20] corresponds to $j=0$, where the outer (Eq. (2)) at $Y=0$ demands $U_S=0$. The boundary condition of no slip at the wall $u(Y=0) = U_S = 0$ is satisfied by the outer layer in the overlap region, and consequently the inner wall layer is not needed. These works [13–17,20–22] adopted $j = -16/R_\tau$ and the outer layer surface slip velocity yields $U_S = C_0 E_0 (-16/R_\tau)^{\gamma_S + \gamma_R}$, a complex relation for fully smooth, transitional, and fully rough surfaces, as their outer velocity scaling is not appropriate. Eaton and Nagib [23] proposed that Afzal highlighted a number of limitations in the asymptotic analysis leading to the power law for the boundary layer theory by George et al. [20] (and later work

Contributed by the Fluids Engineering Division of ASME for publication in the JOURNAL OF FLUIDS ENGINEERING. Manuscript received January 29, 2006; final manuscript received March 4, 2007. Review conducted by Timothy J. O'Hern.

[13–17,21,22]). In particular, the last term in the outer expansion

$$\frac{u}{U_\infty} = U_0(X,Y) - \frac{u_\tau}{U_\infty} U_1(X,Y) \tag{3}$$

derived by Afzal [18,24–26], but ignored by George et al. [17,20–22], Balachandar et al. [13], Bergstrom et al. [14], Koety et al. [15], and Seo and Castillo [16] lead to inappropriate limits. Several other limitations of outer velocity profile in these works have been described in Afzal [18,25,26], and will not be repeated here.

Millikan [27] analyzed fully smooth and transitional rough walls in terms of smooth wall variable Z_+, and for fully rough walls in terms of rough wall variable Z/h and proposed three log law theories, one for each case. The term "roughness function" was introduced by Clauser [28] and Hama [29] as

$$\Delta U_+ = \left(\frac{u}{u_\tau}\right)_S - \frac{u}{u_\tau} \tag{4}$$

a velocity defect representing a shift of velocity between rough and smooth walls in the overlap region, where the suffix S denotes the smooth wall value. It physically represents the shift in the velocity profile in the overlap region due to surface roughness over the smooth surface. When $\Delta U_+ > 0$, the curve is shifted down due to increased drag and where $\Delta U_+ < 0$, the shift is up due to reduced drag. The velocity defect (4) may also be estimated at the boundary layer edge $y=\delta$ where $u=U_\infty$, to yield

$$\Delta U_+ = \left(\frac{U_\infty}{u_\tau}\right)_S - \frac{U_\infty}{u_\tau} = \left(\frac{2}{C_f}\right)_S^{1/2} - \left(\frac{2}{C_f}\right)^{1/2} \tag{5}$$

where $C_f = 2\tau_w/\rho U_\infty^2$ is local skin friction coefficient. The roughness function ΔU_+, like friction velocity u_τ, is a characteristic of the hydraulic wall roughness subjected to oncoming fluid stream. Without loss of generality, the roughness function (4) is also applicable for the power law velocity profile in the overlap region, which is also supported by Eq. (5), arising from the change of skin friction due to surface roughness over the smooth surface. Further, for the power law velocity profile on a rough wall, Balachandar et al. [13] proposed $u_+ = C y_+^\gamma - \Delta U_+$ in analogy with Clauser [28] and Hama [29] traditional log law velocity profile $u_+ = k^{-1} \ln y_+ + B - \Delta U_+$. The estimates of ΔU_+ for sand grains and wire mesh data were made, but no correlations were proposed. Furthermore, for a smooth wall, the constants $C=7.957$ and $\gamma=0.1551$ are not appropriate, because power law constants α and Cdepend on the Reynolds number of the flow. The data gathered for ΔU_+ for various types of roughness have been reviewed by Schlichting [30], Raupach et al. [31], and Jimenez [32].

The present work proposes alternate new nondimensional roughness typical scale ϕ that relates the appropriate form of transitional roughness coordinate y_ϕ to the standard coordinate y by

$$y_\phi = \frac{y}{\phi} \tag{6}$$

Just above the roughness sublayer, all mean relative motions and mean energy-containing components of the turbulent motion do not explicitly depend on surface roughness. The nondimensional roughness scale ϕ, in the present work, is related to the roughness function ΔU_+ as

$$\Delta U_+ = \frac{1}{k} \ln \phi \tag{7}$$

The inner transitional length scale is $\phi\nu/u_\tau$ and a new inner variable ζ for transitional wall roughness is defined as

$$\zeta = \frac{Z_+}{\phi} \tag{8}$$

where $Z_+ = Z u_\tau/\nu$. The coordinate is $Z = y + \epsilon_r$ and ϵ_r is the origin of the coordinate y on the surface, where roughness is caused by irregular protrusions of the hydraulic roughness parameter $h_+ = h u_\tau/\nu$, a particular level between the protrusion bases and heads that automatically satisfies the constraints $0 < \epsilon_r < h$. The method of determining the effective surface roughness origin ϵ_r and friction velocity u_τ may be found in the literature [28–32].

Likewise, the appropriate Reynolds number R_ϕ may be defined as

$$\mathrm{R}_\phi = \frac{\mathrm{R}_\tau}{\phi} \tag{9}$$

where the new parameter R_ϕ can be called the roughness friction Reynolds number, analogous with $\mathrm{R}_\tau = u_\tau \delta/\nu$, the well-known friction Reynolds number. The roughness Reynolds number Re_ϕ may be defined as

$$\mathrm{Re}_\phi = \frac{\mathrm{Re}}{\phi} \tag{10}$$

and $\mathrm{Re} = U_\infty \delta/\nu$ is the traditional Reynolds number. A smooth wall, in terms of the roughness parameters, will have h_+ approaching 0, the ϕ approaching 1, inner variable ζ approaching y_+, the roughness friction Reynolds number approaching the friction Reynolds number, and the roughness Reynolds number approaching the Reynolds number. A fully rough wall in terms of the roughness parameters will have h_+ very large, the roughness scale approaching h_+, inner variable approaching Z/h, and R_ϕ approaching δ/h, the ratio of the boundary-layer thickness to the mean roughness height.

In the present work, a two layer asymptotic theory for open equations of a turbulent boundary layer (without any closure model like eddy viscosity, mixing length, k-ϵ, etc.) has been presented in terms of the inner length scale $\phi\nu/u_\tau$ for transitional rough surface and the inner layer variable $\zeta = Z_+/\phi$. The outer layer has been governed by equations analogous to that of nonlinear wake. The two layers have been matched by the Izakson-Millikan-Kolmogorov (IMK) hypothesis leading to open functional equations. The functional solution in turn produces a power law solution and a log law solution; these contain certain unknown constants that have to be determined from the experimental data or a closure model. This is not surprising, as we are dealing with the open equations of mean turbulent motion.

2 Boundary-Layer Analysis

The boundary-layer equations for a two-dimensional incompressible mean turbulent flow subjected to a pressure gradient in standard notation are [30]

$$\frac{\partial u}{\partial x} + \frac{\partial v}{\partial y} = 0 \tag{11}$$

$$u\frac{\partial u}{\partial x} + v\frac{\partial u}{\partial y} = U_\infty \frac{dU_\infty}{dx} + \nu\frac{\partial^2 u}{\partial y^2} + \frac{\partial \tau}{\rho\, \partial y} \tag{12}$$

subject to the boundary conditions

$$y = 0 \quad u = v = \tau = 0 \tag{13}$$

and

$$y/\delta \to \infty \quad u \to U_\infty(x) \quad \tau \to 0 \tag{14}$$

Here, u and v are the velocity components in x streamwise and y normal directions, and τ is the appropriate Reynolds shear stress. U_∞ is velocity at the edge of the boundary layer with thickness δ, and ν is the molecular kinematic viscosity of fluid. In the present work, the outer and inner asymptotic expansions are matched as described below.

2.1 Outer Wake Layer. The outer layer variables are

$$u = U_\infty U(X,Y) \tag{15}$$

$$U = \frac{\partial F}{\partial Y} \tag{16}$$

$$\tau = \rho u_\tau^2 T(X,Y) \tag{17}$$

where

$$Y = \frac{Z}{\delta} \tag{18}$$

$$X = \int L^{-1} dx \tag{19}$$

$$\frac{\delta}{L} = \epsilon^2 \quad \text{and} \quad \epsilon = \frac{u_\tau}{U_\infty} = \sqrt{\frac{C_f}{2}} \tag{20}$$

Here δ is the outer boundary-layer thickness and L is the scale of flow variations in the x-direction. The boundary-layer equations (11) and (14) in the outer wake layer variables (15)–(20) yield

$$(1-\beta)\chi_1^{-1}T' + FF'' + \beta(1-F'^2) + \delta(1-\beta)(F''F_\delta - F'F'_\delta) = -\frac{(1-\beta)}{\chi_1 \phi \, \mathrm{R}_\phi} F''' \tag{21}$$

subjected to the outer boundary conditions

$$F'(X,\infty) - 1 = T(X,\infty) = 0 \tag{22}$$

Here β is pressure gradient parameter and χ_1 are

$$\beta = \frac{m}{1+m} \tag{23}$$

$$m = \frac{\delta}{d\delta/dX} \frac{dU_\infty}{U_\infty dX} = \frac{\delta}{U_\infty} \frac{dU_\infty}{d\delta} \tag{24}$$

$$\chi_1 = \frac{\delta_X}{\delta} \tag{25}$$

The dash denotes differentiation with respect to Y and suffix δ denotes the differentiation with respect to δ. The outer asymptotic expansions are

$$F = F_o(X,Y) + \epsilon F_1(X,Y) + o(\epsilon) \tag{26}$$

$$U = U_o(X,Y) + \epsilon U_1(X,Y) + o(\epsilon) \tag{27}$$

$$T = T_o(X,Y) + \epsilon T_1(X,Y) + o(\epsilon) \tag{28}$$

The outer layer equations for $F_0(X,Y)$ and $F_1(X,Y)$ from outer Eq. (26) are open and inviscid, which fails to satisfy the no-slip boundary conditions. The lowest-order, outer layer equation for $F_0(X,Y)$ corresponds to a nonlinear wake layer, described in Appendix A, that predicts $F_0'(X,=0)=U(X,0)=b_S$, where parameter $b_S(X)=U_S(X)/U_\infty(X)$ is the ratio of slip velocity $U_S(X)$ of fluid at surface to free stream velocity $U_\infty(X)$. Consequently, an inner wall layer solution containing the viscous term is also needed, in order to satisfy the no-slip boundary condition on the wall.

2.2 Inner Wall Layer. The inner wall variables are

$$\zeta = \frac{Z_+}{\phi} \tag{29}$$

$$u = u_\tau u_+(X,\zeta) \tag{30}$$

$$\tau = \rho u_\tau^2 \tau_+(X,\zeta) \tag{31}$$

and boundary-layer equations (11) and (12), to the lowest order, become

$$\frac{\partial u_+}{\phi \, \partial \zeta} + \tau_+ = 1 + \phi K_+ \zeta + O(\epsilon \mathrm{R}_\phi)^{-1} \tag{32}$$

$$K_+ = \frac{\nu p'}{\rho u_\tau^3} \tag{33}$$

The roughness scale ϕ is of the order of magnitude $1 \le \phi \le \infty$, and it is more appropriate to eliminate ϕ from Eq. (29). In fact, the inner variables have to be expressed as

$$Z_\phi = \frac{Z}{\phi} = \frac{Z u_\phi}{\nu} \tag{34}$$

$$u_\phi = \frac{u_\tau}{\phi} \tag{35}$$

$$u_i(X,\zeta) = \frac{u_+(X,\zeta)}{\phi} \tag{36}$$

and one is tempted with the idea that it is not u_τ that matters, but it is u_τ/ϕ, for better description of the inner layer on the partially rough wall. In view of Eq. (34), the inner variables become

$$\zeta = \frac{Z u_\phi}{\nu} \tag{37}$$

$$u = \phi^2 u_\phi u_i(X,\zeta) \tag{38}$$

$$\tau = \phi^2 \rho u_\phi^2 \tau_+(X,\zeta) \tag{39}$$

The inner layer rough wall equation (32) yields

$$\frac{\partial u_i}{\partial \zeta} + \tau_+ = 1 + K_\phi \zeta + O(\epsilon \mathrm{R}_\phi)^{-1} \tag{40}$$

where

$$K_\phi = \frac{\nu p'}{\phi \rho u_\phi^3} \tag{41}$$

represents the nondimensional pressure gradient parameter. Equation (40), for a constant pressure flow, shows that the total stress remains constant in the inner wall layer.

2.3 Matching in the Overlap Region. In the turbulent motion, the equations are not closed unless a turbulence closure model is adopted. The approaches adopted by Izakson [33], Millikan [27], and Kolmogorov [34] are model free and appeal to an overlap hypothesis (Afzal and Narasimha [35], Afzal [36–38], and Narasimha [39]).

Izakson-Millikan-Kolmogorov (IMK) Hypothesis. Between the viscous and the energetic scales in any turbulent flow exists an overlap domain over which the solutions characterizing the flow in the two corresponding limits must match as the Reynolds number approaches infinity.

The resemblance of the IMK hypothesis to conventional matching associated with closed equations seems peculiar to turbulence theory. For sufficiently large Reynolds numbers, there exists an overlap domain where the inner and outer layer solutions must match. The inner limit (ζ fixed, $\mathrm{R}_\phi \to \infty$) of outer expansions Eq. (27), and the outer limit (Y fixed, $\mathrm{R}_\phi \to \infty$) of inner solution Eq. (38) for matching by Izakson-Millikan-Kolmogorov hypothesis demands

$$\phi u_i(X,\zeta) = U_{\infty +} U_0(X,Y) - U_1(X,Y) \tag{42}$$

$$\zeta = Y \mathrm{R}_\phi \tag{43}$$

as $\zeta \to \infty$, $Y \to 0$ for $\mathrm{R}_\phi \to \infty$ where $U_{\infty +} = U_\infty / u_\tau$. This is an open functional equation connecting four unknown functions. For $\mathrm{R}_\phi \to \infty$, the function $U_{+\infty} \to \infty$ and Eq. (42) require that the inner velocity distribution $u_i(X,\zeta)$ should be unbounded for large ζ.

Note that this matching would be impossible if $u_i(X,\zeta)$ is bounded as $\zeta \to \infty$. The open functional equation possesses a partial solution, and differentiating of Eq. (42) with respect to y yields

$$\zeta \frac{\partial u_+}{\partial \zeta} = U_{\infty +} Y \frac{\partial U_0}{\partial Y} - Y \frac{\partial U_1}{\partial Y} \tag{44}$$

as $\zeta \to \infty$ and $Y \to 0$. For large Reynolds numbers, the function $U_{\infty +} \to \infty$ and the matching of the leading order term in Eq. (44) demands

$$Y \frac{\partial U_0}{\partial Y} = o(\epsilon) \quad \text{while } Y \to 0 \quad \text{as } \epsilon \to 0 \tag{45}$$

Equation (45) permits the simplest solution

$$\frac{\partial U_0}{\partial Y} = \text{finite} \quad \text{at } Y = 0 \tag{46}$$

along with the wall slip velocity $U_0(X, Y=0) = b_S$, where the constant b_S depends on the pressure gradient. This implies that a nonlinear outer layer solution $F_0(X,Y)$ admits the similarity analysis, described in Appendix A, and wall slip velocity $U_S = b_S U_\infty$ is finite. Further, outer equations permit other solutions also, which have not been considered here. In view of these arguments, the matching Eqs. (42) and (44) become

$$u_+(X,\zeta,\mathrm{R}_\phi) = U_{S+}(\mathrm{R}_\phi) - U_1(X,Y,\mathrm{R}_\phi) \tag{47}$$

$$\zeta \frac{\partial u_+}{\partial \zeta} = \mathrm{R}_\phi \frac{\partial U_{S+}}{\partial \mathrm{R}_\phi} = -Y \frac{\partial U_1}{\partial Y} \tag{48}$$

for $\zeta \to \infty$ and $Y \to 0$ for $\mathrm{R}_\phi \to \infty$ and $U_{S+}(\mathrm{R}_\phi) = U_S/u_\tau$. The solution of these equations gives the log laws in the overlap domain, described in Appendix B. Further, it may be pointed out that Izakson [33] considered a functional equation like Eq. (46) and Millikan [27] considered the first derivative such as Eq. (48) and proposed the logarithmic laws, in the shallow outer wake layer where $U_S = U_\infty$ and $b_S = 1$. The approach of Izakson [33] and Millikan [27] for fully developed turbulent pipe or channel flow, has been extended to second-order by Afzal [36] and to third-order by Afzal and Bush [37], and further higher orders by Buschmann and Gad-el-Hak [40]. In turbulent boundary layer flows, the matching by IMK hypothesis has been generalized and composite log laws solutions are obtained by Afzal [38], in the overlap region.

It will now be shown that the functional Eq. (47) also possesses an alternate solution. Differentiating Eq. (48) once more with respect to y, we get

$$\zeta^2 \frac{\partial^2 u_+}{\partial \zeta^2} = \mathrm{R}_\phi^2 \frac{\partial^2 U_{S+}}{\partial \mathrm{R}_\phi^2} \tag{49}$$

and the solution again gives the log laws (Appendix B). It appears that the functional equation may be differentiated as many times as we please, and nothing new or inconsistent would be discovered. The differentiation is one of the keys for solving the functional equations, but other techniques may be employed. The functional Eq. (49) may be divided by Eq. (48) which gives an alternate functional equation

$$\zeta \frac{\partial^2 u_+ / \partial \zeta^2}{\partial u_+ / \partial \zeta} = R_\phi \frac{\partial^2 U_{S+} / \partial \mathrm{R}_\phi^2}{\partial U_{S+} / \partial \mathrm{R}_\phi} \tag{50}$$

Its functional solution may be expressed in the variable separable form as

$$\zeta \frac{\partial^2 u_+ / \partial \zeta^2}{\partial u_+ / \partial \zeta} = \alpha - 1 \tag{51}$$

and

$$\mathrm{R}_\phi \frac{\partial^2 U_{S+} / \partial \mathrm{R}_\phi^2}{\partial U_{S+} / \partial \mathrm{R}_\phi} = \alpha - 1 \tag{52}$$

where constant α is independent of ζ and Y. The integral of these equations gives

$$\frac{\partial u_+}{\partial \zeta} = J \zeta^{\alpha - 1} \tag{53}$$

and

$$\frac{\partial U_{S+}}{\partial \mathrm{R}_\phi} = J \mathrm{R}_\phi^{\alpha - 1} \tag{54}$$

where J is a constant of integration. The two cases $\alpha = 0$ and $\alpha \neq 0$ are presented.

Log Law Solution. For $\alpha = 0$, Eqs. (53) and (54) become

$$\frac{\partial u_+}{\partial \zeta} = J \zeta^{-1} \tag{55}$$

and

$$\frac{\partial U_{S+}}{\partial \mathrm{R}_\phi} = J \mathrm{R}_\phi^{-1} \tag{56}$$

Self-consistency with Eq. (48) demands $J = 1/k$, where k is the classical von Karman constant. The integrations of Eqs. (55) and (56) give the log law solutions described in Appendix B.

Power Law Solution. In the second case $\alpha \neq 0$ the integration produces

$$u_+ = A \zeta^\alpha + b_1 \tag{57}$$

$$U_{S+} = A \mathrm{R}_\phi^\alpha + b_1 + E_S \tag{58}$$

where b_1 and E_s are integration constants and

$$A = \frac{J}{\alpha} \tag{59}$$

The power law velocity profiles (57) and (58) in terms of outer variable Y may be expressed as power law as well as local velocity defect in terms of power law as

$$u_+ = A_1 Y^\alpha + b_1 \tag{60}$$

$$\frac{U_S - u}{u_\tau} = A_1 (1 - Y^\alpha) + E_S \tag{61}$$

where the outer power law prefactor is

$$A_1 = A \mathrm{R}_\phi^\alpha \tag{62}$$

The inner power law prefactor A from Eq. (58) may also be expressed as

$$A = \left(\frac{U_S}{u_\tau} - b_1 - E_S \right) \exp(-\alpha \ln \mathrm{R}_\phi) \tag{63}$$

For large Reynolds numbers, $\mathrm{R}_\phi \to \infty$, $\alpha \to 0$, and the ratio A_1/A approaches a constant value, whereas A becomes unbounded as $U_S/u_\tau \to \infty$.

Uniformly valid solutions of the power law velocity profile obtained from the union of the inner and outer solutions by subtracting the common part above the sublayer is

$$\frac{u}{U_\infty} = F_0'(X,Y) - b_S + \frac{u_\tau}{U_\infty} \left[A \zeta^\alpha + b_1 + \frac{\pi_S}{k} \Omega(X,Y) \right] \tag{64}$$

Where $\Omega(X,Y)$ is the wake function of the power law profile given by the relation

$$\Omega(X,Y)=\left[-U_1(X,Y)+A_1(1-Y^{\alpha})+\frac{\pi_S}{k}\Omega(X,1)\right]\frac{k}{\pi_S} \quad (65)$$

and

$$E_S=\frac{\pi_S}{k}\Omega(X,1) \quad (66)$$

In terms of outer variables, the solution becomes

$$\frac{u}{U_\infty}=F_0'(X,Y)-b_S+\frac{u_\tau}{U_\infty}\left[A_1Y^{\alpha}+b_1+\frac{\pi_S}{k}\Omega(X,Y)\right] \quad (67)$$

$$\frac{U_S-u}{U_\infty}=b_S-F_0'(Y)+\frac{u_\tau}{U_\infty}\left[A_1(1-Y^{\alpha})+\frac{\pi_S}{k}[\Omega(X,1)-\Omega(X,Y)]\right] \quad (68)$$

3 Envelope of Skin Friction Power Law

Let $J=a+b\alpha$ for $\alpha\to 0$ as $\mathrm{R}_\phi\to\infty$, and the power law prefactor Eq. (59) becomes

$$A=\frac{a}{\alpha}+b+\cdots \quad (69)$$

where a and b are constants. The envelope of a function may be defined as the relation which, for each parameter setting of the curve at those parameters, has a point of tangency with the envelope curve. The friction factor power law equations (58) and (69) become

$$\frac{U_S}{u_\tau}=\left(\frac{a}{\alpha}+b\right)\exp(\alpha\ln \mathrm{R}_\phi)+b_1+E_S \quad (70)$$

where parameter α is a function of the Reynolds number. The power law friction factor forms a family of curves in $(U_{S+},\ln \mathrm{R}_\phi)$-plane, where α is the parameter of the family. The family has an envelope that satisfies both Eq. (70) and the equation $\partial U_{S+}/\partial\alpha=0$. The derivative of Eq. (70) with respect to α gives

$$\frac{\partial U_{S+}}{\partial\alpha}=\mathrm{R}_\phi^{\alpha}\left[\left(b+\frac{a}{\alpha}\right)\ln R_\phi-\frac{a}{\alpha^2}\right]=0 \quad (71)$$

which may be simplified as

$$\left(1+\frac{b}{a}\alpha\right)\alpha\ln R_\phi=1 \quad (72)$$

The relation (72) is a quadratic equation in power index α and its solution is given as

$$\alpha=\frac{\Gamma}{\ln \mathrm{R}_\phi} \quad (73)$$

$$\Gamma=\frac{a}{2b}\ln R_\phi\left[\left(1+\frac{4b}{a\ln \mathrm{R}_\phi}\right)^{1/2}-1\right] \quad (74)$$

Equation (62), based on power index α relation (73), becomes

$$A_1=A\exp(\Gamma) \quad (75)$$

The power law prefactors A in the inner layer and A_1 in the outer wake layer depend on the Reynolds number. However, Eq. (74) demands $\Gamma\to 1$ for $\mathrm{R}_\phi\to\infty$, and the prefactors A and A_1 behave in a self-similar manner, such that their ratio $A_1/A=\exp(1)$ is a constant, to the lowest order. The power law prefactor equation (63), in view of Eq. (73), is simplified as

$$A=\left(\frac{U_S}{u_\tau}-b_1-E_S\right)\exp(-\Gamma) \quad (76)$$

The skin friction power law equation (70), after elimination of the power index α from Eq. (73), becomes the skin friction log law

$$\frac{U_S}{u_\tau}=k^{-1}\ln \mathrm{R}_\phi+B+b_1+E_S \quad (77)$$

and

$$k^{-1}=\frac{a}{\Gamma}\exp(\Gamma)\quad\text{and}\quad B=b\exp(\Gamma) \quad (78)$$

Thus, k is the von Karman constant, and B is the intercept of the log law, these depend on Reynolds number through function Γ given by Eq. (74). The results show that the envelope of the skin friction power law equation (70) gives the skin friction log law (77), but constants k and B predicted by relations (78) based on Eq. (74) are functions of the Reynolds number. In the traditional log law solution, the constants k and B are universal numbers, independent of the Reynolds number. In the limiting situation of very large Reynolds numbers, the power law solution becomes equivalent to the log law solution.

The power law prefactor A from Eq. (69) after eliminating constants a and b from Eq. (78), and then using Eq. (77), respectively yield

$$A=\left(\frac{\Gamma}{k\alpha}+B\right)\exp(-\Gamma) \quad (79)$$

$$A=\left(\frac{1}{k}\ln \mathrm{R}_\phi+B\right)\exp(-\Gamma) \quad (80)$$

$$\Gamma=\left(1+\frac{kB}{\ln \mathrm{R}_\phi}\right)^{-1} \quad (81)$$

The power law constants α and A may also be expressed in terms of the friction velocity, by eliminating the $\ln \mathrm{R}_\phi$ term by using Eq. (77) to obtain

$$\alpha=k^{-1}\frac{\epsilon_S}{1-(b_1+E_S)\epsilon_S} \quad (82)$$

$$A=\left(\frac{1}{\epsilon_S}-E_S-b_1\right)\exp(-\Gamma) \quad (83)$$

$$\Gamma=\frac{1-(B+b_1+E_S)\epsilon_S}{1-(b_1+E_S)\epsilon_S} \quad (84)$$

where nondimensional parameter ϵ_S is the ratio of friction velocity to outer layer slip velocity on the surface as

$$\epsilon_S=\frac{u_\tau}{U_S} \quad (85)$$

The power law velocity profile theory presented in this paper holds for any kind of transitional roughness, including the limiting cases of fully rough and fully smooth walls as asymptotic cases. The log law equation (77) obtained from the envelope of the power law, after elimination of the new parameter R_ϕ in favor of classical parameter R_τ, becomes

$$\frac{U_S}{u_\tau}=\frac{1}{k}\ln \mathrm{R}_\tau+B+b_1+E_S-\frac{1}{k}\ln\phi \quad (86)$$

This may also be expressed in terms of fully rough wall parameter δ/h to obtain

$$\frac{U_S}{u_\tau}=\frac{1}{k}\ln\frac{\delta}{h}+B_T+b_1+E_S \quad (87)$$

where

$$\phi=h_+\exp[k(B-B_T)] \quad (88)$$

which from Eq. (7) gives the roughness function. Further, B and $B_T(h_+)$ are the additive terms in the log laws for a fully smooth wall and a transitional rough wall, respectively. In the fully rough

wall, $B_T=B_F$ is a universal constant independent of wall roughness.

4 Results and Discussion

In the shallow outer wake layer, $b_S=1(U_S=U_\infty)$ and the lowest-order outer solution is $F_0(X,Y)=1$. Let in this case $\epsilon_S=\epsilon$ and $E_S=E$. The uniformly valid solution of the power law velocity profile equations (64) and (67) for a partially rough wall, just above the transitional roughness level, become

$$\frac{u}{u_\tau}=A\zeta^\alpha+b_1+\frac{\pi}{k}\Omega(X,Y) \tag{89}$$

$$\frac{u}{u_\tau}=A_1Y^\alpha+b_1+\frac{\pi}{k}\Omega(X,Y) \tag{90}$$

The skin friction power law equation (58) becomes

$$\frac{U_\infty}{u_\tau}=A\mathrm{R}_\phi^\alpha+b_1+E \tag{91}$$

where $E=\pi/k$. The velocity defect equation (68) becomes

$$\frac{U_\infty-u}{u_\tau}=A_1(1-Y^\alpha)+\frac{\pi}{k}[\Omega(X,1)-\Omega(X,Y)] \tag{92}$$

Here, $\Omega(X,Y)$ is the wake function for the power law velocity profile, under the boundary conditions $\Omega(X,0)=0$, $\Omega(X,1)=2$, and $\Omega'(X,1)=-1/\pi$, where $\alpha A_1k=1$. The wake function $\Omega(X,Y)$ may be taken as

$$\Omega(X,Y)=\Omega_0(X,Y)+\frac{1}{\pi}\Omega_1(X,Y)+\cdots \tag{93}$$

where the first wake function $\Omega_0(X,Y)$ is analogous to Coles [41] wake function satisfying the boundary conditions $\Omega_0(X,0)=0$, $\Omega_0(X,1)=1$, and the second wake function $\Omega_1(X,Y)$ is analogous to the modification in basic wake function adopted by Lewkowicz [42], Finley et al. [43], and Granville [44], which satisfy the boundary conditions $\Omega_1'(X,1)=-1$ in addition to $\Omega_1(X,0)=\Omega_1(X,1)=0$. If outer layer is in equilibrium, the two wake functions are independent of X.

The envelope of friction factor power law Eq. (70) gives the log law Eq. (77) whose comparison with log law theory (see Appendix B) demands $b_1=0$ and $E=D$. Further, the power law velocity profiles Eqs. (64) and (67) in the overlap region of the inner and outer layers with $b_1=0$ yield

$$\frac{u}{u_\tau}=A\zeta^\alpha \tag{94}$$

$$\frac{u}{u_\tau}=A_1Y^\alpha \tag{95}$$

The power law index α, prefactor A, and constant Γ are functions of R_ϕ, and the roughness friction Reynolds number and Eqs. (73) and (79)–(81) are summarized below:

$$\alpha=\frac{\Gamma}{\ln \mathrm{R}_\phi} \tag{96}$$

$$A=\left(\frac{\Gamma}{k\alpha}+B\right)\exp(-\Gamma) \tag{97}$$

$$A=\left(\frac{1}{k}\ln \mathrm{R}_\phi+B\right)\exp(-\Gamma) \tag{98}$$

$$\Gamma=\left(1+\frac{kB}{\ln \mathrm{R}_\phi}\right)^{-1} \tag{99}$$

The power law constants α and A from Eqs. (82)–(84), for shallow outer wake in terms of nondimensional friction velocity ϵ are summarized as:

$$\alpha=k^{-1}\frac{\epsilon}{1-E\epsilon} \tag{100}$$

$$A=\left(\frac{1}{\epsilon}-E\right)\exp(-\Gamma) \tag{101}$$

$$\Gamma=\frac{1-(B+E)\epsilon}{1-E\epsilon} \tag{102}$$

where $\epsilon=u_\tau/U_\infty=\sqrt{C_f/2}$. Equations (100)–(102) show that if ϵ is known from local skin friction coefficient C_f, the power law constants α and A may be estimated, and the roughness scale ϕ does not enter the picture.

In the present work, the roughness wall variable $\zeta=Z_+/\phi$, the roughness friction Reynolds number $\mathrm{R}_\phi=\mathrm{R}_\tau/\phi$, and the roughness Reynolds number $\mathrm{R}_\phi=\mathrm{Re}/\phi$, have been proposed to be explicitly independent of roughness scale ϕ. The expressions of roughness function ΔU_+ and roughness scale ϕ proposed in the present work are described in Appendix C, where for inflectional roughness, a simple expression for roughness scale ϕ proposed by Eq. (C3) is

$$\phi=1+\chi h_+\exp\left(-\frac{j}{h_+}\right) \tag{103}$$

and for k-type and d-type roughness, the roughness scale from Eq. (C5) is also given below

$$\phi=h_+ \tag{104}$$

The velocity profiles as log-log plots suitable for display of power law are shown in Figs. 1(*a*)–1(*d*) from the data of Kameda et al. [45], for k-type roughness at various values of Reynolds number. The velocity distribution u_+ in traditional smooth wall-like variables Z_+ is shown in Fig. 1(*a*) as a log-log plot for investigation of power law representation. As h_+ changes, the data in the overlap region shift their location, and the index α and prefactor C are estimated from data fit to the traditional power law $u_+=CZ_+^\alpha$.

There is no universality while using traditional variable Z_+, and different expressions of roughness scale are needed for various types of roughness. The velocity distribution shifted by roughness function $u_++\Delta U_+$ versus smooth wall variable Z_+ is shown in Fig. 1(*b*) on log-log plot. The profile $u_++\Delta U_+=CZ_+^\alpha$ does not depend on wall roughness following Clauser-Hama type similarity for power law velocity profile. The same data of Kameda et al. [45], for the velocity profile u_+ in alternate transitional ζ shown in Fig. 1(*c*) in a log-log plot, do not explicitly depend on surface roughness for proposed power law $u_+=A\zeta^\alpha$ by Eq. (94). The power law index α and prefactor A as a function of roughness friction Reynolds number R_ϕ have been estimated from Fig. 1(*a*).. The outer power law velocity profile, in the outer variables $u_+=A_1Y^\alpha$ given by Eq. (95) is shown as log-log plots in Fig. 1(*d*),which reveal the similarity of the data.

The velocity profile data of Osaka and Mochizuki [46] for d-type roughness is shown in Figs. 2(*a*)–2(*d*). The data of Antonia and Krogstad [47] for wire mesh and rod roughness, and Smalley et al. [48] for rod roughness are shown in Figs. 3(*a*)–3(*d*). The data of Schultz and Flack [49] for sand paper roughness and Schultz and Myers [50] for epoxy pained wall are shown in Figs. 4(*a*)–4(*d*). The data of Schultz and Flack [51] with wall covered by uniform spheres and on the same surface covered by finer scale grit roughness are shown in Figs. 5(*a*)–5(*d*), and the data of Rah-

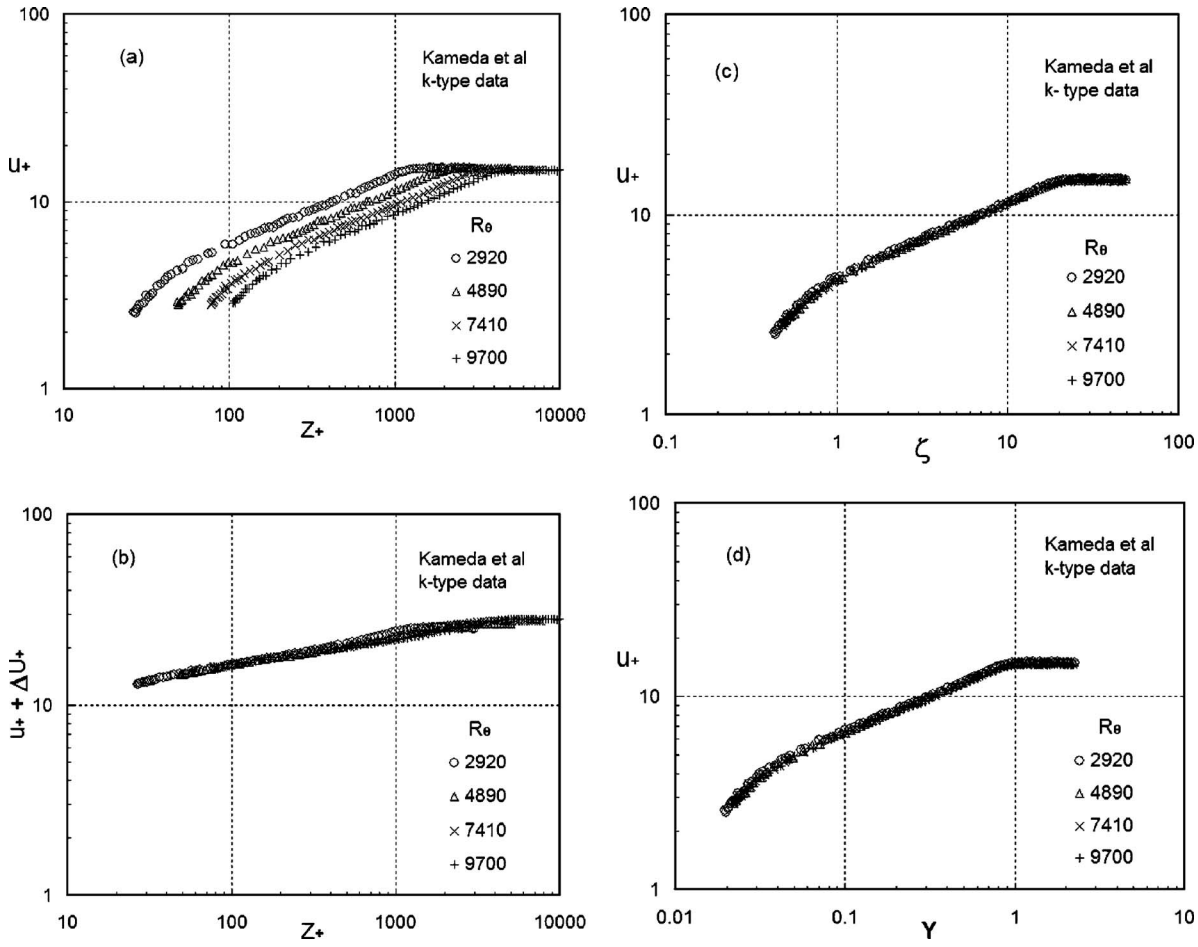

Fig. 1 The power law velocity distribution in log–log plots from data of Kameda, Osaka, and Mochizuki [45] for *k*-type roughness in the turbulent boundary layer: (*a*) Traditional inner power law $u_+ = CZ_+^\alpha$. (*b*) Velocity profile shifted by the roughness function inner power law $u_+ + \Delta U_+ = CZ_+^\alpha$. (*c*) Proposed inner transitionally rough wall power law velocity profile $u_+ = A\zeta^\alpha$. (*d*) Proposed outer power law velocity profile $u_+ = A_1 Y^\alpha$.

man and Webster [52] for bed river roughness are shown in Figs. 6(*a*)–6(*d*), whose behavior is analogous to Figs. 1(*a*)–1(*d*), and no additional comment is needed except that Fig. 6(*d*) shows that outer velocity profile data of Rahman and Webster [52] depend on river bed roughness. Afzal [53] analyzed the power law velocity profiles from DNS data of Leonardi et al. [54] in turbulent channel flow with transverse square bars on one wall. Furthermore, the alternate universal power law velocity profile (u_+, ζ) supports universality, explicitly independent of wall roughness. The corresponding values of power law index $\alpha = \alpha(\mathrm{R}_\phi)$ and prefactor $A = A(\mathrm{R}_\phi)$ are the functions of roughness friction Reynolds number R_ϕ. The power law index α and prefactor A as a function of roughness friction Reynolds numbers have also been estimated from transitional rough channel data of Balachandar et al. [13], Bergstrom et al. [14], Kotey et al. [15], and Poggi et al. [55] for circular perforations arrayed in a hexagonal pattern, wire mesh roughness, and sand grain roughness.

In the case of large Reynolds number flows where $\mathrm{R}_\phi \to \infty$, the Eq. (81) gives $\Gamma \approx 1$ and the log law constants from Eq. (78) become

$$k^{-1} = a\exp(1) \quad \text{and} \quad B = b\exp(1) \tag{105}$$

where the von Karman constant k, and intercept of log law B become universal constants, independent of Reynolds number. For the universal values $k=0.4$ and $B=5.5$ this results in

$$a = 0.92 \quad \text{and} \quad b = 2.02 \tag{106}$$

The power law index α and prefactor A have been compared to experimental data from a turbulent boundary layer on partially rough walls. The power law index for large Reynolds numbers becomes

$$\alpha = 1/\ln \mathrm{R}_\phi \tag{107}$$

and with von Karman constant $k=0.4$ (Schlichting [33]), the prefactors of Eqs. (97) and (98) become

$$A = \frac{0.92}{\alpha} + B\exp(-1) \tag{108}$$

$$A = 0.92\ln \mathrm{R}_\phi + B\exp(-1) \tag{109}$$

The experimental data of the power law constant A have been displayed against α^{-1} in Fig. 7. The data compares very well with the present prediction $A = 0.92/\alpha + 2.1$, corresponding to $B=5.6$ is proposed in Eq. (108). The experimental data shown against $\mathrm{R}_\phi = \mathrm{R}_\tau/\phi$, the roughness friction Reynolds number in Figs. 8 and 9, have some data scatter around the present predictions, which may be due to uncertainties associated with determination of friction velocity u_τ (by indirect methods), roughness function ΔU_+, and boundary-layer thickness δ. The experimental data of power index α against R_ϕ in Fig. 7 can be fruitfully represented, within the data scatter, by Eq. (109). The data of the power law prefactor A

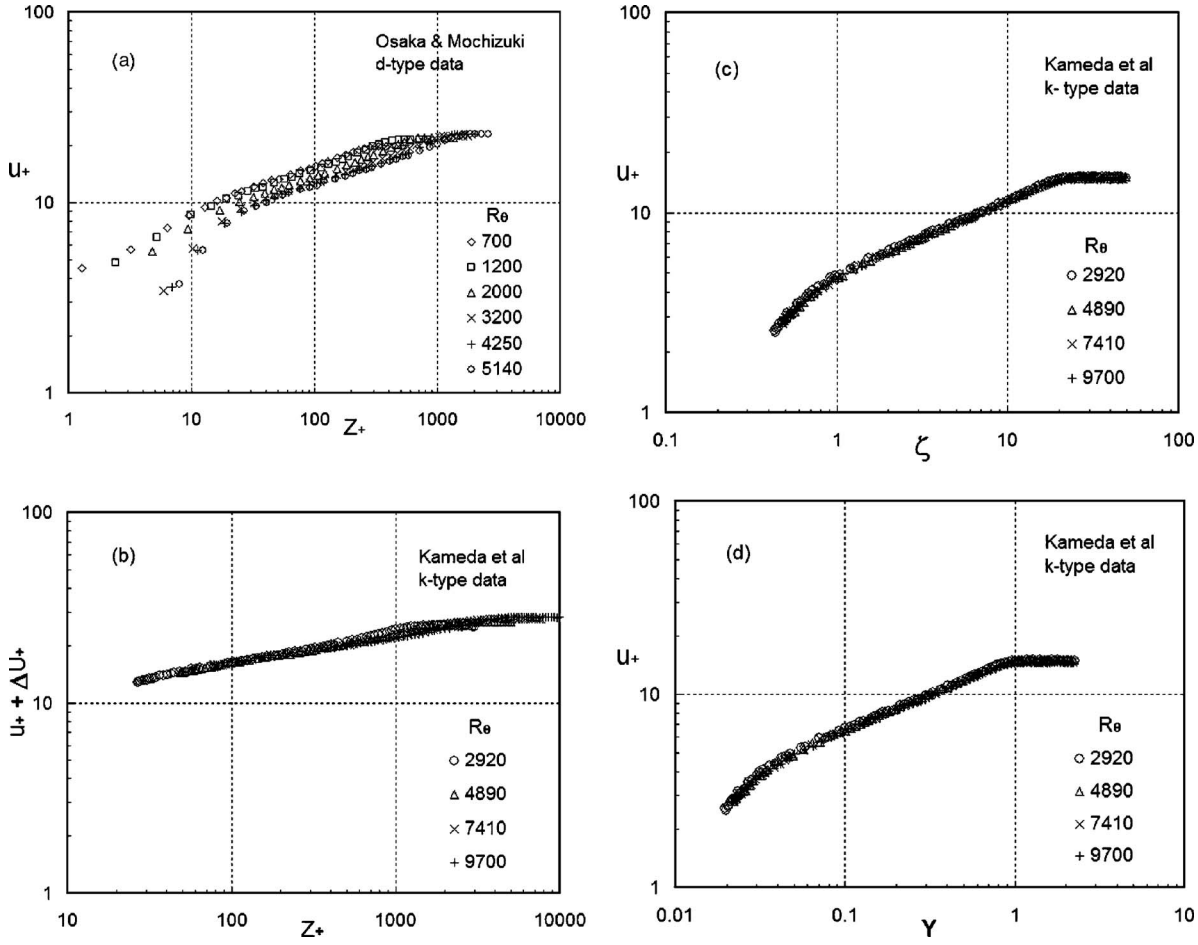

Fig. 2 The power law velocity distribution in log–log plots from data of Osaka and Mochizuki [46] for *d*-type roughness in the turbulent boundary layer. Legend same as in Figs. 1(*a*)–1(*d*).

displayed with R_ϕ in Fig. 9 can be represented, within the data scatter, by the prediction $A=0.92 \ln R_\phi + 1.6$ corresponding to $B=4.4$ proposed by Eq. (109). The mean value $B=5.6$ and $B=4.4$ of the additive intercept of law of the wall yields $B=5$ and $B\exp(-1)=1.84$.

The power law constants α and A from Eqs. (100)–(102) for large Reynolds numbers ($\Gamma \simeq 1$) become

$$\alpha = \frac{2.5\epsilon}{1 - E\epsilon} \tag{110}$$

$$A = \frac{0.368}{\epsilon} - E\exp(-1) \tag{111}$$

The power index α is of the order of the nondimensional friction velocity ϵ (classical velocity scale) and power law constant A of order ϵ^{-1}. The experimental data α and A against ϵ the nondimensional friction velocity displayed in Figs. 10 and 11 show scatter of data around the present predictions of Eqs. (110) and (111), which is due to uncertainties associated with the determination of friction velocity u_τ by indirect methods. The power index α has been compared with the data in Fig. 10, and the present prediction equation (110) required $E_1=4.8$. The prefactor A has been compared with the data in Fig. 11, where the present prediction equation (111) required $E=2$. Further, the values $E=6.2$ and $E=2$ have the mean value $E=4.1$ and $E\exp(-1)=1.51$.

The envelope of the skin friction power law gives the log law, which for a shallow outer wake becomes

$$\sqrt{\frac{2}{C_f}} = \frac{1}{k}\ln R_\phi + B + E \tag{112}$$

This skin friction law may also be expressed as

$$\sqrt{\frac{2}{C_f}} = \frac{1}{k}\ln\left(\mathrm{Re}_\phi \sqrt{\frac{C_f}{2}}\right) + B + E \tag{113}$$

The experimental data on transitionally rough wall for skin friction function $1/\sqrt{C_f}$ against R_ϕ from the relation

$$\frac{1}{\sqrt{C_f}} = 1.76 \ln R_\phi + 5.06 \tag{114}$$

has been linearly represented on a semi-log plot in Fig. 12, and is in good agreement with experimental data, which for $k=0.4$ and $B=5$ require $E=2.2$ in the log law equation (114).

The present prediction of the roughness scale Eq. (103) for inflectional roughness ($j=11$) is compared with data in Fig. 13(*a*). The data of Schultz and Flack [49] marked as Schultz & Flack 1 and Schultz & Flack [51] marked as Schultz & Flack 2 and Schultz and Myers [50] compare well with the prediction for inflectional type roughness. The data of Osaka and Mochizuki [46] for *k*-type roughness, Kameda et al. [45] for *d*-type roughness, and Smalley et al. [48] may be described by following simple predictions $\phi=h_+$. The roughness function $\Delta U_+ = k^{-1}\ln\phi$ with roughness variable h_+ for roughness data, also shown in Fig. 13(*b*), compare very well with the above-mentioned data.

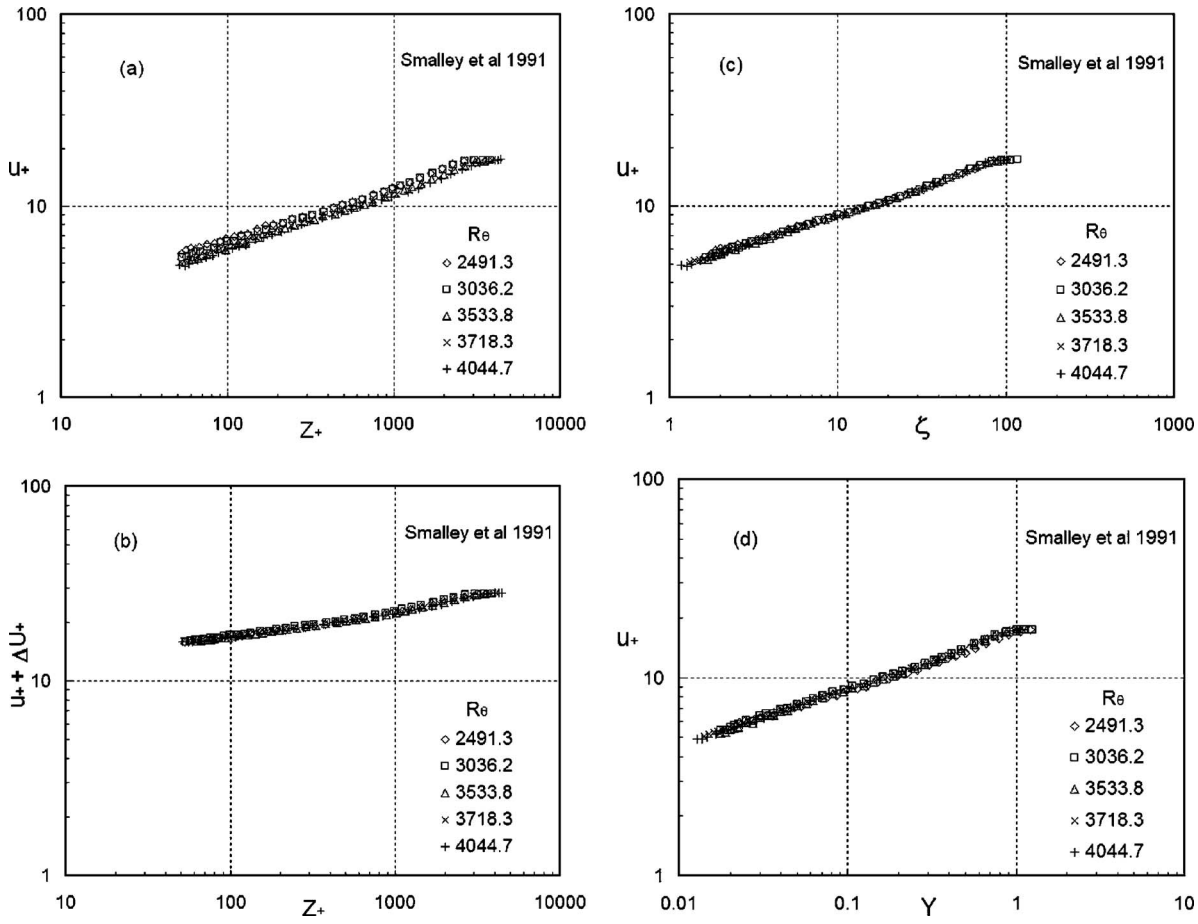

Fig. 3 The power law velocity distribution in log–log plots from data of Smalley et al. [48] for rod roughness in the turbulent boundary layer. Legend same as in Figs. 1(*a*)–1(*d*).

The order layer flow, governed by nonlinear wake equation (A1) subjected to boundary condition (A2) and matching condition (A3), is in nonequilibrium (nonsimilarity). The outer layer equations support Townsend's Reynolds number similarity hypothesis on rough walls [19]. The outer flow is in equilibrium (self-similar) $F_0(X,Y)=F_0(Y)$, and $T_0(X,Y)=T_0(Y)$ provided velocity at edge of the boundary layer

$$U_\infty = \text{const}\ \delta^m \quad \text{and} \quad \delta = \text{const}(x - x_0) \tag{115}$$

and pressure gradient parameter

$$m = \frac{\delta}{U_\infty}\frac{dU_\infty}{d\delta} = \frac{\delta}{U_\infty d\delta/dx}\frac{dU_\infty}{dx} \tag{116}$$

is a constant. Under this situation, outer nonlinear Eqs. (A1)–(A3) are under equilibrium and subjected to constant eddy viscosity closure of Clauser [56] and yield the Falkner-Skan equation (A9), subjected to the boundary condition (A10), and the matching conditions (A11) and (A12) of finite slip velocity on the impermeable wall. The solution to the Falkner-Skan equations (A9)–(A12) or wake and jet-like flows are described in Figs. 14 and 15. The values on m from the experimental data for strong adverse pressure gradient near separation are compared with the present theory in Table 1. The solution to the Falkner-Skan equations (A9)–(A12) representing the effect of the friction parameter ϵ^2/α_c on slip velocity b_S is shown in Fig. 16.

From log law theory, based on outer nonlinear wake layer, a uniformly valid velocity profile (B4), just above the sublayer, is given in Appendix B. For traditional shallow outer wake, the simplified uniformly valid solution is also presented. However, in view of the limitation of Coles [41] wake function $W_0(Y)$ near the outer edge of the boundary layer, a modified wake function $W = W_0(Y) + \Pi^{-1}W_1(Y)$ was considered. The perturbed wake function $W_1(Y)$, estimated from arguments of Lewkowicz [42], Finley et al. [43], Granville [44], and Afzal [38] given by Eqs. (B15)–(B17) of Appendix B, are shown in Fig. 17. Clearly, the proposal (B17) is more appropriate, as it satisfies the integral condition $I_1 = \int_0^1 W_1(Y)dY = 0$.

The classical log law slope k, the von Karman constant and additive term B are universal numbers independent of Reynolds number. The power law solution in the overlap region for large Reynolds numbers R_τ is equivalent to the log law solution. The common overlap region marked COR between the power law and log law velocity profiles has been published elsewhere [6,9,24–26,57]. Above COR there is a region marked PPR where the power law is a better representation of the experimental data. Below COR there is another region marked PLR where the log law is a better representation of the experimental data. The power law solution for large Reynolds numbers R_ϕ shows that the functions k and B are independent of Reynolds number, and it becomes an equivalent classical log law solution. Further, for lower Reynolds numbers R_ϕ, the functions k and B depend on Reynolds number, and the power law is not equivalent to the log law. The reason for developing a power law theory for a turbulent boundary layer over a rough surface is that it provides a better representation of the results for lower Reynolds numbers needed in the design process of actual systems when compared to log law theory.

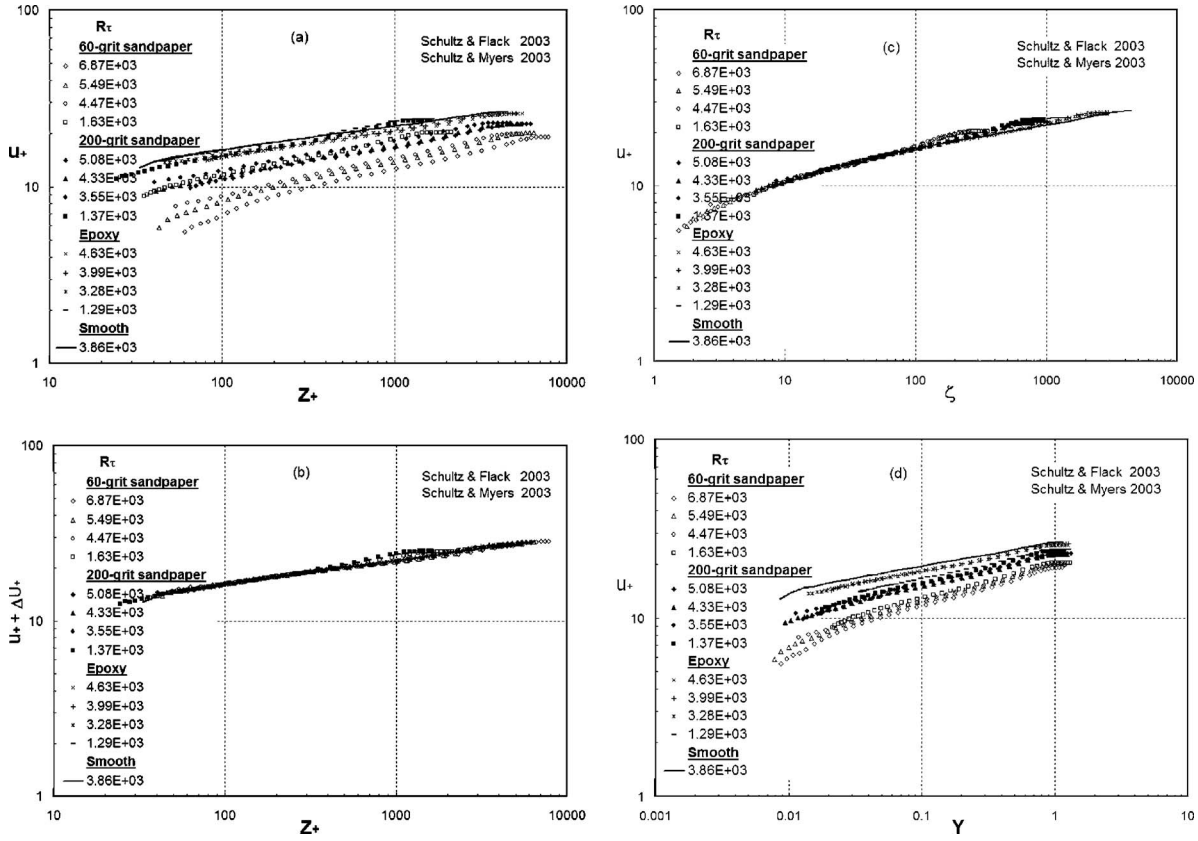

Fig. 4 The power law velocity distribution in log–log plots for turbulent boundary layer data of Schultz and Flack [49] for 60-grit and 120-grid sand grain roughness, and Schultz and Myers [50] for epoxy roughness. Legend same as in Figs. 1(*a*)–1(*d*).

5 Conclusions

(1) Two new parameters, the roughness friction Reynolds number $R_\phi = R_\tau/\phi = u_\phi \delta/\nu$, the roughness Reynolds number $Re_\phi = Re/\phi = U_\phi \delta/\nu$, and new inner variable $\zeta = Z_+/\phi = Z u_\phi/\nu$ for partial rough wall flows have been proposed in the present work. Here, $u_\phi = u_\tau/\phi$ and $U_\phi = U_\infty/\phi$, have been adopted for better description of the inner layer on the partially rough wall. Further, it is not u_τ that matters, but it is u_τ/ϕ that is of significance. The transitional rough wall effects on the mean turbulent shear flow are valid just above the roughness sublayer.

(2) In the present work when dealing with open equations, the matching in the overlap region leads to a functional equation. An alternate functional equation based on the ratio of any two successive derivatives of the functional equation have been matched in the Izakson-Millikan overlap region. This gives two functional solutions: the power law and log law profiles of velocity profile and friction factor.

(3) In the proposed new variable ζ, the velocity profile in the wall region and the skin friction (C_f, Re_ϕ) are universal relations, explicitly independent of surface roughness. This is supported very well by extensive experimental data for all types of transitional surface roughness.

(4) The power law constants α, A, and E, log law constants k, B, and D, and the roughness scale ϕ have to be determined by experiments; matching will not give them. The friction factor power law envelope shows that the power law constants α and A (functions of R_ϕ or C_f) are explicitly independent of roughness scale ϕ. Therefore, the power law constants α and A of a fully smooth wall would suffice for a transitional rough wall also.

(5) The power law constants α and A may be estimated from Eqs. (100) and (101), provided the local skin friction coefficient C_f is known. The roughness scale ϕ enters the picture only if we intend to estimate the power law constants from alternate Eqs. (96)–(99), containing $R_\phi = R_\tau/\phi$ and velocity profile containing $\zeta = Z_+/\phi$.

(6) The velocity profile shift in the overlap region due to transitional wall roughness may either be estimated from experimental data or by the use of an empirical formula for each type of roughness. In the present work, the roughness scale ϕ is related to roughness function ΔU_+ and the expressions for inflectional roughness Eq. (103) and k-type and d-type roughness Eq. (104) compare well with extensive experimental data of transitional surface roughness in the boundary layer and channel flows.

(7) The power law solution for large Reynolds numbers R_ϕ shows that the functions k and B are independent of Reynolds number, and it becomes the equivalent classical log law solution. Further, for lower Reynolds numbers R_ϕ, the functions k and B depend on Reynolds number, and the power law is not equivalent to the log law. The reason for developing a power law theory for turbulent boundary layer over transitional rough surface is that it provides a better representation of the results for lower Reynolds numbers needed in the design process of an actual system when compared to log law theory.

(8) To the lowest order, the outer layer flow is governed by the nonlinear turbulent wake equations which matches with the power law theory as well as log law theory in the overlap region. The outer layer equations support the Townsend's Reynolds number similarity hypothesis on rough walls.

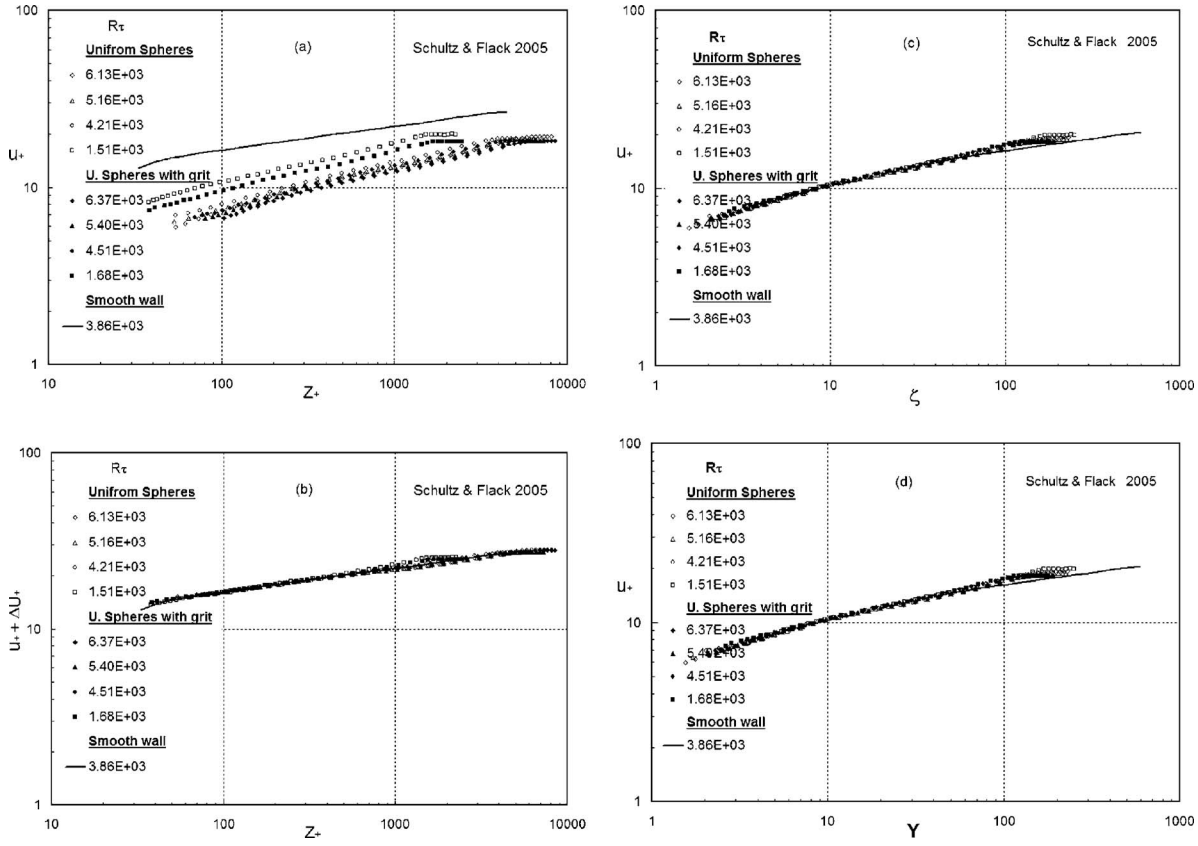

Fig. 5 The power law velocity distribution in log–log plots for turbulent boundary layer from data of Schultz and Flack [51] data for uniform spheres and uniform spheres with grit roughness. Legend same as in Figs. 1(*a*)–1(*d*).

These outer equations are in equilibrium for constant value of m, the pressure gradient parameter, and under constant eddy viscosity closure model; analytical as well as the numerical solutions are presented.

(9) For traditional shallow outer wake, the uniformly valid solution is also presented. A modified wake function $W = W_0(Y) + \Pi^{-1} W_1(Y)$ from arguments of Granville [42], Lewkowicz [43], and Afzal [38] are presented. Clearly, the proposal [38] is more appropriate, as it satisfies the integral condition $I_1 = \int_0^1 W_1(Y) dY = 0$.

Acknowledgment

The support of All India Council of Technical Education, New Delhi is acknowledged. The active help of Dr. Laural Murphy in preparation of the manuscript is also acknowledged.

Appendix A: Lowest-Order Outer Wake Layer

The outer expansions equations (26)–(28) from outer equation (21) yield the lowest order outer variables $F_0(X,Y)$ and $T_0(X,Y)$, which are governed by the following equation:

$$(1-\beta)\chi_1^{-1} T_0' + F_0 F_0'' - \beta(1 - F_0'^2) + \delta(1-\beta)(F_0'' F_{0\delta} - F_0' F_{0\delta}') = 0 \tag{A1}$$

subjected to the boundary conditions (22) at infinity and matching conditions (46) on impermeable surface as

$$Y \to \infty \quad F_0' \to 1 \quad T_0 \to 0 \tag{A2}$$

$$Y \to 0 \quad F_0 \to 0 \quad F_0'' = \text{finite} \quad T_0 \to 1 \tag{A3}$$

The solution of nonlinear wake equations (A1)–(A3) yields the outer layer slip velocity on the surface $F_0'(X.0) = b_S(X)$, which is applicable both to the power law theory as well as log law theory for the overlap region. The outer layer equations support Townsend's Reynolds number similarity hypothesis on rough walls [19,58].

The outer flow equations are closed by the constant eddy viscosity model as

$$\tau = \rho \nu_\tau \frac{\partial u}{\partial y} \tag{A4}$$

$$\nu_\tau = \alpha_c U_\infty \delta^* \tag{A5}$$

$$\delta = \alpha_c a_2 (x - x_o) \tag{A6}$$

$$(1+m) a_2 = \frac{\delta^*}{\delta} \tag{A7}$$

where α_c is a universal constant of Clauser [56], and δ^* is the displacement thickness of the boundary layer. The outer layer is in the equilibrium $F_0(X,Y) = f(Y)$ if the velocity at the edge of the boundary layer is a power law $U_\infty = \text{const}\ \delta^m$, where

$$m = \frac{\delta}{U_\infty}\frac{dU_\infty}{d\delta} = \frac{\delta}{U_\infty d\delta/dx}\frac{dU_\infty}{dx} \quad \beta = \frac{m}{1+m} \tag{A8}$$

pressure gradient parameter is a constant. Equations (A1)–(A3) under the model equations (A4)–(A7) become

$$f''' + f f'' + \beta(1 - f'^2) = 0 \tag{A9}$$

$$f'(\infty) = 1 \tag{A10}$$

$$f(0) = 0 \tag{A11}$$

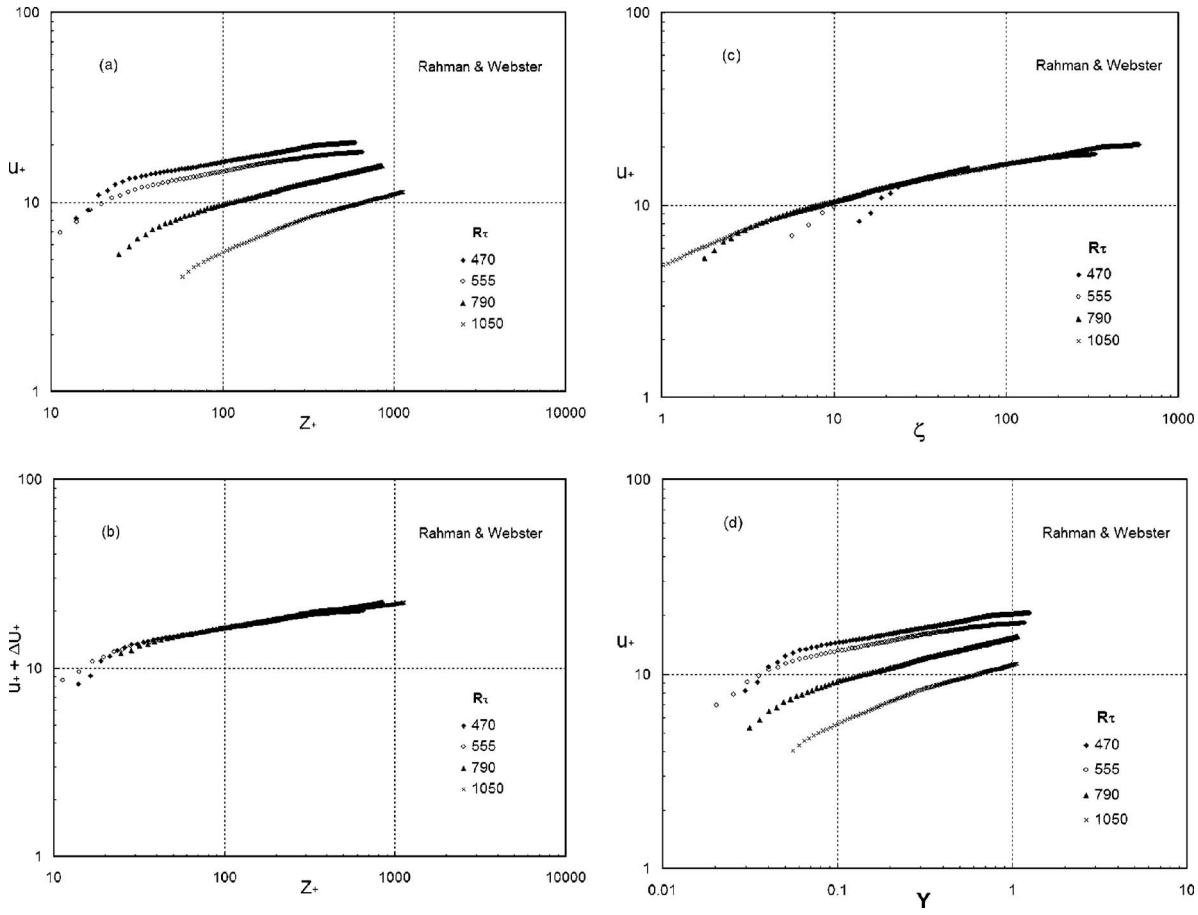

Fig. 6 The power law velocity distribution in log–log plots from data of Rahman and Webster [52] for channel bed roughness. Legend same as in Figs. 1(*a*)–1(*d*).

$$f''(0)\int_0^\infty (1-f')dY = \frac{\epsilon^2}{\alpha_c} = \frac{C_f}{2\alpha_c} \tag{A12}$$

Equation (A9) is the Falkner-Skan equation, where the pressure gradient parameter β differs from classical laminar flow value. The solution under the boundary condition of prescribed wall shear stress equation (A12) gives an outer layer slip velocity $f'(0)=b_S$. The parameter ϵ^2/α_c may be small or of order unity. For $\epsilon\to 0$ for α_c fixed, the boundary condition of Eq. (A12) may lead to the solution $f'(Y)=1$ or $f''(0)=0$ or $f''(0)\neq 0$, as described below.

i) Perturbation Around $f(Y)=1$: This represents a shallow outer wake, where $u-U_\infty$ is small like u_τ, leading to Karman outer

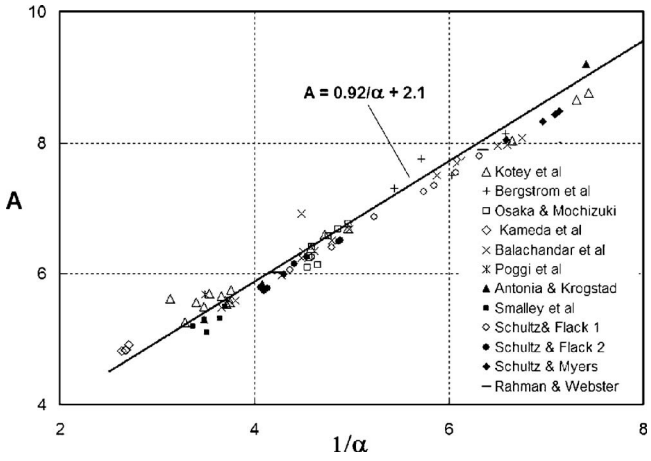

Fig. 7 Comparison of power law constant *A* from Eq. (108) against inverse of the power law index α with the experimental data of turbulent boundary layer on transitional rough wall. Proposed relation $A=0.92/\alpha+2.1$.

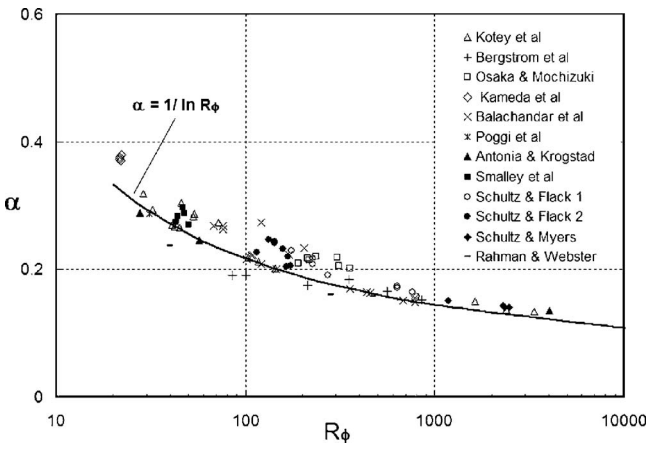

Fig. 8 Comparison of the power law index α from Eq. (107) against roughness friction Reynolds number R_ϕ with the experimental data of the turbulent boundary layer on transitional rough walls. Proposed relation: $\alpha=1/\ln R_\phi$.

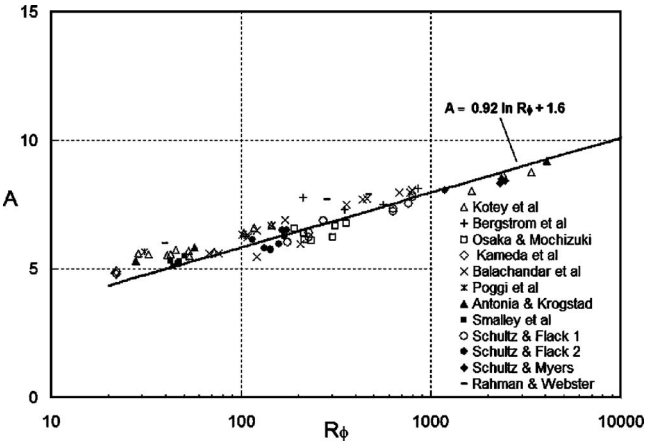

Fig. 9 Comparison of the power law constant *A* from Eq. (109) against roughness friction Reynolds number R_ϕ with the experimental data of turbulent boundary layer on transitional rough walls. Proposed relation: $A=0.92 \ln R_\phi+1.6$.

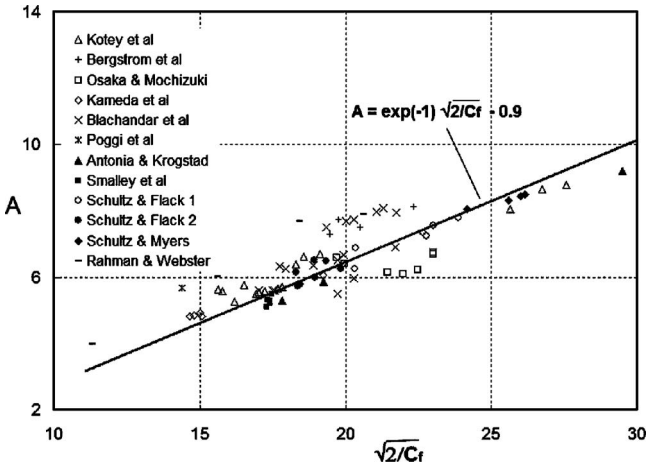

Fig. 11 Comparison of power law constant *A* relation against parameter $\exp(-1)/\epsilon$ based on inverse nondimensional friction factor from Eq. (111) with turbulent boundary layer on transitional rough walls. Proposed relation: $A=\exp(-1)/\epsilon-0.7$.

velocity defect $(U_\infty-u)/u_\tau$ type solution.

ii) $f''(0)=0$, $f'(0)=0$: This solution is of interest at the point of separation. The solution of Eq. (A9) under the boundary conditions $f(0)=f'(0)=f''(0)=f'(\infty)-1=0$ predict $\beta=\beta_0=-0.198838$ and $m=m_0=-0.168585$. The numerical solution of the velocity profile $f'(Y)$ may be normalized as

$$\frac{1}{\delta_e}\int_0^{\delta_e} f'(Y)dY = 1 \tag{A13}$$

where δ_e is the boundary layer thickness at $f'(Y=\delta_e)=0.99$ and the normalized solution may be expressed as

$$f'(Y/\delta_e) = W(Y) \tag{A14}$$

The numerical solution $W(Y)$, as shown in Fig. 14 (after Afzal [59]), compares well with Coles [60] the wake function $W_c(Y)$. The composite log-wake equation of Coles [41,60] is

$$\frac{U_\infty-u}{u_\tau} = -\frac{1}{k}\ln Y + \frac{\Pi}{k}[W_c(1)-W_c(Y)] \tag{A15}$$

where the wake function $W_c(Y)$ satisfies the boundary conditions $W_c(Y=0)=0$ and $W_c(Y=1)=1$ along with the normalizing condition $\int_0^\delta W_c(Y)dY=1$. Although the composite log-wake law (A15) is not valid at the point of separation, from a limiting consideration this yields a relation analogous to Eq. (A14), as shown here. When separation is approached, $u_\tau/U_\infty\to 0$ (i.e., $\lim \tau_w\to 0$), the parameter Π/k tends to infinity, and subjected to the boundary condition $u=U_\infty$ at $y=\delta$, we get a limiting relation

$$\lim\frac{\Pi}{k}\frac{u_\tau}{U_\infty} = 1 \tag{A16}$$

where the velocity profile (at a point of separation (or reattachment) becomes

$$\frac{u}{U_\infty} = W_c(Y) \tag{A17}$$

which may be compared with the present relation (A14).

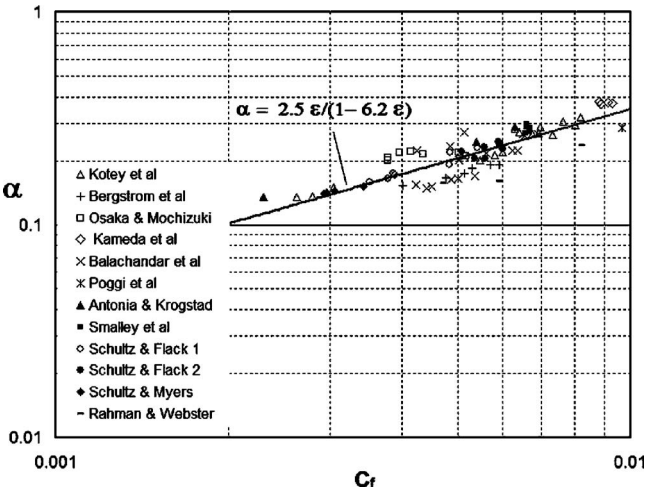

Fig. 10 Comparison of the power law index α against skin fiction coefficient C_f based on Eq. (110) for turbulent boundary layer on transitional rough walls. Proposed relation: $\alpha=2.5\epsilon/(1-6.2\epsilon)$.

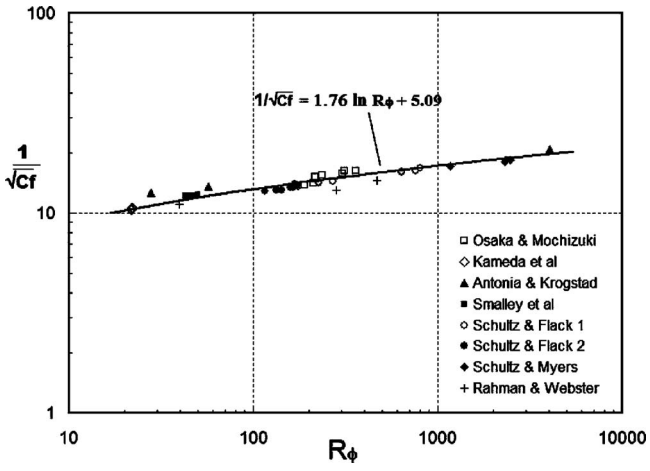

Fig. 12 Comparison of skin friction coefficient C_f against the roughness friction Reynolds number $R_\phi=R_\tau/\phi$ from Eq. (114) for turbulent flow boundary layer on transitional rough wall. Proposed relation: $1/\sqrt{C_f}=1.76 \ln R_\phi+5.09$.

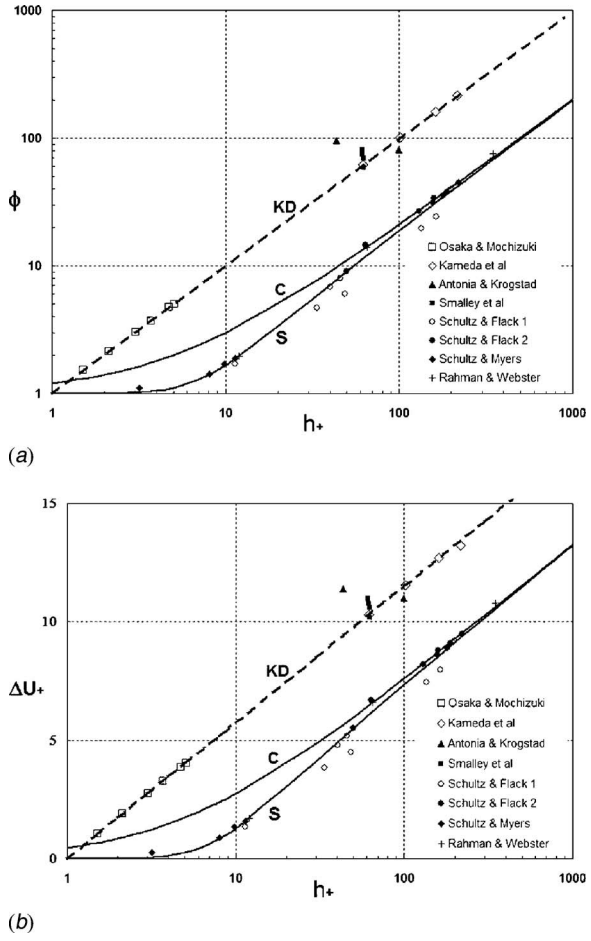

Fig. 13 Comparison of the roughness scales data with present predictions. (*a*) Roughness scale ϕ against wall roughness parameter h_+ for various values of δ/h. (*b*) The roughness function ΔU_+ against wall roughness parameter h_+ for various values of δ/h. The line marked "S" is the inflectional roughness (j=11) and marked "C" is for Colebrook monotonic roughness (j=0) from prediction equation (103) for roughness scale ϕ and roughness function ΔU_+. Line marked "KD" is the prediction Eq. (104) for *k*-type and *d*-type roughness.

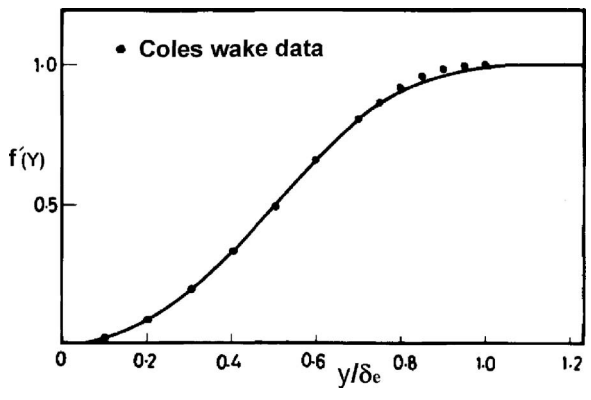

Fig. 14 Comparison of velocity profile from solution of lowest order outer nonlinear wake layer Falkner-Skan equations (A9)–(A12) based on Clauser constant eddy viscosity model, for $m=-0.165858$ ($\beta=-0.198838$) for skin friction $C_f=0$, and slip velocity $b_S=0$ with the wake function of Coles [60]

iii) $f''(0)=0$, $f'(0)\neq 0$: This case represents the wake- and jet-like solutions for outer layer of the turbulent boundary layer flow. In general, $f''(0)=0$, with $f'(0)\neq 0$, gives the wake-like solution for $-1/3<m\leq m_0$ ($-0.5<\beta\leq\beta_0$) with $\beta_0=0.198838$ or $m_0=0.165858$, and jet-like solution for $-1/2\leq m<-1/3$ ($-1\leq\beta<-0.5$). An approximate wake/jet-like solution is

$$f'(Y)=1-[1-f'(0)]\exp(-d_0Y^2) \tag{A18}$$

$$d_0=-\beta[1+f'(0)]/2 \tag{A19}$$

which gives the slip velocity on the surface as

$$f'(0)=-2\frac{m-m_0}{1+2m} \tag{A20}$$

$$d_0=-\frac{1}{2}\frac{m}{1+m}\frac{1-2m_0}{1-2m} \tag{A21}$$

The solution from Eq. (A20) for zero slip velocity yields $m=m_0$ and the solution of Eqs. (A18) and (A19) becomes

$$\frac{u}{U_\infty}=f'(Y)=1-\exp(-d_1Y^2) \tag{A22}$$

$$d_1=-\frac{1}{2}\frac{m_0}{1+m_0}=0.09942\approx 0.1 \tag{A23}$$

The velocity distribution for various values of pressure gradient parameter m are shown in Fig. 15, which clearly displays the wake-like and jet-like solutions in the nonlinear outer layer. The jet-like solutions are of no interest in the present study, and would be useful for wall jet-like flows not considered here. Further, an integral of momentum Eq. (A9) subjected to boundary conditions Eqs. (A10)–(A12) near separation $f''(0)=0$ gives (Afzal [59])

$$m=-\frac{1}{2+H} \tag{A24}$$

that provides the relation of pressure gradient parameter m with shape factor $H=\delta_1/\delta_2$, where

$$\delta_1=\int_0^\infty(1-f')dY \quad \delta_2=\int_0^\infty f'(1-f')dY \tag{A25}$$

The separation domain in the neighborhood $-0.25<m<-0.165858$ ($-1/4<\beta<-0.198838$), and point of separation $m=m_0=-0.165858$ and $\beta=\beta_0=-0.198838$ are of particular interest. Further, the reverse flow solutions also exist, which are wake-like for $m_0<m<0$ ($\beta_0<\beta<0$) and are jet-like for $-\infty\leq m\leq -1/2$ ($1<\beta<-1$), which are not described here. The comparison of values of m from our work with the boundary layer experimental data at the verge of separation is described in Table 1 from various sources (whose citations may be found in [61]). Angele and Klingmann [62] have pointed out that there are several things that indicate that flow of Elsberry et al. [61] is far from separation.

iv) $f''(0)\neq 0$: The numerical solutions with finite shear stress on the wall $f''(0)\neq 0$ for the Falkner-Skan equations (A9)–(A12) have been shown in Fig. 16 (after Afzal [38]) that gives slip velocity $b_S(=U_S/U_\infty)$ against ϵ^2/α_c, for various values of the pressure gradient parameter. Earlier, Clauser [56], in his Fig. 8, p. 47, presented the solution of Eq. (A9) for various values of β subjected to the boundary conditions (A10) and (A11), and prescribed the slip velocity $0\leq f'(0)=u(0)/U_\infty\leq 0.8$ for estimation of velocity gradient $u'(0)/U_\infty=f''(0)$ and $Y=Y^*$ at δ^*. On the other hand, the present work has provided the outer flow matching condition (A11) at $Y=0$, leading to rational solutions, shown in Fig. 16. Further, Clauser [56] did not analyze the solutions $f''(0)=0$ near separation, but considered the strong adverse pressure gradient in the neighborhood of separation domain. These solutions were expressed in terms of velocity defect law $(U_\infty-u)/u_\tau$, which con-

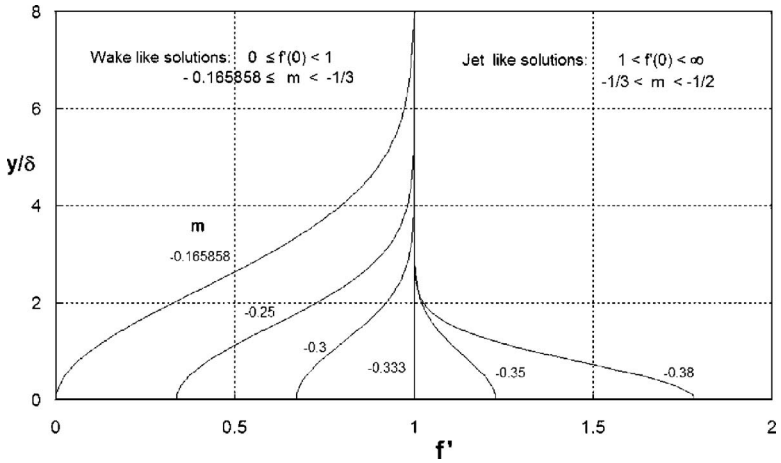

Fig. 15 The wake- and jet-like solutions of the velocity distribution from lowest order outer nonlinear wake layer Falkner-Skan equations (A9)–(A12) for C_f=0, based on Clauser constant eddy viscosity model

strained the solution profile to a shallow outer wake, by imposing a velocity scale u_τ and estimated $\nu_\tau/U_\infty\delta^*=0.018$ (=α_c termed as Clauser's universal constant) by patching it with universal log law, for boundary layer with pressure gradients. This over-constrainment led Clauser [56] to the definition of the equilibrium turbulent boundary layers, in which

$$\beta_1 = \frac{\delta^*}{\tau_w}\frac{dp}{dx} = \text{constant} \tag{A26}$$

Coles [60] carried out this approach of shallow wake one step further, by introducing a wake function $W(Y)$ and parameter Π to account for the outer part of the turbulent boundary layer.

Appendix B: Log Law Theory

The matching Eqs. (55) and (56) are integrated, which gives the log laws for inner velocity and wall shear stress as

$$u_+ = \frac{1}{k}\ln\zeta + B \tag{B1}$$

$$\frac{U_S}{u_\tau} = k^{-1}\ln \mathrm{R}_\phi + B + D_S \tag{B2}$$

The matching of velocity profile Eq. (47) based on Eqs. (B1) and (B2), gives the outer velocity profile

Table 1 Values of *m* from experiments near separation

Experiments	*m*
Ludwieg and Tillmann (1950)	–0.23
Newman (1951)	–0.228
Schubauer and Klebanoff (1951)	–0.257
Stratford (1959)	–0.25
Townsend (1960) theory	–0.234
Simpson et al. (1977)	–0.251
Simpson et al. (1981)	–0.222
Afzal theory [59]	–0.165858
Skare and Krogstad (1994)	–0.22
Alving and Fernholz (1995)	–0.226
Elsberry et al. Case A [61]	–0.21
Elsberry et al. Case B [61]	–0.18
Present work	–0.165858

$$\frac{U_S - u}{u_\tau} = -\frac{1}{k}\ln Y + D_S \tag{B3}$$

A uniformly valid solution for the velocity profile may be obtained from the union of the inner wall layer equation (31) and the outer layer equation (28) subtracted by common part equations (B1) or (B2), above the sublayer, becoming

$$\frac{u}{U_\infty} = U_0(X,Y) - b_S + \frac{u_\tau}{U_\infty}\left(\frac{1}{k}\ln\zeta + B + \frac{\Pi_S}{k}W(X,Y)\right) \tag{B4}$$

where $D_S = W(X,1)\Pi_S/k$ and $W(X,Y)$ is the wake function for log law profile

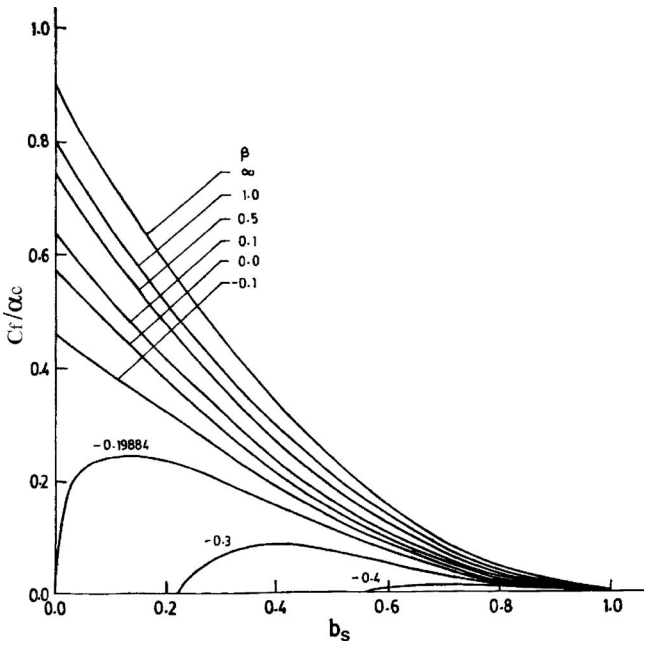

Fig. 16 The skin friction parameter C_f/α_c and wall slip velocity parameter $b_S = U_S/U_e$ from solution outer nonlinear wake layer Falkner-Skan equations (A9)–(A12), based on Clauser constant eddy viscosity model

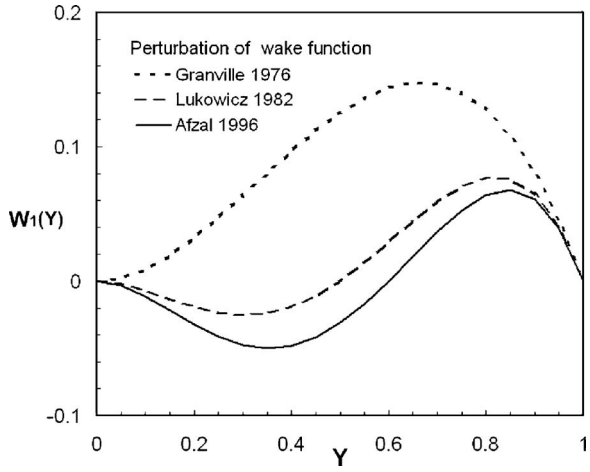

Fig. 17 Comparison of the perturbed wake function $W_1(Y)$ for outer shallow wake layer proposed by Afzal [38] with area $I_1 = \int_0^1 W_1(Y)dY = 0$ with Lewkowicz [42] for $I_1 = 0.0166$ and Finley et al. [43] and Granville [44] for $I_1 = 0.0833$

$$W(X,Y) = \left[-U_1(X,Y) - k^{-1} \ln Y + \frac{\Pi_S}{k} W(X,1) \right] \frac{k}{\Pi_S} \tag{B5}$$

Equation (B4) in outer variables becomes

$$\frac{U_S - u}{U_\infty} = b_S - U_0(X,Y) - \frac{u_\tau}{U_\infty} \left\{ -\frac{1}{k} \ln Y + \frac{\Pi_S}{k} [W(X,1) - W(X,Y)] \right\} \tag{B6}$$

The shallow outer wake $U_0(X,Y) = 1$ ($b_S = 1$, $U_S = U_\infty$), the uniformly valid solution Eqs. (B4) and (B6) yields

$$\frac{u}{u_\tau} = \frac{1}{k} \ln \zeta + B + \frac{\Pi}{k} W(X,Y) \tag{B7}$$

$$\frac{U_\infty - u}{u_\tau} = -\frac{1}{k} \ln Y + \frac{\Pi}{k} [W(X,1) - W(X,Y)] \tag{B8}$$

and the skin friction log law (B2) becomes

$$\frac{U_\infty}{u_\tau} = k^{-1} \ln \mathrm{R}_\phi + B + D \tag{B9}$$

where $U_S = U_\infty$, $D = W(X,1)\Pi(X)/k$ and $\Pi_S = \Pi$. The wake function $W(X,Y)$ satisfies the following boundary conditions $W(X,0) = W(X,1) - 2 = 0$ along with the additional conditions

$$\int_0^1 W(X,Y)dY = 1 \quad \text{and} \quad W'(X, Y=1) = -\frac{1}{k} \tag{B10}$$

The wake function $W(X,Y)$ may be taken as

$$W(X,Y) = W_0(X,Y) + \frac{1}{\Pi} W_1(X,Y) + \cdots \tag{B11}$$

where $W_0(X,Y)$ is the basic wake function (Coles [60]), which satisfies the boundary conditions $W_0(X,0) = W_0(X,1) - 2 = 0$ and integral condition

$$I_0 \equiv \int_0^1 W_0(X,Y)dY = 1 \tag{B12}$$

The perturbation wake function $W_1(X,Y)$ satisfying the boundary conditions $W_1(X,0) = W_1(X,1) = 0$ along with the conditions

$$W_1'(X,1) = -1 \quad \text{and} \quad I_1 \equiv \int_0^1 W_1(X,Y)dY = 0 \tag{B13}$$

For outer layer in equilibrium the wake function $W_0(Y)$ of Moses is

$$W_0(Y) = 6Y^2 - 4Y^3 \quad \text{and} \quad I_0 = 1 \tag{B14}$$

and perturbation of the wake function W_1 proposed by Afzal [38] satisfies the integral condition (B13) is

$$\text{Afzal[38]: } W_1(Y) = \frac{1}{2}(3Y^2 - 8Y^3 + 5Y^4) \quad \text{and} \quad I_1 = 0 \tag{B15}$$

and other authors work, where $I_1 \neq 0$, are stated below

$$\text{Lewkowicz[42]: } W_1(Y) = -Y^2 + 3Y^3 - 2Y^4 \quad \text{and} \quad I_1 = 1/60 \tag{B16}$$

$$\text{Finley et al. [43] and Granville[44]: } W_1(Y) = Y^2 - Y^3 \quad \text{and} \quad I_1 = 1/12 \tag{B17}$$

The earlier work [59,60] more often adopted Eq. (B16) after Lewkowicz [42] ($I_1 = 0.0166$) when compared with Eq. (B17) after Finley et al. [43] and Granville [44] ($I_1 = 0.0833$). However, Eq. (B15) of Afzal [38] is more appropriate as it exactly satisfies the integral condition $I_1 = 0$. The comparisons of the perturbed wake function $W_1(Y)$ for outer shallow wake layer proposed by several workers are shown in Fig. 16.

The velocity profile Eq. (B7) and skin friction Eq. (B9) after elimination of ζ and R_ϕ in favor of the classical variables y_+ and R_τ we get

$$\frac{u}{u_\tau} = \frac{1}{k} \ln Z_+ + B - \Delta U_+ + \frac{\Pi}{k} W(X,Y) \tag{B18}$$

$$\frac{U_\infty}{u_\tau} = k^{-1} \ln R_\tau + B + D - \Delta U_+ \tag{B19}$$

Further, Eq. (B18) of log law theory may be expressed in alternate forms as

$$\frac{u}{u_\tau} = \frac{1}{k} \ln \frac{Z}{h} + B_T + \frac{\Pi}{k} W(X,Y) \tag{B20}$$

that leads to the expression for the roughness function (Raupach et al. [31])

$$\Delta U_+ = \frac{1}{k} \ln h_+ + B - B_T \tag{B21}$$

Here, B and $B_T(h_+)$ are the additive terms in the log laws of wall for fully smooth wall and transitional rough wall, respectively. In fully rough wall, $B_T = B_F$ is a universal constant independent of wall roughness. From Eq. (7) connecting roughness scale with roughness function, we get

$$\phi = \exp(k\Delta U_+) = h_+ \exp[k(B - B_T)] \tag{B22}$$

which is the same as Eq. (88).

Appendix C: Roughness Scale ϕ

The various types of roughness have been considered in the laboratory and atmospheric environments. The roughness function ΔU_+ data from extensive sources may be found in the reviews by Schlichting [30], Raupach et al. [31], Jimenez [32], and Piquet [63]. The experimental determination of the roughness function ΔU_+ by three method are described in Schultz and Myers [50]. Such expressions for all types of roughness are not available, while in other cases the roughness function expressions have a low confidence level.

C.1 Colebrook Monotonic Roughness:

Colebrook [64] in monotonic commercial technical transitional roughness, fortuitously proposed roughness function as composite sum of the log terms of fully smooth wall and fully rough wall as

$$\Delta U_+ = \frac{1}{k}\ln(1+\chi h_+) \tag{C1}$$

where $\chi=\exp(k(B-B_F))=0.306$ with $B=5.5$ and $B_F=8.5$. In terms of roughness scale, ϕ in transitional rough case is a simple sum of the values for fully smooth wall, $\phi=1$, and fully rough wall, $\phi=\chi h_+$, as

$$\phi = 1+\chi h_+ \tag{C2}$$

The Colebrook-type roughness function has been used for random roughness by Grigson [65], and his Table 1, gives values of χ from investigation of the finishes of the hull surfaces.

C.2 Inflectional Roughness:

The sand grain roughness data of Nikuradse is of inflectional type. Loselevich and Pilipenko (see Cebeci [66]) proposed an expression for the roughness function. In present work a simple expression for roughness scale ϕ is proposed for inflectional roughness by introducing an exponential function $\exp(-j/h_+)$ in Eq. (C2) to yield

$$\phi = 1+\chi h_+ \exp\left(-\frac{j}{h_+}\right) \tag{C3}$$

and

$$\Delta U_+ = \frac{1}{k}\ln\phi \tag{C4}$$

where $\chi=\exp(k(B-B_F))$. The roughness scale ϕ in Eq. (C3) with parameter $j\neq 0$ has a point of inflection at origin $h_+=0$. Further, the exponential function in Eq. (C3) approaches unity when $h_+\to\infty$ and zero when $h_+\to 0$, that maintain the traditional skin friction relations of fully rough and fully smooth walls, respectively. For inflectional type roughness, the choice $j=11$ has been in very good agreement with transitional pipe data Nikuradse [7] and Shockling et al. [67] as shown in power law theory of Afzal [9,53] as well as log law theory of Afzal et al. [68,69]. In terms of traditional Reynolds number Re, the work of Afzal et al. [68,69] provides better and more rational predictions of the friction factor when compared with predictions of Allen et al. [70] based on given roughness h_+ and the knowledge of ΔU_+ versus h_+ from one experiment to another, in the situations of machined honed superpipe roughness and Nikuradse's sand grain roughness.

C.3 *k*-Type and *d*-Type Roughness:

In the present work, data of Kameda et al. [45] for *k*-type roughness, Osaka and Mochizuki [46] for *d*-type roughness, Smalley et al. [48] for rod roughness, and Antonia and Krogstad [47] for rod roughness have been predicted by the following simple equations

$$\phi = h_+ \tag{C5}$$

$$\Delta U_+ = \frac{1}{k}\ln h_+ \tag{C6}$$

and referred to as *k*-type and *d*-type roughness.

References

[1] Nikuradse, J., 1932, "Laws of Turbulent Flow in Smooth Pipes," VDI, Forschungsheft N-356 (English Translation NACA TTF-10, p. 359).

[2] Barenblatt, G. I., 1993, "Scaling Laws for Fully Developed Turbulent Shear Flows, Part I: Basic Hypothesis and Analysis," J. Fluid Mech., **248**, pp. 513–520.

[3] Kailasnath, P., 1993, "Reynolds Number Effect and the Momentum Flux in Turbulent Boundary Layer," Ph.D. thesis, Yale University, New Haven, CT.

[4] Zagarola, M., Perry, A. E., and Smits, A. J., 1997, "Log Laws or Power Laws: The Scaling in Overlap Region," Phys. Fluids, **9**, pp. 2094–2100.

[5] McKeon, B. J., Li, J., Jiang, W., Morrison, J. F., and Smits, A. J., 2004, "Further Observations on Mean Velocity Distribution in Fully Developed Pipe Flow," J. Fluid Mech., **501**, pp. 135–147.

[6] Afzal, N., 2001, "Power Law and Log Law Velocity Profiles in Fully Developed Turbulent Pipe Flow: Equivalent Relations at Large Reynolds Numbers," Acta Mech., **151**, pp. 171–183.

[7] Nikuradse, J., 1933, "Laws of Flow in Rough Pipe," VDI, Forschungsheft N-361 (English translation NACA TM 1292, 1950).

[8] Porporato, A., and Sordo, S., 2001, "On the Incomplete Similarity for Turbulent Velocity Profiles in Rough Pipes," Phys. Fluids, **13**(9), pp. 2596–2601.

[9] Afzal, N., Seena, A., and Bushra, A., 2006, "Power Law Turbulent Velocity Profile in Transitional Rough Pipes," J. Fluids Eng., **128**, pp. 548–558.

[10] Barenblatt, G. I., Chorin, A. J., and Prostokishin, V. M., 2000, "Self-Similar Intermediate Structures in Turbulent Boundary Layers at Large Reynolds Numbers," J. Fluid Mech., **410**, pp. 263–283.

[11] Panton, R. L., 2002, "Evaluation of the Barenblatt-Chorin-Prostokishin Power Law for Turbulent Boundary Layers," Phys. Fluids, **14**, pp. 1806–1808.

[12] Osterlund, J. M., 1999, "Experimental Studies of Zero Pressure Gradient Turbulent Boundary Layer," Ph.D. thesis, Royal Institute of Technology, Stockholm, Sweden.

[13] Balachandar, R., Hagel, K., and Blakely, D., 2002, "Velocity Distribution in Decelerating Flow Over Rough Surface," Can. J. Civ. Eng., **29**, pp. 211–221.

[14] Bergstrom, D. J., Tachie, M. F., and Balachandar, R., 2001, "Application of Power Laws to Low Reynolds Number Boundary Layers on Smooth and Rough Surfaces," Phys. Fluids, **13**(11), pp. 3277–3284.

[15] Kotey, N. A., Bergstrom, D. J., and Tachie, T. F., 2003, "Power Law for Rough Wall Turbulent Boundary Layer," Phys. Fluids, **15**, pp. 1396–1404.

[16] Seo, J., and Castillo, L., 2004, "Rough Surface Turbulent Boundary Layer: The Composite Profiles," 42nd AIAA Aerospace Sciences Meeting and Exhibit, Reno, Nevada, Jan. 5–8, Paper No. AIAA 2004–1287.

[17] George, W., and Castillo, L., 1997, "Zero Pressure Gradient Turbulent Boundary Layer," Appl. Mech. Rev., **50**, pp. 689–729.

[18] Afzal, N., 2005, "Scaling of Power Law Velocity Profile in Wall-Bounded Turbulent Shear Flows," 43rd AIAA Aerospace Sciences Meeting and Exhibit, 10–13 Jan Reno, Nevada, Jan. 10–13, Paper No. AIAA-2005-0109.

[19] Flack, K. A., Schultz, M. P., and Shapiro, T. A., 2005, "Experimental Support for Townsend's Reynolds Number Similarity Hypothesis on Rough Walls," Phys. Fluids, **17**, p. 035102.

[20] George, W., Castillo, L., and Knecht, P., 1996, "The Zero Pressure Gradient Turbulent Boundary Layer," Turbulence Research Lab., State University of New York at Buffalo, Technical Report TRL-153.

[21] George, W., Abrahamsson, H., Eriksson, J., Karlsson, R. L., Lofdahl, L., and Wosnik, M., 2000, "A Similarity Theory for the Turbulent Plane Wall Jet Without External Stream," J. Fluid Mech., **425**, pp. 367–411.

[22] George, W., 2005, "Recent Advancements Towards Understanding of Turbulent Boundary Layer," 4th AIAA, Theoretical Fluid Mechanics, Toronto, Canada, June 6–9, 2005, Paper No. AIAA-2005-4669, pp. 1–18.

[23] Eaton, J. K., and Nagib, H. M., 2004, "Report: 'Second International Workshop on Wall-Bounded Turbulent Flows' by H. Nagib & A. J. Smits," Trieste, Italy, Nov. 2–5, 2004.

[24] Afzal, N., 1997, "Power Law in Wall and Wake Layers of a Turbulent Boundary Layer," *Proc. Seventh Asian Congress of Fluid Mechanics*, Allied Publishers, New Delhi, India, pp. 805–808.

[25] Afzal, N., 2001, "Power Law and Log Law Velocity Profiles in Turbulent Boundary Layer Flow: Equivalent Relations at Large Reynolds Numbers," Acta Mech., **151**, pp. 195–216.

[26] Afzal, N., 2005, "Analysis of Power Law and Log Law Velocity Profiles in Overlap Region of a Turbulent Wall Jet," Proc. R. Soc. London, Ser. A, **461**, pp. 1889–1910.

[27] Millikan, C. B., 1938, "A Critical Discussion of Turbulent Flows in Channels and Circular Tubes," *Proc. 5th International Congress on Applied Mechanics* J. P. den Hartog and H. Peters, eds., Cambridge, MA, Wiley/Chapman and Hall, New York, pp. 386–392.

[28] Clauser, F. H., 1954, "Turbulent Boundary Layers in Adverse Pressure Gradients," J. Aeronaut. Sci., **21**, pp. 91–108.

[29] Hama, F. R., 1954, "Boundary Layer Characteristics for Smooth and Rough Surface," Soc. Nav. Archit. Mar. Eng., Trans., **62**, pp. 333–358.

[30] Schlichting, H., 1968, *Boundary Layer Theory*, Mc-Graw Hill, New York.

[31] Raupach, M. R., Antonia, R. A., and Rajagopalan, S., 1991, "Rough-Wall Turbulent Boundary Layer," Adv. Appl. Mech., **44**, pp. 1–25.

[32] Jimenez, J., 2004, "Turbulent Flow Over Rough Walls," Annu. Rev. Fluid Mech., **36**, pp. 173–196.

[33] Izakson, A. A., 1937, "On Formula for the Velocity Distribution Near Walls," Sov. Phys. Tech. Phys., **4**, pp. 155–159.

[34] Kolmogorov, A. N., 1941, "The Local Structure of Turbulence in Incompressible Viscous Fluid for Very Large Reynolds Numbers," Dokl. Akad. Nauk SSSR, **30**, 9–13 (reprinted in Proc. R. Soc. London A 434, 9–13 (1991).

[35] Afzal, N., and Narasimha, R., 1976, "Axisymmetric Turbulent Boundary Layers Along a Circular Cylinder With Constant Pressure," J. Fluid Mech., **74**, pp. 113–129.

[36] Afzal, N., 1976, "Millikan Argument at Moderately Large Reynolds Numbers," Phys. Fluids, **19**, pp. 600–602.

[37] Afzal, N., and Bush, W. B., 1985, "A Three Layer Asymptotic Analysis of

Turbulent Channel Flows," Proc. Indian Acad. Sci., Math. Sci., **94**, pp. 135–148.
[38] Afzal, N., 1996, "Wake Layer in a Turbulent Boundary Layer With Pressure Gradient: A New Approach," *Proc. IUTAM Symposium. on: Asymptotic Methods for Turbulent Shear Flows at High Reynolds Numbers*, K. Gersten, ed., Kluwer Academic Publisher, Dordrecht, pp. 95–118.
[39] Narasimha, R., 1996, "Different Approaches to Asymptotic Expansions of Turbulent Boundary Layer," *Asymptotic Methods for Turbulent Shear Flows at High Reynolds Numbers*, K. Gersten, ed., Kluwer Academic Publisher, Dordrecht, pp. 5–16.
[40] Buschmann, M. H., and Gad-el-Hak, K., 2003, "Generalized Logarithmic Law and its Consequences," AIAA J., **41**, pp. 40–48.
[41] Coles, D., 1968, "Young Person's Guide to the Data," *Proc. Comp. Turbulent Boundary Layer 1968 AFOSR- IFP-Stanford Conference*, Vol. 2, D. Coles, and E. A. Hirst, eds., pp. 1–45.
[42] Lewkowicz, A. K., 1982, "An Improved Universal Wake Function for Turbulent Boundary Layers and Some of its Consequences," Z. Flugwiss. Weltraumforsch., **6**, pp. 261–266.
[43] Finley, P. J., Khoo, C. P., and Chin, J. P., 1966, "Velocity Measurements in a Thin Turbulent Wake Layer," Houille Blanche, **21**, pp. 713–721.
[44] Granville, P. S., 1976, "A Modified Law of the Wake for Turbulent Shear Flows," J. Fluids Eng., **198**, pp. 578–580.
[45] Kameda, T., Osaka, H., and Mochizuki, S., 1998, "Mean Flow Quantities for the Turbulent Boundary Layer Over a *k*-type Rough Wall," 13th Adust. Fluid Mech. Conf., Monash University, Melbourne, pp. 357–360.
[46] Osaka, H., and Mochizuki, S., 1991, "On Turbulence Structure of the Boundary Layer on *d*-type Rough Wall," in *Experimental Heat Transfer, Fluid Mechanics and Thermodynamics*, Keffler, Shah and Ganic, eds., Elsevier Science Pub. Co., Inc., New York, pp. 412–422.
[47] Antonia, R. A., and Krogstad, P. A., 2001, "Turbulence Structure in Boundary Layer Over Different Types of Surface Roughness," Fluid Dyn. Res., **28**, pp. 139–157.
[48] Smalley, R. J., Antonia, R. A., and Djenidi, L., 2001, "Self Preservation of Rough-Wall Turbulent Boundary Layers," Eur. J. Mech. B/Fluids, **20**, pp. 591–602.
[49] Schultz, M. P., and Flack, K. A., 2003, "Turbulent Boundary Layers Over Surfaces Smoothed by Sanding," J. Fluids Eng., **125**, pp. 863–870.
[50] Schultz, M. P., and Myers, A., 2003, "Comparison of Three Roughness Function Determination Methods," Exp. Fluids, **35**(4), pp. 372–379.
[51] Schultz, M. P., and Flack, K. A., 2005, "Outer Layer Similarity in Fully Rough Wall Turbulent Boundary Layers," Exp. Fluids, **38**, pp. 328–340.
[52] Rahman, S., and Webster, D. R., 2005, "The Effects of Bed Roughness on the Scaler Fluctuations of Turbulent Boundary Layer," Exp. Fluids, **38**, pp. 372–384.
[53] Afzal, N., 2006, "Turbulent Boundary Layers on Transitional Rough Surfaces: New Approach to Universal Scaling," 36th AIAA Fluid Dynamics Conference and Exhibit, June 5–8, San Francisco, CA, Paper No. AIAA-2006-2886.
[54] Leonardi, S., Orlandi, P., Smalley, R. J., Djenidi, L., and Antonia, R. A., 2003, "Direct Numerical Simulations of Turbulent Channel Flow With Transverse Square Bars on One Wall," J. Fluid Mech., **491**, pp. 229–238.
[55] Poggi, D., Porporato, A., and Ridolfi, L., 2003, "Analysis of Small Scale Structure of Turbulence on Smooth and Rough Walls," Phys. Fluids, **15**(1), pp. 35–46.
[56] Clauser, F. H., 1956, "The Turbulent Boundary Layer," *Advances in Applied Mechanics*, Academic Press, New York, Vol. 4, pp. 2–52.
[57] Buschmann, M. H., and Gad-el-Hak, K., 2003, "The Debate Concerning the Mean Velocity Profile of a Turbulent Boundary Layer," AIAA J., **41**, pp. 565–572.
[58] Connelly, J. S., Schultz, M. P., and Flack, K. A., 2006, "Velocity-Defect Scaling for Turbulent Boundary Layers With a Range of Relative Roughness," Exp. Fluids, **40**, pp. 188–195.
[59] Afzal, N., 1983, "Analysis of a Turbulent Boundary Layer Subjected to a Strong Adverse Pressure Gradient," Int. J. Eng. Sci., **21**, pp. 563–576.
[60] Coles, D., 1956, "The Law of the Wake in the Turbulent Boundary Layer," J. Fluid Mech., **1**, pp. 191–226.
[61] Elsberry, K., Loefffler, J., Zhou, M. D., and Wygnanssi, I., 2000, "Experimental Study of a Boundary Layer That is Maintained on the Verge of Separation," J. Fluid Mech., **423**, pp. 227–281.
[62] Angele, K. P., and Klingmann, M. B., 2006, "PIV Measurements in a Weakly Separating and Reattaching Turbulent Boundary Layer," Eur. J. Mech. B/Fluids, **25**(2), 209–222.
[63] Piquet, J., 1999, *Turbulent Flow*, Springer-Verlag, Berlin.
[64] Colebrook, C. F., 1939, "Turbulent Flow in Pipes With Particular Reference to the Transition Region Between the Smooth and Rough Pipe Laws," J. Inst. Civ. Eng., **11**, pp. 133–156.
[65] Grigson, C., 1992, "Drag Losses of New Ships Caused by Hull Finish," J. Ship Res., **36**, pp. 182–196.
[66] Cebeci, T., 2004, *Analysis of Turbulent Flows*, Elsevier, New York.
[67] Shockling, M. A., Allen, J. J., and Smits, A. J., 2006, "Roughness Effects in Turbulent Pipe Flow," J. Fluid Mech., **564**, pp. 267–285.
[68] Afzal, N., and Seena, A., 2007, "Alternate Scales for Turbulent Flow in Transitional Rough Pipes: Universal Log Laws," J. Fluids Eng., **129**, pp. 80–90.
[69] Afzal, N., Bushra, A., and Seena, A., 2006, "Effects of Machined Surface Roughness on High Reynolds Number Turbulent Pipe Flow: New Approach to Scaling," *Proc. of the Eleventh Asian Congress of Fluid Mechanics (on disk)*, Institution of Engineers, Malaysia, May 22–25, pp. 542–547.
[70] Allen, J. J., Shockling, M. A., and Smits, A. J., 2005, "Evaluation of a Universal Transitional Resistance Diagram for Pipes With Honed Surfaces," Phys. Fluids, **17**, p. 121702.

Journal of Fluids Engineering

Announcement

ASME Freeman Scholar

The 19th ASME Freeman Scholar committee is soliciting proposals for a person of high capability and considerable experience in an area of fluids engineering to be selected as the Freeman Scholar. He/she will be expected to make a major review of a coherent topic in his/her specialty, prepare a comprehensive statement of the state of the field, and suggest key research needs for the future. After suitable review, the results will be presented publicly at the ASME Fluids Engineering Division conference, and published in the ASME *Journal of Fluids Engineering*.

The honorarium for preparing the review, producing a manuscript in a form for publication and presenting the results at the Congress is $7,500. There will be an additional allowance to cover the cost of travel to present the paper in 2008. The Scholar shall be available, as far as personal commitments permit, for presentation of the lecture at sites of fluids engineering activity in industry, government, or education that so request. In each case, the inviting institution will be expected to bear all expenses and, if necessary, to provide a reasonable honorarium.

Applications for the 2008 Scholarship are to be submitted by **September 1, 2007**. The application shall include:

(1) The applicant's qualifications for undertaking a major study in the field selected.
(2) A statement of the basis for believing that a summary of the state of the art on the proposed topic will make a significant and timely contribution to current or future real problems in fluids engineering practice.
(3) A description of the ideas to be considered and some of the technology to be reviewed.

The Freeman Scholar Program is supported by the ASME Freeman Fund established in 1926 by John R. Freeman, noted Hydraulic Engineer and Scholar, Honorary Member and Twenty-fourth President of ASME. Mr. Freeman suggested a flexible program for utilization of the funds. In early years, it supported fellowships for the study of hydraulic laboratory practice in Europe, later it supported publication of important hydraulic research data, and more recently it was granted to support research programs in hydraulics and fluid mechanics. The Freeman Scholar Program in fluids engineering represents a timely usage of the Fund and is consistent with the intentions of the donor.

For full details, see the Freeman Scholar Program website at
http://www.asme.org/Governance/Honors/SocietyAwards/18th_Freeman_Scholar_Program.cfm.

Timothy O'Hearn
Sandia National Laboratories
Chair, 19th Freeman Scholar

